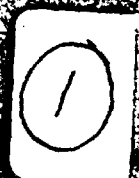


DTIC FILE COPY



17th

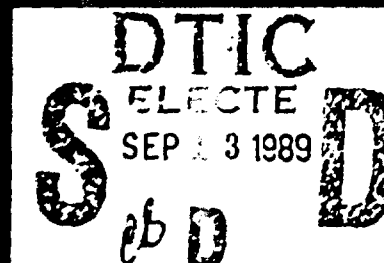
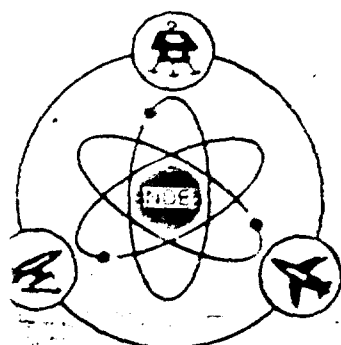
AD-A212 613

SYMPOSIUM

on

NONDESTRUCTIVE

EVALUATION



PROCEEDINGS  
April 17-20, 1989  
San Antonio, Texas

DISTRIBUTION STATEMENT A

Approved for public release  
Distribution Unlimited

Sponsored by

SOUTH TEXAS SECTION  
AMERICAN SOCIETY FOR  
NONDESTRUCTIVE TESTING, INC.,  
SOUTHWEST RESEARCH INSTITUTE,  
and  
NONDESTRUCTIVE TESTING INFORMATION  
ANALYSIS CENTER

89 9 13 09 1

**REPORT DOCUMENTATION PAGE**Form Approved  
OMB No. 0704-0188

Public reporting burden for this collection of information is estimated to average 1 hour per response, including the time for reviewing instructions, searching existing data sources, gathering and maintaining the data needed, and completing and reviewing the collection of information. Send comments regarding this burden estimate or any other aspect of this collection of information, including suggestions for reducing this burden, to Washington Headquarters Services, Directorate for Information Operations and Reports, 1215 Jefferson Davis Highway, Suite 1204, Arlington, VA 22202-4302, and to the Office of Management and Budget, Paperwork Reduction Project (0704-0188), Washington, DC 20503.

<b>1. AGENCY USE ONLY (Leave blank)</b>		<b>2. REPORT DATE</b> April 1989	<b>3. REPORT TYPE AND DATES COVERED</b> Proceedings, April 17-20, 1989	
<b>4. TITLE AND SUBTITLE</b>  Proceedings of the Seventeenth Symposium on Nondestructive Evaluation			<b>5. FUNDING NUMBERS</b>  DLA900-84-C-0910	
<b>6. AUTHOR(S)</b>  F.A. Iddings, D.W. Moore			<b>8. PERFORMING ORGANIZATION REPORT NUMBER</b>	
<b>7. PERFORMING ORGANIZATION NAME(S) AND ADDRESS(ES)</b>  Southwest Research Institute P.O. Drawer 28510 San Antonio, TX 78228				
<b>9. SPONSORING/MONITORING AGENCY NAME(S) AND ADDRESS(ES)</b>  Defense Logistics Agency DTIC-DF Cameron Station Alexandria, VA 22304			<b>10. SPONSORING/MONITORING AGENCY REPORT NUMBER</b>	
<b>11. SUPPLEMENTARY NOTES</b>				
<b>12a. DISTRIBUTION / AVAILABILITY STATEMENT</b>  Approved for public release; distribution unlimited			<b>12b. DISTRIBUTION CODE</b>	
<b>13. ABSTRACT (Maximum 200 words)</b> This Proceedings documents the 17th in a series of symposia which began in 1960. The purpose of this biennial Symposium is to bring together technical and managerial personnel engaged in, and concerned with, fundamental and applied aspects of non-destructive evaluation for the exchange of new ideas, methods, and research and development results. The 17th Symposium was attended by approximately 104 people who heard 45 technical papers presented on a variety of NDE topics. Included were sessions on Ultrasonic Techniques (2 sessions), Radiography and Related Techniques, Advanced Materials Testing, Stress Measurement/Electromagnetic Techniques, NDE of Bonding, and Special Topics in NDE. The Symposium was opened with a keynote address by Dr. Lyle Schwartz, Director, Institute for Materials Science & Engineering, National Institute of Standards and Technology and a Review of the IACs by Dr. Forrest Frank of the Institute for Defense Analyses. A Panel Presentation and Discussion on Government Programs in NDE was held one morning. The 17th Symposium was sponsored by the Nondestructive Testing Information Analysis Center in cooperation with the membership of the South Texas Section, American Society for Nondestructive Testing, Inc.				
<b>14. SUBJECT TERMS</b> Nondestructive Evaluation Radiography Ultrasonics Eddy Current Electromagnetics Composites			<b>15. NUMBER OF PAGES</b> 400	
			<b>16. PRICE CODE</b>	
<b>17. SECURITY CLASSIFICATION OF REPORT</b> Unclassified	<b>18. SECURITY CLASSIFICATION OF THIS PAGE</b> Unclassified	<b>19. SECURITY CLASSIFICATION OF ABSTRACT</b> Unclassified	<b>20. LIMITATION OF ABSTRACT</b>	

PROCEEDINGS OF THE

# **SEVENTEENTH SYMPOSIUM ON NONDESTRUCTIVE EVALUATION**

APRIL 17-20, 1989  
SAN ANTONIO, TEXAS  
F. A. IDDINGS, D. W. MOORE, PROCEEDINGS EDITORS  
C. CUDD, A. WOODS, PUBLICATIONS ASSISTANTS

SPONSORED BY  
NONDESTRUCTIVE TESTING INFORMATION ANALYSIS CENTER  
AT SOUTHWEST RESEARCH INSTITUTE  
and  
SOUTH TEXAS SECTION, AMERICAN SOCIETY FOR  
NONDESTRUCTIVE TESTING, INC.

NOTICE

Responsibility for the submittal and contents of the papers published herein rests upon the individual authors and not on the Nondestructive Testing Information Analysis Center; South Texas Section, American Society for Nondestructive Testing, Inc.; or Southwest Research Institute. Likewise, the legibility, size, layout, or typographic quality of the papers contained herein was predetermined by the quality of the cameraready copy as submitted by the authors for reproduction. All copy of text, photographs, and tables has been reproduced exactly as submitted.

Additional copies may be obtained from:

NTIAC

Southwest Research Institute  
P.O. Drawer 28510  
San Antonio, Texas 78228-0510

Accession For	
NTIS CRA&I	<input checked="checked" type="checkbox"/>
DTIC TAB	<input type="checkbox"/>
Unannounced	<input type="checkbox"/>
Justification	
By <i>80.00 per ltr</i>	
Distribution	
Availability Codes	
Dist	Avail or Special
<i>A-1</i>	<i>21</i>





## PREFACE TO THE 17TH SYMPOSIUM ON NDE

This Proceedings documents the 17th in a series of symposia which began in 1960. The Symposium was conducted on an annual basis through 1963 and since then on a biennial basis. Proceedings have been published for each of the symposia in the series.

The purpose of the 17th Symposium on NDE was to bring together technical and managerial personnel engaged in, and concerned with, fundamental and applied aspects of nondestructive evaluation. The 17th Symposium, attended by a little over 100 people, facilitated the exchange of new ideas, methods, and research and development results. Technical sessions included such topics as Ultrasonics (2 sessions), Radiography and Related Techniques, Advanced Materials Testing, Stress Measurement/Electromagnetic Techniques, NDE of Bonding, and Special Topics in NDE. Also included in the program were keynote addresses by Dr. Lyle H. Schwartz of the National Institute of Standards and Technology and Dr. Forrest R. Frank of the Institute for Defense Analyses. Panel presentations and discussions on Government Programs in NDE were moderated by Dr. A. L. Broz of the Army Materials Technology Laboratory and there was a luncheon presentation on the development of NDE given by John E. Rusing.

The success of the Symposium was due largely to the excellent and diverse contributions by NDE specialists from industry, government, and research sectors, who demonstrated high levels of expertise in the various fields represented. Appreciation is expressed to those organizations and individual participants who have assisted with the successful planning, operation, and conduct of the Symposium. The 17th Symposium was sponsored by the Nondestructive Testing Information Analysis Center in cooperation with the membership of the South Texas Section, American Society for Nondestructive Testing, Inc.

Information regarding additional copies of this Proceedings and information on the 18th Symposium on Nondestructive Evaluation planned for April 1991 may be obtained from:

Dr. F. A. Iddings  
Administrative Director, NTIAC  
Southwest Research Institute  
P.O. Drawer 28510  
San Antonio, Texas 78228-0510  
(512) 522-2737

# CONTRIBUTING AUTHORS

	Page		Page
Ahmed, T. Wayne State University Detroit, Michigan 48202	238	Cline, J. L. Boeing Aerospace and Electronics Seattle, Washington 98124	104
Amin, Kamal E. Norton Company Northboro, Massachusetts 01532	47	Cotter, Daniel J. GTE Laboratories Incorporated Waltham, Massachusetts 02254	94
Annis, M. American Science and Engineering, Inc. Cambridge, Massachusetts 02139	78	Dayal, V. Iowa State University Ames, Iowa 50011	117
Antal, J. J. Army Materials Technology Laboratory Watertown, Massachusetts 02172-0001	62	DeSilets, C. S. Precision Acoustic Devices, Inc. Fremont, California 94539	138
Balasubramaniam, K. Drexel University Philadelphia, Pennsylvania 19104	276	Diercks, K. Jerome Texas Research Institute, Austin Austin, Texas 78733	144
Baukus, W. American Science and Engineering, Inc. Cambridge, Massachusetts 02139	78	Duffer, Charles Texas A&M University College Station, Texas 77843	132
Beissner, R. E. Southwest Research Institute San Antonio, Texas 78228	232	Dunn, Edmund M. GTE Laboratories Incorporated Waltham, Massachusetts 02254	94
Birring, Anmol S. Southwest Research Institute San Antonio, Texas 78228	38	Eberhard, J. W. General Electric Company Schenectady, New York 12301	85
Bjorkholm, P. American Science and Engineering, Inc. Cambridge, Massachusetts 02139	78	Favro, L. D. Wayne State University Detroit, Michigan 48202	238
Bossi, R. H. Boeing Aerospace and Electronics Seattle, Washington 98124	104	Feuer, H. O., Jr. U. S. Army Belvoir Ft. Belvoir, Virginia 22060-5606	173
Bray, Alan V. Texas Research Institute Austin, Inc. Austin, Texas 78733-6201	282	Fraser, J. D. Precision Acoustic Devices, Inc. Fremont, California 94539	138
Bray, Don E. Texas A&M University College Station, Texas 77843	35,197	Friddell, K. D. Boeing Aerospace and Electronics Seattle, Washington 98124	104
Burger, Christian P. Texas A&M University College Station, Texas 77843	132	Golas, Katharine Southwest Research Institute San Antonio, Texas 78228	187
Carignan, Donald A. Instrument Technology, Inc. Westfield, Massachusetts	190	Golis, Matthew J. Advanced Quality Concepts, Inc. Columbus, Ohio	69,197,323
Cervantes, R. A. Southwest Research Institute San Antonio, Texas 78228	1	Hale, Leonard A. Texas Research Institute, Austin Austin, Texas 78733	144
Chou, C. H. Stanford University Stanford, California 94304	138	Harmouche, Mahmoud Texas A&M University College Station, Texas 77843	333

	Page		Page
Hartman, J. K. Morton Thiokol, Inc. Brigham City, Utah 84302-0524	243	Lam, Clive C. Baker Hughes Tubular Services Houston, Texas	224
Hill, R. H., Jr. Southwest Research Institute San Antonio, Texas 78228	173	Lamping, Gerald Southwest Research Institute San Antonio, Texas 78228	329
Hsiao, M. L. General Electric Company Schenectady, New York 12301	85	Larsen, Ronald E. Reinhart & Associates, Inc. Austin, Texas	69,323
Jiao, D. Drexel University Philadelphia, Pennsylvania 19104	276	Light, Glenn M. Southwest Research Institute San Antonio, Texas 78228	251
Jiles, D. C. Iowa State University Ames, Iowa 50011	212,313	Lindenschmidt, K.-E. Ontario Hydro Research Toronto, Ontario, Canada, M8Z 5S4	18
Jin, H. J. Wayne State University Detroit, Michigan 48202	238	Maglic, R. Honeywell Solid State Electronics Division Colorado Springs, Colorado 80906	297
Joshi, Narayan R. Lamar University Beaumont, Texas	268	Marotta, A. S. Army Materials Technology Laboratory Watertown, MA 02172-0001	62
Kamer P. W. Morton Thiokol, Inc. Brigham City, Utah 84302-0524	243	Matzkanin, George A. Texas Research Institute, Austin Austin, Texas 78733	144
Kenyon, D. Honeywell Solid State Electronics Division Colorado Springs, Colorado 80906	296	Moles, M. D. C. Ontario Hydro Research Toronto, Ontario, Canada, M8Z 5S4	18
Kessler, L. W. Sonoscan, Inc. Bensenville, Illinois	167	Mueller, Ted A. Southwest Research Institute San Antonio, Texas 78228	1
Khuri-Yakub, B. T. Stanford University Stanford, California 94304	138	Ngoc, T. D. K. Drexel University Philadelphia, Pennsylvania 19104	276
Kinra, V. K. Texas A&M University College Station, Texas 77843	117	Nottingham, L. D. Electric Power Research Institute Charlotte, North Carolina	329
Koenigsberg, William D. GTE Laboratories Incorporated Waltham, Massachusetts 02254	94	O'Brien, C. Honeywell Solid State Electronics Division Colorado Springs, Colorado 80906	296
Kuo, P. K. Wayne State University Detroit, Michigan 48202	238	Patten, Donald O. Norton Company Northboro, Massachusetts 01532	47
Kwon, Oh-Hun Norton Company Northboro, Massachusetts 01532	47	Reinhart, Eugene R. Reinhart & Associates, Inc. Austin, Texas	197
Kwun, Hegeon Southwest Research Institute San Antonio, Texas 78228	251	Rollwitz, W. L. Southwest Research Institute San Antonio, Texas 78228	212

	Page		Page
Rose, J. L. Drexel University Philadelphia, Pennsylvania 19104	276	Teller, Cecil M. Texas Research Institute Austin, Inc. Austin, Texas 78733-6201	282
Ruescher, Edward H. Southwest Research Institute San Antonio, Texas 78228	31	Thomas, R. E. Santec Systems, Inc. Wheeling, Illinois 60090	111
Sablik, M.J. Southwest Research Institute San Antonio, Texas 78228	212	Thomas, R. L. Wayne State University Detroit, Michigan 48202	238
Salamanca, Teodoro Leon Reinhart & Associates, Inc. Austin, Texas	197	Thumm, E. Honeywell Solid State Electronics Division Colorado Springs, Colorado 80906	296
Salaymeh, S. R. E.I. DuPont DeNemours & Co. Aiken, South Carolina 29808	62	Tweddell, W. R. Karta Technology, Inc. San Antonio, Texas	306
Sandhu, J. S. Santec Systems, Inc. Wheeling, Illinois 60090	111	Utrata, D. Association of American Railroads Chicago, Illinois 60616	313
Sandor, Bela I. University of Wisconsin-Madison Madison, Wisconsin 53706	155	Varallo, T. P. E.I. DuPont DeNemours & Co. Aiken, South Carolina 29808	62
Schafer, D. American Science and Engineering, Inc. Cambridge, Massachusetts 02139	78	Watson, Paul D. Southwest Research Institute San Antonio, Texas 78228	1
Sinclair, A. N. University of Toronto Toronto, Ontario, Canada, M5S 1A4	18	Wey, A. C. Sonoscan, Inc. Bensenville, Illinois	167
Singh, G. P. Karta Technology, Inc. San Antonio, Texas 78228	38,305	Wolfenden, Alan Texas A&M University College Station, Texas 77843	333
Smith, R. Lowell Texas Research Institute Austin, Inc. Austin, Texas 78733-6201	282	Zhang, Daqing University of Wisconsin-Madison Madison, Wisconsin 53706	155
Tam, K. C. General Electric Company Schenectady, New York 12301	85		

### Keynote Address Authors

Dr. Edwin S. Townsley  
Dr. Forrest R. Frank  
Ms. Linda H. Berkhouse  
Science and Technology Division  
Institute for Defense Analyses  
Alexandria, Virginia 22311

xiv

## SYMPOSIUM COMMITTEE

<i>Chairman</i>	F. A. Iddings
<i>Arrangements</i>	B. S. Moreno W. L. Iddings M. F. Ahr
<i>Publications</i>	D. W. Moore C. Cudd A. Woods
<i>Registration and Records</i>	M. F. Ahr B. R. Barnes
<i>Papers Review</i>	F. A. Iddings SwRI Staff

## TABLE OF CONTENTS

<b>Ultrasonic Techniques I</b>		<b>Advancements in and Applications of Backscatter Tomography (ZT)</b>	<b>78</b>
Feasibility of Adaptive Control of an Automatic Welding System by Real-Time Ultrasonic Examinations	1	D. Schafer M. Annis P. Bjorkholm W. Baukus American Science and Engineering, Inc.	
Paul D. Watson Ted A. Mueller R. A. Cervantes Southwest Research Institute			
Sizing Cracks in Thin-Walled CANDU Reactor Pressure Tubes Using Crack-Tip Diffraction	18	Experimental Validation of Incomplete Data CT Image Reconstruction Techniques	85
K.-E. Lindenschmidt M. D. C. Moles Ontario Hydro Research A. N. Sinclair University of Toronto		J. W. Eberhard M. L. Hsiao K. C. Tam General Electric Company	
Field Applications of the Cylindrically Guided Wave Technique on Valve Stems	31	Microfocus Radiography for Nondestructive Evaluation of Ceramics: Principles and Applications	94
Edward H. Ruescher Southwest Research Institute		William D. Koenigsberg Daniel J. Cotter Edmund M. Dunn GTE Laboratories Incorporated	
Applications of the M <sub>21</sub> Ultrasonic Technique to Inspecting Layered Materials	35	X-Ray Backscatter Imaging with a Spiral Scanner	104
Don E. Bray Texas A&M University		R. H. Bossi J. L. Cline K. D. Friddell Boeing Aerospace and Electronics	
Ultrasonic Characterization of Flaws in Ceramics	38	<b>Ultrasonic Techniques II</b>	
G. P. Singh Karta Technology, Inc. Anmol S. Birring Southwest Research Institute		Acoustography: Ultrasonic Imaging Using a Sound-Sensitive Plate/Screen	111
<b>Radiography and Related Techniques</b>		J. S. Sandhu R. E. Thomas Santec Systems, Inc.	
Probability of Detection of Volume Defects in Both Green, Sintered and HIP'ed Zirconia Ceramics by X-Ray Microfocus Radiography	47	Ultrasonic NDE of Thin (Sub-Wavelength) Specimens	117
Kamal E. Amin Oh-Hun Kwon Donald O. Patten Norton Company		V. K. Kinra Texas A&M University V. Dayal Iowa State University	
The Application of Neutron Radioscopy to Lithium-Aluminum Alloy Target Elements	62	Non-Contact Ultrasonic Inspection with Fiber Guided Laser Light	132
J. J. Antal A. S. Marotta Army Materials Technology Laboratory S. R. Salaymeh T. P. Varallo E.I. DuPont De Nemours & Co.		Christian P. Burger Charles Duffer Texas A&M University	
Using X-Radiometry to Count Resin-Bonded Layers in Aramid Ballistic Cloth Composites	69	Application of Ultrasonic Resonance Technique at 300 MHz to the Detection of Disbonds in a Multilayer Structure	138
Ronald E. Larsen, Ph.D. Reinhart & Associates, Inc. Matthew J. Golis, Ph.D. Advanced Quality Concepts, Inc.		J. D. Fraser C. S. DeSilets Precision Acoustic Devices, Inc. C. H. Chou B. T. Khuri Yakub Stanford University	

Detection and Discrimination of Bond Surface Variations in Rubber/Metal Laminates Using Obliquely Incident Ultrasonic Waves K. Jerome Diercks Leonard A. Hale George A. Matzkanin Texas Research Institute, Austin	144	Electromagnetic Wellhead Tubular Inspection Clive C. Lam Baker Hughes Tubular Services	224
<b>Advanced Materials Testing</b>		Theory of Non-Axisymmetric Eddy Currents in Cylindrical Conductors R. E. Beissner Southwest Research Institute	232
Thermographic Analysis of Stress Concentrations in a Damaged Cross-Ply Laminate Daqing Zhang Bela I. Sandor University of Wisconsin-Madison	155	<b>NDE of Bonding</b>	
Nondestructive Detection of Flaws in Ceramics Using Holographic Scanning Laser Acoustic Microscope (Holoslam) A. C. Wey L. W. Kessler Sonoscan, Inc.	167	Infrared Thermal Wave Imaging of Adhesion Defects P. K. Kuo T. Ahmed L. D. Favro H. J. Jin R. L. Thomas Wayne State University	238
Laser-Induced-Fluorescence Inspection of Polyurethane R. H. Hill, Jr. Southwest Research Institute H. O. Feuer, Jr. U. S. Army Belvoir	173	Effect of Surface Roughness on the Ultrasonic Inspection of Space Shuttle Boosters J. K. Hartman P. W. Kerner Morton Thiokol, Inc.	243
Interactive Videodisc Simulation for Engine Inspection Procedures Using a Flexible Borescope Katharine Golas Southwest Research Institute	187	Review of NDE Methodology of Adhesive Bond Quality Determination Glenn M. Light Hegeon Kwun Southwest Research Institute	251
Remote Viewing Donald A. Carignan Instrument Technology, Inc.	190	Chirp Z-Transform in Ultrasonic Interference Spectroscopy for Adhesive Bonds Narayan R. Joshi Lamar University	268
<b>Stress Measurement/Electromagnetic Techniques</b>		Feature Mapping Methodology for Ultrasonic Inspection of Adhesive Bonds J. L. Rose T. D. K. Ngoc D. Jiao K. Balasubramaniam Drexel University	276
Field and Laboratory Applications of an Ultrasonic Method for Measurement of Stress Gradients in Structures Teodoro Leon Salamanca Eugene R. Reinhart Reinhart & Associates, Inc. Donald E. Bray Texas A&M University Matthew J. Golis Advanced Quality Concepts	197	Development of a Resonant Probe for Evaluating the Integrity of Ru <sup>1</sup> Her-to-Metal Bonded Joints R. Lowell Smith Alan V. Bray Cecil M. Teller Texas Research Institute Austin, Inc.	282
A Model for Magabsorption as an NDE Tool for Stress Measurement M. J. Sablik W. L. Rollwitz Southwest Research Institute D. C. Jiles Iowa State University	212	<b>Special Topics in NDE</b>	
		Non-Destructive Tests of Moisture-Induced Current Leakage on IC Packages D. Kenyon E. Thumm C. O'Brien R. Maglic Honeywell Solid State Electronics Division	296

Computer-Based Instruction to Train NDE Technicians 305  
G. P. Singh  
W. R. Tweddell  
Karta Technology, Inc.

Fatigue Induced Changes in the Magnetic Properties 313  
of Ferritic Steels  
D. C. Jiles  
Iowa State University  
D. Utrata  
Association of American Railroads

Programmable Ultrasonic Reflectance of Artificial 323  
Flaws in Materials  
Ronald E. Larsen  
Reinhart & Associates, Inc.  
Matthew J. Golis  
Advanced Quality Concepts, Inc.

**These papers do not appear in program order:**

Nondestructive Examination of Steam Turbine Rotors 329  
by Automated Systems  
Gerald A. Lamping  
Southwest Research Institute  
L. D. Nottingham  
Electric Power Research Institute

An Improved Averaging Method to Predict the 333  
Technical Constants from the Elastic Constants  
Mahmoud Harmouche  
Alan Wolfenden  
Texas A&M University

**Keynote Address**

Evaluation of DOD Information Analysis Center Program: xiv  
Pilot IAC Study  
Dr. Edwin S. Townsley  
Dr. Forrest R. Frank  
Ms. Linda H. Berkhouse  
Science and Technology Division  
Institute for Defense Analyses



## **PREFACE TO KEYNOTE ADDRESS**

This section of the 17th Symposium Proceedings contains the Keynote Address made by Dr. Forrest R. Frank. Other special presentations were not available for inclusion in the Proceedings.

**EVALUATION OF DOD  
INFORMATION ANALYSIS CENTER PROGRAM:  
PILOT IAC STUDY**

*Dr. Edwin S. Townsley  
Dr. Forrest R. Frank  
Ms. Linda H. Berkhouse*

Science and Technology Division  
Institute for Defense Analyses  
1801 N. Beauregard Street  
Alexandria, VA 22311

**Presentation to the 17th Symposium on Nondestructive  
Evaluation**

**by Dr. Forrest R. Frank\*  
18 April 1989**

---

\* The views expressed are those of the presenter and do not necessarily reflect the views of the Department of Defense or the Institute for Defense Analyses.

## **EVALUATION OF DOD INFORMATION ANALYSIS CENTERS: PILOT IAC STUDY**

### **INTRODUCTION**

When Dr. Iddings and I discussed the possibility of a presentation by a representative of the Institute for Defense Analyses to the 17th Symposium on Nondestructive Testing, I was hard pressed to understand why practitioners of the science would be interested in hearing from a Political Scientist about an assessment of the effectiveness or benefits of the DoD Information Analysis Centers Program. It was difficult for me to imagine the circumstances under which the audience would attach much credibility to a speaker who hears about techniques to measure stress using nuclear magnetic resonance and assumes that a patient is about to be x-rayed. However, I concluded that it might be worthwhile to present some of the results of a two year effort to evaluate DoD Information Analysis Centers. As you know the Nondestructive Testing Information Analysis Center (NTIAC) is but one of twenty one such Centers. I hope at the conclusion of this presentation that you will better understand the implications of current public policy debates on the continued existence of and your access to all of the DoD Information Analysis Centers.

As I hope will become clearer at the conclusion of this presentation, the users of NTIAC are the beneficiaries of a public policy that declares Department of Defense will provide to its components and its contractors access to synthesized information in selected disciplines or mission areas in an effort to enhance its research, development, test, and engineering program. NTIAC is one of 21 DoD Information Analysis Centers, and it, like many of these centers, is now at some risk. During the balance of my presentation, I shall explain why I believe your resource is at risk, outline some of the benefits to DoD we have seen provided by NTIAC, and suggest measures you and your organizations might wish to consider taking in order to secure the future for your own research resource.

This presentation is based on a paper *Evaluation of DoD Information Analysis Centers: Pilot Study*<sup>1</sup> prepared by Dr. Edwin S. Townsley and myself. The paper summarizes in considerable detail work performed by the Institute for Defense Analyses under a task order to the Office of the Deputy Director for Defense Research and Engineering for Research and Advanced Technology. The paper should be available in the next few months.

## **INFORMATION ANALYSIS CENTERS DEFINED**

Figure 1 provides a brief overview to the background and definitions of an Information Analysis Center:

---

### **EVALUATION OF DOD INFORMATION ANALYSIS CENTERS**

#### **INFORMATION ANALYSIS CENTERS**

- **ESTABLISHED BY DOD DIRECTIVE 3200.12-R-2 "CENTERS FOR ANALYSIS OF INFORMATION"**
  
  - **SCIENTIFIC AND TECHNICAL INFORMATION IS**
    - **ACQUIRED**
    - **STORED**
    - **EVALUATED**
    - **SYNTHESIZED**
    - **PUBLISHED**
- BY DOD IACS IN A DISCIPLINE OR MISSION AREA**
- 

**Figure 1: Information Analysis Centers Background**

Information Analysis Centers are similar to special libraries in many respects. They perform many functions that are often associated with libraries, but also perform functions which go far beyond those usually associated with library activities. These comparisons are presented below in Figure 2.

---

<sup>1</sup> (Alexandria, VA: Institute for Defense Analyses, 1988).

---

**EVALUATION OF DOD INFORMATION ANALYSIS CENTERS**  
**COMPARISONS OF IAC AND LIBRARY FUNCTIONS**

		IACS	LIBRARIES
<b>ACQUISITIONS</b>	BOOKS	X	X
	JOURNALS	X	X
	PAPERS	X	X
	<i>DATA SETS</i>	X	
	<i>RESEARCH NOTES/DATA</i>	X	
	<i>RAW DATA</i>	X	
<b>CATALOG</b>	CATEGORIZE INFORMATION	X	X
	INDEX	X	X
<b>STORE</b>	ARCHIVE	X	X
	<del>STORE FOR CIRCULATION</del>		X
	STORE FOR SELF USE	X	X
<b>DIGEST/ANALYZE</b>	ABSTRACT	X	X
	<i>ASSESS SIGNIFICANCE</i>	X	
	<i>ASSESS METHODOLOGY</i>	X	
	<i>TECHNOLOGY ASSESSMENTS</i>	X	
	<i>STANDARDIZED METHODOLOGY</i>	X	
	<i>STANDARDIZED DATA SETS</i>	X	
<b>SYNTHESIZE</b>	ANNOTATED BIBLIOGRAPHIES	X	X
	<i>ANNOTATED DATA SETS</i>	X	
	<i>MODELS</i>	X	
<b>PUBLICATION/ CURRENT AWARENESS</b>	ACQUISITION LISTS	X	X
	NEWSLETTERS	X	X
	<i>STUDIES/ANALYSES</i>	X	
	<i>STATE-OF-THE-ART REPORTS</i>	X	
	<i>CRITICAL REVIEWS</i>	X	
	<i>HANDBOOKS</i>	X	
<b>ADVISORY SERVICES</b>	REFERENCE INQUIRIES	X	X
	<i>REFERRALS TO EXPERTS</i>	X	
	<i>TECHNICAL INQUIRIES</i>	X	
	<i>RESEARCH METHODOLOGY</i>	X	
	<i>INSTRUMENTATION/DATA</i>		
	<i>COLLECTION ADVICE</i>	X	
<b>OTHER USER SERVICES</b>			
	<i>CONFERENCE SUPPORT</i>	X	
	<i>CONFERENCE PROCEEDINGS</i>	X	
	<i>SPECIAL STUDIES AND TECHNICAL REPORTS</i>	X	

---

Figure 2: Comparisons of Information Analysis Centers and Libraries

Within the Department of Defense context, Information Analysis Centers are established by DoD Regulation 3200.12-R-2. They are responsible for the performance of several functions which support research, development, engineering, test, evaluation, operations, maintenance, and even technology transfer. Information in all forms is acquired, stored, evaluated, synthesized, and published. Among the most significant differences between IACs and libraries is the collection of raw data extracted from laboratory experiments, field exercises, conferences, and even simulations.

The DoD IAC program, both by directive and as a practical matter, sorts itself into two types of IACs. These are described and examples given in Figure 3.

---

## **EVALUATION OF DOD INFORMATION ANALYSIS CENTERS**

### **TYPES OF DOD INFORMATION ANALYSIS CENTERS**

- **DISCIPLINE-ORIENTED IACS**
  - NON-DESTRUCTIVE TESTING
  - RELIABILITY
  - SOFTWARE
  - INFRA-RED MATERIALS AND TECHNOLOGY
  - METAL MATRIX CERAMICS
- **MISSION-ORIENTED IACS**
  - TACTICAL WEAPON GUIDANCE
  - CHEMICAL/BIOLOGICAL WARFARE
  - NUCLEAR WEAPONS
  - AIRCRAFT SURVIVABILITY
  - CREW SYSTEMS ERGONOMICS

---

**Figure 3: IAC Types and Examples of Subject Matter Coverage**

As is evident from Figure 3, some IACs organize their work along disciplinary lines consistent with the focus of DoD R,D,T, &E interests. Others organize their efforts along mission or functional lines.

The Nondestructive Testing Information Analysis Center is a good example of discipline-oriented IAC. Other examples of discipline-oriented IACs include the Reliability Analysis Center (RAC), which focuses on the reliability of electronic components as well as other aspects of reliability of interest to DoD; the Data Analysis Center for Software (DACS), which examines computer software reliability problems; the Infrared Information Agency (IRIA), which collects and analyzes information on infrared topics; and the Metal Matrix Ceramics Information Analysis Center (MMCIAC), which deals with information on these classes of materials.

Examples of Information Analysis Centers which are organized to collect and analyze information related to DoD mission areas include the following:

- The Tactical Weapons Guidance and Control Information Analysis Center (GACIAC), which collects and analyzes information on precision guided munitions, sensor technology, testing, design, and countermeasures;
- The Chemical Warfare/Biological Defense Information Analysis Center (CBIAC), which collects and analyzes information regarding chemical and biological warfare matters
- The DoD Nuclear Information Analysis Center (DASIAC), which collects, analyzes, and archives information regarding nuclear weapon effects including films and other records of atmospheric and underwater testing of nuclear weapons no longer permitted by the 1962 Partial Test Ban Treaty
- The Survivability/Vulnerability Information Analysis Center (SURVIAC), which collects and analyzes information as well as models and simulations regarding aircraft and vehicle survivability/vulnerability to munitions
- Crew Systems Ergonomics Information Analysis Center (CSERIAC) which will soon be collecting and analyzing information regarding the man/machine interface in vehicles

Each attendee at the Symposium has been provided a directory of DoD Information Analysis Centers which is an extract from a Defense Logistics Agency/Defense Technical Information Center report describing the individual areas of interest and expertise of DoD IACs. Figure 4 is a reproduction of the cover page of that report.

---

**EVALUATION OF DOD INFORMATION ANALYSIS CENTERS**

**DTIC/TR-87/17**

**AD-A184 002**  
**July, 1987**

**INFORMATION ANALYSIS CENTERS**  
**IN THE**  
**DEPARTMENT OF DEFENSE**



**IAC Program Office**

**Approved for public release; distribution unlimited**

**DEFENSE TECHNICAL INFORMATION CENTER**  
**Defense Logistics Agency**  
**Cameron Station**  
**Alexandria, VA 22304-6145**

---

**Figure 4: DoD Information Analysis Centers Report Cover**



One of the things we have learned thus far in our study of the DoD Information Analysis Centers Program is that many users of an IAC are aware of only the IAC that use. Most NTIAC users, for example, were not aware that an additional 20 DoD Information Analysis Centers exist and can be used to assist them in the course of their work. This is perplexing as frequently the subject matter of concern to an IAC user can be addressed by more than one IAC, depending upon the specific problem to be solved.

For example, although the focus of the Symposium is on Nondestructive Testing, it turns out that at least three IACs have knowledge and expertise that might be of interest to an engineer interested in using nondestructive evaluation techniques as an integral part of an industrial process control -- NTIAC, the Manufacturing Technology Information Analysis Center housed at the Illinois Institute of Technology Research, Inc., and the Reliability Analysis Center located near Griffiss Air Force Base.

Nearly all of the 21 DoD Information Analysis Centers operate in approximately the same manner. The NTIAC User's Manual is to first order a useful guide to the day-to-day operations of any DoD Information Analysis Center. It describes a core program oriented towards meeting the needs of users which can be addressed in a brief telephone conversation or short letter. It describes access to the IAC for government agencies which are in need of technical analysis services requiring a larger scale of effort. While there are significant differences among IACs, the NTIAC User's Manual is helpful in describing what IACs generally do.. Figure 5 is a more generic description of IAC programs and summarizes the operations of most DoD Information Analysis Centers.

The DoD IACs typically operate two different activities simultaneously. A basic or "core" program is undertaken to collect, catalog, analyze, synthesize, store, and disseminate information to the user community which is the focus of a particular IAC. Information is disseminated in the form of handbooks, critical reviews, state-of-the-art reports, newsletters, and other current awareness items. Bibliographies and responses to technical inquiries are also provided out of the core program. The costs of the core program are typically born by funds provided under a government contract from the Defense Logistics Agency.

---

## **EVALUATION OF DOD INFORMATION ANALYSIS CENTERS**

### **IAC OPERATIONS**

#### **IACS UNDERTAKE TWO CATEGORIES OF ACTIVITIES**

- **CORE PROGRAM PROGRAM**
  - HANDBOOKS
  - CRITICAL REVIEWS
  - STATE-OF-THE-ART REPORTS
  - NEWSLETTERS
  - BIBLIOGRAPHIES
  - TECHNICAL INQUIRIES
  - REFERRALS TO EXPERTS
- **SPECIAL STUDIES**
  - SPECIFIC TECHNICAL REPORTS
  - TECHNICAL ANALYSIS SERVICES
  - EXTENDED TECHNICAL INQUIRIES

---

**Figure 5: IAC Operations**

IACs also operate a "special task" program. Special tasks are studies or analyses undertaken upon the request of DoD components or other U.S. Government agencies. These typically require the the transfer of funds from the requiring activity to the contracting activity (the Defense Electronics Supply Center in the case of NTIAC) through the use of the Military Interdepartmental Purchase Requisition (MIPR) for DoD components, or analogous purchasing instrument for other Government agencies. Ordering an IAC special task does not require further competition and source selection. This can be of very great importance when the sequence of asking questions and obtaining answers must be sustained as part of a large, expensive, RDT&E effort.

The IAC program as a whole is not well understood. Its contributions to the DoD RDT&E program have not been well documented or defended. Indeed, our study was initiated because the then Deputy Under Secretary of Defense for Research and Advanced Technology was asked to sponsor a new IAC and instead asked the question, "what benefits are IACs providing to my R&D program?" This question was precipitated in large measure by a FY 1986 IAC Program budget reduction in within DoD, coupled with a large reduction in DoD R&D spending mandated by the Gramm-Rudman-Hollings budget balancing law. Figure 6 illustrates the impact of budget considerations on the size of the core IAC program administered by DLA since 1980.

---

## EVALUATION OF DOD INFORMATION ANALYSIS CENTERS

### DOD INFORMATION ANALYSIS CENTERS PROGRAM Recent Budget History\*

(in millions of current dollars)

Fiscal Year	Number of IACs Funded	Planned Program	Requested DoD Program	Appropriation (As Adjusted)	Actual Outlay
1980	8	\$4.0	\$4.0	\$3.64	\$3.64
1981	9	3.9	3.9	3.64	2.982
1982	8	3.992	3.992	3.613	3.2
1983	9	5.3	5.3	4.0	4.0
1984	10	7.0	7.00	4.934	4.5
1985	11	5.75	5.75	5.75	5.75
1986	11	6.550	6.550	6.550	4.075
1987	12	7.926	7.0	5.0	4.579
1988	13	8.6**	5.2	5.175	4.883
1989	13	7.398	5.2	5.2	5.2***
1990	13	7.776****	6.2****		

\* DTIC budget planning records for FY 1988 - 1991 dated 15 November 1988

\*\* includes start up funds for an IAC procurement which was cancelled due to lack of appropriated funds.

\*\*\* estimated outlay at conclusion of current fiscal year

\*\*\*\* estimate based on 5 percent growth over previous fiscal year.

---

**Figure 6: DoD IAC Program Budget History, FY 1980 - FY 1990**

It became apparent from this figure that the program is no longer enjoying the sustained support of the Defense Department and the Congress that it previously had. There are several reasons which may help explain why this is so; it is important to realize that the number of IACs which must be funded out of an ever shrinking pot of available money is growing, even though the pot is shrinking both in terms of current dollars, and especially in terms of constant dollars.

Every year the IAC Program Office in the Defense Technical Information Center at DLA puts together what it thinks the requirements for dollars in the IAC Program are going to be. This amount, represented in the column labeled "Planned Program" is typically calculated by adding the dollars set forth in the core program funding paragraphs of the

existing IAC contracts, the amount of funds required to support proposed new IACs, and an amount needed to support COTRs and special IAC program-wide management and marketing initiatives. The IAC Program Office forwards this proposed budget to the DLA Comptroller for review.

The DLA Comptroller works with two different sets of numbers. First, the Comptroller's budget shop looks at the total DLA R&D budget in the context of total DLA budget authority. Since R&D is a very low priority in the overall DLA program, it is one of the first lines to be scrutinized for reductions whenever the DLA Comptroller feels obligated to reduce requests for budget authority to the Congress. Second, the DLA Comptroller looks at the total dollars in the IAC program for which DLA is responsible. If his financial management system reports that the IAC Program has not used all available financial resources, his reaction to requests for increases is likely to be hostile at best. After all, if the financial management system reports that the IAC Program did not use all funds placed at its disposal in the previous year, why should funds for this program be increased?

In the current budget climate, the result of the pressures to hold the line on funding and the financial reporting system that understates the magnitude of the IAC Program's expenditures results in a DLA Comptroller decision to seek a level of funding that is less than the amount identified by the IAC Program as necessary to sustain the core program in aggregate at the level agreed by the original IAC Proponent and OSD at the time an IAC was established and an IAC contract was written.

The budget crisis encountered in FY 1986 triggered a series of questions for Dr. Kerber, the Under Secretary of Defense for Research and Advanced Technology, regarding the benefits of the DoD IAC Program for his broad responsibilities. These questions in turn led to the IDA study, *Evaluation of the DoD Information Analysis Centers Program*.

## THE IDA STUDY

The IDA study seeks to fulfill the objectives and provide to the Department of Defense the results displayed below in Figure 7. The underlying purpose of the study when we began was to help R&AT form a basis for performing a "triage" among IACs, assuming that the budget authority available could not be increased. IDA was asked in essence to answer the following question:

If there is only \$4 million available to fund IACs, which IACs should be eliminated so that the survivors can do a better job?

In order to help R&AT make these difficult decisions, we had to develop criteria that would help separate IACs into "good", "better", and "best" categories. I might add that we do not believe we have such criteria based on the pilot study; I am not sure we have such criteria based on a more recent review of several additional IACs. We also had to deal effectively with the desire of DoD to quantify everything an IAC does.

As a result of lengthy negotiations over the wording of the task order, we were finally able to arrive at an objective which takes into account the very real problem of attaching numbers as distinct from value to all products and services provided to DoD by 21 very different IACs. Hence, in the objective of our study, one finds the phrase, "qualitative and quantitative assessment methods *where feasible*".

---

## EVALUATION OF DOD INFORMATION ANALYSIS CENTERS

### STUDY OBJECTIVE

**DEVELOP AND APPLY QUALITATIVE AND QUANTITATIVE ASSESSMENT METHODS WHERE FEASIBLE...AND EVALUATE THE EFFECTIVENESS OF INFORMATION ANALYSIS CENTERS IN SUPPORTING DEFENSE-RELATED RESEARCH**

- **STUDY IS TO BE PERFORMED IN FOUR SUBTASKS:**
  - **WORK PLAN**
  - **PILOT STUDY**
  - **REPRESENTATIVE SAMPLE**
  - **EVALUATION OF 12 DLA/DTIC FUNDED IACS**
  
- **EACH STUDY PHASE HAS THREE PARTS**
  - **PROGRAM, POLICY AND TECHNICAL MONITOR'S POINT-OF-VIEW**
  - **THE IAC POINT-OF-VIEW**
  - **THE USER POINT-OF-VIEW**

---

**Figure 7: IDA Study Goals and Perspectives**

In each phase of the study, we have sought to understand the expectations of IAC products and services from the perspective of the DoD technical program manager, the IAC's management, and the IAC's users. It is appropriate to note our heartfelt thanks to the many NTIAC users who so generously gave of their time to answer our questions about the products and services provided to them by NTIAC. The results of our pilot study

were, as I hope you will agree, most interesting. Without the assistance of NTIAC's users, I would be unable to come before you today and report that there is reason to have some hope and expectation that the IAC program can be effectively preserved.

We have been asked periodically why we are conducting an in-depth, program-wide review and evaluation. Figure 8 responds to this important question.

---

## **EVALUATION OF DOD INFORMATION ANALYSIS CENTERS**

### **WHY AN IAC EVALUATION?**

- **EVALUATION IS A NORMAL MANAGEMENT PROCESS**
  - **THE REGULATION REQUIRES PERIODIC EVALUATIONS**
  - **CRITICAL EVALUATIONS CAN LEAD TO IMPROVED OPERATIONS**
  - **THE BUDGET CRUNCH IS FORCING MANAGERS TO DEFEND PROGRAM EXPENDITURES IN GREATER DETAIL**
- 

### **Figure 8: IAC Evaluation**

Why do an evaluation of the DoD IAC Program? Obviously, evaluation is a normal part of the management process. There is strong bureaucratic pressure to perform an evaluation because the DoD IAC Regulation requires one on a biennial basis. Since one hasn't been performed in 20 years, perhaps now is as good a time as any to begin to comply with the Regulation.

More importantly, there is a very strong expectation that a program evaluation can lead to improvements in the operation of and benefits provided by the DoD IAC program. Finally, the budget crunch of FY 1986 dropped available resources at the IACs below critical mass. Several important DoD users of IACs found that as a result of the FY 1986 budget reduction that they were unable to perform their missions. The results of our evaluation will be used, at least by some in OSD, as the basis for justifying the continued existence of one or more DoD IACs.

The objectives of the pilot study are outlined in Figure 9. Our initial focus on study methodology was triggered by our review of existing literature assessing the value of information to the information consumer. Most studies of libraries, special libraries, and reference libraries conclude that it is difficult to attach value to information provided by libraries to their users. As we who work with DoD know, just because something is difficult to accomplish is not an acceptable excuse for failing to provide an answer to the question posed.

We did look at several studies undertaken for the National Science Foundation and the Department of Energy which examined the value of information to their user communities. The results of these studies were instructive. The authors tended to argue that if any benefit of information provided by the NSF or DoE Scientific and Technical Information (STINFO) activities could be identified, the entire value of the resultant was attributable to the STINFO activity. One study concluded that DoE derived some \$30 billion in benefits from its STINFO investment of \$30 million.

---

## **EVALUATION OF DOD INFORMATION ANALYSIS CENTERS**

### **IAC PILOT STUDY OBJECTIVES**

- **INITIAL PURPOSE: DEVELOP AND TEST METHODOLOGY**
- **ADDED EMPHASIS: INCLUDE INFORMATION TO SUPPORT DOD IAC PROGRAM DURING DOD BUDGET PROCESS AND BEFORE OMB AND CONGRESS**
- **ADDITIONAL FOCUS OF STUDY: IDENTIFY PROBLEMS IN ADMINISTRATION, MANAGEMENT, OVERSIGHT, OR EXECUTION OF THE DOD IAC PROGRAM, AND SUGGEST POTENTIAL SOLUTIONS.**

---

### **Figure 9: Pilot Study Objectives**

If the benefit/cost ratio was really this good, one might readily ask, "Why is DoE spending any money on laboratory work at all? Why not simply buy information analysis?" We concluded that the methodologies employed by these studies of NSF and DoE scientific and technical information analysis activities might yield meaningful results for those agencies. Given the skepticism which greets any pronouncement by DoD on the costs, savings, or value of its programs, our judgment was that we needed to develop a different approach to the collection and analysis of information bearing on the question, what is the value to the DoD RDT&E program of the DoD IACs?

The method by which our pilot study was conducted is outlined in Figure 10. As is readily apparent, we chose to rely heavily on program auditing techniques employed widely by various U.S. Government agencies, particularly GAO and DoD program auditors. After completing a far ranging literature review, we looked at the policies governing the DoD IAC Program, discussed their application to specific discipline or mission areas with

technical program managers, the IACs, and finally their users. We put together a preliminary draft report, circulated it for comment, and finally reported to the sponsor an assessment of the benefits and costs of NTIAC to the DoD research program.

---

## **EVALUATION OF DOD INFORMATION ANALYSIS CENTERS**

### **IAC PILOT STUDY METHODOLOGY**

- **REVIEW OF LITERATURE**
  - **GENERAL INFORMATION SCIENCES, LIBRARY EVALUATION, AND IAC SPECIFIC**
- **OPERATIONAL AUDIT**
  - **IDENTIFY PROGRAM GOALS AND OBJECTIVES AS SET FORTH IN DOD DIRECTIVES AND OTHER POLICY STATEMENTS**
  - **ESTABLISH MEASURES OF MERIT TO ASSESS COST, BENEFIT, EFFECTIVENESS, AND PERFORMANCE OF PARTICIPANTS**
  - **DEVELOP INSTRUMENTS NEEDED TO COLLECT DATA**
  - **CONDUCT INTERVIEWS AND REVIEW RECORDS**
  - **ANALYZE DATA**
  - **CIRCULATE DRAFT REPORT FOR COMMENTS**
  - **REVISE REPORT AS APPROPRIATE**

---

### **Figure 10: IDA Pilot Study Methodology**

The initial results we obtained during the course of review of NTIAC were very encouraging. We began to obtain interesting data regarding the benefits to DoD NTIAC products and services very quickly in our pilot study. As a result, we were asked to make note of anecdotes which might be helpful in defending the IAC program as a whole in the DoD and Congressional budget process. Additionally, we were asked to accelerate our review of program-wide operational and management practices.

Let us turn now to a consideration of NTIAC's benefits and costs.

### **NTIAC'S ENVIRONMENT**

Our point of departure in our review of NTIAC was to compare and contrast the institutional "environment" that might be expected from a review of the guiding policy document -- DoD Regulation 3200.12-R-2 -- and its implementation in the field. Figure 11 represents a "map" of the key institutional players that one might expect to find involved in the management and operation of NTIAC based on a reading of the DoD Directive.

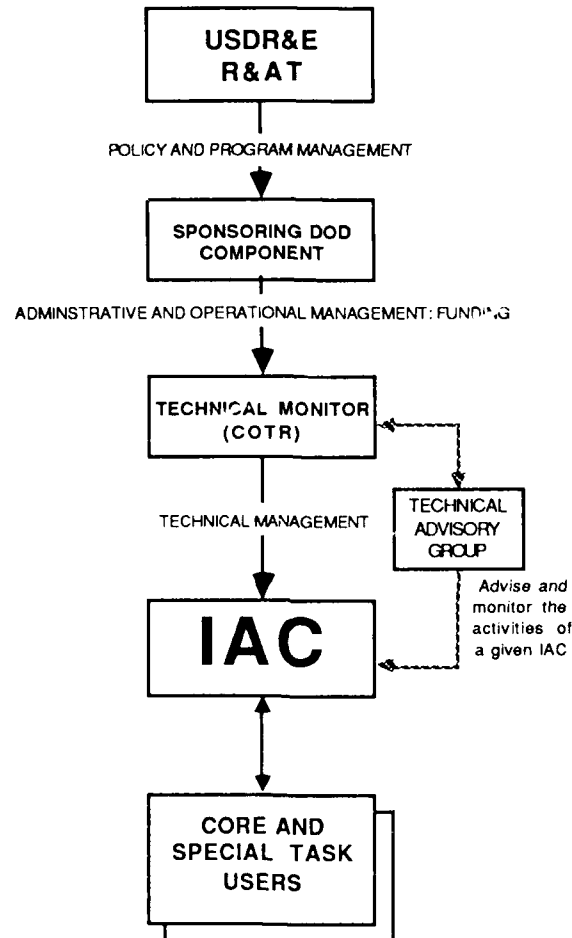


---

## EVALUATION OF DOD INFORMATION ANALYSIS CENTERS

### DOD IAC PROGRAM STRUCTURE

(DOD 3200.12-R-2)



---

**Figure 11: IAC Environment as Defined by IAC Regulation**

According to the Regulation, the Office of the Under Secretary for Research and Engineering (now the Director of Defense Research and Engineering), and his principal staff member, the Deputy Under Secretary of Defense for Research and Advanced Technology (now the Deputy Director of Defense Research and Engineering for Research and Advanced Technology), are supposed to provide overall guidance to all DoD IACs, and the DoD components which sponsor an IAC. The sponsoring DoD component, in turn, provides budget, administrative and technical support, and a technical monitor who

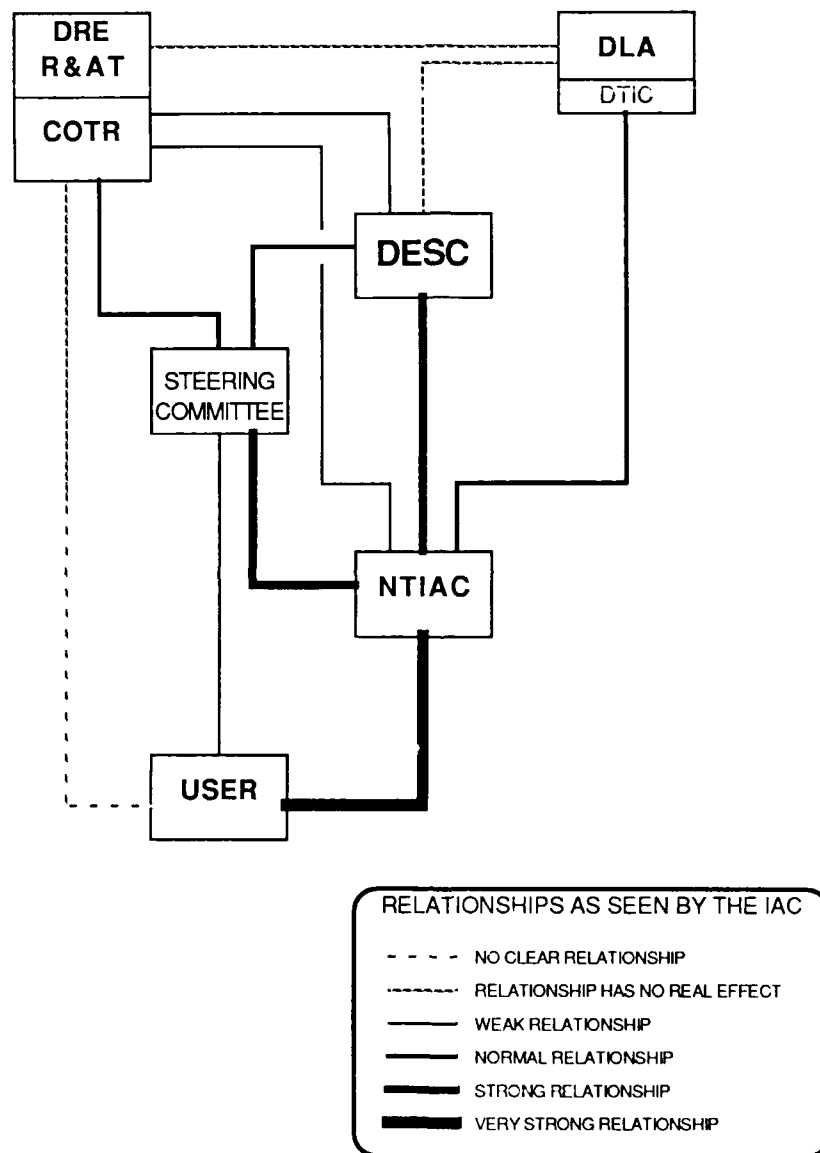
directs the substantive work of a DoD IAC. The technical monitor is assisted by an *ad hoc* advisory committee composed of DoD members of the IAC's technical community.

On paper, the linear relationships among policy, technical management, and contract administration appear straightforward. However, as is often the case, the real world is at considerable variance with the world as envisioned by directives and regulations. Figure 12 illustrates the environment of NTIAC as perceived by the IAC.

The differences between Figure 11 and Figure 12 are striking. First, there are substantially more actors in NTIAC's environment than would be expected based on a reading of the IAC Regulation. For example, DLA staff, the Defense Electronics Supply Center staff, the IAC Program Office at DTIC, and the *ad hoc* Steering Committee play more prominent roles in the direction, administration, and management of NTIAC than would be anticipated by a reading of the Regulation.

---

## EVALUATION OF DOD INFORMATION ANALYSIS CENTERS



---

Figure 12: NTIAC Environment as Perceived by NTIAC

NTIAC receives guidance from Mr. Persh, its COTR and a member of the R&AT staff on the technical content of its core program. Mr. Persh has delegated to Dr. Broz, Chairman of the Tri-Services Steering Committee, considerable responsibility for providing guidance to NTIAC on special tasks. NTIAC receives guidance on contract administration and management matters from its Procuring Contracting Officer at DESC; it also receives guidance on the administration of certain contract matters from an Administrative Contracting Officer in the Defense Contract Administration Services (DCAS) office in San Antonio. It is paid out of another DCAS office in Dallas. NTIAC receives guidance on overall budget and IAC-wide policies from the IAC Program Office at DTIC.

In the final analysis, NTIAC works for three or four different people, often simultaneously because seemingly simple and straightforward matters of tasking often involve differing interpretations of NTIAC's contract, the DoD Directive, and conflicting interpretations of DLA procurement rules and regulations.

Sponsorship responsibilities defined by the DoD Regulation are carried out by several organizations. DLA provides administrative management and guidance; Mr. Persh (OSD) and Dr. Broz (Army Materiel Technology Laboratory) provide technical guidance; IAC program guidance is provided by the IAC Program Office. This arrangement works reasonably well most of the time. However, when differences of view arise, the diffusion of responsibilities and authorities can be troublesome for the IAC and its users.

DLA has not been able to provide adequate budget defense for the core IAC program for some years. As noted above, the DLA Comptroller's budget organization is constrained by its understanding of Congressional limitations on budgets and its own financial management system which is understating the use of dollars by all DoD IACs reporting to it. From an institutional standpoint, DLA has little incentive to change. The IAC program represents a \$6 million budget line in an area of research and development support as part of a \$9 billion dollar procurement and logistics support agency. Given the disparity between DLA's primary mission -- support and sustain DoD forces in the field -- and its tertiary mission -- support the DoD RDT&E community -- it is easy to understand why DLA does not invest its political capital in defense of this small program.

Figure 13 summarizes the manner in which NTIAC has adapted to the differences between the environment one might expect to find based on a quick reading of the IAC Regulation and the environment we found upon inspection of the NTIAC case.

---

## EVALUATION OF DOD INFORMATION ANALYSIS CENTERS

### NTIAC'S ENVIRONMENT

- SPONSORSHIP RESPONSIBILITIES ARE BEING CARRIED OUT BY DLA WHICH HAS NO RESPONSIBILITY FOR DOD NDE PROGRAMS
  - DLA DOES NOT CONSIDER ITSELF TO BE THE SPONSOR
  - DLA DOES NOT PROVIDE OPERATIONAL MANAGEMENT OF NTIAC
- FROM NTIAC'S PERSPECTIVE, IT HAS THREE DIFFERENT "ADMINISTRATORS"
  - DESC FOR ALL CONTRACT MATTERS
  - THE IAC PROGRAM OFFICE FOR CORE ACTIVITIES
  - THE COTR AND THE CHAIRMAN OF THE TRI-SERVICES STEERING COMMITTEE FOR SPECIAL TASK GUIDANCE
- DLA/DTIC FUNDING FOR NTIAC HAS BEEN LESS THAN ANTICIPATED IN THE CONTRACT
- SOUTHWEST RESEARCH INSTITUTE HAS PROVIDED CONSIDERABLE SUPPORT FOR NTIAC
- NTIAC HAS FOCUSED EFFORTS ON UPDATING DATA BASE AND PERFORMING SPECIAL TASKS
- STATE-OF-THE-ART STUDIES, SELF-EVALUATION, PROACTIVE CURRENT AWARENESS ACTIVITIES, AND OTHER CORE FUNCTIONS HAVE BEEN GIVEN A LOWER PRIORITY DUE TO LACK OF RESOURCES
- NTIAC IS USING MODERN ADP SYSTEMS AND TECHNIQUES
- NTIAC HAS BEEN MOST ACTIVE IN TRYING TO IDENTIFY AND SEEK REMEDIES TO HARDWARE AND SOFTWARE PROBLEMS THAT HAVE IMPACTED UPON COMMUNICATION OF DATA BETWEEN DTIC AND THE IACS

---

Figure 13: NTIAC's Environment

NTIAC has recognized the problem for resources imposed upon it by the environment. Southwest Research Institute, NTIAC's parent organization, has been especially supportive. It has provided overhead resources to support NTIAC's director and staff in the pursuit of information collection and dissemination. It has provided IR&D resources to develop computer software for NTIAC's use as part of its information cataloging and synthesis responsibilities. It has procured from overhead and fee dollars modern computer equipment to support information storage, retrieval, and dissemination.

NTIAC and its technical managers, Mr. Persh and Dr. Broz, have also adapted to the current environment by winnowing away certain tasks or subtasks included in the core

program statement of work. Given the limitations of resources, my personal view is that NTIAC and its technical managers have made very reasonable choices about sacrificing certain parts of the core program, e.g. self-evaluation, in favor of continuing to provide services to the NTIAC user community. NTIAC has preserved its current awareness program, but has done so at the expense of producing handbooks, state-of-the-art reports, and some critical reviews. While this is frustrating to many NTIAC users, it appears on balance to be reasonable because NTIAC has been able to maintain its core collection of information necessary to support more expansive inquiries in the form of special studies or special tasks.

NTIAC with the support of its parent has done an excellent job of substituting computers for people. Indeed, not only is NTIAC using modern ADP, a requirement of the IAC Regulation, it appears to be well ahead of DTIC, the governmental agency to whom it looks for broad policy guidance on use of ADP and other information collection and dissemination techniques.

Having established that NTIAC has adapted reasonably well to its environment, the question still remains to be answered, "Is NTIAC providing benefits to DoD"? Let us turn to the results of our study on this key point.

## **BENEFITS TO DOD FROM NTIAC PRODUCTS AND SERVICES**

In order to understand how NTIAC products and services might be of benefit or value to DoD, we first had to characterize and define what we meant by benefits. We concluded that there are four categories of benefits provided by a DoD Information Analysis Center. Figure 14 summarizes our approach to the problem categorizing IAC benefits. We retained in our analysis the concern about trying to assess benefits for which quantified data could not be divined. We acknowledged in our analytical framework the possibility that IACs might provide DoD benefits which are important, even if savings of dollars, labor hours, or months in the acquisition cycle could not be directly attributed to an IAC product or service.

---

## EVALUATION OF DOD INFORMATION ANALYSIS CENTERS

### IAC BENEFIT/COST ANALYSIS

- **FOUR CATEGORIES OF BENEFITS TO DOD**
    - **BENEFITS WHICH CAN BE QUANTIFIED AND FOR WHICH DATA WAS DEVELOPED**
    - **BENEFITS WHICH CAN BE QUANTIFIED BUT FOR WHICH NO DATA WAS DEVELOPED**
    - **BENEFITS WHICH CAN BE DEFINED, BUT CAN NOT BE MEASURED QUANTITATIVELY WITH PRECISION OR CONFIDENCE**
    - **BENEFITS WHICH CANNOT BE DEFINED OR MEASURED IN A MEANINGFUL WAY**
  - **BENEFITS CATEGORIES APPLY TO CORE AND SPECIAL TASKS**
  - **COSTS ARE DIRECT CONTRACT COSTS**
- 

**Figure 14: IAC Benefit/Cost Analysis**

We sought to avoid a situation in which we would produce quantitative results subject to interpretation by budget analysts and accountants which would fail to take into account the value of the products and services to NTIAC's users -- scientists, engineers, and bench level technicians trying to solve real-world, military technology problems.

Figure 15 summarizes the results of our efforts to obtain an assessment of NTIAC's benefits from its user community. To those who want numbers, I can report that our study produced quantitative benefits. We have numbers -- we are not 100 percent confident that the numbers are good, representative, and above reproach. But we found numbers.

We also found other benefits to which numbers could be attached if only NTIAC users had taken the time, had attached importance, or had bothered to collect appropriate data. In some cases, we found that benefits were quantifiable, but the results were too new to have any significant or meaningful supporting data to report just yet.

We also found benefits reported by a significant number of NTIAC users that cannot be quantified. We have been told and have been able to document significant benefits from NTIAC Products in terms of operational readiness, combat capability, improvement in R&D planning, and overall improvement in technician competence. Users told us that these benefits were of great value; NTIAC's continued existence was terribly important to them, even if the benefits they derive from NTIAC could not be quantified.

## EVALUATION OF DOD INFORMATION ANALYSIS CENTERS

### NTIAC BENEFIT SUMMARY

BENEFIT CATEGORY	SAVINGS IN TIME AND EFFORT	SAVINGS FROM CHANGES IN OPERATIONS	OTHER BENEFITS	TOTALS
DEFINED QUANTIFIABLE	SEVEN CORE USERS ONE SPECIAL TASK	ONE CORE USER TWO SPECIAL TASK USERS	ONE SPECIAL TASK USER	
QUANTIFIED	BENEFITS - \$2,192,500 COSTS - \$ 701,065	BENEFITS - \$11,000,000 COSTS - \$ 1,490,000	BENEFITS - \$400,000 COSTS - \$ 90,000	BENEFIT-\$13,592,500 COSTS \$ 2,228,065
DEFINED QUANTIFIABLE	TWO CORE USERS	ONE CORE USER FOUR SPECIAL TASK USERS		
UNQUANTIFIED	BENEFITS - @ 1.5 WEEKS COSTS - \$100	BENEFITS - TOO SOON TO SAY (4) -DID NOT TRY TO CALCULATE (1) COSTS - \$679,079		BENEFITS - 1.5 WEEKS COSTS-\$679,179
DEFINED NOT QUANTIFIABLE		TWO SPECIAL TASK USERS	FOUR CORE USERS THREE SPECIAL TASK USERS	
		BENEFITS-OPERATIONAL READINESS COSTS - \$ 165,537	BENEFITS - NEW KNOWLEDGE COSTS- \$ 606,314	COSTS -\$ 771,851
UNDEFINED NOT	ONE CORE USER		TWO CORE USERS COTR AND CHAIRMAN STEERING COMMITTEE	
	BENEFIT - ? (LIBRARIAN)		BENEFITS - NEW KNOWLEDGE, BETTER PROGRAM PLANNING	
	COSTS - \$100		COSTS - CORE PROGRAM	
TOTAL	BENEFITS - \$2,192,500 COSTS - \$ 701,265	BENEFITS -\$11,000,000 COSTS - \$ 2,33 4,616	BENEFITS - \$400,000 COSTS - \$696,314	

Figure 15: NTIAC's Benefits to DoD -- Summary



Figure 15 illustrates our success in identifying savings or other financial benefits accruing to DoD as a result of DoD component and contractor use of NTIAC core and special task programs.

These results were obtained by interviewing NTIAC core and special task users. We divided NTIAC core users into two categories:

- users of general distribution products
- users of products prepared in response to individual inquiries

Figure 16 illustrates some of NTIAC's products produced for the entire NDE community during the period 1983 - 1988.

---

## **EVALUATION OF DOD INFORMATION ANALYSIS CENTERS**

### **NTIAC CORE PROGRAM BENEFITS**

- **GENERAL DISTRIBUTION PRODUCTS**
  - AVAILABLE TO ALL WHO ASK AND WHO ARE APPROVED DTIC CUSTOMERS
  - VERY WIDESPREAD GEOGRAPHIC DISTRIBUTION OF USERS
- **NTIAC CORE GENERAL DISTRIBUTION PRODUCTS**
  - QUARTERLY NEWSLETTER (INCLUDES A LEAD TECHNICAL ARTICLE)
  - OTHER TITLES/ACTIVITIES
    - ULTRASONIC TRANSDUCERS
    - AUTOMATED RADIOGRAPHY, 2ND EDITION
    - DEPOT MAINTENANCE HANDBOOK
    - ACE/AACE INSPECTION AND ANALYSIS HANDBOOK
    - PROCEEDINGS OF THE 15TH SYMPOSIUM ON NDE
    - 16TH SYMPOSIUM ON NONDESTRUCTIVE EVALUATION

---

**Figure 16: NTIAC Core Products**

Figure 17 illustrates the distribution of NTIAC's core users who made individual requests for assistance during FY 1987.

---

## EVALUATION OF DOD INFORMATION ANALYSIS CENTERS

### NTIAC CORE INDIVIDUAL RESPONSE USERS FOR FY 1987

ORGANIZATION		TYPE SERVICE	
AIR FORCE	14	BIBLIOGRAPHY	29
ARMY	11	GENERAL INFORMATION	5
NAVY	4	DOCUMENTS	18
DLA	3	REFERRALS	10
DOD CONTRACTOR	18	TECHNICAL INQUIRIES	13
FOREIGN	2		
COMMERCIAL ENTITY	16		
OTHER	4		

---

**Figure 17: NTIAC Individual Response Core Users, FY 1987**

These figures suggest that NTIAC enjoys broad, DoD-wide support for its core programs. Most NTIAC core users with whom we spoke were receiving newsletters or other current awareness publications. Figure 18 outlines the kinds of users and the kinds of benefits they reported to us.

In summary, we found interviewed 18 individual response core users of NTIAC. Of these 18, we found that 15 had asked NTIAC for special bibliographies and three had requested answers to technical inquiries. Several commercial users were billed \$100 for the for a bibliography or obtaining an answer to a technical inquiry, consistent with the DLA contract mandated cost recovery policy and an implementing schedule prepared by NTIAC. Government users paid no additional fee for NTIAC service.

We were told by five users who paid not additional fee for service that the bibliographies prepared by NTIAC saved them in aggregate, an estimated \$11,500. These estimates reflected the users' judgment of the value of their time or the costs of obtaining similar information from alternative sources.

Three users who were charged for NTIAC services reported significant benefits. The three users estimated that they saved or received in value more than \$91,000 worth of information.

---

## **EVALUATION OF DOD INFORMATION ANALYSIS CENTERS**

### **NTIAC CORE USERS SURVEY--INDIVIDUAL RESPONSE SERVICE USERS**

<b>USER AGENCY</b>	
8	DOD AGENCIES
1	DOD CONTRACTOR
2	UNIVERSITY-BASED USERS
7	COMMERCIAL VENTURES (INCLUDING COMPANIES AND CONSULTANTS)
<b>NATURE OF TASK</b>	
15	ANNOTATED/CRITICAL BIBLIOGRAPHIES
3	TECHNICAL INQUIRIES
<b>FUNDING</b>	
8	COMMERCIAL USERS/DOD CONTRACTOR BILLED \$100 EACH
9	GOVERNMENT USERS FUNDED IN DLA/DTIC CORE FUNDS
1	UNSPECIFIED FUNDING OF SERVICE
<b>AMOUNT OF BENEFIT</b>	
5 OF 9 CORE-FUNDED TASKS WITH USER-QUANTIFIED BENEFITS	
TOTALING \$11,500	
3 OF 8 BILLED TASKS WITH USER-QUANTIFIED BENEFITS OF MORE THAN	
\$91,000 (\$80,000 FROM ONE TASK)	
1 CORE-FUNDED TASK REPORTED NO QUANTIFIED BENEFITS	

---

**Figure 18: Individual Response Core User Summary Benefits**

When we look behind these aggregate figures, we find a fairly consistent pattern of benefits being provided by NTIAC to users who have a specific inquiry. NTIAC typically saves them time, effort, and money. Much of the information available from NTIAC is available from other vendors, but at substantially greater cost, in less detail, in more diffuse and less focused nature, and in some instances substantially less useful form. Figure 19 summarizes some of the specific benefit-cost relationships individual users provided.

---

## EVALUATION OF DOD INFORMATION ANALYSIS CENTERS

### SAMPLE CORE INDIVIDUAL RESPONSE USER BENEFIT COST ESTIMATES

REQUEST ORIGINATOR	RATIO	BASIS
KELLY AFB NDE OFFICE	3:1*	IN-HOUSE MAN HOURS
USAF NDI PROGRAM	3:1*	ALTERNATIVE SOURCES
AVSCOM, APPLIED TECHNOLOGY DIVISION	4:1*	ALTERNATIVE SOURCES
ADVANCED CONSTRUCTION TECHNOLOGY CENTER	5:1*	IN-HOUSE MAN-HOURS
REINHARD ASSOCIATES	10:1	IN-HOUSE MAN-HOURS
ARMY CORPS OF ENGINEERS	100:1*	APPLICATION OF INFORMATION
SCIENTIFIC MEASUREMENT SYSTEMS	800:1	ALTERNATIVE SOURCES

\* ASSUMES THAT THE COST OF THE TECHNICAL INQUIRY WAS \$100, EVEN THOUGH NO CHARGE TO THE USER WAS MADE BY NTIAC

---

**Figure 19: Sample Benefit/Cost Ratios**

These numbers reflect some very specific data and in several instances are thought to be anomalous. In the case of the Corps of Engineers, NTIAC was asked to comment on the effectiveness of the use of radiography as a test of the integrity of 55-gallon drums containing unknown substances stored on Johnston Atoll. NTIAC responded to this technical inquiry by suggesting that radiography was not likely to provide useful information; alternative methods were proposed. The Corps told us that as a result of NTIAC's response to their inquiry, they concluded that no meaningful information on the condition of the 55 gallon drums could be obtained within the \$10,000 budget. The project was cancelled and the Corps estimated that it saved \$10,000.

We believe that if the Corps had posed this question as a commercial customer, it would have been charged \$100. Hence, simple arithmetic shows that the benefit cost ratio in this instance was 100:1.

In the case of Scientific Measurement Systems, we learned of a much more significant valuation of information. In this case, the requestor had commissioned another technical engineering house to perform a study on NDE techniques to evaluate bridge structures. Scientific Measurement Systems was not satisfied with the resulting study by this contractor. It turned to NTIAC for assistance.

We were told by the firm that it had invested the best \$100 of corporate money ever! We were told that the value to the firm of the NTIAC response exceeded the value of the \$80,000 study. Again, by arithmetic, we conclude in this case the benefit/cost ratio was 800:1.

Our data suggest that the 100:1 and 800:1 ratios reported here are anomalous to the extreme. However, the ratios of 3:1 up to 10:1 based on the in-house cost of labor used to answer questions or the costs of obtaining similar information from alternative sources seem reasonable and are internally consistent with one another.

The benefits reported by special task users of NTIAC are equally impressive. Figure 20 summarizes the total population of NTIAC's special task users through FY 1987 from whom information on benefits could have been sought.

---

**EVALUATION OF DOD INFORMATION ANALYSIS CENTERS**  
**NTIAC SPECIAL TASK USERS**

---

SERVICE	TASKS	TOTAL COST
ARMY	15	\$1,897,054
NAVY	13	\$1,521,319
AIR FORCE	5	\$692,294

---

**Figure 20: NTIAC Special Task Users**

As in the case of NTIAC's core users, we see widespread distribution of special task users throughout the Department of Defense. Figure 21 summarizes our approach to the collection of information on special task benefits to DoD resulting from NTIAC products and services.

---

## EVALUATION OF DOD INFORMATION ANALYSIS CENTERS

### ESTIMATION OF SPECIAL TASK BENEFITS

- **METHODOLOGY**
  - IDENTIFIED LIST OF NTIAC SPECIAL TASK USERS
  - FOCUSED ON USERS WITH LARGE DOLLAR VOLUME
  - IDENTIFIED USERS IN SAME APPROXIMATE GEOGRAPHIC AREA
  - CONDUCTED DETAILED INTERVIEWS
    - 13 OF 19 SPECIAL USER ORGANIZATIONS
    - 28 OF 34 SPECIAL TASKS
    - TOTAL VALUE OF \$3,731,495
    - APPROXIMATELY 83% OF THE TASKS AND 92% OF THE DOLLAR VALUE OF NTIAC SPECIAL TASKS THROUGH FY 1987
- **ASKED USERS TO QUANTIFY BENEFITS WHERE POSSIBLE**
- **IDA REVIEWED METHOD BY WHICH QUANTIFIED VALUE OF INFORMATION WAS ESTIMATED WHERE PROVIDED**
- **IDA ADJUSTED ESTIMATES OF VALUE IN SEVERAL INSTANCES**
  - EXCLUDE PURELY SUBJECTIVE ESTIMATES
  - ACCEPT ONLY THAT PORTION OF AN ESTIMATE THAT DID NOT REQUIRE RETROFIT OF AIRCRAFT ALREADY FIELDIED
  - PARTITION THE VALUE BETWEEN NTIAC AND U.S. GOVERNMENT EFFORTS
    - EXCLUDE DOLLAR VALUE OF RECURRING BENEFITS BEYOND THE FIRST YEAR.

---

**Figure 21: Estimation of Special Task Benefits**

We typically asked users to quantify benefits where possible. Many were able to do so. Having been told the value of NTIAC's special task products or services to users, we asked them to explain how they arrived at their judgments. In some instances, we accepted these estimates at face value. In other instances, we chose to partition the variance in benefits reported between NTIAC and others. In the case of the Army Aviation Depot at Corpus Christi Naval Air Station, we divided the benefits between NTIAC and the Army, even though as a practical matter we agree with the Army's judgment that if NTIAC had not performed the services needed to install a reliability centered maintenance program, the work would not have been accomplished. In other instances, we deeply discounted the user's estimate of benefit because NTIAC had been successful in proving the first part of a two part problem false, thereby eliminating the need for the second part of the solution which would have resulted in astronomical savings to the government.

Figure 22 summarizes the overall results of our assessment of special task benefits provided to DoD by NTIAC.

---

## **EVALUATION OF DOD INFORMATION ANALYSIS CENTERS**

### **NET ASSESSMENT OF SPECIAL TASK BENEFITS**

- **NO INFORMATION ON 6 OF 19 USERS, 6 OF 34 TASKS**
- **UNDEFINABLE AND UNMEASURABLE BENEFITS FROM 2 USERS (NOT INCLUDED)**
- **DEFINED BUT UNMEASURABLE BENEFITS FROM 2 USERS (NOT INCLUDED)**
- **DEFINED, MEASURABLE, BUT UNQUANTIFIED BENEFITS FROM 4 USERS (NOT INCLUDED)**
  - **3 TOO SOON TO HAVE COST SAVINGS DATA**
  - **1 DID NOT COLLECT COST SAVINGS DATA**
- **DEFINED, SUBJECTIVELY ESTIMATED BENEFIT FROM 1 USER (not Included)**
- **DEFINED, QUANTIFIED BENEFITS FROM THREE USERS (discounted and Included)**
- **DEFINED AND QUANTIFIED BENEFITS FROM ONE USER (Included at face value)**

<p><b>\$12,800,000 OF SPECIAL TASK BENEFITS WHERE WE HAVE GOOD CONFIDENCE IN THE ESTIMATED VALUE OF THE BENEFITS. (TOTAL COST OF ALL SPECIAL TASKS - \$4,110,668)</b></p>
---

---

**Figure 22: Net Assessment of NTIAC Special Task Benefits**

We were able to obtain a considerable amount of information about the benefits to special task users from NTIAC products and services. For example, in six of 19 tasks, users were unable to tell us very much about the kind of benefits they received. However, these users were at the basic or early applied research end of the R,D,T & E spectrum. Their mission is to take information from various sources, add new information generated from their laboratory work, and disseminate the combined results.

Several users told us of benefits they received, even though they could not quantify the benefits in terms of hours saved, dollars saved, shortened acquisition time, etc. Other users were able to tell us that they could quantify benefits being accrued as a result of NTIAC products at some future time, but the results had just begun to roll in and the data was not available. One user stopped mid sentence when describing the benefit of an NTIAC task to the government and told us it would cost the government between \$200

million to \$800 million or more to recreate the results of data being collected and analyzed by NTIAC.

Several other users gave us both qualitative and quantitative assessments of benefit. In some instances, we were able to accept the quantitative judgments without qualification; in other instances as noted above, we partitioned the quantitative benefits reported among others and NTIAC. In still other cases, we simply discounted the benefits reported. Figure 23 highlights some examples of quantitative benefits reported.

One of the users who was able to quantify the benefits of NTIAC products was the Pacific Missile Test Center (PMTC) at Point Mugu, California. NTIAC addressed several problems for PMTC. One problem dealt with the failure of a sensor in an obsolescent munition to work properly. Unless a solution to the problem of sensor failure could be found, the entire inventory would have to be destroyed. Since the item was no longer manufactured, and since the munition, while obsolescent, was still deployed with the fleet, PMTC strongly wished to find a solution with a minimum amount of destructive testing. NTIAC was able to come up with a method to analyze the failure of the sensor to operate correctly. It was also able to come up with an inexpensive solution.

In another PMTC task, NTIAC was able to identify the cause of serious deformation in HARPOON missile shipping containers which was resulting in water damage to missiles. In this case, NTIAC was able to determine that empty HARPOON shipping cases were being stored vertically. As a result of this storage practice, the cases were deforming, the water-tight seals were separating from the cases, and gaps between the top and bottom halves of the case were forming when missiles were placed in them for horizontal storage. NTIAC suggested changes in procedures so that empty HARPOON cases would continue to be stored flat. In so doing, NTIAC was successful in reducing water damage to HARPOON missiles being stored in the reusable shipping containers.

The PMTC staff told us that NTIAC was half as expensive as in-house PMTC staff, assuming PMTC staff were available to address these problems. Furthermore, the judgment of PMTC staff was that NTIAC technical work was equal to or superior to the work that would have been performed by PMTC in-house staff had they been available to work on these problems. The quantitative benefit to PMTC was therefore estimated at \$2.1 million.



---

## **EVALUATION OF DOD INFORMATION ANALYSIS CENTERS**

### **QUANTITATIVE BENEFITS OF NTIAC SPECIAL TASKS**

- **PACIFIC MISSILE TEST CENTER**
  - ESTIMATED VALUE OF NTIAC SPECIAL TASK--\$2,100,000
  - ESTIMATE BASED ON COST SAVINGS HAVING WORK PERFORMED BY EXPERTS RATHER THAN IN-HOUSE PERSONNEL
  - IDA DID NOT INCREASE VALUE OF NTIAC SPECIAL TASK TO REFLECT PMTC ESTIMATE OF NTIAC'S SUPERIOR QUALITY
- **NAVAL ELECTRONICS SYSTEM ENGINEERING CENTER**
  - ESTIMATED VALUE OF NTIAC SPECIAL TASK - \$8,800,000
  - ESTIMATE BASED ON PROCUREMENT SAVINGS RESULTING FROM COMPETITION IN PROCUREMENT OF ELECTRONIC SPARE PART COMPONENTS FACILITATED BY NTIAC DEVELOPMENT OF NDE PROCEDURES FOR CERTIFICATION OF SPARES
  - ESTIMATE ACCEPTED BY IDA BASED ON NESC WORKING PAPERS
- **ARMY AVIATION SYSTEMS COMMAND--RELIABILITY CENTERED MAINTENANCE PROJECT**
  - ESTIMATED SAVINGS BY ARMY--\$18,400,000
  - SAVINGS ESTIMATED FROM DETAILED LABOR AND MATERIALS RECORDS FOR 20 MAJOR AIRCRAFT COMPONENTS; NTIAC PROVIDES 5 PROFESSIONALS TO SUPPLEMENT 37 PROFESSIONALS PROVIDED BY THE ARMY (ALTHOUGH ALL 37 DO NOT WORK ON THIS PROJECT)
  - IDA ESTIMATES NTIAC'S SHARE OF THE BENEFITS IS 5/42 OR \$2,100,000
  - IDA FURTHER ESTIMATES THIS VALUE IS A ONE-TIME BENEFIT EVEN THOUGH THE MAINTENANCE PROGRAM WILL USE TECHNIQUES DEVELOPED FOR SPECIFIC AIRCRAFT COMPONENTS FOR THEIR ENTIRE LIFE CYCLE
- **ARMY AVIATION SYSTEMS COMMAND--WIRING HARNESS**
  - ESTIMATED SAVINGS BY ARMY
  - \$200,000 TIMES 2 PRODUCTION LINES
  - \$100,000 PER AIRCRAFT TIMES MORE THAN 1500 AIRCRAFT
  - TOTAL SAVINGS: AT LEAST \$15,400,000
  - IDA ACCEPTED PRODUCT LINE CHANGE SAVINGS ONLY AND ESTIMATED VALUE OF NTIAC BENEFIT TO THE ARMY OF \$400,000

---

**Figure 23: Quantitative Benefits of NTIAC Special Tasks**

In the case of the Naval Electronics Systems Engineering Center, the value of NTIAC's information products was estimated to be in excess of \$8 million. This estimate was arrived by a careful review of procurement costs to the Navy of spare electronic parts

before and after NTIAC devised test methods to qualify alternative suppliers for original manufacturer spares. The mere threat of competitive procurement of spare electronic components resulted in a 25 percent reduction in cost; effective competition or second source development of spares often resulted in as much as a 50 percent reduction in spare parts costs. NESC staff built detailed case histories of the NTIAC experience; we accepted at face value their judgment of savings.

In the case of the Army Aviation Systems Command helicopter depot repair facility at Corpus Christi Naval Air Station, we found that NTIAC had made a substantial contribution to the development of alternative methods of performing depot level maintenance on helicopters. As a result of NDE evaluation of major airframe and propulsion system components, NTIAC had substantially reduced time and costs of depot maintenance. The Army had collected data on repair costs before and after NTIAC products were prepared and concluded that NTIAC's work had resulted in an initial savings of more than \$18 million. We looked at this data and came to a somewhat more conservative figure. We argued that since the Army had a staff of engineers who, in principle, could have participated in the development of the reliability centered maintenance program, it was appropriate to credit NTIAC with only a share of the savings. Even so, our more conservative calculation shows that NTIAC's work accounted for more than \$2 million in savings.

In another instance, the Army ran into a problem that illustrates both quantitative and qualitative benefits provided by a DoD IAC. The specifics of this case were as follows.

An unsuccessful bidder on a helicopter wiring harness contacted a Congressional office to allege that the wiring harness being installed in a helicopter was defective at the level of design; furthermore, it was being implemented with additional defects. If these allegations were correct, the Army would have to redesign the wiring harness, retool two production lines, and rewire more than 1000 aircraft.

Aviation Systems Command turned to NTIAC to examine these issues. It elected to use NTIAC because NTIAC was technically competent, was not involved in the design of the subsystem, and was not involved in its manufacture. The Army expressed to us its belief that only a technically competent consultant organization with no obvious interest in the outcome of the analysis would satisfy the desire for objectivity stimulated by the Congressional office inquiry.

As a result of the NTIAC study, the Army concluded that the initial design was not defective. It credited NTIAC with a benefit from this study of \$400,000 (two production lines at \$200,000 retooling cost each). We agreed with this assessment because had NTIAC not performed an evaluation of the wiring harness the Army would have retooled the two production lines. The Army credit NTIAC with an ultimate savings of more than \$15 million (\$100,000 per aircraft to rewire 1500 aircraft). We chose to accept the savings associated with the verification of the existing wiring harness design but we did not include in our estimate of NTIAC benefits the savings associated with not having to rewire 1500 helicopters.

Figure 24 illustrates some of the problems we encountered in attempting to quantify benefits of NTIAC special tasks. In several instances, NTIAC had recently completed work which would eventually produce data related to savings of time, labor, or dollars. The results were too current to be translated into meaningful data on quantitative benefits. In other instances, we could see a mechanism for collecting and analyzing data which would permit the calculation of quantitative benefits; the users either could not see such mechanisms, or did not believe it necessary to collect and report such data to their management.

---

## **EVALUATION OF DOD INFORMATION ANALYSIS CENTERS**

### **ADDITIONAL QUANTIFIED BENEFITS NOT YET CALCULATED**

- **FOUR USERS BELIEVE THEY HAVE BENEFITED FROM NTIAC SPECIAL TASKS IN MEASURABLE WAYS BUT HAVE NO DATA TO REPORT**
  - **IN THREE CASES THE APPLICATION OF NTIAC SPECIAL TASK RESULTS IS SO NEW THAT NO DATA HAS YET BEEN GENERATED WHICH COULD BE USED TO QUANTIFY BENEFITS**
  - **IN ONE CASE THE SPECIAL TASK USER HAD MADE NO EFFORT TO COLLECT OR QUANTIFY SUCH DATA, EVEN THOUGH THE USER THOUGHT SUCH DATA MIGHT BE DISCERNABLE**
- **ONE USER PROVIDED AN ESTIMATED DOLLAR VALUE OF BENEFIT BUT IDA CHOSE TO EXCLUDE IT FROM OUR CALCULATION BECAUSE WE COULD NOT DEVISE A METHOD TO PARTITION THE VALUE OF NTIAC'S CONTRIBUTION TO A VERY LARGE PROGRAM**

---

**Figure 24: Additional Quantitative Benefits Not Yet Calculated**

In addition to quantified benefits described above, we found several instances in which NTIAC was providing DoD with products and services which yielded

nonquantifiable benefits which could nevertheless be described in detail. Figure 25 summarizes some of the more interesting examples we found in our study.

---

## **EVALUATION OF DOD INFORMATION ANALYSIS CENTERS**

### **UNQUANTIFIED BENEFITS OF NTIAC SPECIAL TASKS**

- **TWO USERS REPORTED TANGIBLE BENEFITS TO OPERATIONAL READINESS WHICH CANNOT BE MEASURED QUANTITATIVELY BUT ARE CLEARLY IMPORTANT TO MILITARY DEPARTMENTS**
  - **HELICOPTER READINESS**
  - **NEW MATERIALS TO SUPPORT RAPID OVER-THE-BEACH DELIVERY OF PETROLEUM PRODUCTS IN AMPHIBIOUS ASSAULT OPERATIONS (WITH BENEFITS ALSO ACCRUING TO UNDERWAY REPLENISHMENT CAPABILITIES)**
- **TWO USERS REPORTED TANGIBLE BENEFITS IN HAVING A QUALIFIED EXPERT NOT ASSOCIATED WITH A MILITARY DEPARTMENT PRIME CONTRACTOR WHO COULD ASSIST THE GOVERNMENT IN IDENTIFYING PROBLEMS RELATED TO QUALITY OF MILITARY SYSTEMS ALREADY IN THE INVENTORY**
- **TWO USERS ARE RESEARCHERS WHOSE REPORTS INCORPORATE RESULTS OF WORK PERFORMED BY NTIAC ON THEIR BEHALF.**

---

**Figure 25: Unquantified Benefits of NTIAC Special Tasks**

Two users reported significant improvements in operational capability as a result of NTIAC special tasks. One of these two users also reported great benefit in being able to turn to NTIAC as a neutral, competent source of technical information in lieu of a contractor or a government design bureau. Other users reported significant benefits in terms of the quality of their research as a result of NTIAC inputs into larger research projects.

The Army Aviation Systems Command came to NTIAC shortly after it had grounded the fleet of Blackhawk helicopters due to a composite rotor hub spindle failure. AVSCOM needed to find a neutral third party to do some failure analysis and develop an NDE technique that would permit the troops in the field to determine quickly and reliably whether or not a helicopter was safe to fly.

This task occurred during a period in which the father of a Marine Corps aviator had the U.S. Government and Sikorsky before the Supreme Court alleging negligence and liability in another fatal helicopter accident case. In that case, it was alleged that the Navy had designed and Sikorsky had implemented a defective emergency exit in a Marine Corps helicopter. The plaintiff was seeking damages from both the U.S. Government and the

manufacturer. The U.S. Government was invoking the principle of sovereign immunity as its defense; Sikorsky and the government were seeking to extend sovereign immunity to the contractor as well.

In the case of the Blackhawk helicopter, AVSCOM was concerned that the logic of the court in the case then before the Supreme Court could be extended to any subsequent litigation resulting from Blackhawk crashes. Therefore, AVSCOM did not want the AVSCOM design bureau (the designer of the rotor hub spindle) or the prime contractor (Sikorsky) performing an analysis of failure or involved in the development of test methods to detect cracked rotor hub spindles prior to flight. NTIAC was selected because of its preeminence in the field of NDE. The NTIAC contract was modified through a special task, and within a matter of a few short weeks, AVSCOM had an answer to its question.

Although AVSCOM ultimately elected to remanufacture the rotor hub spindles using non-composite materials, the NTIAC report provided a test method that would have allowed the Army to use NDE techniques to inspect each Blackhawk immediately prior to flight to determine whether or not the aircraft was safe to fly. During wartime, this test method would have made an incalculable difference to helicopter readiness.

Our interview with the Naval Civil Engineering Laboratory discovered another instance in which an NTIAC special task yielded results with immediate benefit to operating forces. In this case NTIAC had been asked to develop both destructive and nondestructive techniques to evaluate samples of new material for use in over-the-beach delivery of POL to support amphibious operations. The special task was highly successful in its own right. In addition, the NDE techniques had immediate application to the Navy's underway replenishment activities (UNREP). Hoses carrying POL and other UNREP materials could be examined and discarded or repaired before transfer of material actually began. As a result, the Navy was able to report fewer casualties due to parting hoses or breaking hawsers, smaller losses of material, and fewer instances of environmental damage which might occur if a hose carrying POL should part.

## **LESSONS LEARNED**

The NTIAC study, our pilot study evaluating the DoD Information Analysis Centers Program, has several lessons for scholars, for the DoD IAC Program, and for users of DoD IACs. Figure 26 summarizes key lessons we believe are of special interest.

---

## **EVALUATION OF DOD INFORMATION ANALYSIS CENTERS**

### **LESSONS LEARNED**

- **STABILIZATION OF CORE FUNDING FOR NTIAC**
  - **MAKE NTIAC MEANINGFUL TO THE DEFENSE LOGISTICS AGENCY**
    - DEFENSE ELECTRONICS SUPPLY CENTER STANDARD DRAWING PARTS PROGRAM**
    - DEFENSE FUEL SUPPLY CENTER**
    - DEFENSE CONSTRUCTION MATERIALS CENTER**
  - **INCREASED SUPPORT FOR NTIAC VOICED BY OSD TO DIRECTOR, DEFENSE LOGISTICS AGENCY**
- **MARKETING OF NTIAC PRODUCTS AND SERVICES**
  - **IMPROVED NTIAC UNDERSTANDING OF THE DOD BUDGET CYCLE**
  - **IMPROVEMENTS IN DISTRIBUTION OF NTIAC PRODUCTS TO MEMBERS OF THE COMMUNITY**
- **NDE COMMUNITY SUPPORT FOR NTIAC**
  - **IMPROVED VISIBILITY FOR NTIAC**
  - **IMPROVED USER FEEDBACK TO NTIAC**
  - **IMPROVED USER FEEDBACK TO OSD**
- **IAC OPERATIONS**
  - **PREPARATION OF REQUESTS FOR SPECIAL TASKS BY U.S. GOVERNMENT AGENCIES**
  - **COLLECTION OF FOREIGN-ORIGIN INFORMATION**
  - **COLLECTION OF U.S. GOVERNMENT TEST AND EVALUATION INFORMATION**
  - **NTIAC INTERFACE WITH THE DEFENSE TECHNICAL INFORMATION CENTER (DTIC)**

---

**Figure 26: Lessons Learned**

It is important for DoD to stabilize the core funding of the DoD IACs at the level anticipated at the time an IAC was established as documented in the contract between the IAC parent and DoD if DoD does not wish to see core efforts eviscerated over time. While NTIAC has adapted well to its shrinking core budget, its adaptations have not been painless to either the IAC or its user community. Handbooks, data books, state-of-the-art reports, and critical reviews helpful to the community have not been prepared. The costs imposed by the inability of NTIAC to produce these documents have not been documented; it is my personal sense that many of the benefits that NTIAC could provide DoD have not been

realized because of the reductions in the level of effort in the core program in response to the budget crunch.

NTIAC has not been as aggressive as one might have expected in building support within DLA for its products and services. For example it has not marketed its ability to develop NDE techniques to qualify alternative suppliers of electronic components demonstrated to the Naval Electronics Systems Laboratory to DLA's Defense Electronics Supply Center. NTIAC has not demonstrated its technique to detect the level of peroxidation of aviation fuels developed for the Naval Air Propulsion Research and Development Center for the DLA's Defense Fuels Supply Center. NTIAC has not taken its expertise in nondestructive evaluation to the DLA's General Supply Center or the Construction Materials Supply Center. These are major DLA field activities and if properly approached could become significant DLA users of NTIAC products and services. Were this to happen and were NTIAC's core program resources to be reduced, it would be DLA activities who would be affected; it would be DLA activities who would complain to the DLA Comptroller that they were unable to perform because of reduced budget support to the NTIAC core program.

Our study also suggests that Office of the Deputy Director for Defense Research and Engineering for Research and Advanced Technology (DDDR&E/R&AT) must do a better job cultivating the support of DLA for an R&AT program. The R&AT staff have not been successful in impressing upon DLA that the IAC Program is an integral part of much larger and very diverse research, development, and acquisition program. As a result, the DLA Comptroller responds to familiar stimuli -- the perceptions of the Congress and the financial management information available within DLA. The results are DLA requests to the Congress for appropriation of funds which are substantially less today in real terms than they were at the time DLA assumed management responsibility for the IAC Program in 1971.

It is also clear from our study that NTIAC, its user community, its technical monitor, and the staffs of the DoD components who depend heavily on NTIAC must do a better job collecting information about the benefits NTIAC provides. While NTIAC can help collect this data, often times it is the Technical Monitor, the IAC Program Office, or an OSD staff member who must query NTIAC users. Our study found many government employees who told us that they were reluctant to respond to NTIAC questionnaires regarding their use of NTIAC for fear that much deserved praise would show up in sales brochures or other literature. In addition, the present ethics climate makes it difficult for

contractors to elicit any evaluation from government employees beyond a simple statement to the effect that the deliverables met the terms of the contract. In this climate, it falls upon the shoulders of the technical and program overseers to elicit comments and collect data on the utility of NTIAC products and services.

Our study also suggested that NTIAC needed to improve its distribution of products throughout the user community. We specifically have suggested that the NTIAC newsletter be circulated to every special task user.

As noted in Figure 26, we found some areas of IAC administration and management that could be improved. For example, it appears that the process of modifying the NTIAC contract for special tasks is not going as smoothly today as it was some time ago. There are several reasons for this; we suspect upon further review of other Information Analysis Centers that the process will be shown to be more bureaucratic, requiring greater attention to regulatory and procedural detail.

It would also appear that NTIAC could benefit from changes in DTIC and DoD policy regarding dissemination of test and evaluation data to DoD IACs. NTIAC reported substantial delay in receiving information which had to be requested through its COTR. While much of this information is not usually released to contractors, it would appear that NTIAC had a very legitimate need for test and evaluation data in order to build and maintain working data bases on materials attributes, test techniques, test equipment, etc. Since NTIAC does not make secondary distribution of any reports for which it is not the author, the unauthorized secondary distribution of data -- the usual objection to release of test and evaluation data -- would appear to be minimal.

Our review of NTIAC identified several areas in the overall IAC program which we have been examining in our present study. These are noted in Figure 26 above. We do believe that NTIAC, like other IACs, should be given broader access to a variety of official U.S. Government documents which describe scientific and technological developments throughout the world. These documents, while not excessively detailed, would be useful in making some very tentative estimates of the need to look at NDE technology in foreign countries.

Finally we observed that NTIAC was experiencing several problems in working with DTIC. Some of these problems seemed small -- e.g. not being able to receive hard copy of material supplied to DTIC via electronic means for several weeks. Others were quite significant, e.g. overwriting bibliographic records in the DROLS system shared with



other IACs. DTIC seemed unable to resolve most of these issues over the period of our pilot study

## **SUMMARY AND CONCLUSIONS**

Figure 27 summarizes the findings and conclusions of our pilot study evaluating a single DoD Information Analysis Center. In our pilot study, we successfully developed and demonstrated an analytical technique which allowed access to information needed to identify benefits offered to DoD and DoD contractors by a single DoD IAC.

---

### **EVALUATION OF DOD INFORMATION ANALYSIS CENTERS**

#### **SUMMARY AND CONCLUSIONS**

- **NTIAC HAS A HIGHLY FAVORABLE BENEFIT COST RATIO**
    - **QUANTIFIED \$14 MILLION IN BENEFITS ON COSTS OF \$4.2 MILLION**
    - **IDENTIFIED OTHER DEFINED BUT UNQUANTIFIED BENEFITS OF PARTICULAR INTEREST TO THE DEPARTMENT OF DEFENSE**
      - **IMPROVED COMBAT READINESS**
      - **IMPROVED TRAINING**
      - **IMPROVED LOGISTICS PROCEDURES**
  - **DEMONSTRATED AN EFFECTIVE STUDY AND ANALYSIS TECHNIQUE**
    - **EXPANDED STUDY TO INCLUDE A REPRESENTATIVE SAMPLE OF DOD IACS**
    - **IDENTIFIED ADDITIONAL BENEFITS TO DOD PROVIDED BY OTHER DOD IACS**
    - **IDENTIFIED IAC PROGRAM MANAGEMENT AND OVERSIGHT PRACTICES WHICH COULD BE CHANGED TO THE BENEFIT OF DOD USERS**
- 

#### **Figure 27: Summary and Conclusions**

In addition we were able to identify specific benefits provided to the NDE community by NTIAC.

We hope that NTIAC's users will find this presentation useful in guiding their response to inquiries from NTIAC and others regarding the utility of NTIAC products and services. We hope that future inquiries about benefits will be received with the same spirit of cooperation as we were received and that the efforts to document NTIAC's support of the DoD NDE community will continue to receive your effective cooperation and support.

FEASIBILITY OF ADAPTIVE CONTROL  
OF AN AUTOMATIC WELDING SYSTEM BY REAL-TIME ULTRASONIC EXAMINATIONS

Paul D. Watson  
Ted A. Mueller  
R. A. Cervantes  
Southwest Research Institute  
San Antonio, Texas

ABSTRACT

This research and development program has established the feasibility of monitoring the molten pool-base metal interface generated during welding operations. The investigation included development and construction of special transducers and shoes to interrogate the localized welding zone. The data acquisition system was configured to obtain the necessary data and subsequent analysis of that data revealed that the interface produces ultrasonic signals of sufficient amplitude to track and measure the depth of weld penetration. In addition, the generation of welding flaws such as inadequate penetration and cracking can be detected shortly after weld pool solidification. The transducer arrangement could be modified to perform weld joint tracking. Using these features, it would be possible to construct an ultrasonic monitoring system to adaptively control the welding variables and to ultrasonically examine the weldment on a pass-by-pass basis which would provide a basis for acceptance/rejection of the welding operation in real-time. The program identified certain difficulties, particularly the changes in sound velocity and attenuation in the high thermal gradient zone, that must be addressed to improve the accuracy of measurement.

1. INTRODUCTION

Recent industry and government goals have put precedence on the development of the technology and techniques to fully automate welding systems. Such systems produce higher reliability weldments and thus reduce costs and increase productivity. The objective of this research project was to determine the feasibility of using real-time ultrasonic examination techniques

to accomplish three major tasks, i.e.:

- 1) Weld quality examination
- 2) Seam tracking and weld penetration monitoring
- 3) Monitor weld bead profile.

The accomplishment of the above tasks would provide the mechanism necessary for real-time adaptive control of the welding system.

## 2. BACKGROUND

In recent years, there has been a major effort in the welding industry to more fully automate certain of the welding processes in an effort to provide higher reliability weldments with increased efficiency, thus increasing productivity. One engineering discipline engaged in this activity is robotics and the associated process controls of vision systems, seam tracking, etc. There is another area of development centered around hard automation. These emerging fields apply adaptive control of the welding process by real-time monitoring of the various parameters.

In-process (real-time) examination of the weldment has a dual potential, i.e., (1) the results of a suitable Non-Destructive Examination (NDE) immediately available after welding is complete and (2) a monitoring device which can provide the information necessary for adaptive control of the welding process.

Ultrasonic Testing (UT) has unique characteristics which can allow its use in real-time.<sup>(1)</sup> The potential for real-time UT examination during the welding operation makes this approach very attractive in that welding flaws formed during any given layer of a multiple pass weld would be immediately detected. This would allow termination of the welding and repair of the flaw prior to deposition of any additional weld metal.

The second potential, i.e., real-time adaptive control of the welding process, has an even larger impact on the welding industry. Mr. L. A. Lott<sup>(2)</sup> has conducted experiments in UT detection of the molten weld metal/base metal interface using both shear wave and longitudinal wave

transducers. He concluded that monitoring this interface could be used to detect the penetration depth and puddle location and would provide information necessary for real-time control of the welding process.

Concurrent work by D. L. Hardt and J. M. Katz<sup>(3)</sup> at MIT came to the same conclusion based on work in detection and measurement of molten pools in cylindrical rods using longitudinal wave transducers. Robert Fenn<sup>(4)</sup> and R. R. Stroud<sup>(5)</sup> in the United Kingdom have been working with the same concept and investigated shear wave and longitudinal wave examination of molten metal interfaces using the submerged arc welding process. Their work led to the development of an ultrasonic monitoring system claiming  $\pm 1$  mm accuracy. Subsequent to Lott's work by EG&G Idaho, Inc., at the Idaho National Engineering Laboratory (INEL), J. A. Johnson and N. M. Carlson<sup>(6)</sup> describe further development in the use of shear waves to examine newly deposited weld metals. Their results show that pattern recognition techniques can be used to characterize the resultant weld and discriminate between different types of flaws. In a subsequent paper<sup>(7)</sup> presented at the 68th Annual AWS Convention in Chicago, March 1987, Carlson and Johnson discussed using pattern recognition techniques on molten pools and developed an algorithm capable of discriminating between acceptable weld pool geometries and those judged to be unacceptable.

All of the investigators have experienced difficulties in the following areas:

- (1) High thermal gradients at the weld-base metal interface causes greater attenuation and velocity changes of the ultrasound.

- (2) The reflected signals are difficult to interpret due to a small signal-to-noise ratio.
- (3) Sophisticated data acquisition equipment is necessary to obtain the information necessary for subsequent analysis.

### 3. PROGRAM RESULTS

The program was initiated in August 1985 and work progressed through February 1987. Several iterations of the experimental program and equipment were necessary to obtain the desired results.

#### 3.1 INITIAL TRIALS

Initial welding trials disclosed that the signals returning from the molten pool interface displayed a small signal-to-noise ratio and thus amplification of the signals was necessary. These trials also indicated that the signals were best transmitted and received using a 5 MHz shear wave transducer at 40° and that a temperature-resistant material (Vespel SP-1) was necessary for the transducer shoe. A video camera was used to record the UT instrument display for subsequent playback in slow motion and stop action allowing more accurate analysis of the signals. Two new 5 MHz, high sensitivity, highly damped transducers were designed and fabricated to increase the signal-to-noise ratio and produce a much more sensitive response.

The test sequence was to produce a small notch in the plate surface and peak the UT signal on that notch. The welding torch was positioned directly over the notch and the arc initiated. Immediate melting obliterated the notch which eliminated the UT signal. Power was increased

until a molten pool was established. UT signals appeared on the oscilloscope at a position closer in time than the previously established notch position. This was clearly the molten weld pool interface. As the plate heated up, that signal shifted out in time due to sound velocity change. Both pulse-echo and RF wave forms were monitored. The audio-video system recorded the signals with voice commentary on arc initiation, power settings, gain settings, etc. Replay of the resultant tape was made in slow-motion and stop-action to analyze the signals. Measurement of the signal position of the molten pool and the notch was possible.

The next series of tests was performed on a moving arc. The signals were clear and were recorded. Cross-sectioning of the weld after recording allowed measurement of the puddle depth at 0.175 to 0.185 inches and analysis of the video tape yielded a measurement of 0.16 to 0.20 from signal spacing. It must be noted that these are dynamic signals and are moving across the screen and changing in amplitude due to velocity and attenuation changes caused by temperature increases and, thus, precise selection of the desired signal was difficult.

The video-recorded signals of the preliminary tests were adequate for the purpose of establishing the existence of the molten metal interface. However, it was decided that a transient recorder should be used to capture the data in digital form for subsequent analysis.

#### 3.2 DATA ACQUISITION SYSTEM

A Nicolet Model 204A transient recorder with a Model 2090 III oscilloscope and a 2081 interface was married to a Hewlett

Packard Model 9000-217 computer with appropriate disk drives and printer. The new hardware configuration allowed the acquisition of waveforms with 50 nano second sample rate. Once acquired, the waveforms can be stored at a rate of three per second.

Software was written to control the Nicolet digitizer to capture the UT waveforms during the welding process. The Nicolet digitizes the waveform and transfers it to the HP computer which stores the data in its memory. The software was written to capture 64 waveforms at a maximum rate of three waveforms per second. The time interval between waveforms can be increased if coverage over a longer period of time is required. Additional software was written to display the waveform data in a hidden line form on the monochrome CRT with the ability to transfer the image to the printer for hardcopy.

The ultrasonic instrumentation consists of a Tektronix 465 oscilloscope with an MP-215 pulser and an MR 101 receiver. The special 5 MHz transducers and heat-resistant shoes provide enhanced sensitivity of the examination. The previously assembled audio-visual system was utilized to record all welding trials.

### 3.3 STATIC WELDING TESTS

Welding trials were reinitiated and static welds were made on preplaced notches as in previous trials. The signals from the molten weld pool were recorded by the new data acquisition system as well as the video system. Analysis of these test results indicated that the molten weld pool could be monitored from initiation of melting through full molten pool development. Test Numbers 101, 102, and 103 were made with welding amperage of 185,

160, and 135 amperes, respectively. This was intended to produce welding pools of varying penetration to test accuracy of the UT system.

The digital UT data was analyzed to determine the depth of the molten pool. The data was acquired in the following manner:

- (a) A long shallow notch was placed in a 0.75 inch steel plate. The notch served as a strong UT reflector and is used as a reference point.
- (b) A UT waveform of the notch was recorded before the welding was started. This waveform serves as a reference of the location of the surface with the plate cold.
- (c) The welding arc was initiated and the data acquisition was started with waveforms being acquired at the rate of three per second. Sixty-two waveforms were recorded.
- (d) Immediately after the welding process was stopped, another UT waveform is recorded of the reference notch with the plate in hot condition so that the velocity changes due to temperature increase can be recorded.

Figures 1, and 2 represent the graphic plots of Tests 101, 102 and 103. The front signal (indicated in Figure 1) represents the cold notch signal. The back (last) signal represents the hot notch signal after weld termination. The signals to the left of the graphs represent the molten pool interface. Note that the cold notch signal rapidly decreases in amplitude and shifts to the right as the welding pool increases in size. The presence of any signal from the notch

as fusion takes place is due to beam spread which detects the notch on either side of the molten pool. The shift to the right (further out in time) is due to heat-up of the plate. The distance (in microseconds) between the interface signal and the hot notch signal is directly proportional to the "B" dimension shown in Figure 1. The same dimension can be taken directly from the video display which is calibrated in inches of metal path.

To augment the monochrome display, a program was written to transfer the waveform data to the Division 17 SUN System for color display. This takes advantage of existing software for the display of waveform data which uses color as the amplitude dimension for display. In addition, this display allows selection of a single waveform of the 64 recorded waveforms. The waveform at the beginning of the test (cold plate) is zero and the final waveform (No. 64) is the hot notch at the end of the test. Each waveform has a time base of 50 nano seconds (sample rate) and, thus, the information can be used to calculate the hot velocity ( $V_h$ ) for each welding test as follows:

$$V_h = MP \div (T_c + \Delta T)$$

where:

$V_h$  = Average Hot Velocity in inches per  $\mu$  sec

MP = Metal Path (one way)

$T_c$  = Time required for one way MP in the cold condition in  $\mu$  sec

$\Delta T$  = Difference in time between hot and cold notch - one way.

$V_h$  averaged 0.123 inches per  $\mu$  second. The weld pool depth is then calculated by determining the total difference in time between the hot notch and the interface signal as  $\Delta T_p \div 2$  (one way) and multiplying by  $V_h$ .

Comparison of Tests 101, 102, and 103 were taken from welds made at 185, 160 and 135 amperes, respectively and clearly show that the separation of the molten pool signal and the notch signal are progressively less for lower amperages. Thus, the penetration depth is measured smaller for the lower amperage welds.

Welding pool depth was calculated from the video and digital data using the location of the notch on the hot plate as an average velocity reference for the calculation. Table I is a listing of the depths in the "B" dimension as calculated from the data.

The data from the digital display agrees very well with the data from the video, however, the data from the sectioning of the welds did not agree with the digital and video recorded UT data. Two possible explanations for the difference in the observed UT results and the sectioning data are:

- (a) Change in the referenced angle due to the increased temperature of the welding process.
- (b) A curved UT sound path due to the temperature gradient in the material between the molten pool and the search unit.

The first possibility has been investigated and the change in metal path due to a change in refracted angle has been calculated along with the velocity in steel necessary to produce the refraction change.

Based on the location of the hot plate reference notch, the average velocity in steel of the hot plate was calculated at  $1.23 \times 10^{-5}$  inches/sec. This would

amount to a refracted angle change of over one degree with a change in metal path of over 0.030 from the cold refracted angle. The shorter metal path, due to the change in refracted angle, would tend to make the pool depth appear smaller than its real dimension and, thus, account for some of the observed error. At this time, the effects of UT beam curve due to temperature gradient has not been investigated.

### 3.4 DYNAMIC WELDING TESTS

A method was established that allows tracking of a moving welding arc with the transducer. Dynamic welding tests were run under the same data acquisition method as the static test. Movement of the welding head along the notch was at a speed of 2.5 inches/minute. Waveform data was acquired from the cold reference notch followed by 62 waveforms taken after the welding process was started and completed by the acquisition of a hot reference waveform immediately after the completion of the welding pass. The data was analyzed and the pool depths ("B" dimension) were calculated from the digital UT data and the video data. Metallographic cross-sections were measured for molten pool depth. Table II shows the results of these tests.

Figure 3 shows the graphic plots for Tests 125, 128 and 129 welded at 185, 160 and 135 amperes, respectively. Figure 4 shows the photomicrographs of the solidified weld pool. The "B" dimension of the molten pool was measured from these photographs.

A review of the figures reveals that the data acquisition system is capable of recording the desired information in both the static as well as the dynamic welding modes. The difficulty is in the present accuracy of these measurements. A review

of the two tables shows undersizing the molten pool by approximately 0.060 inches and this error is very consistent from test to test in both static and dynamic modes. It is believed that the error is a combination of several smaller errors as follows:

- (a) The refracted angle of the transducer changes as the plate heats up which re-directs the ultrasound to a shallower portion of the weld. Further, the velocity of sound changes which affects the distance calibration of the UT instrument.
- (b) There is the probability that the sharp thermal gradients near the molten pool would cause curving of the sound path.
- (c) Ultrasonic beam spread over the two-inch metal path does not allow measurement at discrete points. Thus, the reflected signals are likely to be averages over an area of the molten pool interface whereas the metallographic measurements are at discrete points.
- (d) Hot notch measurements are taken as quickly as possible after arc termination, however, some recovery (cooldown) is bound to occur prior to that measurement.

### 3.5 FINAL WELDING TRIALS

In light of the inaccuracy of the measurements, a series of tests were conducted in an effort to refine the data acquisition and investigation. These included introducing two notches close together and welding on the ligament between. This effort was to determine the velocity changes with more accuracy, but the results were

inconclusive. However, it was noted that recovery, i.e.; shift to the left (shorter metal path) of the hot notch, was very rapid after arc termination. This accounts for some of the inaccuracy in undersizing the puddle depth. In addition, it was discovered that maximizing the signal at the notch corner in the cold condition and then scanning forward during welding produced stronger and more widely spaced signals. This is surmised to be caused by the change in angle accompanying the welding heat which would require a forward scan to intersect the puddle at a normal (cold) location. The data acquisition system was not used for these tests.

The very high gain settings utilized in these tests allow resolution of the non-metallic inclusions (plate flaws) within the carbon steel plate. A notch was milled in the plate surface which was 0.06 inch wide by 0.1 inch deep. The notched plate was scanned to locate an area displaying such plate flaws that were located on the maximized notch sound beam path. Figure 5 is a graphic reproduction of the rationale behind these tests. Note that the position of the transducer is set to maximize the corner reflector of the notch. The satellite pulse is shorter in metal path and the signal appears closer in time. The plate flaw is selected to fall within the beam path at a location only slightly removed from the expected molten pool depth. Thus, the plate flaw will be very close to the molten pool and be subjected to very high temperatures. The resultant UT signal from this flaw should be a good gage of hot velocity changes during welding.

Welding Tests No. 173 through 176 were performed with plate flaw(s) in the beam path. The resultant digital plots, SUN displays, and video images were analyzed

to determine the hot velocity and weld pool depths. The  $V_h$  calculations using the hot notch averaged 0.122-inch per  $\mu$  sec. There was more scatter in  $V_h$  calculations using the plate flaws due to the varying distance from the molten pool, however,  $V_h$  varied from 0.120 to 0.123 inch per  $\mu$  sec. The subsequent calculations for puddle depth used  $V_h$  as 0.122-inch per  $\mu$  sec. Each weld was sectioned at the centerline, etched and the actual puddle depth measured. Table III summarizes the testing performed in this series.

A review of the Table III information shows that the data from each of the three methods of calculation, i.e.; video image, digital plot and SUN display are in general agreement. Test 173 was conducted at 160 amps producing a puddle depth of 0.181 inches and was undersized an average of 0.028 inches. Test No. 174 was welded at 130 amps and was undersized an average of 0.027 inches. Test No. 175 was welded at 180 amps and was oversized in one case and undersized in the other five calculations. The average error was only 0.009 inches. Test No. 176 was welded at 180 amps and the results were similar to Test 175 with an average error of 0.003 inches.

Figure 6 shows the metallographic cross section of Test Numbers 175 and 176. The flaw positions are marked and the "B" dimension shown in ink. Note that the flaws fall directly on the notch corner intercept line and is nearly at the fusion zone. Test 176 contained three different plate flaws near the weld pool. Figure 7 is the digital plot of this test which shows the three flaws. The flaw closest to the notch was consumed by the molten pool. The next closest flaw is very near the fusion line and the third is on the



edge of the heat affected zone. Note that Figure 6 indicates a centerline fracture at the weld nugget. This is caused by rapid cooldown and the presence of the notch at each edge. The last signals received after arc termination and solidification are representative of these cracks and can be clearly shown on the video records. The hot signals include the unconsumed plate flaws, and the crack intersection with the plate surface. These signals are apparent in each of Test No.'s 173 through 176 and verify that welding flaws can be detected immediately after solidification.

#### 4. CONCLUSIONS

The program was initially intended to investigate the feasibility of adaptive control of welding systems using real-time ultrasonic examination techniques. Task I was to study the ultrasonic response to weld pool penetration characteristics. The investigators performed a total of 177 welding trials to that end. These tests necessitated development and construction of appropriate ultrasonic transducers, identification of an appropriate data acquisition system, including the ultrasonic equipment, transient recorders, computer data processing and appropriate software and specialized data presentation and analysis. Unfortunately, the task I effort expended the funds available and the intended investigations of Task II, weld quality, and Task III, weld profile, were not formally addressed. There were, however, individual welding tests in Task I that indicated that weld quality can be determined shortly after solidification of the weld bead.

Based upon the results of this work, the following conclusions can be made:

- (1) The base metal-molten metal interface produced during welding can be detected by using ultrasonic examination techniques.
- (2) The position of the molten metal interface can be determined with reasonable accuracy.
- (3) The position of the sidewall of the weld joint relative to the transducer can be located accurately and there is strong evidence that this could be used as a seam tracking device.
- (4) Weld quality can be monitored shortly after solidification. This has been demonstrated during the static weld tests, many of which produced centerline cracks upon solidification. Figure 1 (Test No. 101) is an example, and review of the video tape disclosed a very strong signal being reflected from that crack immediately after solidification. The dynamic tests did not produce this cracking and, thus, no signals were detected.
- (5) Feasibility of the use of ultrasonics to adaptively control an automatic welding system has been established.

#### 5. RECOMMENDATIONS

A review of the results will reveal that the monitoring of molten pools, i.e.; weld penetration, needs further development in the following areas:

- (1) Design and construct appropriate transducer positioning equipment that will allow controlled movement with three degrees of freedom and join that equipment to the welding torch. This will produce more controlled

experiments during arc movement down the weld joint.

- (2) Conduct a series of experiments that more fully define the capabilities of flaw detection in real-time. This would involve deliberate generation of flaws such as hot cracking, inadequate penetration and incomplete fusion.
- (3) Conduct a series of experiments that more fully define the capabilities of weld bead profile monitoring.
- (4) Development of an algorithm to compensate for, or compute, the effects of increased temperature near the molten pool and the even greater changes experienced in the heat affected zone. This includes both sound velocity changes and refracted angle changes.
- (5) Design and conduct experiments that will verify the algorithm.
- (6) Investigate the use of focused transducers to more precisely locate discrete points on the molten interface.
- (7) Investigate the use of phased array (multiple) transducers to interrogate the molten pool with multiple angles.
- (8) Identify the problems associated with data acquisition and signal processing in real-time for adaptive control of the welding system.

#### REFERENCES

- (1) Grothues, H.L., Southwest Research Institute Project 17-9336, "Search Unit Tracking and Recording System - Real Time Processing and Display," Final Report, June 1984.
- (2) Lott, L. A., "Ultrasonic Detection of Molten/Solid Interfaces of Weld Pools," Materials Evaluation, Vol. 42, March 1984.
- (3) Hardt, D. E., and Katz, J. M., "Ultrasonic Measurement of Weld Penetration," Welding Research Supplement, Welding Journal, September 1984.
- (4) Fenn, R., "Ultrasonic Monitoring and Control During Arc Welding," Welding Journal, September 1985.
- (5) Fenn, R., and Stroud, R., "Development of an Ultrasonically Sensed Penetration Controller and Scan Tracking System for Welding Robots," Paper C471/84, UK Robotics Research 1984, London, December 1984.
- (6) Johnson, J. A., and Carlson, N. M., "Weld Energy Reduction by Using Concurrent Nondestructive Evaluation," NDT International, Vol. 19, No. 2, June 1986.
- (7) Carlson, N. M., and Johnson, J. A., "Ultrasonic Sensing of Weld Pool Penetration," Welding Research Supplement, Welding Journal, November 1988.

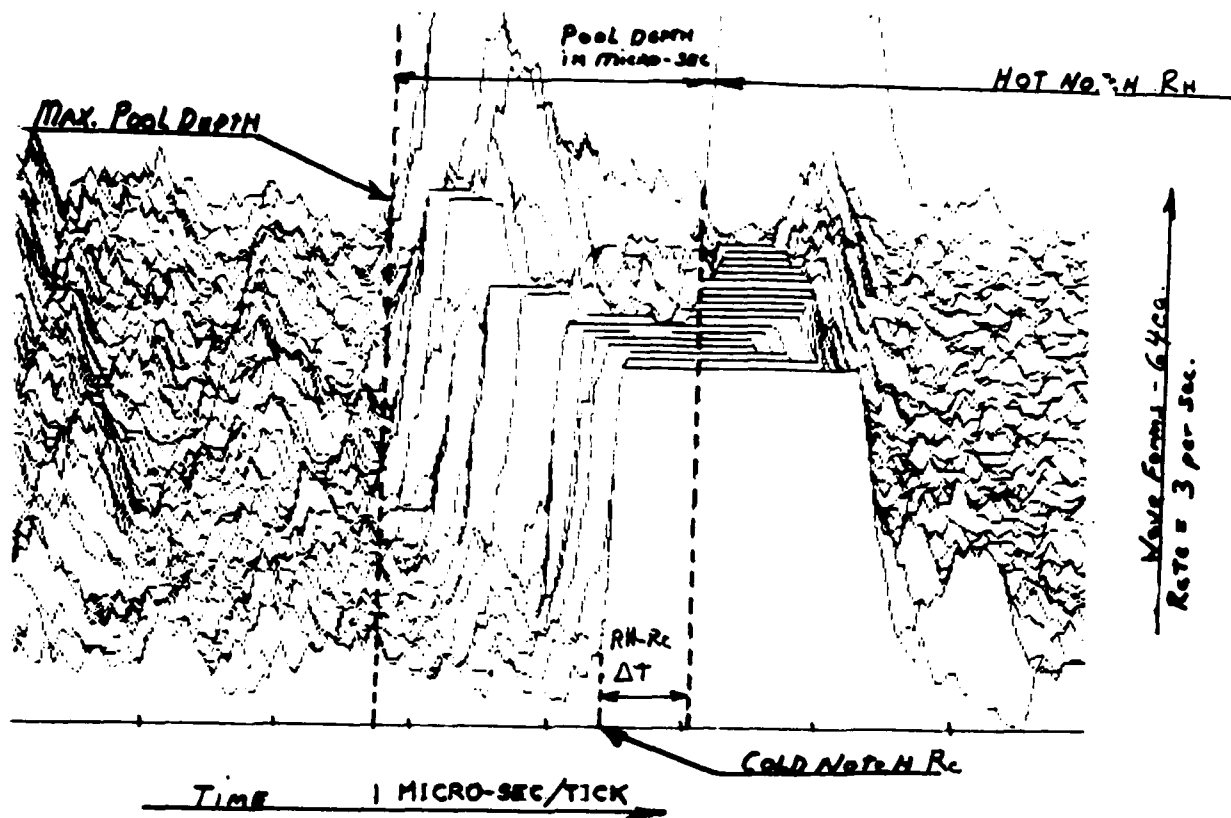
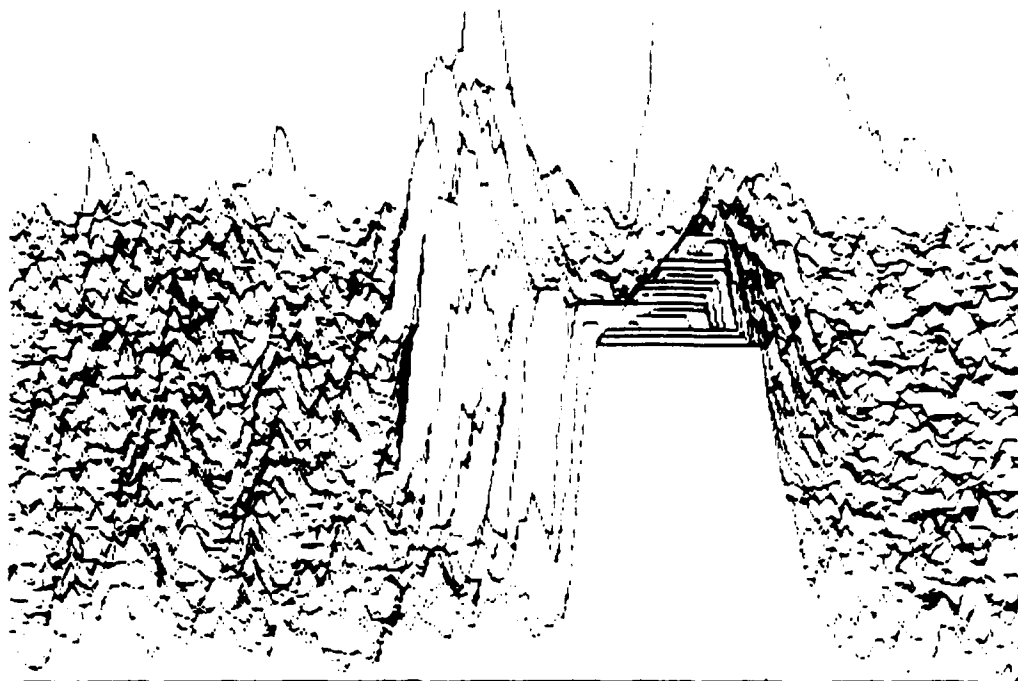


FIGURE 1  
DIGITAL PLOT AND PHOTOMICROGRAPHS OF TEST NO. 101 AT 185 AMPERS

TEST 102  
165 AMP



TEST 103  
135 AMP

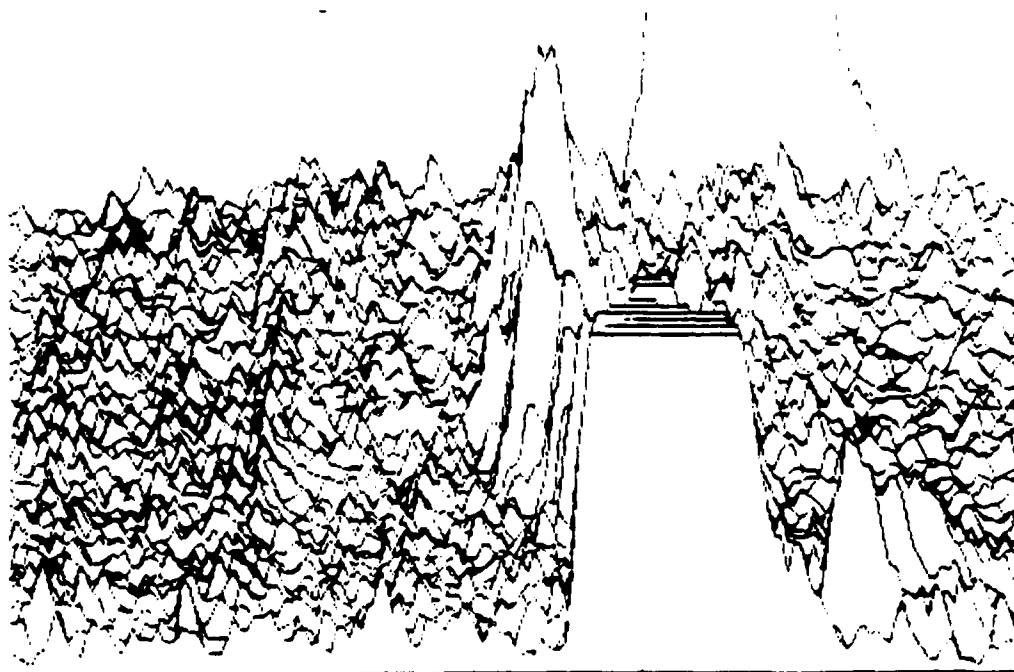
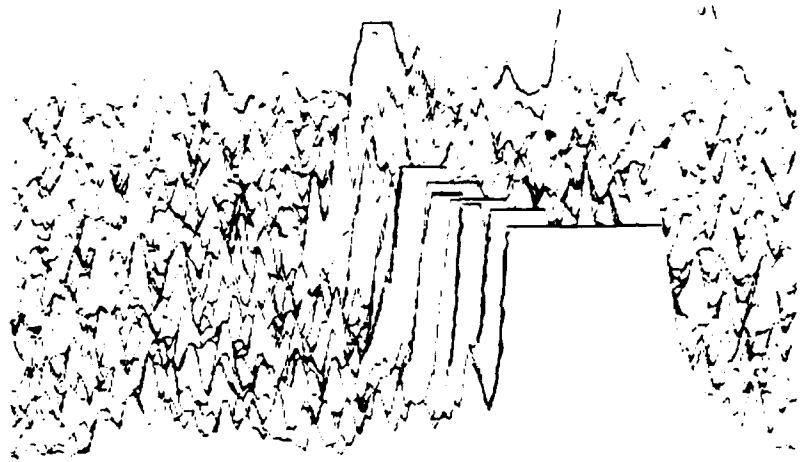
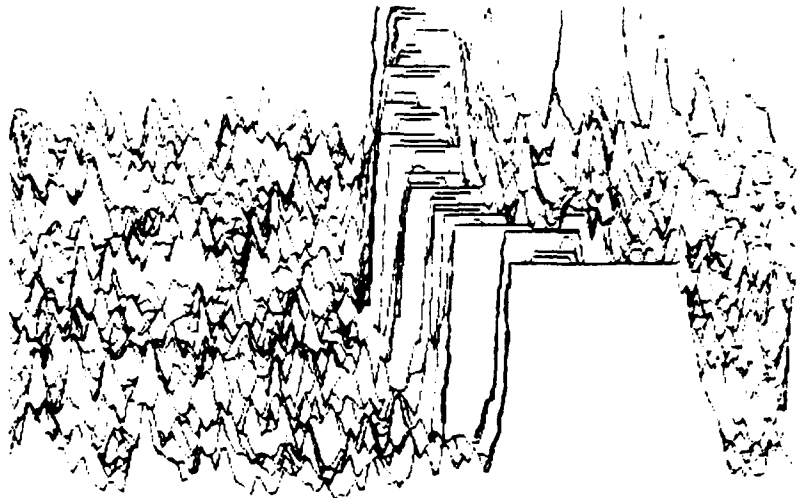


FIGURE 2  
DIGITAL PLOTS OF TEST NO'S 102 AND 103 REDUCED TO 80% FOR REPRODUCTION

TEST 125



TEST 128



TEST 129

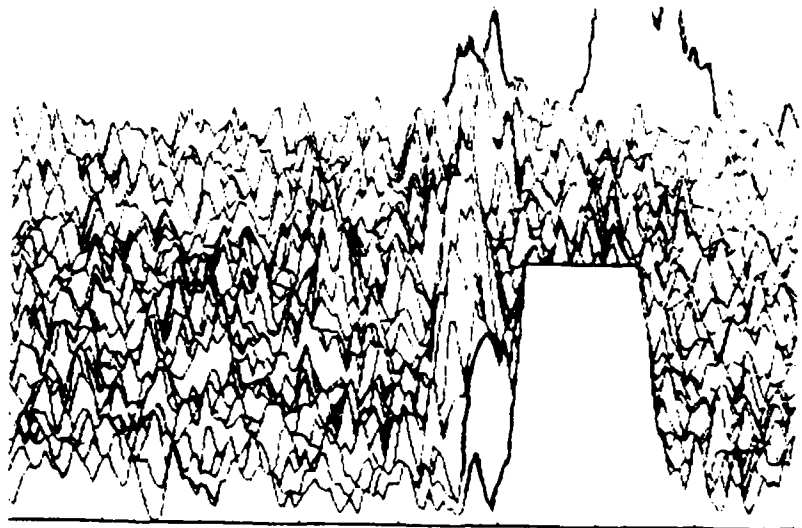
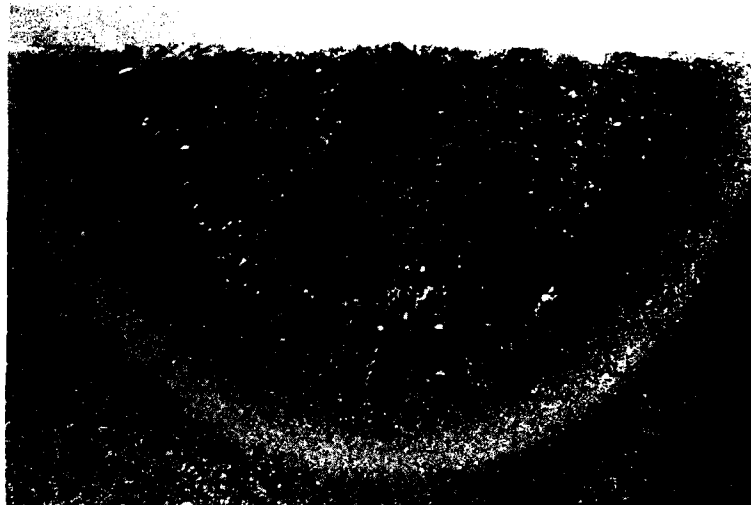
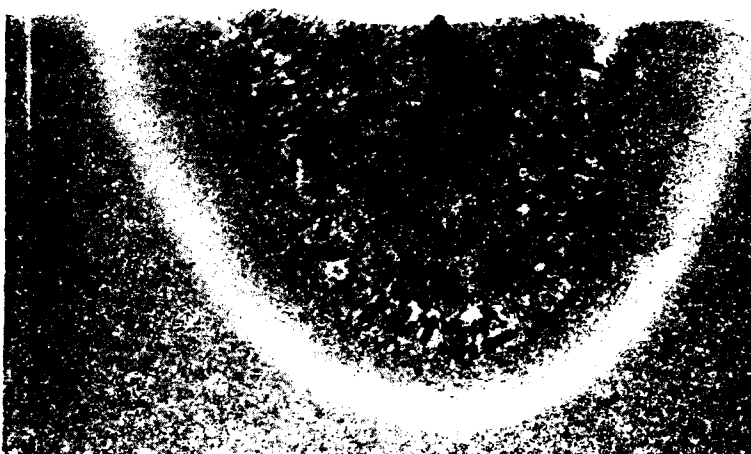


FIGURE 3  
DIGITAL PLOTS FOR TEST NO'S 125, 128 AND 129, WELDED AT 183, 160 AND  
130 AMPERS, RESPECTIVELY. DYNAMIC WELD AT 2.5 INCH PER MINUTE



TEST 125  
B = 0.194



TEST 128  
B = 0.178



TEST 129  
B = 0.156

FIGURE 4  
PHOTOMACROGRAPHS OF TEST NO'S 125, 128 AND 129, WELDED AT 185, 160 AND  
130 AMPERS, RESPECTIVELY

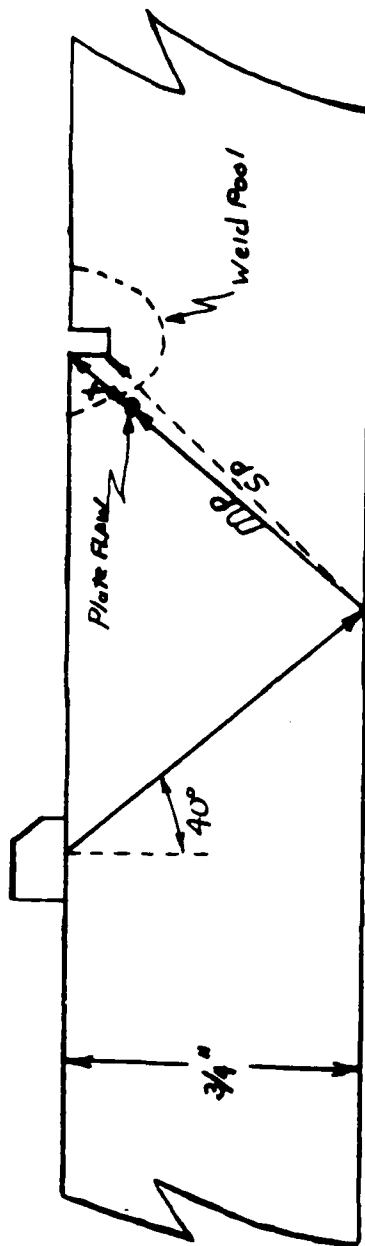
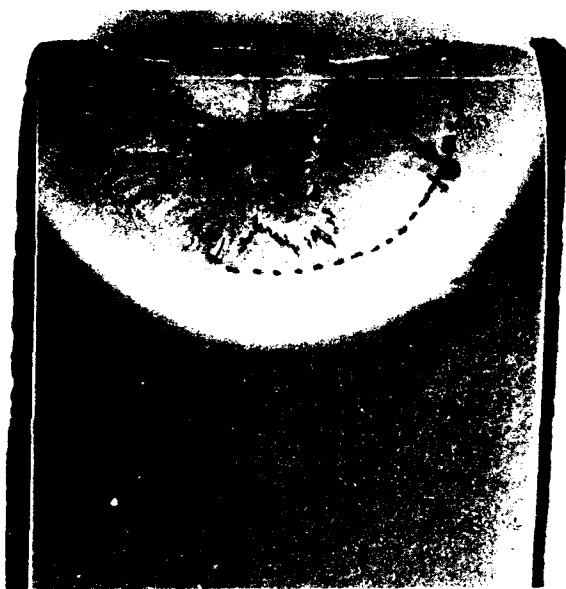


FIGURE 5. SKETCH OF THE CALIBRATION CONFIGURATION FOR TEST NO.'S 173 THROUGH 176.  
 THE 40 DEGREE ANGLE BEAM TRANSDUCER ESTABLISHES THE NOTCH CORNER AT A METAL PATH (MP) OF 1.958 INCHES.  
 THE PLATE FLAW MP ESTABLISHES DISTANCE "X", I.E.,  $MP_M - MP_P$ . THE BOTTOM OF THE NOTCH PRODUCES A SATELLITE PULSE SIGNAL WHICH IS PROPORTIONAL TO THE DEPTH OF THE NOTCH.



CROSS-SECTION OF TEST NO. 175  
SHOWING FUSION ZONE AND FLAW  
LOCATION. THE UT BEAM PATH  
WAS FROM THE RIGHT SIDE.

5X



CROSS-SECTION OF TEST NO. 176  
SHOWING FUSION ZONE AND FLAW  
LOCATION(S). THE UT BEAM PATH  
WAS FROM THE LEFT SIDE AND THE  
PREVIOUS NOTCH POSITION IS SHOWN.

5X

FIGURE 6  
PHOTOMICROGRAPHS OF TEST NO'S 175 AND 176



TEST 176 FLAW IN PLATE REPEAT OF 180 AMP TEST  
16 Dec 1966 11:35:30 DELTA-T = .292

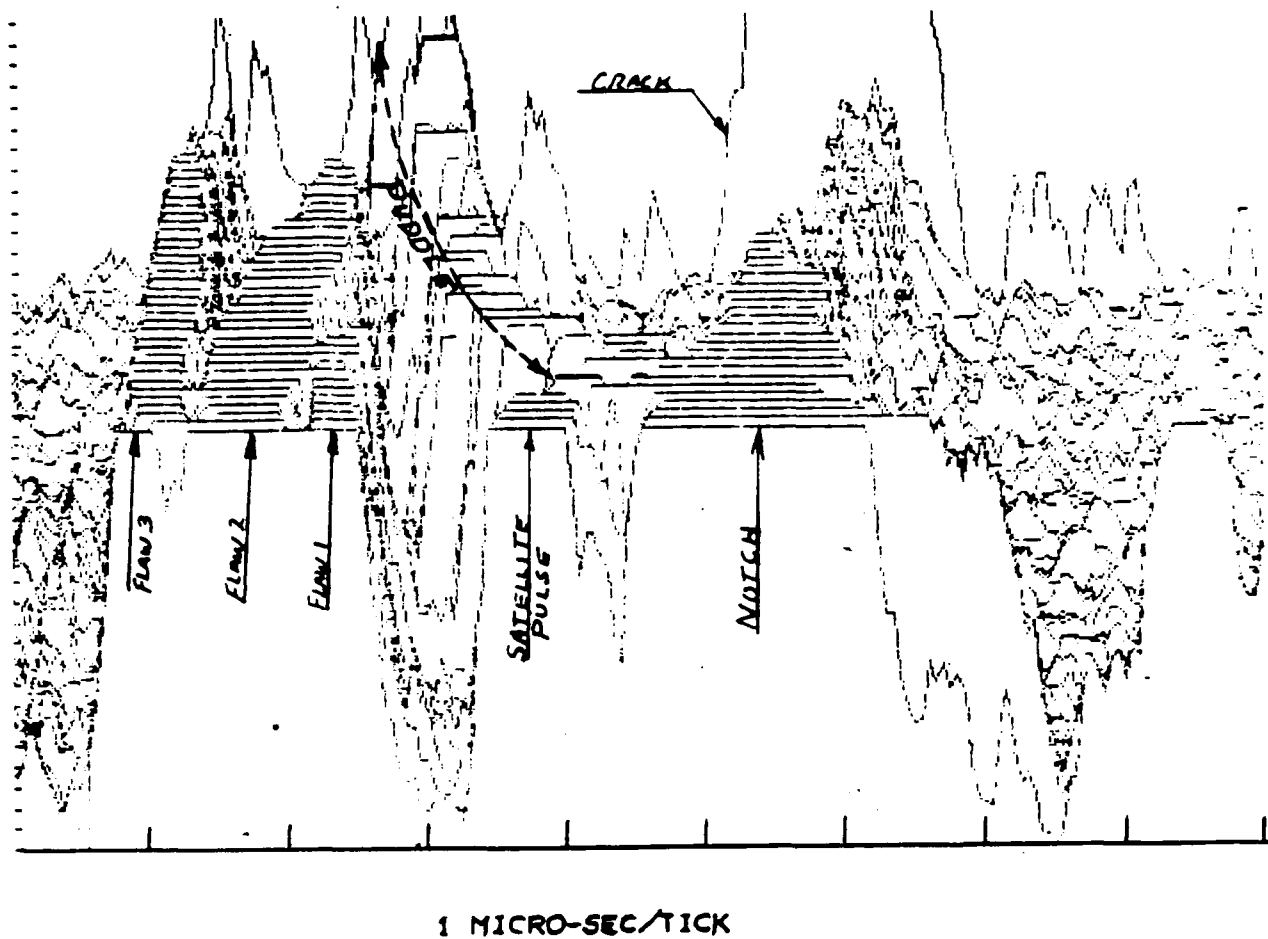


FIGURE 7  
DIGITAL PLOT OF TEST NO. 176 SHOWING NOTCH,  
SATELLITE PULSE FROM THE BASE OF THE NOTCH,  
THREE PLATE FLAWS AND A COOLDOWN CRACK

TABLE I  
CALCULATED FUSION DEPTH VERSUS MEASURED DEPTH

POOL DEPTH IN INCHES (B DIMENSION)

<u>TEST NO.</u>	<u>AMPS</u>	<u>UT (DIGITAL)</u>	<u>UT (VIDEO)</u>	<u>SECTIONING</u>	<u>AVE. ERROR</u>
100	185	.13	.133	.190	.059
101	185	.14	.127	.190	.057
102	165	.11	.102	.160	.054
103	135	.07	.064	.155	.088
106	200	.13	.114	.190	.086
108	185 <sup>(1)</sup>	.14	.127	.190	.057

NOTE: <sup>(1)</sup>DYNAMIC TEST

TABLE II  
CALCULATED FUSION DEPTH VERSUS MEASURED DEPTH

POOL DEPTH IN INCHES (B DIMENSION)

<u>TEST NO. (1)</u>	<u>AMPS</u>	<u>DIGITAL UT (2)</u>	<u>VIDEO UT</u>	<u>SECTIONING</u>	<u>AVG. ERROR</u>
125	185	.128	.128	.194	.066
128	160	.118	.115	.178	.062
129	130	.098	.083	.156	.067

NOTES: <sup>(1)</sup>ALL TESTS ARE DYNAMIC AT 2.5 INCH/MINUTE TRAVEL.

<sup>(2)</sup>DIGITAL CALCULATIONS MADE WITH  $V_h = 0.123$  INCH/MICROSECOND.

TABLE III  
CALCULATED FUSION DEPTH VERSUS MEASURED DEPTH

POOL DEPTH (1)

<u>TEST NO.</u>	<u>AMPS</u>	<u>VIDEO</u>		<u>DIGITAL PLOT</u>		<u>DIGITAL SUM</u>		<u>METALLOGRAPHIC (2)</u>
		<u>HN</u>	<u>HF</u>	<u>HN</u>	<u>HF</u>	<u>HN</u>	<u>HF</u>	
173	160	.152	.146	.148	.165	--	--	.181
174	130	.140	.121	.138	.111	--	--	.154
175	180	.216	.191	.196	.160	.183	.192	.199
176	180	.216	.203	.217	.182	.195	.192	.204

NOTES: <sup>(1)</sup> HN IS MEASUREMENTS BASED ON HOT NOTCH VELOCITY DATA AND HF IS BASED ON HOT FLAW VELOCITY DATA.

<sup>(2)</sup> "B" DIMENSION ALONG A PATH TO THE NOTCH CORNER.

# **SIZING CRACKS IN THIN-WALLED CANDU REACTOR PRESSURE TUBES USING CRACK-TIP DIFFRACTION**

K.-E. Lindenschmidt\*, M.D.C. Moles\* and A.N. Sinclair\*\*

\* Nondestructive and Fracture Evaluation Section  
Metallurgical Research Dept., Ontario Hydro Research  
800 Kipling Ave., Toronto, Ontario, Canada, M8Z 5S4

\*\* University of Toronto, Dept. of Mechanical Engineering  
5 King's College Rd., Toronto, Ontario, Canada, M5S 1A4

## **ABSTRACT**

The most practical nondestructive means of measuring the depth of cracks approximately 0.4 mm deep in CANDU reactor pressure tubes is the ultrasonic crack-tip diffraction method. Initially, optimum ultrasonic parameters for wave mode, transducer frequency, main-bang pulse characteristics, incident and diffracted angles were obtained on three fatigue cracks, based on the criteria of maximum signal amplitude and accuracy in determination of crack depth. In addition, three signal processing techniques, auto and cross-correlation, rectification and smoothing and the magnitude of the analytic signal, were used to obtain time measurements. Except for the first fatigue crack, the depth calculations were accurate to within the specified range of  $\pm 0.1$  mm. The optimum signal parameters determined from the fatigue cracks were used to measure the cracks in laboratory hydride blisters cracked under four-point bending. The measurements came within the error range of  $\pm 0.1$  mm for cracks measuring 0.38 and 0.54 mm.

## **1. INTRODUCTION**

The CANDU (Canadian Deuterium Uranium) nuclear reactor core contains several hundred horizontal pressure tubes which hold uranium fuel bundles. Heavy water is pumped through the pressure tubes where it is heated to a temperature of

approximately 300°C before it is passed to the steam generators. A pressure tube, shown in Figure 1, is made of a Zirconium - 2.5 wt.% Niobium alloy. The tube is six meters in length with an inside diameter of 103 mm and a wall thickness of 4.2 mm. The pressure tube is housed by another zirconium alloy

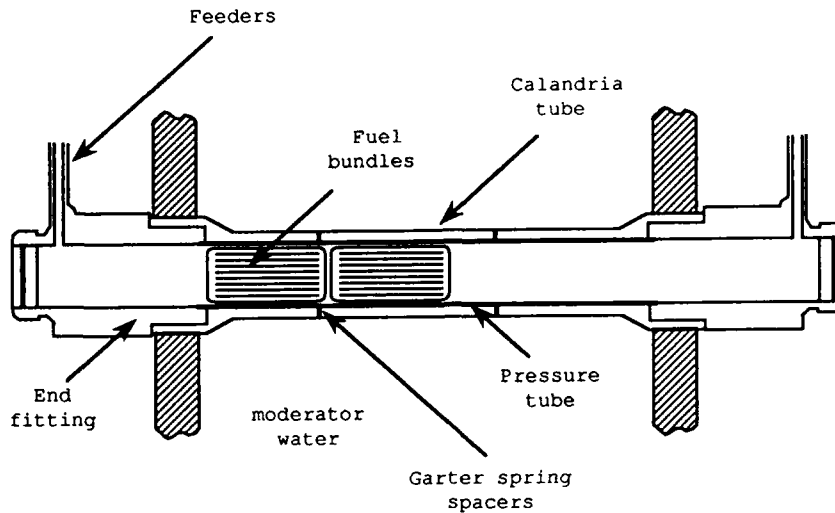


FIGURE 1: Fuel channel consisting of a Zr-Nb pressure tube.

tube, the calandria tube, which isolates the pressure tube from the surrounding moderator water environment contained in the reactor vessel. The two tubes are separated by garter spring spacers. The gap between the two tubes is filled with an inert gas to insulate the high temperature pressure tube from the cooler temperature calandria tube.

The research presented here is geared to measure the depths of cracks in hydride blisters, which are pockets of accumulated hydride platelets. They are extremely brittle and allow for easy crack initiation. Hydride blisters usually form on the outside surface of the pressure tube due to the pressure tube sagging and coming in contact with the outside calandria tube. This forms a temperature gradient to where hydrogen, produced from the oxidation of the zirconium, migrates<sup>(1)</sup>. This forms a high concentration area of hydrogen and the resulting hydrogen embrittlement.

A remote automated inspection system called CIGAR (Channel Inspection and Gauging Apparatus for Reactors) has been design by Ontario Hydro. CIGAR uses ultrasonic angled probes in a pulse-echo configuration to detect defects in the tube. Currently, only the length of a crack can be measured. There is no accurate means of determining the depth of a crack.

Various specifications must be kept in mind in developing a crack depth measurement technique:

- (1) the technique has to measure crack depths 0.4 mm or greater with a maximum error of 0.1 mm;
- (2) the depth measurements must be made via the CIGAR system since it is the only inspection mechanism available for reactor tube inspections;
- (3) the measurements are to be made ultrasonically due to the restrictions of the high radiation and high temperature environment;
- (4) the measurements must be made from the inside of the tubes. Access to the outer tube wall is

blocked by the calandria tube and moderator.

There are a number of possible ultrasonic techniques for measuring radial defect depths in thin-walled pressure tubes. Direct measurements of amplitude have been used for sizing but are very subject to defect parameters such as crack orientation, transparency and roughness. Decibel drop-off techniques suffer similar deficiencies.

Attempts to detect crack tips using only one normal beam or focused angle beam transducer have generally not been successful since signal amplitudes from crack-tips are so low, it is difficult to differentiate the tip echo from the noise<sup>(2)</sup>. Shadowing techniques have been used but are subject to errors from multiple cracking, orientation and transparency factors. Surface or creeping wave techniques are possibilities but are likely to suffer from the natural variations in blister cracking patterns.

The most promising ultrasonic technique is the crack-tip diffraction method which uses two transducers, one as the transmitter and the other as the receiver. The signal-to-noise ratio is higher than for any of the aforementioned techniques<sup>(2)</sup>.

## 2. CRACK-TIP DIFFRACTION

### 2.1 PRINCIPLE

The crack-tip diffraction technique, illustrated in Figure 2, is a two probe method with both pulser and receiver probes angled with respect to the surface.  $\eta$  represents the measured angles. The probes lie on opposite

sides of the defect plane but on the same side of the test sample. Defects can be embedded or break either surface. The ultrasonic beam strikes the defect, which reflects, absorbs, transmits, mode converts and diffracts the beam. The tips of the defect, which are typically much thinner than the ultrasound wavelength, diffract ultrasound and radiate rays like a tuning fork radiates sound waves. These crack-tip diffracted rays are very directional with the amplitudes a function of the ultrasound beam angle and frequency, and crack parameters, particularly orientation and transparency.

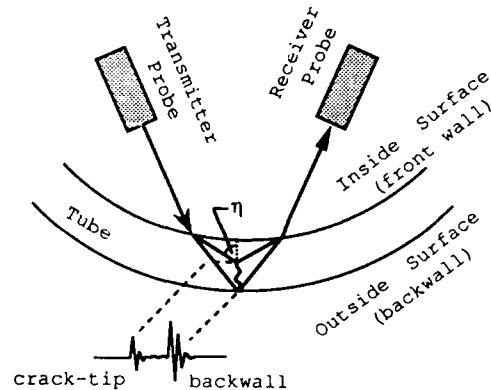


FIGURE 2: The crack-tip diffraction method.

The difference in time-of-flight between the crack-tip echo signal and the echo from the crack base is used to determine crack depth. This is done by considering wave velocity and the geometry of the probes and the defect. In pressure tubes, blister crack depths are measured relative to the tube backwall. Since time-of-flight can be measured to considerable accuracy, crack-tip diffraction permits the reproducibility and accurate measurement of crack depths, in principle. Unfortunately, crack-tip signals are very

weak, often around the noise level and thus can be easily missed.

## 2.2 PREVIOUS WORK ON CRACK-TIP DIFFRACTION

The earliest practical work on ultrasonic diffraction was the Delta technique, a special case of the dual probe pitch-catch technique with the receiver probe set at  $0^\circ$  ie. in the plane of the defect, developed by Posakony and Cross<sup>(3)</sup>. Despite the apparent potential of the technique, little follow-up research was performed, with a few exceptions<sup>(4)</sup>. The current interest in crack-tip diffraction started from work by Böttcher et al<sup>(5)</sup> where diffracted rays from crack-tips were mistaken for scattering from grain boundaries. This work prompted Silk and Lidington<sup>(6)</sup> to perform more work on sizing notches using time-of-flight techniques. Their work was extended to fatigue cracks with considerable success in the sizing of these defects<sup>(7)</sup>.

The work by Silk and Lidington<sup>(6)</sup> <sup>(7)</sup> initiated the development of a commercial system, called Zipscan, for measuring defect depths in thick-walled vessels. The original Zipscan system used low frequency probes (about 2 MHz) primarily in contact mode for reactor pressure vessels. Zipscan used  $45^\circ$  longitudinal waves with signal averaging to improve signal-to-noise ratio, synthetic aperture focusing and image correction. More recently, an off-shore model for oil rigs has been developed, and a number of probe configurations are possible.

The development of the technology includes optimizing the method to obtain the best accuracy of the depth calcu-

lations and the greatest signal-to-noise ratio. Parameters affecting the optimization are flight-path geometry, ultrasonic wave mode and defect characteristics. Research by Silk and Lidington<sup>(8)</sup>, Golan<sup>(9)</sup> <sup>(10)</sup> and Temple<sup>(11)</sup> have applied the technique to varying defect depths, probe separations, transmitted and received beam angles and test specimen thicknesses. Ultrasonic waves of various waves - longitudinal, transverse, and surface - and combinations of waves were also investigated for potential improvement of the method. Temple<sup>(12)</sup> <sup>(13)</sup> extended this investigation to defects of various orientations (tilt and skew angle) and shapes (aspect ratio).

From the previous literature, it is known that different optimum configurations of the ultrasonic delivery system exist for various conditions of specimen thickness, defect orientation, etc. Based on the conditions present in our case - very thin specimen (4.2 mm through-wall thickness), shallow crack depth (less than  $1/2$  wall thickness) and crack orientation (Figure 2) - initial ultrasonic parameters were selected. Probes of 15 MHz frequency or higher should be used. Beam angles of  $70^\circ$  to  $80^\circ$  for longitudinal waves and  $40^\circ$  to  $50^\circ$  for transverse waves generally gave the best results by many of the aforementioned researchers. Both longitudinal and transverse waves have advantages and disadvantages in their uses. It must be remembered that these conclusions were drawn, for the most part, from work done on flat surfaced specimens made from steel. Our specimens have curved surfaces made out of Zr-Nb alloy. Hence, deviations from these results with our experimental tests are

to be expected.

The accuracy and repeatability of crack-tip diffraction has been proven by others, Charlesworth and Temple<sup>(14)</sup>, Aikawa and Nakayama<sup>(15)</sup> and Springfellow and Perring<sup>(16)</sup> to name a few. Mastroianni et al<sup>(17)</sup> have performed crack-tip diffraction studies on notches 2.5 mm deep and less in CANDU pressure tubes and obtained accuracies of  $\pm 0.1$  mm using  $45^\circ$  shear waves and transducer frequencies of around 20 MHz. An accuracy of  $\pm 0.2$  mm was obtained on a fatigue crack.

### 3. EXPERIMENTAL

#### 3.1 APPARATUS AND EQUIPMENT

A block diagram of the experimental apparatus is shown in Figure 3.

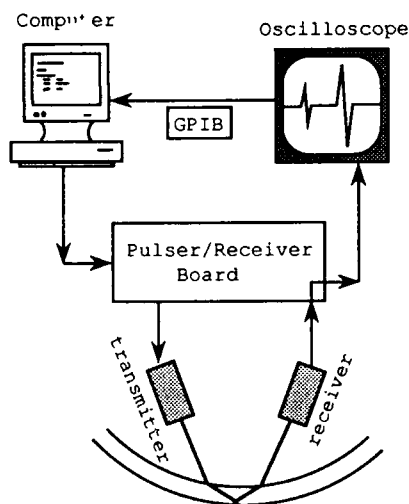


FIGURE 3: Experimental apparatus.

An Adaptronics PCPR-100 Ultrasonic Pulser board, which fits into a personal computer, was used to generate the main-bang pulse, the shape of which can be controlled via computer soft-

ware. The parameters of the pulse shape include the output voltage (12 - 400 volts), shape (unipolar or bipolar square wave with leading edge either in the negative or positive direction), number of cycles, frequency (640 kHz - 20 MHz), and damping.

The main-bang pulse excites the transmitter probe. Ultrasound is sent from the transmitter into the water and test specimen where it interacts with the test specimen surfaces and defects. The reflected and diffracted sound waves are then picked up by the receiver probe. This signal is sent to the pulser board where the gain can be regulated. The signal is then forwarded to an oscilloscope (Tektronix 7854) for display and digitizing. Using a GPIB interface bus, the digitized waveforms are stored on computer disk for future signal processing. Both the oscilloscope and the pulser board are simultaneously triggered by an external source.

Two of each of the following probes were tested in preliminary studies: unfocused probes of 15, 20, 25 and 35 MHz and focused probes of frequency 25 MHz. Active elements were 3.2 mm in diameter. The transducer pairs used for the pitch-catch configuration were always of the same frequency.

The probes were mounted in magnetic holders on a flat steel plate with a 2 mm marked square grid. The pressure tube sections were mounted in a groove on the steel plate and could be rotated. Typically, a pressure tube specimen was mounted with the crack in line with the grid's axis for probe positioning. Probe positions were calculated using an iterative computer pro-

gram, described by Lindenschmidt (2), and the probes located manually.

### 3.2 TEST SPECIMENS

Initial tests were performed on three specimens cut from Zr-2.5 wt% Nb pressure tubes. These specimens were fatigue cycled to produce an axial crack in each specimen approximately half-way through the thickness of the tube grown radially from the outside surface. To assist the pre-cracking, an EDM (Electron Discharge Machining) starter notch was first machined onto the outside surface of each specimen to produce a stress concentration point. Starter notches on the specimens FC #1 (Fatigue Crack #1), FC #2 and FC #3 were 5, 10 and 15 mm long, respectively, and 0.5, 0.75 and 1.0 mm deep.

The experiments on the fatigue cracked specimens were performed to determine the optimum transducer geometry, the main-bang pulse parameters and the transducer frequency to be used for this particular crack-tip diffraction application. Once these parameters were optimized, tests were performed on cracks formed in hydride blisters. Specimens with hydride blisters on the outside surfaces were cut from pressure tubes and then cracked under four-point loading.

### 3.3 SIGNAL PROCESSING TECHNIQUES

Three signal processing techniques were used to enhance time-delay readability between the crack-tip diffracted and the backwall reference signals: auto and cross-correlations, rectification and smoothing and the magnitude of the analytic signal. These techniques overcame some of the problems faced in

time measurements such as small signals and signals very close together or overlapping.

#### 3.3.1 Auto and Cross-Correlations

These techniques were chosen to give an indication of how the crack-tip diffracted signal and the backwall reflected signal correlate together in time. The autocorrelation was found using a Fourier spectroscopy routine. First, using a FFT (Fast Fourier Transform) algorithm described by Bendat and Piersol (18), the estimated spectral density of a time signal,  $x(t)$ , is found in terms of its real and imaginary frequency components,  $\text{Re}[X(f)]$  and  $\text{Im}[X(f)]$ , respectively, as,

$$S_{xx}(f) = \frac{\sqrt{(\text{Re}[X(f)])^2 + (\text{Im}[X(f)])^2}}{N \Delta t}$$

where  $N$  is the number of points in the waveform and  $\Delta t$  is the sampling time space. The estimated autocorrelation,  $R_{xx}(r\Delta t)$ , is the inverse Fourier transform of  $S_{xx}(f)$  and can be computed using an inverse FFT algorithm (18),

$$R_{xx}(r\Delta t) = \frac{N}{N-r} \cdot [\text{invFFT} \{S_{xx}(f)\}]$$

where  $r$  is a signal point.

The cross-correlation was also found of a waveform containing just the crack-tip signal correlated with a waveform containing only the backwall signal. It was found in a similar manner as the autocorrelation (18).

#### 3.3.2 Rectification and Smoothing

The crack-tip diffracted signal and the backwall reflected signal both consist of a number of cycles giving the sig-



nals several negative and positive peaks. Rectifying and lowpass filtering the signal yields one broad positive peak with a single clear maximum. This takes the ambiguity out of time-delay measurements. However, the resolution of the signal decreases and loss of information due to removal of the signal high frequency components is apparent. The Butterworth filter, proven to work successfully by Clark(19), was used for lowpass filtering because the filter computations are done in the time domain, not the frequency domain, avoiding extra computation time.

### 3.3.3 Magnitude of the Analytic Signal

Physically, the square of the analytic signal magnitude is proportional to the total energy arriving at the receiver transducer(20). This total energy consists of kinetic and potential energy. Defining the waveform as a complex analytic signal allows both kinetic and potential energy to be represented, one as the real component, the other as the imaginary component. This technique has advantages over the rectification and smoothing method as it permits better time resolution and there is no loss of frequency information.

## 4. RESULTS

### 4.1 RESULTS ON FATIGUE CRACKS

Initially, the three fatigue cracks, FC #1, FC #2 and FC #3, were tested using 15, 20, 25 and 35 MHz probes to determine the optimum transducer frequencies. Beam angles impinging on the crack-tip were varied between 40° and 70° incident and diffracted angles to determine the optimum configuration.

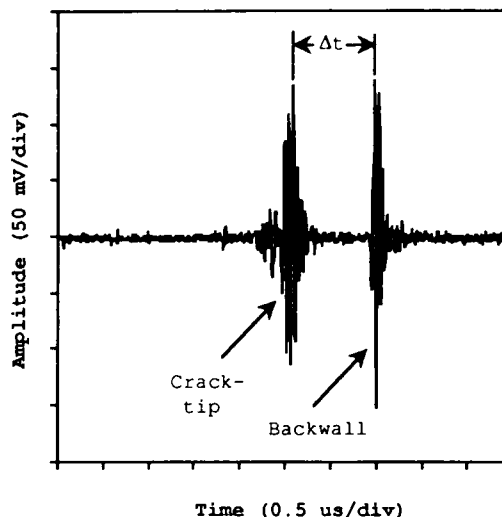


FIGURE 4: Raw rf fatigue crack waveform.

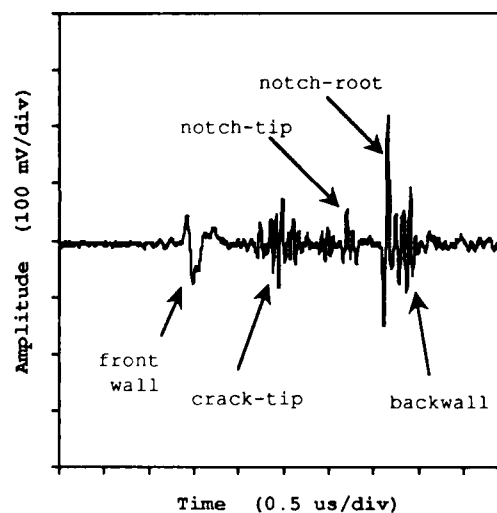


FIGURE 5: A-scan with interfering signals from notch.

The two criteria used were:

- 1) maximum diffracted signal amplitude, and
- 2) accuracy in crack depth measurements.

Figure 4 shows a sample raw rf (radio frequency) waveform from one of the fatigue cracks with the crack-tip signal clearly defined. In general, the

fatigue cracks gave good tip signals but there were often signals from the EDM starter notches which confused the waveforms (see Figure 5 for an example which also shows a lower crack-tip signal). The backwall signal was often distorted due to the presence of the notch. In practice, it was desirable to move the probes back from the backwall so the probe beams met at or near the crack-tip to give maximum signal amplitudes. With the fatigue cracks roughly half way through the wall and using these small high frequency probes, the amplitude of the backwall signal was substantially reduced.

#### 4.1.1 Signal Processing

In addition to measuring the time difference between the maximum signal peaks of the crack-tip diffracted and backwall reflected signal of the raw rf and rectified rf waveforms, several signal processing methods were implemented to determine the time difference. Figure 6 shows the autocorrelation of the waveform from Figure 4.

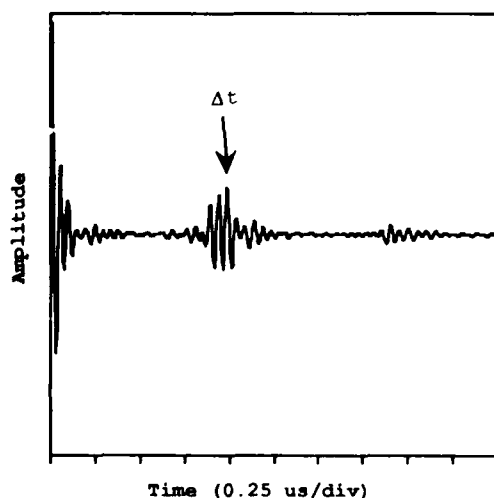


FIGURE 6: Autocorrelation of raw rf signal.

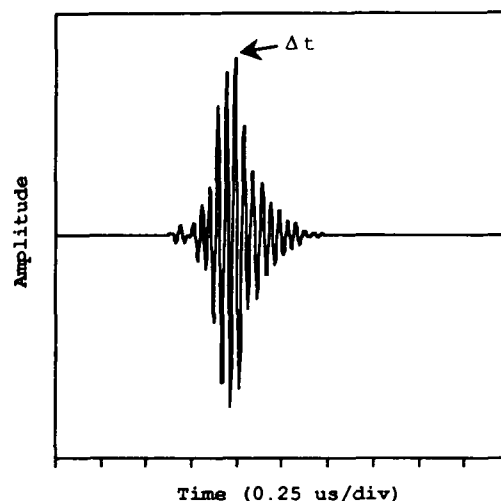


FIGURE 7: Correlation of crack-tip signal crossed with back-wall reflection.

Figure 7 shows a cross-correlation of a waveform containing only the crack-tip signal crossed with a waveform containing only the backwall reflection.

Figure 8 shows the rectification and smoothing of the signal in Figure 4. Again, this technique provides a more readily interpretable trace but information is lost in the process. Figure 9 shows the magnitude of the complex analytic signal from Figure 4 showing a readily interpretable signal. Overall, the signal processing results can be summarized by saying that all the techniques improve signal readability but none of them is convincingly superior in all cases.

#### 4.1.2 Wave Mode and Amplitude Measurements

All of the signals received from the fatigue cracks were obtained using shear waves, both in transmission and receiving. Longitudinal waves were tried but the signal amplitudes of the crack-tip diffracted signals were too

small and in most cases undetectable. Hence, longitudinal waves were rejected as a possible wave mode for the ultrasonic measurement system.

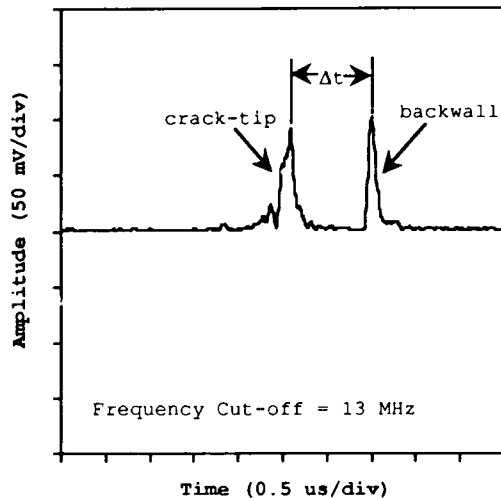


FIGURE 8: Rectification and smoothing.

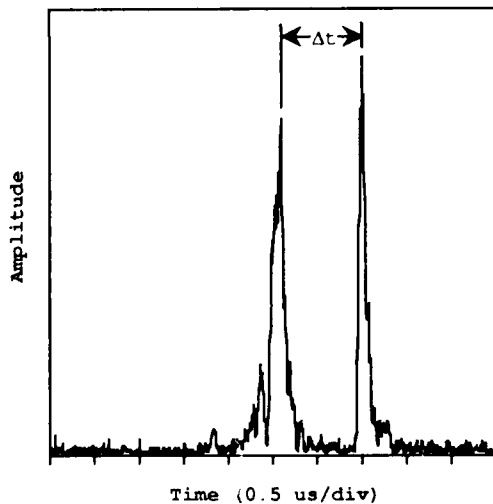


FIGURE 9: Magnitude of the analytic signal.

Sample results on the amplitude measurements of the crack-tip diffracted signal is given in Figure 10 for FC #2 using 25 MHz probes. Amplitudes were typically higher at higher incident and diffracted angles and at lower trans-

ducer frequencies. Using focused probes showed no improvement in signal gain.

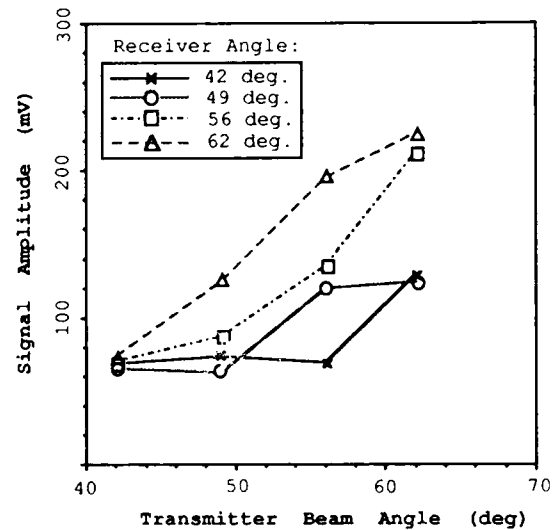


FIGURE 10: Crack-tip signal amplitudes for FC #2 (25 MHz probes).

#### 4.1.3 Depth Measurements and Errors

The depths of the broken open cracks FC #1, FC #2 and FC #3, as measured by optical microscopy, were 2.07, 2.30 and 2.60 mm. The following results are taken from time measurements determined by the cross-correlation method. The error graph for FC #1, 25 MHz probes is shown in Figure 11. Errors greater than  $\pm 0.1$  mm were obtained for angles ranging from  $55^\circ$  to  $62^\circ$ . The error graphs for FC #2 are given in Figures 12 and 13 for the 20 and 25 MHz unfocused probes, respectively. For the 20 MHz probes, all errors for the  $56^\circ$  transmitter probe angles were within  $\pm 0.1$  mm. The like-angle beam configurations,  $49^\circ - 49^\circ$  and  $56^\circ - 56^\circ$ , gave the smallest errors. For the 25 MHz transducers, all the like-angle geometries gave errors greater than 0.1 mm. The same conclusions can be drawn from FC #3 results as from FC #2. In

general, the 20 MHz transducers produced smaller errors than the 25 MHz probes. The angle configurations for the most accurate results are  $49^\circ - 49^\circ$  and  $56^\circ - 56^\circ$ . The  $55^\circ - 55^\circ$  will be suggested for the delivery system because greater amplitudes are obtained for higher angles.

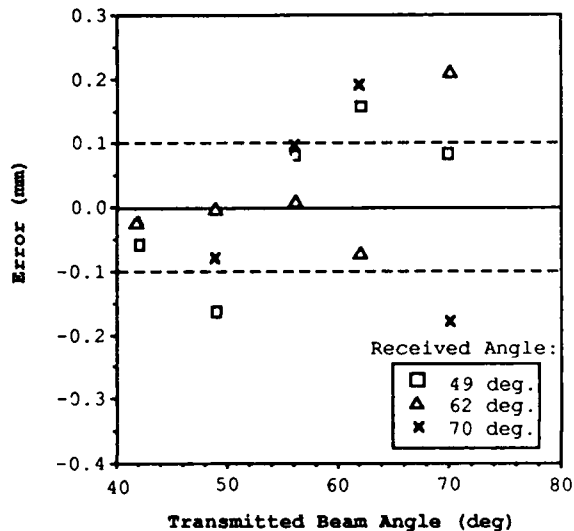


FIGURE 11: Errors for FC #1 (25 MHz probes).

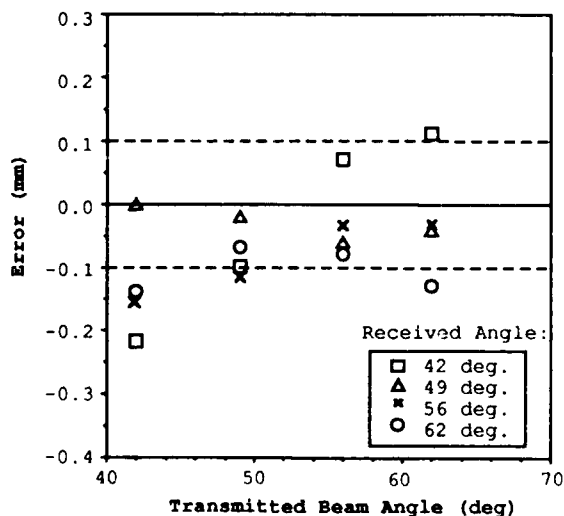


FIGURE 12: Errors for FC #2 (20 MHz probes).

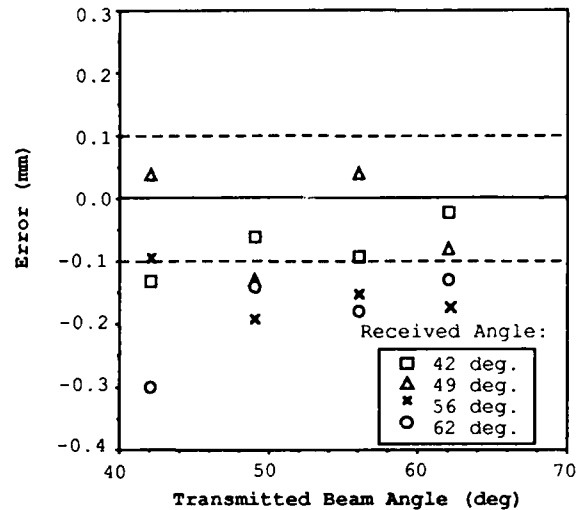


FIGURE 13: Errors for FC #2 (25 MHz probes).

#### 4.1.4 Main-Bang Pulse Parameters

The main-bang pulse characteristics were varied to see their effect on signal amplitude and depth accuracy. The parameters, pulse shape, frequency, voltage, damping and the number of cycles in the pulse, did not greatly affect the accuracy of the time measurements but significantly altered the amplitude received from the diffracted signal. To obtain maximum amplitude, the main-bang pulse parameters were set at maximum voltage (400 volts), negative bipolar (-B) pulse shape, frequency coinciding with the central frequency of the transducer, and maximum damping and only one excitation wave cycle to eliminate after-ringing in the signals.

#### 4.2 RESULTS ON HYDRIDE BLISTER CRACKS

Due to time limitations, the HBC (Hydride Blister Crack) depths were measured using only selected optimum probes and incident/diffracted angles. These were the 20 and 25 MHz unfocused

TABLE 1								
Depths and Errors Hydride Blister Cracks								
HBC #1 0.38 mm HBC #2 0.54 mm	Original rf Signal		Cross - Correlation		Rectify and Smoothing		Magnitude of Anal. Signal	
	depth (mm)	error	depth (mm)	error	depth (mm)	error	depth (mm)	error
HBC #1 20 MHz 50°- 50°	0.38	-0.00	0.38	-0.00	0.32	-0.06	0.30	-0.08
HBC #2 25 MHz 50°- 50°	0.43	-0.11	0.42	-0.12	0.46	-0.08	0.47	-0.07
HBC #2 25 MHz 55°- 55°	0.56	-0.02	0.49	-0.05	0.50	-0.04	0.53	-0.01

probes and either the 50° - 50° or 55° - 55° angles. Table 1 shows the results from HBC #1 and HBC #2. Subsequent optical measurements showed the depths to be 0.38 and 0.54 mm, respectively. The depth measurements in Table 1 are within the  $\pm 0.1$  mm range with two minor exceptions.

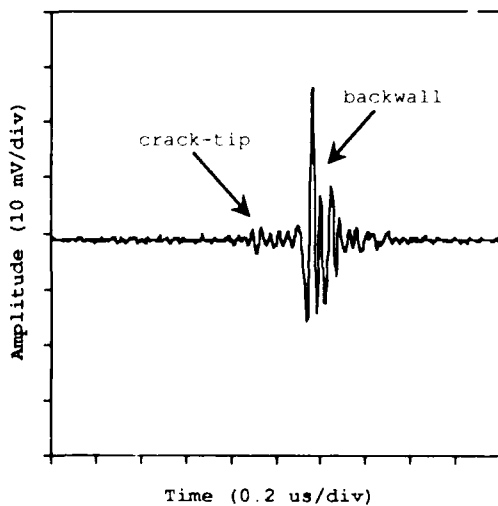


FIGURE 14: HBC #2 (50° - 50°)

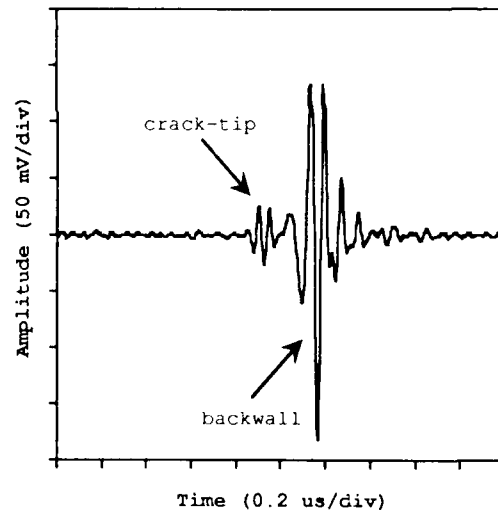


FIGURE 15: HBC #2 (55° - 55°)

Figure 14 shows a waveform from HBC #2 using a 50° - 50° probe arrangement with the crack-tip signal barely detectable. This signal would be difficult to distinguish during an in-reactor inspection without signal processing. In contrast, the crack-tip signal using the 55° - 55° angles is much clearer as shown in Figure 15. Note

the increase in amplitude of the crack-tip diffracted signal and the improved accuracy of the depth calculations when the transmitter and receiver angles are increased.

## 5. DISCUSSION

The results on the three fatigue cracks and the two cracked blisters show that the crack-tip diffraction technique is capable of measuring crack depths on the outside surface of the pressure tubes within a range of  $\pm 0.1$  mm on real defects. The optimization criteria for the flight path geometry in obtaining errors this small and obtaining reasonable crack-tip diffracted signal amplitudes has been met. Maximum signal amplitude was sacrificed to obtain more accurate depth estimates and greater time difference resolution between the crack-tip and backwall signals. The use of a fixed probe module, as opposed to the manual floating probe arrangement used here, should improve repeatability and accuracy further. The three signal processing techniques used here primarily gave an improvement in readability rather than accuracy. At present, data is being collected using a fixed module in B-scan format. Using SAFT (Synthetic Aperture Focusing Technique), a substantial improvement in signal-to-noise ratio, accuracy and repeatability can be obtained.

## 6. CONCLUSIONS

The optimum parameters for the ultrasonic delivery system are:

- 1) the probe angle configuration must be  $55^\circ - 55^\circ$ ,
- 2) 20 MHz transducers should be used, and

- 3) pulse shaping should be used to give the largest signal amplitudes.

## REFERENCES

1. Price, E.G., "Highlights of the Metallurgical Behavior of CANDU Pressure Tubes", AECL-8338 (Prelim.), Sept. 1984.
2. Lindenschmidt, K.-E., "Sizing Cracks in Reactor Pressure Tubes Using the Crack-Tip Diffraction Method", M.A.Sc. Thesis, University of Toronto, 1989.
3. Posakony, G.J. and Cross, B.T., United States Patent Number 3,712,119, January 23, 1973.
4. Granville, R.K. and Taylor, J.L., "Improvement in Signal-To-Noise Ratio During the Ultrasonic Testing of Titanium Alloys", British Journal of NDT, July 1986.
5. Böttcher, B., Schultz, E. and Wüstenberg H., "A New Method for Crack Depth Determination in Ultrasonic Materials Testing", 7th International Conference on Nondestructive Testing, Warsaw, Poland, June 1973.
6. Silk, M.G. and Lidington, B.H., "An Investigation of the Potential of the Use of Scattered Ultrasound in the Determination of Crack Depth", AERE-7649, Jan. 1974.
7. Silk, M.G. and Lidington, B.H., "Defect Sizing Using an Ultrasonic Time Delay Approach", British Journal of NDT (17), March 1975.
8. Silk, M.G. and Lidington, B.H., "Defect Sizing Using the Time Delay of Diffracted Ultrasound", in 'The Detection and Measurement of Cracks', Welding Institute, Abington Hall, Abington, Cambridge, 1976.
9. Golan, S. "Sizing of Cracks with Scattered Ultrasonic Waves". National Bureau of Standards Special Publication

596, in 'Ultrasonic Materials Characterization', Berger, H. and Linzer, M., eds., Proc. 1st International Symposium on Ultrasonic Materials Characterization, Gaithersburg, Md., June 1978.

10. Golan, S., "Defect Characterization and Dimensioning of Cracks in Welds by the Ultrasonic Diffraction Method", (U.S.) National Bureau of Standards, Washington, D.C., March 1980.

11. Temple, J.A.G., "Time-of-Flight Inspection: Theory", Nucl. Energy, (22)5, Oct. 1983.

12. Temple, J.A.G., "The Amplitude of Ultrasonic Time-of-Flight Diffraction Signals Compared with Those from a Reference Reflector", Int. J. Pres. Ves. & Piping (16), 1984.

13. Temple, J.A.G., "Calculated Signal Amplitudes for Time-of-Flight Diffraction Signals for Tilted or Skewed Cracks", AERE-TP-1188, 1986.

14. Charlesworth, J.P. and Temple, J.A.G., "Ultrasonic Time-of-Flight Inspection Through Anisotropic Cladding", Proc. Periodic Inspection of Pressurized Components, Institute of Mechanical Engineers, Oct. 1982.

15. Aikawa, Y. and Nakayama, M.,

"Measurement of Crack Height by Tip Echo Interference Method", 7th NDE Nucl., 1985.

16. Springfellow, M.W. and Perring, J.K., "Detection and Sizing of Inner Radius Defects in DDT Plate 4 (Simulated PWR Nozzle) by the Ultrasonic Time-of-Flight Diffraction Technique", British Journal of NDT (26), Feb. 1984.

17. Mastroianni, F., Moles, M.D.C. and Sinclair, A.N., "Ultrasonic Crack-Tip Diffraction in CANDU Reactor Pressure Tubes", Fifth Pan Pacific Conference on NDT, Vancouver, April 1987.

18. Bendat, J.S. and Piersol, A.G., 'Random Data: Analysis and Measurement Procedures', 2<sup>nd</sup> Edition, John Wiley and Sons, Inc., 1986.

19. Clark, B.D., "Second Order Recursive Digital Filters for Offline Processing on Apple II Computers: Machine Language Subroutines Using Floating-Point Arithmetic in Applesoft ROM", Intelligent Instruments and Computers, Nov./Dec. 1986

20. Gammell, P.M., "Improved Ultrasonic Detection Using the Analytic Signal Magnitude", Ultrasonics, (19)2, March 1981.

## FIELD APPLICATIONS OF THE CYLINDRICALLY GUIDED WAVE TECHNIQUE ON VALVE STEMS

Edward H. Ruescher, NDE Analyst  
Nondestructive Evaluation Science and Technology Division  
Southwest Research Institute  
San Antonio, Texas

### ABSTRACT

Over the last few years, the need for inspecting stud bolts in nuclear power plants has increased due to several documented stud bolt failures. Some of these stud bolts were very long and accessible from one end only. Conventional techniques used for short stud bolts or stud bolts with heater hole access were not adequate for these longer studs. Therefore, a new technique, the cylindrically guided wave technique (CGWT), was developed. This paper discusses the theory, results of the evaluation, and application procedures of the CGWT on cylindrical test objects other than bolting. One example of a failed valve stem is shown.

### INTRODUCTION

The cylindrically guided wave technique (CGWT) was developed to answer a direct need in the nuclear power industry to examine bolting. Engineers at several nuclear power plants had become concerned about stress corrosion cracking in the threads of bolts used in the reactor pressure vessels and primary coolant systems. Several instances of failure were noted in these areas, particularly in the primary coolant system bolting. Southwest Research Institute (SwRI), under contract with the Electric Power Research Institute (EPRI), developed the basic CGWT technology.

Subsequent to the initial development, further applications of the CGWT were and are being explored by SwRI. In the search for applications of the CGWT, the essential elements of the technology were evaluated and listed: (1) the object should have a length-to-diameter ratio of four to one or greater; (2) the object should have a relatively simple geometry; (3) the object should not have threads for the major portion of its length; and (4) either detailed drawings of the part or a known good spare part should be made available to be used for baseline information. This paper discusses the theory of operation for the CGWT\* and discusses some of the applications for the CGWT technology other than for bolting.

### THEORY

The CGWT is based on the fact that an ultrasonic wave traveling in a long cylinder becomes, in effect, guided by the geometry of the cylinder. That is, instead of a normal beam spread, the ultrasonic beam interacts with the surface of the cylinder and mode converts.

In theory, the CGWT is described by the transmission of the longitudinal beam and the various orders of mode-

converted waves that occur when the ultrasonic beam is constrained to propagate down a cylindrical geometry. These mode-converted signals are effective for recording the end of the stud reflection (backwall) as well as reflectors in the stud (such as cracks). In fact, one can positively detect flaws by using the following criteria:

- (1) The backwall reflection from the end of the stud will always be present.
- (2) The primary longitudinal backwall reflection with its various longitudinal-to-shear-to-longitudinal (LSL) mode-converted will always be present.
- (3) Any signals that occur prior to the backwall with their associated LSL modes are indicative of flaws.
- (4) Signals between the L and mode-converted pulses are also indicative of flaws.

The time at which signals occur prior to the backwall also enables the inspector to determine the location of the flaw relative to the end of the stud.

In order to exploit the presence of mode-converted (secondary or trailing) signals, it is necessary that they appear separately from the main reflected pulse or the echo. The extent of this separation depends upon the incident pulse width and the diameter of the cylindrical waveguide under inspection. Several orders of mode conversion occur, as shown in Figure 1. The first signal (called the backwall echo) is from the far end (the end opposite to the end on which the transducer was mounted) on the stud. The signals that follow the backwall echo immediately are mode-converted end-of-stud or backwall-trailing pulses. (These trailing pulses are also called the secondary echoes.) The time separation between the 0-degree L signal and the first

\*Light, G. M., N. R. Joshi, and S. N. Liu, "Stud Bolt Inspection Using Ultrasonic Cylindrically Guided Wave Technique," presented at the ASME Pressure Vessel and Piping and International Computers in Engineering Conference and Exhibition, Chicago, Illinois, July 20-24, 1986.



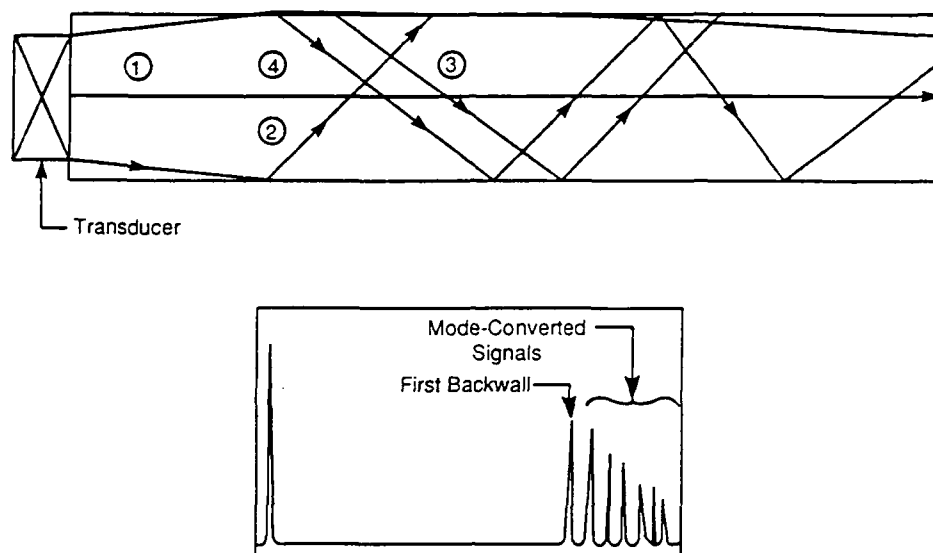


Figure 1. Schematic view illustrating the principles of the CGWT. The first signal to return is from the edge of the bolt (backwall). The following signals are due to backwall reflections that have undergone mode conversion.

mode-converted signal is directly related to the diameter of the stud. The successive mode-converted signals are separated by the same interval of time.

The first backwall echo signal is denoted as the longitudinal (L); the first trailing pulse that follows it is denoted as the longitudinal-to-shear-to-longitudinal (LSL); the second trailing pulse is denoted as the longitudinal-to-shear-to-longitudinal-to-shear-to-longitudinal (LSLSL), etc. The time interval (t) between the L and LSL returned from the end of the stud is the time needed to travel the distance S (S-wave path) at shear velocity minus the time needed to travel the distance X at longitudinal velocity (as shown in Figure 2). That is, the time difference is

$$\Delta t = \frac{d}{V_s} \left( \frac{1}{V_s} - \frac{1}{V_l} \right) \quad (1)$$

where d is the diameter of the stud and  $V_s$  and  $V_l$  are the shear and longitudinal velocities in the steel.

Ordinarily, signals from threads appear as noise and hence pose a problem in identifying a weak signal from a shallow notch in a thread. This could be overcome, however, by the proper combination of transducer frequency and diameter in relation to the diameter of the specimen and the position of the transducer at a suitable location, not necessarily at the center, on the end face of the specimen. Properly addressed, these conditions could change thread noise into an identifiable echo from the first thread at the other end followed by its trailing pulses. This transformation would certainly help to locate a weak signal from the shallow notch in the threads.

The trailing pulses are also effective for recording the end of the stud reflection (backwall) as well as small reflectors

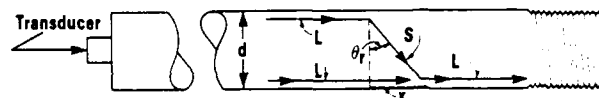


Figure 2. Schematic view illustrating the path-length difference between the 0-degree longitudinal wave and a similar wave that undergoes mode conversion. The path difference is the tangential component X of the shear wave, S, going across the bolt diameter.

in the stud, such as notches or cracks. The time at which signals occur prior to the backwall also enables the inspector to determine the location of the flaw relative to the end of the stud. The fact that the mode-converted signals are at a time spacing that is constant and related to a measurable parameter--the bolt or stud diameter--allows use of the technique for signature analysis. This becomes important when inspecting noisy material and when the critical crack size is very small.

Successful ultrasonic inspection depends on the proper selection of transducers for given specimen geometry and material specifications. The specimen geometry, in turn, decides detectability, penetration, sensitivity, and resolution.

Prior to any field trials of the CGWT, an operating procedure for the use of the CGWT technology was developed, along with the appropriate data and calibration recording forms using the referenced paper as a guideline. The initial field trials of the CGWT were performed on conventional studs and bolts for which the technique was originally developed. However, it became apparent that other configurations of parts could be examined. These included valve stems, lift rig pins, pump shafts, and reactor pressure vessel studs.

## APPLICATION NO. 1 - REACTOR LIFT RIG PIN

Prior to the start of any examination, the anticipated times to the backwall, any known geometric reflector or calibration notches, and mode-converted delta times are calculated. These calculations are based upon drawings, dimensional sketches, or dimensions taken from known good spare parts. An example of this would be the reactor lift rig pins at a reactor site where no calibration or known good standard was available. Figure 3 shows the dimensions taken from a dimensional sketch of the lift rig pin. As can be seen from the sketch, when the transducer is placed on the head of the lift rig pin, a reflector should be received corresponding to a metal path of approximately 10.6 and 16.4 inches. These represent the land area and the backwall of the pin. Also noted and observed was the cotter pin hole drilled near the opposite end of the lift pin. When scanning from the nut end of the lifting pin, the land area at approximately 3.7 inches would give a signal, as would the backwall at the full length of the pin at 15.75 inches. In addition to the calculated arrival times, the critical areas of the lift pin were also identified—the area from 1.5 to 10.6 inches from the head of the pin and the land area approximately 11.2 inches from the head. When examining the pin from the threaded end, the critical area is identified as being 5.75 inches and from 5.75 to 14.9 inches from the threaded end of the lift pin. When the examinations were performed, no flaws were found and the ultrasonic signals were well within acceptable tolerances of the anticipated time of arrival.

## APPLICATION NO. 2 - VALVE STEMS

The CGWT was also used to examine valve stems at several nuclear power plants, with the same type of preexamination planning. Spare valve stems were available for calibration or base line data purposes. Figure 4 shows the CRT presentation of the entire length of the valve stem. Figure 5 shows a composite view of the valve stem with an expanded view showing the mode-converted delta signals. Figure 6 is a sketch of a typical valve stem showing the instrumentation hole, the upper threaded portion, the main shank of the valve stem, the attached fitting, the attachment point, and the back of the valve stem. This corresponds to the signals shown on the known good valve stem. There are other configurations for valve stems; however, by utilizing a known good spare valve stem for baseline data, a meaningful examination of the valve stems can be performed (see Figure 7).

The next set of figures (see Figures 8 and 9) were taken from a plant at which a defective valve stem was detected. Figure 8 shows the baseline data for a known good valve stem, and Figure 9 shows the defective valve stem. In this case, the valve stem had a total fracture in its shank portion at a severe angle to the longitudinal axis of the valve stem. The defective valve stem was clearly identified and the data taken from the valve stem agreed with the location of the flaw within one-half inch of its length, which was in excess of 37 inches from the ultrasound's entry surface.

## CONCLUSION

The CGWT is a meaningful examination for selected cylindrical objects, including bolting and other components. When known good parts can be used for baseline or calibration information, evaluation of the results is positive and immediate. However, where no known good part is available for baseline data, the evaluation of the data must be made by comparing data (1) on all known parts examined,

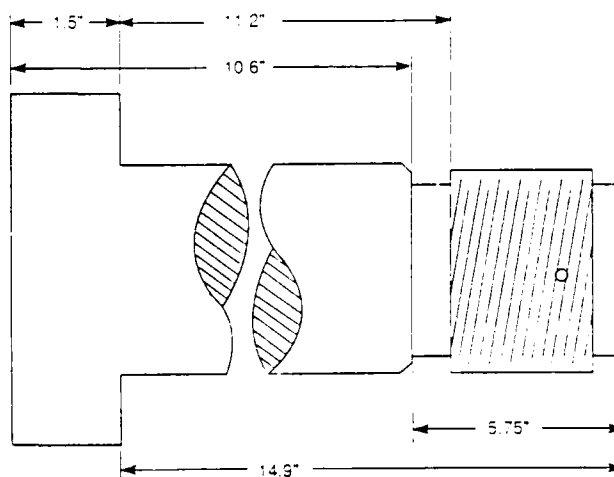


Figure 3. Dimensioned Sketch of Lift Rig Pin



Figure 4. Valve Stem Baseline Data (Overall)

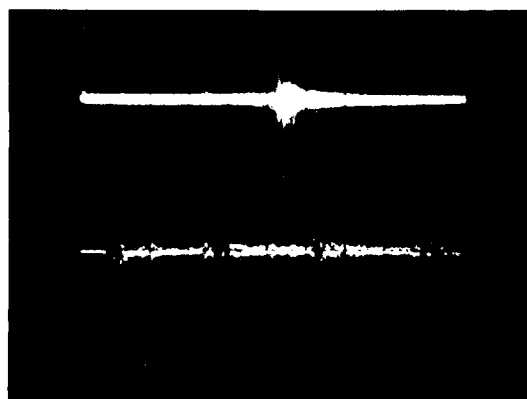


Figure 5. Valve Stem Baseline Data (Overall and Delta Time of Mode-Converted Signals)

provided there are several to be examined, or (2) on a mathematical basis using the time domain for signal arrival time if only one part of its type is to be examined.

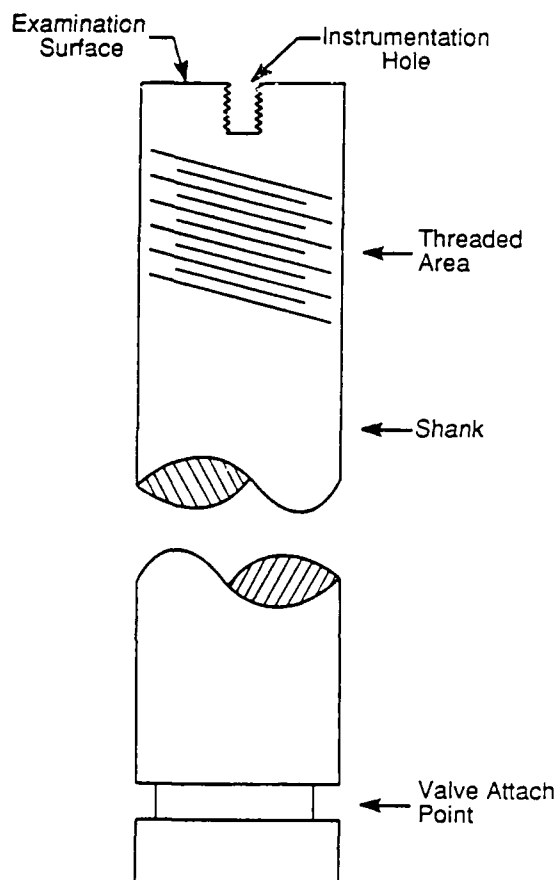


Figure 6. Sketch of Typical Valve Stem

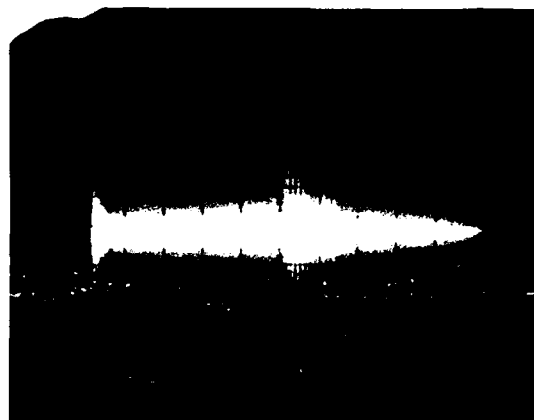


Figure 7. Typical Valve Stem Examined

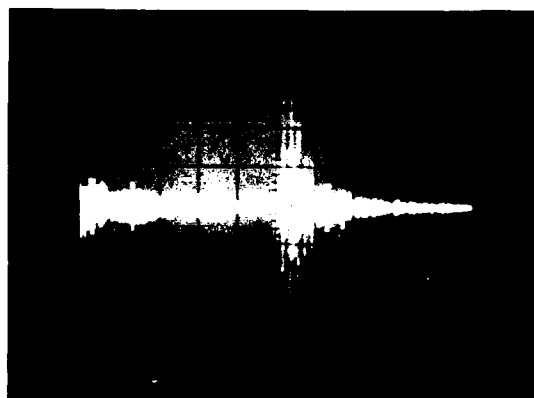


Figure 8. Valve Stem Baseline Data

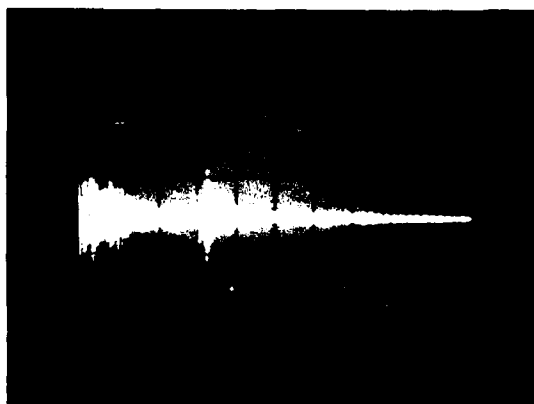


Figure 9. Failed Valve Stem

# APPLICATIONS OF THE $M_{21}$ ULTRASONIC TECHNIQUE TO INSPECTING LAYERED MATERIALS

Don E. Bray  
Associate Professor  
Department of Mechanical Engineering  
Texas A&M University  
College Station, Texas 77843

## Abstract

Engineering structures and systems often utilize components which are composed of multiple layers of dissimilar materials, enabling the unique characteristic of each material to be used to the greatest advantage. Ceramic liners in steel pipe, stainless steel overlays on alloy steel and hardened layers at wear surfaces are typical examples of layered materials used in engineering applications. While the dissimilar properties of the materials are used to a performance advantage, they may create difficulties for an inspection. Layered waves, however, may be useful in performing this inspection since they travel in the various materials with different characteristics. In a case where a low speed layer is joined to a high speed, underlying material, the first higher order Rayleigh wave, labeled the  $M_{21}$  mode, is shown here to be useful in inspecting several combinations of layered materials.

## 1. INTRODUCTION

A typical layered structure which supports the propagation of the  $M_{21}$  wave is shown in Fig. 1 where the wave is excited with a Plexiglas wedge incident at angle  $\theta$ . The excitation angle is estimated initially using Snell's law and the bulk shear wave speed in the upper layer. Experimental optimization often is required, however, to establish the angle for the peak amplitude  $M_{21}$  wave. The bulk shear wave speed in the upper layer,  $C_2^u$ , must be less than the bulk shear wave speed in the lower layer,  $C_2^l$ . With the layer thickness designated by  $H$ , the travel speeds of the fundamental and first higher-order modes ( $M_{11}$  and  $M_{21}$ , respectively) are a function of the excitation frequency, as shown in Fig. 2.

The dispersion curves in Fig. 2 are for a single layered model where the speed of the upper layer is one-half that of the lower layer, i.e.  $C_2^u = (1/2) C_2^l$ . At high frequencies the speeds of the  $M_{11}$  and  $M_{21}$  waves approach the speeds of the fundamental Rayleigh and the bulk shear waves in the upper layer, respectively. As the frequency is lowered, the speed of the fundamental mode stays constant down to about 500 kHz. The higher-order mode, on the other hand, becomes highly dispersive.

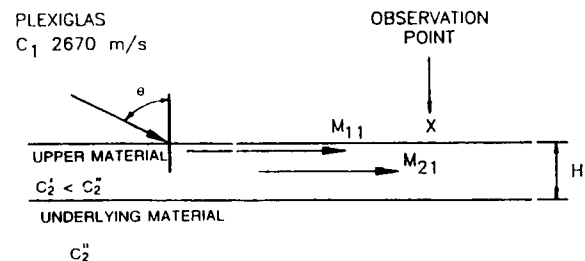


Fig. 1 Typical layered structure for propagating fundamental ( $M_{11}$ ) and higher-order ( $M_{21}$ ) waves with Plexiglas wedge.

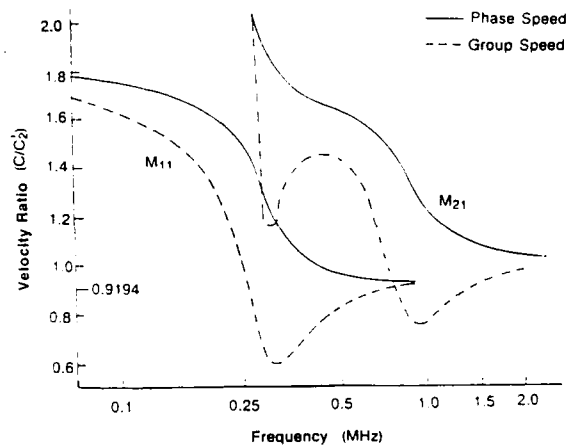


Fig. 2 Dispersion curves for Rayleigh waves in a low speed zone over high speed zone. (Parameters from earth model in Table 1).  $H = 5$  mm.

Further reduction of the frequency causes a complete disappearance of the higher-order mode at a "cut-off" frequency of approximately 300 kHz. At still lower frequencies, the speed of the fundamental wave approaches the speed of the fundamental Rayleigh wave in the underlying layer, largely uninfluenced by the upper layer.

Typical arrivals for the two waves are shown in Fig. 3 with the  $M_{21}$  leading the  $M_{11}$ . The separation time of the two arrivals is a function of the relative speed of the two waves which, for the higher frequencies, is a function mostly of the bulk shear wave speeds in the upper and underlying material. The frequency region where the speeds are nondispersive, of course, is determined by the layer thickness.

The dispersion curves for the 2:1 speed ratio provide easily distinguishable descriptions for the two modes. In applications for engineering structures, however, the speed ratios are not as great as seen here with the result that the arrivals of the two modes will be much closer than expected for the 2:1 model.

## 2. APPLICATIONS OF $M_{21}$ IN MATERIALS INSPECTION

A description of an application of the  $M_{21}$  to inspecting stainless steel overlay material has been given in Ref. 1. In that case, an upper

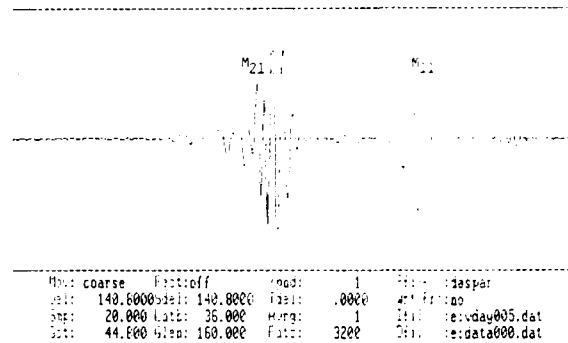


Fig. 3 Typical arrivals of  $M_{21}$  and  $M_{11}$  waves along a cold worked surface of railroad rail. (See Table 1 for material parameters.) (Courtesy American Society of Mechanical Engineers).

layer of type 347 stainless steel was welded in rows about 25 mm (1 inch) apart over a type A387 structural steel base. The overlay thickness was about 5 mm. The  $M_{21}$  mode could be excited in the overlay material with the Plexiglas probe slightly skewed on the perpendicular to the weld rows. A 2.25 MHz probe was used. Side drilled holes at the interface as well as defects in the weld were located with the  $M_{21}$  wave. The advantage of the wave is that a region several inches in front of the probe may be inspected from one probe position, thus increasing the coverage area for a single probe location.

Another application is the analysis of the percent of cold work in layers developed by Hertzian type stresses, as encountered by railroad wheels and rails and roller bearings. Further analysis of the cold worked material and the excitation of the  $M_{21}$  wave showed a correlation between the appearance of the wave and the initial hardness of the steel.<sup>(2)</sup>

## 3. OTHER APPLICATIONS OF THE $M_{21}$ WAVE

A variety of other material combinations are candidates for inspection with the  $M_{21}$  ultrasonic wave. Some of these are listed in Table 1, along with the earth model used for Fig. 2 and the railroad rail and stainless steel applications described in Refs. 1 and 3. The most important parameter for predicting the excitation and detection of the  $M_{21}$  waves is the shear wave speed ratio  $C_2^s/C_1^s$ . A higher value, as seen for the 2:1 model, has a greater likelihood of propagating an easily distinguishable  $M_{21}$  wave. The railroad rail, however, produced a very pronounced wave at a ratio of only 1.052. The other material combinations are suggested as potential

Table 1

Parameters for various models for excitation of higher-order Rayleigh waves in single layered material

	Earth	Rail	Stainless Steel ----- Alloy Steel	Steel ----- Al <sub>2</sub> O <sub>3</sub>	Copper ----- Nickel	Copper ----- Alumin.	Gold ----- Silver
$C_1$ (m/s)	6235	6134	5790	5940	4700	4700	3240
$C_2$ (m/s)	3600	3125	3100	3250	2260	2260	1200
$v_1$	0.250	0.325	0.299	0.286	0.33	0.33	
$C_1'$ (m/s)	12471	6153	5940	9000	5630	6300	3600
$C_2'$ (m/s)	7200	3289	3250	5500	2960	3130	1590
$v_2$	0.250	0.300	0.286	0.202		0.31	
$C_1'/C_1$	2.0	1.003	1.026	1.5	1.20	1.34	1.11
$C_2'/C_2$	2.0	1.052	1.048	1.69	1.31	1.38	1.32
$\rho_2/\rho_1$	1.5	1.0		0.45	1.003	3.31	1.84

candidates for inspection with this wave. All have speed ratios considerably greater than the railroad rail which should make the waves easily excited.

#### 4. SUMMARY

$M_{21}$  waves with the energy isolated within a layer may be used to inspect layered materials typically found in modern engineering structures. The wedge used to excite these waves has an incident angle near to that of the fundamental Rayleigh wave. Commercial probes are used. With the probe assembly located at one spot on the item being inspected, the waves may be used to inspect for defects at the boundary between the two materials as well as for defects within the upper material.

The exact design parameters for  $M_{21}$  probe systems have not been fully established for the material combinations listed in Table 1. Further work would require a study of the variations in material wave speed, the thickness and uniformity of the layer as well the type of defects being sought.

#### 5. REFERENCES

1. Bray, D. E., "Application of the First Higher-order ( $M_{21}$ ) Mode Rayleigh Wave to the Inspection of Stainless Steel Overlays," New Directions in the Nondestructive Evaluation of Advanced Materials, MD-Vol. 9, Winter Annual Meeting, American Society of Mechanical Engineers, Chicago, Illinois, 1988, pp. 73-77. (To be published Journal of Engineering Materials and Technology).
2. Bray, D. E., "Higher-order Mode Rayleigh Waves in the Cold-worked Zone of Railroad Rails," Proceedings 14th Symposium on Nondestructive Evaluation, Nondestructive Testing Information and Analysis Center, San Antonio, Texas, April 1983, pp. 520-525.

## ULTRASONIC CHARACTERIZATION OF FLAWS IN CERAMICS

G.P. Singh  
Karta Technology, Inc.

Anmol S. Birring  
Southwest Research Institute

### ABSTRACT

Ceramics are currently being evaluated as a replacement for metals and polymers in many applications. Their superior corrosion and wear resistance, light weight, low cost, excellent electrical and optical properties, limited thermal expansion, and their ability to withstand high temperatures make them inviting materials for use in structural, aerospace, electronic, and biotechnology areas. Despite their desirable properties, the use of ceramics is greatly restricted in structural applications because ceramics are brittle and their physical properties are nonuniform. To assure ceramic product reliability, it is important that they be examined nondestructively. A feasibility study to apply high frequency ultrasonics to detect and characterize surface breaking cracks and voids was conducted. Results show that extremely small cracks and voids can be easily detected. However, characterization of flaws requires application of sophisticated signal processing algorithms. This paper discusses the application of deconvolution to detect and size flaws

### 1. INTRODUCTION

Ceramics are being widely considered for replacement of metals and polymers in many engineering applications. Their corrosion resistance, small coefficients of thermal expansion, light weight, low cost, excellent mechanical properties under heavy stress, outstanding electrical and optical properties, and exceptional resistance to high temperatures make them very attractive in structural, microelectronic and biotechnology areas.

Because ceramics have high heat resistance, they have been used in automotive and jet engine components, burner noz-

zles, and heat exchangers. Their special electrical properties are useful in capacitors, piezoelectric devices, thermistors, solar cells, and integrated circuit substrates. Their optical properties make them valuable for infrared transmission windows, as well as in lasers and high-pressure sodium vapor lamps. Because of their hardness and wear resistance, they find use in cutting tools and bearings, and, because some are biocompatible, they are used as substitutes for bones and joints and in artificial heart valves (1,2).

Despite their desirable properties, the use of ceramics is greatly restricted in structural applications because of the following major reasons:

frequency domain signal. The same approach was applied to determine the extent of surface breaking cracks. Results show that void diameter and crack extent can be estimated rather accurately. Results further show that the accuracies would increase significantly if the test frequencies and probe positioning precision were further increased. The focus of this paper is on the detection and characterization of flaws in silicon carbide samples.

The presence of minute voids, inclusions or cracks can severely reduce ceramic material strength. For example a 10 micron flaw in high performance  $\text{Si}_3\text{N}_4$  can reduce the expected strength from approximately 1500 MPa to 250 MPa (3). Therefore, detection and measurement of these flaws are of considerable importance to the reliable application of high performance ceramics as structural components.

The objective of this study was to detect and characterize strength limiting flaws. Specific objectives were to:

1. Detect and locate near-surface voids in silicon carbide.
2. Estimate the size of voids located in the bulk of the material.
3. Detect and estimate the size of surface breaking cracks in silicon carbide materials.

The following sections describe the theoretical background, specimens used in the study, experimental set up, data acquired, results, conclusions, and recommendations.

## 2. THEORETICAL BACKGROUND

To detect near-surface flaws, size voids located in the bulk material, and determine the extent of surface breaking cracks spectral and deconvolution analysis were employed. These three problems although very different in physics of wave propagation yield signals which, from signal processing viewpoints, are very similar in nature and can therefore be analyzed using the same approaches. For example, near-surface

1. It is difficult to make advanced ceramic parts with uniform physical properties from one batch to the next or even within a single batch. As a result, ceramic parts often fail to meet specifications.
2. Properties of ceramics are much more sensitive to imperfections, such as pores at grain boundaries or impurity inclusion, than their metallic counterparts.
3. Ceramics are quite brittle leading to severe failure. They fail catastrophically instead of retaining some load-carrying capability after reaching their maximum sustainable loads.
4. Ceramics, during production, may develop random microcracks, voids, or other flaws that, by acting as stress concentrators, ultimately may cause a part to fail.

It is therefore extremely important that nondestructive evaluation (NDE) techniques be developed and used to distinguish good ceramic components from bad due to material defects. From a NDE point of view the ceramic inspection problem can be divided into the following categories:

1. Detection and characterization of surface flaws, and
2. Detection and characterization of inclusions and voids (occurring close to the near-surface or in the bulk material).

A feasibility study to evaluate the application of high-frequency ultrasound to detect the flaws mentioned above was conducted. Flaw detection and characterization studies were limited to silicon carbide samples. Some of the samples were obtained from NASA Lewis Research Center. Voids located close to the front surface, not detectable using conventional high frequency ultrasonics, were detected using spectral and deconvolution analysis. Location of these voids could be determined within 11% error. Average diameter of voids located in the bulk material (away from front or back surface) was determined using average differential frequency between the maximas or the minimas in the deconvolved



flaws are composed of two signals one from the front surface of the specimen and the second from the flaw. However, these are superimposed and flaws in time domain cannot be detected (Figure 1).

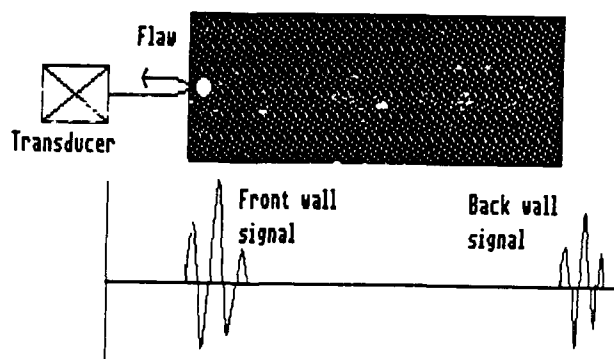


Figure 1. Typical signal from near-surface flaw. Flaws close to the surface are not detectable using arrival time analysis.

Similarly, the physical model for void sizing shown in Figure 2 indicates that:

1. A main signal would appear when the wave front first encounters a void, and
2. A second signal results from part of the wave front which travels around the void. These waveforms appear as small signals after the main signal (Figure 2) and are known as creeping or Franz waves.

Similarly, for surface breaking crack sizing, two signals are obtained. These signals could be from the tip and base of the crack as shown in Figure 3 (a) or from the two edges [Figure 3 (b)].

For comparatively large defects, or relatively higher frequencies, the two signals appear separated by a distinct time delay. For example, the advantage of using a higher frequency for the sizing of voids is evident between the 25 MHz and 100 MHz transducer. The higher frequency because of better axial resolution tends to separate the two signals. The delay time in this case can be directly measured and the size of the flaw calculated. However, for smaller defects such as

those encountered in ceramic inspection the two signals are superimposed and advanced signal processing, such as spectral and deconvolution analysis, is necessary to determine the differential time.

Deconvolution analysis is explained using a linear systems model. Figure 4 shows a simple linear model of interaction between ultrasonic energy transmitted by the transducer, its interaction with the material flaw, and reception by the transducer.

Let  $f(t)$  be the input ultrasonic pulse which after interaction with the material and flaw is picked up by the transducer as  $h(t)$ . Obviously the characteristics of the output pulse are altered due to the interaction. Let  $g(t)$  be the function which is responsible for altering  $f(t)$  to  $h(t)$ . For a linear system, output  $h(t)$  can be written as a convolution of  $f(t)$  and  $g(t)$ . Mathematically,

$h(t) = f(t) * g(t)$  where  $*$  represents convolution integral defined as

$$h(t) = \int_{-\infty}^{\infty} f(\tau) g(t - \tau) d\tau$$

Although the equation appears very simple its numerical evaluation in time domain is computationally intensive. To simplify computation a convolution theorem may be used which states that if  $f(t)$  has the Fourier transform  $F(f)$  and  $g(t)$  has the Fourier transform  $G(f)$ , then  $f(t) * g(t)$  has the Fourier transform  $F(f)G(f)$ . In other words  $h(t) = f(t) * g(t)$  can be obtained by first Fourier transforming  $f(t)$  into  $F(f)$  and  $g(t)$  into  $G(f)$  and then taking the inverse Fourier transform of the product  $F(f)G(f)$ . Thus, to find the transfer function  $g(t)$  which alters the input  $f(t)$  into  $h(t)$  the following relation holds

$$g(t) = \text{IFFT} \{H(f)/F(f)\}$$

This equation signifies that the function responsible for altering  $f(t)$  to  $h(t)$  can simply be obtained by complex division of the Fourier coefficients and taking their inverse Fourier transform. Physically, this equation implies that a flaw can be represented as a time or frequency domain function which is independent of the variables such as transducer, couplant thickness, etc. From a practical viewpoint complex

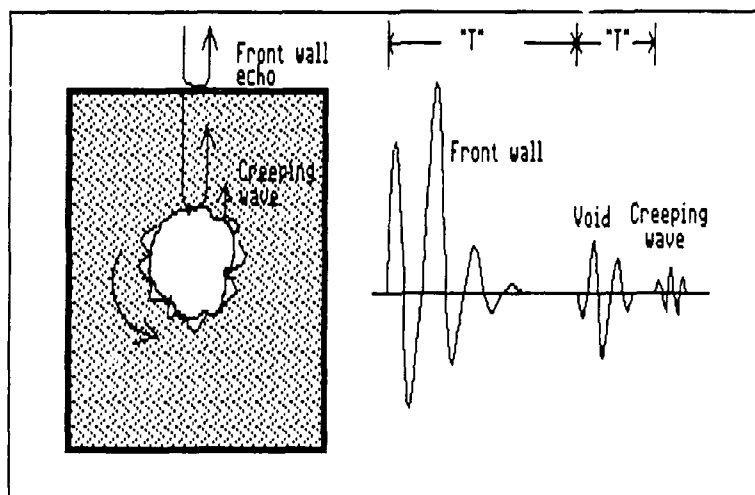


Figure 2. Physical model for determining void diameter. Creeping waves which travel around a void are used to determine the void diameter.

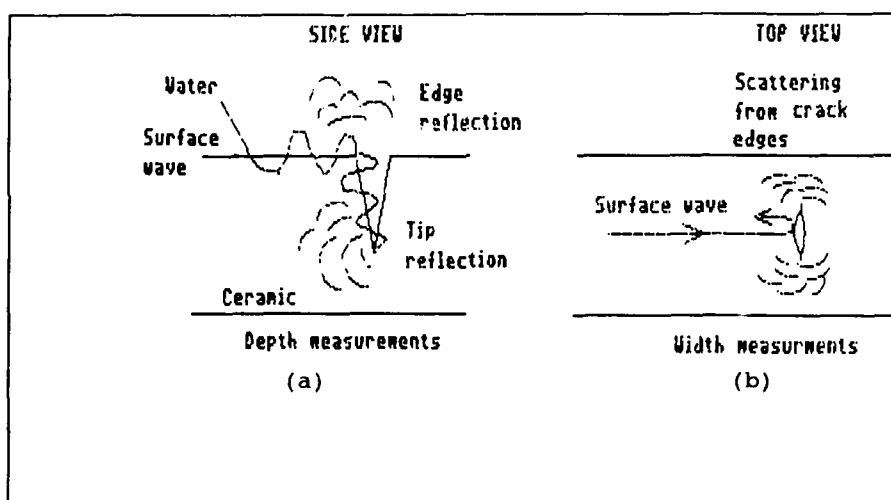


Figure 3. Physical model for determining crack extent. Interference signals from crack tip and edges are superimposed.

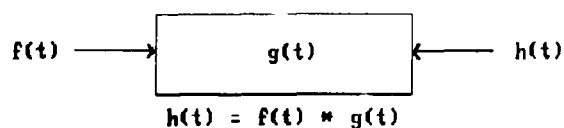


Figure 4. Simple linear model of ultrasonic interaction.

division magnifies inflections in the spectrum due to wave superposition. For example, Figure 5 shows an RF signal which is composed of two superimposed time domain signals.

A frequency spectra shows inflection points indicating the presence of a second signal. The ratio of spectra, prior to taking IFFT for deconvolution, clearly magnifies the inflections.

Location of near-surface voids and the average size of voids located in the bulk of material is calculated by obtaining the mean of frequency differences in maximas and minimas.

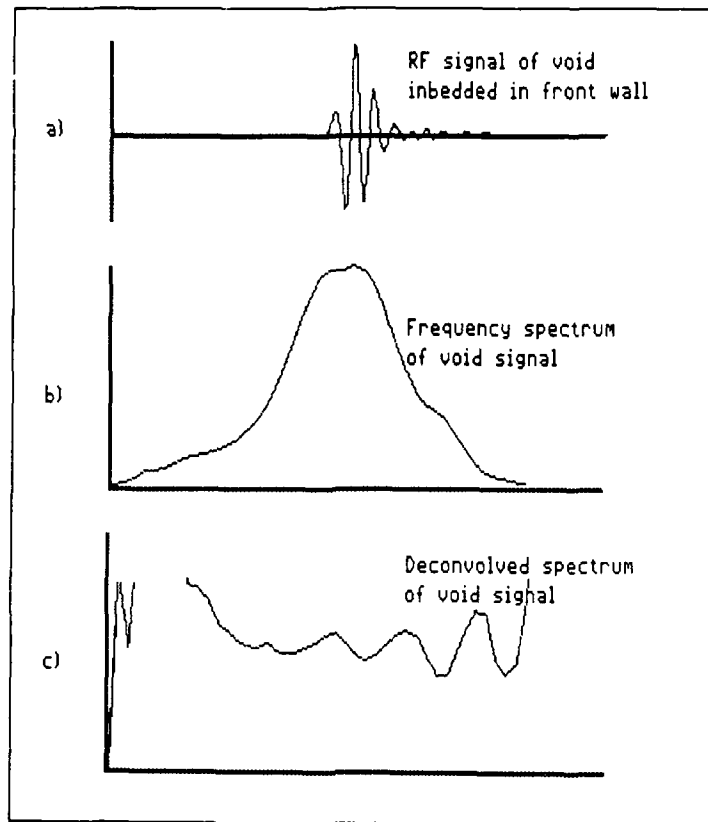


Figure 5. Typical signal for near-surface flaw detection. Deconvolution can improve resolution of the maximas and minimas. (a) RF waveform (b) frequency spectrum, and (c) deconvolved spectrum.

### 3. EQUIPMENT AND SPECIMEN

Hot-pressed (HP) silicon carbide (SiC) specimens with flaws were used. One of the specimens was provided by NASA Lewis Research Center and specified as having seeded voids. The voids ranged from 200 to 500 micrometers in diameter located at depths of 0.2 to 1.1 millimeters. Specimens containing surface breaking cracks were generated in the laboratory using the Vickers indentation technique.

Flaw characterization apparatus consisted of a Panametrics 5600T pulser-receiver, a Tektronix 7854 digital oscilloscope, and an IBM personal computer with a 20 MByte hard drive, a color monitor, a high density disk drive, and 640 K of Random Access Memory. 512 points were digitized and transferred through an IEEE 488 bus from the digital scope to the personal computer for storage and further processing. 25, 50, and 100 MHz transducers were used to detect, locate and size various flaws in the silicon carbide sample. Special

software for data acquisition and processing was developed. Algorithms included temporal averaging, spatial averaging, spectral analysis, and deconvolution.

### 4. RESULTS

The following sections discuss the results as they pertain to near-surface flaw depth measurement, void size, surface crack detection and sizing.

Two transducers 25 and 100 MHz nominal frequency were used to determine depth of 19 voids. The 25-MHz transducer has an axial resolution of 0.78 mm, i.e., flaws located at a distance greater than 0.78 mm from the test surface could be detected using a conventional arrival time approach. Conversely, defects located at a distance less than 0.78 mm would not be detected using a 25 MHz transducer and the conventional arrival time analysis. Figure 6 shows a typical RF-waveform from the front surface of the SiC specimen.

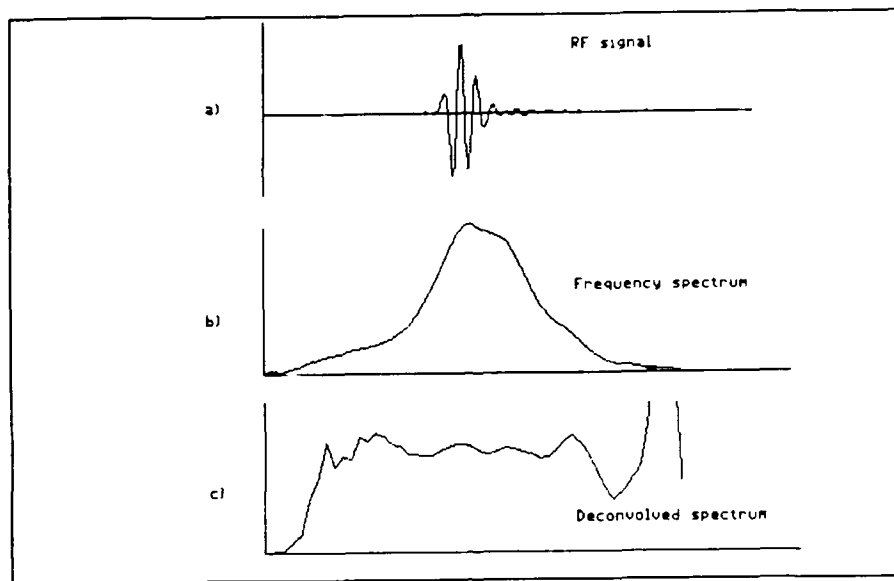


Figure 6. Typical near-surface flaw signal. (a) RF signal, (b) frequency spectrum, (c) and deconvolved spectrum.

Notice that a void 300 microns in diameter, located at 0.6 mm below the front surface is not detected in the time domain. However, the frequency spectrum shows several inflection points indicating the presence of another signal (Figure 6). The deconvolved spectrum clearly shows several maximas and minimas which can be used for confirming the presence of the flaw and calculating its distance from the front surface. Table 1 shows that the flaws located at 0.5 to 0.6 mm can be located using 25 MHz transducer. However, voids located 0.2 mm below the surface could not be located using 25 MHz transducer. This was due to the fact that the bandwidth of the transducer is limited. Therefore, presence and location of these voids was confirmed by a 100 MHz transducer (Table 2). Note that voids located 200 microns from the surface are accurately located.

During any characterization procedure it is important to determine the location of flaws; however, the determining factor whether a flaw renders a component defective is the size of the flaw.

In this part of the study, a sample secured from NASA Lewis with twenty-two seeded voids in a silicon carbide sample was used. The voids ranged from 200 to 500 microns in diameter. Table 3 shows the data for sizing the 500 micron voids with the 25 MHz transducer. Data on the 500 micron voids was

analyzed because only these voids provided a fully resolved signal. Such a signal was necessary to allow the implementation of the same characterization technique as used for the near-surface flaw location measurements.

The main flaw signal and the creeping wave or 'Franz' waves form two superimposed signals which can be resolved using spectral and deconvolution techniques. Tables 3 and 4 show experimentally measured void diameters.

Notice the improvement in the definition of the minimas in the deconvolved representation. Averaging several maximas or minimas reduces the error in the differential frequency. The number of minimas or maximas can be increased by using a higher frequency bandwidth transducer.

Data in Tables 3 and 4 clearly establishes the engineering feasibility of measuring void sizes. However, it is recommended that much more data on smaller size voids and different materials be acquired to establish reliability and accuracy of these techniques.

Table 5 shows estimated crack depth and surface dimension. Estimated crack sizes are also shown in this table. It was discovered that the measured crack sizes correlated rather well with the surface dimension of the crack. It is believed

TABLE 1. EXPERIMENTAL DATA FOR DEPTH MEASUREMENT OF VOIDS AT 25 MHZ

NASA Lewis Specimen, # 23 - Silicon Carbide (SiC)

FILE	NOMINAL SIZE (mm)	DEPTH (mm)	TIME MEASURE (u sec)	DELTA "F" (MHz)	DEPTH FROM TIME MEASURE	EXPR DEPTH (mm)	% ERR
41F	0.20	0.20	N.A.	N.A.	N.A.	N.A.	----
42F	0.20	0.20	N.A.	N.A.	N.A.	N.A.	----
43F	0.20	0.20	N.A.	N.A.	N.A.	N.A.	----
44F	0.20	0.20	N.A.	N.A.	N.A.	N.A.	----
81F	0.30	0.60	N.A.	6.61	N.A.	0.72	19.30
82F	0.30	0.60	N.A.	8.08	N.A.	0.58	2.80
83F	0.30	0.60	N.A.	7.64	N.A.	0.62	3.60
84F	0.30	0.60	N.A.	7.94	N.A.	0.60	0.50
85F	0.30	0.60	N.A.	6.91	N.A.	0.69	14.60
86F	0.30	0.60	N.A.	6.66	N.A.	0.71	18.60
87F	0.30	0.60	N.A.	6.47	N.A.	0.74	22.50
88F	0.30	0.60	N.A.	7.40	N.A.	0.64	6.80
6F	0.50	0.50	N.A.	8.09	N.A.	0.58	16.60
7F	0.50	0.50	N.A.	7.50	N.A.	0.63	26.20
1F	0.50	1.10	0.24	4.26	1.14	1.11	0.90
2F	0.50	1.10	0.24	4.56	1.14	1.04	5.40
3F	0.50	1.10	0.23	5.15	1.10	0.92	16.30
4F	0.50	1.10	0.23	4.32	1.10	1.10	0.00
5F	0.50	1.10	0.23	4.75	1.10	1.00	9.00
AVERAGE % ERROR							10.83

TABLE 2. EXPERIMENTAL DATA FOR DEPTH MEASUREMENT OF VOIDS AT 100 MHZ

NASA Lewis Specimen # 23 - Silicon Carbide

FILE	NOMINAL SIZE (mm)	DIRECT TIME MEASURE	NOMINAL DEPTH (mm)	DELTA "F" (MHz)	EXPMNTAL DEPTH (mm)	% ERR
V100-42V	0.20	N.A.	0.20	23.52	0.20	0.50
V100-41V	0.20	N.A.	0.20	20.00	0.24	18.50
V100-44V	0.20	N.A.	0.20	17.94	0.27	32.50
V100-43V	0.20	N.A.	0.20	17.65	0.27	32.50
V100-61V	0.30	N.A.	0.60	8.82	0.49	10.50
V100-62V	0.30	N.A.	0.60	11.28	0.54	18.85
V100-7FV	0.50	N.A.	0.50	10.50	0.45	25.00
AVERAGE % ERROR						18.85

TABLE 3. EXPERIMENTAL DATA FOR SIZING OF VOIDS AT 25 MHZ

NASA Lewis Specimen, # 23 - Silicon Carbide

Specimen # 23 : With seeded voids

Thickness - 3.048 mm

Longitudinal velocity - 9.49 mm/microseconds

Shear velocity - 6.02 mm/microseconds

Wavelength - 0.379 mm

25 MHz Panametrics focused transducer - V324 | 0.25/1.5 "

#75157

FILE	MEASURED SIZE (mm)	DEPTH (mm)	DELTA "F" (MHz)	VOID SIZE (mm)
41F	0.20	0.20	N.A.	N.A.
42F	0.20	0.20	N.A.	N.A.
43F	0.20	0.20	N.A.	N.A.
44F	0.20	0.20	N.A.	N.A.
81F	0.30	0.60	N.A.	N.A.
82F	0.30	0.60	N.A.	N.A.
83F	0.30	0.60	N.A.	N.A.
84F	0.30	0.60	N.A.	N.A.
85F	0.30	0.60	N.A.	N.A.
86F	0.30	0.60	N.A.	N.A.
87F	0.30	0.60	N.A.	N.A.
88F	0.30	0.60	N.A.	N.A.
6F	0.50	0.50	N.A.	N.A.
7F	0.50	0.50	5.80	0.51
1F	0.50	1.10	5.88	0.51
2F	0.50	1.10	4.85	0.62
3F	0.50	1.10	4.41	0.68
4F	0.50	1.10	4.12	0.73
5F	0.50	1.10		

TABLE 4. EXPERIMENTAL DATA FOR SIZING VOIDS AT 100 MHZ

NASA Lewis Specimen, # 23 - Silicon Carbide (SiC)

FILE	NOMINAL SIZE (mm)	DEPTH (mm)	"F" (MHz)	VOID SIZE (mm)
V100-42V	0.20	0.20	N.A.	N.A.
V100-41V	0.20	0.20	N.A.	N.A.
V100-44V	0.20	0.20	N.A.	N.A.
V100-43V	0.20	0.20	N.A.	N.A.
V100-61V	0.30	0.60	0.05	0.14
V100-62V	0.30	0.60	0.05	0.15
V100-7FV	0.50	0.60	0.12	0.36

TABLE 5. EXPERIMENTAL DATA USED FOR SIZING SURFACE CRACKS

FILE	LOAD (grams)	MEASURED WIDTH (mm)	DELTA "F" (MHz)	EXPERIMENTAL DIMENSION (mm)	% ERR
5A	8000.000	0.188	17.930	0.192	2.100
9B	8000.000	0.195	19.920	0.173	11.300
6B	2000.000	0.098	16.870	0.204	108.200
6A	2000.000	0.113	21.760	0.158	39.800
7A	4000.000	0.143	20.880	0.165	15.400
2B	4000.000	0.173	22.350	0.154	11.000
2A	4000.000	0.158	20.580	0.167	5.700
7B	4000.000	0.150	23.790	0.145	3.300
8B	6000.000	0.195	15.580	0.221	13.300
3B	6000.000	0.173	16.910	0.204	17.900
5B	8000.000	0.203	16.160	0.207	2.000
3A	6000.000	0.180	20.050	0.172	4.400
9A	8000.000	0.225	17.490	0.197	12.400
10A	10000.000	0.240	18.820	0.183	23.600
4A	8000.000	0.248	16.320	0.211	14.900
4B	8000.000	0.225	18.380	0.187	16.800
11A	10000.000	0.248	17.860	0.193	22.200
10B	10000.000	0.248	20.580	0.167	32.700
11B	10000.000	0.248	21.660	0.159	35.900

that knowing the aspect ratio in a particular material the depth could be estimated.

## 5. CONCLUSIONS AND RECOMMENDATIONS

Based on the results the following conclusions can be drawn:

1. Flaws located near the front-wall surface can be located accurately using deconvolution analysis.
2. Voids located in the bulk of material can be sized using spectral and deconvolution analysis.
3. Leaky surface waves are an excellent means for detecting surface breaking cracks. Sizing the crack depth is difficult.
4. Measurement accuracy in locating flaws beneath the surface or sizing them is dependent on transducer center frequency and bandwidth.

It is recommended that

1. Techniques described in this report be applied to smaller diameter voids in a host of different materials.

2. A detailed metallurgical study which provides quantitative measures be conducted and the results correlated with ultrasonic velocity and attenuation measurements.

3. Advanced signal processing techniques including imaging should be given preference to characterize flaws.

## 6. REFERENCES

1. Hench, L.L. and Ulrich, D.R., editors Ultrasonic Processing of Ceramics, Glasses, and Composites, Wiley: New York, 1984.
2. Sanders, H.J., "High Tech Ceramics," C&EN, July 1984.
3. Nicholson, P.S., "A Pedagogical Development of the Ultrasonic Characterization of Flaws in Advanced Ceramics," Ceramic Engineering Research Group, McMaster University, Hamilton, Ontario, Canada.

Probability of Detection of Volume Defects  
In Both Green, Sintered and HIP'ed Zirconia Ceramics  
By X-Ray Microfocus Radiography

Kamal E. Amir, Oh-Hun Kwon and Donald O. Patten  
Norton Company, Advanced Ceramics, Northboro, MA 01532

ABSTRACT

The sensitivity of seeded void detection at a 90/95 probability of detection/confidence level is around 8% of specimen thickness for sintered Y-TZP (2.5 mol% yttria zirconia) ceramics, while for green (molded/ unfired) samples it is around 7.5%. Microscopic examination reveals that the size of voids seeded in the sample bulk decreases to  $<5\text{ }\mu\text{m}$  after HIP'ing while a small percentage of the remained surface voids are detected by radiography. On the other hand, the sensitivity of detection of Fe inclusions at 90/95 probability of detection/confidence level is around 8% for HIP'ed material and 7% for green samples. It has been demonstrated that microfocus radiography can be useful in evaluating the effectiveness of HIP'ing in eliminating voids and pores in thin section parts.

A Fortran program was written to allow for rapid and efficient calculations of the probability of detection statistics for a large number of seeded defects using a numerical root finding approach.

**Introduction:**

Zirconia base ceramics are known to have the highest fracture toughness among all ceramic monoliths (1). In addition, they possess high strength and good wear resistance (2). The material's improved fracture toughness is usually a result of the volume and shape changes associated with transformation phenomena such as martensitic transformation from tetragonal to monoclinic (3). Linear elastic fracture mechanics models stress the importance of understanding the crack instability in relationship to the critical stress intensity factor. Crack geometry plays a major role in this process. Such cracks may be associated with the presence of voids and other volume defects in the material (4). It is therefore essential that inspection procedure

be established for the detection and quantification of those defects. Numerous NDE techniques are available for such purpose. However, data on the quantitative detection sensitivity of defects in ceramics and particularly zirconia base materials hardly exist.

The present investigation was carried out to determine the probability of detection statistics for volume defects in zirconia ceramics using microfocus film radiography techniques. Moreover the intention was to monitor and evaluate the efficiency of hot isostatic pressing, HIP'ing, in reducing and eliminating voids in such materials. Microfocus film technique was chosen over real time due to the fact that zirconia base materials have very high x-ray



absorption coefficients which makes inspection of thick sections nearly impractical. Very high acceleration voltages are usually needed which reduce the real time image contrast and quality. On the other hand film techniques provide higher sensitivity/contrast for defect recognition than real time with fewer image problems.

#### Method of Analysis:

Methods for analyzing the reliability of NDE inspection techniques are detailed in reference 5. There are usually four terms to be considered when assessing the reliability of inspection decisions. These are:

- a - Quality index,  $\alpha$
- b - Error-Probability Ratio -  $\beta$
- c - Success-Probability Ratio -  $\gamma$
- and d - Probability of detection,  $P_d$  (both conditional and non-conditional, see reference 5).

The main objective of statistical evaluation of the reliability of non-destructive inspection is to estimate the probability of detection,  $P_d$ , with as few trial inspections as possible. This is done by defining a lower limit (lower bound),  $P_d$ , for the range of values that is expected to contain the true probability of detection. The degree of confidence,  $G$ , in the probability of detection is limited by the number of seeded/existing flaws. The exact binomial distribution function is commonly used to find  $P_d$  for a given total number of flaws/defects as follows:

$$1 - G = \sum_{x=0}^N \left[ \frac{N!}{x!(N-x)!} \right] P_d^x (1-P_d)^{N-x} \quad 1$$

where  $X$  is the total number of detected flaws and  $N$  the initial total number of flaws in the material.

Radiographic detectability of defects is often expressed as a percent of thickness sensitivity as given by:

$$\text{Thickness sensitivity} = (D/T) * 100 \quad 2$$

where  $T$  is the sample thickness in the direction of the x-ray beam, and  $D$  the defect size.

#### Details of the Fortran Computer Program Approach:

The immediate difficulty in computing the probability of detection lies in the fact that one cannot solve equation 1 above directly for  $P_d$  because the lower bound probability of detection,  $P_d$ , is embedded in the summation. The problem was addressed previously by NASA (6, 7) using a computer program which approximates the value of  $P_d$  using an expansion. The intention in the present investigation is to solve the relationship directly using a numerical root finding approach. An initial Fortran program was written, which successfully provided solution for small values of  $N$ . Problems were encountered when computing very large as well as very small values of  $N$  in the factorial. A second look at equation 1 revealed the source of these difficulties. As  $P_d$  can only fall between 0 and 1 the  $P_d^x$  terms and  $(1-P_d)^{N-x}$  have the potential to be extremely small numbers. On the other hand  $N!/X!(N-X)!$  can be either very large or very small. Both accuracy considerations and the maximum and minimum numbers which can be handled by the digital computer forced some minor adjustments. Double precision (16 digit Mantissa) was employed for the appropriate variables and a strategy was devoted to minimize the size of the  $N!/X!(N-X)!$  term for all possible values of  $N$  and  $X$ . In order to allow  $N$  to hold values of up to 500 logic was adopted to factor out either  $1 \times 10^{30}$  or  $10 \times 10^{-30}$  multiple times as the size of the factorial term approaches the maximum and minimum numbers which the computer could handle ( $9.99 \times 10^{38}$  or  $9.99 \times 10^{-38}$ ). The power terms of  $P_d^x$  and  $(1-P_d)^{N-x}$  were handled with double precision natural logarithm.

The root finding routine employed to solve equation 1 is of a type called A Binary Cut Search (Method of Bisection). The logic begins with an initial guess for  $P_d$  and calculates the resulting error. The guess is incremented by an empirically chosen value and the error is again calculated. This continues until the sign of the guessing procedure has stepped past the actual solution. When this occurs the increment is divided by two and another solution is performed. By this approach the program homes in on the exact solution. An error tolerance is selected beyond which the accuracy of the solution is not significantly affected. Although more rapid root-finding routines exist (one was attempted in this effort) they are not as stable and thus have difficulties with sensitive functions. The solution generated

The root finding routine employed to solve equation 1 is of a type called A Binary Cut Search (Method of Bisection). The logic begins with an initial guess for  $P_d$  and calculates the resulting error. The guess is incremented by an empirically chosen value and the error is again calculated. This continues until the sign of the guessing procedure has stepped past the actual solution. When this occurs the increment is divided by two and another solution is performed. By this approach the program homes in on the exact solution. An error tolerance is selected beyond which the accuracy of the solution is not significantly affected. Although more rapid root-finding routines exist (one was attempted in this effort) they are not as stable and thus have difficulties with sensitive functions. The solution generated

with this program agrees with those found by other methods for values of  $N$  in the range of 50 or less. However, we are not aware of other solutions for larger values of  $N$ , the results generated by the program behave exactly as one would expect. The program details are described in Appendix A.

#### Experimental Procedure:

Two spray dried Y-TZP (toughened zirconia polycrystals with yttria) powders were chosen for this study: YZ-110 (2.5 mol%  $Y_2O_3$ , Norton) and TZ-3YA (3mol%  $Y_2O_3$ , Tosho). Classified polymethyl methacrylate, PMMA, and iron spheres with discrete sizes were seeded in the material so as to simulate naturally occurring voids and inclusions. Nominal diameters of PMMA were 50, 100, 125 and 250  $\mu m$  and those of Fe were 78, 95, and 165  $\mu m$ ; table 1 shows the size distribution of those particles as measured using Princeton Gamma Technics, PGT, digital image analysis system IV.

Both 30 and 300 spheres of PMMA and Fe were randomly dispersed into Y-TZP powders in a small vial using a commercial mixer, SPEX Mixer/mill. The powder mixtures were then uniaxially pressed at 200 MPa into a round steel die. Thickness of the green compact was typically 1.3 mm. Dummy pellets of various thicknesses were also pressed using the same technique to provide a thickness range for the probability of detection study. After x-ray microfocus examination of the green pellets, the samples were sintered at 1500°C for 30 minutes to a density around 98-99% of the material's theoretical density. After microfocus investigation of those sintered samples they were HIP'ed at 1500°C under pressure to full density and finally inspected.

A Ridge HOM X-161 X-ray microfocus unit was used for producing the film data. The operating parameters for the microfocus X-ray system were 60 to 115 KV excitation voltage, with a beam current of .28 to .50 mA. The exposure times were varied from 12 to 30 minutes to achieve film densities in the range 1.5 to 2.2 using data from the characteristics exposure charts which were generated in-house for Agfa films (D4). A special filter screen was placed in the path of the x-ray beam after it travelled through the sample which resulted in improved film contrast. The film

exposures were conducted at magnifications of 8 to 13X. For image quality, exposures were made using the ASTM # 5, 10, 15, and 20 Molybdenum penetrameters for each specific sample thickness. The exposed films were processed using an Agfa Structur-ex NDT 1 film processor unit. An 8 minute film processing cycle was selected.

Samples were sliced with a diamond saw then polished and given a final finish using 1  $\mu m$  diamond paste and examined optically for void detection.

#### Results & Discussion:

Densities of green compacts were found to be around  $55 \pm 1\%$  of the theoretical. The sintered samples gave density values around  $98 \pm .50\%$  of the theoretical value and underwent around 18% linear shrinkage. As HIP'ed the material achieved a density around  $99.5 \pm .40\%$  of the theoretical value.

#### Microstructure:

Figure 1 shows the distribution of PMMA simulated pores after HIP'ing. It is noted that the distribution of pores in the zirconia matrix is quite random with variable distances to neighboring macropores thus simulating the random distribution of defects in actual materials. Figure 1 also shows the reduction in both the number and size of seeded PMMA particles (simulated voids) during HIP'ing. After complete densification only those pores  $< 1 \mu m$  were present in the matrix.

Those voids in the samples bulk, which were  $< 125 \mu m$ , were completely eliminated during HIP'ing. Figure 2 shows an example of both surface and near surface pores which remained after HIP'ing. The shape of such pores changes during densification as a result of plastic deformation/diffusion induced by the isostatic pressure and high temperature. Ultimately such mechanism eliminates volume and near surface voids but not surface ones.

Samples sintered with Fe spheres were cracked due to the volume expansion resulting from oxidation of Fe (see Figure 4); therefore, they were not HIP'ed.

#### Radiography Data:

Figures 3 to 5 provide typical examples of microfocus projection radio-

graphs obtained for both green, sintered and HIP'ed zirconia samples containing seeded defects.

#### Probability of Detection Statistics:

Figures 6 to 9 give the lower bound probability of detection as a function of thickness sensitivity as defined in equation 2 above. The defect size used in the plots is the as seeded Fe and PMMA size. Hot isostatic pressing has significantly reduced the as-seeded size of the PMMA induced pores and eliminated some of the simulated ones.

It can be seen that the probability of detection of simulated voids, PMMA in molded zirconia at 95% confidence level drops below 90% at a thickness sensitivity of <8%, see Figure 6. It drops to less than 50% for void size smaller than 3.5% of the sample thickness. The minimum size detected using microfocus radiography was 20  $\mu\text{m}$  in samples 1.3 mm thick; however, the data obtained on such samples was not used for statistical analysis because some of the detected sites were due to the presence of clusters and agglomerates and not single particles. From Figure 6 we can conclude that microfocus radiography technique can provide reliable detection of defects which are larger than 8% of the material thickness (i.e. with less than 10% uncertainty).

After sintering and HIP'ing the probability of detection of the simulated voids was reduced, see Figure 7. A first look may lead us to believe that  $P_d$  for HIP'ed material is much lower than that for sintered samples. A low fraction of the seeded voids were detected therefore yielding  $P_d$  values much lower than 90% (Figure 8). Microstructural observations discussed above show a shrinkage of the pores created by seeded PMMA and close up of some of them. Therefore the data of the HIP'ed material may be interpreted as representing a different void size range, probably at least 2-3 times smaller than the as seeded size range. This means that the thickness sensitivity for the pore size at which  $P_d$  values were reported for HIP'ed samples should be about 1/3 the values plotted. If we then use the corrected values for thickness sensitivity the curve for the HIP'ed material will shift to coincide with the curve for sintered material (see curve 3 - HIP'ed/normalized thickness). All

this means is that the probability of detection of simulated voids in HIP'ed material is the same as that in sintered one.

The HIP'ed samples show differences in both density and chemistry as compared to sintered ones. Although this results in different mass absorption coefficients of the two matrices for the x-rays, the differences are not significant enough to provide better detection capability for defects in HIP'ed material versus sintered one. This means that the detection of voids by x-rays should be comparable for materials densified by various techniques in agreement with our previous hypothesis (Figure 7 data).

In the case of Fe seeds, the probability of detection by x-ray radiography is slightly higher for green material as compared with sintered one as seen from examining both Figures 8 and 9. For example the 90%  $P_d$  at 95% confidence level occurs at around 7% thickness sensitivity (smaller defect size) for green compacts as compared to 8% for sintered ones. There has been no size reduction for the Fe particles as a result of sintering as confirmed by both radiographs and metallography; the material's density increased from around 55 to 98% of the theoretical value. Since the density of Fe is around 7.8 g/cc, the density difference between Fe and zirconia matrix is therefore reduced on going from green to sintered state. Such reduction in density difference translates into a reduced difference in the x-rays mass absorption coefficients of Fe w.r.t. the matrix. Consequently the differential contrast effect of the Fe inclusions which is a function of the x-ray mass absorption is reduced by sintering. Therefore, the detection sensitivity of x-ray radiography for Fe in sintered material is lower than that in green one. This also may be supported by the fact that Fe reacts with the zirconia matrix during sintering; the reaction zone has absorption characteristics similar to that of the matrix. In terms of radiography this may be thought of as a reduction of the effective absorption cross section of Fe seeds to x-rays and consequently a reduction in detection sensitivity with densification.

One of the main outcomes of this work is that the simulated voids which were as large as 250  $\mu\text{m}$  underwent

significant shrinkage, many of the smaller size seeds (125, 100 and 50  $\mu\text{m}$ ) disappeared and some shrank to < 5  $\mu\text{m}$  during the HIP'ing process.

Another finding is that x-ray microfocus radiography technique has demonstrated its ability to detect both inclusions and simulated voids in zirconia samples which are reasonably thin. Thick samples ( $\geq 25$  mm) require much higher excitation voltage in excess of 150 KV to enable x-rays to penetrate through. Most microfocus radiography units are not designed for over 165 KV excitation voltage. Units with higher KV usually have x-ray focal spot sizes around 300  $\mu\text{m}$  and larger. The image geometric unsharpness of such systems is higher than the focal spot size (depends on the image magnification) and therefore such equipment exhibit zero sensitivity to detecting defects smaller than 100  $\mu\text{m}$ .

Having said this, it is believed that complementary techniques such as ultrasonics are needed to help evaluate high density ceramics which contain finer size defects and flaws such as zirconia.

#### Conclusions:

- 1- Microfocus radiography film technique is capable of detecting both voids and inclusions (Fe) in zirconia base ceramics which are reasonably thin (< 25 mm).
- 2- The probability of detection of Fe inclusions at 95% confidence level is 90% for defect size around 7% of the sample thickness or larger in molded zirconia and 8% or larger in sintered material.
- 3- The probability of detection of simulated voids is 90% at confidence level of 95% in molded samples (green compacts) for defect size around 8% of the part thickness or larger. For both HIP'ed and sintered YZ110 samples the same detection statistics are achieved for voids which are larger than 8% of the material's thickness. This thickness sensitivity is for the as seeded defect sizes.
- 4- The process of hot isostatic pressing, HIP, has shown to be capable of healing/eliminating voids and in significantly

reducing their size during the densification process.

- 5- Microfocus radiography film techniques may be used as a monitoring tool along with microscopy and other complementary NDE techniques (ultrasonics) to evaluate the efficiency of HIP'ing.

#### Acknowledgment:

The authors would like to thank Gary Lambert for conducting the radiography exposures.

#### References:

- 1- R.C. Garvie and R.T. Pascoe, in "Processing of Crystalline Ceramics" edited by H. Palmour III, R.F. Davis and T.M. Hare (Plenum Press, New York, 1978) P. 263.
- 2- T.E. Fischer, M.P. Anderson, S. Jahanmir, and R. Salher, "Friction and Wear of Tough and Brittle Zirconia in Nitrogen, Air, Water, Hexadecane and Hexadecane Containing Stearic Acid", Wear, 124, 1988, P. 133.
- 3- N. Claussen and P. Petzow, in "Energy and Ceramics" edited by P. Vincenzini (Elsevier, 1980), P. 680.
- 4- F.F. Lange, "Transformation Toughening, Part 2 Contribution to Fracture Toughness", J. Materials Science, 17, 1982, P. 235.
- 5- P.F. Packman, S.J. Klima, R.L. Davies, J. Malpani, J. Mayzis, W. Walker, BGW Yee, and D.P. Johnson, "Reliability of Flaw Detection by Nondestructive Inspection", Metals Handbook, Vol. 11, 8th ed., 1976, P. 414, ASM, Metals Park, OH.
- 6- Don J. Roth, Stanley J. Klima and James D. Kiser, "Reliability of Void Detection in Structural Ceramics Using Scanning Laser Acoustic Microscopy", NASA Technical Memorandum 87035, Spring Meeting of the American Society for Nondestructive Testing, Washington, D.C. March 11-14, 1985.



a-As Seeded



b-HIP'ing C1

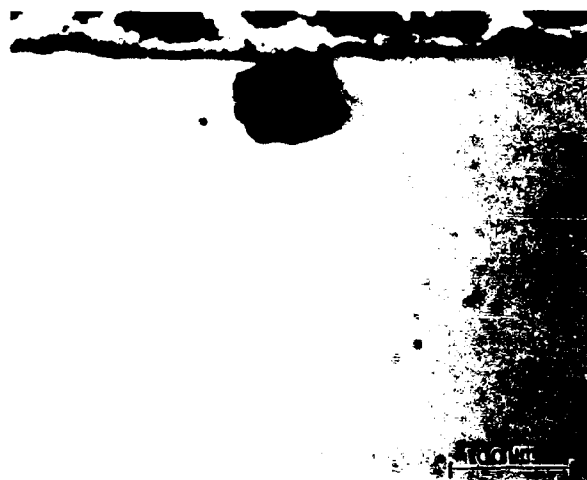


c-HIP'ing C2

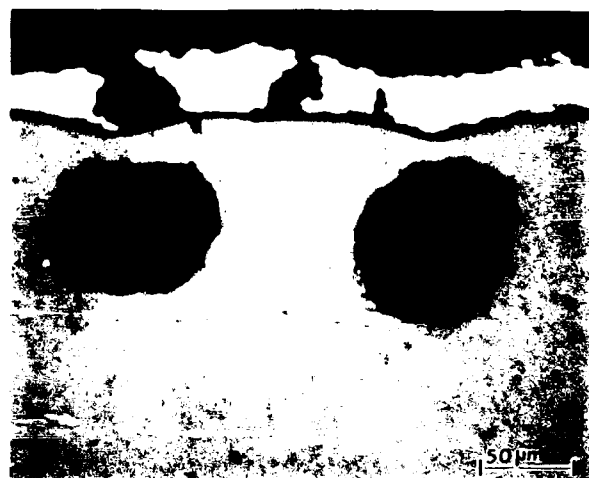
Figure 1. Effect of HIP'ing Conditions on the Number and Size of Macropores in Zirconia Ceramics. Seeded Pore Size is 125  $\mu$ m

Table 1  
Particle Size Analysis of the Defects Seeded in Zirconia ( $\mu$ m)

Fe		PMMA	
Average	Std. Dev.	Average	Std. Dev.
76	9	24	14
107	14	60	14
175	26	95	21
		168	19
		250	18



a-Surface Pore



b-Near Surface Pores

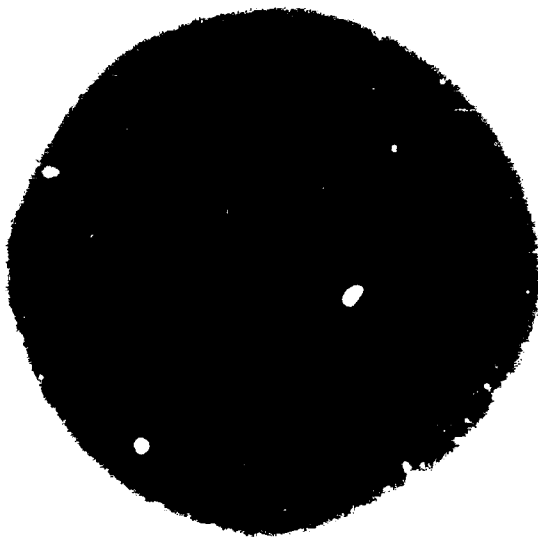
Figure 2. Cross Section of HIP'ed Zirconia Showing the Presence of Pores Only at and near the Surface of the Samples. The Effect of Plastic Deformation during HIP'ing is Revealed through the Depressions near Individual Pore Sites.



a- 16X



a- 7X



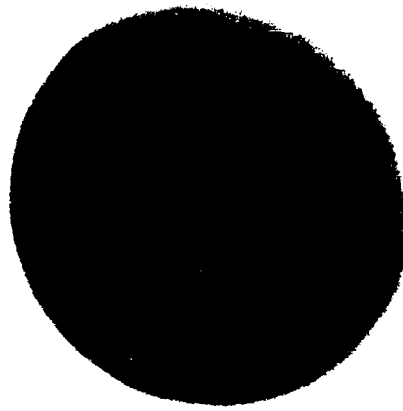
b- 11X



b- 8X

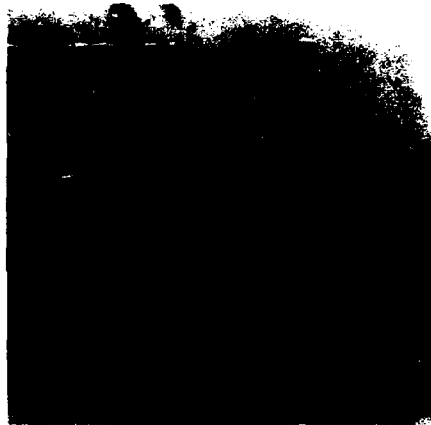
Figure 3. X-Ray Radiographs of Zirconia with Fe Seeds, 100  $\mu\text{m}$  Nominal Size. Samples are 1.5 mm Thick. a-Molded, b-Sintered.

Figure 4. X-Ray Microfocus Radiographs of Both Molded and Sintered Zirconia Containing 150  $\mu\text{m}$  Nominal Size Seeded Fe Inclusions. a-Molded, b-Sintered



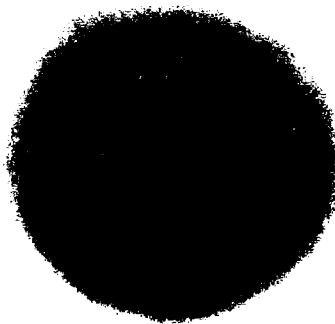
a-

7X



b-

14X



c-

7X

**Figure 5. X-Ray Radiographs of Molded Zirconia Discs, 1.5 mm Thick, Seeded with PMMA Particles with the following Nominal Sizes  
a-20  $\mu\text{m}$ , b-50  $\mu\text{m}$ , c-100  $\mu\text{m}$**

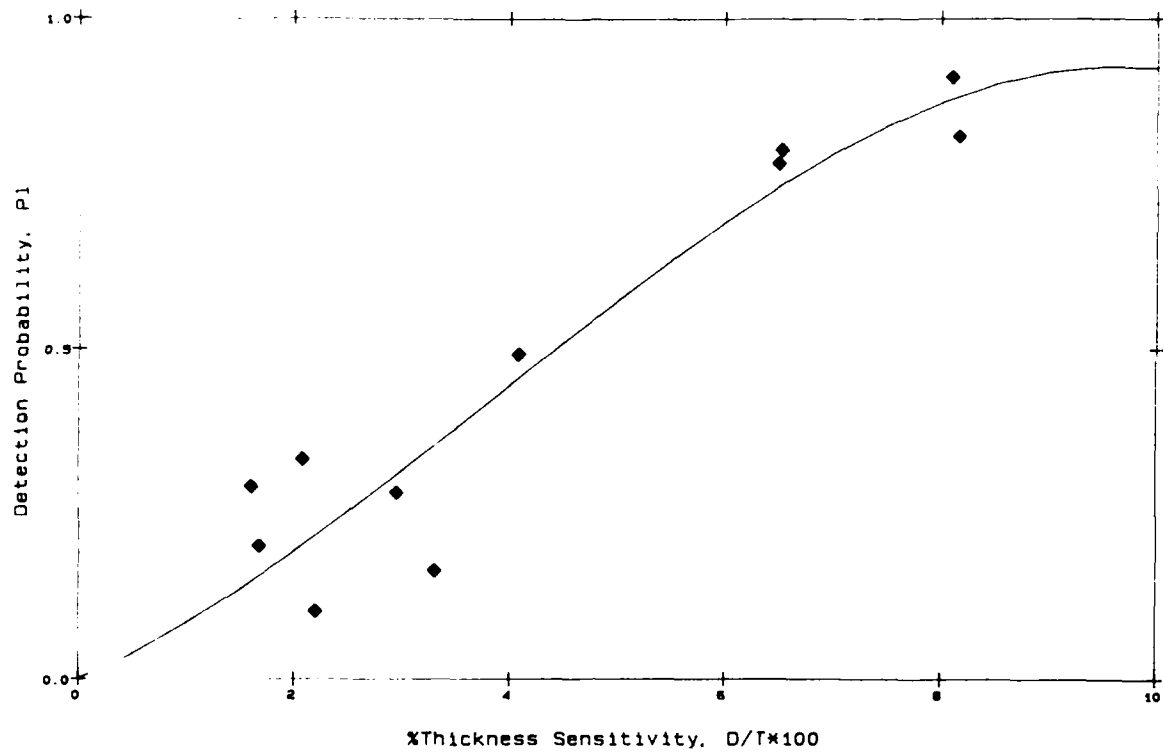


**Figure 6. Lower Bound Probability of Detection of Voids in Molded ZrO<sub>2</sub>**

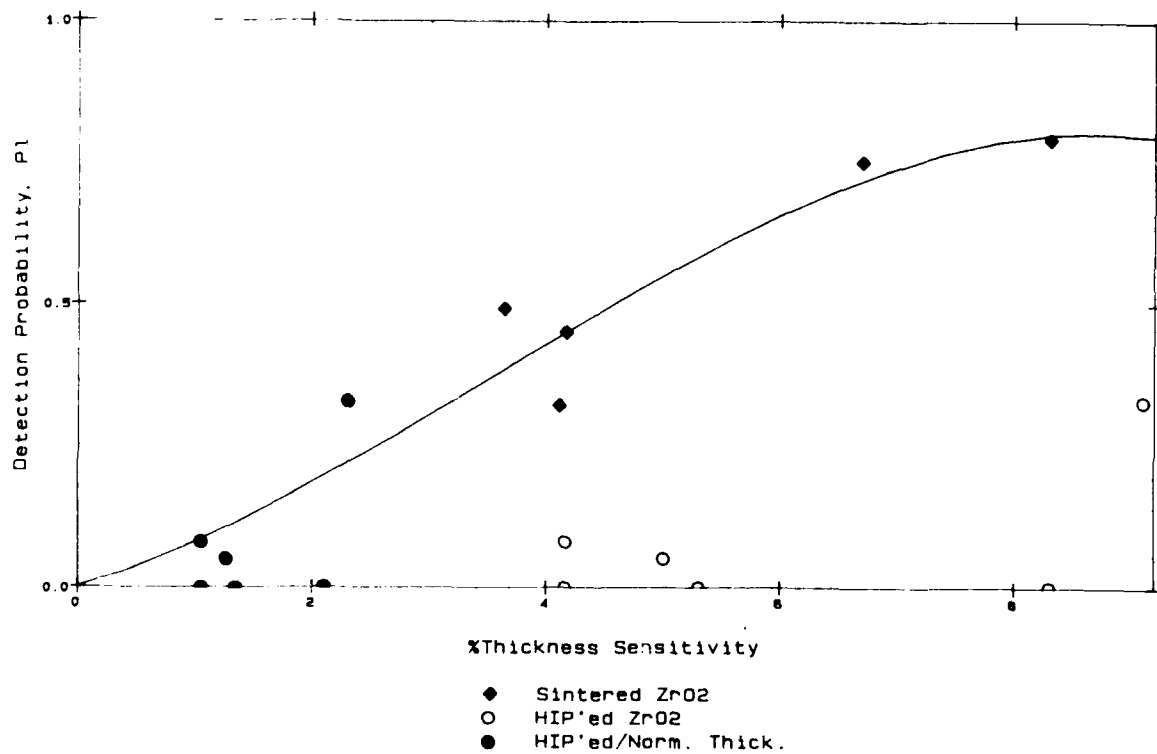


**Figure 7. Lower Bound Probability of Detection of Voids in Sintered and HIP'ed ZrO<sub>2</sub>**



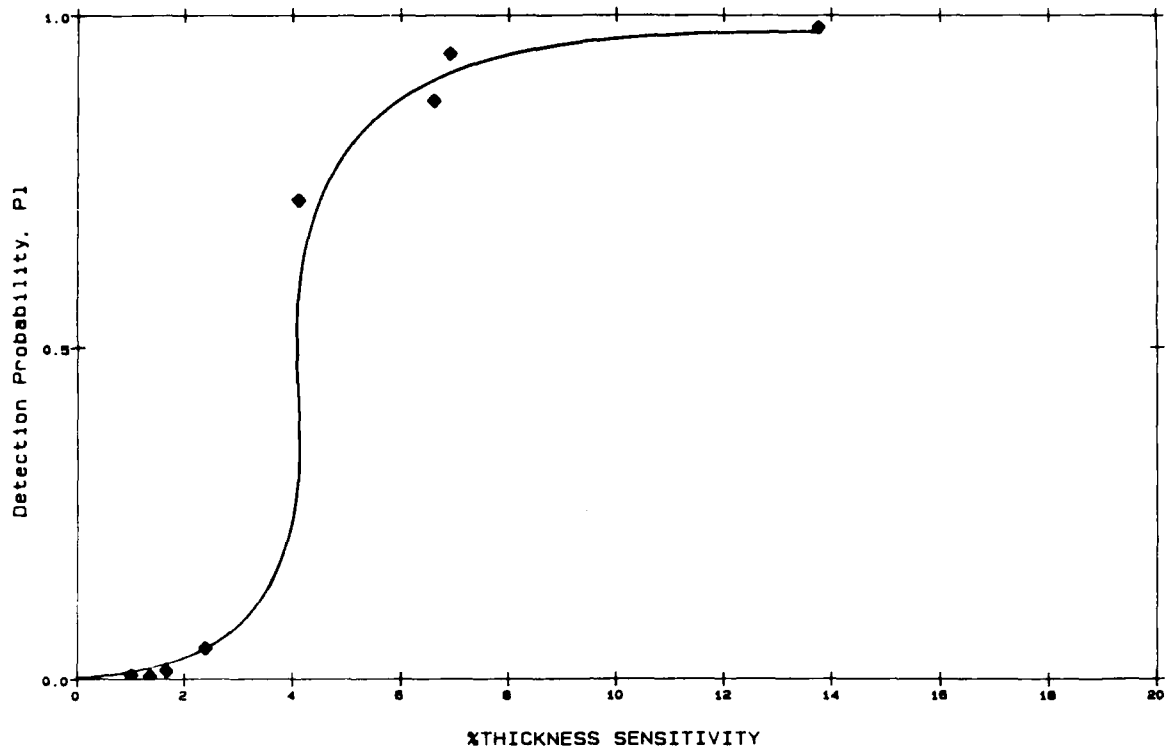


**Figure 8. Lower Bound Probability of Detection of Fe in Molded ZrO2**

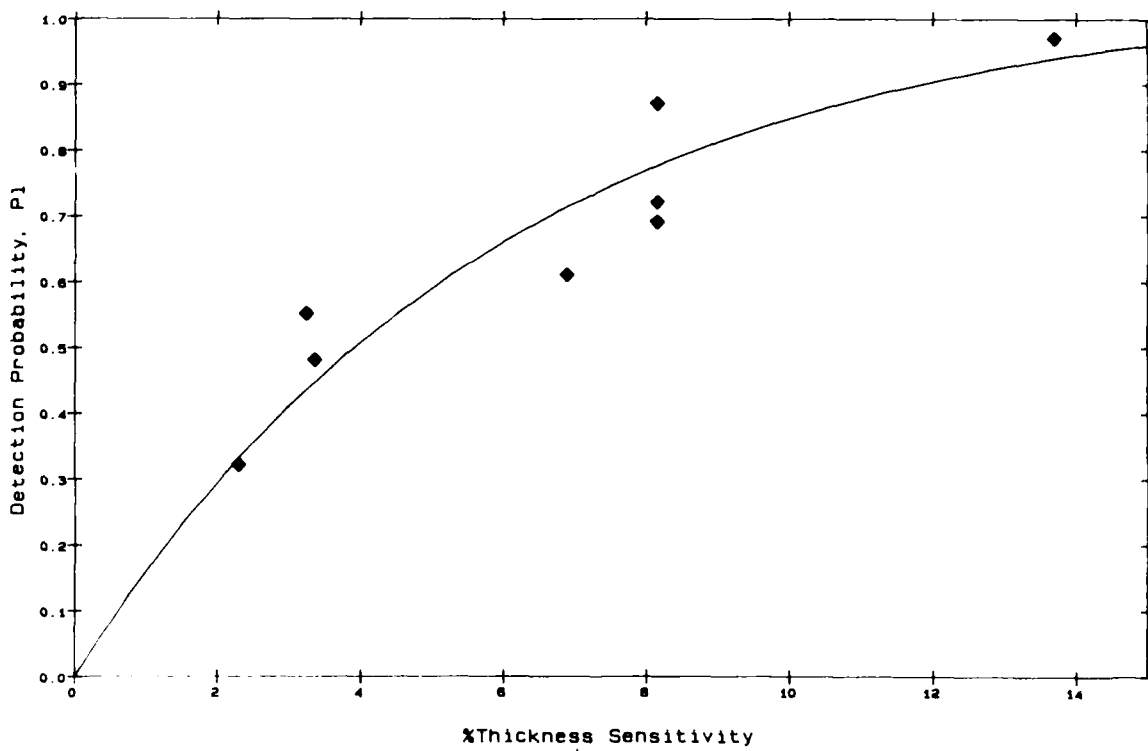


**Figure 9. Lower Bound Probability of Detection of Fe in Sintered ZrO2**

## APPENDIX A

### FORTRAN COMPUTER PROGRAM FOR COMPUTING LOWER BOUND PROBABILITY OF DETECTION STATISTICS

The following Fortran program was written for a Digital VAX 750 minicomputer to allow for computing the lower bound Probability of detection,  $P_d$ , at any level of Confidence,  $G$ .

The program guesses an initial approximate value for  $P_d$  which is used to find an exact solution of the Binomial Distribution Function for the lower bound Probability of detection using a binary cut search route finding routine. It also allows for inputting an initial value of  $P_d$  by the operator.

Plots of  $P_d$  as a function of thickness sensitivity on curve fitting functions were carried out using a commercially available statistical/graphics package (PSI Plus by BBN & Associates in Cambridge, MA).

## VARIABLES

### Double Precision

F - Intermediate value of factorial term  
FLAG2 - Counter for # of times F is divided by IE-30  
FLAG3 - Counter for # of times F is divided by IE-30  
N - Number of uniform-sized, seeded defects, used as Do loop limit  
S - Number of defects actually detected, Do loop lower limit  
NF - Used to pick up value of N as separate from Do loop limit  
NFF - Decremental value of NF in factorial loop  
PL - Probability of detection  
Q -  $Q = N - X$   
QF - Decremental value of Q in factorial loop  
SUM - Sum of values of Z.  $\text{Sum} = \sum_{x=s}^N \frac{N!}{x!(N-x)!} P_1^x (1-P_1)^{N-x}$   
X - Double precision value of X used in factorial loop  
Z -  $Z = \frac{N!}{x!(N-x)!} (P_1)^x (1-P_1)^{N-x}$

### Regular Precision

G - Confidence level  
I - Summation loop counter  
IDO - Search loop counter  
IFA - Factorial loop counter  
IFLAG1}  
IFLAG2}- Flags used to improve success rate of search  
IFLAG3}  
IN}  
IS} - Integer forms of N and S for printing purposes  
J - Search loop counter used to identify first pass  
J1 - Overall iteration counter, stops program after 1000 iterations  
ZINC - Increment used in binary cut search loop

```

      DOUBLE PRECISION F,N,S,NF,NFF,ZIP,Q,ZIPF,QF,PL,Z,
      $SUM,FLAG2,FLAG3
1     WRITE(6,*)'ENTER G'
      READ(5,*,ERR=1)G
2     WRITE(6,*)'ENTER S'
      READ(5,*,ERR=2)S
3     WRITE(6,*)'ENTER N'
      READ(5,*,ERR=3)N
      PL=((S/N)**2.0)*LOG(N)/LOG(400.0)*.95/G
4     WRITE(6,*)'ENTER INITIAL GUESS OR 2 IF YOU WANT PROGRAM TO GUESS.'
      WRITE(6,*)'IF YOU HAVE MADE AN ERROR IN PREVIOUS INPUT, ENTER 10.'
      READ(5,*,ERR=4)GUESS
      IF (GUESS.GT.9) GO TO 1
      IF (GUESS.LT.0) GO TO 4
      IF (GUESS.LT..95) PL=GUESS
      IFLAG1=0
      IFLAG2=0
      IFLAG3=0
      FLAG3=0D0
      FLAG2=0D0
C*****BEGINNING OF SEARCH
      J1=0
6     J=0
      ZINC=.05
      IF (N.GT.200) ZINC=.025
      IF (N.GT.300) ZINC=.01
      DO 3000 IDO=1,100
      J=J+1
      J1=J1+1
      IF (J1.GE.1000) THEN
      WRITE(6,*)'TERMINATED BECAUSE J1 GREATER THAN 1000'
      STOP
      ENDIF
      SUM=0
      WRITE(6,*)'PL=',PL,'    INC=',ZINC,'    ERR=',FCN2
      NF=N
      DO 1000 I=S,N
      NFF=NF
      X=I
      Q=NF-X
      QF=Q
      IF (QF.LT.1.0) QF=1D0
      XF=X
      F=1D0
      DO 101 IFA=1,N
      F=(NFF/(XF*QF))*F
      IF (F.GT.1.0E30) THEN
      F=F/1.0D30
      FLAG3=FLAG3+1D0
      IF (FLAG3.EQ.25) WRITE(6,*)'ALARM CONDITION FLAG3=25'
      ENDIF
      IF (F.LT.1.0E-30) THEN
      F=F/1.0D-30

```

```

FLAG2=FLAG2+1D0
IF (FLAG2.EQ.25) WRITE(6,*) 'ALARM CONDITION FLAG2=25'
ENDIF
QF=QF-1D0
XF=XF-1D0
NFF=NFF-1D0
IF (XF.LT.1.0) XF=1D0
IF (QF.LT.1.0) QF=1D0
101  CONTINUE
      Z=DEXP(DLOG(F)+FLAG2*DLOG(1D-30)+FLAG3*DLOG(1D30)+X*DLOG(PL)
      $+Q*DLOG(1D0-PL))
      FLAG3=0D0
      FLAG2=0D0
      SUM=SUM+Z
1000  CONTINUE
      IF (J.EQ.1) THEN
        FCN1=SUM+G-1.0
        IF (ABS(FCN1).LT.0.00001) GO TO 200
        PLOLD=PL
        PL=PL+ZINC
        IF ((PL.GE.1.0).AND.(IFLAG1.EQ.0)) THEN
          PL=.9999999
          IFLAG1=1
        ELSE IF (PL.GE.1.0) THEN
          IFLAG1=0
          PL=.000001
          GO TO 6
        ENDIF
        GO TO 3000
      ENDIF
      FCN2=SUM+G-1.0
      IF (ABS(FCN2).LT.0.00001) GO TO 200
      IF (FCN2*FCN1.LE.0.0) THEN
        ZINC=ZINC/2.0
        PL=PLOLD+ZINC
        IF ((PL.GE.1.0).AND.(IFLAG2.EQ.0)) THEN
          PL=.9999999
          IFLAG2=1
        ELSE IF (PL.GE.1.0) THEN
          IFLAG2=0
          PL=.000001
          GO TO 6
        ENDIF
        GO TO 3000
      ENDIF
      PLOLD=PL
      PL=PL+ZINC
      IF ((PL.GE.1.0).AND.(IFLAG3.EQ.0)) THEN
        PL=.9999999
        IFLAG3=1
      ELSE IF (PL.GE.1.0) THEN
        IFLAG3=0
        PL=.000001
        GO TO 6
      ENDIF

```

```

FCN1=FCN2
3000 CONTINUE
      WRITE(6,*) 'PROGRAM FAILED TO FIND SOLUTION'
      IN=INT(N)
      IS=INT(S)
      WRITE(6,303) IS, IN, PL, FCN1
      WRITE(28,303) IS, IN, PL, FCN1
303   FORMAT(2X,I3,5X,I3,5X,F11.9,5X,F11.9)
      GO TO 4000
200   WRITE(6,*) ' '
      WRITE(6,*) ' '
      WRITE(6,*) ' '
      WRITE(6,*) ' '
      IS=INT(S)
      IN=INT(N)
      WRITE(6,*) 'PL = ', PL, ' S= ', IS, ' N= ', IN, ' ITER = ', J
      WRITE(6,*) ' '
      WRITE(6,*) ' '
      WRITE(6,*) ' '
      WRITE(6,*) ' '
      WRITE(29,*) '*****'
      WRITE(29,300) G, IN, IS
      WRITE(28,302) IS, IN, PL
302   FORMAT(2X,I3,5X,I3,5X,F9.7)
      WRITE(29,*) 'PL = ', PL
300   FORMAT(1X,'G = ',F4.3,' N = ',I3,' S = ',I3)
4000 CONTINUE
301   WRITE(6,*) 'ENTER 1 IF YOU WISH ANOTHER RUN, 0 TO STOP'
      READ(5,*,ERR=301) IR
      IF (IR.NE.0) GO TO 1
      STOP
      END

```

\$

THE APPLICATION OF NEUTRON RADIOSCOPY  
TO LITHIUM-ALUMINUM ALLOY TARGET ELEMENTS

J. J. Antal and A. S. Marotta  
Army Materials Technology Laboratory  
Watertown, Massachusetts 02172-0001  
and

S. R. Salaymeh and T. P. Varallo  
E. I. DuPont De Nemours & Co.\*  
Savannah River Laboratory and Plant  
Aiken, South Carolina 29808

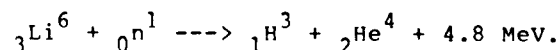
Abstract

We have shown that neutron radiography is very useful in locating the position of a Li-Al alloy core enriched in Lithium-6 in tubular aluminum target elements. The alloy core is displaced during a forming process and its location must be redetermined before processing can be completed. The Army's low-flux mobile neutron radiography system was employed in these studies as a model system for possible on-line, in-plant use. A series of core end sections of target tubes containing from 0.1 to 4.6 grams of Lithium-6 per foot of length were examined radiographically with thermal neutrons. The system was able to determine the extent of lithium alloy core from the highest concentrations down to about 0.2 grams of Lithium-6 per ft within one minute of data collection time. A marked loss of sensitivity below this level could be recovered by providing higher geometrical resolution in the images obtained or by using image enhancement techniques. Film radiography was used to verify the accuracy of radiographic determinations at the lowest lithium concentrations.

INTRODUCTION

The goal of the studies described here was to provide an accurate alternate method for determination of the post-extrusion location of Li-Al alloy core in aluminum target elements to be used in the production of tritium in nuclear reactors. The work is an effort stemming from a mutual interest of the Department of the Army and the Depart-

ment of Energy in diverse applications of the Li-Al alloy system. Lithium-aluminum alloys with lithium content in the 0.8 to 2.5 weight-percent range are used as target material in the production of tritium at Department of Energy facilities. Tritium,  $H^3$ , is produced through the reaction:<sup>(1)</sup>



\*The information contained in this paper was developed during work under contract No. DE-AC09-76SR00001 with the U. S. Department of Energy.

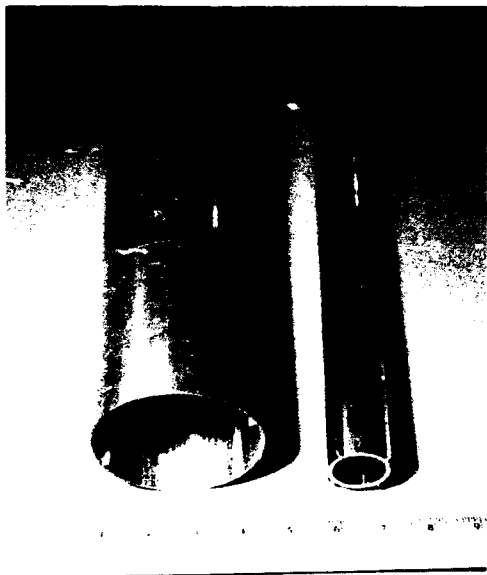


Fig. 1. Photograph of typical target tubes.

The target material,  $^6\text{Li}$ , is in the form of an aluminum-clad Li-Al alloy hollow tube. After a controlled period of irradiation with neutrons in a nuclear reactor, the tube is removed and the tritium generated is recovered from the alloy.

#### TARGET TUBES

Aluminum tubes approximately 12 feet in length and varying in diameter from about 1.3 inches to 3.6 inches are used as carriers of target material in this application. Figure 1 is a photograph of typical tube sections. The target material may be natural lithium or lithium enriched in the  $^6\text{Li}$  isotope in the form of a lithium-aluminum alloy.\* It is common practice to express the lithium content in units of grams of  $^6\text{Li}$  per foot of tube length. The lithium-

aluminum alloy, having essentially the same physical properties as pure aluminum, readily bonds to aluminum in an extrusion cladding operation which results in a uniform metallic tube with the lithium element entirely sealed within aluminum.

Unfortunately, this forming operation displaces the Li-Al alloy in a manner which results in a very nonuniform distribution of the alloy at the two ends of the finished tube. In order to retain all of the target lithium and not defeat the integrity of the cladding seal, it is important to locate the exact extent of the alloy at the core ends. This allows excess aluminum at the core ends to be cut off and disposed of in a later operation.

The present practice is to determine the location of the end of the embedded alloy core with an eddy current probe. An independent nondestructive method for confirming the location of the core end was desired.<sup>(2)</sup> Ultrasonic pulse-echo time of flight measurements were tried, but consistent results could not be obtained at low Li-Al alloy concentrations. The method explored and described here is to provide a neutron radiologic image of a 10-inch section of the core end which maps out the distribution of the alloy completely. The distribution of uranium fuel in aluminum-clad reactor fuel elements can be determined using x-ray radioscopy in a similar manner. Another requirement was to provide this determination within a short (1 or 2 minute) time frame.

\*Lithium occurs in nature as a mixture of two isotopes, 7.5%  $^6\text{Li}$  and 92.5%  $^7\text{Li}$ ; enrichment alters the ratio of these isotopes in the target alloy. Lithium-6,  $^6\text{Li}$ , and  $\text{Li}^6$  all refer to the same isotope.



## THE NEUTRON RADIOSCOPY SYSTEM

The use of neutron radiation for this work is particularly favorable because enrichment of the Li-Al alloy with its  $^6\text{Li}$  isotope gives the alloy a very high cross section for neutron removal (typically 940 barns) relative to that of the aluminum (0.9 barns)<sup>(4)</sup> thereby providing excellent image contrast. Radioscopy refers to the technique of imaging hidden components of an object with radiation transmitted through the object and recorded in a non-permanent manner. In the radioscopy described in this report, the image is stored electronically and presented to the operator on a CRT screen. The Army has an interest in neutron imaging systems for aircraft examination and other nondestructive examination purposes which requires that the neutron source be mobile. This requirement has led the implementation of neutron radiography away from the use of nuclear reactor sources and towards the use of less encumbered, small californium-252 and accelerator sources. The radioscopy in these studies was accomplished primarily with a small accelerator source system which provides about 1/500 of the thermal neutron flux provided by reactor sources for radioscopy.<sup>(5,6)</sup> The accelerator generates 14.3 MeV neutrons which are moderated in oil to thermal energies for radioscopy. It is shown in operation in Figure 2. The source and collimator system is mounted on a mobile frame, weighs 4900 pounds (2200 kg), and occupies a volume of approximately 15 ft x 5 ft x 4 ft (4.6 m x 1.5 m x 1.2 m). It was appropriate to utilize this unit for this work because it provides a model system for possible installation within a target fabrication plant.



Fig. 2. View of the radioscopic setup. The white sphere in the foreground houses the accelerator source and moderator. The collimated neutron beam from the source head illuminates the two tube sections set up horizontally in front of the 10in x 10in screen of the imaging system.

The electronic imaging system employed is of very high sensitivity, specifically designed to work with the low fluxes of small neutron source systems.<sup>(7)</sup> In this imaging system, the neutrons are detected by a lithiumloaded phosphor whose light emission is detected with a cooled silicon intensified target tube from which the image is scanned out and placed in memory in digital form under control of a computer. Special hardware and software intervene at the scanning stage to provide a very low noise environment. Normally a series of scanned images is summed and then presented for viewing so that the minimum "exposure" time in these studies was about 3 seconds. Electronic imaging of this type has the advantage of allowing the operator to terminate the exposure when the image has built up sufficient contrast to provide a clear decision regarding the condition of the object under

TABLE 1. TARGET TUBE CHARACTERISTICS

Tube No.	Diameter (in.)	<sup>6</sup> Li Content (g/ft)	<sup>6</sup> Li Density (mg/cm <sup>2</sup> )	Approx. Imaging Time (sec.)
1	1.3	3.21	10.2	less than 3
2	3.6	4.09	4.67	less than 5
3	1.3	0.65	2.06	10
4	3.6	0.81	0.93	30
5	1.3	0.29	0.92	30
6	3.6	0.55	0.63	60
7	1.3	0.19	0.60	60
8	1.3	0.13	0.41	see text
9	1.3	0.10	0.32	see text

examination. Neutron activation of the object is kept at a minimum by this technique and by the inherently low flux of a small source.

#### RESULTS ATTAINED

A representative series of tubes examined is listed in Table I. They cover a range of practical interest with lithium-6 isotope contents from 0.1 g/ft to 4 g/ft. For comparison with radiosopic image densities, these concentrations have been expressed as an areal density in mg/cm<sup>2</sup> in column 4 of Table 1. For tubes at the top of the concentration range, clear radiosopic images were presented for viewing in less than 5 seconds. It should be possible to view the lithium distribution in real time for these tubes. Images collected in less than 1/20th second and presented consecutively would allow viewing while the tube is rotated to ensure that the most extreme extent of lithium is located. Our image collection software does not allow for true real-time presentations, so we were unable to demonstrate this during our work.

Clear images from which core end determinations could be made were obtained within one minute of exposure time for all but those having the lowest

areal lithium-6 concentration, those noted as 0.10 and 0.13 g/ft. Thus for concentrations above 0.2 g/ft, small source neutron radioscopy would appear to be a satisfactory nondestructive tool. The detection sensitivity seemed to drop markedly for the lowest lithium-6 concentrations, however.

In order to reduce exposure times to a minimum, the radiography system was operated with a low L/D ratio of 14/1, which was expected to provide sufficient resolution in the images for the purpose intended. A radiological determination made from an item having curved surfaces such as cylinders is often difficult because a sharp edge with a well defined contrast change is not available. A typical radiosopic image which shows three tube core ends is reproduced in Figure 3. The tube having the highest concentration of lithium-6 readily shows the location of the Li-Al alloy and graphically demonstrates its nonuniform distribution. Here one can use the whole image to make a determination of the extreme extent of the alloy. The tube on the left in Figure 3 contains a moderate amount of lithium-6 and the contrast over the center region of the tube does not provide a good measure of the core end. Here one relies on the view of the curved edges of the tube where the cylindrical shape places some



Fig. 3. A neutron radioscopic image of three small diameter target tubes in the region of the core ends. The tubes have average areal densities of Lithium-6, left to right, of 2.06, 0.32, and 10.2 mg/cm<sup>2</sup>. This CRT image is reversed in radiographic density, black delineates an absorber. L/D is 14.1.

depth of lithium-6 in line with the radiation beam. For routine determinations, the tube would be rotated to assure that the extreme of the core end is being viewed. The center tube in Figure 3 contains so little lithium-6 that the low contrast and low resolution has lost even the curved edge image to the casual viewer. The ability to see the edge of any of the core ends is further hindered by the thinning of the alloy core to a shallow wedge shape as the end is approached. It is apparent that greater care with the radiological setup and the sacrifice of a longer image collection time may be needed to attain success at the lowest lithium-6 concentrations.

A neutron film radiograph of a low concentration tube, taken at an L/D ratio of 27.4/1 for improved resolution, Figure 4, makes the factors discussed above clear. Using the radiograph presented in Figure 4, the location of

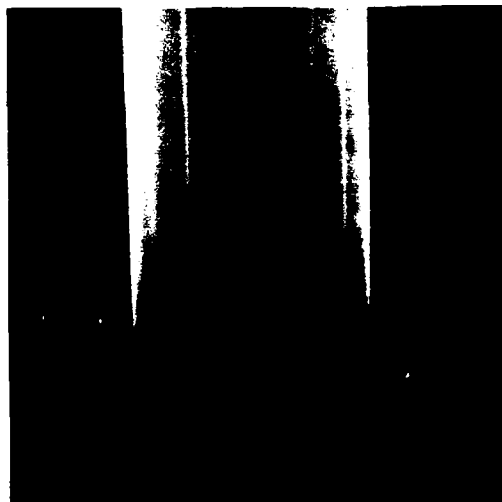


Fig. 4. A neutron radiograph (on x-ray film) of one of the large diameter target tubes with an areal density of Lithium-6 of 0.63 mg/cm<sup>2</sup>. It illustrates the need for better resolution when dealing with very low lithium loadings. L/D is 27.4.

core end can be identified easily. Also visible is the wedge-shaped character of the alloy core near its end. This suggests the need for higher resolution or other image improvements to outline the core distribution at the lowest areal densities.

#### IMAGE PROCESSING

We have found that some form of image processing or enhancement is beneficial to making determinations of core end locations in tubes containing less than about 0.4 g/ft of lithium-6. The extent of the processing is probably best determined by the facilities available at the place where the determinations are made and by the difficulty in making an individual determination. Take the example of the 0.1 g/ft tube shown in the center of Figure 3. A trained viewer can see the general location of the lithium alloy core in this CRT screen view (at the top of the figure), but cannot determine its exact extent.



Fig. 5. A CRT screen view showing the result of applying a "masking" process to the radioscopic image in Figure 3 to clarify the location of Li-Al alloy in the center tube.

As a first try, the following simple image enhancement procedure may be executed quickly. A determination is made of the maximum and minimum screen illuminance in the suspected core area. This is usually available as a profile

of brightness across the selected portion of the image or as maximum and minimum values of brightness within a selected rectangular area of the image. All values of brightness between the maximum and minimum are then set to "1" (white) in the computer memory and all other brightness values in the image are set to "0" (black). This is a common process sometimes called "masking". The result of applying this process to Figure 3 is shown in Figure 5. The low concentration center tube now shows the presence of alloy core much more clearly. This rather simple enhancement procedure may suffice in many cases. Here, the extent of the core is still questionable.

Adding additional processing steps eliminates any question of core extent. Figure 6(a) is a CRT image of the same tube shown at the center of Figure 3. The tube is now translated along its long axis so that only an all-aluminum

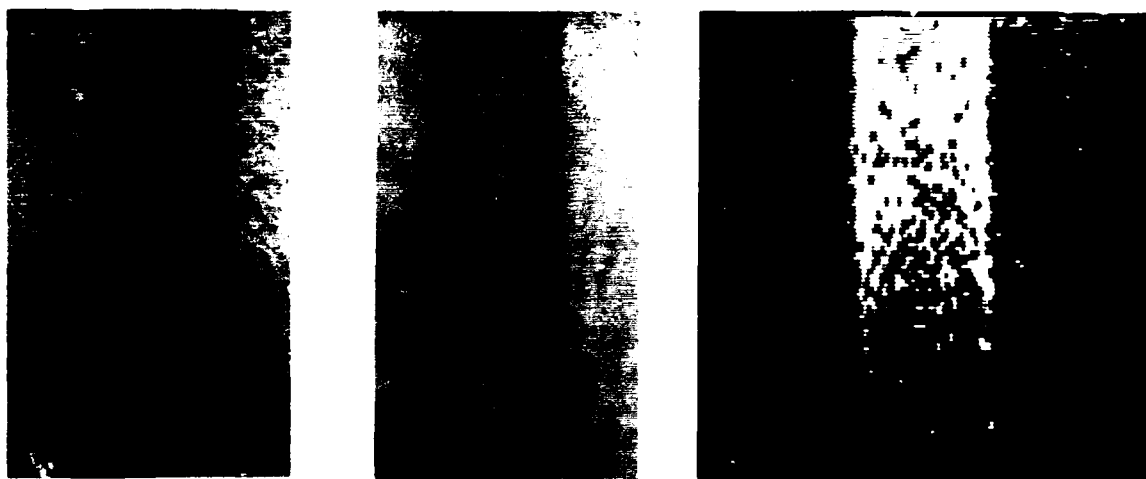


Fig. 6. (a) A neutron radioscopic image of the low lithium-6 content tube ( $0.32 \text{ mg/cm}^2$ ) shown in the center of Figure 3. The Li-Al alloy extent from the top of the tube is uncertain. (b) A neutron radioscopic image of an all-aluminum portion of the same tube. (c) The image resulting from applying a masking process to the pixel-by-pixel quotient of image (a) divided by image (b). The extent of the Li-Al alloy core is now quite certain.

portion of the tube is imaged, Figure 6(b). This image is now subtracted from or divided into that containing the alloy core, pixel by pixel, which results in an image of the core alone. The masking process can now be applied to the resultant image to provide stark contrast for the remaining significant illuminance levels, as shown in Figure 6(c). The full extent of the lithium core is now readily visible. This type of image processing eliminates the clutter in the background which makes it difficult for the human eye to isolate the image information of importance.

#### SUMMARY

The feasibility of using neutron radioscopy utilizing a small neutron source and electronic imaging to determine the location of Li-Al alloy core ends in target tubes fabricated for tritium production has been demonstrated. Accurate determinations appear to be possible by straightforward application of radioscopy within practical time constraints for target tubes containing concentrations of lithium-6 isotope above 0.2 g/ft of tube length. Below this concentration the usual trade-off between image resolution and exposure time must favor higher resolution in the images and require longer times for a determination to be made. The application of some image enhancement may also be traded off to obtain a shorter exposure time. In a particular application, the available software and its ease of application should determine the most suitable enhancement technique. It was demonstrated further that the required neutron radiology could be accomplished with a neutron source small enough that its installation within the tube

fabrication plant should be possible.

#### REFERENCES

- (1) K. H. Beckurts and K. Wirtz, Neutron Physics, Springer-Verlag, New York, 1964, p. 14.
- (2) S. R. Salaymeh and T. P. Varallo, Savannah River Laboratory, Technical Division internal reports, June-December, 1988.
- (3) Analysis Report, U. S. Army Materials Technology Laboratory, MT&E Branch, 1988.
- (4) D. I. Garber and R. R. Kinsey, Neutron Cross Sections, BNL 325, 3rd Ed, Vols. I & II, 1973.
- (5) J. J. Antal, W. E. Dance, S. F. Carollo and J. D. Moravec, "Experience with an On-Off Mobile Neutron Radiography System", in Neutron Radiography, J. P. Barton, G. Farney, J. Person and H. Rottger, Eds., D. Reidel Publishing Company, Dordrecht, Holland, 1987.
- (6) J. J. Antal and A. S. Marotta, "A Neutron Radiography system for Field Use", in Nondestructive Testing and Evaluation for Manufacture and Construction, H. Reis and W. J. McGonagle, Eds, Hemisphere Publishers, 1989 (in press).
- (7) W. E. Dance and S. F. Carollo, "High Sensitivity Real Time Imaging System for Reactor or Non-Reactor Neutron Radiography", in Proceedings of the 2nd World Conference on Neutron Radiography, J. P. Barton, G. Farney, J. Person and H. Rottger, Eds, D. Reidel Publishing Company, Dordrecht, Holland, 1987.

USING X-RADIOMETRY TO COUNT RESIN-BONDED  
LAYERS IN ARAMID BALLISTIC CLOTH COMPOSITES

Ronald E. Larsen, Ph.D.  
Reinhart & Associates, Inc.  
Austin, Texas

Matthew J. Golis, Ph.D.  
Advanced Quality Concepts, Inc.  
Columbus, Ohio

ABSTRACT

The Army Paratroopers and Support Ground Troops (PASGT) helmet is a composite consisting of nominally 19 layers thickness aramid (Kevlar) ballistic cloth heat-bonded in a press with rolled-on phenolic resin. Inadvertent omission or poor fitting of layers during lay-up or the occurrence of undetected shifts in layers during hot pressing can significantly weaken the helmet and thereby drastically impair its effectiveness under combat conditions. Currently, helmets are accepted or rejected on a lot basis using ballistic projectile penetration destructive tests on a statistically significant sample from each lot. A Phase I Small Business Innovative Research (SBIR) was performed to assess the feasibility of nondestructively counting layers by through-transmission x-radiometry, a technique that would allow 100 percent testing of helmets for layer count if proved feasible. Tests were conducted on flat panels, crown panels containing gaps, and actual helmets using 14-18 keV Pu x-rays from a 30-mCi Cm-244 source, a sodium iodide scintillation counter, several collimators, and a multichannel analyzer. Variations of 1 layer in 19 were easily detected in the flat panels free of lateral gaps in layers. The infusing of resin into artificially produced lateral gaps in the crown specimen and into actual lateral gaps in the helmet during press-curing impaired the effectiveness of the radiometric method by introducing high radiometric density material into the beam path. It is concluded that radiometry should be combined with visual inspection to assure helmet integrity. Modified approaches are discussed.

INTRODUCTION

Bonded and unbonded aramid cloth is used widely by military and law-enforcement organizations in personnel protection applications. The Army Paratroopers and Ground Support Troops (PASGT) helmet is a rigid resin-bonded aramid (Kevlar 29) ballistic cloth composite. The helmet is assembled from precut phenolic resin prepreg, which is laid up either in a pinwheel or in a rectangular panel and pinwheel pattern.

Engineering specifications require that all regions of the helmet contain at least nineteen layers. The lay-up is cured in a hot press mold. Inadvertent omissions or misplacements of prepreg layers and shifts during the molding cycle can cause the finished helmet to be less than nineteen layers thick, compromising its integrity and impairing its effectiveness as personnel protection apparel.

Currently, all helmets are inspected visually after hot pressing to detect obvious manufacturing defects, such as crimping, unbonding, surface blemishes, and lateral gaps in surface layers with associated inflow of resin. The helmets that pass this inspection are then accepted or rejected on a lot basis using ballistic projectile penetration destructive tests on a statistically significant sample from each lot. Combined, these two evaluation methods provide some assurance of helmet integrity. However, there is clearly a need for a nondestructive method for counting layers in the helmets. The availability of portable, low-cost (less than \$10,000 each) instruments based on this method would allow 100 percent testing of helmets for layer count at production and depot levels. These tests would augment the existing visual and impact tests, thereby giving greater assurance of helmet integrity.

A six-month research and development program, partially supported by 1987 Phase I SBIR funding provided by the U.S. Army, was performed to evaluate the feasibility of developing a portable, radiographic or radiometric device capable of detecting missing (or excessive) layers in Kevlar composite helmets. The objective of this research was to devise and evaluate a method capable of detecting a variation of one layer out of nineteen layers in the composite.

#### SPECIMENS AND METHODS

Several flat Kevlar composite panels, seven helmets that had been rejected from production lots due to wrinkling and other surface blemishes, and a helmet crown panel containing built-in regions of missing Kevlar were obtained from three manufacturers. All helmets had pinwheel construction. Initially the parts were radiographed using a conventional x-ray tube source operated at 25

kV to characterize their lay-up patterns and locate obvious lateral layer gaps and resin in-flow regions.

Radiometry tests were performed with a laboratory through transmission system fabricated from modular components. The source was 30 mCi of curium-244, which furnished 14-18 keV x-ray photons for the radiometry tests on the Kevlar parts. The through-transmitted x-ray photons were detected with a sodium iodide tube and photon counts were processed, energy-analyzed, and displayed using a multi-channel analyzer and a microcomputer. Both tube and source were fitted with collimators that limited the beam diameter in the parts to 1/4-inch or less.

#### RESULTS

Initial radiometry tests were performed to assess the ability of this method to detect changes in the layer counts of flat specimens free of gaps and resin inflow regions. The test pieces used in these tests were made from a single 6-inch x 6-inch x 16-layer Kevlar composite panel obtained from Unicore Prison Industries (UPI). A 1-inch square coupon was cut from the panel and soaked overnight in methylene chloride to soften the resin enough to allow careful separation of the square into 16 separate layers. These layers were allowed to dry thoroughly.

The x-ray transmission of the 16-layer stack of test coupons was measured using the laboratory system and compared with the transmission of the intact 16-layer panel. The difference between the two attenuation values was found to be less than the system sensitivity under ideal conditions, or 0.3 percent.

The relationship between x-ray transmission and the total number of layers was determined experimentally. The first radiometric

measurement was performed on the basic 16-layer panel. Then the number of layers was increased, adding squares of the cured composite one at a time. The data recorded was the total number of counts under open tube (no panel) and panel-in-place conditions.

The test results are shown in Figure 1, which is a semi-log plot of relative counts (fractional transmission) versus the total number of layers. The data points fit on a straight line that passes through 1 on the log scale, which demonstrates the exponential relationship between fractional transmission and the total number of layers in a Kevlar composite panel. The attenuation coefficient equals 0.0695 per Kevlar layer. A change of effective panel thickness of one layer produced approximately a 2 percent change in the relative transmission (or attenuation) of the beam. Standard pulse counting statistics showed uncertainty in the number of counts to be less than 0.6 percent at a 99.95-percent confidence level. Thus, the system was determined to be sensitive to changes as small as 1/2 layer if the effects of variabilities in the resin/fiber quantity ratio do not impair the measurement.

In a second set of tests using the 16-layer panel, the effect of adding known thicknesses of cured resin, spray paint, bonded Kevlar and Kevlar cloth to this panel was measured by radiometry. The objective of these tests was to assess the degree to which the presence of these materials might influence radiometric counting of layers in helmets. Table 1 summarizes the test results. Notice that the beam attenuation coefficient of resin is seven times that of Kevlar cloth, and that spray paint is even more attenuative than resin. These results suggest that the radiometric method should be limited to use on unpainted production-line helmets and that radiometric testing be limited to the testing

of helmets that have passed thorough visual inspection for evidence of surface gaps and resin inflow.

A helmet crown specimen containing cut-outs in layers was inspected by radiometry to assess the effect of inflow of resin into the gaps on the x-ray beam attenuation. The specimen contained cut-outs simulated 1, 2, and the missing layers. The cut-outs were all 1 inch long and varied in width from 1 inch down to 1/16-inch. The test results are shown in Figure 2. Sampling locations at the widest cut-outs are on the left of this figure and those at the narrowest are on the right. Notice that the deviation of the predicted (computed) attenuation values increase as the widths of cut-out gaps decrease. This effect is caused by inflow of resin into the gaps, which is more pronounced for narrower gaps than wider gaps. The presence of resin was observed visually as darkening of the surface layers over the cut-outs.

All seven helmets were surveyed by radiometry. Figure 3 shows a typical result. The beam attenuation is nearly constant in the crown region where there are no designed-in layer overlaps. There is a considerable variation of attenuation in the skirt region, where legs of the pinwheel overlap at their edges giving rise to inflow of resin.

An attempt was made to correlate the degree of surface resin darkening and lightening with beam attenuation. A significant degree of correlation would support our tentative conclusion that radiometry would be an effective layer counting method for helmets visually observed to be free of surface flaws and localized resin-rich and resin-poor areas. In the tests, five observers were asked to grade the lightness and darkness of twenty locations on a helmet on a scale of -4 to +4. Their numbers were plotted against



the measured beam attenuation values for the corresponding locations, and a linear regression analysis was performed. The test results are shown in Figure 4. The correlation coefficient (R) is 0.68 and the confidence level is 95%.

The totality of results obtained from this research suggests that radiometry might be an effective layer counter method. However, the restrictions already noted should be observed. Furthermore, it is imperative that a larger data base be established and data from unflawed, visually acceptable helmets be included.

#### CONCLUSIONS

The radiometry technique evaluated is a useful technology for counter layers in Kevlar composites. However, the inflow of resin into existing gaps in the prepreg layers can impair the accuracy of the method. To minimize this effect, only those helmets that have passed a rigorous visual inspection should be surveyed by radiometry.

All helmets surveyed by radiometry in this study had been rejected on the basis of visual inspection before they were turned over to this research project. A statistically chosen quantity of helmets that have passed visual inspection should be surveyed by the radiometric method in order to build up a valid data base for establishing a standard for this technique. Work is planned in this area as a next step in developing a field-portable radiometric layer counter for Kevlar composites. Utilization of ancillary techniques, including sonic and infrared testing, will be included in the following step of the planned development work.

#### ACKNOWLEDGEMENTS

This research was partially supported under 1987 Phase I SBIR funding through contract number DAAK60-87-C-0039, issued by The Department of the Army, U. S. Army Troop Support Command, Natick Research, Development and Engineering Center (NRDEC), Natick, Massachusetts, 01750-5011. Technical monitoring for this contract was performed at NRDEC by Ms. Jane Astle and Mr. Stanley Waclawick.

The authors and Reinhart & Associates, Inc., thank Mr. Tim Browder of Unicore Federal Prison Industries, Mr. B. J. Richmond of Devil's Lake Sioux Manufacturing Company, and Mr. Henry Tracy of Geonautics, Inc., who furnished Kevlar helmets and test panels for this research free-of-charge, and provided a wealth of background information and helpful advice. Mr. Gene Lewis of Lewcott Chemicals furnished samples of phenolic resin and Kevlar fabric on very short notice, and we are grateful for his help.

## Beam Transmission vs. Number of Bonded Kevlar Layers in Flat Panel

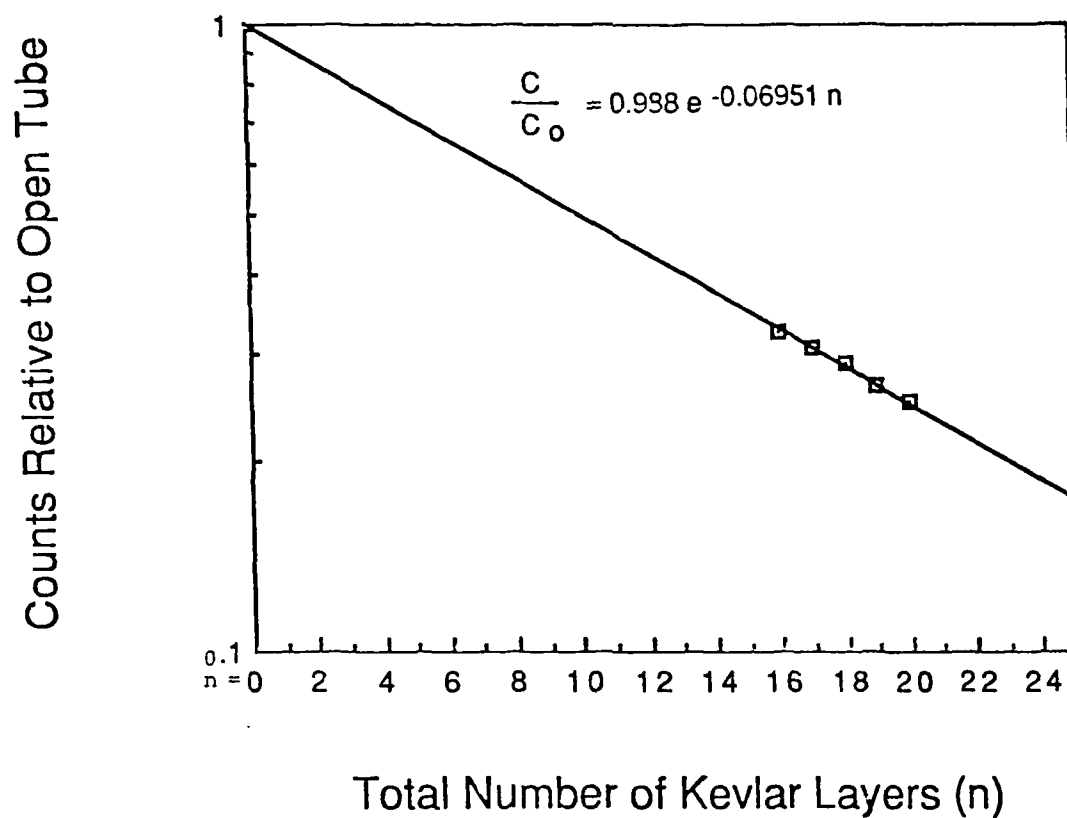


Figure 1. Variation of x-ray photon transmission with total number of Kevlar layers in test panel.

TABLE 1 Relative Attenuation of X-rays by Various Helmet Fabrication Materials.

Material	Attenuation coefficient, $\mu$ (in units of percent layer of bonded Kevlar composite)	Radiometric equivalent to 1-layer bonded Kevlar	Relative effectiveness of equal thickness of material in attenuating beam
Spray Paint	0.194	6.6 mils	8.5
Resin	0.169	7.5 mils	7.0
Bonded Kevlar	0.0695	-	3.0
Prepreg	0.071	0.97 layer	3.1
Kevlar Cloth	0.0228	3.0 layers	1.0

## Analysis of UPI Crown Specimen Data

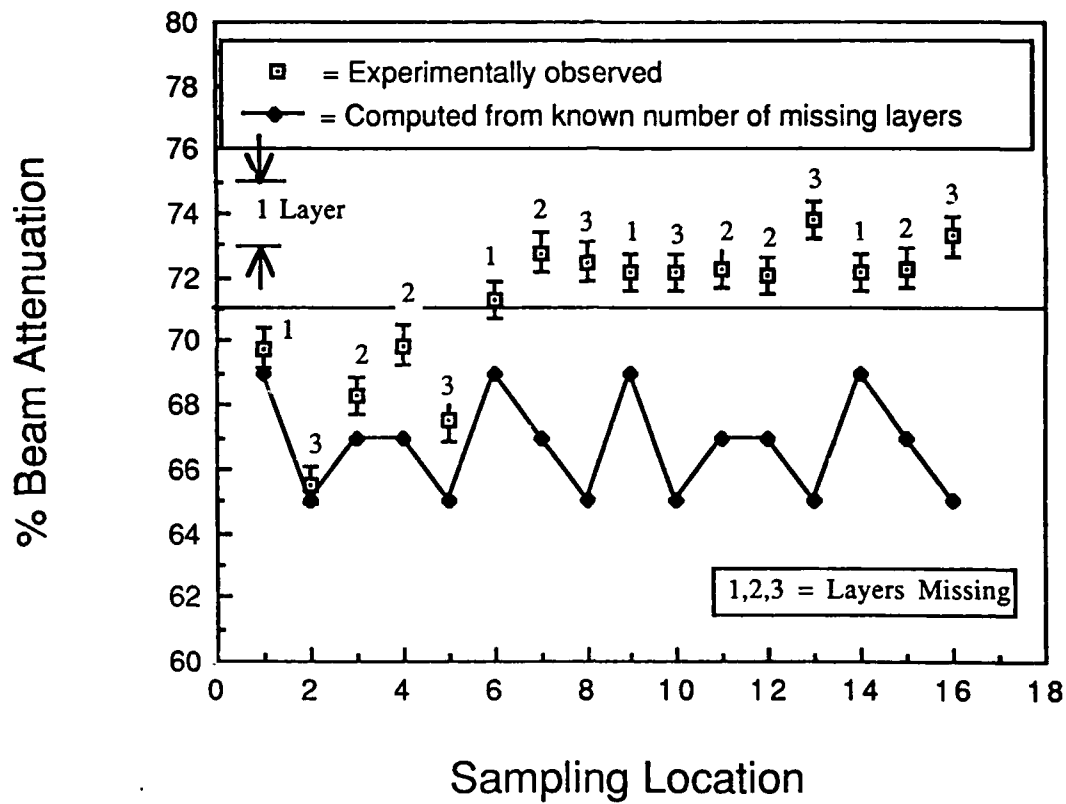


Figure 2. Beam attenuation in helmet crown specimens containing layer gaps.

# Beam Attenuation vs. Sampling Location DLS Helmet #6

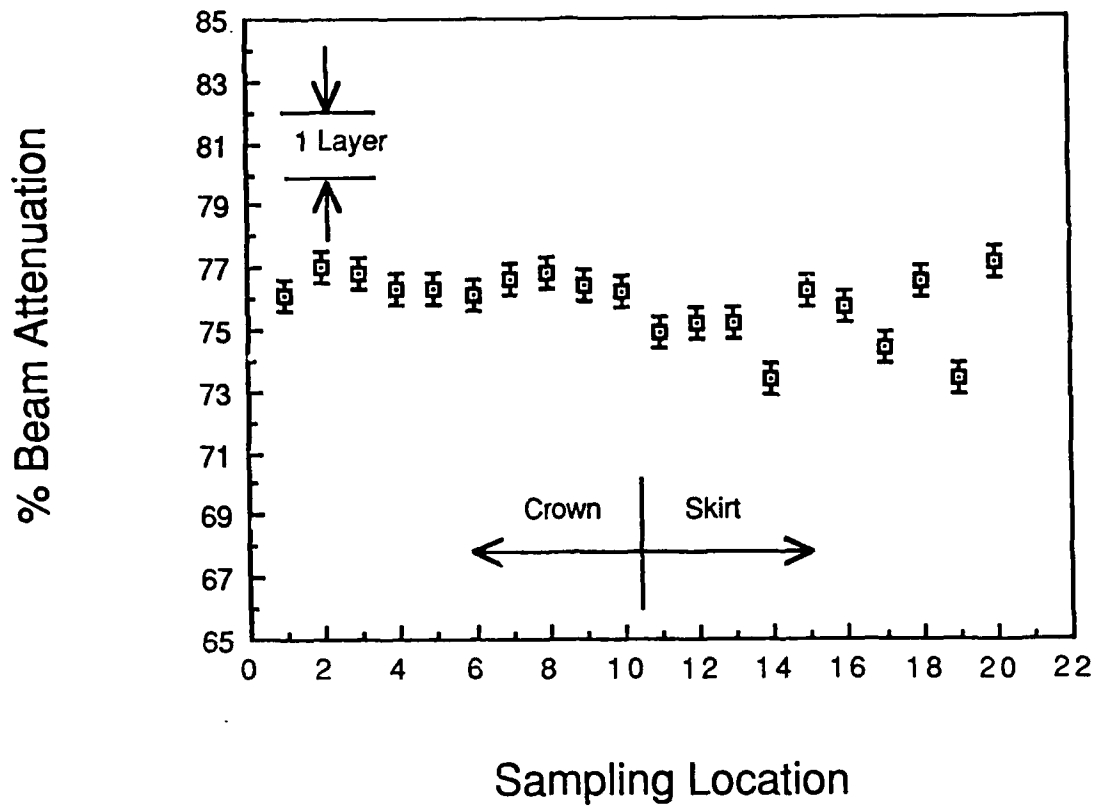


Figure 3. Beam attenuation for 20 sampling attenuations in crown and skirt regions of helmet DLS-6.

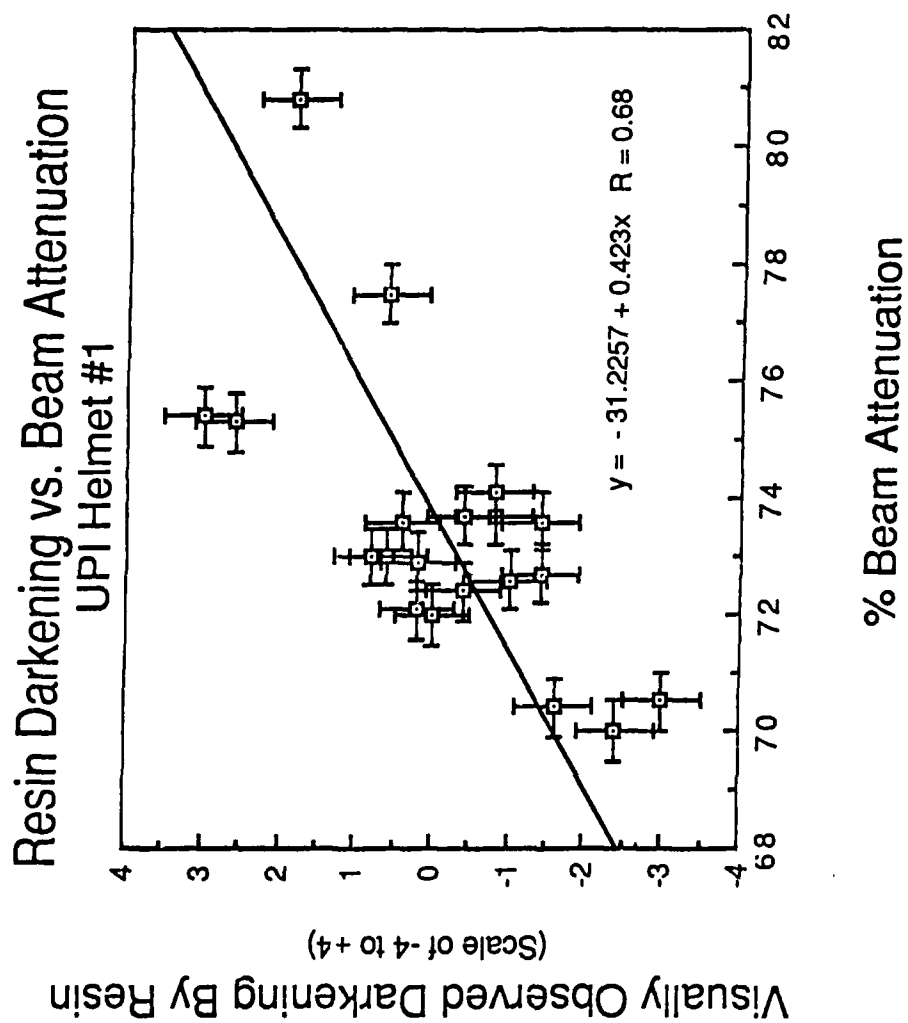


Figure 4. Correlation of resin darkening on helmet surface with x-ray beam attenuation.

## ADVANCEMENTS IN AND APPLICATIONS OF BACKSCATTER TOMOGRAPHY (ZT)

D. Schafer, M. Annis, P. Bjorkholm, and W. Baukus  
American Science and Engineering, Inc.  
Cambridge, Massachusetts 02139

### ABSTRACT

American Science and Engineering, Inc., is currently under contract to the Air Force Astronautics Laboratory to design, construct and install a laboratory based Backscatter Tomography System (trademarked by AS&E as ZT™). This project results from the successful Phase I SBIR program conducted by AS&E which showed the usefulness of ZT for detecting anomalies in thin walled composite structures. The equipment has been designed to meet the requirements of an AFAL specification.

This paper will detail the second phase of the program and highlight the advancements made in the ZT system with respect to system speed, spatial resolution, and slice thickness. The system configuration will be presented and specific operating parameters discussed. In addition, AS&E will present the results of company-sponsored investigations which dramatically depict applications of the one-sided ZT system to the inspection of other composite materials and structures. The presentation will include ZT images taken of a variety of objects. The usefulness of ZT as a materials evaluation, process control and production based inspection system will be discussed.

### 1. INTRODUCTION

Thin walled, carbon-carbon and filament wound composite structures are finding use in many fields because of their high strength and low weight. In particular, there are many applications of these components in rocket motor chambers and nozzles and in advanced aircraft components. Sub-millimeter defects are possible due to the fine structure of these materials. These small defects can have catastrophic consequences. As an example, in

a nozzle, a delamination can affect the flame front and dramatically increase the rate of erosion of the nozzle surface. Clearly a burn through in a nozzle can cause dramatic failure of the rocket. Due to the small size of the defects, non-destructive evaluation of these materials is difficult.

American Science and Engineering, Inc., has developed a new technology for non-destructive testing that has specific application to the inspection of composite structures. This

technique utilizes detection of backscatter radiation from a specific depth into the test article. Phase I of the ZT program has been completed, and Phase II is in progress.

## 2. ZT TECHNICAL DESCRIPTION

The ZT technique requires a source of scanning radiation and a collimated detector. The source produces a well defined pencil beam of radiation that can be moved within a fan shaped region as shown in Figure 1. The detector collimator, which is constructed of sheets of radiation absorbing material, allows scattered radiation from only a small region of the object to reach the detector. The measured signal is then representative of the scattering from the small subsurface section of the object. This subsurface volume element is called a voxel.

As the pencil beam is scanned, the total subsurface volume is traced out. If the object is then moved in a direction perpendicular to the plane of the beam (relative to the source/collimator) at a speed slower than the X-ray scan, a slice parallel to the surface is traced out. Sampling the signal many times (e.g., 512) over the time for one pencil beam sweep, digitizing, storing, and displaying produces a visual image of the subsurface slice of the object. A schematic of a typical ZT system is shown in Figure 2.

The unique ZT geometry has several advantages over traditional X-ray scatter techniques. First, because of the flying spot technology, a ZT system can use large efficient detectors. These detectors collect a large fraction of the scattered flux from the voxel under inspection, and therefore images are produced faster than in other systems. Second, the flexibility of ZT allows for inspection at depths up to 5". Third, the patented ZT system can be customized for a particular application. The result is a flexible system

that is capable of inspecting objects of various shapes and sizes.

## 3. PHASE I

To demonstrate the capability of the ZT system to image defects typical of thin walled structures, ZT scans were made of delamination, porosity, and density phantoms as well as of several composite structures provided by AFAL.

In general, scans were done using our maximum available X-ray flux, i.e., at 90 kV, the maximum kilovoltage at which the X-ray tube would operate without arcing, and at 4 mA, the maximum fluoroscopic current usable at that kilovoltage.

Scans of AFAL-supplied composites were made in one of two scan geometries as illustrated in Figure 3. Figure 3a shows a "radial" scan for cylindrical objects. It obtains a slice which represents an annular ring of the cylinder. The resolution in this geometry within the slice is determined by the scanning beam size, typically 1 mm x 1 mm. The slice thickness is determined by the collimator and is about 3 mm.

Figure 3b illustrates a "tangential" scan for cylindrical objects. It also produces an annular slice, but in this case the slice thickness is determined by the fan beam slit and is about 1 mm. This geometry has significantly better sensitivity for circumferential cracks or delaminations. The resolution can be sharpened by simply reducing the slit size.

Figure 4a shows a photograph of a carbon composite sample supplied by the AFAL for Phase I of this program. A ZT image at a depth of 0.450" taken using tangential geometry is shown in Figure 4b. The image shows angular fiducial marks in the form of two lengths of solder (one long, one short). Furthermore, the solder shadows the detector



during part of the rotations, producing a reduced signal during that time. These shadows are observable to the left of the black bars produced when the solder blocks the primary beam. Neither the solder bars nor their shadows are real features of the sample. The structure shown in the defects themselves is real. This defect is confirmed by visual inspection of the "Y" shaped defect near the top of the cylinder.

On the basis of these preliminary measurements, several phantom studies were performed to determine the resolution and selectivity of ZT for delamination, porosities, density fluctuations, and chemical species variation. All of the phantom studies were done on flat plate objects. The results of the phantom studies were compared to a simple theory based on visual identification related to expected signal to noise. As expected increases in S/N ratio will improve system sensitivity. Several improvements in system design will increase the S/N ratio without increasing the total image acquisition time.

#### 4. PHASE II

Phase II of the program involves an implementation of improvements into a design for a laboratory based ZT system which will be delivered to the AFAL. These improvements have included design changes in the X-ray pencil beam source, the scatter collimator and detector, and the system electronics.

The Phase I ZT system was an adaptation of existing flying spot technology using a rotating chopper wheel. The backscatter collimator and detector had to be placed on the object side of the chopper wheel, making the source to object distance no less than 26". This did not allow for efficient use of the available X-ray flux. The Phase II design employs a different flying spot mechanism that allows for a reduction in the source to object

distance to 12" thus improving the flux utilization. Increased flux allows for either reduction in the scan time, or, for a given scan time, improvement in the image resolution.

The Phase II system reduces the distance from the final beam collimating aperture to the object from 13" to 3". While the pencil beam has sharp edges at the beam defining apertures, as the beam travels from these apertures two effects change its shape and produce a broader beam. First, the beam gets larger simply because of magnification. Second, the edges tend to blur because of the finite focal spot size of the X-ray tube. The Phase II system has sharper edges and this translates into better detectability for sharp edged defects.

The Phase II system will use an X-ray tube with a peak voltage of 160 kV. This higher kV tube will result in greater penetration capabilities as well as increased X-ray flux. The Phase II system will also be easily upgradable to use a 320 kV tube if required. The higher kV tube will allow inspection of more diverse types of objects. For example, at a slice depth of 10 g/cm<sup>2</sup> Fe, the ratio of detected signal at 300 kV to that at 100 kV is about 100:1.

In the Phase I system, the scatter collimators/detectors were located in the backscatter position shown in Figure 3a. For the Phase II system, the detectors are moved to the side scatter position. This tangential geometry, shown in Figure 3b, has several advantages over the previous geometry for detection of defects particularly in cylindrical objects: First, the slice thickness is now defined by the X-ray beam and is easily adjustable using the precollimator. Second, the partial volume that the void occupies in the voxel is increased over that of the old geometry. Third, because the X-ray beam width rather than the collimator defines the slice thickness, a new

simpler collimator vane geometry is possible. This geometry greatly increases the collimator efficiency for collecting photons scattered from the inspected voxel without increasing the collection of multiply scattered photons, and therefore increases the signal to noise ratio of the image. In addition, the new collimator will be of improved design employing thin tungsten vanes instead of steel vanes further increasing the collimator efficiency.

The Phase I ZT system used a detector comprised of a scintillating material coupled to a set of photomultiplier tubes. The Phase II system will use a similar detection scheme. The system electronics, however, will be different. The Phase I system used a charge integration circuit whereby the current output from the photomultiplier was integrated over the pixel time, converted to a voltage, amplified, digitized, and sent to a computer for image display. This is the same procedure that is used for digital radiography in a standard transmission system. The problem with applying this method to ZT is that the signal levels are low, and electronic baseline noise then becomes a more serious problem. In addition, because a single X-ray photon interacting in a scintillator produces a number of visible photons proportional to the energy of the X-ray, this system actually measures the total X-ray energy deposited in the detectors. A high energy X-ray photon will therefore produce more current in the electronic system than a low energy photon. This situation is addressed in the Phase II electronics system by counting pulses rather than integrating charge. In the pulse counting scheme, each X-ray photon that interacts in the scintillator produces visible light as before. The PMT's convert this visible light into a charge pulse which will simply be counted instead of integrated. This is possible in the ZT system because the expected count rates are much lower than in

transmission radiography. In a transmission system, the counts are typically many orders of magnitude higher than this pulse counting maximum. With pulse counting, low level electronic noise is no longer a problem, and each detected X-ray photon counts as 1 event regardless of energy.

The Phase II ZT system will be interfaced to an personal computer complete with image processing hardware and software. The operator will control the inspection and then see a real-time image appear as the object is scanned. After the scan, several digital image manipulation algorithms will be available to enhance the image for detection of defects. The system is easily expandable to allow for addition of specific user-defined algorithms.

The Phase II ZT program is well under way. This system will be able to inspect cylindrical objects of up to 36" in length and 24" in diameter. In addition to the cylindrical objects, the system can inspect flat objects of height no greater than 36" and virtually any length.

## 5. OTHER APPLICATIONS

In an ongoing research and development program conducted using company funds in our imaging laboratory, we are investigating the application of ZT to several different materials. Figure 5 shows a ZT scan of a piece of graphite laminate. This material is typical of the new composite materials that are currently being used on modern aircraft. These materials have high strength and low weight, however, they are difficult to inspect for defects. The ZT scan clearly shows a large defect in the sample. This defect is a delamination between the surfaces of the layered composite and is not apparent from visual inspection of the object. The ZT technology is very well suited to inspection of these flat plate materials.

One-sided inspection also gives ZT the capability of inspecting objects that are otherwise inaccessible. The water carrying pipes on a submarine or in a nuclear reactor are just a couple of examples of the types of objects that may be inspected using a ZT system. These pipes may develop pits that can lead to serious failures. We are currently investigating the use of ZT in early detection of these pits.

ZT technology offers a unique method for inspecting other high technology materials and systems. Figure 6 shows a ZT image of a section of the strut in a Helicopter rotor blade. The bond lines between the Kevlar, the Honeycomb, and the strut are evident. Delaminations in these bond lines could lead to loss of equipment and/or life.

The Phase II laboratory based ZT system to be delivered to the AFAL will be used specifically to inspect rocket motors, however, the technology has potentially far reaching applications in the NDT industry.

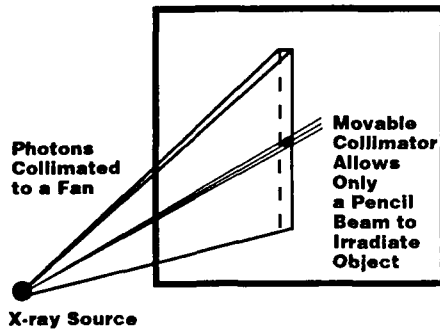


Figure 1. Scanning X-Ray Beam Technique.

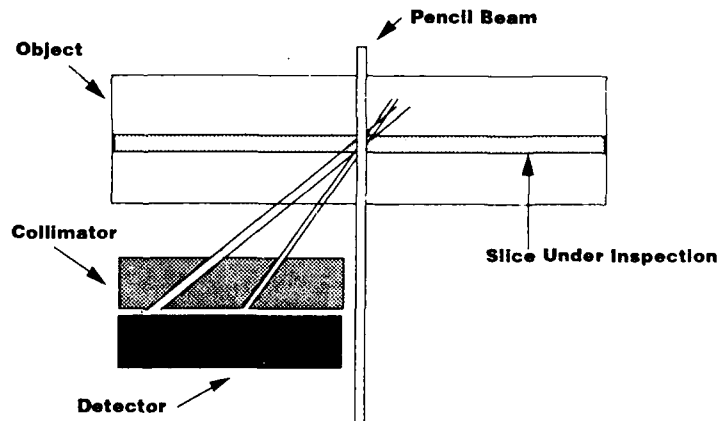


Figure 2. ZT System - Top View.

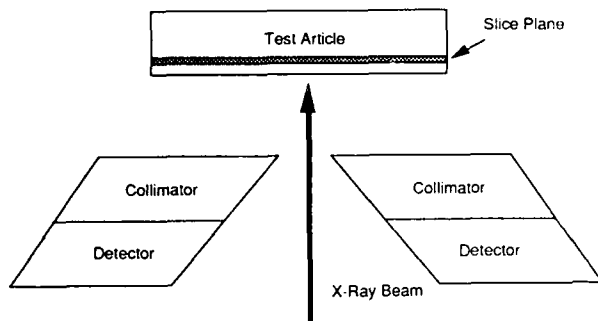


Figure 3a. ZT System Normal Geometry.

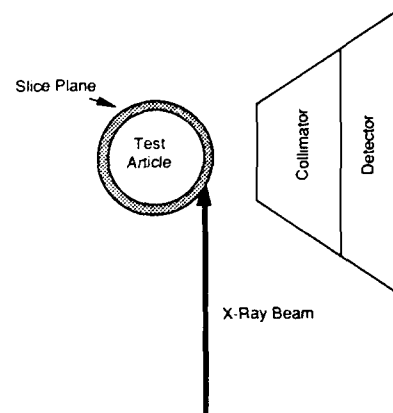


Figure 3b. ZT System Tangential Geometry.

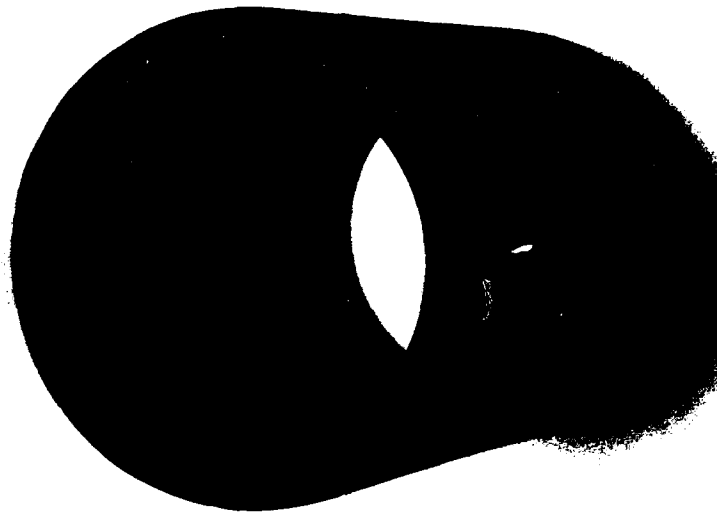


Figure 4a. Photograph of 8" Diameter Carbon-Carbon Composite.



Figure 4b. ZT Image at Depth 0.450".



Figure 5. ZT Image of Graphite Laminate.

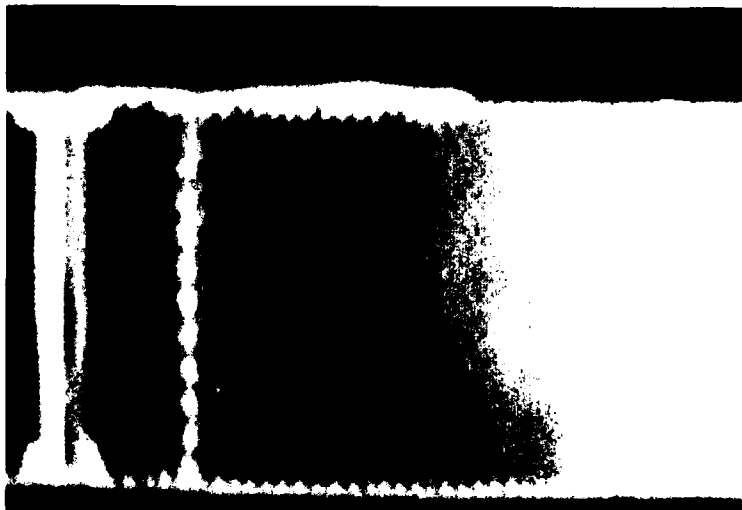


Figure 6. ZT Image of Helicopter Rotor Blade.

## EXPERIMENTAL VALIDATION OF INCOMPLETE DATA CT IMAGE RECONSTRUCTION TECHNIQUES

J.W. Eberhard, M.L. Hsiao, and K.C. Tam  
Corporate Research and Development  
General Electric Company  
Schenectady, New York 12301

### ABSTRACT

X-ray CT inspection of large metal parts is often limited by x-ray penetration problems along many of the ray paths required for a complete CT data set. In addition, because of the complex geometry of many industrial parts, manipulation difficulties often prevent scanning over some range of angles. CT images reconstructed from these incomplete data sets contain a variety of artifacts which limit their usefulness in part quality determination. Over the past several years, GE has developed 2 new methods of incorporating a priori information about the parts under inspection to significantly improve incomplete data CT image quality. This work briefly reviews the methods which were developed and presents, for the first time, experimental results which confirm the effectiveness of the techniques. The new methods for dealing with incomplete CT data sets rely on a priori information from part blueprints (in electronic form), outer boundary information from touch sensors, estimates of part outer boundaries from available x-ray data, and linear x-ray attenuation coefficients of the part. The two methods make use of this information in different fashions. The relative performance of the two methods in detecting various flaw types is compared. Methods for accurately registering a priori information with x-ray data are also described. These results are critical to a new industrial x-ray inspection cell built by GE for inspection of large aircraft engine parts.

### 1. INTRODUCTION

Computerized Tomography (CT) image reconstruction is a powerful technique for creating two-dimensional cross-sectional images of a wide variety of objects. It is becoming important in manufacturing, where it allows identification of very small flaws and provides new design freedom because of its ability to image internal structure, which cannot be inspected

effectively with alternative techniques. Figure 1 shows the data acquisition configuration for both digital radiography (DR) and CT images using a linear array x-ray detector. In computerized tomography, the image of an object is reconstructed from its projection data. The angular range of the projection data is determined by the projection theorem, or the central slice theorem, which states that the one-dimensional Fourier transform of the projection  $P_{\theta}(x)$  of a two-dimensional object  $f(x,y)$  at view angle  $\theta$  relative to the x-axis

gives rise to a line of Fourier components of  $f(x,y)$  in the Fourier space, with the line passing through the origin and oriented at the angle  $\theta$  relative to the  $y$ -axis. The consequence of this theorem is that one would need the projections of the object in a full angular range and with sufficiently fine angular spacings in order to reconstruct its image uniquely. The object can be mathematically expressed in terms of these projections, such as an inverse Fourier transform or an inverse Radon transform, and therefore the projections can be inverted mathematically to yield the image.

In certain cases, however, complete data sets for CT imaging are not available. Physical limitations in the data acquisition process and considerations of throughput, data set size, and computation time can limit the CT data set. In both these cases, image quality is degraded by the absence of complete data. For most manufactured parts, however, a great deal is known about the structure, since the parts were built from a designer's blueprint. Incorporation of this a priori information has the potential to significantly improve image quality. Indeed, various techniques have been developed for dealing with the incomplete data CT image reconstruction problem over the last decade<sup>(1)-(13)</sup>.

GE Corporate Research and Development has been actively involved in CT imaging with a priori information for most of the last decade<sup>(5)-(13)</sup>. Two major types of incomplete CT data set have been addressed. (See Figure 2). In the limited angle CT case, sections of a complex part obstruct the data acquisition scan over a portion of the angular range. In the penetration limited CT case, x-ray path lengths through certain sections of the part are too great to allow sufficient x-ray penetration for meaningful measurement. Two techniques to enhance CT image quality using a priori information have been developed and validated for application to these problems. The model-based CT reconstruction technique, using a priori information extracted from designer's blueprint in electronic form, is described in Section 2. The interactive reconstruction technique, which requires less complete a priori

information than a complete electronic model, is described in Section 3. Experimental validation of both techniques is presented in Section 4. Section 5 summarizes the results.

## 2. MODEL-BASED CT RECONSTRUCTION TECHNIQUE

Because most manufactured parts were built from a designer's blueprint or solid modeling electronic database, incorporating a priori information extracted from a CAD model has the potential to enhance incomplete projection CT image quality. In general, the incomplete projection situation can be divided into two categories: limited-angle and the penetration-limited. For the limited-angle situation, incomplete data results when sections of a complete part obstruct the data acquisition scan over a portion of the angular range. Using the model-based CT reconstruction method, projection data acquired over the available angular range and projection data calculated from the model image over the missing angular range are used for reconstruction. For the penetration-limited situation, the x-ray path length through certain sections of the part is too great to allow sufficient x-ray penetration for meaningful measurement. Projection substitution is applied to the penetration-limited portion of the projection data. Image quality improves significantly. The use of a priori information from solid models has proved to be a powerful technique for enhancing the quality of incomplete data CT images. The model-based CT reconstruction approach involves CAD model creation, model-image extraction, registration, and the projection substitution scheme and is described as follows.

A CAD electronic database can be created using a solid modeling development tool such as the TRUCE solid modeler developed by the solid modeling program at GE-CRD. A two-dimensional cross section can be derived from a three-dimensional solid model electronic database. The GE Aircraft Engine F404 high-pressure turbine blade is shown in Figure 3.(a); its polygon shaded complete 3D solid model is represented in Figure 3.(c) and the 2D cross-section model im-

age extracted from a 3D solid model with the desired orientation and position of the cross-section plane is shown in Figure 3.(d). Engineering database matching has been conducted to correlate the electronic model, blueprint specification, and the data acquisition setup so that a 2D cross section corresponding to the CT projection plane can be successfully extracted from a three-dimensional solid model.

To properly utilize a priori information from a CAD model for limited-angle CT reconstruction, accurate registration between the model image and the CT image is required. A 2D moment-based registration method has been developed and applied to ensure proper use of a priori information for model-based CT reconstruction<sup>(7)</sup>. A geometric transformation is estimated based on the first and second moment of the model image and the reconstructed CT image with incomplete projection. The translation factor is calculated from the offset of the object central gravity point, which can be computed as the first moment about the  $x$  and  $y$  axes. The rotation is computed from the variations of the orientation angle. The axis of elongation, defined as the line for which the integral of the square of the distance to points in the object is a minimum, is used to represent the object orientation. The orientation angle is the angle between the axis of elongation and the  $x$  axis. This angle can be computed as function of the second moments about the central gravity point. A transformation matrix containing both the translation and rotation factors is then applied to the CT image such that the resultant image is geometrically correlated to the 2D model image extracted from a solid model.

A projection substitution scheme has also been developed. It consists of projection alignment and automatic scaling algorithms. Since the center detector number and the first viewing angle of the projection computed from the registered model image may be different from those used in the real projection acquired from the CT cell, projection alignment must be conducted. In addition, the a priori information extracted from a 3D solid model is represented as a binary image.

The scaling factor applied to the projection calculated from this model image is unknown. In order to ensure the proper projection substitution, an automatic scaling method has been developed in which the projection data calculated from a model image can be automatically rescaled to match the projection data acquired from the detector. It uses the averaged ratio of area covered by a co-existing projection pair over the available angular range. The co-existing projection pair are the projection data acquired from the available angular range and its corresponding projection data calculated from the registered model image. It is assumed that the scaling factor is unique for a uniform density cross section. This method ensures the proper alignment of the projection data set and establishes the success of the model-based CT reconstruction.

### 3. ITERATIVE RECONSTRUCTION TECHNIQUE

An iterative algorithm designed to reconstruct images from limited-angle data was first proposed by Tam<sup>(5)</sup> et al. The idea is to make use of the available a priori information about the object to compensate for the missing projection data. The iterative transform algorithm is schematically illustrated in Figure 4. The image is transformed back and forth between the object space and the projection space, being corrected by the a priori information on the object in the object space, and by the known projections in the projection space. The a priori information in the object space includes a boundary enclosing the object, and an upper bound and a lower bound of the object density.

The upper and lower bounds of the object density are usually available. For example, they can be estimated from the a priori knowledge about the composition of the object; in fact, the lower bound is usually taken to be zero. The exterior boundary of the object can be estimated by touch sensor or modelling. If the shape of the object is not too concave, its exterior boundary can also be estimated using the same x-ray data that are used to reconstruct the CT image without requiring additional equipment. The approach is to construct the convex hull of the object using x-ray



data, and to use the convex hull as an approximation of the actual object boundary. The convex hull of a two-dimensional object is the smallest convex region containing the object. If the object is convex in shape, its convex hull is the same as its support. If the object is not convex, its convex hull is a good approximation of the object support if its shape is not too concave. In general, these conditions are fulfilled in industrial inspection, since most of the industrial objects are convex in shape, such as cylinders, spheroids, parallelepipeds, etc. Hence the use of the object convex hull as an approximation of the object boundary is justified.

#### 4. EXPERIMENTAL VALIDATION

##### 4.1 MODEL-BASED CT RECONSTRUCTION

Consider a specific aircraft engine part, the pressure-welded blade disk (BLISK). The CT cross section is about 7.0" high and 0.5" wide. Because of the relatively high aspect ratio of this section, x-ray penetration in the long path length direction could be a problem, and incomplete data CT reconstruction is required to inspect this part. To validate the model-based CT reconstruction technique, two incomplete projection cases have been studied: a limited-angle projection case and a penetration limited projection case.

The limited-angle projection is simulated when the limited-angle scanning caused by an obstruction on the scanning path results in the inaccessibility of some view angles. Two missing cones each with 40° angles are placed in the most penetration limited projection angle. Figure 5.(a) shows the limited-angle sinogram data with 80° missing angle out of 360° full scanning viewing angular range. The reconstructed CT image with this limited-angle sinogram data is shown in Figure 5.(b). Note that the reconstructed image is seriously distorted. A major portion of the walls is missing and many streak artifacts are present. It is hardly possible to use this image for any quantitative measurement.

Using the enhanced model image shown in Figure 5.(c), which is properly registered with the orientation and position of the reconstructed incomplete projec-

tion CT image, the model sinogram data can be calculated via the reprojection method and is shown in Figure 5.(d). Applying the projection alignment, rescaling, and projection substitution schemes, the model-enhanced limited-angle sinogram results by combining the limited-angle sinogram data and the model sinogram data (Figure 5.(e)). The reconstructed CT image with model-enhanced limited-angle sinogram data is produced and is shown in Figure 5.(f). The improvement in image quality is substantial.

In addition, applying the model-based CT reconstruction method to enhance penetration-limited CT image quality has also been studied and validated. Figure 6.(a) shows the complete sinogram data of the pressure-welded blade disk. Due to the relatively high aspect ratio, the penetration-limited situation has occurred by over-attenuation. The reconstructed CT image with the penetration-limited sinogram is shown in Figure 6.(b). Note that those walls parallel to the most penetration limited direction are not as dense as the others. Using the model-based CT reconstruction technique, the model-enhanced sinogram is generated (Figure 6.(c)) and the reconstructed image with model-enhanced sinogram data is presented in Figure 6.(d). The result shows significant improvement and those low density walls have been rebuilt.

##### 4.2 ITERATIVE TRANSFORM ALGORITHM

The iterative transform algorithm has been validated on simulated data<sup>(5)(9)(10)</sup>. The reconstructed images showed improvement after iterations at all angular ranges, and the extent of improvement increased as the iterations progressed. These results are partially reproduced in Figure 7. Figure 7.(a) shows a point object reconstructed from limited angle projection data. Data were available only in a 53.1° angular range, and missing in the other 126.9°. (In the simulations, parallel beam geometry was used, so a complete data set requires an angular scan of only 180 degrees.) The missing projection data caused blurring of the point object as well as the presence of positive and negative ridges radiating from the point object. Figure 7.(b) shows the improved point object after 10 iterations. The bound-

ary constraint used in the iterations was a square of 11 by 11 pixels, with the point object located at the center of the square. After the iterations the image became much narrower, and the artifacts were much reduced.

Recently the iterative transform algorithm has also been validated<sup>(11)-(13)</sup> on experimental data. X-ray sinogram data of the cross-section of a F404 high-pressure turbine blade made of Ni-based superalloy were acquired on a GE X-Ray Inspection Module at the GE Aircraft Engine Business Group at Cincinnati, Ohio. The results corresponding to two back-to-back 40° missing cones oriented along the x-axis are reproduced in Figure 8. Figure 8.(a) shows the image reconstructed from complete data. Figure 8.(b) shows the image reconstructed from limited-angle data, and the images after 1 and 2 iterations using the iterative algorithm are shown in Figures 8.(c) and 8.(d) respectively. The a priori information used consisted of the upper and lower bounds of the object density and the exterior boundary. After the iterations there are obvious improvements inside the cavities and on the wall regions.

The iterative transform algorithms was also applied to the pressure welded blade disk (BLISK) which was used to evaluate the Model-Based CT Reconstruction algorithm. In this case, as for the blade data, the results corresponding to two back-to-back 40° missing cones oriented along the x-axis. Figure 9.(a) shows the image reconstructed from complete data. Figure 9.(b) shows the image reconstructed from limited-angle data, and the images after 1 and 4 iterations using the iterative algorithm are shown in Figures 9.(c) and 9.(d) respectively. After the iterations there are again obvious improvements inside the cavities and on the wall regions.

## 5. CONCLUSION

Two techniques have been developed for incorporating a priori information into incomplete data CT images. Both techniques have been extensively tested, both with simulations<sup>(6),(7)-(10)</sup> and with experimental

data (Section 4). The Model-Based Technique requires detailed a priori information about the part, since missing data are calculated directly from the part model. However, it provides excellent image quality and rapid calculation of the final image, since no iterations are required. The Iterative Transform Technique, on the other hand, requires less detailed a priori information about the part, but requires greater computation to arrive at the improved image. Also, this technique deals with manufacturing variability more effectively, since it does not rely on detailed information about the part internal structure from the blueprint. Both techniques substantially reduce the level of artifacts in the incomplete data CT images, and therefore make operator interpretation much more feasible. Both show dramatic improvement in image quality compared to incomplete data CT images.

## 6. REFERENCE

1. Sato, T., Norton, S.J., Linzer, M., Ikeda, O., and Hirama, M., "Tomographic Image Reconstruction from Limited Projections using Iterative Revisions in Image and Transform Spaces," *Applied Optics*, 20, 1981, pp. 395-399.
2. Tuy, H., "Reconstruction of A Three-Dimensional Object from A Limited Range of Views," *J. Math. Anal. Appl.*, 80, 1981, pp. 598-616.
3. Nassi, M., Brody, W.R., Medoff, B.P., and Macovski, A., "Iterative Reconstruction-Reprojection: An Algorithm for Limited Data Cardiac-Computed Tomography," *IEEE Trans. Biomed. Eng.*, BNE-29, 1982, pp. 333-341.
4. Stark, H. ed. *Image Recovery: Theory and Application*, Academic Press, Inc., New York, 1987.
5. Tam, K.C., and Perez-Mendez, V., "Tomographical Imaging with Limited-Angle Input," *J. Opt. Soc. Am.*, 71, 1981, pp. 582-592.
6. Tam, K.C., "Improving the Accuracy of Limited-Angle Reconstruction by Multispectral Imaging,"

- Proceedings of the VIIth International Conference on Information Processing in Medical Imaging, Stanford University, June 22-26, 1981, pp. 414-427.
7. Eberhard, J.W., Hedengren, K.H., and Hsiao, M.L. "Effects of Manufacturing Variability on Model Based CT Image Reconstruction," presented at the Eighth Annual Review of Progress in Quantitative NDE, University of California, San Diego, July 31 - August 5, 1988. Also, to be published in Thompson, D.O., and Chimenti, D.E., eds., Review of Progress in Quantitative Nondestructive Evaluation, vol. 8, Plenum Press, New York, 1989.
  8. Eberhard, J.W., and Hedengren, K.H., "Use of a Priori Information in Incomplete Data X-Ray CT Imaging," Review of Progress in Quantitative Nondestructive Evaluation, Thompson, D.O., and Chimenti, D.E., eds., vol. 7A, Plenum Press, New York, 1988, pp. 723-730.
  9. Tam, K.C., "Reducing the Fan-Beam Scanning Angular Range," *Physics in Medicine and Biology*, 33, 1988, pp. 955-967.
  10. Tam, K.C., "Limited-Angle Image Reconstruction in Non-Destructive Evaluation," Proceedings of the 1987 NATO Advanced Workshop on Signal Processing and Pattern Recognition in Non-destructive Evaluation of Materials, Quebec City, Canada, August 18-22, 1987.
  11. Tam, K.C., Eberhard, J.W., and Mitchell, K.W., "Incomplete-Data Image Reconstructions in Industrial X-Ray Computerized Tomography," presented in Review of Progress in Quantitative NDE, San Diego, July 31-August 5, 1988; also to be published in the proceedings.
  12. Tam, K.C., "The Application of Convex Hull in Industrial X-Ray Computerized Tomography," presented in Review of Progress in Quantitative NDE, San Diego, July 31-August 5, 1988; also to be published in the proceedings.
  13. Tam, K.C., Eberhard, J.W., and Mitchell, K.W., "Limited-Angle X-Ray CT Image Reconstructions in Industrial NDT," to be published in the Proceedings of the 12th World Conference on Non-Destructive Testing, Amsterdam, The Netherlands, April 23-28, 1989.
  14. Huesman, R.H., Gullberg, G.T., Greenberg, W.L., and Budinger, T.F. Donner Algorithms for Reconstruction Tomography, Lawrence Berkeley Laboratory, University of California, Pub. No. 214, 1977.

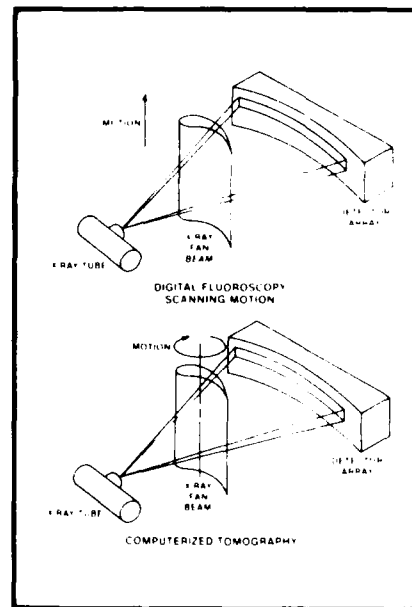
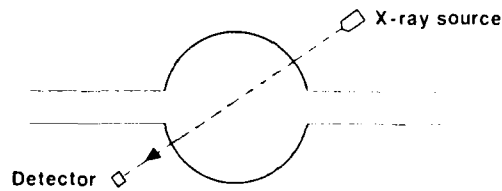
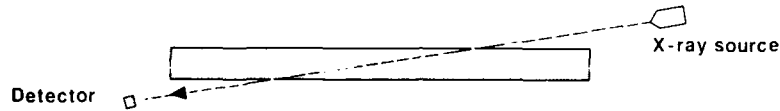


Figure 1: Digital Radiography (DR) and Computerized Tomography (CT)



e.g. 1 Scanning obstructed in some angular range



e.g. 2 Object very long in one direction

Figure 2: Incomplete Data Situations

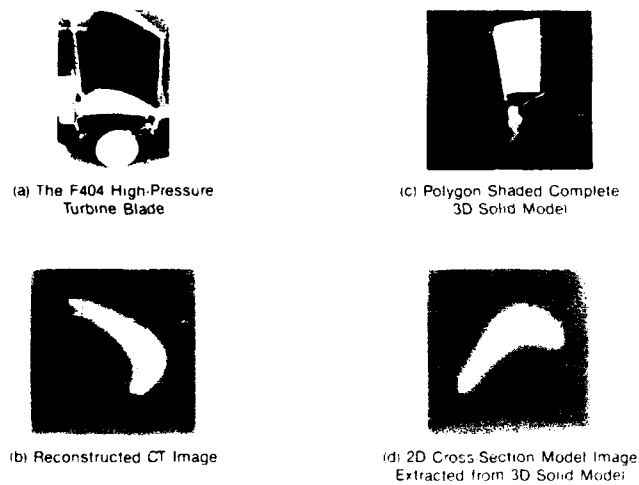


Figure 3: Model Information of the AE's F401 Blade

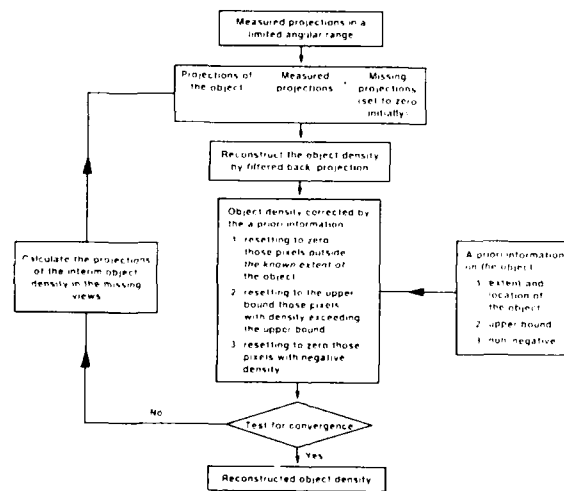


Figure 4: The Iterative Transform Algorithm

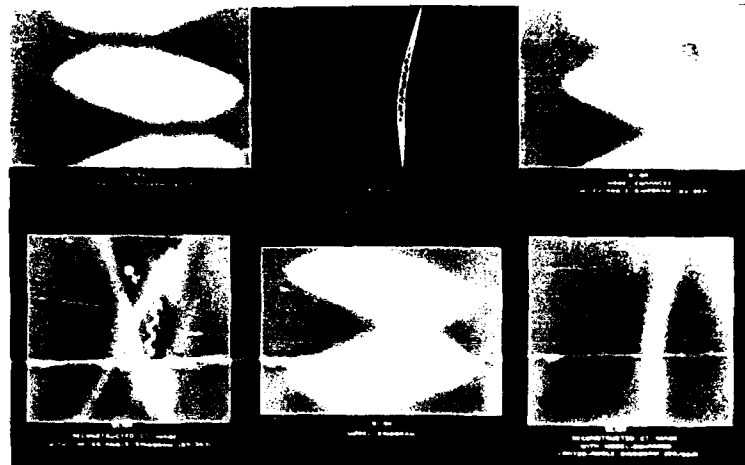


Figure 5: Model-Based Reconstruction with Limited-Angle Projection



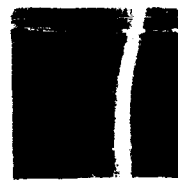
(a) Penetration-Limited BLISK Sinogram



(c) Model-Enhanced Sinogram



(b) Reconstructed CT Image with Penetration-Limited Sinogram



(d) Reconstructed CT Image with Model-Enhanced Sinogram

Figure 6: Model-Based Reconstruction with Penetration-Limited Projection

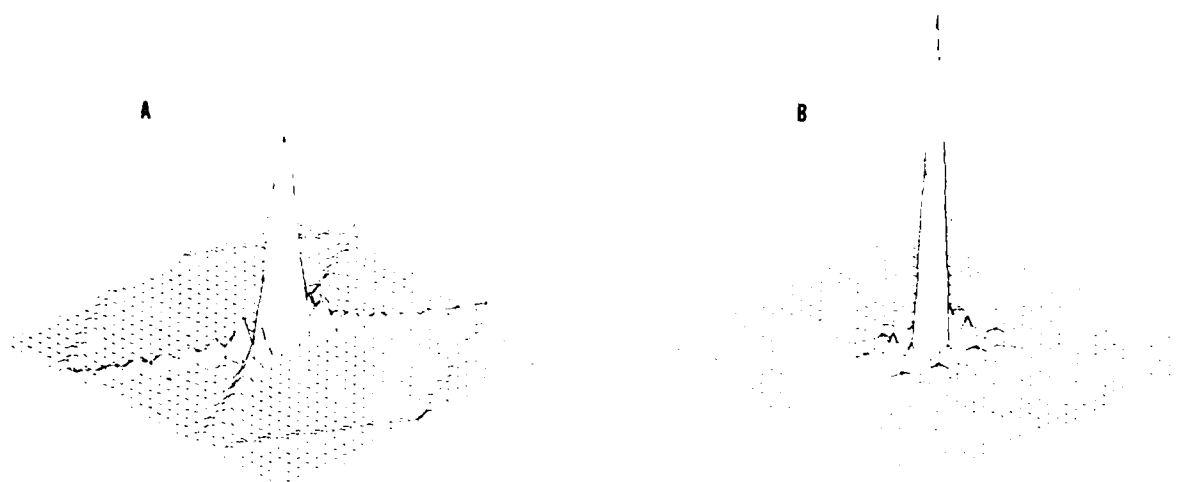


Figure 7: Simulation Results of the Iterative Transform Algorithm



Figure 8: Experimental Results (F404 Blade) of the Interactive Reconstruction Method

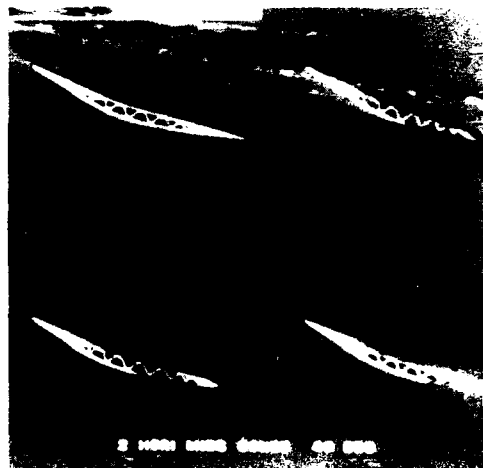


Figure 9: Experimental Results (Blisk) of the Interactive Reconstruction Method

## **MICROFOCUS RADIOGRAPHY FOR NONDESTRUCTIVE EVALUATION OF CERAMICS: PRINCIPLES AND APPLICATIONS**

**William D. Koenigsberg, Daniel J. Cotter, and Edmund M. Dunn**

**GTE Laboratories Incorporated  
40 Sylvan Road  
Waltham, MA 02254**

### **ABSTRACT**

Microfocus radiography is one of the most effective methods for the nondestructive evaluation (NDE) of ceramic components. Theoretical and practical limitations on the defect detection capability of microfocus radiography are presented. The simultaneous need for adequate resolution and contrast in x-ray projection imaging is reviewed. Reliability of defect detection is assessed by measuring the probability of detection (POD) for x-ray images of laser-machined voids in a silicon nitride sample. Probability of detection curves are determined for x-ray film and real-time fluoroscopic imaging. Comparison of the curves obtained under identical conditions reveals differences in shape and level. The significance of these differences is discussed. An application of microfocus radiography is the NDE of ceramic-to-metal brazed joints. In-process NDE of silicon nitride ceramic brazed to Incoloy 909 metal was performed. Correlation between NDE and subsequent destructive evaluation of the brazed test samples is discussed.

### **INTRODUCTION**

Microfocus radiography is one of the most effective methods for inspection of ceramics.<sup>(1,2)</sup> The x-ray technique is nondestructive, capable of detecting internal and surface defects, applicable to complex-shaped objects, and it produces real-time images which are the basis for automatic inspection in a production environment. For any nondestructive evaluation system which generates images of internal or surface structure, it is essential that adequate resolution and contrast exist simultaneously. Radiographic physics allows for tradeoffs among controlling variables, including accelerating potential, beam current, and exposure time. Research has been performed to optimize defect detectability by establishing microfocus imaging parameters (accelerating potential, magnification, etc.) for a wide range of silicon nitride components.

Microfocus x-radiography has advanced to a point where image resolution has improved by a factor of 50 over conventional x-ray sources. Specifically, a focal spot diameter of 10  $\mu\text{m}$  is commonplace, compared with a nominal 500- $\mu\text{m}$  diameter for a conventional x-ray source. This improvement alone is largely responsible for the success achieved in the NDE of ceramics using microfocus x-ray radiography. Decreasing the dimensions of the focal spot still further realizes diminishing returns and engenders other fundamental difficulties. Therefore it is reasonable to explore other approaches for improving the detectability of defects in ceramic components.

Ultimately a measure of the degree to which defect detectability has improved is required. Such a measure is the probability of detection (POD) and is described in the literature.<sup>(3)</sup> The POD

for seeded defects in  $\text{Si}_3\text{N}_4$  has been reported,<sup>(1,4)</sup> with x-ray film providing outstanding resolution and contrast characteristics among the available imaging media. In this paper, a baseline POD for laser-machined defects in silicon nitride ceramic is established using a real-time imaging system. Results from in-process NDE studies for ceramics joining are presented. First the meanings of defect detectability, resolution, and contrast limitations are discussed.

## DEFECT DETECTABILITY

Detectability is a broad term which reflects the ability of an inspector to distinguish a difference between a uniform background and a local inhomogeneity in a two-dimensional image. Two conditions must be satisfied to achieve detection. Sufficient resolution and image contrast must exist simultaneously. As illustrated in Figure 1, resolution is a measure of the clarity of the two-dimensional outline of a flaw or inhomogeneity. Contrast sensitivity is a measure of the degree to which the third dimension (depth) is represented by a change in film opacity on the radiograph.

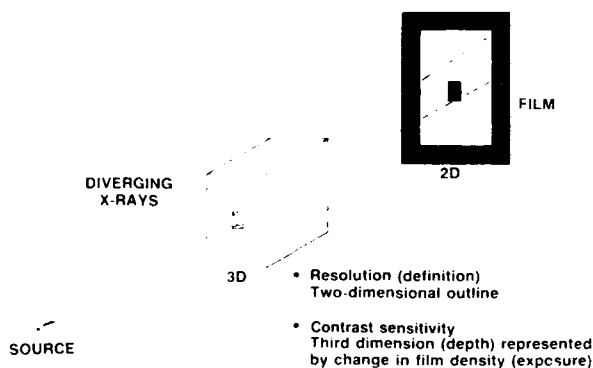


Figure 1. Radiographic Sensitivity. Radiographic sensitivity is dependent on both resolution and contrast sensitivity. Resolution is concerned with the two-dimensional outline of a flaw or inhomogeneity; contrast sensitivity is indicative of how the third dimension (depth) is represented by a change in film density on the radiograph.

## RESOLUTION

As shown in Figure 2, forming an ideal image using projection radiography requires a point source. The microfocus system has a source of small but finite size ( $10\text{-}\mu\text{m}$  focal spot) which substantially reduces geometric unsharpness. The illustration

shows that an extended source causes unsharpness that degrades definition of an object's outline. This unsharpness also limits resolution of internal structure such as voids or other flaws. In fact, by using the real-time imaging capability of the microfocus system at a 10X magnification, one can watch a  $100\text{-}\mu\text{m}$  defect disappear from view as the x-ray source is electronically increased in size from its  $10\text{-}\mu\text{m}$  minimum.

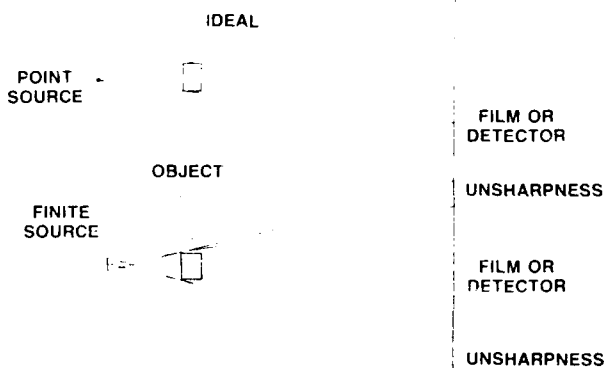


Figure 2. Unsharpness. Forming an ideal image requires a point source. The microfocus system has a source of small but finite size ( $10\text{-}\mu\text{m}$  focal spot) which can cause geometric unsharpness at high magnification. This reduces definition of the object outline and limits resolution of internal detail.

Unsharpness is displayed in Figure 3 for a typical imaging situation. A focal spot of  $10\text{-}\mu\text{m}$  diameter is used at a magnification of 10X to view a  $100\text{-}\mu\text{m}$  defect. In this case, the  $100\text{-}\mu\text{m}$  defect is imaged as a  $1\text{-mm}$  defect with  $0.09\text{-mm}$  unsharpness, or just less than 10%. Experience has shown that detectability of voids this size is not limited by 10% unsharpness.

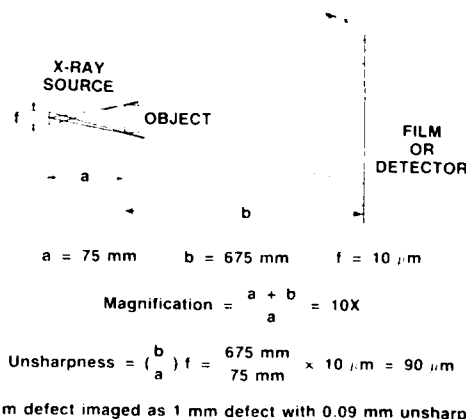


Figure 3. A Typical Imaging Situation. A focal spot of  $10\text{-}\mu\text{m}$  is used at a 10X magnification to view a  $100\text{-}\mu\text{m}$  defect. The  $100\text{-}\mu\text{m}$  defect is imaged as a  $1\text{-mm}$  defect with  $0.09\text{-mm}$  unsharpness, or just less than 10%.



By combining the equations for unsharpness and magnification, an expression can be derived relating the two variables

$$U_g = (M-1)f, \quad (1)$$

where  $U_g$  is the unsharpness,  $M$  is magnification, and  $f$  is the focal spot size. This shows that unsharpness increases linearly with increasing magnification. The ratio of unsharpness to magnified defect size is given by

$$\frac{U_g}{M \cdot x} = \frac{f}{x} \left( 1 - \frac{1}{M} \right) \quad (2)$$

where  $x$  is the actual defect size. This result shows that increasing magnification has a diminishing influence on the ratio. In fact, the ratio of unsharpness to magnified defect size asymptotically approaches the ratio of the focal spot size to actual defect size as magnification increases. These results are valid regardless of the nature of the imaging detector, i.e., for film or real-time image intensifier. Other characteristics of the imaging media will, of course, exert additional influences on the detectability of defects.

## CONTRAST SENSITIVITY

Contrast sensitivity is a measure of the degree to which the third dimension (depth) of an object is represented by a change in film density on a radiograph. The interaction of penetrating radiation with the object and film influence the contrast sensitivity. A model of the interaction can be approximated as shown in Figure 4.<sup>(5)</sup> This is an approximation because it is based on attenuation of monochromatic radiation, and the microfocus x-ray tube is a polychromatic radiation source. The equations in the figure express as a ratio the change in transmitted radiation intensity when a void or inclusion is encountered within an object. Maximizing the change in intensity improves subject contrast and increases the likelihood of detecting flaws.

In practice, subject contrast is typically improved by reducing the kilovoltage (accelerating potential) used for x-ray generation. This reduction increases the minimum wavelength of the penetrating radiation<sup>(6)</sup> and affects the attenuation of x-rays by the material. Mass attenuation coefficient values for the constituent elements<sup>(7)</sup> can be used to calculate the linear attenuation coefficient of silicon nitride and common inclusion (contaminant) materials. Continued reduction of the accelerating potential is not practical because the x-ray intensity

decreases still further, resulting in excessively long film exposure requirements. The improvement in subject contrast with decreasing accelerating potential is simple to demonstrate with a calibrated silicon nitride step wedge.<sup>(12)</sup>

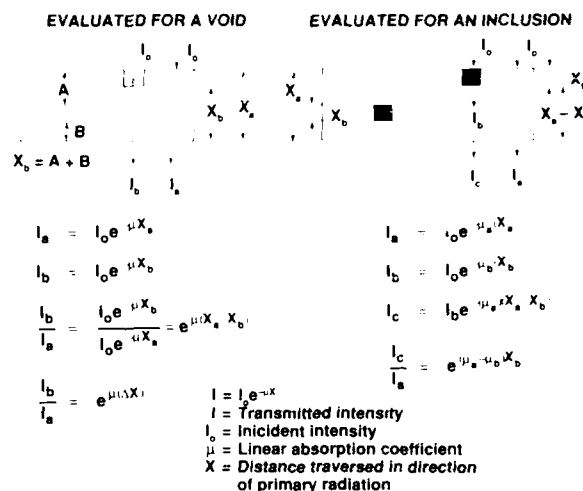


Figure 4. Contrast Sensitivity. The equations shown express, as a ratio, the change in x-ray intensity through an object when a void or inclusion is encountered.

Contrast sensitivity is also dependent on the film used for imaging. The effect, which is determined by the film characteristic curve, can be expressed by<sup>(5)</sup>

$$\text{Void} \quad \frac{\Delta D}{G} = (0.43)\mu_a(\Delta X), \quad (3)$$

$$\text{Inclusion} \quad \frac{\Delta D}{G} = (0.43)(\mu_a - \mu_b)(\Delta X), \quad (4)$$

where  $\Delta D$  is the change in film density,  $G$  is the slope of the film's characteristic curve,  $\mu_a$  is the linear attenuation coefficient of the object,  $\mu_b$  is the linear attenuation coefficient of the inclusion, and  $\Delta X$  is the thickness of the void or inclusion in the direction of primary radiation. A properly exposed x-ray film that is readily viewable with a high intensity illuminator has a slope of approximately 5. By specifying (or determining) the smallest change in film density detectable by an inspector, one can calculate the minimum void size detectable as a function of accelerating potential.<sup>(12)</sup>

An improvement in contrast can be realized by increasing image magnification.<sup>(8,9)</sup> This occurs because placing the object further away from the film (closer to the microfocus x-ray source) reduces the contribution of x-ray scatter to image forming radiation. This can often result in higher contrast in the film image.

Understanding how radiographic sensitivity is affected by resolution and contrast aids in optimizing defect detectability; however, theoretical limits on detection may not be realized in practice. For instance, when radiographing a 3-inch-thick (76.2 mm) silicon nitride object, reducing the kilovoltage to improve contrast becomes impractical because of insufficient photon flux (excessive exposure time). Defect detectability has to be evaluated for the given imaging situation and is part specific.

## DEFECT DETECTION

Image Quality Indicators (IQIs), objects with machined defects, can be used to determine defect detectability. One type of IQI used with the microfocus x-ray system is the penetrameter. The basic approach is to determine the minimum change in thickness which is detectable in the x-ray image of the penetrameter when exposed in the direction of primary radiation. Defect detectability can be quantified by introducing the ratio, thickness sensitivity:

$$\text{Thickness Sensitivity} = \frac{\Delta X}{X}, \quad (5)$$

where  $X$  is the thickness of the object and  $\Delta X$  is a change in object thickness in the direction of primary radiation.

Defect detectability measurements over a wide range of object thickness were made with a silicon nitride slot penetrameter.<sup>(2)</sup> Slots of varying depth were ground into one block, and additional blocks were added to build the penetrameter up to the object thickness of interest. The thickness sensitivity measurement is made by objectively noting the slot of least depth detectable on the radiograph.

Microfocus x-ray images of the slot penetrameter were stored in computer memory. The images were frame averaged to reduce random noise.<sup>(10)</sup> The penetrameters were 1.0 inch thick (25.4 mm) and were imaged at 100 kV. The thickness sensitivity measured was 1.0%. Under similar conditions, film radiographs of the penetrameters yielded a thickness sensitivity of 0.5%.

Voids tend to be the most prevalent defect in silicon nitride,<sup>(11)</sup> and evidence suggests that they are one of the most critical.<sup>(11,12)</sup>

Voids in objects of large cross section are difficult to detect because of thickness sensitivity limitations. Therefore, reliability of void detection was investigated.

## PROBABILITY OF DETECTION

Reliability of flaw detection can be assessed by determining a lower-bound probability of detection.<sup>(7)</sup> In this case, the probability of detecting voids in sintered silicon nitride was studied. Two outcomes are possible when inspecting a part containing known voids; an existing void is detected or not detected. The inspection process can be characterized with a binomial distribution because it has only two outcomes.<sup>(13)</sup>

Lower-bound probability of detection can be calculated at a given confidence level according to the expression<sup>(3)</sup>

$$1 - G = \sum_{X=S}^N \frac{N!}{X! (N-X)!} P_1^X (1 - P_1)^{N-X}, \quad (6)$$

where  $N$  is the number of existing flaws,  $S$  is the number of flaws detected,  $P_1$  is the lower-bound probability of detection, and  $G$  is the confidence level (range 0.0–1.0). The confidence level is a measure of the expectation that the true probability of detection exceeds the calculated lower-bound probability of detection. The level of confidence employed depends on the reliability required for a particular application. The greater the confidence level, the more conservative is the calculated lower-bound probability of detection.

Probability of detection data were acquired using a test specimen containing simulated voids. The specimen was a block (0.100 x 0.300 x 1.00 inches) of sintered AY6 silicon nitride ( $\text{Si}_3\text{N}_4 + 6 \text{ w/o } \text{Y}_2\text{O}_3 + 2 \text{ w/o } \text{Al}_2\text{O}_3$ ) machined to a 320 grit surface finish. A pulsed Nd-glass laser machined the voids (nominally 100  $\mu\text{m}$  in diameter and 100- $\mu\text{m}$  deep) into the surface of the block. Individual voids were formed using a single 2-ms pulse, and their dimensions were controlled by the focus of the laser beam. Some effort was required to overcome tapering of the hole to a point, due to attenuation of the beam entering the specimen, but the final result was a consistent void with a circular opening, uniform diameter, and rounded bottom. Once the laser operating parameters were established, 100 simulated voids were reproducibly machined into the block at random locations.

Probability of detection was determined as a function of thickness sensitivity under specific imaging conditions. Thickness sensitivity, which was discussed for the  $\text{Si}_3\text{N}_4$  slot penetrometer, is the ratio of minimum change in thickness radiographically detectable to thickness of the object being radiographed in the direction of primary radiation. It was varied by placing additional blocks of the same material under the one containing the machined voids. Projection radiographs were made at 10X magnification using high-contrast film. The voltage was held constant at 45 kV, and a tungsten anode (x-ray target) was used. Current and time were varied as the object thickness was changed to maintain a consistent exposure suitable for viewing (film density approximately 2.4). The radiographs were examined with a high intensity illuminator by a skilled radiographer who had knowledge of the nature of the voids. The number of voids detected at each thickness sensitivity was recorded, and the value of  $P_L$  (lower-bound probability of detection) was determined at a confidence level of 95%, i.e.,  $G = 0.95$  from Equation 6 using a table of the cumulative binomial distribution.<sup>(14)</sup> The plot is shown in Figure 5. The value of  $P_L$  was determined at 5 thickness sensitivities for the 100 voids. The value of the  $P_L$  plotted corresponds to the maximum value of void depth for the group (maximum was 108  $\mu\text{m}$ , minimum was 84  $\mu\text{m}$ , nominal was 100  $\mu\text{m}$ ). This makes the value of  $P_L$  conservative because its calculation is biased by voids of less depth (smaller changes in thickness). The plot is valid only for a specific set of conditions and should not be applied generically. Probability of detection and the sensitivity of a nondestructive evaluation technique depend on the specific object being inspected. In fact, this is why the laser-machining approach to void simulation was pursued; it can be applied to complex-shaped objects.

The procedure outlined above was repeated for the real-time imaging system built into the microfocus equipment.<sup>1</sup> The same 100-hole  $\text{Si}_3\text{N}_4$  test block was utilized and probability of detection (POD) was determined as a function of thickness sensitivity. Frame averaging was exercised to reduce the effects of random noise. The number of voids detected at each of five thickness sensitivities (the same values as before) was recorded, and  $P_L$  was determined at a confidence level of 0.95 from Equation (6) and a comprehensive table of the binomial distribution. The results are displayed in Figure 6. Comparison

of Figures 5 and 6 reveal distinct differences which are discussed here.

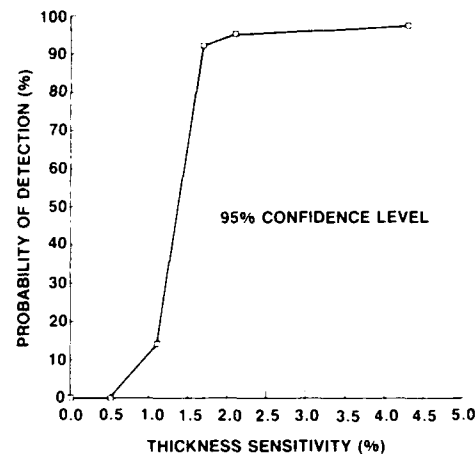


Figure 5. Lower-Bound Probability of Detection for Film Radiography. Lower-bound probability of detection was evaluated as a function of thickness sensitivity at a confidence level of 95%. The value of  $P_L$  was calculated at 5 thickness sensitivities for a group of 100 voids. The value of  $P_L$  is plotted, as a point, at the maximum value of void depth for the group. A straight line is used to connect the points.

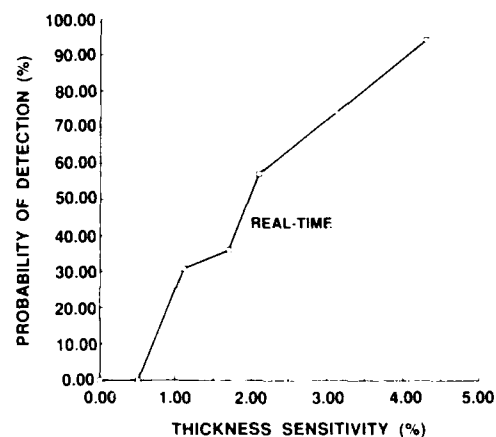


Figure 6. Lower-Bound Probability of Detection for Real-time Radiography. Results from a baseline study of real-time probability of detection are shown. Real-time probability of detection levels are approaching the superior film results. Improvement is expected with further parametric studies of the influence of imaging variables on real-time flaw detection.

<sup>1</sup>IRT-Ridge Model HOMX 161

Figure 5 shows a sharp increase in the probability of detection starting at a thickness sensitivity of about 1% and nearly reaching the 0.95 level at a thickness sensitivity of about 2%. This behavior is characteristic of a properly operating film imaging system and points out that the reliability of detecting defects whose dimensions are less than or "near" the thickness sensitivity threshold (in this case centered at about 1.4%, i.e., where  $POD = 0.5$ ) must be questioned. Conversely, this result shows that the probability of defect detection is reliable (i.e. > 95%) at a thickness sensitivity greater than or equal to 2%.

Inspection of Figure 6 shows a marked difference in the general character of the probability of detection curve. The monotonic increase in POD with thickness sensitivity is much more gradual when the real-time imaging system is employed, reaching 0.92 at a thickness sensitivity of about 4.5%. In fact, except for a small region between 0.5% and 1.0% thickness sensitivity, the real-time POD is everywhere less than the film-determined POD. This result was at first disconcerting because every attempt was made to assure that measurement conditions were identical. Additional experiments with differing operational parameters quickly revealed the cause of the apparent discrepancy. In particular, increasing the magnification for real-time imaging caused the POD to approach the film-determined POD.

This is a consequence of the superior resolution characteristics of film compared to a real-time image intensifier, all other factors being the same. By increasing the magnification (i.e., by moving the object closer to the x-ray source), the effective resolution of the image intensifier is improved. This important result points out that it is not appropriate to compare probability of detection data obtained by film and real-time imaging on a one-to-one basis. Rather, studies of this nature must be performed to maximize probability of detection for each imaging situation. A pertinent example of the utilization of microfocus radiography for NDE of high performance materials is inspection required for ceramics joining.

#### NDE FOR CERAMICS JOINING

The utilization of advanced ceramics in high performance applications such as in heat engines requires the development of suitable joining methods. Ceramic-ceramic and ceramic-metal joints are needed in a variety of circumstances, for

example, coupling ceramic turbine rotors to metal shafts in hybrid automotive engines and attachment of ceramic coupons in critical wear areas or local high temperature zones. Silicon nitride is a prime candidate for heat engine applications because of its high temperature strength, oxidation resistance, and excellent thermal shock resistance.

Silicon nitride has a low thermal expansion coefficient relative to the structural materials to which it is commonly joined. This mismatch results in expansion differences at elevated temperatures which can cause high stresses at the interface, compromising the structural integrity of the joint. Brazing is the preferred method for ceramic-metal joining because the ductile braze alloys are able to accommodate the thermal expansion mismatch. In ceramic-ceramic joining, brazing is favored because flow of the molten braze alloy allows less stringent joint tolerances than methods such as diffusion bonding. A number of braze materials for joining ceramics are now commercially available,<sup>(15)</sup> and research to develop new alloys is ongoing.

Silicon nitride components for heat engines must generally experience fewer failures than one part per million to satisfy reliability requirements in engine production. Ceramic joining reliability must be commensurate. Nondestructive evaluation plays a key role in ceramic joining, by serving as a materials research tool both for process development and for inspection of the final product.

#### INFLUENCE OF THE BRAZE ON NDE SIGNALS

Wetting and bonding are the crucial criteria for an effective braze.<sup>(16)</sup> The ability to monitor the distribution of braze material is advantageous because the degree of wetting and potential for bonding is revealed. Microfocus radiography can be used to measure the presence and distribution of braze material at the interface between joined components because x-ray attenuation is sensitive to small changes in the composition and thickness of the braze material. The factor which governs x-ray attenuation is the atomic number of the constituent elements. Fortunately, the braze materials contain elements with high atomic numbers compared to the materials being joined. This results in x-ray images with high contrast between the braze and surrounding area, easing radiographic interpretation.

A comparison of linear attenuation coefficients is given in Figure 7 for silicon nitride, Incoloy<sup>2</sup> 909 metal, and Nioro<sup>3</sup> braze material (82 w/o Au, 18 w/o Ni) as a function of x-ray energy level. The calculated linear attenuation coefficients are based on tabulated values of mass attenuation coefficients of the constituent elements.<sup>(7)</sup> These calculated values are approximate because they are based on monochromatic radiation and the microfocus x-ray system has a polychromatic radiation source. The graph exhibits large differences in x-ray attenuation of the materials. These results favor x-ray imaging because the contrast in the image is directly related to differences in linear attenuation coefficient. Decreasing the accelerating potential (kilovoltage) of the x-ray system increases the minimum wavelength of the penetrating radiation and typically improves contrast.<sup>4</sup>

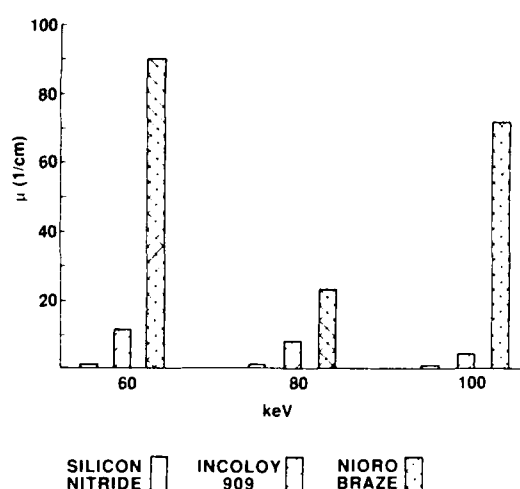


Figure 7. Comparison of Linear Attenuation Coefficients. A comparison of linear attenuation coefficients for silicon nitride, Incoloy 909 metal, and Nioro braze material (82 w/o Au, 18 w/o Ni). Large differences in x-ray attenuation coefficients result in high contrast images which ease radiographic interpretation.

Microfocus x-ray imaging was used in the present study to examine silicon nitride-silicon nitride and silicon nitride-Incoloy brazed with Nioro. It was expected that images of the ceramic-ceramic braze could be used to detect varying degrees of the distribution of the braze material; however, the similar detectability that occurred in the ceramic-metal braze images

was unexpected. Fortunately, imaging was done at low accelerating potentials (60-120 kV), and the large difference between linear x-ray attenuation coefficients of the ceramic, metal, and braze material provided sufficient contrast. In particular, the 82% Au component of the Nioro braze material dominated the effect on contrast.

## MICROFOCUS RADIOGRAPHY OF CERAMIC-CERAMIC BRAZED SAMPLES

The microfocus x-ray images shown in Figure 8 are representative of NDE of one ceramic-ceramic brazing operation. In this case, rectangular silicon nitride bars with chamfered edges are viewed after Nioro brazing. The pictures are of processed real-time x-ray images made at approximately 10X magnification. The only image processing performed was frame averaging to reduce random noise. The accelerating potential was 65 kV. The bars were positioned with a slight rotation and tilt with respect to the image plane. In this orientation, a uniform distribution of braze material could be imaged as a complete rectangle of consistent brightness. The resultant high contrast image reveals varying degrees of distribution of the braze material. Such variations are a measure of the degree of wetting at temperature and potential for bonding.

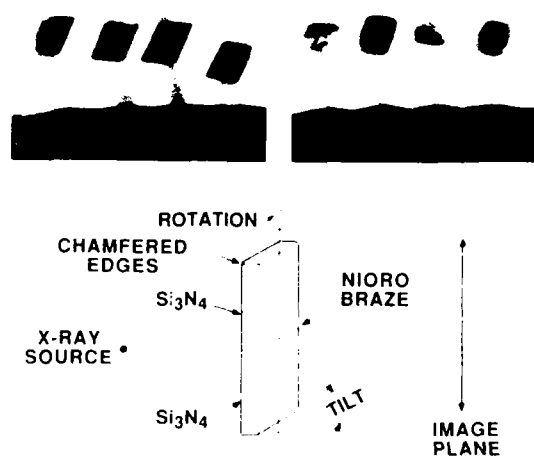


Figure 8. X-ray Image of Ceramic-Ceramic Brazed Samples. Silicon nitride bars with chamfered edges joined with the Nioro braze are viewed. The bars are positioned with a slight rotation and tilt with respect to the x-ray source and image plane. Varying degrees of distribution of the braze material are revealed.

<sup>2</sup> Incoloy is a trademark of Huntington Alloys, Inc., Huntington, West Virginia

<sup>3</sup> Nioro is a trademark of GTE Electrical Products, Belmont, California

<sup>4</sup> An exception occurs in the graph shown because of a K edge for Au at 80.9 keV

The microfocus radiographs shown in Figure 9 are representative of cylindrical and square brazed ceramic-ceramic samples that were used to study the effect of brazing parameters and substrate coatings on wettability. Samples were imaged in transmission, with the braze plane perpendicular to the direction of primary radiation. The total thickness of silicon nitride was approximately 20 mm. Variation in the distribution of braze material was still detectable.

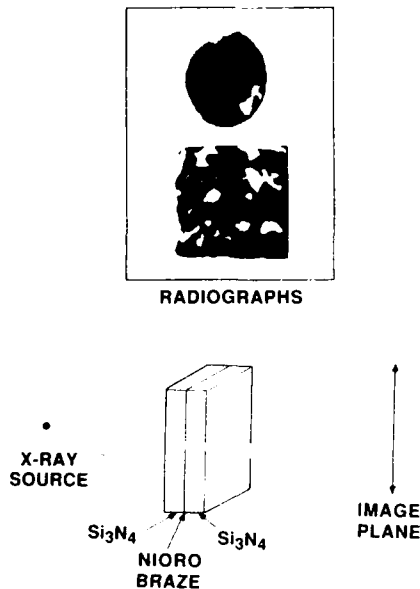


Figure 9. Through Transmission Radiographs of Ceramic-Ceramic Brazed Samples. Samples were imaged with the braze perpendicular to the direction of primary radiation. Nonuniform distribution of the braze material is discernible.

#### MICROFOCUS RADIOGRAPHY OF CERAMIC-CERAMIC BRAZED SAMPLES

An immediate requirement is the attachment of ceramic turbine rotors to metal shafts in automotive engines. A simplified illustration of a prototype ceramic-metal joint situated for imaging is shown in Figure 10. The joint can be viewed as a ring of metal brazed to a cylindrical ceramic rod. In this study, silicon nitride (SNW1000<sup>5</sup>) was joined to Incoloy 909 with a Nioro braze.

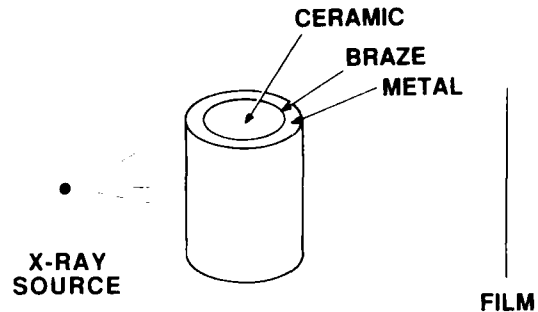


Figure 10. Prototype Ceramic-Metal Joint. The simplified illustration of a prototype ceramic-metal joint can be viewed as a ring of metal brazed to a cylindrical ceramic rod.

The in-process NDE test procedure is shown in Figure 11 for ceramic-metal joining process development. This approach was applied to samples under a variety of braze conditions (e.g., braze cycle time, quantity of braze material, etc.). The flow diagram illustrates the concept of in-process NDE, where x-ray images are obtained at each process step. In this way, the final condition of the specimen can be traced back to intermediate process steps. For instance, if a crack is detected in the ceramic after brazing, was it a result of brazing or was the crack present in the sample before brazing? Perhaps the most important feature of in-process NDE is that it simplifies interpretation of the final image.

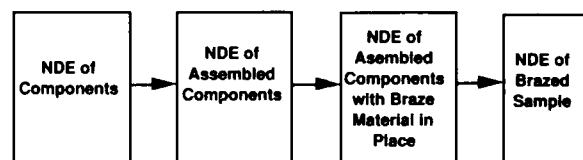


Figure 11. In-Process NDE Test Matrix. In-process NDE allows tracing the final condition of the sample to intermediate processing steps, simplifying interpretation of the image.

In-process NDE was used to inspect four mechanical shear test samples brazed over different braze cycle time intervals. Microfocus film radiography was used to take advantage of the superior contrast of the film compared to the real-time image intensifier. Gamma radiography with an IR-192 (radioactive isotope) source was also performed. For comparison, representative radiographs are shown in Figure 12.

<sup>5</sup>SNW1000-GTE Electrical Products, Belmont, California

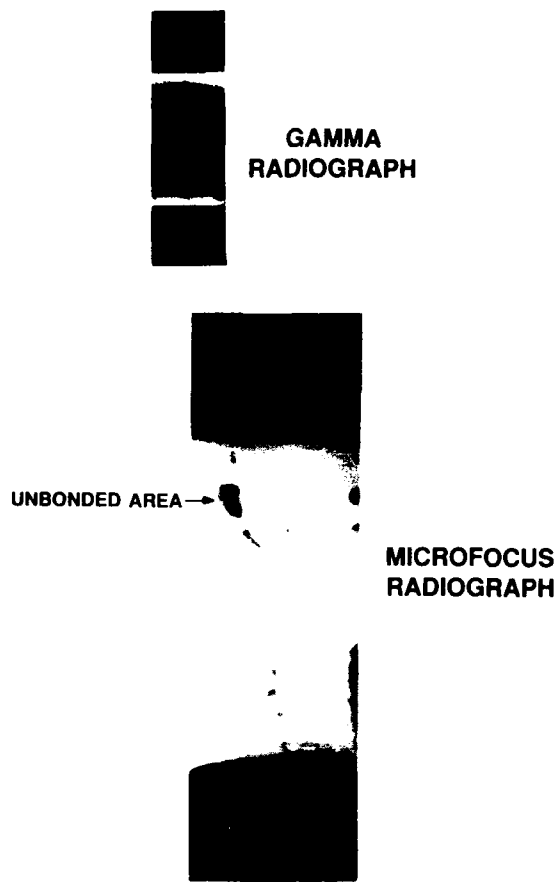


Figure 12. Radiographs of a Braze Specimen (a) from gamma rays, (b) from microfocus x-rays about 6X magnification. The microfocus radiographs showed superior contrast and resolution. The gamma radiographs had wider imaging latitude, and multiple samples could be viewed simultaneously.

The gamma radiographs exhibited wide imaging latitude, and several samples could be examined simultaneously without magnification. The microfocus radiographs showed superior contrast and resolution. Each sample was radiographed in two orientations (rotated 90°) so the entire braze could be studied. By comparing radiographs of the samples before and after joining, it was determined that one braze insert had incompletely melted. Unlike the other samples, the structure of the insert was still visible after brazing. This sample experienced the shortest braze cycle time. Varying degrees of distribution of the braze material were noted. The samples were mechanically tested by placing the braze joint in shear, and test results are given in Table 1.

Table 1  
Mechanical Property Measurements of Brazed Prototype  
Ceramic-Metal Joints

Sample No.	Shear Test		Comments
	MPa	Pounds/in <sup>2</sup>	
A	231	33,500	Substantial unbonded area
B	252+	36,500*	Unbonded area
C	252+	36,500*	No unbonded area visible
D	237	34,400	Ceramic cracks
			Incomplete melting

\* Denotes sample did not break. Test discontinued because of load cell limitation.

Correlation of the NDE results with mechanical performance was only partially possible. For example, the substantial unbonded area in Sample A, compared with the complete bonding in Sample C, was consistent with relative mechanical strength. Also, the incompletely melted braze insert resulted in visible unbonded area in Sample D and lower strength than Sample C. Comparisons between samples with significant unbonded areas such as A and B could not be used to accurately predict relative strength. Image processing algorithms capable of quantifying the braze distribution area are under development. At this point, the use of NDE to predict mechanical strength is qualitative.

## SUMMARY AND CONCLUSIONS

Reliability of defect detection was assessed by determining the lower-bound probability of detection of simulated voids in silicon nitride ceramics. Utilizing film radiography, detection of these irregularly shaped and randomly located voids was accomplished with a high degree of reliability, for example a POD of 92% was determined, with a confidence level of 95%, for voids at 1.2% thickness sensitivity. Real-time probability of detection was assessed in a baseline study which showed that POD levels are approaching the superior film results; however, further parametric studies of the influence of imaging variables on detection are required.

Studying the effects of process modifications with microfocus radiography has aided understanding of structural ceramic joining. Detection of varying degrees of the distribution of the braze material was possible for both ceramic-ceramic and ceramic-metal joints. Correlation of the NDE results with

mechanical performance was only partially possible. Samples with substantial differences in distribution of braze material had relative strengths consistent with NDE results; however, more subtle comparisons could not be made. The correlation of NDE results with mechanical performance should improve with advances in quantitative image analysis and expansion of the database on relevant testing.

## REFERENCES

1. G.Y. Baaklini, J.D. Kiser, and D.J. Roth, "Radiographic Detectability Limits for Seeded Voids in Sintered Silicon Carbide and Silicon Nitride," *Adv. Ceram. Mater.*, Vol. 1, No. 1 (1986).
2. D.J. Cotter and W.D. Koenigsberg, "Microfocus Radiography of High Performance Silicon Nitride Ceramics," *Proceedings of the Conference on Nondestructive Testing of High Performance Ceramics*, Boston, MA, Aug. 25-27, 1987, pp. 233-253, American Ceramic Society.
3. R.F. Packman, S.J. Klima, R.L. Davies, J. Malpani, J. Moyzis, W. Walker, B.G.W. Yee, and S.P. Johanson, "Reliability of Flaw Detection by Nondestructive Inspection," pp. 414-424, in *Metals Handbook*, Vol. II, 8th Ed., H.E. Boyer, ed., American Society for Metals, Metals Park, OH (1976).
4. K.E. Amin and T.P. Leo, "Radiographic Detectability Limits for Seeded Defects in Both Green and Densified Silicon Nitride," *Proceedings of the Conference on Nondestructive Testing of High Performance Ceramics*, Boston, MA, Aug. 25-27, 1987, pp. 222-232, American Ceramic Society.
5. E.P. Bertin and R.J. Longobucco, "Practical X-ray Contact Microradiography," *Scientific Instruments*, Vol. 6, No. 1, February 1961, pp. 1-3 (1961).
6. W.T. Sproull, *X-Rays in Practice*, McGraw-Hill, pp. 20-43 (1946).
7. P. McIntire, *Nondestructive Testing Handbook*, published by the American Society for Nondestructive Testing, Vol. 3, pp. 227-232 (1985).
8. R.L. Smith, "The Effect of Scattering on Contrast in Microfocus Projection X-Radiography," *Br. J. NDT*, pp. 236-239 (September 1980).
9. A. Macovski, *Medical Imaging*, Prentice-Hall, Inc. (1983).
10. P. Mengers, "Technological Advances in Computer Aided Real-Time X-Ray Image Processing," *Proc. Qualtest 3 Conf., Soc. for Manufact. Engineers* IQ84-672 (1984).
11. A.E. Pasto, J.T. Neil, and C.L. Quackenbush, "Microstructural Effects Influencing Strength of Silicon Nitride," *Proc. of Int. Conf. on Ultrastructure Processing of Ceramics, Glasses and Composites* (1983).
12. A.G. Evans, *Progress in Nitrogen Ceramics*, ed. by F.L. Riley, Marinus Nijhoff Publ., Boston, MA (1985).
13. A. Papoulis, *Probability, Random Variables, and Stochastic Processes*, 2nd Ed., McGraw-Hill (1985).
14. *Tables of the Cumulative Binomial Probability Distribution*, Harvard University Press (1955).
15. R.E. Loehman and A.P. Tomsia, *Ceramic Bulletin*, Vol. 67, No. 2, 1988.



## X-RAY BACKSCATTER IMAGING WITH A SPIRAL SCANNER

R. H. Bossi, J.L. Cline, K.D. Friddell  
Boeing Aerospace and Electronics  
P.O. Box 3999, M/S 87-60  
Seattle, WA 98124

### Abstract

X-ray backscatter imaging allows radiographic inspections to be performed with access to only one side of the object. A collimated beam of radiation striking an object will scatter X-rays by Compton scatter and X-ray fluorescence. A detector located on the source side of the part will measure the backscatter signal. By plotting signal strength as gray scale intensity vs. beam position on the object, an image of the object can be constructed. A novel approach to the motion of the collimated incident beam is a spiral scanner. The spiral scanner approach can image an area of an object without the synchronized motion of the object or detector, required by other backscatter imaging techniques. X-ray backscatter is particularly useful for flaw detection in light element materials such as composites. The ease of operation and the ability to operate non-contact from one side of an object make X-ray backscatter imaging of increasing interest to industrial inspection problems.

### 1. INTRODUCTION

Radiation scatter is present in all radiographic inspections. Normally it is a detriment to the image quality and actions are taken to reduce its effect or presence. However, the scattered radiation can be usefully employed as the measurement method itself. This can allow one-sided inspection of objects.

X-ray interaction with materials involves photoelectric effect, incoherent (or

Compton) scatter, coherent scatter and pair production. Pair production occurs at energies greater than 1.022 MeV. Coherent scatter (the photon does not change energy) is a relatively minor effect, although it can be significant at low energies and in precise measurement studies. At typical radiographic energy ranges of 50 keV to 1 MeV, photoelectric effect and Compton scatter are the predominate X-ray interaction modes. The photoelectric effect is an absorption, while the Compton effect is a scattering

mode in which the photon changes direction and loses energy. Compton scatter is predominate over most of the energy ranges used by radiographers. Figure 1 shows this effect in several materials. This explains why scatter control is important in radiography. Also, the photoelectric effect can give rise to X-ray fluorescent emission and this can add significantly to the scattered radiation signal.

Calculations of scatter performance using computer X-ray interaction codes, have shown that backscatter signal variations as a function of material thickness, atomic number, density and x-ray energy, are sufficient for imaging to be useful.<sup>(1)</sup> The fluorescence effect of high atomic number elements is a significant contributor to the signal and can be discriminated by X-ray beam energies set above and below the K edge. The sensitivity of backscatter relative to through transmission imaging is also favorable.<sup>(2,3)</sup>

## 2. IMAGING METHOD

A variety of techniques can be and have been used to obtain backscatter images in both medicine and industry.<sup>(1-27)</sup> A useful concept for field inspection is shown in figure 2. This system is based on a flying spot x-ray source using a spiral scan technique. In the flying spot approach, a pencil beam of radiation strikes the object and the total scatter from the interaction through the part is detected by a large area detector.

Figure 3 is a schematic diagram of the spiral scanner prototype system. The collimated X-ray beam which illuminates the test object is created by concentric collimating disks with slits which rotate

at the end of the collimation tube. One slit is radial and the second slit is a spiral. Figure 4 shows the two disks. As the spiral slit rotates, a collimated X-ray beam is swept along the direction of the radial slit. The beam is a spot that strikes the objects and X-rays are scattered back to a detector. Readings of signal strength at the detector as a function of the spiral slit location are recorded. By indexing the radial slit, another region is scanned. When a full circle of radial data has been obtained, it can be reformatted to create an image with the normal perspective. The detector is a large annular piece of scintillating plastic with photomultiplier tubes. The detector has an inner diameter of 15 inches and an outer diameter of 30 inches. A personal computer is used to control the scanning, acquire the digitized data and display the image.

The spiral scan approach has the advantage, over other techniques, of being self contained for all mechanical motions. The scanner is simply positioned in the front of the area to be scanned. Other backscatter imagers require synchronized motion of either the part or source/detector or a combination of motions.

The spiral scanner approach can also be used in other configurations.<sup>(28)</sup> The geometry can be reversed by placing the detector at the source location and observing an object that is emitting radiation of a type and spectra for which the detector is sensitive. Similarly the spiral scanner could be mounted in front of a large detector and used as a direct, collimated imaging system for through transmission radiography with minimal scattering components.

### 3. RESULTS

The prototype scanner has been tested on composite honeycomb panels. Figure 5 shows an image of a panel with water in the honeycomb. The X-ray source energy was about 80kVp at 5 mA. The Boeing letters are made of plastic. The hole at the center of the image is an image artifact of the spiral scanner device. Radial streaks in the image are due to x-ray machine current/voltage fluctuations. Typically the unit is operated with an approximate 2 feet source-to-disk distance and a 2 feet disk-to-object distance. With six inch diameter disks, the area of object scanned is about 12 inches.

The speed of the scanner is a function X-ray source strength, distances, slit size, disk speed and computer digitization rates. Disks with about 2 mm wide slits have been used. The computer digitization rate has been a limitation in scanning speed on the prototype system requiring the scanner to operate at scans of 12 to 20 minutes. The X-ray machine has also shown limitations. A high stability, high output device is desirable. An industrial optimized scanner based on the design tested here should be capable of obtaining scans in the range of 1 to 2 minutes.

### 4. CONCLUSIONS

X-ray backscatter imaging with a spiral scanner has been shown to be feasible. The device could be useful for one-sided field inspections of defects due to thickness, material, and/or density variations.

### 5. REFERENCE

1. Back scatter X-ray Imaging, R.H. Bossi, K.D. Friddell, J.M. Nelson., Materials Evaluation, Vol. 46, No. 11, October 1988.
2. J. Kosanetzky, G. Harding, K.H. Fischer, and A Meyer, "Comscan X-ray Imaging", Philips GmbH, Hamburg, W. Germany.
3. R.Bossi, J. Cline, K. Friddell, J. Nelson, "One Sided Radiographic Inspection Using Backscatter Imaging", Review of Progress Quantitative NDE, Vol. 8, D. O. Thompson, D. E. Chimenti, Eds., Plenum Press, 1989.
4. Karl-Hans Reiss and W. Schuster, "Quantitative Measurements of Lung Function in Children by Means of Compton Backscatter", Pediatric Radiology, Vol. 102, March, 1972.
5. Leon Kaufman, Gordon Gamsu, Charles Savoca, Sybil Swann, Louis Murphey, Bernard Hruska, David Palmer and John Ullman, "Measurement of Absolute Lung Density by Compton-scatter Densitometry", IEEE Transaction on Nuclear Science, Vol. NS-23, February, 1976.
6. P. G. Lale, "The Examination of Internal Tissues, using Gamma-ray Scatter with a Possible Extension to Megavoltage Radiography", Physics in Medicine and Biology, Vol. 4, 1959.
7. R. L. Clarke, E. N. C. Milne, and G. van Dyk, "The Use of Compton Scattered Gamma Rays for Tomography", Investigative Radiology, Vol. 11, 1976.

8. F. T. Farmer and Margaret P. Collins, "A New Approach to the Determination of Anatomical Cross-sections of the Body by Compton Scattering of Gamma-Rays", *Physics in Medicine and Biology*, Vol. 16, 1971.
9. F. T. Farmer and Margaret P. Collins, "A Further Appraisal of the Compton Scattering Method for Determining Anatomical Cross-sections of the Body", *Physics in Medicine and Biology*, Vol. 19, 1974.
10. Bruce C. Towe and Alan M. Jacobs, "X-ray Backscatter Imaging", *IEEE Transactions on Biomedical Engineering*, Vol. BME-26, September, 1981.
11. Bruce C. Towe and Alan M. Jacobs, "X-ray Compton Scatter Imaging Using a High Speed Flying Spot X-ray Tube", *IEEE Transactions on Biomedical Engineering*, Vol. BME-28, October, 1981.
12. J.J. Battista and M.J. Bronskill, "Compton-scatter Tissue Densitometry: Calculation of Single and Multiple Scatter Photon Fluences", *Physics in Medicine and Biology*, Vol. 23, No.1, 1978.
13. Peter R. Duke and James A. Hansen, "Compton Scatter Densitometry with Polychromatic Sources", *Medical Physics*, Vol. 11, No. 5, 1984.
14. Alan L. Huddleston and Jay P. Sacklerh, "The Determination of Electron Density by the Dual Energy Compton Scatter Method", *Medical Physics*, Vol. 12, No. 1, 1985.
15. G. Harding and R. Tischler, "Dual-energy Compton Scatter Tomography", *Physics in Medicine and Biology*, Vol. 31, May, 1986.
16. L. Brateman, A. M. Jacobs and L. T. Fitzgerald, "Compton Scatter Axial Tomography with X-rays: Scat-Cat", *Physics in Medicine and Biology*, Vol. 29, November, 1984.
17. S. Bukshpan, Dan Kedem and Drora Kedem, "Detection of Imperfections by Means of Narrow Beam Gamma Scattering", *Materials Evaluation*, Vol. 33, October, 1975.
18. G. A. Arkhipov, E. G. Golukov, B. L. Dvinyaninov, P. P. Zol'nikov, Yu. A. Kovyazin, and K. A. Sukhanova, "Using Scattered Gamma \*Radiation for Detecting subsurface defects in Metal", translated from *Defektoskopia*, No. 3, May-June, 1976.
19. B. Bridge, "A Theoretical Feasibility Study of the use of Compton Backscatter Gamma-Ray Tomography (CBGT) for Underwater Offshore NDT", *British Journal of NDT*, November, 1985.
20. D.G. Costello, J. A. Stokes, and A. P. Trippe, "Theory and Applications of Collimated Photon Scattering", 14th Symposium on Nondestructive Evaluation, San Antonio, TX, 1983.
21. G. Harding, "On the Sensitivity and Application Possibilities of a Novel Compton Scatter Imaging System", *IEEE Transactions on Nuclear Science*, Vol. NS-29, No.3, June 1982.

22. H. Strecker, "Scatter Imaging of Aluminum Castings Using an X-ray Fan Beam and a Pinhole Camera", Materials Evaluation, Vol. 40, September 1982.
23. H. Berger, Y. T Cheng, and E. L. Criscuolo, "High Sensitivity, One-Sided X-ray Inspection System", NSWC TR 85-292, July 1985.
24. S. Ashley, "Airport X-ray Spots Invisible Weapons", Popular Science, May 1986.
25. J. Stanely and J. Le Page, "Development of a Prototype Backscatter Tomography," AFWAL-TR-85-4140, Feb. 1986.
26. Marin Annic, Paul Bjorkholm and Richard Mastonardi, "ZT: A Tomographic Backscatter Technique for Nondestructive Evaluation", 16th Symposium on Nondestructive Evaluation, San Antonio, TX, April 1987.
27. N.K. Gupta, R.F. Rodenbaugh, M.D. Silver, and E.A. Sivers, "Backscatter Imaging Tomography with High Efficiency Detectors: Work in Progress", Review of Progress in Quantitative NDE, Williamsburg, VA, June 1987.
28. Ken Friddell, Boeing Invention Disclosures A-86-094, A-86-097.

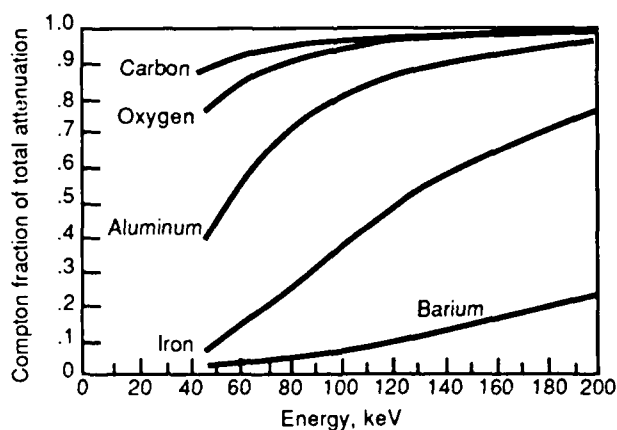


Figure 1. Fraction of Compton scatter in the total X-ray attenuation as a function of energy for selected elements.

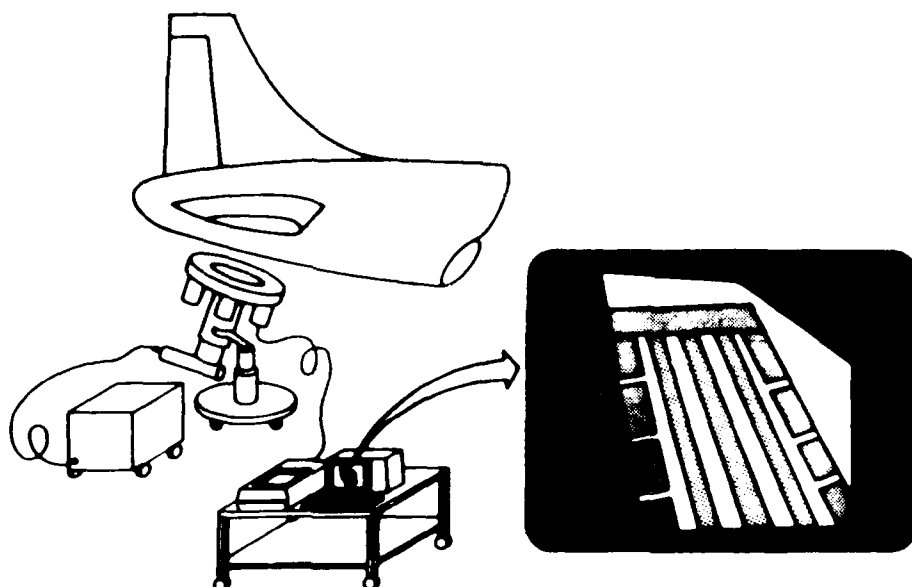


Figure 2. Field inspection concept for X-ray backscatter imager.

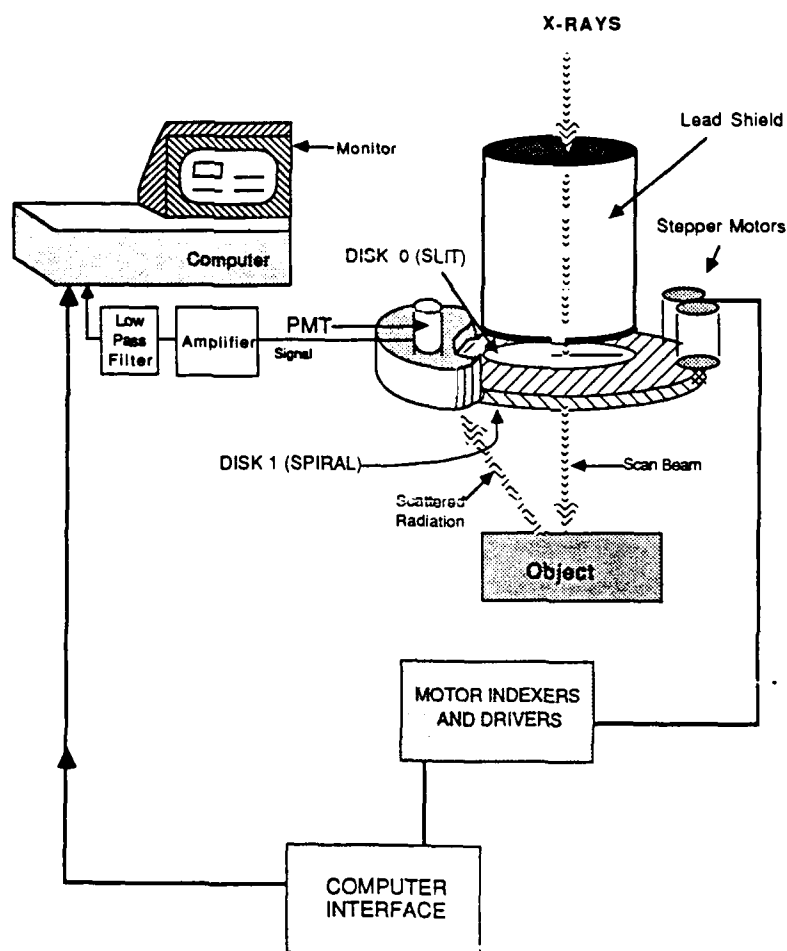
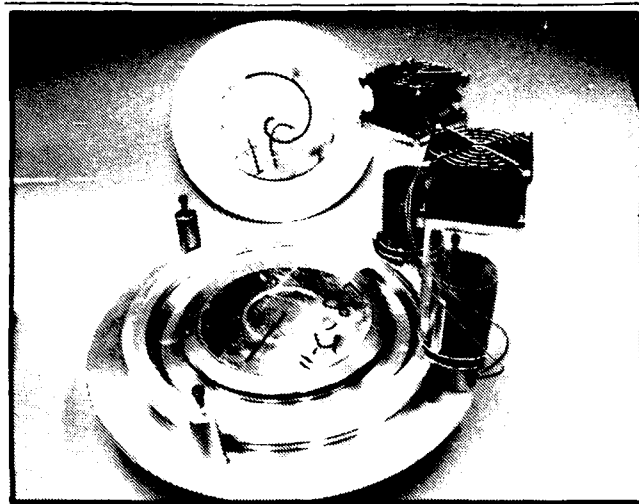
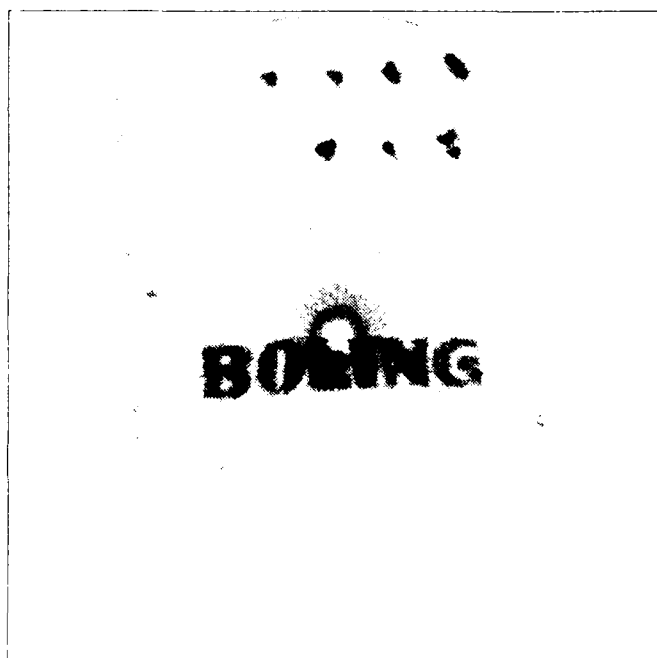


Figure 3. Schematic diagram of a prototype spiral scan imaging system.



*Figure 4. Spiral scan disks. One disk mounts above the other in the rotating mechanism.*



*Figure 5. Backscatter image of composite honeycomb containing water.*

ACOUSTOGRAPHY: ULTRASONIC IMAGING  
USING A SOUND-SENSITIVE PLATE/SCREEN

J.S. Sandhu and R.E. Thomas  
Santec Systems, Inc.  
Wheeling, Illinois 60090

Abstract

Many attempts have been made in the past to use a sound-sensitive plate/screen to produce ultrasonic images in a manner similar to Radiography and Fluoroscopy, but technical drawbacks such as poor screen sensitivity, limited dynamic range, long image-generation times and artifacts have kept this approach from becoming practical. We have used a sound-sensitive plate/screen based upon the "acousto-optical" properties of liquid crystals to generate ultrasound images. Screen sensitivities in the  $\mu\text{W}/\text{cm}^2$ , dynamic range of 15-20 dB and image-generation times of 5-10 seconds have allowed us to successfully image discontinuities in composite materials, currently gaining a widespread use in the aerospace and other industries. Image artifacts have been greatly reduced by making use of "partially incoherent" ultrasound to insonify the test specimens. This approach to ultrasonic imaging, which we have called Acoustography, offers some unique advantages over conventional ultrasonic methods including high inspection speeds, ability to inspect curved and complex geometry structures and real-time monitoring of specimens under service-simulating loads. This paper will discuss principles underlying the acoustographic process and its use as a nondestructive testing technique.

1. INTRODUCTION

In the past, many attempts have been made to produce ultrasonic images in a manner analogous to radiography, fluoroscopy or photography. Although reasonable images were produced by some researchers, the systems produced had

many technical drawbacks including poor screen sensitivity, limited screen dynamic range, long image generation times, and poor image quality due to artifacts<sup>1</sup>. These drawbacks have prevented the applicability of this approach to non-destructive testing of materials and



medical diagnosis.

In this paper, we report on the use of liquid crystal based sound-sensitive detector screen/plate<sup>2</sup> for generating full-field projection images with ultrasound. Screen sensitivity and dynamic range have been improved to allow nondestructive inspection of some real world composite structures. The image quality has been greatly improved by using "partially incoherent" sound to insonify specimens.

## 2. ACOUSTOGRAPHY

### 2.1 THE PROCESS

In acoustography, an ultrasonic source is placed on one side of a specimen and a detector screen on the other side in a medium that has low attenuation coefficient, e.g. water, Figure 1. In passing through the specimen, ultrasonic waves are differentially attenuated and cast a shadow image of the discontinuities. This image is converted into a visual image by the sound-sensitive detector screen/plate.

### 2.2 THE SOUND-SENSITIVE SCREEN/PLATE

The physical mechanism by which the sound-sensitive screen/plate converts the ultrasound into visual images is based upon the birefringent properties of the liquid crystal material contained in the screen. Initially, the liquid crystal molecules are parallel to each other, Figure 2. When the display is viewed under polarized light with crossed polarizer/analyzer, it shows a uniform dark field of view. When ultrasound interacts with the display, the orientation of the liquid crystal molecules changes. This reorientation

of the molecules is seen as a brightness change in the field of view. The amount of molecular reorientation, which determines the brightness level, depends upon the ultrasonic intensity. This allows the screen brightness to be modulated by ultrasonic intensity and allows ultrasonic images, which are intensity maps, to be converted into visual images.

The relation between ultrasonic intensity and brightness is expressed by an acousto-optical transfer curve, analogous to an H&D curve for radiographic film, and depends upon the design characteristics of the screen. Therefore, proper selection of screen characteristics is necessary to achieve optimum results.

### 2.3 THE SOUND SOURCE

The sound source employed in the acoustographic imaging process emits "partially incoherent" sound, so that interference artifacts can be minimized. The source can be designed to generate any sound frequency with collimated, converging or diverging beams. Proper choice of frequency and beam characteristics are necessary for optimum results.

## 3. NONDESTRUCTIVE TESTING

Acoustography was employed for detecting defects in graphite/epoxy composite laminates and to visualize ultrasonic fields of a transducer. The frequency of the sound source was approximately 3.5 MHz which was also the operational frequency of the sound-sensitive screen/plate. Since the specimens were all flat, a collimated beam was used for

insonification. The distance between the specimen and the screen was minimized to optimize image sharpness. Figure 3 shows the acousto-optical transfer of the screen employed in this work.

Figure 4a shows the acoustograph (image) of a woven graphite/epoxy composite. This specimen contained two circular inclusions with diameters of 0.375 in. (9.52 mm) and 0.625 in. (15.9 mm). The inclusions were 0.001 in. (0.025 mm) thick. The circular inclusions were easily detected along with the fibrous nature of the composites. The inclusions were measured from the acoustograph to be 0.346 in. (8.8 mm) and 0.692 in. (17.6 mm), which was well within our measurement errors. Figures 4b and 4c show acoustographs of braided graphite/epoxy composite laminates with 0.75in.x 0.75in. and 0.75in.x 0.25in. inclusions respectively.

Figure 5a shows the acoustograph of a 16-ply quasi-isotropic graphite/epoxy laminate. The specimen had been subjected to impact of 202 gram (0.44 lb) impactor from a height of 1.83 meters (72 in.). The damage is clearly delineated with acoustography along with the fibrous nature of the specimen. Figure 5b shows the acoustograph of a woven graphite epoxy specimen subjected to impact of a 2 lb. hammer blow.

Figure 6 shows the ultrasonic intensity distribution of a 3.5 MHz piezo-electric transducer (unfocussed) in the near-field zone. The fields were generated by placing the transducer at various distances from the screen. The positions of maxima and minima along the transducer radiation axis coincided with their calculated values.

#### 4. CONCLUSIONS

The formation of full-field projection images analogous to radiography and fluoroscopy is demonstrated. A sound-sensitive screen, which is analogous to a fluoroscopic screen, is used to visualize the images. The possibility of using this method for the non-destructive inspection of composites is demonstrated by insonifying the specimens with partially incoherent ultrasound.

#### 5. REFERENCES

1. H. Berger, J. Acoust. soc. Amer. 45, no. 4, 859-867, 1969.
2. J.S. Sandhu, U.S. Patent 4 379 408 Apr. 12, 1983.
3. J.S. Sandhu, U.S. Patent 4 651 567 March, 1987.

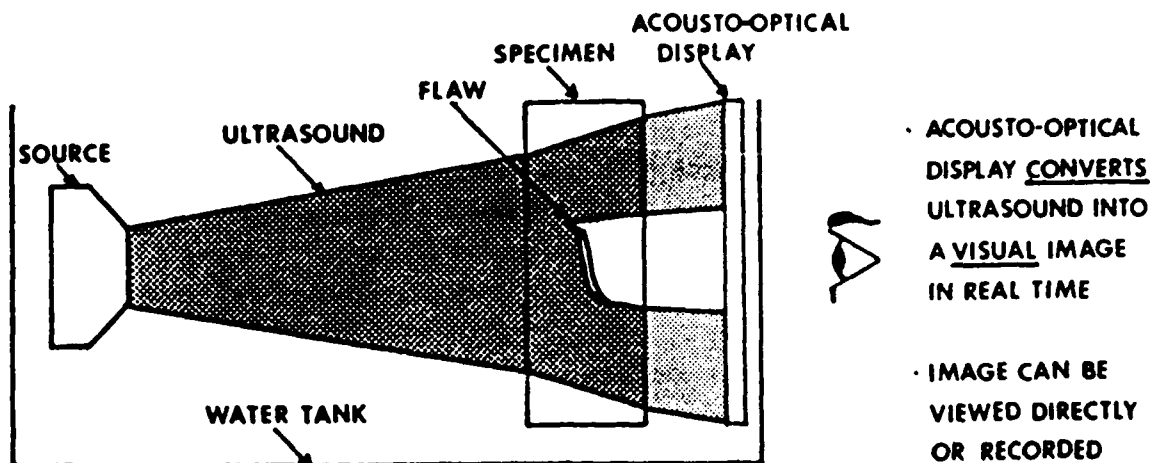


FIGURE 1 - THE ACOUSTOGRAPHIC IMAGING PROCESS

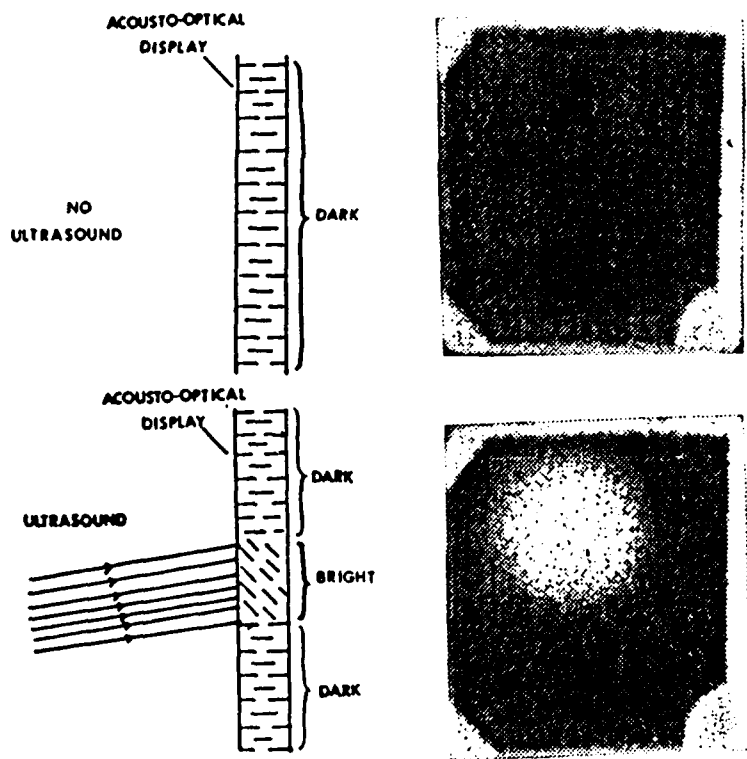


FIGURE 2 - PHYSICAL MECHANISM BY WHICH SOUND-SENSITIVE SCREEN CONVERTS ULTRASOUND INTO VISUAL IMAGES

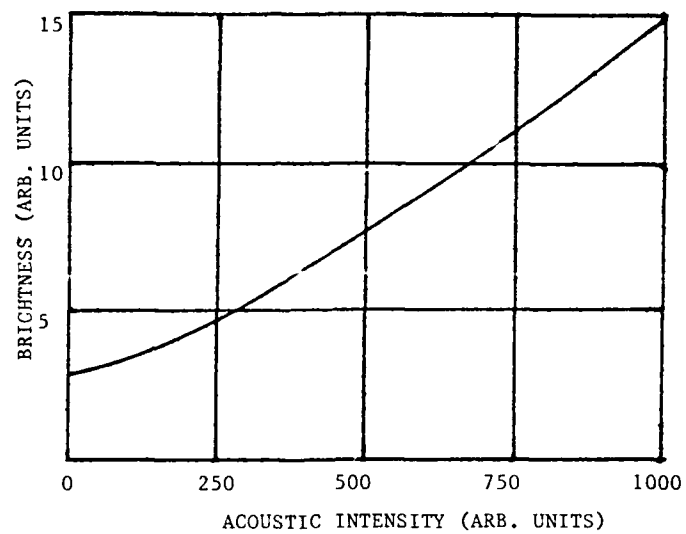


FIGURE 3 - ACOUSTO-OPTICAL TRANSFER CURVE OF THE SCREEN



FIGURE 4 - ACOUSTOGRAPHS OF GRAPHITE/EPOXY COMPOSITES CONTAINING INCLUSIONS (a) WOVEN SPECIMEN, (b) & (c) BRAIDED SPECIMENS

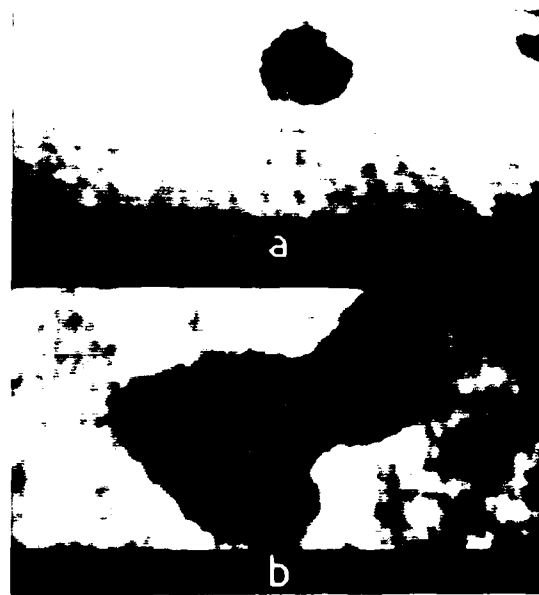


FIGURE 5 - ACOUSTOGRAPHS OF GRAPHITE/EPOXY COMPOSITES CONTAINING IMPACT DAMAGE  
(a) IMPACTOR CASE (b) HAMMER CASE

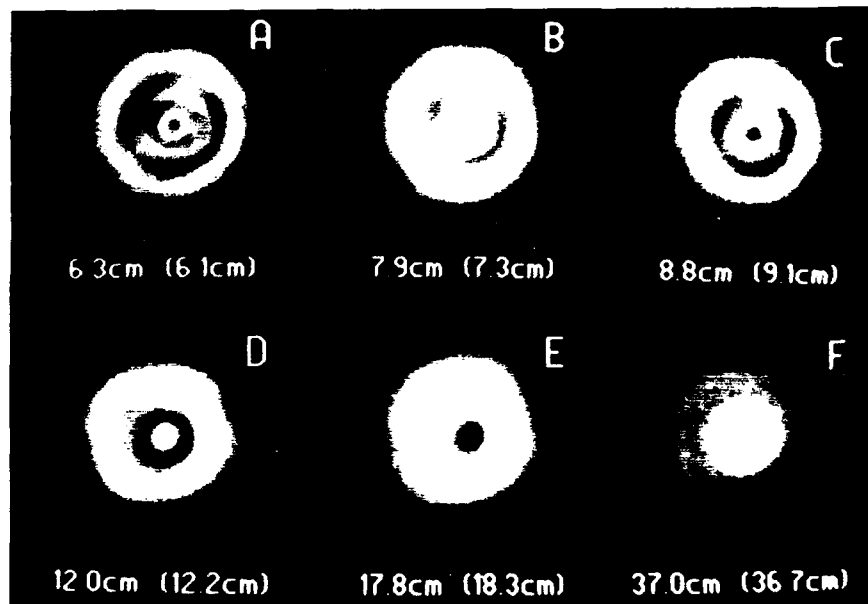


FIGURE 6 - ULTRASONIC FIELD INTENSITIES OF THE 3.5 MHz TRANSDUCER IN THE NEAR-FIELD ZONE, (---) INDICATES THEORETICALLY CALCULATED VALUE OF THE MAXIMA AND MINIMA ALONG RADIATION AXIS

# ULTRASONIC NDE OF THIN (SUB-WAVELENGTH) SPECIMENS

V.K. Kinra  
Department of Aerospace Engineering  
Texas A&M University  
College Station, Texas 77843

and

V. Dayal  
Department of Aerospace Engineering  
Iowa State University  
Ames, IA 50011

## ABSTRACT

The classical methods of ultrasonic inspection break down when the thickness of the specimen becomes comparable to the wavelength. By combining elementary theory of Fourier Transforms and conventional ultrasonics hardware, we have developed a new technique for measuring the phase velocity, group velocity, and attenuation in ultra-thin (submillimeter or subwavelength) specimens. The technique is equally effective for thin or thick specimens, for dispersive or non-dispersive media and for elastic or viscoelastic materials.

## LIST OF SYMBOLS

$F^*(\omega), G^*(\omega)$	fourier transform of $f(t), g(t)$	$k_0$	wavenumber in water, real, $\text{mm}^{-1}$
$R_{ij}$	Reflection coefficient in medium $i$ from medium $j$	$k_1$	$\omega/c$ , wavenumber in specimen, $\text{mm}^{-1}$
$T_{ij}$	Transmission coefficient for a wave incident in medium $i$ and transmitted into medium $j$	$k_2$	attenuation coefficient, nepers/mm
$a$	a characteristic length; half crack length or particle radius, mm	$t$	time, $\mu\text{s}$
$c, c_1$	longitudinal phase velocity in specimen, $\text{mm}/\mu\text{s}$	$u$	particle displacement
$c_0$	longitudinal phase velocity of wave in water, $\text{mm}/\mu\text{s}$	$x$	distance
$c_g$	group velocity in specimen, $\text{mm}/\mu\text{s}$	$\alpha$	normalized frequency, $2\pi fa/c_1$
$f$	frequency, MHz	$\lambda$	wavelength, mm
$h$	plate thickness, mm	$\xi$	normalized wavenumber, $2\pi fa/\langle c_1 \rangle$
$k$	complex wavenumber = $k_1 + ik_2$ , $\text{mm}^{-1}$	$\rho_0, \rho$	density of water, specimen, $\text{g/ml}$
		$\omega$	circular frequency, $\text{rad}/\mu\text{s}$
		$\langle \rangle$	aggregate property of a composite

## 1. INTRODUCTION

The classical method of measuring the speed of sound is the time-of-flight method<sup>(1)</sup>. This requires specimens which are at least five-wavelength thick, i.e. for steel, at one MHz, at least 30 mm thick, for example. The advent of high strength composites implies use of thin panels: many applications of graphite/epoxy and metal-matrix composites require thickness less than one mm. All of the existing techniques break down in this situation because the front-surface and the back-surface reflections cannot be separated. By combining elementary theory of Fourier transforms with conventional ultrasonics, we have developed a new technique of measuring phase velocity, group velocity, and attenuation of a sub-wavelength, sub-millimeter viscoelastic specimen. The classical methods use the amplitude information. Our method exploits the phase information (in addition to the amplitude information) in the the Fourier domain. Up to an extent, as the thickness decreases, the efficacy of our technique increases. We will illustrate the use of this technique on three distinctly disparate materials: aluminum (non-dispersive, non-attenuative), epoxy (non-dispersive, weakly attenuative), a particulate composite (highly dispersive, highly attenuative). Finally, we will demonstrate the use of this technique for monitoring the growth of transverse cracks in graphite fiber reinforced composite materials.

## 2. THEORY

Consider an infinite elastic plate immersed in an elastic fluid (water). A Lagrangian diagram indicating the space-time location of a wavefront which occupied the position  $x=0$  at time  $t=0$  is shown in Fig. 1. A plane-fronted finite-duration pulse, Ray 1, is normally incident on the plate. This results in an infinite series of reflected and transmitted pulses.

Let the displacement in the incident field be given by

$$u^{inc} = f_0(\omega t - k_0 x) \quad (1)$$

where  $f_0(s) \equiv 0$  for  $s < 0$ ,  $\omega$  is the circular frequency,  $k_0$  is the wavenumber in water and  $c_0 = \omega/k_0$ . The entire reflected field,  $u^r = u^2 + u^6 + u^{10} + \dots$ , may be written as

$$u^r = R_{12} f_0(s-s_2) + T_{12} R_{21} T_{21} \sum_{m=1}^{\infty} R_{21}^{m-1} f_0(s-s_{4m+2}) \quad (2)$$

where  $s_{4m+2} = 2 k_0 a + m 2kh$ ,

$$R_{12} = \frac{\rho_0 c_0 - \rho c}{\rho_0 c_0 + \rho c} = -R_{21},$$

$$T_{12} = \frac{2\rho_0 c_0}{\rho_0 c_0 + \rho c} = 2 - T_{21}.$$

In an exactly analogous manner, one can write down the expressions for the total transmitted field as

$$u^t = T_{12} T_{21} \sum_{m=0}^{\infty} R_{21}^{2m} f_0(s-s_{4(m+1)}) \quad (3)$$

where  $s_{4(m+1)} = h [(2m+1)k - k_0]$

In eqs (2) and (3)  $m$  is the number of complete round trips taken by the wave across the plate thickness  $h$ .

In this paper the qualifiers "thick," "moderately thick" and "thin" are used in the following sense. When toneburst which are ten cycles long can be separated in the time-domain, the specimen is considered "thick"; when short duration pulses can be separated, the specimen is considered moderately thick; when even the short-duration pulses cannot be separated, the specimen is considered "thin". However, the duration (or length) of the pulse depends on the center-frequency of the transducer. Hence, with reference to the

absolute dimensions of the specimen the use of the word "thick" is quite arbitrary. On the other hand the word "thick" is not arbitrary with respect to the wavelength i.e. a specimen is "thick" if, approximately,  $h > 5\lambda$ , "moderately thick" if  $3\lambda < h < 5\lambda$ , and "thin" if  $h < 3\lambda$ .

## 2.1 ANALYSIS FOR MODERATELY THICK SPECIMENS

In an effort to fill the gap between "thick" and "thin" specimens we first consider the case of a "moderately thick" specimen such that short-duration pulses in Fig. 1 can be clearly separated from each other in the time-domain. Let  $f(t)$  be the signal corresponding to ray 2 and  $g(t)$  be the combined signal corresponding to rays 2 and 6 as sensed by a transducer at  $x=0$ . (This is the so-called pulse-echo mode). Then

$$f(t) = R_{12} f_0(\omega t - 2k_0 a) \quad (4)$$

and

$$g(t) = f(t) + T_{12} R_{21} T_{21} f_0(\omega t - 2k_0 a - 2kh). \quad (5)$$

The Fourier transform of a function  $f(t)$  is defined as

$$F^*(\omega) = \frac{1}{\sqrt{2\pi}} \int_{-\infty}^{\infty} f(t) e^{i\omega t} dt, \quad -\infty < \omega < \infty \quad (6)$$

with the associated inverse transform given by,

$$f(t) = \frac{1}{\sqrt{2\pi}} \int_{-\infty}^{\infty} F^*(\omega) e^{-i\omega t} d\omega \quad (7)$$

Let  $F^*(\omega)$ ,  $G^*(\omega)$  and  $F_0^*(\omega)$  be the Fourier transforms of  $f(t)$ ,  $g(t)$  and  $f_0(t)$ , respectively. Then, a straightforward application of the shifting theorem for Fourier transforms yield

$$\frac{G^*(\omega)}{F^*(\omega)} = 1 - T_{12} T_{21} e^{i2kh} \quad (8)$$

The key term in eq (8) is  $e^{i2kh}$  or  $e^{i2h\omega/c}$ . Thus, in eq (8) if one plots  $|G^*(\omega)|$  vs  $\omega$  it will be characterized by a series of resonance peaks whose spacing is given by  $\Delta(2h\omega/c) = 2\pi$ , or in view of  $\omega = 2\pi f$

$$c = 2h \Delta f \quad (9)$$

Measurement of  $c$  in aluminum using eq (9) is illustrated in Fig. 2. Here  $F(\omega) = |F^*(\omega)|$  and  $G(\omega) = |G^*(\omega)|$ . Note that  $G(\omega)$  consists of the transducer response,  $F(\omega)$ , superimposed by an oscillation due to  $e^{-i2h\omega/c}$  term. A further improvement in the measurement method can be achieved by plotting  $|G^*(\omega)/F^*(\omega) - 1|$ . This is illustrated in Fig. 3. By taking out the shape of the transducer response we are left with oscillations due to the constructive and destructive interference between the front-surface (ray 2) and back-surface reflections (ray 6).

Although eq. (8) was derived on the assumption that the specimen behaves in an elastic manner, it can be readily shown by a straightforward application of the Correspondence Principle [17] that eq. (8) is rigorously valid even for linear viscoelastic materials. Eq. (8) yields the complex-valued wavenumber  $k = k_1 + ik_2$ , the phase velocity is given by  $c = \omega/k_1$ , and  $k_2$  is the attenuation in nepers/mm. Now consider the transmitted field for a moderately thick specimen. Two measurements are made. In the first, the specimen is removed from the water path i.e. the wave travels solely through water. Let the receiving transducer be located at some  $x = l > b$ . Then  $u^{inc}(l, t) \equiv f(t) = f_0(\omega t - k_0 l)$ . The specimen is now inserted in the wavepath and the signal due to ray 4 alone is recorded. Thus,

$$g(t) = u^4(l, t) = T_{12} T_{21} f_0(\omega t - k_0 l - 2k_0 a - kh).$$



Then,

$$\frac{G^*(\omega)}{F^*(\omega)} = T_{12} T_{21} e^{-i(kh+k_0 n)} \quad (10)$$

which is the desired equation for the complex-valued wavenumber  $k$ .

In the following, for brevity, this method will be referred to as the Separable-Pulse method.

## 2.2 ANALYSIS FOR THIN SPECIMENS

The total reflected field comprising rays 2, 6, 10, 14 .....  $\infty$  at  $x=0$  may be found from eq (2).

$$g(t) = u^r(0, t) = R_{12} f_0(\omega t - 2k_0 a) + T_{12} R_{21} T_{21} \sum_{m=1}^{\infty} R_{21}^{2(m-1)} f_0(\omega t - 2k_0 a - m 2kh) \quad (11)$$

Let the front surface reflection be labeled  $f(t)$ , then

$$f(t) = R_{12} f_0(\omega t - 2k_0 a)$$

Let  $Z = R_{21}^2 e^{i2kh}$  then  $|Z| < 1$ , and

$$\frac{G^*}{F^*} - 1 = \frac{T_{12} T_{21}}{R_{12} R_{21}} \sum_{m=1}^{\infty} Z^m \quad (12)$$

Observing that for  $|Z| < 1$ ,  $(1-Z)^{-1} = 1+Z+Z^2 + \dots \infty$ , and defining

$$\beta = \frac{R_{12} R_{21}}{T_{12} T_{21}} \left( \frac{G^*(\omega)}{F^*(\omega)} - 1 \right) \quad \text{we get} \quad Z = \frac{\beta}{1+\beta} \quad (13)$$

From  $Z$  one can readily calculate the complex-valued wavenumber  $k(\omega)$ .

We now consider the transmitted field. Here a second transducer is used as a receiver at some  $x = l > b$ . To obtain a reference signal the specimen is removed and the signal through water is recorded.

$$f(t) = u^{inc}(l, t) = f_0(\omega t - k_0 l)$$

Let  $g(t)$  be the total transmitted field, rays 4, 8, 12, ...  $\infty$  then from eq. (3)

$$g(t) = T_{12} T_{21} \sum_{m=0}^{\infty} R_{21}^{2m} f_0[\omega t - k_0 l - h\{(2m+1)k - k_0\}] \quad (14)$$

$$\frac{G^*(\omega)}{F^*(\omega)} = \frac{T_{12} T_{21} e^{ih(k-k_0)}}{1 - R_{21}^2 e^{i2kh}} \quad (15)$$

In the following, these methods will be referred to as the Non-Separable-Pulse methods.

Finally, it is noted that the theoretical procedures developed in this section are equally valid for both the longitudinal as well as the shear disturbances.

## 3. EXPERIMENTAL PROCEDURES

A schematic of the apparatus is shown in Fig. 4. The heart of the system is a pair of accurately-matched, broad-band, water-immersion, piezoelectric transducers. An experiment is initiated at time  $t=0$  by a triggering pulse produced by a pulser/receiver; the pulse is used to trigger a digitizing oscilloscope; simultaneously the pulser/receiver produces a short-duration (about 100 ns) large-amplitude (about 200 volts) spike which is applied to the transmitting transducer. In the reflection mode it also acts as a receiver. The received signal is post-amplified (to about one volt) and then digitized with maximum sampling rate of 100 MHz (or 10 nanoseconds per point). To reduce the ubiquitous random errors, each measurement is averaged over a sample size of 64. A laboratory computer controls all operations of the digital oscilloscope through an IEEE bus. The built-in signal processor of the oscilloscope performs FFT on the acquired signals and the relevant parts of the data are then transferred to the computer for further analysis.

#### 4. RESULTS AND DISCUSSIONS

The experimental procedures developed during the course of this investigation were used to interrogate three rather disparate materials:

- (1) Non-dispersive, non-attenuative (elastic)
- (2) Non-dispersive, weakly-attenuative (linear viscoelastic)
- (3) Highly-dispersive, highly-attenuative

In the following the results are presented in the same order.

##### 4.1 NDE OF A NON-DISPERSIVE MATERIAL

The main objective of this work is to develop techniques suitable for very thin specimens. Therefore, we subjected our techniques to the following critical test. A thick aluminum plate ( $2.807 \pm 0.0025$  mm) was first tested using the conventional toneburst method. Then the thickness was gradually machined down to 0.258 mm (about 10 mil, a very thin foil) in five steps. In non-dimensional terms the thickness was reduced from about 4.4 to 0.4 wavelengths; a frequency of 10 MHz was used. At each step  $c$  was measured. We could have used five different samples. Instead we adopted the foregoing procedure in order to ensure that we are always testing exactly the same material. The density was measured by the Archimedes principle. Our estimate of the error in density is  $\pm 0.015\%$ . The results are presented in Table 1. The first measurement was made using the conventional toneburst method<sup>(8,9)</sup>. The time-domain signal is shown in Fig. 5(a). A particular peak (say the fourth peak) near the center of the toneburst is selected as the reference peak. The twice-transit-time,  $2h/c$  could be measured to an accuracy of 1 ns. Our estimate of error in the phase velocity is 0.1%. In the second measurement the toneburst was reduced to about one cycle; see Fig. 5(b). Note that the pulses can be clearly separated. The Separable-Pulse method, eq (8) was used to

analyze this data. Since only the first two pulses are needed for data analysis, the remaining pulses are electronically gated out or nulled. In the third measurement, the data analysed remains the same i.e. Fig. 5(b). However, the Non-Separable Pulse method, eq (15), is used. In other words,  $g(t)$  is now viewed as the sum of all transmissions. For the remaining measurements the specimen was gradually machined down. Non-Separable Pulse method was used to analyze the data. The pulses for  $h=1.686$  mm are shown in Fig. 5(c). Note that the conventional toneburst method can no longer be used; though both methods developed in this work can be used, we used the Non-Separable-Pulse method. The pulse for the next three thicknesses,  $h=1.001$ , 0.613 and 0.258 mm are shown in Figs. 5d, 5e, 5f, respectively. Because of the reduced thickness the pulses cannot be separated in the time domain. Therefore, even the Separable-Pulse method cannot be used; here we have to use the Non-Separable-Pulse method. For the thinnest specimen the round trip time is only 82 ns; the pulse duration is roughly 200 ns. This gives rise to what appears to be "ringing" in Fig. 5f.

With reference to Table 1, the average of all the measurements is  $6.342 \text{ mm}/\mu\text{s} \pm 0.25\%$ . We conclude that the Non-Separable-Pulse method developed for ultra-thin (sub-wavelength) specimens and the Separable-Pulse method for moderately thin (about one wavelength) specimens yield results which agree to 0.25% with the conventional toneburst method. (We hesitate to make absolute claims on accuracy because for the given piece of aluminum we do not know the true value of the phase velocity).

##### 4.2 NDE OF A NON-DISPERSIVE, WEAKLY-ATTENUATIVE MATERIAL

Next, we tested our experimental method on a medium which is non-dispersive but attenuative. An epoxy (EPON 8282) was

selected for this purpose. The results are presented in Table 2. Note that three frequencies, spanning nearly a decade, were used. The phase velocity measured by the toneburst method on a thick specimen is 2.915 mm/ $\mu$ sec and agrees very well with that measured with the Non-Separable-Pulse method.

#### 4.3 NDE OF A HIGHLY-ATTENUATIVE, HIGHLY-DISPERSIVE MATERIAL

Finally, we applied the new technique to a material which is simultaneously highly dispersive as well as highly attenuative, namely, a random particulate composite consisting of lead spheres in an epoxy matrix. These composites have been described in (12,13). Transducers with 0.25 MHz center-frequency were employed. Separable-Pulse method in through-transmission mode, eq (10), was used. In Fig. 6  $F^*(\omega)$  is the received signal with the specimen removed while  $G^*(\omega)$  is the signal with the specimen in place;  $\bar{c}$  is the volume fraction of inclusions. The dip in the amplitude of  $G^*(\omega)$  corresponds to the cut-off frequency. The present measurement,  $f_c = 0.21$  MHz, agrees quite well with the earlier measurement<sup>(12)</sup> using the conventional toneburst method. We now introduce a normalized frequency  $\Omega \equiv k_1 a = 2\pi f a / c_1$  and a normalized wavenumber  $\xi \equiv \langle k_1 \rangle a = 2\pi f a / \langle c_1 \rangle$  where  $\langle \rangle$  refers to an aggregate property of the composite. Fig. 7 shows the frequency vs wavenumber plot. As expected<sup>(12)</sup>, along the (lower) acoustical branch at low frequencies the behavior is non-dispersive; a straight line fitted through the data points passes through the origin ( $\langle c_1 \rangle / c_1 = \Omega / \xi$ ). Same was noted at high frequencies along the (higher) optical branch. These two observations serve as critical checks on the accuracy of our measurement. The normalized phase velocity is given by the slope of the secant,  $\langle c_1 \rangle / c_1 = \Omega / \xi$ , and the group velocity is given by the slope of the tangent,  $\langle c_g \rangle / c_1 = d\Omega / d\xi$ . The discrete

toneburst data from the earlier work<sup>(12-14)</sup> is also plotted; the agreement is considered quite satisfactory. The present technique is tremendously faster; the entire dispersion and attenuation curve is produced in a single experiment. Another major advantage of this method is as follows. When one uses the toneburst method, each point suffers a scatter due to random errors; see Fig. 7. In the present method the whole curve may shift up or down but the shape of the curve will not be altered by the random errors. Fig. 8 shows the normalized phase velocity versus frequency. The arrow labeled HASHIN is the velocity calculated from the lower (appropriate) static bound due to Hashin and Shtrikman<sup>15</sup>. The agreement between the theory and the low-frequency results is considered quite satisfactory. As  $\Omega$  increases the effective inertia of the lead spheres ( $\sim \rho \omega^2$ ) increases and the phase velocity decreases. At very high frequencies (it is conjectured) the inertia becomes so large that the spheres become essentially motionless. Thus they no longer contribute to the inertia of the composite as perceived by the effective wave. Hence the velocity increases dramatically across the cut-off frequency and becomes frequency-independent at very high frequencies. Fig. 8b shows the group velocity i.e. the speed with which energy flows in a composite. As expected, the group velocity is essentially constant at low and high frequencies; around the cut-off frequency,  $\Omega_c$ , it undergoes large fluctuations. Theoretically,  $c_g \rightarrow \infty$  at two points around the cut-off frequency. Perhaps the most interesting feature is that the group velocity becomes negative around  $\Omega_c$ , i.e. as the wave propagates in the positive x-direction, the energy flows in the negative x-direction. In Fig. 7 this corresponds to those points on the curve where the slope is negative.

In Fig. 9 we have plotted attenuation versus frequency. The peak in the curve defines the

cut-off frequency. For comparison  $k_2\lambda$  for the neat epoxy alone is 0.13 which is negligibly small compared to the peak attenuation. Thus all of  $k_2\lambda$  may be attributed to the scattering effects.

#### 4.4 NDE OF DAMAGE IN COMPOSITE MATERIALS

We now demonstrate the application of our technique to fiber-reinforced composite materials. Graphite/Epoxy AS4/3502 crossply  $[0_6/90_4/0_2]_s$  laminates were tested. These were subjected to monotonic tensile loading. As a result transverse cracks develop. Edge replication was made to obtain a record of the transverse cracks. The loading was interrupted at several points along the load axis, the coupon was subjected to an ultrasonic examination and the loading was resumed. The Separable-Pulse method in the reflection mode, eq (8), was used. In Fig. 10 we have also shown the portion of the edge replication which is insonified by the ultrasonic beam. The number of cracks seen by the beam is also listed. Note that we have not plotted the attenuation  $k_2\lambda$  but rather the changes in  $k_2\lambda$  caused by this damage. To guard against fortuitous results, three different frequencies were used, namely, 2.25, 5.00 and 7.50 MHz. We note that attenuation changes quite significantly and monotonically with the number of transverse cracks. We also note that in the range of frequency tested, the attenuation decreases with frequency. This may be attributed to the fact that these experiments were conducted at very high values of the wavenumber:  $k_1a=1.23$ , 2.70 and 4.02 ( $a$  is the half crack length) at 2.25, 5.00 and 7.50 MHz, respectively. Fig. 11 shows the longitudinal phase velocity at the same three frequencies. Within the errors of measurement,  $\pm 0.1\%$ , the phase velocity remains constant with damage. This is not at all surprising, in view of the fact that here the wave-vector (or the particle displacement vector) is parallel to the crack face i.e. the crack-wave interaction is very weak. Thus we

conclude that for the present case while the attenuation is sensitive to the presence of transverse cracks, velocity is not. Here we have presented just one example of the application of the new technique to ultrasonic NDE of fiber-reinforced composites. A detailed investigation of the problem has been carried out and the interested reader is referred to a follow-up paper [16].

#### 5. CONCLUSIONS

We have described a new experimental technique which can be used to measure phase velocity and attenuation of ultrasonic waves in very thin plates (down to a thickness which is one order of magnitude smaller than the wavelength). We emphasize that in the development of this technique we have taken a "black-box" approach i.e. it would work for any material so long as it behaves in a linear viscoelastic material and the attenuation is not large.

#### 6. ACKNOWLEDGEMENTS

This research was supported by the Air Force Office of Scientific Research Contract No. F49620-83-C-0067 to Texas A&M University. Thanks are due to Connie Rice for a careful preparation of the manuscript.

#### REFERENCES

1. T.R. Tauchert, and A.M. Guzelsu., "An Experimental Study of Dispersion of Stress Waves in a Fiber-Reinforced Composite," ASME Journal of Applied Mechanics, 39, 98-102 (1972).
2. H. Kolsky, "Stress Waves in Solids," DOVER (1953).
3. F.H. Chang, J.C. Couchman, and B.G.W. Yee, "Ultrasonic Resonance Measurements of Sound Velocity in Thin Composite Laminates," J. Comp. Matl. 8, 356-363 (Oct. 1974).
4. J.S. Heyman, "Phase Insensitive Acoustoelectric Transducer," J. Acoust. Soc. Am., 64(1), 243-249 (July 1968).

5. J.D. Achenbach, "Wave Propagation in Elastic Solids," North-Holland Publishing Company (1973).
6. H. Kolsky, "The Propagation of Stress Pulses in Viscoelastic Solids" The Philosophical Magazine, 8(1), 693 (Aug. 1956).
7. E.O. Brigham, "The Fast Fourier Transform," Prentice Hall (1974).
8. V.K. Kinra, M.S. Petraitis, and S.K. Datta "Ultrasonic Wave Propagation in a Random Particulate Composite," Int. J. Solids Structures, 16, 301-312 (1980).
9. V.K. Kinra, and A. Anand, "Wave Propagation in a Random Particulate Composite at Long and Short Wavelength," Int. J. Solids Structures, 18(5), 367-380 (1982).
10. V.K. Kinra, and E.L. Ker, "Effective Elastic Moduli of a Thin-Walled Glass Microsphere/PMMA Composite," J.Comp. Matl, 16, 117-188 (Mar. 1982).
11. A. Wolfenden, M.R. Harmouche, G.V. Blessing, Y.T. Chen, P. Terranova, V. Dayal, V.K. Kinra, J.W. Lemmens, R. Phillips, J.S. Smith P. Mahmoodi, and R.J. Wann, "Dynamic Young's Modulus Measurements in Nickel-Based Alloys: Six Methods," J. Testing Evaluation, Vol. 17, No. 1. pp. 2-13 (1989).
12. V.K. Kinra, and P.N. Li, "Resonant Scattering of Elastic Waves by a Random Distribution of Inclusions," Int. J. Solids Structures, 22(1), 1-11, (1986).
13. V.K. Kinra, "Dispersive Wave Propagation in Random Particulate Composites," Recent Advances in Composites in the United States and Japan, ASTM STP 864, J.R. Vinson and M. Taya, Eds., 309-325 (1985).
14. V.K. Kinra and C.Q. Rousseau, "Acoustical and Optical Branches of Wave Propagation: Some Additional Results," Proc. Multiple Scattering of Waves in Random Media and Random Rough Surfaces, The Pennsylvania State Univ., Ed. V.K. Vardan and V.V. Vardan, 603-613 (1985).
15. Z. Hashin and S. Shtrikman, "A Variational Approach to the Theory of The Elastic Behavior of Multiphase Materials," J. Mech. Phys. Solids, 11, 127-140 (1963).
16. V.K. Kinra, V. Dayal, and J.G. Eden, "Ultrasonic Nondestructive Testing of Matrix Cracks in Fiber-Reinforced Composites" to be submitted to Experimental Mechanics.
17. R.A. Schapery, "Viscoelastic Behavior and Analysis of Composite Materials," 2, ed. G. Sendeckji, Academic Press, New York (1974).

TABLE 1. Test Results on Aluminum Sample

Material: Aluminum  
Wave Type: Longitudinal  
Mode: Transmission  
Frequency: 10 MHz  
Density:  $2.8177 \pm 0.0004$  g/ml

h mm	h/ $\lambda$	c mm/ $\mu$ s	$\bar{\sigma}/c$ %	Technique	Reference Figure
2.807	4.4	6.3572		Toneburst	5a
2.807	4.4	6.3239	0.013	Separable-Pulse	5b
2.807	4.4	6.3275	0.010	Non-Separable Pulse	5b
1.683	2.7	6.3461	0.040	Non-Separable Pulse	5c
1.001	1.6	6.3538	0.030	Non-Separable Pulse	5d
0.613	0.96	6.3594	0.130	Non-Separable Pulse	5e
0.258	0.4	6.3231	0.140	Non-Separable Pulse	5f

TABLE 2: Test Results on Epon 828-Z Epoxy

Material: Epon 828-Z epoxy  
Wave Type: Longitudinal  
Mode: Transmission

Specimen thickness  $1.869 \text{ mm} \pm 0.0025$   
Specimen density  $1.2069 \pm 0.0004 \text{ g/ml}$

Test Frequency MHz	Wavespeed mm/ $\mu$ s	$\frac{\sigma}{\epsilon}$ %	$k_2 \lambda$	$\frac{\sigma}{\epsilon}$ %	Technique
1.0	2.874	0.1	0.1340	1.4	Non-Separable Pulse
5.0	2.884	0.14	0.0924	1.5	Non-Separable Pulse
10.0	2.915	0.08	0.0975	1.0	Non-Separable Pulse
10.0	2.915	0.24	0.0979	2.2	Toneburst

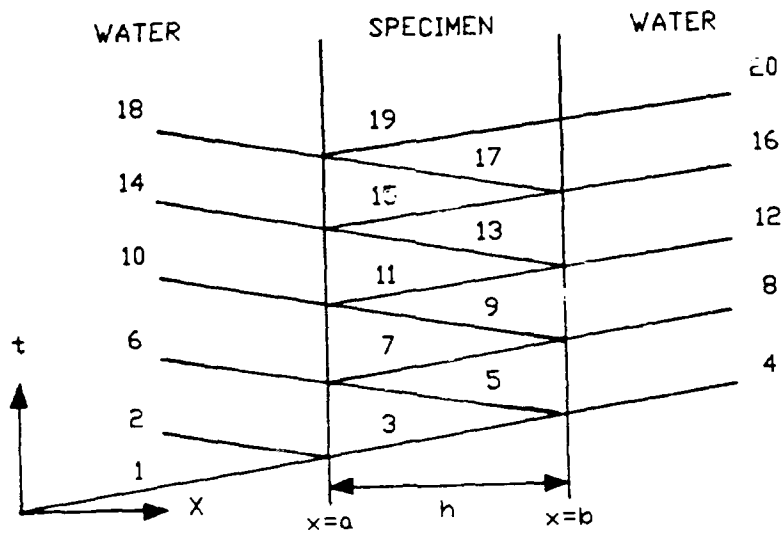


Fig. 1 Various reflections and transmissions from a plate immersed in water.

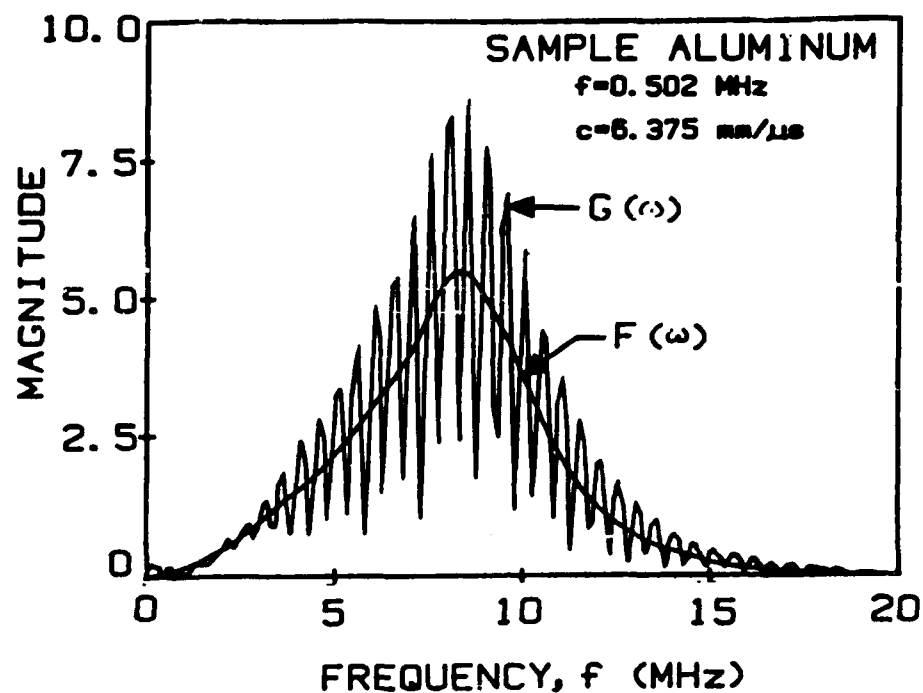


Fig. 2 Magnitudes of Fourier Transforms of  $f(t)$  and  $g(t)$  when pulses can be separated.

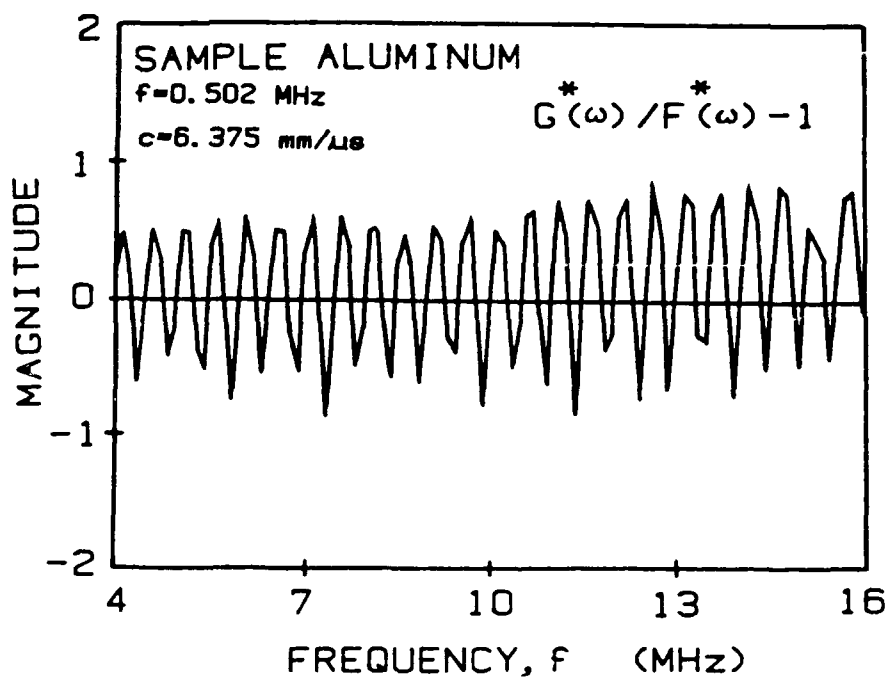


Fig. 3 Magnitude of  $G^*(\omega)/F^*(\omega) - 1$ , from Fig. 2. Resonance spacing can be measured easily from the zero line crossings.

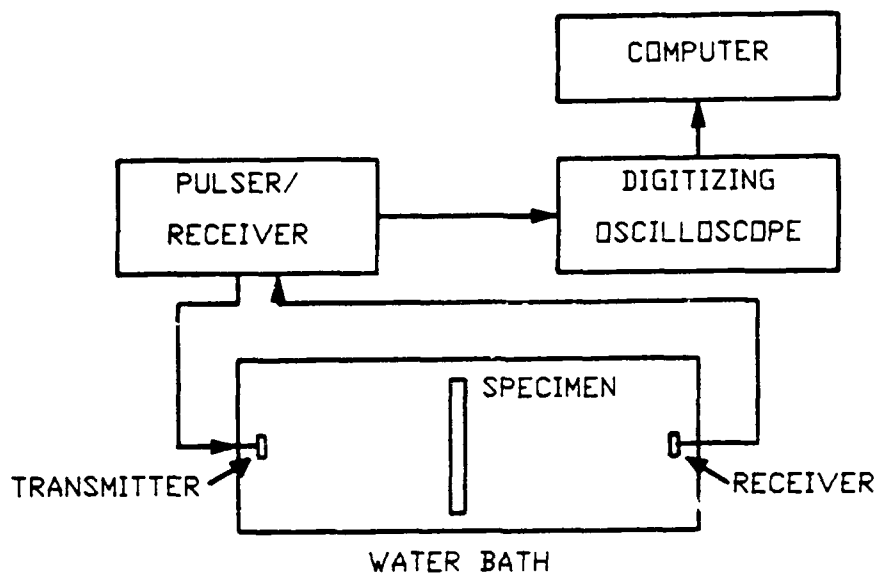


Fig. 4 Block diagram of the experimental set up.

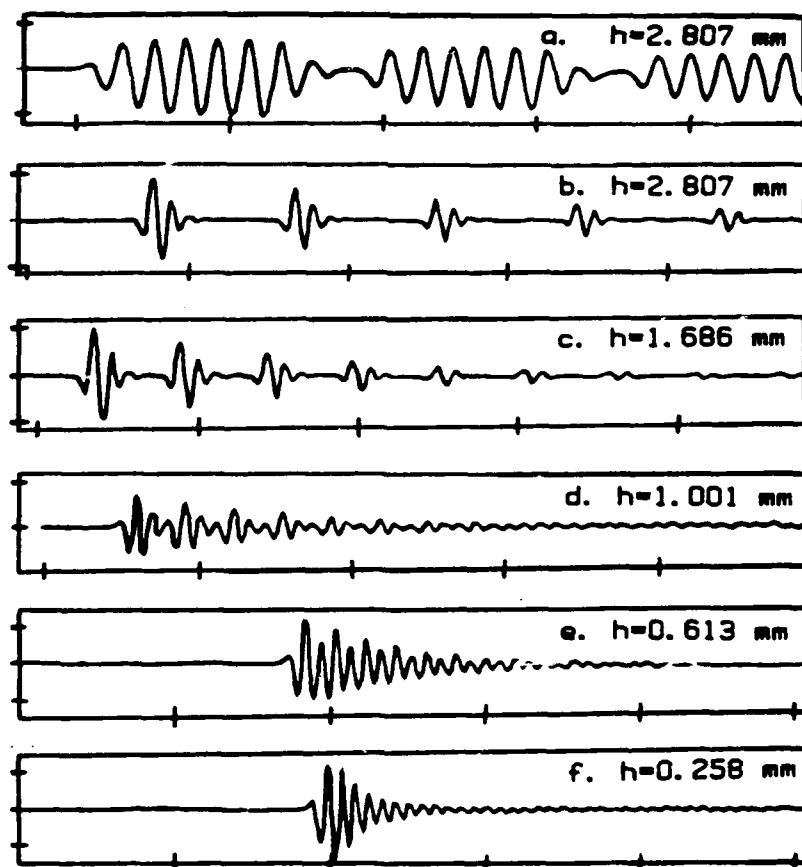


Fig. 5 10 MHz signal through aluminum plates of different thickness. (a) is for toneburst. Others are for a single pulse of signal. Plate thickness given on each signal.



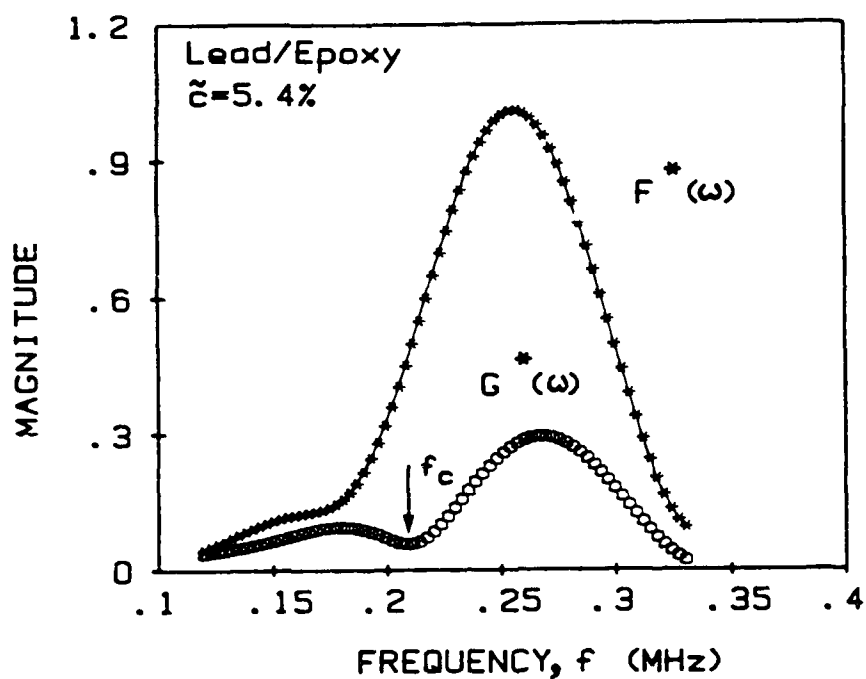


Fig. 6 Magnitude of  $F^*(\omega)$  [FFT of signal through polystyrene delay rod] and  $G^*(\omega)$  [FFT of signal through polystyrene and Lead/Epoxy specimen]. Note the dip in amplitude at the cut-off frequency,  $f_c$ .

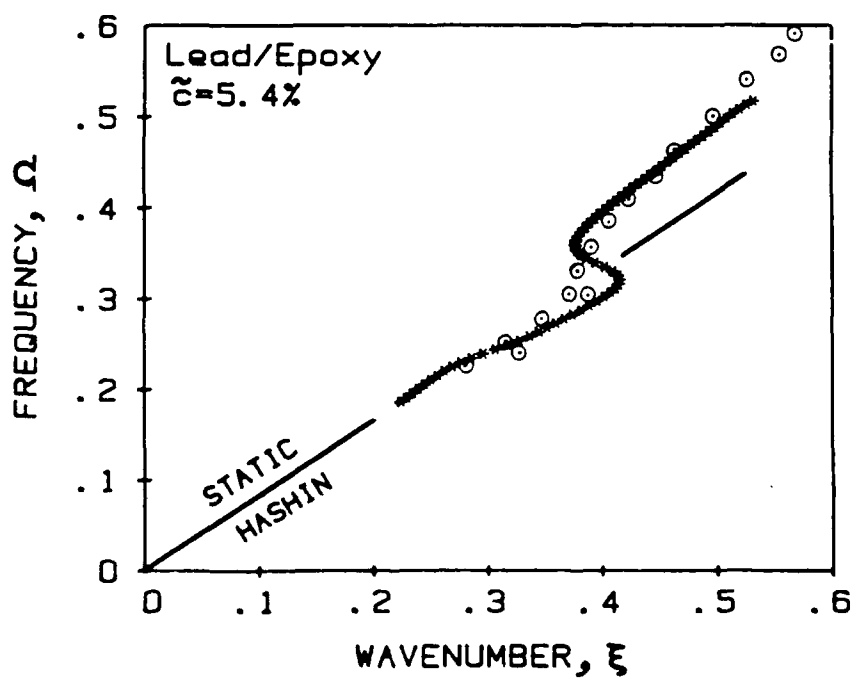


Fig. 7 Frequency;  $\Omega = k_1 a$  and wavenumber;  $\xi = \langle k_1 \rangle a$  curve for a dispersive Lead/Epoxy specimen. Circled points are data from reference 12-14.

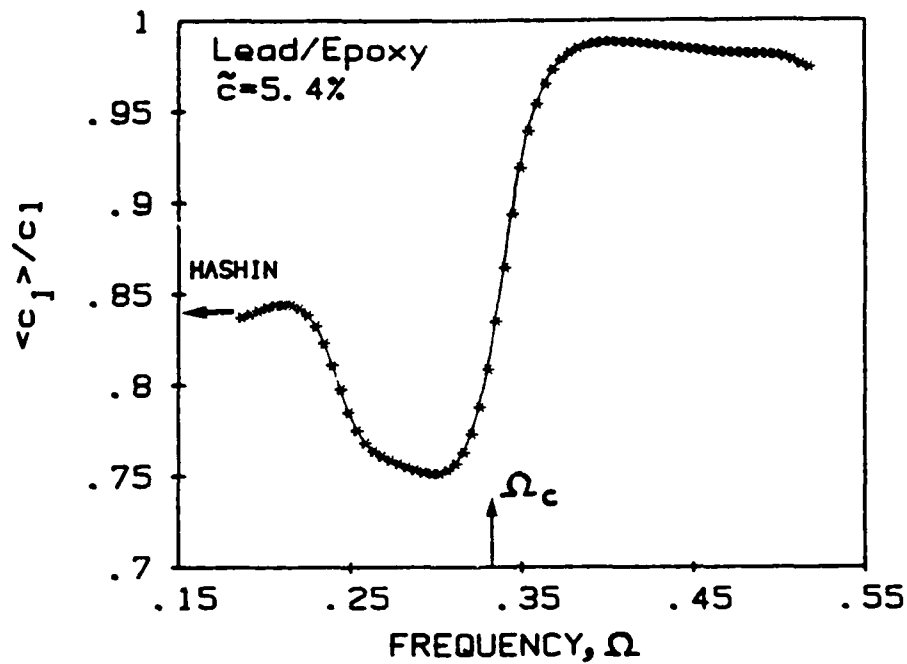


Fig. 8a Normalized phase velocity and frequency curve for the dispersive Lead/Epoxy specimen.

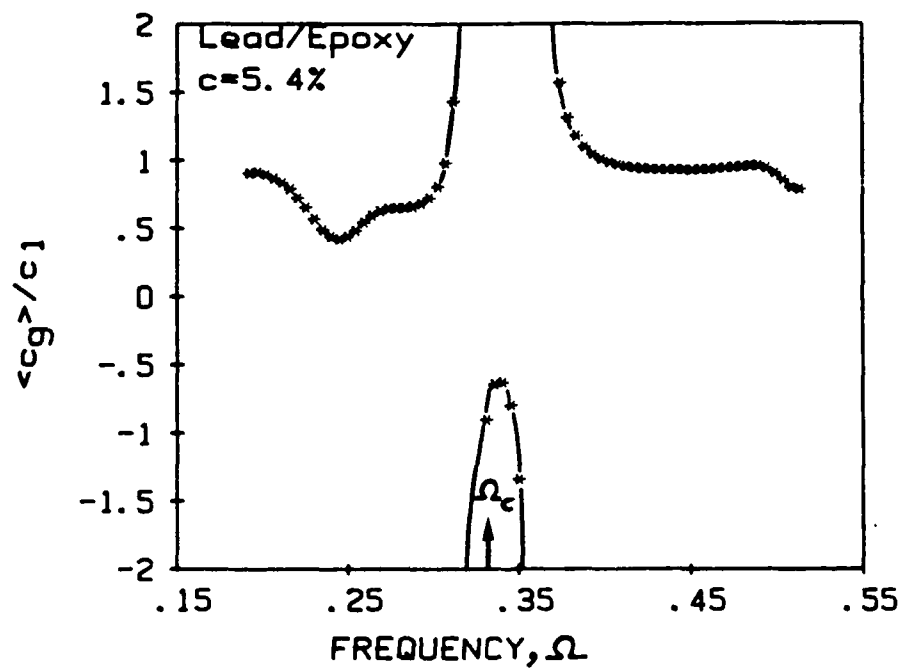


Fig. 8b Normalized group velocity and frequency curve for Lead/Epoxy specimen.

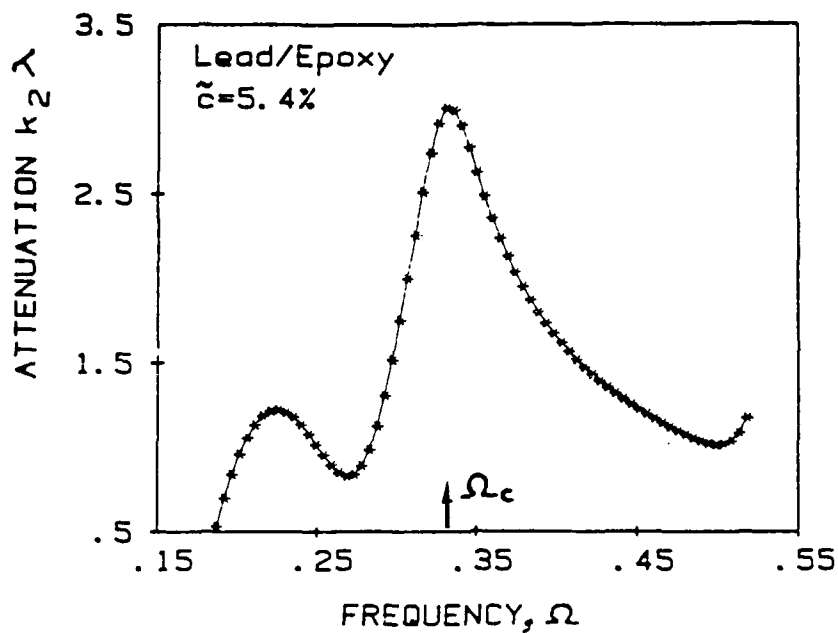


Fig. 9 Normalized attenuation and frequency curve. Note a very high attenuation (large energy absorption) due to dispersion at the cut-off frequency,  $\Omega_c$ .

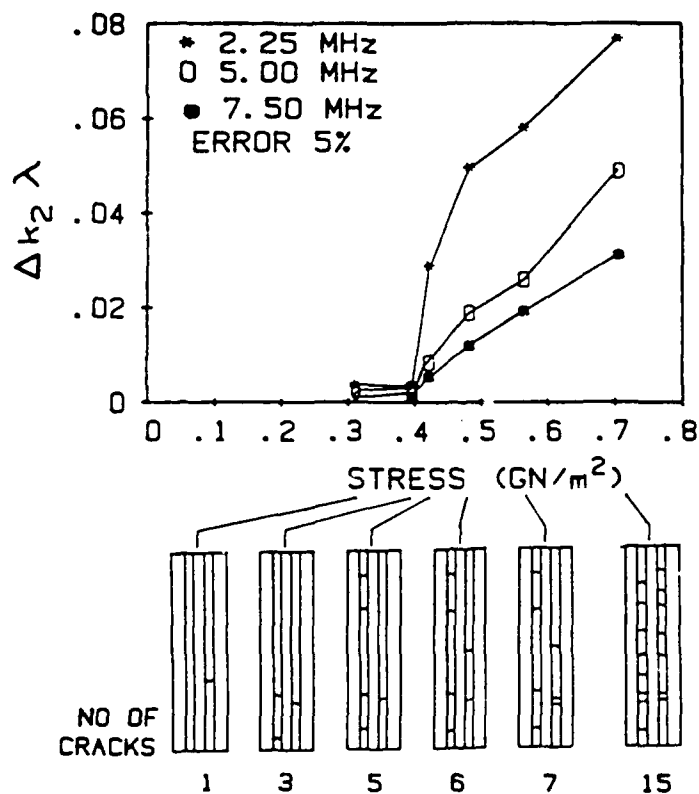


Fig. 10 Attenuation increases dramatically with transverse cracks in Gr/Ep,  $[0_6 90_4 0_2]_S$  laminate at all three frequencies tested. Extent of damage is shown in the edge replication sketches.

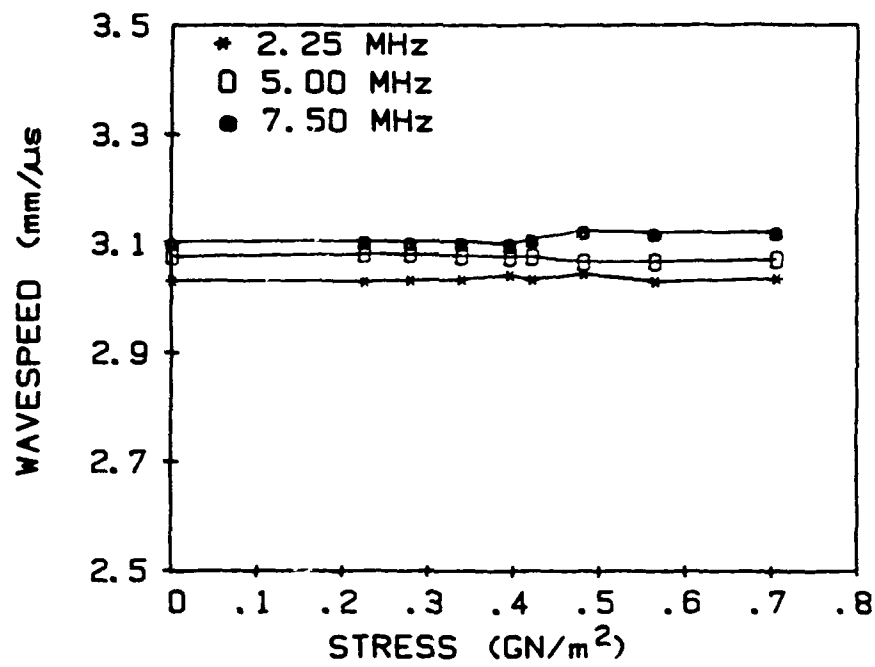


Fig. 11 Longitudinal wavespeed variation at three different frequencies with transverse cracks in a Gr/Ep,  $[0_2 90_4 0_2]_S$  laminate.

## NON-CONTACT ULTRASONIC INSPECTION WITH FIBER GUIDED LASER LIGHT

Christian P. Burger & Charles Duffer  
Texas A&M University

### 1. ABSTRACT

Thermal Acousto Photonic NDE (TAP-NDE) generates ultrasonic waves in steel through a very short duration (order of 20ns) thermal shock from a high energy laser pulse guided through optical fibers. This wave interrogates the material and can be read with standard ultrasonic transducers or with the newer fiber tip interferometers. This paper discusses the latest developments in this technology and shows how this technology provides remote non-contact energy input onto rough surfaces or into areas where the use of traditional transducers are either difficult or impossible. It further discusses the possibilities for spatial and temporal conditioning of the energy input to produce waves with pre-determined characteristics, e.g. collimated beams, plane wave fronts and focused waves.

### 2. INTRODUCTION

In the research described here, a high energy laser pulse is coupled into an optical fiber bundle which is then used to guide the pulse into otherwise remote and inaccessible locations in or on metallic structures and components. Here the fiber is pointed at the surface so that the pulse will illuminate a small area of the surface at the position where it is desired to excite an ultrasonic inspection wave. The energy absorbed from the pulse by the surface very suddenly and very locally heats a small

volume of material near the surface. Unless the material is very thin, it acts as a half-plane and the heated volume, which needs to expand rapidly, is constrained from doing so by the cold material that surrounds it. The resultant thermal jerk generates acoustic waves that radiate along the surface (Rayleigh or R-waves) and propagates into the half plane (bulk waves).

These waves interrogate the material and are sensed (or read) at a different position with a fiber optic interferometer. In this device the coherent light from a continuous wave

laser is coupled into a single mode optical fiber which guides the light to the point on the surface where the ultrasonic wave is to be read. The output end of the fiber is approximately normal to the surface and is located close to, but not in contact with, the material. A small percentage (3-5%) of the light in the fiber is internally reflected from the free surface of the fiber tip. This is the reference wave. The remaining light emerges from the fiber and is scattered by the surface of the material. A small portion of this light is reflected back onto the fiber tip where it enters the fiber as the object wave and interferes with the reference wave.

The phase difference between these two waves is a measure of the gap length (difference in optical path length) between fiber tip and material surface. When a wave passes underneath the tip the small change in the gap is recorded as a dynamic phase change. Since the light traverses the gap twice the phase shift relates to double the change in the gap.

The combined wave propagates back through the fiber and is directed onto a photodetector which converts the phase dependent changes in intensity to an electrical signal.

### 3. GENERATION OF ACOUSTIC WAVES WITH FIBER OPTICS

The generation of an ultrasonic wave from a high energy laser pulse guided through an optical fiber was first achieved in 1987(1) with a pulsed ruby laser. The set-up is shown in Fig. 1. Current work is with a pulsed Nd-YAG laser with an optical pulse width of ~8ns and maximum pulse energy of 1Joule at the normal

wavelength of 1064 nm or at the frequency doubled wavelength of 532 nm. A single pulse is coupled into non-coherent fiber optic bundles with circular input ends and variously shaped output ends. The pulse is then guided through the fiber to a steel block where it is used to produce a Rayleigh wave. This wave is detected with a standard Rayleigh wave set-up consisting of a P-cut piezo electric transducer mounted on a 90° wedge. As in reference 1, it is necessary to shield the transducer from light scattered from the laser pulse in order to prevent a noisy signal. The Piezoelectric transducer is connected directly to a digitizing oscilloscope which is triggered from the laser's Q-switch. The output end of the fiber or fiber bundle is mounted on an x, y, z,  $\theta$  positioner to control the position, size and orientation of the input area with respect to the R-wave transducer. In this way both the distance between fiber end and the specimen surface (h) and the distance between illumination spot and transducer (b) can be varied. This arrangement allows a transverse scan of the acoustic beam to be performed in the y-direction. The layout is shown in Figure 1 which also defines the notation used in this paper.

The parameters that control the efficiency with which ultrasonic waves are generated in the material, as well as their amplitude, nature (shape) and the mix between surfaces and body waves are:

- (1) The surface properties of the exposed material  
(Absorptivity/reflectivity of the surface for the wave length of light used;  
thermal diffusivity of the material;  
surface roughness; the extent of transparency or opacity of the material

to the light being used).

(2) The properties of the light pulse (Pulse duration; distribution of energy in the pulse, both temporally and spatially; frequency/wavelength of the radiation being used).

(3) The geometry of the spot that is being irradiated (Size; shape).

(4) The temporal distribution of radiation energy along the geometry of the spot and/or over its area (Energy is not put into the material at the same time everywhere in the exposed area).

#### 4. WAVE SHAPES PRODUCED FROM INPUTS WITH DIFFERENT GEOMETRIES

The first and most natural shape for the illuminated spot is the normal circular spot from a single core 1mm diameter multi-mode fiber. The result is shown in fig. 2a. The next two tests were conducted with fiber bundles. The fibers are arranged into a round 1mm active input area and are rearranged to have an output end with

1) All the fibers arranged in a straight line approximately 4mm long.

2) The fibers arranged over a semi circular area with diameter just over 1mm.

In each case the fiber bundles consisted of 19 plastic clad silica fibers arranged non-coherently to the desired configuration. The results for these two tests are shown in figs. 2b and 2c.

These experiments show how changes in the shape of the area subjected to thermal shock, that is, of the illuminated spot on the surface of the steel specimen, affect the shape and amplitudes of the ultrasonic waves. Only the analog shapes of the waves were considered. The energy in each pulse from the laser was about 400 mJ. For the single fiber the best

position was with the fiber tip almost touching the specimen. This resulted in a 1mm illumination spot. Both the line and semi-circular inputs produced their maximum amplitudes at 1mm away from the specimen. The single fiber produced a 15mv peak to peak amplitude; the line input 18 mv peak to peak and the half-circle fiber bundle 11 mv peak to peak.

As shown in reference 1, the size of the illuminated spot changes the shape and quality of the resulting wave. As the fiber tip is moved further away from the surface of the specimen the divergence of the output beam causes the spot size to change linearly with distance. As the end of the fiber moves away from the surface, the amplitude of the wave decreases, the illumination spot size becomes larger and the waves acquire secondary features suggesting multiple effective sources which cause overlapping of thermal shocks emanating from different regions of the input areas.

Figure 3 shows the waves when the stand-off distance between the fiber tips and the steel surface was 7mm. When compared to Figure 2 it is clear that line and semi-circular sources now produce waves which are not suitable for high resolution NDE.

#### 5. FIBER OPTIC SENSING

A basic interferometer consists of two coherent beams of light: an object beam, which passes through, or is reflected by, the specimen under observation, and a reference beam, which is unaffected by the specimen. If the wave fronts of the two beams are coherent with respect to each other, they interfere when superimposed. The design of the

interferometer used in this research is based on the Fizeau configuration as described in reference 2 and shown in fig. 4.

Since the optical fiber interferometer (OFI) is excited by coherent light, the two beams interfere destructively whenever the optical path lengths of the internally and externally reflected light beams differ by a half wavelength or odd multiple thereof as shown in fig. 5. When the change in the displacement induced length of the Fizeau cavity is less than  $1/4$  wavelength the pure phase from OFI will define the displacement. If the intensities and polarizations of the internal and external reflections are reasonable equal, the intensity of the combined beams traveling back along the optical fiber will be seen to brighten and darken as the cavity length changes. A change in the cavity length greater than  $1/4$  wavelength will shift the output signal intensity through one or more maxima and minima.

The intrinsic self-alignment of the reference and object beams is one important feature of the OFI. In addition, throughout most of the interferometer both beams experience the same environment - the relative phase of the two beams can change only in the Fizeau cavity. That is, the only place where the reference and object beams are not subject to the same temperature, pressure, vibration, etc. is in the cavity between the fiber tip and the specimen.

If the displacements are large enough for the phase changes to produce several changes from light to dark data is quantified by counting maxima and minima

and the only critical alignments are those associated with launching the light into the fiber. However, when the displacement is of the order of  $1/4$  wave length the fiber tip must be located at any quadrature point of the signal as shown in fig. 5 ( $\Delta = \pi/4, 3\pi/4, 5\pi/4, \dots$ ). The location of the fiber tip, i.e. the initial length of the Fizeau cavity, is critical. In ref. 2 very careful alignment of the fiber tip produced well separated waves with very accurate time of flight measurement capabilities. A set-up of that complexity is not practical for on-site inspection. Our current research is concerned with methodologies that will remove this restriction.

## 6. CONCLUSION

Current research is demonstrating the feasibility of using fiber-optic based generators and sensors of ultrasound for advanced NDE. The potential advantages of a system based on this technology are:

- (1) Energy input is without contact between an input transducer and the surface.
- (2) Input can be remote and can be precisely located with the aid of focused fiber-scopes, etc.
- (3) Input can be rapidly scanned.
- (4) The energy level can be adjusted and the nature of the input modified by correct conditioning.
- (5) Because of the small source point, the acoustic wave will more nearly approximate its analytical or "pure shape".
- (6) Since readout is at a point over time, wave shapes are sharply defined, closely spaced waves are already separated and time of flight data has high resolution.



(7) Readout is also non-contacting and can be conducted in remote locations.

#### 7. ACKNOWLEDGEMENTS

The research reported here was performed with support from the Texas Advanced Technology Program under project number 70080.

#### 8. REFERENCES

1. T.D. Dudderar, C.P. Burger, J.A. Gilbert, J.A. Smith, and B.R. Peters, "Fiber Optic Sensing for Ultrasonic NDE," J. of Nondestructive Evaluation, Vol. 6, No. 3, 1987.
2. C.P. Burger, T.D. Dudderar, J.A. Gilbert, B.R. Peters, and J.A. Smith, "Laser Excitation Through Fiber Optics for NDE," J. of Nondestructive Evaluation, Vol. 6, No.. 1, 1987.

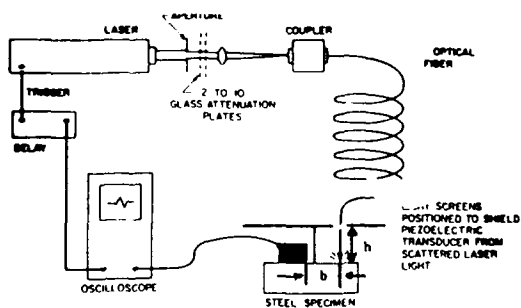


Figure 1. Set-up for laser generation of sound.

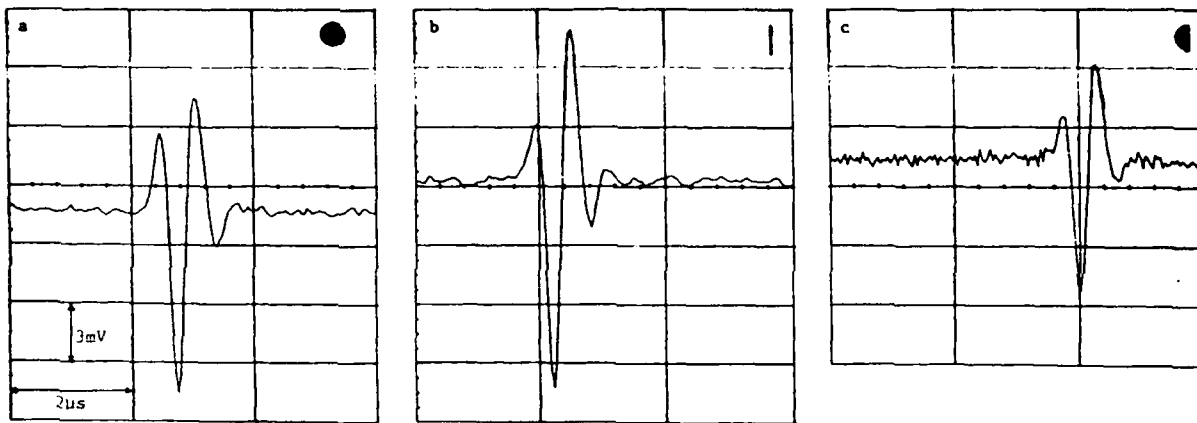


Figure 2. Comparison between maximum amplitudes obtained for optimum positioning and orientation of three different input shapes:  
a) circular input:  $h = 0$   
b) line input:  $h = 1\text{mm}$   
c) half circle input:  $h = 1\text{mm}$ .

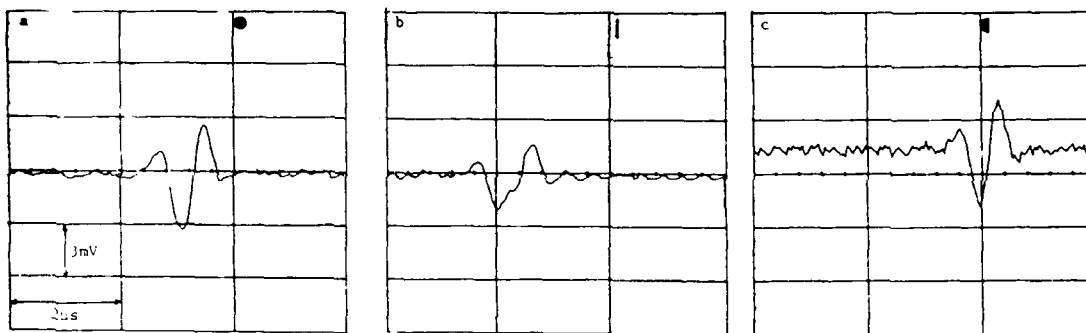


Fig. 3 Rayleigh waves generated for three input shapes with  $h = 7\text{mm}$ .

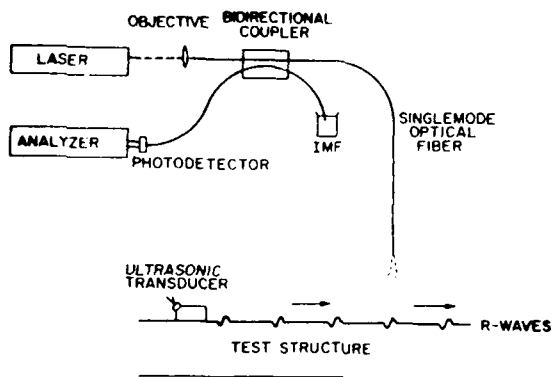


Figure 4. Fiber tip interferometer.

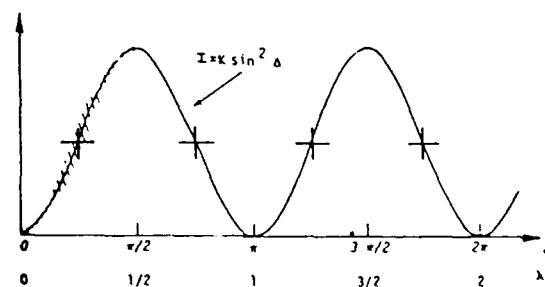


Figure 5. The  $\sin^2$  variation of the intensity of the output beam from FTI.  
 $\Delta$  = phase angle  
 $\lambda$  = wavelength

APPLICATION OF ULTRASONIC RESONANCE TECHNIQUE AT  
300 MHZ TO THE DETECTION OF DISBONDS IN A MULTILAYER STRUCTURE

J.D. Fraser and C.S. DeSilets, Precision Acoustic Devices, Inc., 200 Hammond Ave., Fremont, CA 94539  
C.H. Chou and B.T. Khuri-Yakub, Ginzton Laboratory, Stanford University, Stanford, CA 94304

ABSTRACT

This paper describes the results of work on the feasibility of using high frequency ultrasound to determine the degree of bondedness of multilayer structures. A sandwich structure of two identical metal sheets of thickness on the order of 25  $\mu\text{m}$ , bonded together by a dissimilar third layer of thickness 10  $\mu\text{m}$  was examined. The primary disbond was expected to be in the region of the interface between the top two metal layers. Frequency domain analysis using a Wiener-filtered FFT was used to extract a signature related to the properties of the upper metal strip as an acoustic resonator, which is strongly dependent on the boundary conditions on its back surface. The frequency range of 200 to 300 MHz was determined to be the appropriate range at which to perform the inspections. The sandwich structure was modelled for varying degrees of bondedness, and frequency domain measurements were made on a number of samples using a 300 MHz acoustic transducer and electronic setup. Experimental results have indicated strong correlation between the depth and width of nulls in the Wiener-filtered spectrum and the state of bondedness. The results correspond well to the acoustic resonance of the disbonded upper metal layer as predicted by the theory.

STATEMENT OF PROBLEM AND APPROACH

The problem to be addressed is the state of bondedness between the first and second layers of a thin, bonded metal sandwich. In this case, the sandwich was formed of two 25  $\mu\text{m}$  layers with a 10  $\mu\text{m}$  layer of a dissimilar metal between. Disbonds or voids between the top and second layers were leading to reliability and inspectability problems. The authors were approached to determine the feasibility of an ultrasonic inspection technique and demonstrate an implementation of that technique. The extremely small thicknesses of the layers and the small sizes of the voids to be detected made the problem a difficult one.

The effect used to accomplish the inspection is the reflection of sound waves from interfaces

between dissimilar materials. The reflection coefficient of a metal to metal interface is much smaller than that of a metal-vacuum, metal-air, or metal-water interface. If geometrical factors and material properties are amenable, bondedness can be measured by interrogating the sample with a sound pulse in a water bath to measure the reflection coefficient of the metal-metal interface. If the frequency and bandwidth of the sound pulse can be made high enough, the echoes from the various surfaces will be distinct in time, and the echo from the desired interface may be measured directly. If separation of echoes in the time domain cannot be achieved, frequency domain analysis by Fourier Transform may be used to extract a signature related to the properties of the upper metal

strip as an acoustic resonator, which are strongly dependent on the boundary conditions on its back surface. Interpretation of frequency domain results is simplified by use of the Wiener filter, which presents the useful data in normalized form, and suppresses the noisy portions of the data.

The Wiener filter is a frequency-domain signal processing technique which divides the signal power spectrum by a reference spectrum (obtained in our case from a simple reflector) at frequencies where the reference spectrum is not noisy, and reduces the spectral amplitude gracefully to zero where the reference spectrum is below a specified noise level. This has the effect of presenting the significant portions of the reflection coefficient function of the sample in a normalized fashion, and removing portions of the spectrum which do not contain meaningful information.

For these particular samples, in the time domain, the echo from the interface to be inspected arrives about 11 nanoseconds after the front surface echo. Evaluation of this echo may be confused easily by the finite pulse duration of a practical transducer, as well as by lead height variations, surface roughness, and beam irregularities. A center frequency of at least 1.5 GHz would be required to directly inspect this interface. Technical difficulties would be great. However, in the frequency domain, the time delays between multiple echoes in the layered structure lead to periodicities of about 30 MHz in bonded regions, while periodicities of about 100 MHz are obtained in disbonded regions. The interfering factors mentioned above do not severely affect the effectiveness of the technique because a frequency domain technique uses a long interval of signal and adds the effects of multiple echoes.

Figure 1 shows the geometry of the structure to be inspected and the relationship of the acous-

tic transducer and beam to the sample. A 300 MHz zinc oxide transducer on a sapphire buffer rod was chosen to give a usable bandwidth covering the range of frequencies over which resonances of the structure useful for signature analysis were found. In our case, signature extraction from the spectrum required operation over frequencies ranging from 200 to 300 MHz. Our setup had a useful signal to noise ratio over a frequency range of 100 to 300 MHz. The beam was focussed to a diameter of approximately 30  $\mu\text{m}$ , minimizing sensitivity to roughness of the surfaces and giving excellent sensitivity to small disbanded regions.

Factors which affect the performance of the measurements described above include the acoustic velocities of the two metals, which determine the delay times between echoes; their attenuation coefficients, which govern weakening of the echoes from internal interfaces and help to determine the maximum usable frequency; and the acoustic impedances of the water transmission medium and the two metals, which determine the reflection coefficients of the front surface and internal interfaces.

The acoustic properties of the two metals were measured and the structure was modelled for varying degrees of bondedness. Figures 2 and 3 show calculated reflection coefficients versus frequency for the fully bonded structure and for the unbonded top layer. The differences in null location and depth between the two structures are readily apparent. In order to simulate the signals expected in a real measurement, the frequency response of a transducer and the frequency dependent attenuation in the water path between the transducer and the sample were added. The results are shown in Figures 4 and 5 for the three layer and unbonded layer structures. Comparison of these graphs shows which resonances will form the basis of a bondedness signature for this structure.

## EXPERIMENTAL TECHNIQUE

The following inspection procedures were used:

- (1) Align a flat reference surface under the transducer for maximum echo amplitude and compactness, at the proper focal depth. Record the echo waveform and save it for use as a reference for Wiener filtering.
- (2) Replace the reference surface with the sample and record the RF echo. Calculate the spectrum and normalize the spectrum of the reference echo using a Wiener filter.
- (3) Inspect the resultant spectrum for signature information.

## RESULTS

Figure 6 shows the Wiener filtered power spectrum obtained from an echo received from a sample of the well-bonded three layer structure.

No deep nulls are seen. The signature corresponds approximately to that shown in Figure 4, within variations to be expected from uncertainty in the thicknesses of the metal layers.

Figure 7 shows the same result obtained from an identical sample, but with a void behind the first layer. Here, a deep null is easily noted at a frequency of 230 MHz. This corresponds almost exactly with the theoretical result shown in Figure 5. The agreement is excellent. This demonstrates that Wiener filtering can be used to extract meaningful information from signals when the experimental conditions do not allow adequate bandwidth to resolve the structures to be inspected in the traditional amplitude versus time method.

Measurements were made on a large number of samples. A statistical study has indicated strong correlation between Wiener filter analysis of return echoes to extract the acoustic resonance of the disbanded metal layer, and the actual fraction of disbanded area as determined by postmortem SEM photographs of peeled samples.

## CONCLUSIONS

We have identified and studied an acoustic technique for evaluating bonded metal sandwiches when time separation of echoes is not readily achieved. The technique depends on the measurement of the relative strengths of front surface echoes and echoes from the back surface of the top layer. A Fourier analysis method utilizing the Wiener filter was used to isolate the desired effect and produce readily quantifiable signatures; the width and depth of a null in the power spectrum of the return signal after broadband excitation. Correlation was found between bondedness as determined by SEM photography of peeled samples and null depth.

## NOTE

This paper published previously in the proceedings of the symposium at the Quantitative NDE Meeting held in LaJolla, CA, 7/31 - 8/5, 1988.

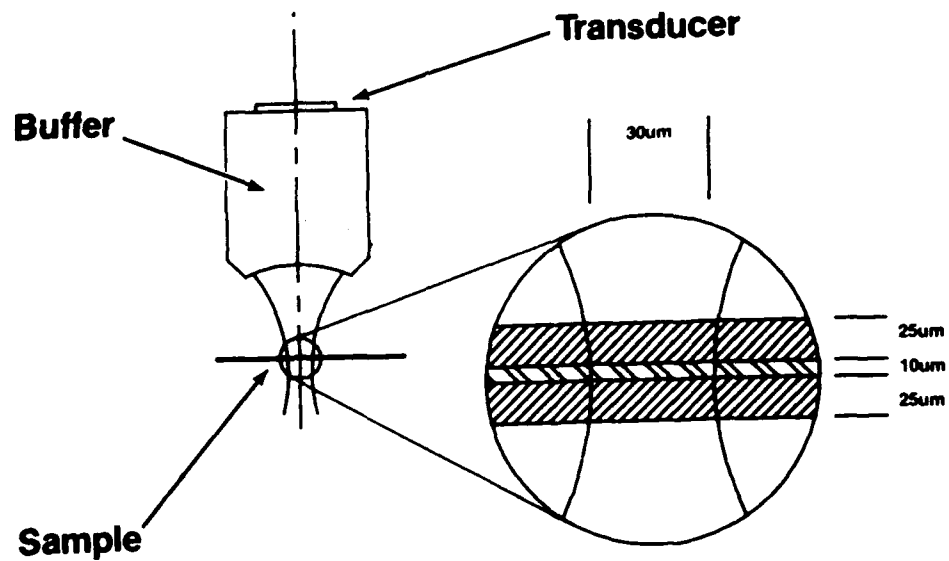


Figure 1. Diagram of the Relationship of the Transducer and Sound Beam to the Three-Layer Metal Sandwich to be Inspected.

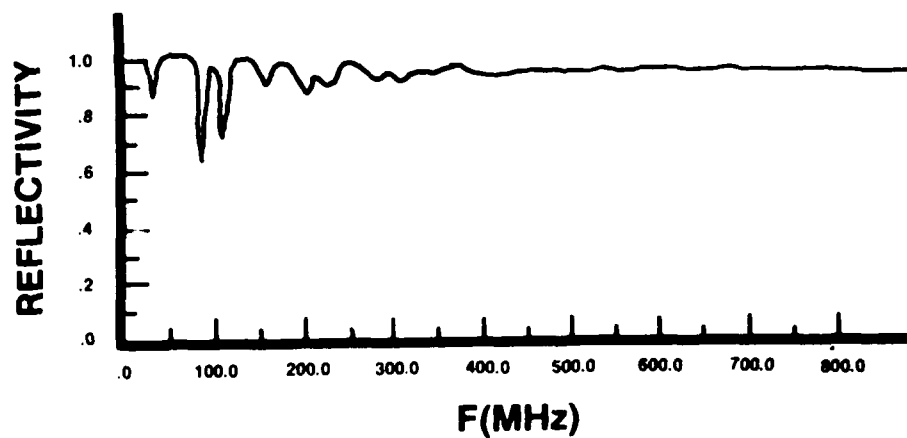


Figure 2. Theoretical Reflectivity vs. Frequency of a Well-Bonded Three-Layer Structure.

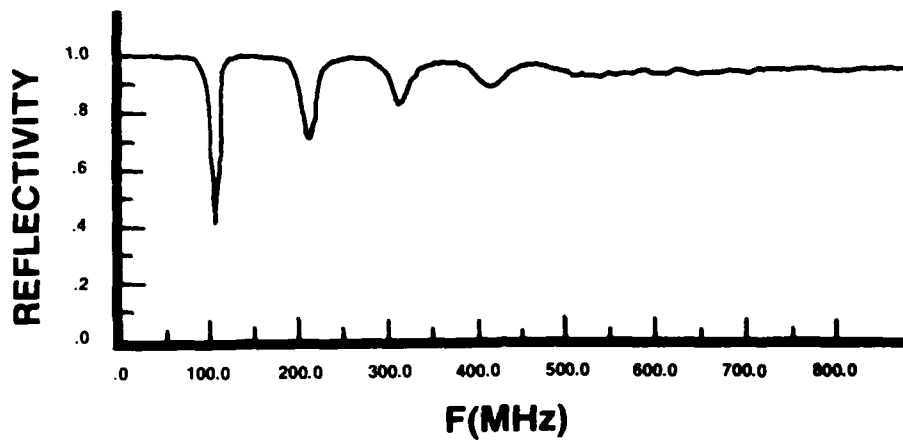


Figure 3. Theoretical Reflectivity vs. Frequency of an Unbonded Metal Layer.

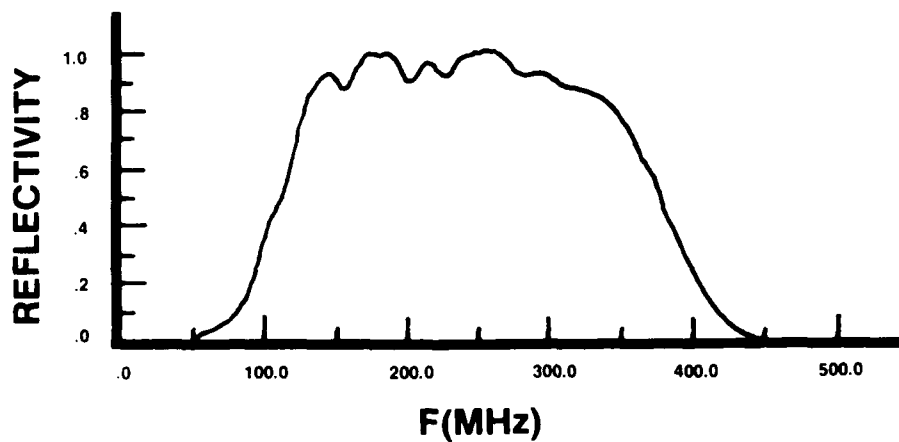


Figure 4. Theoretical Received Signal vs. Frequency of a Well-Bonded Three-Layer Structure, Including Transducer Response and Water Path Loss.

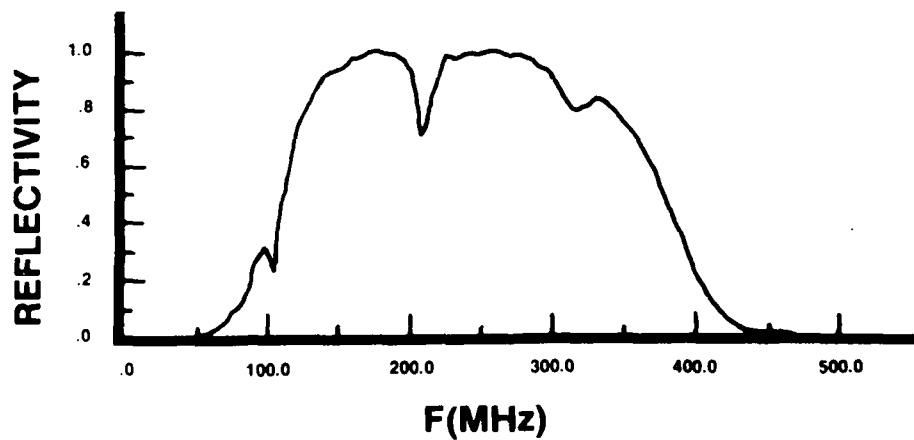


Figure 5. Theoretical Received Signal vs. Frequency of an Unbonded Metal Layer, Including Transducer Response and Water Path Loss.

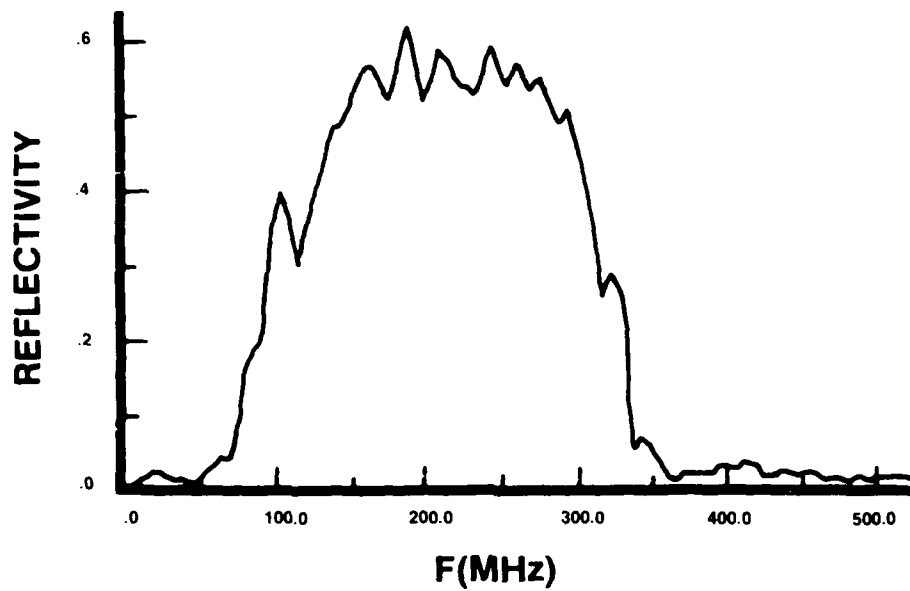


Figure 6. Experimental Received Signal vs. Frequency of a Well-Bonded Three-Layer Structure with Wiener Filtering.

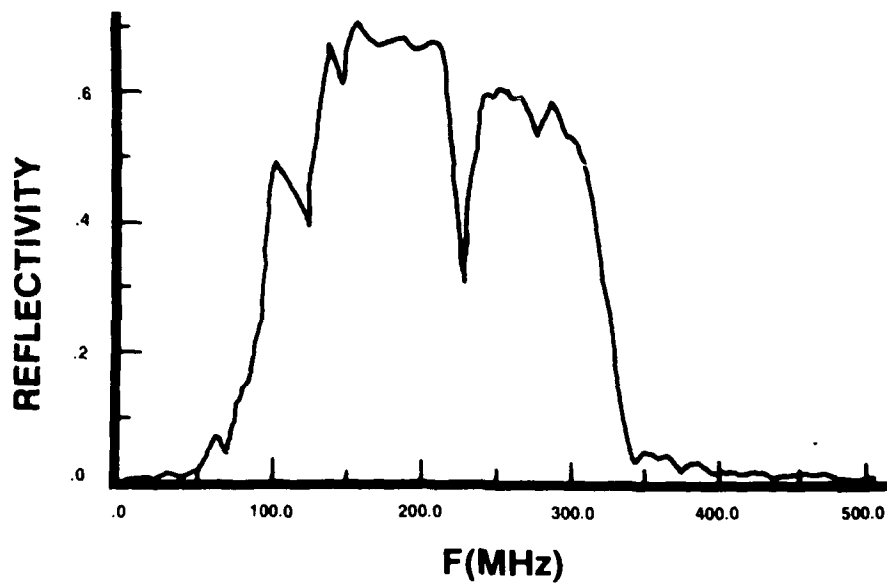


Figure 7. Experimental Received Signal vs. Frequency of an Unbonded Metal Layer, with Wiener Filtering.



DETECTION AND DISCRIMINATION OF  
BOND SURFACE VARIATIONS IN RUBBER/METAL LAMINATES  
USING OBLIQUELY INCIDENT ULTRASONIC WAVES

K. Jerome Diercks, Leonard A. Hale and George A. Matzkanin  
Texas Research Institute, Austin  
Austin, TX 78733

**Abstract**

Scans of bonded rubber-to-metal specimens were performed using an incidence angle of 20 deg re normal to the surface of the metal adherend (cold-rolled SS304 plate). This angle is greater than the critical angle for exciting compressional waves in the plate, but less than that for exciting transverse waves. Other, e.g., Lamb, waves may also be excited, but at a relatively much lower amplitude. The measured parameter was the level of the transverse wave after reflection at the bond surface. Variations in bond surface quality as well as disbonds between the layers were readily discriminated. Comparable results were achieved whether measuring the wave after one or several reflections. The "noise" in a scan that is due to directional scattering by the microstructure in the metal adherend was reduced by recording several scans using different ensonification directions and averaging them. This enabled discrimination of subtle differences in the quality of the bond surface. A simple, effective algorithm for assigning signal level measurements to plotting bins for display is described. This work was funded by the Office of Naval Research under a Phase II Small Business Innovative Research contract.

**INTRODUCTION**

Recent measurements at Texas Research Institute (TRI), in an ongoing program of ultrasonic rubber-to-metal bond evaluation, revealed unexpected sensitivity in detecting and discriminating variations in bond surface quality using the transverse wave mode excited in the metal adherend (cold-rolled SS304 plate). In the TRI work, the specimen is immersed in water, and the exposed metal surface is ensonified by a compressional wave at an oblique angle of incidence. The transverse wave is excited by mode conversion at the ensonified surface of the plate and propagates at an angle determined by Snell's Law. The propagating wave intersects the bondline and is specularly reflected back toward the exposed surface. The wave is re-converted to a compressional wave in the surrounding water and propagates in a direction determined by Snell's Law (in this case, specular with respect to the incident wave). These events will prevail through several internal reflections, until the energy losses from reflection and reradiation render the signal not detectable.

If the plate thickness is greater than about one-half wavelength at the ensonifying signal frequency, the individual reflections of the transverse wave can be

resolved in time. If the width of the ensonifying beam is smaller than the separation between reflection/reradiation loci, sequential reflections can also be resolved in space. Other wave modes, e.g., Lamb, that may also be excited will sometimes appear at lower levels between the reradiation loci, and can also be resolved in the receiver. If the acoustic geometry permits, the signal resulting from a single reflection or from several sequential reflections may be selected for measurement. The work described here includes all of these conditions to some extent.

Rokhlin *et al* have described the use of obliquely incident transverse waves to monitor the cure state of adhesives and the strength of the resulting bonds (1,2). They identify two basic boundary conditions: (1) a rigid boundary, with continuity of tractions and displacements on the interface; and (2) a slip boundary, with continuity of the normal traction and displacement, but absence of the tangential traction component. The acoustic coupling between layers is high at a rigid, i.e., bonded, boundary; reflectivity, and, thus, measured signal level, is accordingly low. The coupling is low at a slip, i.e., disbonded, boundary; reflectivity and measured signal level are high. It may be speculated that in regions

where there is poor bonding, intermediate conditions will prevail.

Application of obliquely incident transverse waves to evaluation of bondline quality, particularly in rubber/metal laminates, has not received much attention in the literature. The work reported here is considered at least an extension of existing technology, if not a new application. Results of a multiple-scan averaging technique for improving signal-to-background ratio are presented, and a simple, but effective, algorithm for distributing the signal level measurements to plotting bins for display is described.

## METHODS AND PROCEDURES

**Specimens.** Specimens were prepared by bonding (vulcanizing) neoprene 5109S to Type 304SS cold-rolled plate using procedures developed and proved in-house. Specimen size was 6 in. x 6 in. Plate thicknesses of 1/4 and 1/8 in. were included. The thickness of the rubber layer was 1/8 in.

The standard specimen format used in the TRI work is one-third (2 in. x 6 in.) of the lower surface area bare metal; this section includes one long edge of the plate. The remaining two-thirds (4 in. x 6 in.) of the lower surface area is covered with the rubber layer. Variations in "bondedness," or bond flaws, are included in the rubber-to-metal interface in a variety of ways. The bonding procedure specifies surface grit-blasting, followed by applications of a primer and an adhesive before vulcanization. Variations in bondedness are effected by failure to prepare the surface, or omission of the primer or adhesive, or both. Bond flaws are created by rubbing a mold release into the prepared surface; the flaws are then sometimes coated with primer/adhesive and sometimes not. Both variations in bondedness and bond flaws are generally included in all specimens prepared.

**Set-Up Procedures.** Set-up ("initialization") was done over the bare metal section of the specimen. The procedure was to begin with the transducer couple at sufficient distance above the plate surface that the field of view of the receiver was aligned with the reflected incident beam (or stated differently, the spots generated by the intersection of the transducers' beams with the plate surface overlay each other). The transmitted signal was a short burst of 3-5 cycles at the resonant frequency of the transducers. The couple-surface distance was then reduced, which had the effect of causing the field of view of the receiver to move away from the reflected incident beam. As the transducers approached the plate surface, the receiver viewed less and less of the specularly reflected beam and began to intersect one or more loci of reradiation of the internally propagating (and

reflecting) transverse wave. The couple-surface separation was fixed at a distance that allowed resolution of the desired signal (reflected/reradiated pulse or pulses), or was reduced to "zero," i.e., the nearest edge of the transducers was essentially in contact with the plate surface. When operating "in contact," it was sometimes necessary to adjust the separation between the transmitting and receiving transducers to maximize the signal from the nearest reradiating locus. Depending on the geometry, the first, or a subsequent, reflection of the transverse wave was gated for measurement in the receiver. Or if the field of view of the receiver included several reflections of the wave, all were sometimes included in the measurement gate.

## RESULTS

Figure 1 is a diagram of the bond surface of a 1/4 in. thick plate with three areas of differing "bondedness," called the P4 specimen. The view is from the upper surface, or through the metal plate. The left one-third of the surface is bare metal, i.e., no rubber layer. The upper one-third of the rubber covered area is a "well-bonded" area; that is, it was prepared in accordance with the accepted TRI rubber-to-metal bonding procedure. The lower one-third of the rubber covered area is a "poorly bonded" area; it was prepared without the use of primer/adhesive. The rubber is bonded to the plate in this area—it cannot readily be pulled away—but the adherence is presumably less than in the upper area. The center one-third of the rubber covered area is a disbonded area. It was prepared by rubbing mold release into the area and also without primer/adhesive. The rubber covering this area can be lifted away from the metal plate. The broken line delineates the area scanned, as defined by the axis of the rod supporting the transducer couple.

Figure 2 is a C-scan of the P4 specimen. The transmitter driving signal was 3 cycles at 5.0 MHz; the acoustic signal was 5 cycles at about 4.5 MHz. The transducer couple-surface distance allowed resolution in time of the first reflection of the internally propagated transverse wave (the edge of the reflected incident beam was also seen by the receiver). The scan format is 51 lines of 128 points each. Measured signal level is indicated by the darkness, or density, of the points; the higher the level, the darker the points. Five levels are displayed. The algorithm for establishing the levels and distributing the points is: five level bins with an equal number of points in each bin. This scan discriminates and delineates the bare metal area (left side of scan) and the disbonded area (center right of scan). It does not differentiate the two bonded areas.

A common procedure for improving the ratio of signal-to-noise (S/N) is to sum or average over several independent records of the signal-in-noise. This increases

the S/N by reducing the level of the noise relative to the level of the signal. The signals, being coherently related to some time reference, sum to  $n$  times their average value, where  $n$  is the number of records. The noise components of the records, being incoherently related to the time reference, sum toward zero. The same rationale may be applied to scanning, specifically, to the detection and discrimination of bond surface variations or flaws in the presence of a high background level. The latter is caused principally by scattering and reflection of signal energy at the various impedance boundaries related to inhomogeneity or anisotropy in the metal adherend. Surface disturbances—bumps or dents—may also contribute. Variations and flaws in the bond surface are ordinarily detected and delineated independent of the direction from which they are ensonified (the transducer couple orientation angle), whereas the contributors to "background" have a directional nature: their level depends on the direction of ensonification. Performing multiple scans, each employing a different orientation angle (direction of ensonification), and averaging them, should yield an increase in the signal-to-background ratio analogous to, and resulting from the same processes as, that observed when averaging signal-in-noise. The scans are averaged point-by-point.

This was done in the present work. Eight scans were obtained essentially simultaneously in the following manner. The transducer couple was stepped from point to point across the specimen surface. At each point the couple was rotated in 45 deg increments from 0 deg orientation angle to 315 deg orientation angle. An acoustic signal was transmitted at each angle to yield eight measurements per point. When the point-by-point scan of the specimen was complete, the measurements were subdivided into eight "subscans," one for each orientation angle, each with one-eighth of the total number of measurements recorded. These were then processed in a variety of ways, but usually by simply averaging all eight. To save time in both scanning and data processing, fewer surface points are evaluated: the area scanned is the same; the resolution is diminished.

Figure 3 is a scan of the P4 specimen using the above described scanning/processing procedure. The scan format was 21 scan lines with 21 points per line. The transducer couple-surface separation distance was the same as for the scan of Figure 2, i.e., the measured signal was the fourth reflection of the internally propagating transverse wave. The acoustic signal was 5 cycles at about 4.5 MHz. As in Figure 2, the bare metal and disbonded areas—left side and center right of scan—are readily discerned, with relatively little degradation in essential resolution. However, the two differently bonded areas (see description of Figure 1, above) which were not discriminable in Figure 2, are now discriminated: the "well-bonded" area at the top of the scan

presents a lower average signal level than does the "poorly-bonded" area at the bottom. This is in agreement with the hypothesis that the reflectivity, as manifested in the signal level, at the bond surface is an indicator of "bondedness," that is, of the acoustic coupling between the bonded layers.

If we extrapolate Rokhlin *et al*'s description of the different boundary states (see above) to our specimens, a well-bonded surface exemplifies a rigid boundary, and a fluid-backed surface (bare metal), a slip boundary. The relative signal levels recorded from these surfaces in Figures 2 and 3 support this notion. And, as evidenced by Figure 3, it is not unreasonable to postulate that the higher signal level measured over the less-well-bonded area indicates poorer acoustic coupling, or diminished adhesion. A disbond, where there is likelihood of entrapped gas, however thin a layer, will manifest with a higher signal level than is recorded over the bare metal. For the disbonded area of this specimen (right center area, Figures 1-3), it is likely that there was water ingress into the end regions, with gas entrapped between. This expectation is supported by the results of the scans, in concert with the "model."

Figure 4 is a diagram of another specimen, called the BC specimen, prepared with the same materials as the P4 specimen, but with differing bond surface conditions and flaws. Again, the view is from the top, or through the plate. The left one-third of the lower (bonded) surface is bare metal, the center one-third is rubber bonded according to the accepted TRI rubber-to-metal bonding procedure, and the right one-third is rubber bonded according to the same procedure, but without preparation of the metal surface by grit blasting. Included in the right one-third of the rubber covered area are two circular disbonds formed by masking the circular areas with metal disks during vulcanization of the rubber, then removing the disks after vulcanization to expose two circular bare metal areas. These areas were then sealed with transparent plastic tape to form two air-backed circular flaws in the rubber layer.

Figure 5 is a C-scan of this specimen. The transducer couple-surface separation distance allowed spatial overlap of the reflected incident and reradiated transverse waves; the signal duration allowed temporal overlap. The transducers were resonant at about 0.5 MHz. Initialization, or set-up, was done as follows. A short duration signal was generated and the couple-surface distance was adjusted until the amplitudes of the reflected and reradiated components were about equal. The signal duration was then lengthened until the two wave components overlapped in time. By chance, this yielded an interference null waveform. The measurement gate was positioned over the "offset" portion of the waveform, i.e., over that portion of the

reradiated wave component that was not interfered with by the reflected wave component. Figure 5, then, is the variation in measurement signal amplitude recorded with this set-up. The three different surface conditions, bare, well-bonded and poorly-bonded, as well as the circular flaws are readily discriminated. The image quality is acceptable, but not good.

Figure 6 is a C-scan of the same specimen with the same set-up, but is the average of 8 scans recorded as described earlier (discussion preceding Figure 3). Again, the three bond surface conditions are clearly discriminated, with somewhat better imaging than in Figure 5. (Edge artifacts caused by the transmitter or receiver swinging past the edge of the plate as the couple rotated are more evident in this scan than in that of Figure 3.) The same relative amplitude differences prevail for the different surface and flaw conditions of this specimen as for the conditions and flaws of the P4 specimen.

Figure 7 is a diagram of another specimen, called the GM specimen, prepared with a 1/8 in. thick plate. Again, the view is from the top, or through the plate. As with the P4 and BC specimens, the left one-third of the bonded surface is bare metal. The right two-thirds of the surface is 5109S neoprene bonded to the metal according to the TRI bonding procedure. The circular and diagonal disbonds were formed by rubbing mold release into the metal surface, and omitting the primer/adhesive; the circular area included a small, narrow "vent" to the bare metal area to allow any gas formed during vulcanization to escape. The triangular flaw was prepared by omitting the primer/adhesive over this area. Again, the broken line delimits the area actually scanned. Except for the one-third bare/two-thirds rubber surface allocation, the nature and characteristics of this specimen were unknown to the investigator at the time of scanning.

Figure 8 is a C-scan of this specimen. The incident acoustic signal was 5 cycles at about 4.5 MHz. The transducer couple-plate surface separation distance allowed the receiver to view both the reflected incident wave and the reradiated first reflection of the internally propagated transverse wave, but they were resolved in time. The reradiated wave was gated for measurement. This scan shows that all features of this specimen were clearly discriminated and imaged. It indicates, also, that the portion of the bonded rubber surface below the circular disbond and adjacent to the bare metal area was probably not as well bonded as the rest of the surface (this has not yet been confirmed by any destructive testing). This scan was repeated after moving the receiver's field of view to the locus of the third internal reflection of the transverse wave, and to the locus of the fifth reflection.

The transducer couple-surface separation distance was then reduced to "zero," i.e., in contact with the plate surface (in reality, there was about a 0.010 in. thick water layer separating them). The geometry of the couple/plate placed the receiver's field of view over the locus of the fourth internal reflection of the transverse wave. (The third and fifth reflections were also detected, but at about one-tenth the amplitude of the fourth, and they were resolved in time.) The acoustic signal, as determined from the waveform of the detected, internally reflected signal, was the same as in the preceding scan: about 5 cycles at about 4.5 MHz.

Figure 9 is the C-scan recorded with "zero" couple-surface separation distance, i.e., "in contact" with the plate. All of the programmed features of the bond surface are again discriminated and are as well, if not better, imaged than in Figure 8. The principal evaluative difference between these two scans is that Figure 9 does not indicate a poorly-bonded area below the circular disbond.

## DISCUSSION

The C-scans presented here are typical of those being achieved using a resolved-signal, transverse-wave measurement format. The transverse wave, by itself, is demonstrably sensitive to programmed differences in "bondedness," i.e., to the quality of the bond as defined by the procedures used to prepare it, and to flaws—separations between the adherends—in the bond surface. Differently bonded surfaces and flaws manifest as differences in recorded signal amplitude in a predictable way. Disbonds—areas with zero adhesion—are readily detected and imaged. While the transverse wave yields a relative indication of differences in bond quality, it remains to be demonstrated that there is a usable relationship between the measurement—reflected signal amplitude—and bond, or adhesion, "strength."

Of practical import is the simplicity of the method. Precise frequency control is not required, although the results to date indicate that some frequency versatility may be; i.e., there appears to be a wavelength-thickness dependence which needs further investigation. Transducer-surface separation distance is not critical and, theoretically, may be reduced to zero, i.e., to surface contact. The principal advantage of the latter is that it would eliminate the need to immerse the object being examined. The obvious disadvantage of a contact implementation is potential variations in signal level—the measurement—due to poor acoustic coupling between the transducers and the surface of the object.

Information about the bond surface is all contained in the internally propagated, reflected and reradiated wave, transverse or other. Gating out that component of the

detected signal caused by near-surface reflection of the incident wave appreciably reduces the background level in a scan and thus improves the signal-to-background ratio. Recording several different measurements at each interrogated point on the bond surface and then averaging these is also effective in improving the signal-to-background ratio. The different measurements are obtained by ensonifying the point from different directions; in our work we used eight directions, each 45 deg around the compass. Different scans are thus produced, and averaging these is akin to the process of averaging signal-in-noise: the noise (background) sums to a low level, while the signal level is relatively unaffected. Application of this procedure enabled discrimination of differing quality bond surfaces in our specimens (see Figures 2 and 3) that were not discriminable using a unidirectional scan. The method we implemented, rotating the transducers, was time-consuming, and to compensate, we interrogated many fewer points of the bond surface; imaging of flaws was, accordingly, poor. An array of transducers scanned electronically would accomplish the eight (or however many) "scans" in essentially the same amount of time that is needed to achieve a single scan, and with good image quality.

A C-scan facilitates detection and delineation of the features of a bond surface. However, depending on how the measurements are assigned to the different colors or shades used, and how many of these there are, the scan can as easily mask or smear features as enhance or delineate them. Too many shades or too many colors can make interpretation of the scan difficult. We have found five colors, or shades, to be satisfactory for discriminating the essential features of a (programmed) bond surface. The algorithm used for distributing the measurement values among the shades is simply to assign an equal number of data points to each shade (amplitude bin). This results in five amplitude bins with differing widths, i.e., magnitudes of differences between maximum and minimum values. This algorithm was employed for all of the scans presented here; its effectiveness is evident in the figures. Sometimes, when the distribution of measurement levels is obviously multi-modal, operator selection of bin values based on the distribution will improve the "quality" of the display (C-scan), generally without, however, significantly altering the relative discriminability of the bond surface features. The decision/distribution process for doing this is a rational one that does not require any *a priori* knowledge of the bond surface; the levels/shades established are dictated by the distribution of the measurement levels.

## CONCLUSIONS

Based on our work to date, and the discussion and results presented here, we conclude that:

1. A resolved-signal, transverse-wave measurement format is sensitive to, and readily discriminates differences in, bond surface quality and disbonds. The format does not require precise frequency control, and may potentially be used with transducers in contact with the surface of the object, thus eliminating the need for immersing the object.
2. Forming multiple scans of the bond surface by ensonifying in different directions at each interrogation point, then averaging the scans on a point-by-point basis can improve the signal-to-background ratio, and thus the discriminability of bond surface characteristics or features. It does not improve feature resolution.
3. A simple algorithm to distribute the data points into five amplitude, or level, bins with an equal number of points in each bin is effective for displaying the results of a bond surface scan in a C-scan format.

## REFERENCES

1. S.I. Rokhlin, M. Hefets and M. Rosen, "An Ultrasonic Interface-Wave Method for Predicting the Strength of Adhesive Bonds," *J. Appl. Phys.* **52**, 2847 (1981).
2. S.I. Rokhlin and D. Marom, "Study of Adhesive Bonds Using Low-Frequency Obliquely Incident Ultrasonic Waves," *J. Acoust. Soc. Am.* **80**, 585 (1986).

P4 SPECIMEN

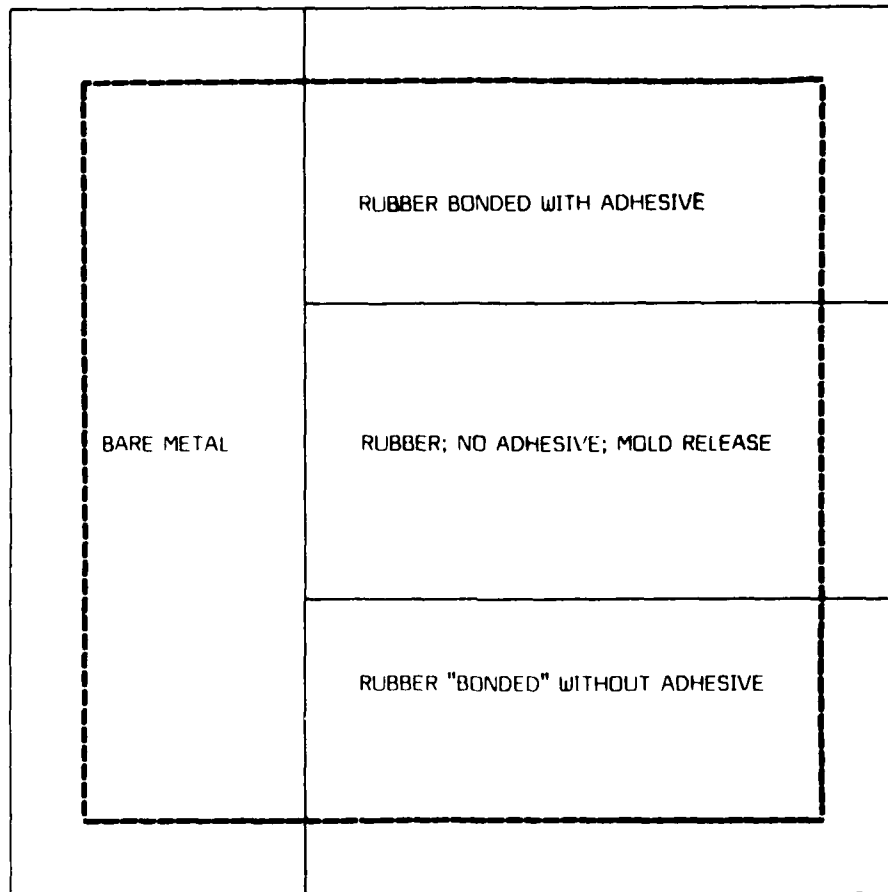


Figure 1. Diagram of the bond surface of a rubber/metal laminate, called the P4 specimen, with three programmed areas of differing bond quality.

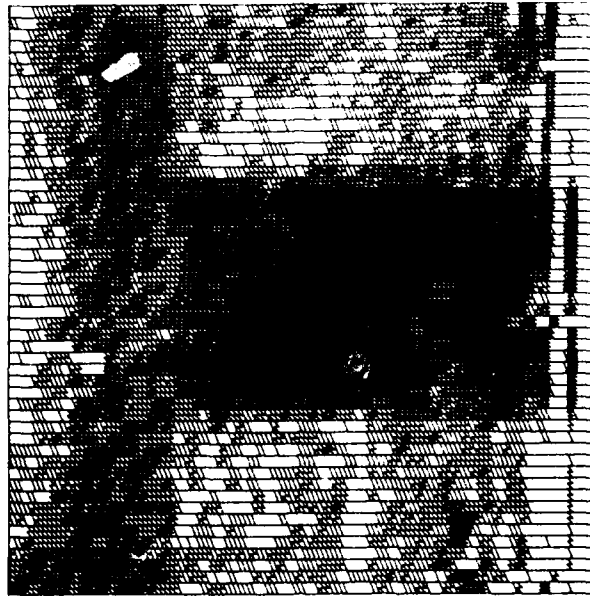


Figure 2. C-scan of the P4 specimen obtained using the resolved-signal, transverse-wave measurement format. The acoustic signal was 5 cycles at a frequency of about 4.5 MHz. The level of the first reflection of the internally propagated transverse wave was measured. Signal level is indicated by the darkness, or density, of the points; the higher the level, the darker the points. The scan format is 128 points in the x-direction, 51 lines in the y-direction.

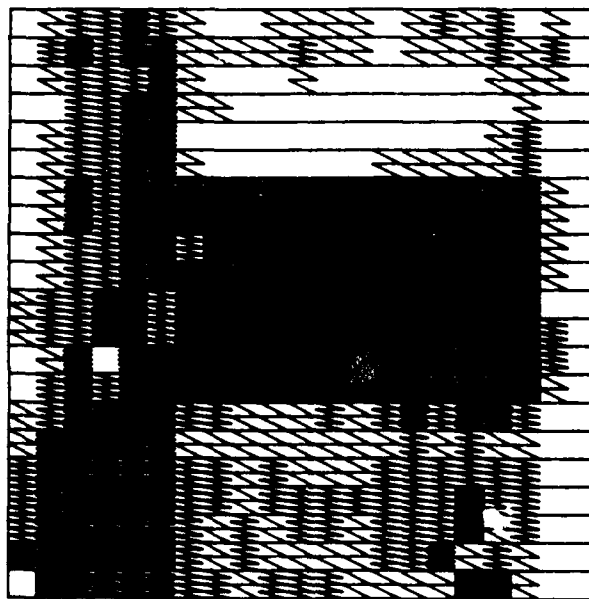


Figure 3. C-scan of the P4 specimen obtained by averaging eight different scans (see text). The signal, measurement and display formats are as described for Figure 2. The scan format is 21 points in the x-direction, 21 lines in the y-direction. Note the improved discriminability of the upper and lower bonded areas (see Figure 1)

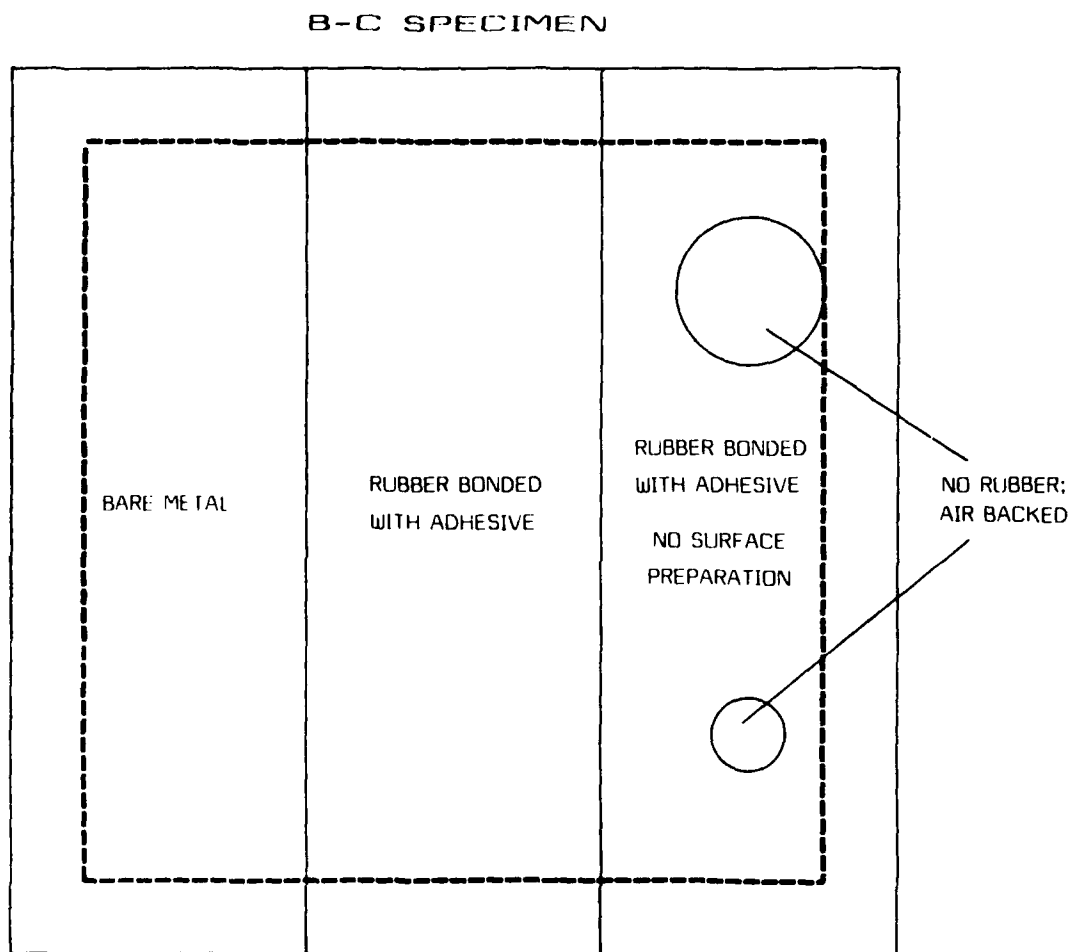


Figure 4. Diagram of the bond surface of a rubber/metal laminate, called the BC specimen, with two programmed areas of differing bond quality and two programmed, air-backed circular disbonds.



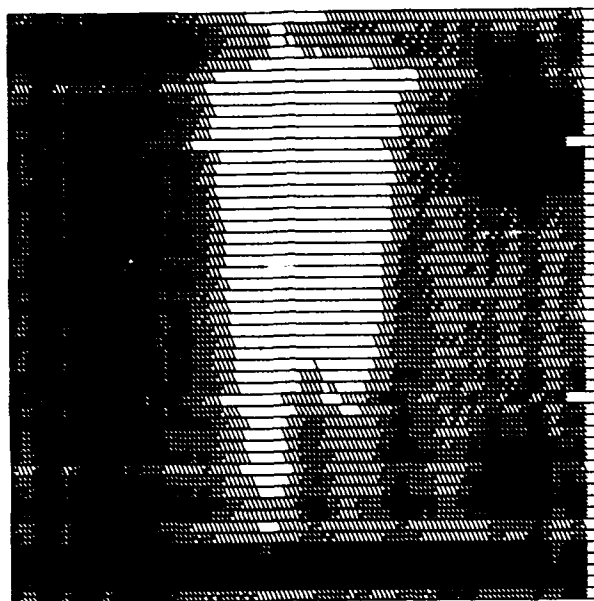


Figure 5. C-scan of the BC specimen obtained using the resolved-signal, transverse-wave measurement format. The signal was 10 cycles at a frequency of 0.4 MHz, which allowed overlap of the reflected and reradiated waves to form an interference-null waveform. The "offset" portion of the detected signal—that portion of the reradiated wave not interfered with by the specularly reflected incident wave—was gated and measured. The display format is as described for Figure 2.

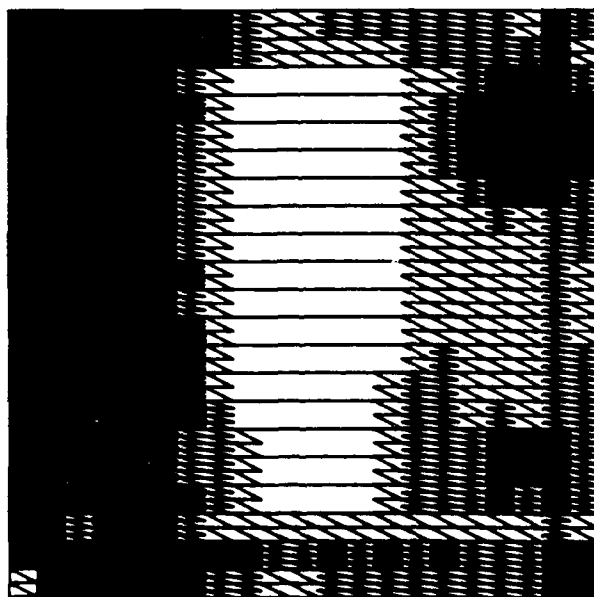


Figure 6. C-scan of the BC specimen obtained by averaging eight different scans (see text). The signal, measurement and display formats are as described for Figure 5.

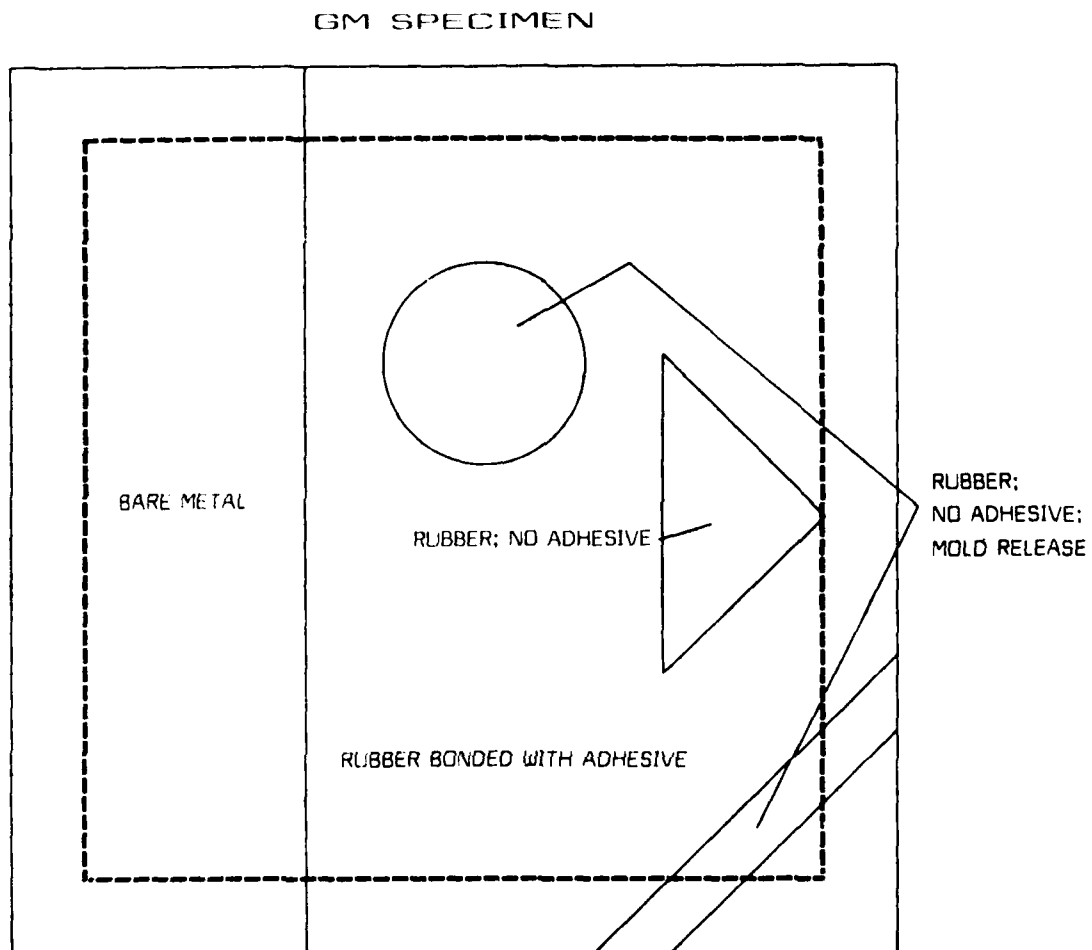


Figure 7. Diagram of the bond surface of a rubber/metal laminate, called the GM specimen, with three disbonded areas of two different kinds in the laminated portion of the surface.



Figure 8. C-scan of the GM specimen obtained using the resolved-signal, transverse-wave measurement format. The acoustic signal was 5 cycles at a frequency of about 4.5 MHz. The measurement, display and scan formats are as described for Figure 2.



Figure 9. C-scan of the GM specimen obtained using the resolved-signal, transverse-wave measurement format. The transducer couple-surface separation distance was about 0.010 in., essentially "in contact." The measured signal was the fourth reflection of the internally propagated, reflected and reradiated transverse wave.

## THERMOGRAPHIC ANALYSIS OF STRESS CONCENTRATIONS IN A DAMAGED CROSS-PLY LAMINATE

Daqing Zhang and Bela I. Sandor  
Department of Engineering Mechanics  
University of Wisconsin-Madison  
Madison, WI 53706

### ABSTRACT

Based on a new thermoelasticity theory for damage, an effective stress concentration factor  $K^e$  is defined for thermographic stress analysis (TSA; also SPATE method). This method was used to measure the stress concentrations due to transverse matrix cracking in a  $[0/90]_5$  glass/epoxy laminate subjected to static and cyclic loading. With characteristic full-field stress measurements,  $K^e$  is not unique. A three-parameter Weibull function reveals the distribution of  $K^e$  with excellent results. When 50% probability values were chosen, a three-parameter expression between  $K^e$  and cycles of loading, and a linear relationship between  $K^e$  and stress in static loading were established. It has been shown that  $K^e$  decreases with increased damage, and that once  $K^e$  reaches unity, the laminate is in a uniform and stable damage state, which is equivalent to the characteristic damage state (CDS) defined by others.

### 1. INTRODUCTION

Transverse matrix cracking in cross-ply laminates results in stiffness reduction, stress redistribution, stress concentration, delamination and fiber fracture. Over the last 20 years, the transverse cracking associated with degradation of mechanical properties in composite laminates under static and dynamic loading has been the subject of extensive theoretical, numerical and experimental research. Several proposed analytical models in terms of strength and linear fracture mechanics can be used to predict the first-ply cracking strain, cracking density, and stress distribution<sup>(1-7)</sup>.

In experimental aspects, prior research was mainly on investigating transverse cracking density and measurements of stiffness reduction under static and cyclic loading. It is not possible to use conventional experimental techniques to determine the stress redistribution

quantitatively due to progressive material damage; the stress redistribution can be determined only by theoretical modeling and numerical analysis. Following recent developments, quantitative, full-field, nondestructive, and noncontacting stress measurements are possible by measuring the change in infrared radiant emission produced by dynamic loading. A thermoelasticity theory for damage in anisotropic materials has been developed by introducing an effective damage tensor<sup>(8)</sup>. This theory has been used in conjunction with the TSA method to evaluate the damage parameter  $D$ , normalized mass density  $\rho^e/\rho$ , and effective Young's modulus  $E^e$  in anisotropic materials<sup>(8)</sup>. In this paper this theory will be used to study stress redistribution in a damaged cross-ply laminate under static and cyclic loading conditions.

### 2. METHOD OF THERMOGRAPHIC STRESS ANALYSIS

The TSA signal  $S$  recorded by a sensitive and linear detecting system is the cyclic change  $\Delta\phi$  in the infrared emission  $\phi$  resulting from a small temperature change  $\Delta T$ , at the surface of a cyclically loaded specimen. The signal is given by (9)

$$S = \Delta\phi = 3eBT^2 \Delta T \quad (1)$$

where  $e$  is the surface emissivity,  $B$  is the Stefan-Boltzman constant, and  $T$  is the absolute temperature.

For an undamaged orthotropic material in a biaxial state of stress,  $\Delta T$  can be expressed as<sup>(10)</sup>

$$\Delta T = - \left( \frac{T}{\rho C_p} \right) (\alpha_1 \Delta\sigma_1 + \alpha_2 \Delta\sigma_2) \quad (2)$$

where  $C_p$  is the specific heat at constant pressure,  $\rho$  is the mass density,  $\alpha_1$  and  $\alpha_2$  are the coefficients of thermal expansion in the directions of principal axes, and  $\Delta\sigma_1$  and  $\Delta\sigma_2$  are the stress changes in the corresponding directions.

A generalized thermoelasticity theory for damage in anisotropic materials can be expressed as<sup>(8)</sup>

$$\Delta T = \frac{T}{\rho^e C_e} \left( \frac{\partial M_{ij}}{\partial T} C_{jk} \epsilon_k + M_{ij} \frac{\partial C_{jk}}{\partial T} \epsilon_k - M_{ij} C_{jk} \alpha_k \right) \Delta \epsilon_i \quad (3)$$

where  $C_e$  is the specific heat capacity for  $\epsilon_i = 0$ ,  $M_{ij}$  is the effective stress tensor,  $C_{jk}$  is the stiffness matrix, and  $\epsilon_k$  is the strain tensor.

Substituting Eq. 3 into Eq. 1 and considering a uniaxial stress case, Eq. 1 can be written as

$$S = \left( - \frac{3eBT^3\alpha}{\rho C_p} \right) \left[ \frac{\Delta\sigma}{(1-D)^2} \right] \quad (4)$$

or

$$S = C_f \left[ \frac{\Delta\sigma}{(1-D)^2} \right] \quad (5)$$

where  $C_f = (-3eBT^3\alpha/\rho C_p)$  is the calibration factor corresponding to the state of undamaged material and  $D$  is the damage parameter.

### 3. MATERIAL AND EXPERIMENTS

Material used in this investigation is a glass fiber/epoxy laminate with  $[0/90_5]_s$  lay-up. This laminate is a special case of orthotropic composites in which the strength and stiffness in the  $0^\circ$  direction are much lower than those in the  $90^\circ$  direction. Figure 1 shows the geometry of the laminate. The Young's modulus and the ultimate strength in one of the principal material symmetry axes are 11.4 GPa and 110 MPa, respectively. A typical loading and unloading behavior of the laminate is shown in Fig. 2; the strains were measured by an extensometer. When the static stress reached 67 MPa, which is 58% of the ultimate strength, the first crack occurred. A knee point is shown in Fig. 2 with a rapid increase of strain and without increase of stress. Once the first crack formed the specimen was unloaded. A nondestructive cyclic stress range  $\Delta\sigma = 10$  MPa (with the peak stress equaling 10% of the material's ultimate strength) with a cyclic stress ratio of  $R = 0.1$  was applied for the full-field measurements of TSA. After the area scan was completed, the static loading was set to generate a second crack. Area scans for progressively more transverse cracks under damaging prior static loading and corresponding typical line plots are illustrated in Fig. 3. The developments of transverse cracks due to cyclic loading are shown in Fig. 4. The changes in signal  $S$  caused by stress redistribution in these scanned areas clearly reveal the transverse cracks and stress concentrations in the surface ply of the laminate (color photographs provide much better details of the stress patterns).

### 4. DEFINITION OF EFFECTIVE STRESS CONCENTRATION FACTOR $K^e$

Equation 5 can be expressed as<sup>(8)</sup>

$$\Delta\sigma^e = S \frac{(1-D)}{C_f} \quad (6)$$

where  $\Delta\sigma^e$  is the effective stress range after damage occurred.

Equation 6 may also be written as

$$(\Delta\sigma^e)_a = S_a \frac{(1 - D_a)}{C_f} \quad (7)$$

where  $(\Delta\sigma^e)_a$ ,  $S_a$ , and  $D_a$  are average effective stress range, average signal and average damage parameter of the scanned area, respectively.

On the other hand, at any specific point of the scanned area, Eq. 6 has the form

$$(\Delta\sigma^e)_s = S_s \frac{(1 - D_s)}{C_f} \quad (8)$$

where  $(\Delta\sigma^e)_s$ ,  $S_s$ , and  $D_s$  are effective stress range, the TSA signal and damage parameter at a specific point, respectively.

Thus, an effective stress concentration factor  $K^e$  can be defined as

$$K^e = \frac{(\Delta\sigma^e)_s}{(\Delta\sigma^e)_a} \quad (9)$$

The distributions of  $(\Delta\sigma^e)_s$  and  $(\Delta\sigma^e)_a$  are schematically shown in Fig. 1.

The characteristics of  $K^e$  are significant as follows:

Equation 9 has the same physical meaning as the stress-concentration factor defined for isotropic materials.  $(\Delta\sigma^e)_s$  and  $(\Delta\sigma^e)_a$  correspond to notch tip stress and nominal stress in a notched member, respectively.

Equation 9 can be used to describe the characteristics of transverse cracking caused by static or cyclic loading as well as other damaging sources.

$K^e$  decreases with increased damage, because  $(\Delta\sigma^e)_a$  increases with increased damage or an increase in transverse cracks (referring to the changes in signal  $S$  shown in Figs. 3 and 4) and  $(\Delta\sigma^e)_s$  may stay the same or may decrease since the delamination reduces the stress concentration.

We define the phenomenon of damage evolution and

distribution of stress concentrations uniquely characterized by the TSA method as damage absorption spectra. On the basis of the line spectra shown in Figs. 3 and 4, effective stress concentration factors  $K^e$  were calculated (using Eq. 9) for both static and cyclic loadings, Figs. 5 and 6. Note that the maximum  $K^e$  is approximately 1.8 and the minimum is 1.0 for both loading conditions, and the  $K^e$  of a fixed point (shown in Fig. 5) on the earliest crack decreases as the stress increases (or as damage increases). The effective stress concentration factors are functions of stress range  $\Delta\sigma$  and progressive cycles  $N$  (see Fig. 6).

## 5. STATISTICAL DISTRIBUTION OF $K^e$ AND PREDICTION OF CHARACTERISTIC DAMAGE STATE (CDS)

Experimental data normally show some scatter, and so do the effective stress concentration factors obtained by the TSA method. It is important to apply statistical methods to analyze the distribution of these data. The three-parameter Weibull distribution function is employed to describe the distributions of effective stress concentrations. The Weibull distribution function is given by<sup>(11)</sup>

$$P(x) = 1 - \exp \left[ - \left( \frac{x - x_u}{x_0} \right)^\phi \right] \quad (10)$$

where  $\phi$ ,  $x_0$ , and  $x_u$  are the shape, scale, and location parameters.

Three-parameter Weibull function has been widely used in the analysis of statistical properties of fatigue life and crack length distribution in metallic materials, and of static strength and fatigue life distributions in composite materials. However, the two-parameter Weibull distribution function, assuming  $x_u$  to be zero, is also applied in many situations. This is so because the two parameters may be easily estimated if a substantial accuracy can be assured. Whether the distribution of chosen data is best presented by a three-parameter or a two-parameter Weibull function depends on the data plotted on a Weibull paper showing a linear relation.

The data for effective stress concentration factors for statistical analysis were obtained from 25 mm wide

transverse cracks, which are the same width as the specimen shown in Fig. 1. The total number of data points obtained from the TSA scans is 45, and each of the data represents the stress concentration in a line segment of 0.5 mm length. The data shown in Fig. 7 represent a variation of the effective stress concentrations in one transverse crack with progressively increased damage produced by static loading. As shown in Fig. 6, the  $K^e$  values decrease with increasing cycles.

The parameters of the Weibull distribution obtained by the least squares method<sup>(12)</sup> are listed in Tables 1 and 2 (only the parameters for the cyclic stress range of  $\Delta\sigma = 52$  MPa are given in Table 2). The distributions of  $K^e$  are plotted on Weibull papers shown in Figs. 8 and 9. Some of the values of  $x_u$  in Table 1 and 2 are small and others are zero, so in this case the two-parameter Weibull function can be used to describe approximately the distributions of the effective stress concentration factors.

With regard to damage, Reifsnider et al.<sup>(13)</sup> defined a characteristic damage state (CDS) as a laminate property. The damage state is considered unique for each laminate stacking sequence. It was shown that at this state the transverse cracks were uniformly distributed and retained at a stable pattern of the ply cracks. As discussed before,  $K^e$  decreases with increased damage. When  $K^e$  reaches unity, the material is in a uniformly damaged and stable state, so this state is equivalent to the characteristic damage state. In order to predict this state, 50% probability values of  $K^e$  are chosen and the following equations are established based on these values.

$$K^e = 2.82 - 0.017 \sigma \quad \text{for static loading} \quad (11)$$

$$K^e = A \left( 1.0 + \frac{C}{N^\beta} \right) \quad \text{for cyclic loading} \quad (12)$$

where A, C, and  $\beta$  are experimental constants and are presented in Table 3. The characteristic damage state can be obtained from the two equations by setting  $K^e = 1$  for either the static or the cyclic loading case; such curves are shown in Figs. 7 and 10. The stress and cycles when  $K^e = 1$  are presented in Tables 1 and 2.

## 6. CONCLUSIONS

In terms of the thermoelasticity theory for damage, the definition of effective stress concentration factor for the TSA method demonstrates that this parameter adequately characterizes the stress redistribution and damage in a cross-ply laminate. It is shown that the distribution of  $K^e$  obeys the Weibull distribution. As predicted when  $K^e$  approaches unity, the material is in a homogeneous and stable damage state which is equivalent to the characteristic damage state defined by Reifsnider. Therefore, the definition is a realistic and rational description of damage. The experiments showed that the TSA method can be applied to detect sub-surface cracks and measure the full-field stress redistribution in a damaged composite material.

## 7. ACKNOWLEDGMENT

The authors would like to thank Professor R. E. Rowlands for providing test material.

## REFERENCES

- 1 Hahn, H. T. and Tsai, S. W., "On the Behavior of Composite Laminates after Initial Failure," *J. Composite Materials*, 1974, pp. 288-305.
- 2 Garrett, K. W. and Bailey, J. E., "Multiple Transverse Fracture in 90° Cross-Ply Laminates of a Glass Fiber-Reinforced Polyester," *J. Material Science*, 1977, pp. 157-168.
- 3 Manders, P. W., Chou, T. W., Jones, F. R. and Rock, J. W., "Statistical Analysis of Multiple Fracture in 0/90/0 Glass Fiber/Epoxy Resin Laminates," *J. Materials Science*, 1983, Vol. 18, pp. 2876-2889.
- 4 Highsmith, A. L. and Reifsnider, K. L., "Stiffness-Reduction Mechanisms in Composite Laminates," *ASTM STP 775*, 1982, pp. 103-117.
- 5 Han, Y. M. and Hahn, H. T., "A Simplified Analysis of Transverse Ply Cracking in Cross-Ply Laminates," *Composites Science and Technology*, 1988, Vol. 31, pp. 165-177.
- 6 Ohira, H., "Analysis of the Stress Distributions in the Cross-Ply Composite after Transverse Cracking,"

- Fifth Int. Conf. on Composite Materials, ICCM-V*, San Diego, CA, 1985, Edited by Harrigan, W. C. Jr., Strife, J. and Dhingra, A. K., pp. 1115-1124.
- 7 Charewicz, A. and Daniel, I. M., "Damage Mechanism and Accumulation in Graphite/Epoxy Laminate," *Composite Materials: Fatigue and Fracture, ASTM STP 907*, Edited by Hahn, H. T., American Society for Testing and Materials, Philadelphia, 1986, pp. 274-297.
  - 8 Zhang, D. and Sandor, B. I., "A Theory of Thermoelasticity for Damage in Anisotropic Materials," submitted to *Fatigue & Fracture of Engineering Materials & Structures*, 1989.
  - 9 Oliver, D. E., "Stress Pattern Analysis by Thermal Emission," Chapter 14, *Handbook of Experimental Mechanics*, Edited by Kobayashi, A. S., Prentice-Hall, 1986, pp. 610-620.
  - 10 Stanley, P. and Chan, W. K., "The Application of Thermoelastic Stress Analysis Techniques to Composite Materials," *Proc. of the 1987 SEM Spring Conf. on Expt. Mechs.*, Houston, 1987, TX, pp. 536-544.
  - 11 Weibull, W., "A Statistical Distribution Function of Wide Applicability," *J. of Applied Mechanics*, Vol. 8, 1951, pp. 293-297.
  - 12 Zhang, D. "Anisotropic Damage: A Thermoelasticity Theory and Verifications," Ph.D thesis, Department of Engineering Mechanics, University of Wisconsin-Madison, 1989.
  - 13 Reifsnider, K. L. and Masters, J. E., "Investigation of Characteristic Damage States in Composite Laminates," American Society of Mechanical Engineers, Paper No. 78-WA/Aero-4, *Winter Annual Meeting*, San Francisco, 1978.

Table 1. Parameters of Weibull Distribution Function Under Static Loading  
Material:  $[0/90]_s$  Laminate

Stress(MPa)	$\phi$	$x_u$	$x_0$	$r$	Mean	$x_{50}$	Prediction
65	22.32	0.06	1.67	-0.983	1.69	1.70	1.67
68	25.23	0.02	1.59	-0.965	1.57	1.58	1.61
77	22.08	0.01	1.46	-0.990	1.44	1.45	1.46
93	19.66	0.00	1.17	-0.961	1.14	1.15	1.17
96	26.09	0.00	1.16	-0.991	1.13	1.14	1.12
103							1.00



Table 2. Parameters of Weibull Distribution Function Under Cyclic Loading  
Material:  $[0/90_5]_s$  Laminate  
 $\Delta\sigma = 52$  MPa and  $R = 0.1$

N(cycles)	$\varphi$	$x_u$	$x_0$	$r$	Mean	$x_{50}$	Prediction
800	14.48	0.05	1.56	-0.993	1.56	1.57	1.54
1520	17.49	0.01	1.47	-0.999	1.43	1.44	1.43
2720	16.61	0.01	1.35	-0.984	1.32	1.34	1.34
4920	14.85	0.02	1.24	-0.991	1.21	1.20	1.27
17130	19.76	0.00	1.19	-0.965	1.16	1.17	1.14
19430	16.34	0.02	1.13	-0.996	1.12	1.13	1.13
27430	16.70	0.02	1.13	-0.993	1.11	1.12	1.10
146000							1.00

Table 3. Experimental Constants as Shown  
in Eq.12 Under Different Cyclic Stress Ranges  
Material:  $[0/90_5]_s$  Laminate

$\Delta\sigma$ (MPa)	A	C	$\beta$
41	0.87	6.34	0.22
52	0.80	4.98	0.25
57	0.85	2.70	0.24

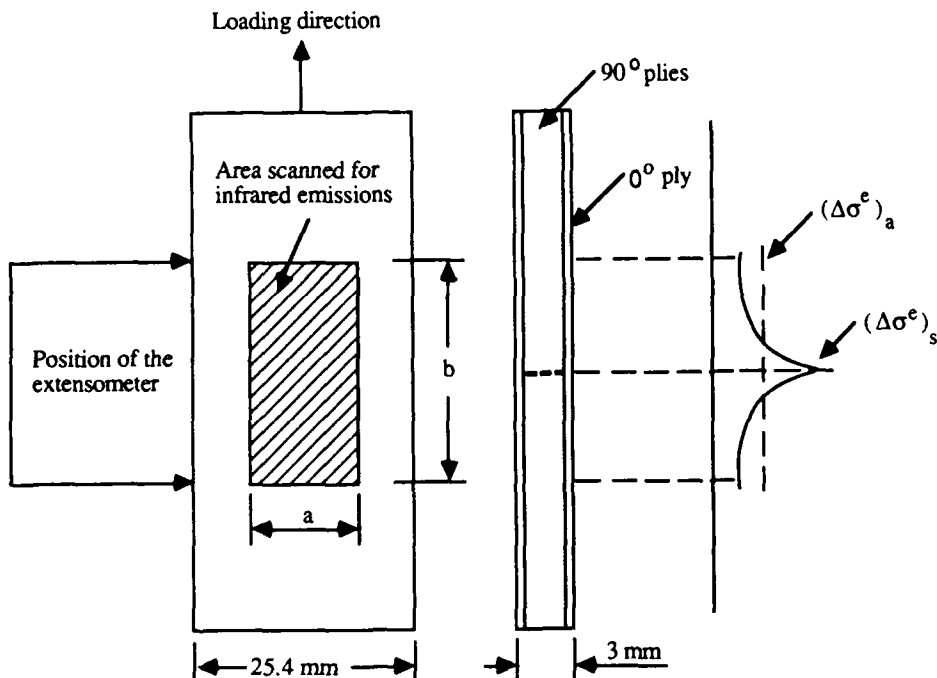


Fig. 1 Schematic diagram of a cracked  $[0/90_5]_s$  laminate.  $a = 11.0$  mm and  $b = 25.4$  mm for the data shown in Fig. 3.  $a = 17.7$  mm and  $b = 25.4$  mm for the data shown in Fig. 4

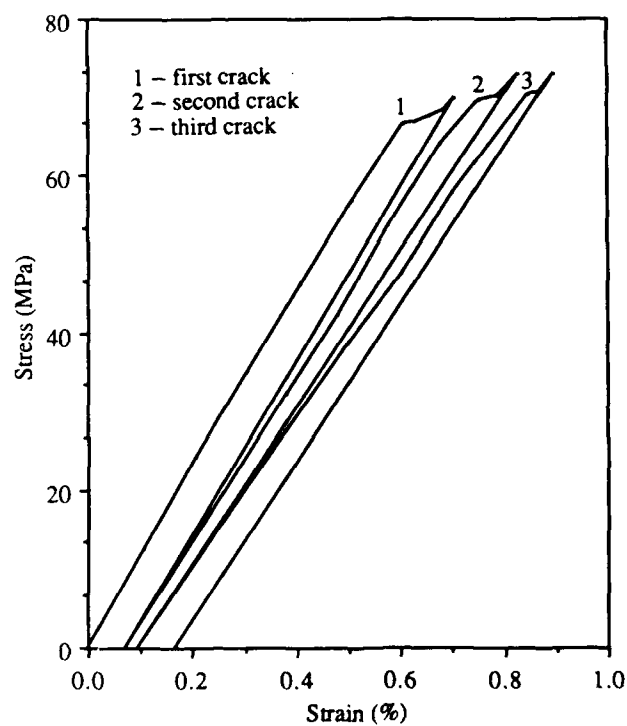


Fig. 2 Typical loading and unloading behavior of  $[0/90_5]_s$  laminate. Note jumps in strain at transverse cracking

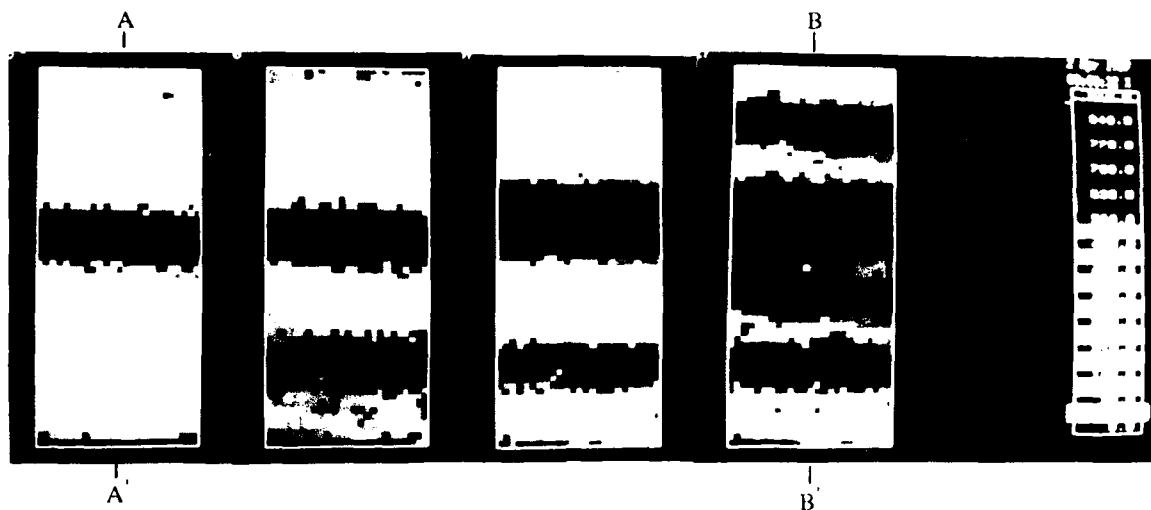


Fig. 3a  $\sigma = 67$  MPa Fig. 3b  $\sigma = 70$  MPa Fig. 3c  $\sigma = 71$  MPa Fig. 3d  $\sigma = 83$  MPa

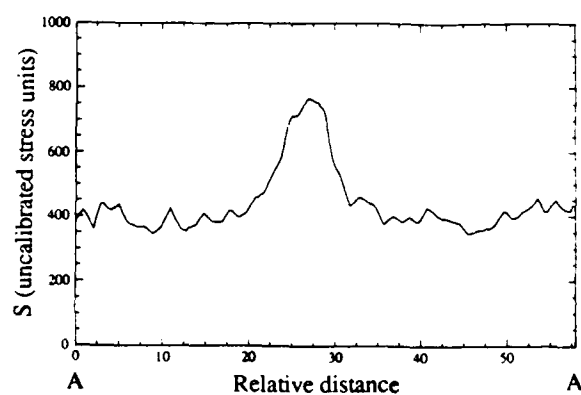


Fig. 3e Line plot on section AA

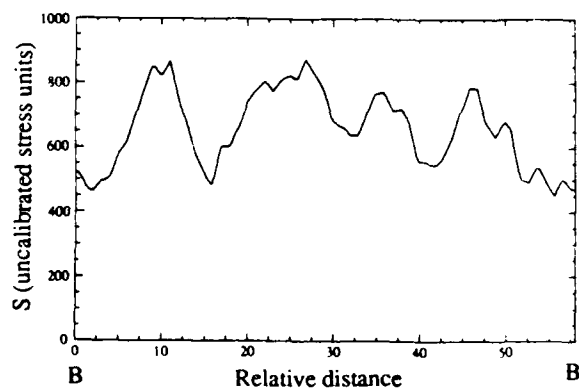


Fig. 3f Line plot on section BB'

Fig. 3 TSA scans of a  $[0/90_5]_s$  laminate at various damaging prior static stresses.  
Nondestructive stresses for TSA:  $\Delta\sigma = 10$  MPa,  $R = 0.1$

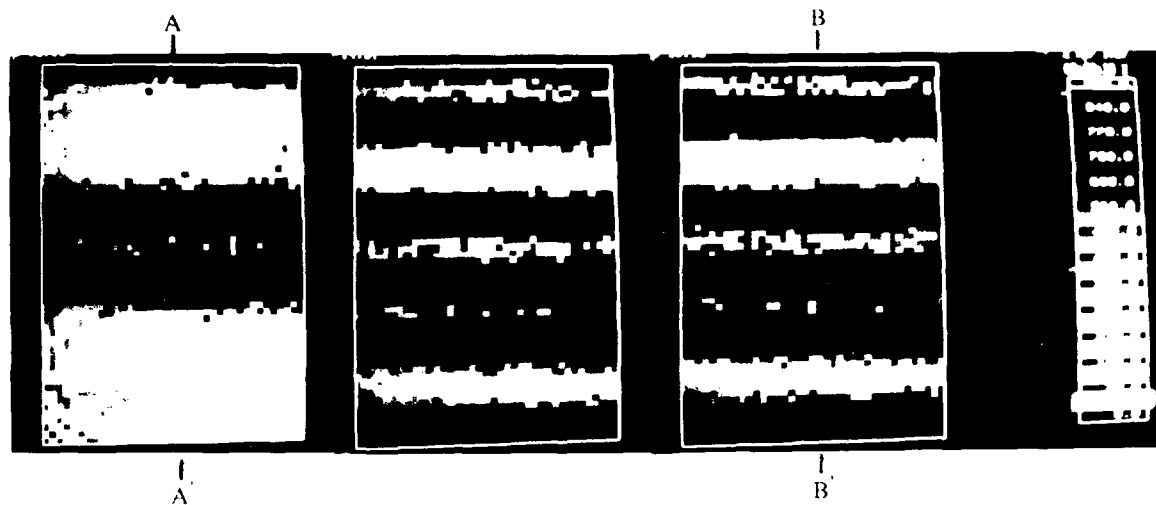


Fig. 4a N=3000 cycles

Fig. 4b N=7500 cycles

Fig. 4c N=10,000 cycles

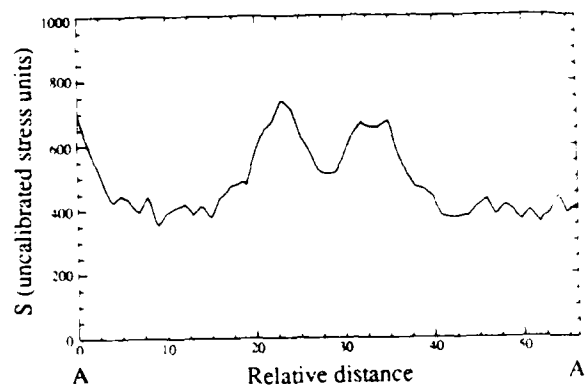


Fig. 4d Line plot on section AA'

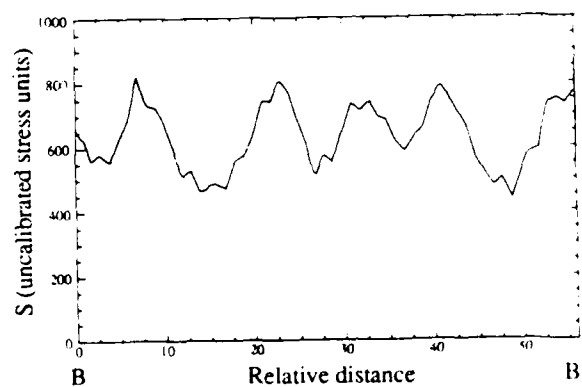


Fig. 4e Line plot on section BB'

Fig. 4 TSA scans of a  $[0/90_5]_s$  laminate at various stages of fatigue damage. Destructive stresses:  $\Delta\sigma = 51$  MPa,  $R = 0.1$  and nondestructive stresses for TSA:  $\Delta\sigma = 10$  MPa,  $R = 0.1$

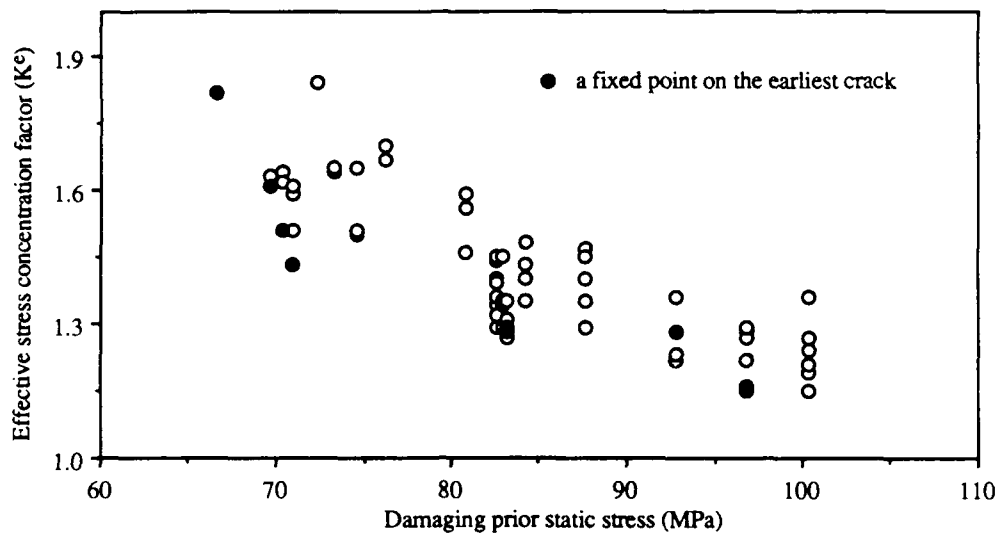


Fig. 5 Stress concentrations of  $[0/90_5]_s$  laminate due to transverse-ply cracking under static loading  
Nondestructive stresses for TSA:  $\Delta\sigma = 10$  MPa,  $R = 0.1$

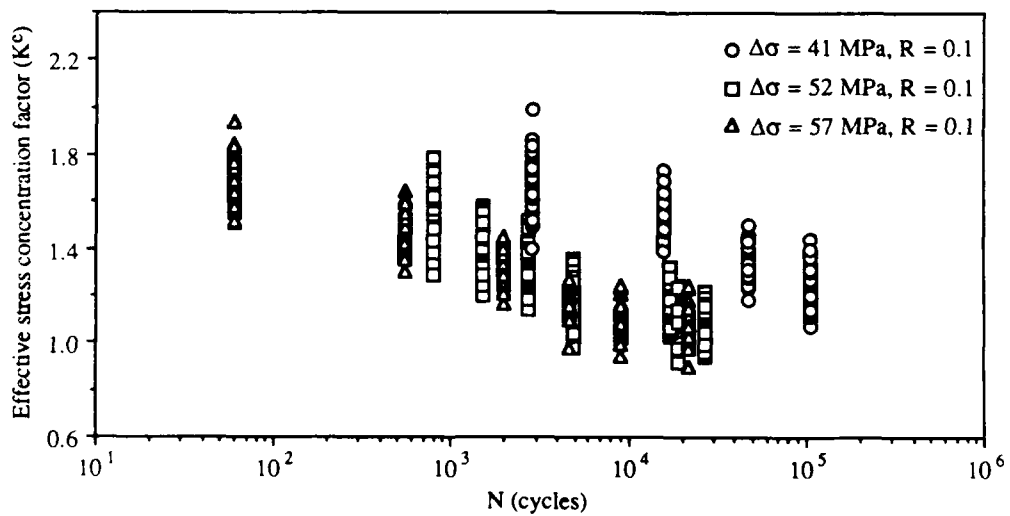


Fig. 6 Effective stress concentrations of  $[0/90_5]_s$  laminate due to transverse-ply cracking under cyclic loading  
Nondestructive stresses for TSA:  $\Delta\sigma = 10$  MPa,  $R = 0.1$

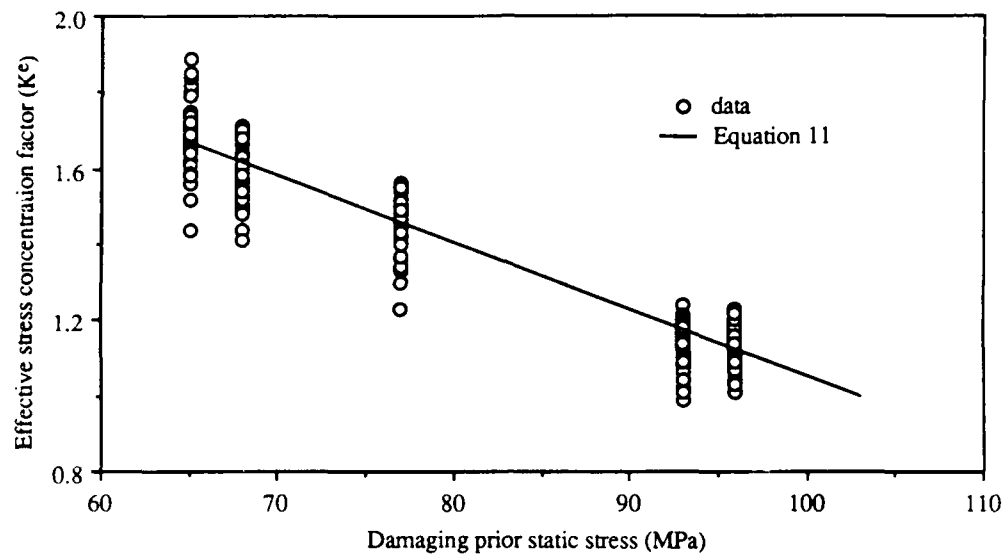


Fig. 7 Effective stress concentration decrease of  $[0/90_5]_s$  laminate with increase of static loading  
Nondestructive stresses for TSA:  $\Delta\sigma = 10$  MPa,  $R = 0.1$

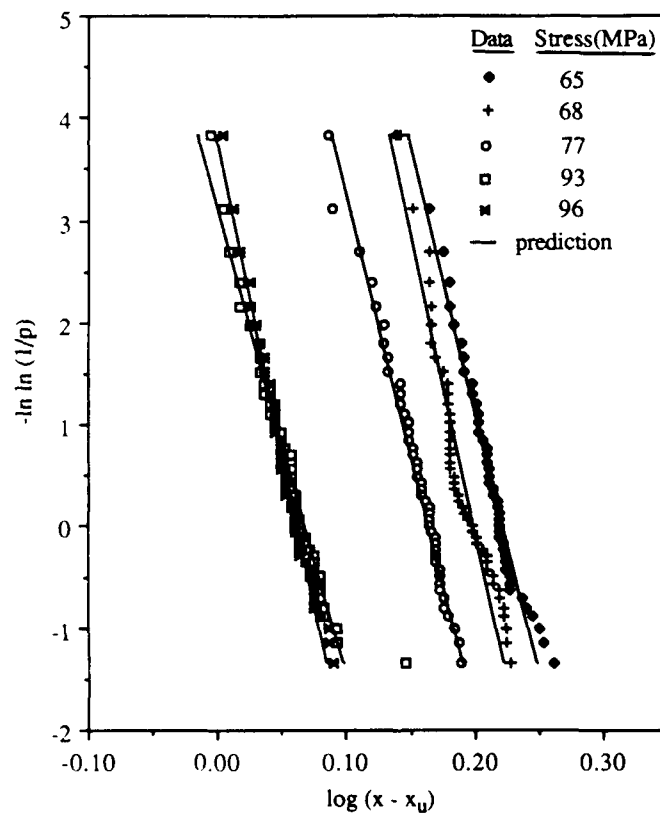


Fig. 8 Distribution of effective stress concentration factor,  $K^e$ , of  $[0/90_5]_s$  laminate under static loading. Data are the same as shown in Fig. 7. Here  $x$  represents the sample of effective stress concentration factor

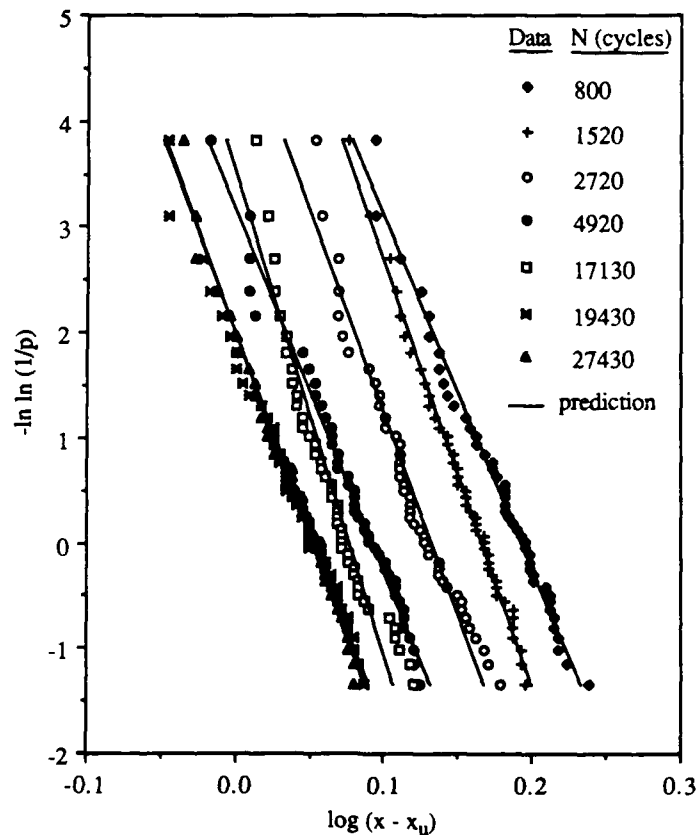


Fig. 9 Distribution of effective stress concentration factor,  $K^e$ , of  $[0/90_5]_s$  laminate under cyclic stresses;  $\Delta\sigma = 52$  MPa,  $R = 0.1$ . Data are also shown in Fig. 6. Here  $x$  represents the sample of effective stress concentration factor

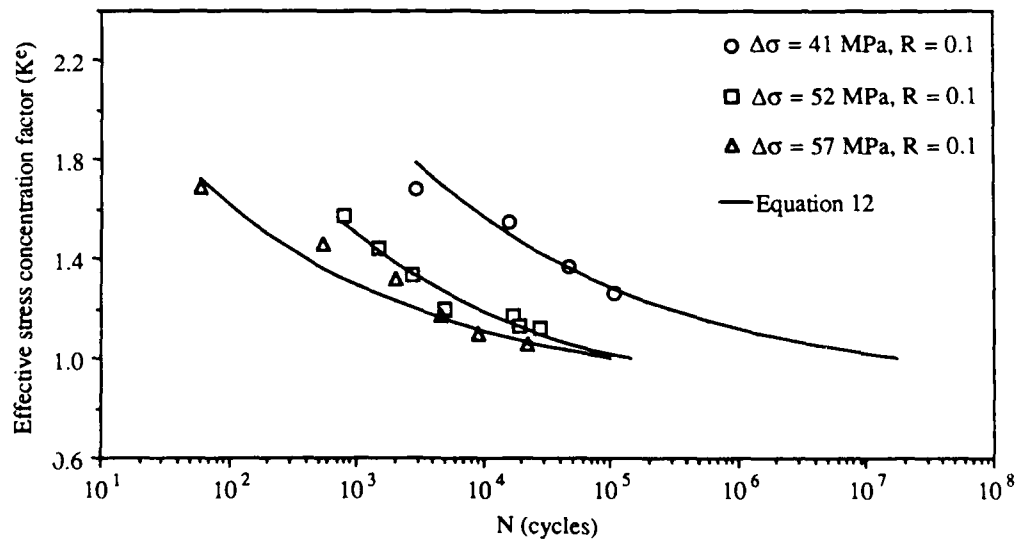


Fig. 10 Effective stress concentration decrease of  $[0/90_5]_s$  laminate with increase of cycles for three different cyclic stress ranges. Data are obtained from Eq. 10 by setting 50% probability  
Nondestructive stresses for TSA:  $\Delta\sigma = 10$  MPa,  $R = 0.1$

# NONDESTRUCTIVE DETECTION OF FLAWS IN CERAMICS USING HOLOGRAPHIC SCANNING LASER ACOUSTIC MICROSCOPE (HOLOSLAM)

A. C. Wey, and L. W. Kessler  
Sonoscan, Inc.  
530 E. Green Street, Bensenville, Illinois

## ABSTRACT

Scanning Laser Acoustic Microscopy (SLAM) is an important nondestructive testing (NDT) tool which provides real-time flaws detection in ceramics with high resolution for imaging the detailed structure of flaws. The SLAM operates in a transmission mode and the micrograph produced by SLAM is, however, a two dimensional (2-D) shadowgraphic view of 3-D object. Because of diffraction, the resultant images are often unfocused. To overcome this problem we developed a holographic image processing technique for SLAM which used the principles of acoustical holography and the calculation of wavefield propagation so that the wavefield could be digitally backpropagated to any plane of specified depth. In this paper, we review the SLAM technology and its application in nondestructive flaw detection for ceramics. We also describe the holographic reconstruction process and demonstrate the power of this technique by providing 3-D localization of flaws in structural ceramics. The actual type, shape, size and depth of voids and inclusions in silicone nitride samples were experimentally determined.

## 1. INTRODUCTION

The mechanical properties of ceramic components are often degraded by the presence of flaws, such as pores, inclusions, and many other microstructural irregularities. The mechanical behavior is very much affected by the size, number, and distribution of internal flaws. For example, for a spherical inclusion in an infinite matrix, the residual stresses resulting from the mismatch in thermal expansion coefficients are approximately proportional to the cubic of the ratio of the radius of the inclusion to the radial

distance from the inclusion (1). The fracture mechanics of pores may be quite different from that of inclusions, but the dependence of strength on pore size can also be described by several statistical models (2). Although the quantitative prediction of mechanical degradation of ceramics as a result of inclusion and/or void is difficult, the application of an appropriate NDE technique to detect and characterize the type, shape and size of defects can be a significant quality-control measure for ensuring the mechanical integrity of ceramic components.



The scanning laser acoustic microscopy (SLAM) is an important branch of acoustic microscopy which uses ultrasound in the range of 10 to 200 MHz to produce high resolution ultrasonic images (3). SLAM has demonstrated its unique capability of real-time detection of flaws such as cracks, voids, inclusions, porosity and delaminations in structural ceramics (4,5). In contrast to the familiar pulse-echo techniques used in most of ultrasonic inspection systems, SLAM operates in the transmission mode so that it can interrogate the entire thickness of the sample in real time. However, the micrograph produced by conventional SLAM is a composite shadowgraphic image which contains both in-focus and out-of-focus information and makes the interpretation of the image difficult. Important information about the size, shape and depth of flaws are lost because of diffraction. To overcome this problem, we have developed a holographic SLAM system which incorporates holographic image reconstruction technique into a modified SLAM to produce hologram of the internal structure of a ceramic sample. This new holographic SLAM can reconstruct an entire object field at any depth from the acquired hologram and provides 3-D information about the object. In this paper, we shall review the SLAM technology and describe how SLAM can actually "see inside" objects and locate defects not evident at the surface. The required modification of a conventional SLAM to acquire both amplitude and phase data and the use of these data in holographic image reconstruction process is described. We demonstrated the power of this technique by identifying the type, size, shape and depth of the flaws in silicone nitride samples.

## 2. SLAM TECHNOLOGY

The SLAM uses high frequency ultrasound in combination with a scanning laser beam detector to create real-time images of elastic characteristics of materials at a microscopic level. Figure 1 illustrates schematically the operation

of a commercially available SLAM. A sample is placed between an insonifying transducer and detector. The transducer is a piezoelectric element and the detector is a scanning focused laser beam.

The transducer transmits a continuous plane wave of ultrasound through the entire thickness of the sample. As the ultrasound travels through the material, defects within the sample spatially alter its transmission. The ultrasound is reflected, refracted or absorbed by internal discontinuities such as cracks, delaminations, voids or inclusions. This results in a nonuniform wave pattern at the other side of the sample, which can be detected by a low power scanning laser. The laser acts as a point-by-point detector of the ultrasound wave motion and can translate information on internal features of the sample into video signals through the use of a photodiode and knife-edge detection technique (6). In order to provide a specularly reflecting surface for the scanning laser beam, the specimen is covered with a partially silvered coverslip.

The variations in ultrasound transmission are displayed on a TV monitor where the bright regions correspond to defect-free areas of high transmission through the sample, whereas, the darker areas correspond to regions of higher ultrasonic attenuation attributed to defects or changes in elastic properties because of scattering, reflection or absorption of ultrasound.

Many potential applications involve imaging defects which are far below the surface of the sample. Such images are actually far-field diffraction patterns. These patterns are easily recognizable with minimal training, and thus identification is routine. However, without a detailed knowledge of the sample, little more than the most basic characterization of the flaws is possible. The regular SLAM micrographs does not explicitly provide important information such as actual size and distribution of

flaws. It is thus expected that the power of SLAM could be greatly enhanced through the use of holography to yield more precise information about the internal structure of a given sample.

### 3. HOLOGRAPHIC IMAGE PROCESSING

To perform holographic image reconstruction, a complex amplitude of acoustic wavefield propagating through the specimen is required and thus phase information of the wavefield must be preserved. The SLAM receiver was modified to become a quadrature receiver<sup>(6)</sup> for practical acquisition and extraction of the necessary amplitude and phase data. Quadrature detector requires multiplying the received signal with two coherent electronic references, one phase shifted 90 degrees with respect to the other. A block diagram of the quadrature receiver is shown in Figure 2.

In SLAM, ultrasonic plane wave propagates through the specimen and is scattered by internal defects. The wavefield is detected at the coverslip by using a scanning laser and knife-edge demodulation. The SLAM imaging processing can be modeled by a simple linear system as shown in Figure 3.a. The system uses two linear filters: one characterizes the wave propagation through the homogeneous portion of the specimen, and the other represents the response of knife-edge detection. To reconstruct images, we employ an inverse filter to compensate for the response of knife-edge detection and another filter to account for diffraction. The reconstruction block diagram is shown in Figure 3.b. The transfer functions for these filters can be found in the reference<sup>(8)</sup>.

The holographic SLAM contains a standard SLAM with modified electronic circuit for quadrature receiver and an IBM Personal Computer AT compatible with a 10 MHz 32 bit co-processor board. The control program was written in the C programming language and runs on the 32-bit co-processor which acts as the main computer using the MS-DOS computer as an

I/O controller. The outputs of quadrature receiver are digitized by a video-rate frame grabber. The data acquisition algorithm extracts phase and amplitude data from the digitized outputs of quadrature receiver and then uses them to reconstruct a complex wavefield. The backpropagation algorithm can digitally propagate the wavefield backward to any plane of specified depth in the specimen in a matter of seconds. The advantage of holographic SLAM system is that by recording one set of holographic data an acoustic micrograph can be produced at any time and at any depth within the sample. With other reflection-mode techniques, sequential scans must be made at each level.

### 4. EXPERIMENTAL RESULTS

We demonstrated the power of holographic SLAM by performing 3-D localization of flaws in silicone nitride specimens. The thickness of test specimens was 5 mm. The ultrasound source used in experiments operated at 105.96 MHz and the field of view was 3 mm by 2.81 mm. The sample was placed 0.3 mm below the coverslip to avoid damage to coverslip and the gap was filled with water. The compressional wave velocity inside the sample was 9,780 m/sec and the velocity of ultrasound in water was 1,500 m/sec. Figure 4 shows a standard SLAM amplitude image which displays diffraction patterns of flaws below the sample surface. One can easily locate flaws from the SLAM image, but may have difficulty in identifying the actual shape, size and depth of the defects.

Figure 5 shows a series of reconstructed images produced by holographic SLAM. It demonstrated that holographic SLAM could focus object in the same fashion as an optical microscope. Figure 5.a displays the reconstructed image at the top surface of the sample which was 0.3 mm below the coverslip. As the images were reconstructed backward at a depth below the sample surface, more defects were brought into focus and consequently the type, size, shape and depth could easily be determined. For example, the solid

black round spot in Figure 5.b, as pointed by an arrow, indicates a void of 100  $\mu\text{m}$  in diameter at a depth of 0.5 mm below the surface. Figure 5.c reveals another 120  $\mu\text{m}$  size void 0.6 mm deep while 6.d shows a 200  $\mu\text{m}$  wide inclusion at 1.2 mm depth. The type of defects being either voids or inclusions could be determined by the fact that void completely blocked the transmission of ultrasound and would show a black solid round spot in acoustic image, while inclusion refracted, but not blocked, ultrasonic transmission and were represented by a donut-type pattern.

## 5. SUMMARY

We have reviewed briefly the principles of scanning laser acoustic microscopy and discussed the required modification of a conventional SLAM to become holographic SLAM. Inverse-filtering techniques used in the digital holographic image process are described. Our experimental results clearly show that holographic SLAM is capable of providing 3-D localization of flaws in structural ceramics. The actual type, size, shape and depth of subsurface defects can be accurately identified by using holographic SLAM.

## ACKNOWLEDGMENT

This work was supported by NSF, National Science Foundation, ISI-8604227.

## References

1. J. Selsing, "internal Stress in Ceramics", J. Am. Ceram. Soc. 44 (8) P. 419 (1961).
2. R. A. Sack, "Extension of Griffith's Theory of Rupture to Three Dimension", Proc. Phys. Soc. London 58, P.729(1946).
3. L. W. Kessler and D. E. Yuhas, "Acoustic Microscopy- 1979", Proc. IEEE, Vol. 67, No. 4, P. 526 (1979).
4. L. W. Kessler and Gasiel, T. M., "Acoustic Microscopy Review: Nondestructive Inspection of Advanced Ceramic Materials", Advanced Ceramic Materials, Vol. 2, No. 7, P. 107 (1987).
5. D. J. Roth, E. R. Generazio, G. Y. Baaklini, "Quantitative Void Characterization in Structural Ceramics by use of Scanning Laser Acoustic Microscopy" Material Evaluation, 45, P. 958 (1987).
6. R. L. Whitman, A. Korpel, "Probing of Acoustic Surface Perturbations by Coherent Light", Applied Optics, Vol. 8, No. 8, P. 1567 (1969).
7. Z. Lin, H. Lee, G. Wade, M. Ovarecz and L. W. Kessler, "Data Acquisition in Tomographic Acoustic Microscopy", Proc. IEEE Ultrasonic Symp., P. 627 (1983).
8. G. Wade and A. Meyyappan, "Scanning Tomographic Acoustic Microscopy: Principles and Recent Developments", SPIE Vol. 768, P. 267 (1987).

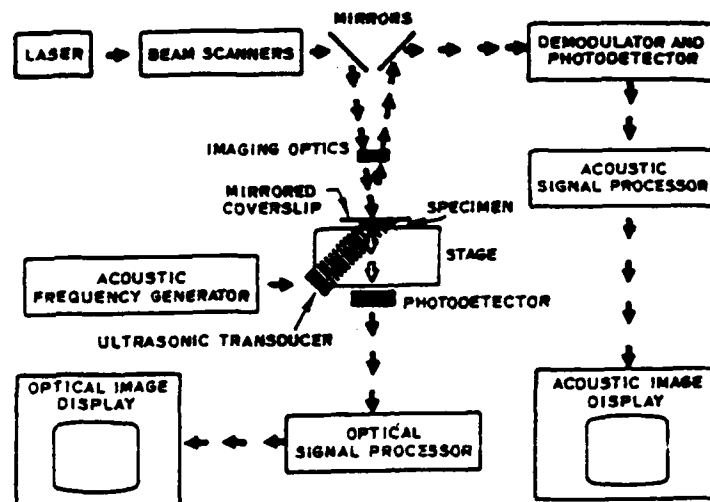


Fig. 1. Schematic Diagram of Scanning Laser Acoustic Microscope.

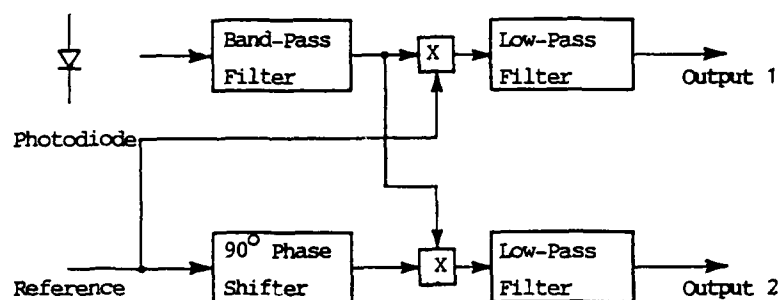


Fig. 2. Block diagram of the quadrature receiver.

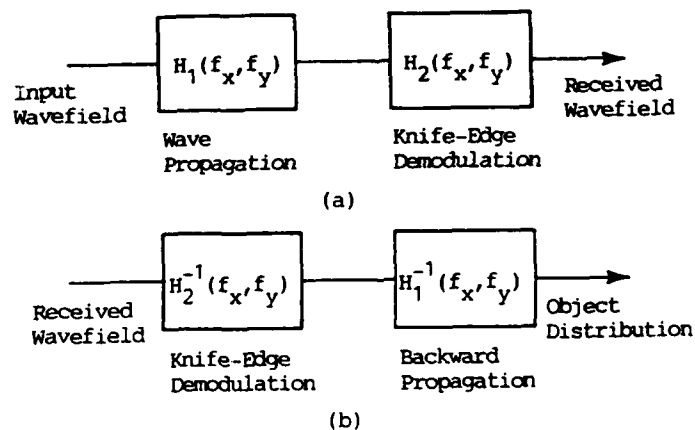


Fig. 3. (a) A linear system model for SLAM imaging process, and (b) inverse filtering for holographic reconstruction.

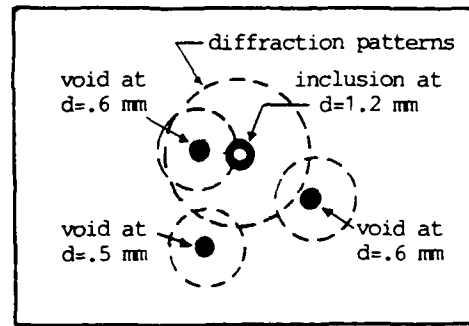
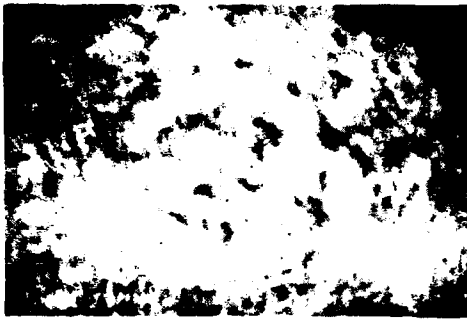


Fig. 4. Standard acoustic image produced by 100 MHz SLAM showing diffraction patterns of internal flaws within ceramics.

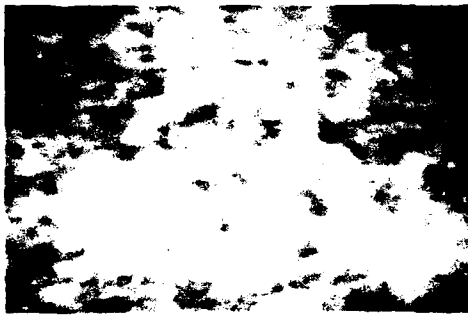


Fig. 5.a Reconstructed image by HOLOSLAM at the top surface of a  $\text{Si}_3\text{N}_4$  sample.



Fig. 5.b Reconstructed image at a 0.5 mm depth showing a 100  $\mu\text{m}$  void.



Fig. 5.c Reconstructed image at a 0.6 mm depth showing two 120  $\mu\text{m}$  voids.



Fig. 5.d Reconstructed image at a 1.2 mm depth with a 200  $\mu\text{m}$  inclusion.

## LASER-INDUCED-FLUORESCENCE INSPECTION OF POLYURETHANE \*

R. H. Hill, Jr.  
Southwest Research Institute  
Instrumentation and Space Research Division  
6220 Culebra Road  
San Antonio, TX 78284

and

H. O. Feuer, Jr.  
U. S. Army Belvoir  
Research, Development, and Engineering Center  
Materials, Fuels, and Lubricants Laboratory  
Ft. Belvoir, VA 22060-5606

### Abstract

Laser-induced fluorescence has been used as the basis for a new nondestructive-inspection technique. With the monochromaticity and power densities available with lasers, molecular transitions that are not normally thought of as fluorescent can be probed. For instance, some chromophores that exhibit ultraviolet absorption can be induced to fluoresce using laser excitation and detection in the visible-wavelength region of the spectrum. Quantitative measurements show that there is sometimes a very strong correlation between the laser-induced fluorescence and some physical characteristic of the material. Many times this is due to the fact that fluorescence reveals relationships between molecular functional groups -- in contrast to infrared-absorption techniques, which are mainly used to reveal only the presence of certain groups. Laser-induced fluorescence can be used as a monitor because alterations of these relationships occur during degradation processes. A strong correlation between laser-induced-fluorescence intensity and tensile strength of several polyurethane-based systems has been demonstrated. Successful laboratory experiments employing fiber-optic bundles indicate that practical implementation of this method is possible. A portable instrument to determine the physical condition of fabric-reinforced polyurethane fuel tanks used by the U.S. Army is one future application, but the method may also be applicable for use on other elastomeric materials.

---

\* The findings in this report are not to be construed as an official Department of the Army position unless designated by other authorized documents. Use of trade names or manufacturers in this report does not constitute an official endorsement or approval of the use of such hardware or software.

## 1.0 INTRODUCTION

### 1.1 THE PROBLEM

The U.S. Army currently has a large number of fabric-reinforced elastomer tanks, ranging in size from 100 gallons to 200,000 gallons, used for storing fuel or other liquids. These tanks must hold liquids for extended periods of time while exposed to the elements and then be folded and stored worldwide in crates for years before being needed again. The combination of heat and humidity is very deleterious to the materials used in the construction of these tanks. Although the tanks are drained after use and prior to storage, residual liquid usually remains in them. Exposure to the liquid can degrade the polymer after a long period of time and cause leakage. The current procedure is to discard tanks which have been stored for five years or more, even if they have never been in service. Nondestructive-inspection techniques for determining the condition of these tanks are needed.

### 1.2 BACKGROUND

#### 1.2.1 Polymer Degradation

Polyurethanes are a broad class of chemically divergent polymers. The two main subgroups are ether-based polyurethanes comprising flexible polyether segments joined by rigid urethane segments and ester-based

polyurethanes where flexible aliphatic or aromatic polyester segments are joined by urethane links. The types and lengths of flexible and rigid segments in polyurethane determine whether the resins are soft, rubbery, or glassy. Polyurethanes are widely employed as films, foams, moldings, and specialty items. In general, there are several mechanisms that initiate degradation in polyurethanes.<sup>(1)</sup> Hydrolysis: In ether-based polyurethanes, only the urethane linkage undergoes hydrolysis, and quite severe conditions are required. In contrast, ester-based polyurethanes may undergo scission at either ester or urethane linkages; in fact, the ester group is an order of magnitude more sensitive to hydrolysis than the urethane linkage. Chain cleavage is accompanied by an increase in crystallinity which accentuates changes in mechanical properties. Thermal reactions: At temperatures above 150°C, the urethane link cleaves to give a variety of reaction products. In the presence of oxygen, all polyurethanes oxidize, especially in the flexible segments. Ether segments are particularly prone to oxidation. Photoreactions: In general, all polyurethanes are light-sensitive to some degree, from either direct photoreactions or complex reactions involving free radicals. The wavelengths and power densities of the light involved are very important parameters in these processes.

Other elastomers may have better weathering characteristics than the ester-based or ether-

based polyurethanes originally studied. Therefore, limited measurements on several other elastomers were also conducted during the course of the work.

### 1.2.2 Laser-Induced Luminescence

Laser-induced luminescence (LIL) is emission of light resulting from absorption of laser energy by a substance. The wavelengths of the reradiated light contain a major component at the wavelength of the exciting laser light (reflected light), but there are also many new wavelengths present (luminescence) that are determined by the molecular structure of the substance. Laser-induced luminescence includes both laser-induced fluorescence (LIF), which is fast luminescence occurring on time scales of the order of nanoseconds, and laser-induced phosphorescence (LIP), which is slower luminescence occurring on time scales as long as several seconds. The luminescence spectrum is not only a function of time, but also a function of the excitation spectrum. Fluorescence and phosphorescence have been studied for a number of years and have been used in numerous ways in the laboratory environment. Laser-induced luminescence is finding widespread use in many new and diverse applications; for example, it is currently being used to study energy redistribution collisions in vapors, for fingerprint detection, to map flowfields in chemical lasers, and in medical applications. In recent years, technological advances have

increased reliability and portability of lasers and also generally reduced costs; this is readily demonstrated by the wide use of helium-neon lasers in bar-code scanners found in many supermarkets.

In many applications, fluorescence dominates phosphorescence. Fluorescence is characterized by many spectra depending on the excitation wavelength. A fluorescent molecule emits a fluorescence spectrum after it absorbs radiation within its excitation spectrum. The spectral distribution of the fluorescent radiation is a physical and absolute characteristic of a given substance for a given excitation wavelength and is useful for qualitative considerations. The emission intensity of fluorescence at a given wavelength is useful for quantitative analysis with a given instrument after standardization. Quantitative measurements show that there is sometimes a very strong correlation between laser-induced luminescence and some physical characteristic of the material. Many times this is due to the fact that fluorescence reveals relationships (e.g., conjugation) between molecular functional groups; this is in contrast to infrared absorption techniques, which are mainly used to reveal presence of individual molecular functional groups. Because alteration of these relationships between certain molecular functional groups occur during degradation, laser-induced luminescence can be used to monitor degradation processes.



Polymer photophysics<sup>(2)</sup> has received much attention recently. Molecules containing absorbing groups, called chromophores, undergo electronic transitions which result in the characteristic absorption of the compound. Chromophores occur naturally or may be artificially introduced as a label (e.g., a fluorescent-dye molecule) attached to the polymer. Commonly occurring chromophores include: ether (-O-), ester (-COOR), and nitrile (-CN) with peak absorptions at 185 nm, 205 nm, and 160 nm, respectively.<sup>(3)</sup> If these chromophores lose excess energy through non-radiative transitions (such as heating), they are considered chromophores only; however, if excess energy is re-emitted as luminescence, chromophores can also be considered as fluorophores.

With the monochromaticity and power density available with lasers, molecular transitions that are not normally thought of as fluorescent can be probed. For instance, chromophores that exhibit ultraviolet absorption can sometimes be induced to fluoresce with laser excitation in the visible region of the spectrum; this effect can be very important from the viewpoint of practical implementation of instruments based on these properties.

NOTE: When a spectrum is dominated by the fluorescent component, luminescence is commonly referred to as fluorescence. A distinction is usually made only when the

phosphorescence dominates or is intentionally measured after fluorescence has decayed. (A common example of this slightly ambiguous terminology is "fluorescent glow-in-the-dark paint"--phosphorescence is actually the process that causes the paint to glow in the dark.)

### 1.2.3 Literature Survey

The versatility and sensitivity of luminescence as a technique in polymer chemistry stem from multiple aspects of interactions of the electronically excited states with their immediate environment.<sup>(4)</sup> Luminescence has been used to study some thin-film polyurethane systems<sup>(5)</sup> where it was found that luminescence characteristics may be very different, although absorption spectra may be very similar. These differences were dependent on the manufacturing processes because of the impurity concentrations. Fluorescence has also been used to monitor polymerization (viscosity) in systems such as methyl methacrylate.<sup>(6)</sup> Use of fluorescent probes (dyes) has been investigated for similar applications. Fluorescent probes have been used in polyurethane systems<sup>(7,8)</sup> and several<sup>(9-11)</sup> other polymer systems. Disadvantages of adding fluorescent probes are (1) the material may also change in color, (2) interaction between the probe molecule and the polymer may adversely affect the polymer, and (3) some of the probe molecules may leach out as the polymer degrades, thus

complicating interpretation of the data. A research group in Helsinki has recently reported a new instrument (PEXSCANNER) that can be used to estimate the relative degree of cross-linking in polyethylene plastic. Their results were good for peroxide-linked polyethylene and in most cases for radiation-linked polyethylene. Their instrument used a helium-cadmium laser operating at 442 nm to induce fluorescence in the visible region of the spectrum.<sup>(12)</sup>

### 1.3 RESEARCH APPROACH

A systematic research plan was established with the ultimate goal of developing an instrument capable of determining in the field degradation of fabric-reinforced elastomer fuel tanks. Basic research was conducted to determine if laser-induced-fluorescence intensity could be correlated to degraded mechanical characteristics. Laboratory experiments were conducted using standard spectroscopic techniques. A wide variety of samples was studied. The next step was to determine if complex, bulky, and expensive laboratory equipment could be replaced with simpler, smaller, and lower-cost equipment. Similar experiments were then conducted with the incident laser beam and resulting fluorescent light being conducted through fiber-optic bundles. Highlights of the fiber-optic bundle work are described below.

## 2.0 BIFURCATED FIBER-OPTIC BUNDLE EXPERIMENTS

### 2.1 INTRODUCTION

When laser-induced fluorescence is measured using optical filters instead of a narrow-bandwidth spectrometer, fluorescence signals of several wavelengths are measured simultaneously. Laser-induced fluorescence measured in this fashion is referred to as "integrated fluorescence" because the signal is related to the integral of the fluorescent-light intensity, weighted by the filter-detector response, over the wavelengths to which the system responds. Hence

$$I(\lambda_e) = \int \text{LIF}(\lambda_e, \lambda) D(\lambda) f(\lambda) d\lambda, \quad (1)$$

where

$I(\lambda_e)$  = integrated fluorescence for excitation wavelength  $\lambda_e$ ,

$\text{LIF}(\lambda_e, \lambda)$  = laser-induced fluorescence at wavelength  $\lambda$  when excited with wavelength  $\lambda_e$ ,

$D(\lambda)$  = detector response at wavelength  $\lambda$ ,

$f(\lambda)$  = filter response at wavelength  $\lambda$ .

## 2.2 SAMPLES

Samples were artificially aged by immersion in hot distilled water (160°F for periods up to 70 days). A partial list of samples and nomenclature is shown in Table I. The samples included ester-based polyurethanes (UA, UB), ether-based polyurethanes (UC), and nitriles (G) all of which were commercially available. The samples were slightly cleaned using a mild detergent and a toothbrush.

The samples were approximately 1.3-mm thick and were essentially optically "opaque". All of the samples described in this report could be commonly described as "amber" in color. (For instance, using the 1931 CIE standard color definitions with illumination standard "C", the unaged material designated as "UA" had the color coordinates:  $Y = 27.7$ ,  $x = 0.443$ , and  $y = 0.432$ .)

TABLE I. SAMPLES

Code	Manufacturer*	Description
UA	Uniroyal	ester-based
UB	Uniroyal	ester-based
UC	Uniroyal	ether-based
G	Goodyear	nitrile-based

\* Use of trade names or manufacturers in this report does not constitute an official endorsement or approval of the use of such hardware.

## 2.3 EQUIPMENT, PROCEDURES, AND DATA

## 2.3.1 Tensile Strength

Tensile-strengths are shown in Figure 1. Estimation of uncertainty in this data can be

made based on irregularities of the curves, and is in the range of  $\pm 5\%$ . These data were measured using a Precision Scientific Group model CRE-1000 strength-of-materials tester. Procedures for the measurements conformed to the American Society for Testing and Materials (ASTM) standards.

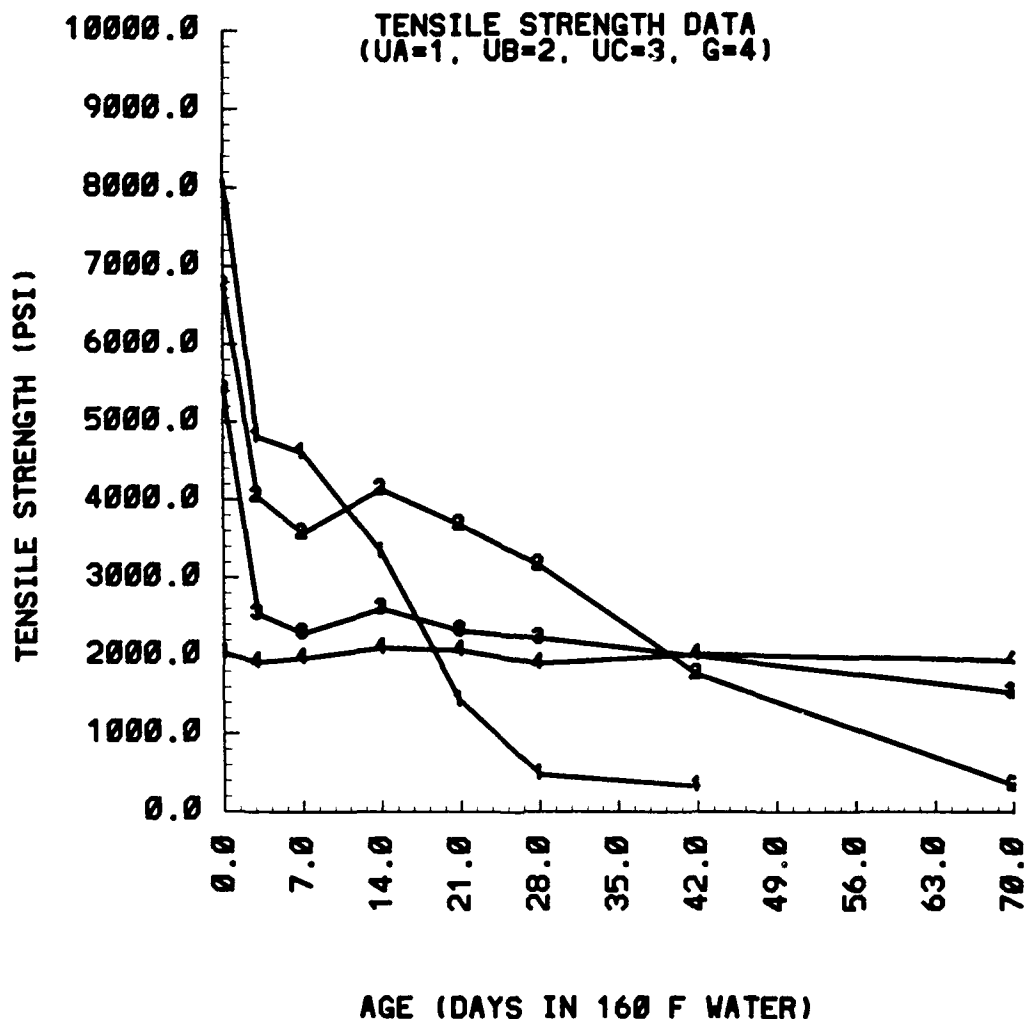


FIGURE 1. TENSILE STRENGTH AS A FUNCTION OF AGE (Samples: UA, UB, UC, G; Aging Method: Hot Water)

### 2.3.2 Laser-Induced Fluorescence

Experimental apparatus for measuring laser-induced fluorescence through a bifurcated (two-channel) fiber-optic bundle is shown in Figure 2. Typical experimental parameters were as follows:

Laser:	Spectra Physics (SP) model 2025 argon-ion laser (see discussion below), 488 nm, power 0.5 mW measured at input to fiber,
Modulator:	Princeton Applied Research (PAR) model 125A mechanical chopper, 2.0 kHz,
Filter F1:	Edmund P/N 030907, Interference filter @ 488 nm,
Fiber:	Oriel P/N 77533, 1-m (nominal) bifurcated bundle, numerical aperture (NA)= 0.55, material: glass, average loss over visible wavelength region: 45%, stand-off distance "d" from sample: 22mm,
Filter F2:	Schott OG570, 2 each, 3.0-mm thick,
Detector:	United Detector Technology (UDT) PIN-10 Schottky-barrier silicon photodiode operated in the photoconductive mode (-9 V bias, 100-k $\Omega$ load resistor), a 19-mm-focal-length lens (36 mm from the detector) imaged the output from the bundle (44 mm from lens) onto the detector,

Electronics: PAR model 124A lock-in amplifier with a model 116 preamplifier: sensitivity 10- $\mu$ V scale, quality factor  $Q = 10$  at 2.0 kHz, time constant 300 ms, monitored with a Keithley model 177 digital multimeter.

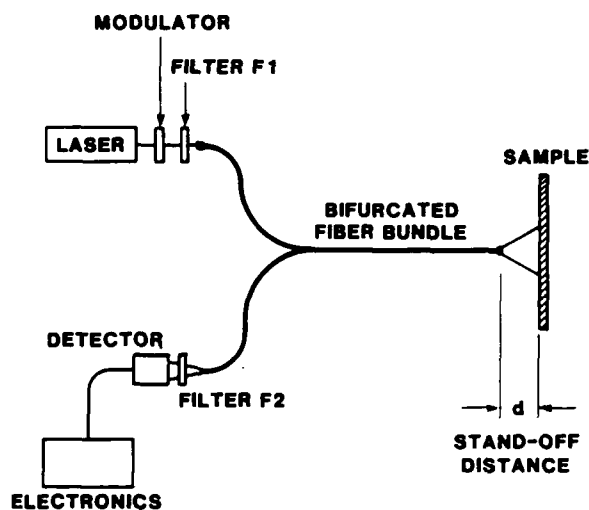


FIGURE 2. EXPERIMENTAL APPARATUS USING A BIFURCATED FIBER-OPTIC BUNDLE

An argon-ion laser operated in the constant-light-output mode was usually used. It was highly attenuated to simulate a small portable laser. (Other lasers were also used for additional experimentation, for instance, a PMS Electro-Optics model LHGR-0050 0.5-mW-helium-neon laser operating at a wavelength of 543.5 nm.) No lenses were used to image the laser beam into the bundle because the bundle diameter was larger than the diameter of the laser beam. Standard modulation

techniques were used to minimize any interferences that may have been present, such as stray room light.

The fiber-optic bundle set-up was used with the experimental parameters listed above to measure laser-induced fluorescence as a function of sample age for several elastomers. (See

Figure 3.) Standard deviations for each data point were typically 3% of the mean. For reference it should be noted that the y-axis units (labelled as "arbitrary units") of Figure 3 were actually volts (V) where 10 V corresponded to full-scale deflection of the lock-in amplifier (operated on the 10- $\mu$ V range).

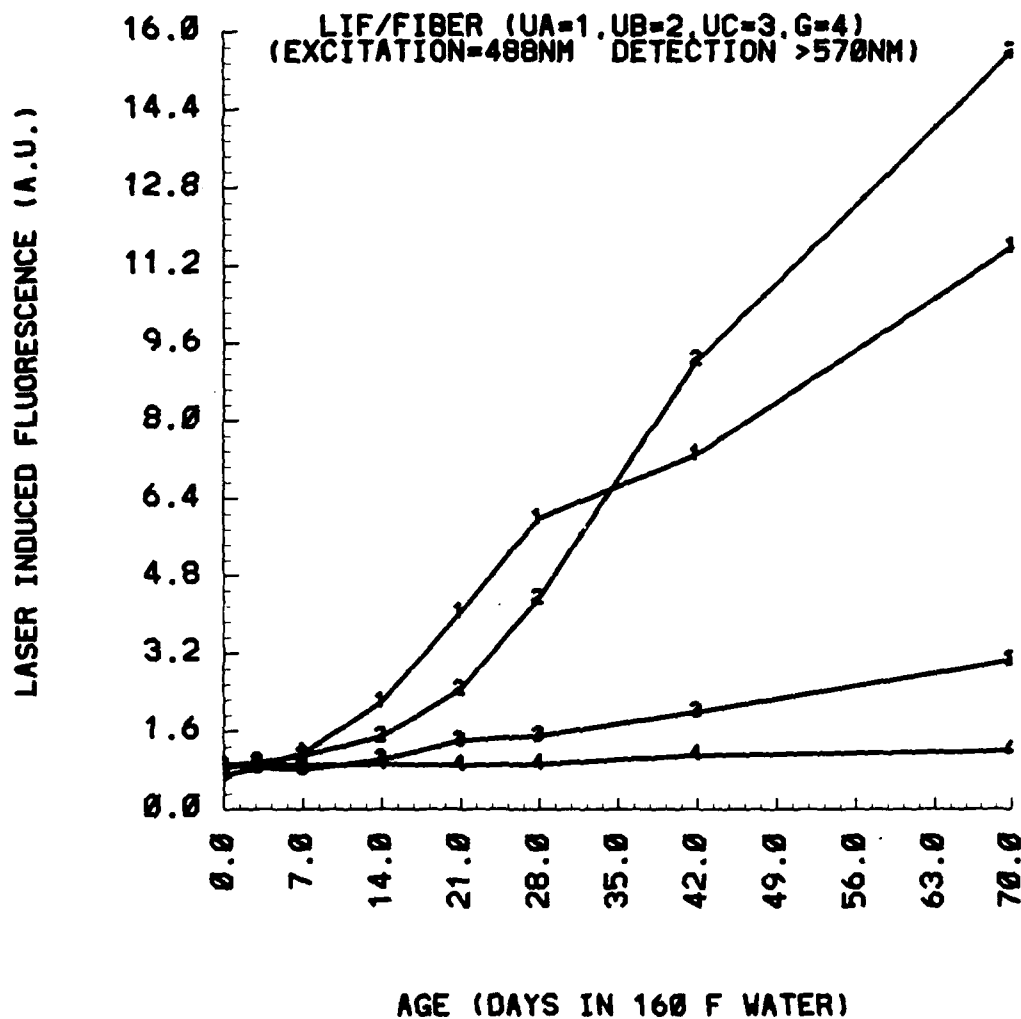


FIGURE 3. INTEGRATED LASER-INDUCED-FLUORESCENCE INTENSITY MEASURED THROUGH A FIBER-OPTIC BUNDLE AS A FUNCTION OF AGE (Excitation Wavelength: 488 nm; Detection Wavelengths: >577 nm; Samples: UA, UB, UC, G; Aging Method: Hot Water)

The kind of material behind the samples had only a very small effect (typically less than 1%) on the laser-induced-fluorescence intensity. This effect was small because of the thickness of the samples. Black vinyl tape was routinely used as the backing material for all of the tests described here.

Linearity of laser-induced-fluorescence intensity as a function of laser-power density was investigated. For power densities below  $20 \text{ mW/cm}^2$ , laser-induced-fluorescence intensity was linearly related to the laser power density. (This is probably true at higher power densities; however, no measurements were made above that power-density regime. Linearity testing was conducted only at relatively low-power densities because the envisioned end-use of this technique will be based on a low-power laser unit.) A linear-least-squares analysis indicates the slopes deviated less than 3% from unity with linear-correlation coefficients better than 0.99, for both degraded and nondegraded samples.

While using integrated-fluorescence through the fiber-optic bundle, optimization of the filter-detector combination was also investigated. For example, with the set-up shown in Figure 2, 488-nm excitation and the UDT PIN-10 detector, a better differentiability resulted for the UB material by using a Schott OG630 filter. (Although the absolute signal strength was decreased by about a factor of 2.5, the differentiability was better by a factor

of approximately 2.) This work implies that some accommodation for changing filters may be advantageous for a field unit.

## 2.4 RESULTS

### 2.4.1 Correlation of Laser-Induced Fluorescence with Tensile Strength

Typical scatter diagrams which relate laser-induced fluorescence to tensile strength are shown in Figures 4A-4C. A strong correlation exists for UA, UB, and UC materials. Correlation can be approximated by a linear function for each material if the data point from the unaged sample (highest tensile strength) is not considered; this type of very rapid initial degradation has been observed by other researchers.<sup>(13)</sup> Correlation from the nitrile G samples is not strong over the range investigated, because the material has just started to degrade over the range of aging in the present study.

It can be seen from these scatter diagrams that for the UA material, correlation may be slightly better described by a nonlinear function or combinations of functions; however for comparison purposes, a linear-least-squares analysis has been used for all three materials UA, UB, and UC, linear-correlation coefficients being -0.90, -0.99, and -0.94, respectively. Notice that the slopes (laser-induced-fluorescence change for the same geometrical/experimental set-up per unit

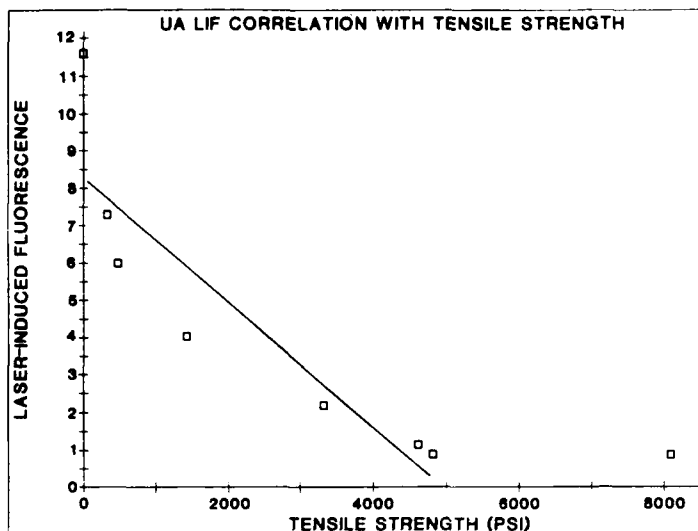


FIGURE 4A. SCATTER DIAGRAM OF LASER-INDUCED-FLUORESCENCE INTENSITY AS A FUNCTION OF TENSILE STRENGTH (Excitation Wavelength: 488 nm; Detection Wavelengths: >570 nm; Samples: UA; Aging Method: Hot Water; Comments: Straight line is the linear least-squares fit neglecting data point from the unaged sample)

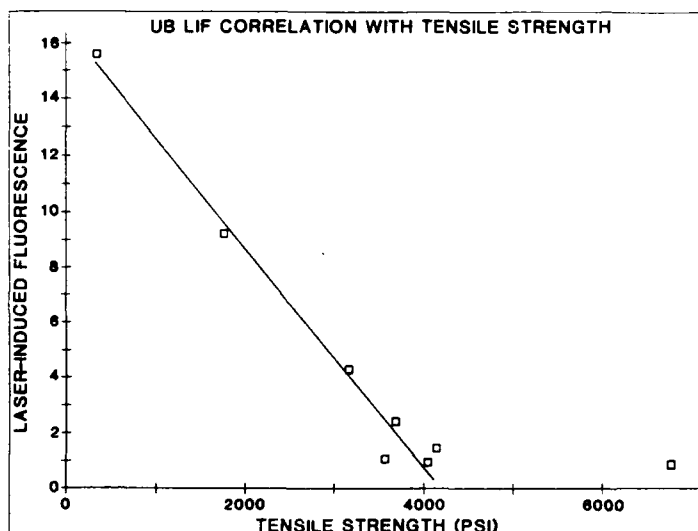


FIGURE 4B. SCATTER DIAGRAM OF LASER-INDUCED-FLUORESCENCE INTENSITY AS A FUNCTION OF TENSILE STRENGTH (Excitation Wavelength: 488 nm; Detection Wavelengths: >570 nm; Samples: UB; Aging Method: Hot Water; Comments: Straight line is the linear least-squares fit neglecting data point from the unaged sample)

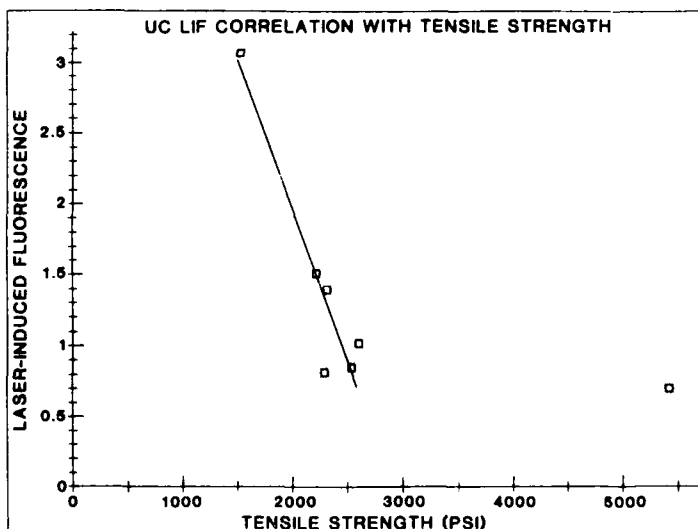


FIGURE 4C. SCATTER DIAGRAM OF LASER-INDUCED-FLUORESCENCE INTENSITY AS A FUNCTION OF TENSILE STRENGTH (Excitation Wavelength: 488 nm; Detection Wavelengths: >570 nm; Samples: UC; Aging Method: Hot Water; Comments: Straight line is the linear least-squares fit neglecting data point from the unaged sample)



change in tensile strength) are different (-0.0017, -0.0039, and -0.0021, respectively). This indicates that a different correlation relationship exists for each type of material.

#### 2.4.2 Discussion

The strong correlation exists for only the right combination of excitation and detection wavelengths. Correlation exists because of the complex molecular and intermolecular relationships that are altered as the material ages. Generally, structural changes that induce rigidity tend to promote fluorescence, because internal-vibrational-relaxation (non-radiative) processes are minimized. By using an excitation wavelength longer than the primary absorption wavelength, in conjunction with low-power densities, bleaching and photodegradation effects can be avoided because the photon energies are not enough to break most chemical bonds. Additionally, choice of excitation wavelength is somewhat influenced by impurities in the polymer; that is to say, if a certain excitation wavelength causes impurities in the polymer to strongly fluoresce, then that would not be a suitable choice for excitation. (For example, the strong ultraviolet-excited fluorescence of scavenger additives can be avoided.)

These data demonstrate that the method of "integrated fluorescence" can be used through a fiber-optic bundle to differentiate the degree of degradation of elastomers. Small, relatively

low-cost equipment can be used for the measurements. For certain materials, a very high degree of correlation exists between laser-induced fluorescence and tensile strength.

### 3.0 CONCLUSIONS AND RECOMMENDATIONS

Correlation between laser-induced fluorescence and material degradation exists for many of the materials tested because of the complex molecular and intermolecular relationships (such as cross-linking, scission, oxidation) that are altered during degradation. Intensity of laser-induced fluorescence is promoted because of the decrease of internal relaxation processes when degradation modifies these relationships. Because the excitation photon energies are not high enough to break most chemical bonds or excite fluorescence from most of the impurities, many complications normally associated with fluorescence measurements can be avoided.

A conceptual diagram for a developmental prototype, shown in Figure 5, is based on a low-power laser with a fiber-optic bundle to deliver the laser beam and collect fluorescent light. The advantages of an inspection device based on these principles are that it is non-destructive, portable, and easy to use. The samples may be of a wide variety and require minimal surface preparation. Disadvantages are that the method does not work well on

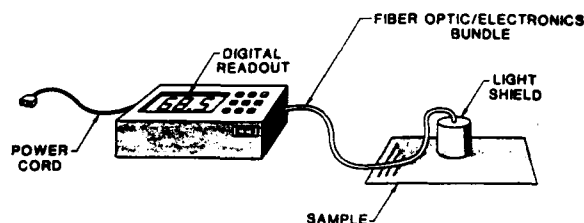


FIGURE 5. CONCEPTUAL DIAGRAM FOR FUTURE APPLICATIONS

some "black" materials and an instrument based on laser-induced-fluorescence changes must be calibrated for each type of material tested.

The work described above demonstrates that practical application of the laser-induced-fluorescence inspection technique to polyurethane elastomers is very promising, and further development should be conducted. Investigation of its applicability to other materials is presently underway.

#### 4.0 ACKNOWLEDGMENTS

Laser-induced-fluorescence inspection of polymer-based materials has recently been patented by SwRI.<sup>(14)</sup> The development of an instrument based on this concept has been partially supported by the U.S. Army Belvoir Research, Development, and Engineering Center (STRBE-VU, Ft. Belvoir, VA 22060-5606) through a special task for the

Nondestructive Testing Information Analysis Center (NTIAC) under Contract No. DLA 900-84-C-0910 CLIN 0001AX, Mods: P00043, P00046, and P00060.

#### 5.0 REFERENCES

1. Encyclopedia of Polymer Science and Engineering, John Wiley and Sons, Wiley-Interscience, (New York, NY) 1986, Vol. 4, pp 630-693, Vol. 6, pp. 636-638.
2. "Polymer Photophysics," J. M. Torkelson, *Physics Today*, pp. S-64 (Jan. 1987).
3. Instrumental Methods of Analysis, H. H. Willard, L. L. Merritt, Jr., and J. A. Dean, 4th Ed., Van Nostrand Reinhold Co., (New York, NY) 1948, p. 85.
4. "Effect of Polymer Chain Tacticity on the Fluorescence of Molecular Rotors," R. O. Loutfy and D. M. Teegarden, *Macromolecules* **16**, pp. 452-456 (1983).
5. "Photochemical Reactions in an MDI-Based Elastomeric Polyurethane," N. S. Allen and J. F. McKellar, *J. of Appl. Polymer Sci.* **20**, pp. 1441-1447 (1976).

6. "Novel Excimer Fluorescence Method for Monitoring Polymerization," F. W. Wang, R. E. Lowry, and W. H. Grant, *Polymer* **25**, pp. 690-692 (1984).
7. "A Study of Polymers Using Fluorescent Dyes," C. A. Byrne, E. J. Pozniomek, O. I. Kutai, S. L. Suib and S. J. Huang, in Materials Characterization for Systems Performance and Reliability, (Proceedings of the Sagamore Army Materials Research Conference: 1984) Ed. by J. W. McCauley and V. Weiss, Plenum Press (New York, NY) 1986, pp. 495-503.
8. "Fluorescence in Polymers," C. A. Byrne, E. J. Pozniomek, O. I. Kutai, S. L. Suib, and S. J. Huang in Polymers as Biomaterials, Ed. by S. W. Shalaby, A. S. Hoffman, B. D. Ratner, and T. A. Horbett, Plenum Press (New York, NY), 1985, pp. 111-120.
9. "Fluorescence Probes for Solid Polymer Films," R.O. Loutfy, *SPIE* **743**: Fluorescence Detection, Ed. by E. R. Menzel, p. 54-59, (1987).
10. "Cure Monitoring of Epoxy Resins by Fluorescent Spectroscopy," F.W. Wang, R.E. Lowry and B.M. Fanconi, *Polymeric Materials Science and Engineering*, **53**, pp. 180-185, (1985).
11. "Cure Monitoring of Epoxy Resins by Fluorescence Recovery After Photo-bleaching," F.W. Wang and E. Wu, *Polymer Commun.* **28**, pp. 73-75, (1987).
12. "Pex Scanner, A New Instrument to Measure On-Line the Degree of Cross-Linking in Polyethylene Plastics," M. Luukkala and J. Viirto, *J. of Indust. Irradiation Tech* **2** (3,4), pp. 353-366, (1984).
13. Reference 7, p. 498.
14. "Optical Inspection of Polymer-Based Materials," Ralph H. Hill Jr., U.S. Patent No. 4,802,762.

INTERACTIVE VIDEODISC SIMULATION FOR ENGINE  
INSPECTION PROCEDURES USING A FLEXIBLE BORESCOPE

Katharine Golas, Ph.D.  
Southwest Research Institute  
6220 Culebra Road  
San Antonio, Texas 78284

Abstract

This paper discusses an Interactive Videodisc (IVD) training program developed to teach the operation of a flexible borescope for inspection of engines on the F-16 aircraft. The paper describes the IVD technology and presents current information regarding how the technology relates to current research on adult cognition. The paper describes the borescope training program design, in which a simulation using full motion video segments was developed to provide students with very realistic and practical training on fault isolation and corrective actions using the flexible borescope during nondestructive evaluation procedures.

1. DESCRIPTION OF IVD

Interactive videodisc technology is a form of instruction that uses an optical disc recorded with analog signals (DeBloois, 1988). A computer is added to the laser-read videodisc, thus permitting instant and direct access to large textual, visual, and audio data bases. Pre-designed still and motion images, audio segments, and text or graphic screens are retrieved from this data in a pattern that each learner determines through continued interaction by his or her individual input. There are several capabilities of an optical disc interfaced with a computer: direct, uncomplicated access to data, vast storage capacity, both motion and still visuals, and rapid response time. Other forms of instruction can allow a learner to actively participate with the knowledge imparted, but the videodisc and computer combination permits

enhancements that combine various media so that instruction can be interactive and therefore more effective. A complete interactive system consists of the following components:

- (1) a computer provides the system's "intelligence," i.e., the programming and search algorithm created by the instructional designer;
- (2) a magnetic hard disk drive allows the program information and computer text and graphics to be loaded into computer random-access memory (RAM) very quickly; interface and graphic overlay cards allow the computer and videodisc player to "talk" to each other; and the RGB video monitor displays the images for both the computer and videodisc player;

- (3) the software programs stored on a floppy or hard disk and/or on the optical videodisc contain the visual images and audio signals selection menus, test items, simulations, student management files, and diagnostic routines;
- (4) the optical videodisc player rapidly retrieves the video and audio segments which are stored on the optical videodisc, as initiated by the learner and according to the computer program;
- (5) an optical videodisc contains up to 54,000 video still frames and two tracks of audio;
- (6) User input devices such as a keyboard, touch screen, light pen, mouse, or voice recognition unit allow the user to interact with the system.

Additional components to IVD systems can include:

- (1) authoring languages which help courseware designers to prepare the computer presentation of the instructional design;
- (2) still frame audio is sound that is prerecorded on the videodisc either as digital or analog signals. It is loaded into a buffer at the same time a single frame of video is searched and displayed. Previously, the audio on a videodisc could only be played when the laser head reads 30 frames per second, playing motion video.
- (3) synthesized sound chips in the computer provide simple word or sentence instructions and feedback to learners;

- (4) digitized video stored on the magnetic medium in the form of graphics or video is played in conjunction with the analog video stored on the optical disc;
- (5) bar code readers can quickly read a code from a page of a training manual or troubleshooting guide and enter the data into the computer and integrate instructional or information contained in the manual with the interactive program resident in the computer;
- (6) compact disc-read only memory (CD-ROM) or write once/read many (WORM) disc players can hold vast amounts of data and add unprecedented data storage capacity to the training station.

## 2. INTERACTIVE TRAINING AND USER PERFORMANCE: CONCLUSIONS FROM THEORETICAL STUDIES RELATED TO ADULT COGNITION

Although opinions vary among learning theorists as to what internal processes occur as an individual learns, there is considerable agreement that certain conditions improve learner performance. These conditions include active participation, practice, feedback, repetition, and motivation. Studies have also shown that information taken in through multiple senses is more readily learned than through a single sense.

IVD offers the learner an opportunity to respond to stimuli and to receive almost immediate feedback, reinforcement, practice, and remediation as required. According to Fleming and Levie (1978), the core feature of the technology, interaction, is a sound educational principle:

"In general, where the learner reacts to or interacts with the criterial stimulus, learning is facilitated and that facilitation increases with the degree of learner activity or involvement."

DeBloois (1988) notes that there are other message design principles available with IVD simply by the nature of the medium:

- (1) pictures promote better memory and learning than words alone;
- (2) concepts about concrete objects are more readily learned than concepts about abstractions. Observing the attributes of a concept from an image, and then distinguishing them visually from non-attributes (features not related to the concept) helps a person learn and remember the concept;
- (3) observing a person performing some activity and then modeling the observed behavior is a very powerful instructional approach, especially for teaching problem solving.

Fleming and Levie (1978) suggest that more learning occurs as the user's involvement with the prepared materials deepens, from simple attending (reading, looking, listening) to covert responding (repeating words subvocally) to overt responding (concrete actions). DeBloois (1988) reports that a well-designed, high-quality IVD training program draws learners into more intense, overt responses, by creating a learning environment which addresses many of the factors which are known to improve learner performance.

### 3. APPLICATION OF IVD TO BORESCOPE TRAINING

In the borescope IVD, real images from inside the engine are presented to the student, and the student is asked to identify problems (e.g., cracking, rust, oxidation, corrosion, etc.) and decide how best to handle any problems they do encounter (e.g., pull the engine from the aircraft, fly 10 hours and recheck the situation, notify supervisor). The IVD simulation replaces the need for hands-on practice during training on actual equipment. Data reveals that students

are able to perform immediate on-the-job inspections after receiving IVD training. They learn more information without tying up actual equipment or valuable supervisor time.

### 4. DESCRIPTION OF THE BORESCOPE IVD PROGRAM

The IVD program begins with an instructional sequence and graphic descriptions on how to operate the borescope and what to inspect for. This is followed by individualized practice exercises in which the student is asked to identify the parts of the borescope, set up the borescope for probing the engine, probing a certain area of the aircraft, isolate problems, and take corrective actions. Student data collection routines keep track of the student's performance (e.g., number of problem areas they overlooked, number of incorrect decisions the student made during the inspection, incorrect analysis of problems encountered, etc.).

The borescope IVD training program is delivered on the IBM InfoWindow System. IBM InfoWindow is an integrated IVD hardware delivery system with a touch screen, graphic overlay, and audio capability. The InfoWindow system uses an IBM personal computer, a videodisc player, and a high-resolution color monitor to actively interact with the user. The borescope program was authored with the program called TenCORE. TenCORE is one of 35 IVD language authoring programs available on the market today.

## REMOTE VIEWING

Donald A. Carignan  
Instrument Technology, Inc.  
Westfield, Massachusetts

### ABSTRACT

This paper defines Remote Viewing and describes the various principles involved, namely: rigid optics, fiber optics and video systems. A brief explanation is included to detail the similarities between each and to outline performance versus cost that distinguishes each system. Also included is discussion on how each of the systems can be fabricated to withstand severe environments.

Perhaps the greatest advancement in Remote Viewing during the last few years has been in miniaturization. This paper takes a close look on how small systems have evolved and how discoveries and development in other non related fields has greatly improved the science of Remote Viewing. Miniaturization of optics, fibers and video is covered. Most recent advancements include the digitizing of obtained information for image processing, recording and transmission.

A brief illustration of various applications and how Remote Viewing plays an important role in the requirements for Non Destructive Testing is presented herewith. Examples of systems for measurement, observation and documentation are discussed, including several cases in severe hostile environments.

### 1.0 INTRODUCTION

Remote Viewing has been growing in popularity over the last few years and is experiencing healthy growth throughout industry due to:

- (a) Recent advancements in technology
- (b) Broadening of the base, that is, a general growth in NDT requirements along a broader range of industries
- (c) Requirements for inspection documentation

This presentation submits a verbal definition of Remote Viewing and then goes on to define the terms by illustration. Recent advancements and the current state-of-the-art is discussed along with recommendations for performance evaluation. In

closing, systems performance will be explained along with recent typical examples of Remote Viewing Systems.

### 1.1 DEFINITIONS

Remote Viewing - The ability to view into areas that are inaccessible or hostile. In other words, to be able to look into areas where you cannot stick your head into, or, do not want to stick your head into.

### 1.2 SCHEMATIC DEFINITION

Fig. 1. provides a schematic definition of the complete concept of Remote Viewing. An object to be viewed is separated from the observer by a barrier. The barrier is anything that prevents an observer from walking up to the object to view it.

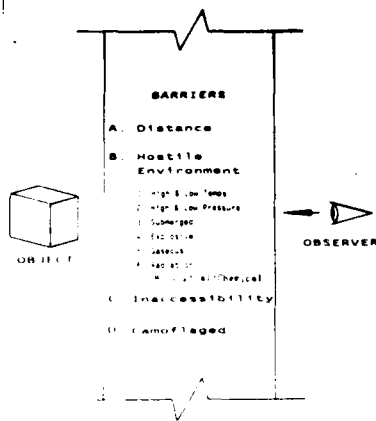


FIG. 1 - BARRIERS

The barrier may be a physical barrier, such as a wall, jacket or shroud, that prevents internal viewing, or it may be an opening such as a rifle barrel or tube, which provides too small an opening for the observer's head to enter.

The barrier may also be a protective barrier intended to protect the observer from a very severe and hostile environment.

Hostile environments that might require observation include:

- High/Low Temperatures
- High/Low Pressures
- Explosive
- Submerged
- Radiation
- Gaseous
- Biological/Chemical

Another barrier to consider is distance, when the observer and the object are separated and close visual inspection is necessary.

## 2.0 TYPES AND ILLUSTRATIONS

Available instruments, for Remote Viewing, are broken down into three main classifications as illustrated in Fig. 2.

- (a) Rigid Optics - These include Telescopes, Periscopes, Borescopes and Microscopes.
- (b) Flex Optics - Fiber Scopes
- (c) Video - Video Scopes

In all systems, penetration of the barrier takes place with an objective lens. The lens and the distal end of the instrument are, therefore, susceptible to the environment and have to be protected, if necessary.

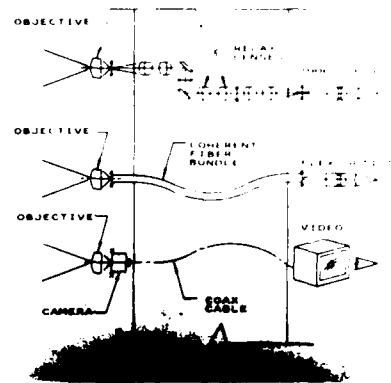


FIG. 2 - REMOTE VIEWING - HOW?

### 2.1 RIGID OPTICAL SYSTEMS

The objective lens forms a primary image. In rigid optical systems, sets of additional lenses, called relay lenses, are then used to form secondary images which are relayed along a straight line path. Secondary images are created and formed as often as required to move the image along until the barrier is exited. Once outside the barrier, the final image is formed with the choice of adding an eyepiece for visual use or camera adapters for camera use.

### 2.2 FLEXIBLE SYSTEMS

In flex systems, the same type of objective lens is used to form a primary image. This time, however, the primary image is placed on the face of a coherent bundle. By its nature, the bundle creates or reforms this image at its other end. There are, therefore, no secondary images, just the primary image and the final image. With the final image located outside the barrier, an eyepiece or camera adapter can be applied as in the rigid system.

### 2.3 VIDEO SYSTEMS

In Video Systems, the same objective is again used to form a primary image, but this time the image is formed on the image plane of the video camera. The optical image is then transformed into an electronic signal that travels the length of the coax cable and then is transferred back into a visual image at the monitor.

### 2.4 SYSTEM COMPARISONS

If we then make an assumption that a video camera will most likely be attached to both the rigid system and



the flex system and thus present a video image to the user, we see very strong similarities between all three systems. Each starts with an objective lens forming a primary image and each ends with a video image on the monitor. The basic difference between the three systems remains in the manner in which the information is transferred through the barrier.

And there lies the crux of the problem in selecting the system that best meets the requirements. Now the potential user has to go through an analysis of-

Performance vs. Benefits vs. Cost.

### 3.0 SYSTEM PERFORMANCE

When specifying or evaluating a Remote Viewing System, remember that the reason for even contemplating such an item is the requirement or need to see something. It should follow that the first criteria to be concerned with is "how well can the system see?", as measured in resolution.

Manufactures, unfortunately, do not make life any easier for the user in terms of resolution. Each of the three principals involved, optic, fiber and video, talk in different foreign languages. Optical people talk in terms of diffraction limits, and of arc secs of resolution. Fiber people talk in terms of fiber size, packing, density and pixels. The video people talk in terms of horizontal and vertical lines of resolution and line pair per mm. It does get a bit confusing.

#### 3.1 RESOLUTION MEASUREMENT

The accepted method and means for specifying and testing for resolution has become the USAF 1951 Bar Chart. The Bar Chart is a series of geometrically diminishing set of lines and spaces. Each set is identified by a group and sub group number. Fig. 3.

The resolution limit of any viewing instrument is obtained when it is no longer possible to determine spaces between lines. The target is viewed in decreasing pattern sizes until a group can no longer be resolved. The previous pattern is then said to be the resolution limit.

#### 3.2 RESOLUTION SAMPLES

It is necessary to state the bar group to be resolved at some specified distance. It is totally useless to only

specify one without the other. USAF Bar Charts are available in high contrast and in low contrast forms and it is necessary to determine and specify which target best illustrates the requirements.

Once a resolution limit has been set using USAF Bar Charts, there can be no argument between supplier and user as to whether the instrument or system meets specifications. Either it resolves as stated or it doesn't.

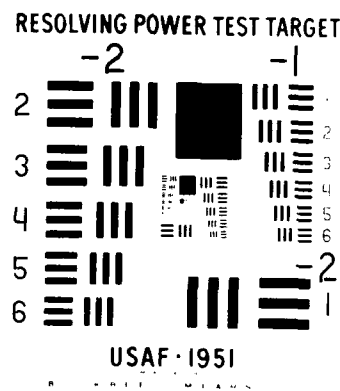


FIG. 3 - USAF BAR CHART

#### 3.3 ENVIRONMENT

In dealing with hostile environments, consideration must be given to the distal tip of the instrument as it penetrates the barrier and enters the environment. The exposed tip must be able to withstand whatever environment is present or must be protected from that environment.

#### 3.4 ANALYSIS-RELIABILITY-PERFORMANCE-COST

In attempting to select the proper balanced system and going through an analysis of critical features, performance standards, reliability and cost, you will find that the rigid systems will come out on top in most cases.

Rigid Optical Systems have all the features in their favor except one (1), they can get big and bulky and cannot bend around corners. When size, weight and the need to bend around corners comes into play, rigid optical systems

have to take a back seat. That leaves a choice between fibers and video. At the moment, fibers are holding a slight edge in cost, reliability and availability in small diameter size, but video systems are coming on strong. The cost of video systems is steadily decreasing while their reliability keeps improving. The manufacturers of coherent fiber bundles are getting a little concerned.

#### 4.0 TECHNICAL ADVANCEMENTS

Several technological advancements have had a great impact recently, on Remote Viewing; first of which is miniaturization.

##### 4.1 BORESCOPES

Not too long ago, a 10mm diameter Borescope was the norm. It was driven by medical requirements and met the needs. Early jet engines finally added 10mm diameter holes to their outer cases so that these medical scopes could be used for internal inspection. When engines became smaller, borescopes became smaller, down to 8mm - 5.5mm and finally down to 4.0mm.

At about this time, however, the search for super conductors was receiving a great deal of attention and a great deal of funding. Corning Glass was experimenting with dopeing glass rods in order to change the glass index of refraction and thereby promote super conductivity. Although we are not sure of intended results, a new gradient rod lens was formed as a by product, a strange long thin cylindrical lens that could form images. The Japanese took advantage of the results, worked on it, perfected it and now we have the Gradient Rod Lens. A major break through. Today, using this principle and these lenses, a new series of borescopes is available with instruments as small as 0.5mm diameter.

##### 4.2 FIBERSCOPES

After the introduction of coherent bundles and the development of 10mm fiberscopes for the medical market, development and advancements in fiber technology went nowhere fast. From approximately 1955 to 1980, there were few advancements in fiber technology.

The communication industry, by then, recognized the potential for using fibers in communications and along came huge R&D programs. Fiber technology took off. Now thanks to recent developments, fiberscopes have gone

through great improvements in resolution, transmission efficiency and cost. The Japanese again took advantage of technological improvements and applied it to coherent bundles.

Today, it is possible to obtain fiberscopes as small as 0.7mm diameter and with greatly improved performance characteristics. If you haven't viewed through a fiberscope in some time, you will be pleasantly surprised at the performance of today's scopes.

##### 4.3 VIDEO SCOPES

What can I say of video advancements in recent years. It was inconceivable just a few years ago to even consider tube type cameras for Remote Viewing applications. Cameras were much to large, fragile and extremely unreliable.

Then along came the computer revolution and solid state technology. High R&D budgets were established by all game players to produce better, smaller and less expensive chips. This never ending drive produced the solid state camera. Again, the Japanese took the initiative and applied it to producing high resolution color chip cameras. The result is that today we have video color scopes as small as 14mm in diameter and as small as 6mm in black and white.

##### 4.4 INFORMATION HANDLING

After the right probe has been selected, the barrier penetrated, and information received, the most common requirement today is to attach a video camera to the system. What we have in essence, whether rigid optics or flex optics, is a very sophisticated camera lens. The probe becomes the lens and the video camera becomes the information receiver.

With today's video technology, one of the greatest advancements has been in information handling. Information received through the probes can now be analyzed, recorded, measured, identified, enhanced, computer analyzed, transmitted, etc.

Systems such as MI II are now portable and can be attached to any visual system for complete information handling. Fig. 4.

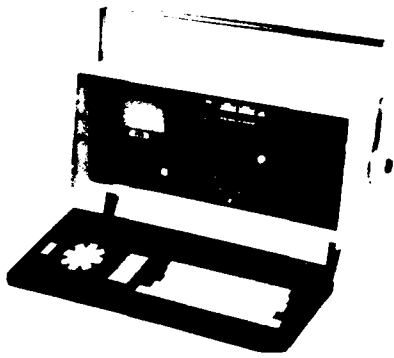


FIG. 4 - MI II

## 5.2 OBSERVATION

The user of observation systems, on the other hand, is primarily concerned with coverage area rather than viewing detail, that is, how much can be seen and not how small a detail can be seen.

## 5.3 ALIGNMENT

In this application, the user is more concerned with line-of-sight and pointing accuracy than resolution or field coverage.

## 5.4 REQUIREMENTS

It becomes important, therefore, when selecting the proper Remote Viewing Instrument, to consider applications. If more than one application is intended, decisions then have to be made for either dedicated instruments or perhaps a universal instrument with compromises.

## 6.0 SYSTEMS

It appears that the three (3) ingredients required to put together Remote Viewing Systems have come of age together and have arrived in place at approximately the same time. They are:

### 6.1 HIGH TECHNICAL PROBES

New generation of high performance probes as previously discussed in this article are now available.

### 6.2 POSITIONING SYSTEMS AND MOTOR CONTROLS

Simple, straight forward, PC controlled positioning and motor controlled systems are now readily available.

## 6.3 INFORMATION PROCESSING

Thanks to current, state-of-the-art, image analysis systems, similar to MI II, the information can be displayed, identified, measured, recorded, freeze framed, enlarged, computer enhanced and transmitted. Computer programs are readily available for complete and total analysis of the received image. There is virtually no limit to the sophistication that can be applied to the information received from the Remote Viewing probes. The technology is here today.

## 6.4 ILLUMINATION

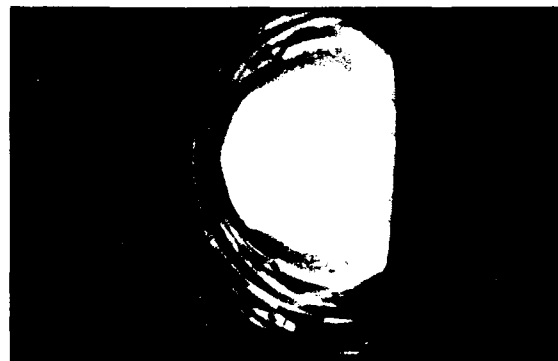
Not enough can be said of the importance of proper illumination when selecting the proper Remote Viewing System. Just as anyone with 20/20 vision finds it difficult to see in a room without illumination, the best Remote Viewing System cannot properly operate without adequate illumination. Not only is quantity of illumination important, but quality plays a very important role. Glare is the common enemy.

Although white light remains the choice of many customers, Remote Viewing Systems are as easily applied to applications requiring Ultra Violet or Infrared illumination. Today's systems, whether rigid, flex or video, can handle intense U.V. illumination as required by MIL-STDs for Dye Penetrant and Particle inspection.

## 7.0 EXAMPLES

Five examples have been selected to demonstrate variations in Remote Viewing Systems.

### 7.1 FUSION PROGRAM - PRINCETON UNIVERSITY - FIG. 5



This is a photograph of the first fusion reaction to take place on U.S. soil. The time is December 24, 1982 and the place is the Tokamak Reactor at Princeton University.

A set of three periscopes were designed to penetrate through the floor of the Tokamak Reactor Room and to extend through the large magnets required to suspend the reaction. The periscopes had to be designed to withstand severe magnetic fields, radiation and temperatures.

The periscopes contained nine (9) computer controlled drive functions, rotation, azimuth and elevation scan, power select, focus, image roll, aperture and camera selection. Operation of the periscopes was completely computer controlled without any human in the area.

#### 7.2 ENGINE CASE INSPECTION - WHITE/U.V. ILLUMINATION

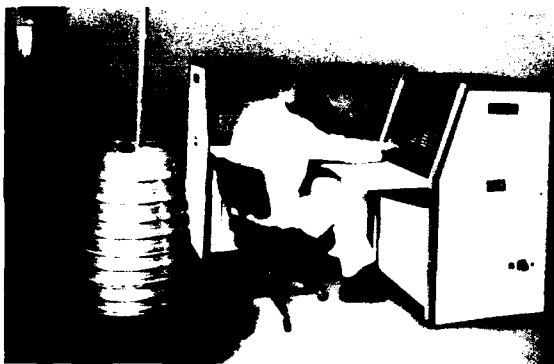


FIG. 6 - ENGINE CASE INSPECTION

New generation turbine engine cases are to be cast in sections and then E. B. welded into an assembly. This particular case had nine (9) welded sections. The problem was to view the interior for surface quality. Of concern were weld splatter, shoot peen surface quality and weld cracks, viewed under white light and U.V. illumination.

This particular unit is a four (4) axis, numerical control system that enables a rigid probe to track the inner contour of the case for complete, 100%, inside inspection. In this particular semi-automatic model, the operator performed visual inspection via the monitor but advanced models anticipate that inspection will be handled through computer processing.

#### 7.3 B-1 BOMBER WING ASSEMBLY



FIG. 7 - B-1 BOMBER WING ASSEMBLY

To bolt the composite wing of the B-1 Bomber to its pivot casting, called for over 400 fasteners. To secure the dovetail sections together, manufacturing specifications required that no gap over .003 inches be allowed between mating surfaces. Gaps in excess of .003 inches would produce unacceptable stress in the material when the bolts were torqued to proper levels.

Therefore, to meet these requirements, it was necessary to inspect each fastener hole and to measure the gap at each level in four (N-S-E-W) quadrants.

A rigid optical probe with video camera attached was developed to enter each hole and to measure the gap to accuracies of  $\pm .0001$  inches. The measurements for each gap were recorded on floppy disks and, similar to a cad/cam operation, the disks were used to operate automatic shim manufacturing equipment.

The wing was then separated from the pivot and each gap position received its own custom made shim, most often tapered. The wing was put back into position and the 400 fasteners secured.

#### 7.4 TUBE WELDING

Corrosion in stainless steel heat exchanger tubes has become a serious problem in power plants, especially Nuclear Plants. Corrosion was discovered to be universally located at the ends of the tubes. Corrective action was to sleeve the I.D. of the corroded tube, i.e., insert a sleeve length (approximately 24") into the existing tube and weld it in place at top and bottom.



FIG. 8 - TUBE WELDING

Because of low level radiation, a completely automatic system had to be developed to index across the exchanger, insert the sleeve, weld the sleeve, and inspect the weld. At first, an ultrasonic probe was used for weld inspection, but, because of possible error and for the need of additional documentation, a Remote Visual System was desired also.

A rigid optical probe was developed, with camera attached and with motorized controls for scan and focus. After welding, the Remote Viewing Probe was automatically positioned and inserted into each sleeve and visual inspection and recording of each weld was accomplished.

#### 7.5 C.E.G.B. - FUEL INSPECTION

In order to improve performance and safe operation of nuclear plants in England, it was determined necessary to visually inspect fuel rods and bundles immediately upon their removal from the reactor.



FIG. 9 - C.E.G.B. FUEL INSPECTION

An underwater Remote Viewing device with rigid probe coupled to a color camera was developed. The unit contained miniature motors for scan and focus control.

The probe, with illumination attached and secured in a positioning system, is lowered 30 feet underwater to the bottom of the spent fuel pool. A fuel bundle is then positioned in the unit and through use of positioning controls, the probe is lowered between the rods into the bundle to a penetration depth of 1/2 meter.

Visual examination of the conditions of the fuel determine if the reactor has to be shut down for refueling or whether it can remain operating.

FIELD AND LABORATORY APPLICATIONS OF AN ULTRASONIC  
METHOD FOR MEASUREMENT OF STRESS GRADIENTS IN STRUCTURES

Teodoro Leon Salamanca, Ph.D., Eugene R. Reinhart  
Reinhart & Associates, Inc., Austin, Texas

Donald E. Bray, Ph.D.  
Texas A&M University, College Station, Texas

Matthew J. Golis, Ph.D.  
Advanced Quality Concepts, Columbus, Ohio

ABSTRACT

An ultrasonic technique using critically refracted longitudinal waves (CRLW) is described and shown capable of measuring stress changes (stress gradients) in a laboratory test on welded plates and in a field test on generator retaining rings. In the welded plates case, residual stress changes were obtained by measuring the relative velocity changes in different plate conditions, namely as received, after welding, and after stress relieving of the plates. Preferred orientation of crystals is known to produce similar effects as stress does on velocity; therefore, a neutron diffraction technique was used to study the (001) [110] texture in the plates and found no significant changes throughout the weld and parent metal. In the case of the generator retaining ring, measurements were taken when the ring was installed and off the rotor. It was found that high tensile hoop stresses are set up in the ends of the ring when the rotor is stationary and the hoop stress vanishes when the ring is off the rotor. In both cases, the CRLW technique was able to discriminate between the two different states of stress.

INTRODUCTION

New and more demanding structural engineering designs have, in the past, increased the safety factor of a structure to prevent mechanical failures. The emerging of the nondestructive evaluation (NDE) field as an alternative to estimate remaining service life in a structure or component has assisted in the improvement of the design process by allowing lower safety factors and weight reduction. The NDE schemes are dependent upon many factors including defect detection and characterization, material degradation, and applied and residual stresses among others.

Concerning residual stress measurement, many nondestructive techniques to measure stress (residual and/or applied) have been investigated and resulted in successful laboratory techniques. Some of these techniques have also been developed into field applicable techniques such as X-ray diffraction [1] and Barkhausen noise [2]. Laboratory and field applicable techniques are useful under given favorable conditions and have their own disadvantages.

An ultrasonic technique, which is described in the following pages, is explained and applied in two cases, namely laboratory and field cases. The ultrasonic technique measures the critically refracted longitudinal wave (CRLW) velocity in a material that is subjected to applied and/or residual stress. The first case, in a laboratory use, a pair of steel welded plates (cold rolled and hot rolled plates) were used to measure the longitudinal residual stress field before and after partial stress relieving treatment. In the second case, a field use, the applied hoop stress is measured in a generator retaining ring. Two different stress conditions are studied; when the retaining ring is installed on the rotor (stationary) and when the ring is taken off of the rotor.

In both cases, steel welded plates and retaining ring, a relative zero stress travel-time value is defined based on areas assumed to be unstressed.

#### TECHNIQUE

Stress measurement using ultrasonic techniques is dependent on the acoustoelastic effect, i.e., strain-induced ultrasonic wave velocity variations. The acoustoelastic theory predicts that such variations behave linearly provided the material is elastically deformed. The effect is distinct for different kinds of waves. These effects were measured by Egle and Bray [3] in a railroad steel sample and they found that ultrasonic velocities vary linearly with strain as predicted by the acoustoelastic theory. Their results show that the most strain-sensitive wave is the longitudinal wave propagating parallel to the stress axis and the least strain-sensitive wave is the shear wave propagating perpendicular to the stress axis. Since the longitudinal wave

propagating parallel to the stress axis is most sensitive to stress (strain), a technique able to propagate a longitudinal wave in a material is desirable. A method to excite a longitudinal wave is by using mode conversion and Snell's Law of refraction. By using mode conversion, an appropriate incident beam is used to excite a critically refracted longitudinal wave in the subsurface of the test medium. In the case of plexiglass as the incident medium (transducer with a shoe made of plexiglass) and steel the test medium, the angle of incidence at the first critical angle is approximately equal to 28 degrees. The excited subsurface wave can be detected by placing another transducer similar to the transmitting transducer in front of the transmitting transducer.

Due to ultrasonic velocity changes induced by strain, the technique was developed to measure the velocity of the CRLW in a linear path and in a constant gage length, therefore, the velocity changes will be effectively measured by measuring travel-time changes. There are two ways to measure travel-time as described above. One way is by using one transmitting transducer and two receiving transducers assembled on a properly aligned frame. Another way is by using one transmitting transducer and one receiving transducer assembled on a properly aligned frame. In both cases, a test or reference block must be used to calibrate the distance between transducers, i.e., standard travel-time. The ultrasonic probes consist of transmitting and receiving transducers made of plexiglass wedges and air-backed or highly damped commercial transducers coupled on to the wedges. The ultrasonic signal received is composed of refracted longitudinal and shear waves, but since the longitudinal waves are faster they arrive earlier in time. Once the first arriving pulse is identified, the first and second positive crossings are marked and measured. The probe measures

stress (strain) in the linear direction that the CRLW is propagating by correlating the travel-time measured to the acoustoelastic constant of the test material.

## RESULTS

### Case 1. Steel Welded Plates Before and After Stress Relieving

During the process of welding, due to the shrinking and plastic deformation caused by the thermal process, residual stresses are set up inside the part being welded. Residual stresses created as a result of welding of steel plates are studied and measured in Reference [4]. It was found that residual tensile stress almost as high as the yielding point of the base metal is generated in the weld in the longitudinal direction parallel to the weld bead axis; this stress is compressive in areas away from the weld, and gradually approaches zero towards the edges of the plate (see Figure 1). The residual shear stress perpendicular to the weld bead axis is usually lower than the residual longitudinal stress either near or away from the weld. The stress distribution described above indicates that the residual longitudinal stress may be more detrimental to the plate integrity in the event an applied tensile stress is superimposed on the residual stress. Therefore, the residual longitudinal stress is to be measured.

A pair of steel (1018) welded plates of dimensions 762 mm (30 in) x 254 mm (10 in) and thickness of 19 mm (0.75 in), one cold rolled and one hot rolled were used for this case. There was a third plate used in the measurements as a control plate made of 1018 steel fully annealed. The probe configuration with one transmitter and two receivers was used by positioning the probe parallel to the weld and the rolling

direction of the plates. The receiving transducers were separated by a fixed constant distance of 216 mm (8 in). Travel-time measurements were taken in different conditions of the plates, namely as received, before welding, after welding, and after partial stress-relief treatment (1100 degrees Fahrenheit for 1 hour). The refracted waves were captured by using a digital data acquisition system capable of transient sampling of 20 MHz and equivalent sampling of 160 MHz.

The results shown in Figures 2 - 5 were obtained by using two probes with air backed transducers [5] (piezoceramic material EC64 1 in x 1 in) having nominal frequencies of 1 MHz and 2.25 MHz and all the measurements were performed at room temperature (approximately 21 degrees Celsius). The travel-time values obtained for the annealed control plate were 37 microseconds for the 1 MHz probe and 36.5 microseconds for the 2.25 MHz probe; the same values were obtained from measurements on the hot rolled and cold rolled plates before welding (these values are marked by the line on the left axes of Figure 2 - 5). Figures 2 - 5 show plots of the ultrasonic wave travel-time variations as a function of distance from weld centerline obtained during these tests. Observe that the travel-time obtained before stress relief is much larger in the vicinity of the weld centerline than in the base metal. The region near the weld, especially the centerline, is known to be the area of highest tensile longitudinal residual stress in welded plates. Had the centerline been under compression instead of tension, the travel-time would have been less there than in areas away from the centerline into the parent metal.

Notice also, after stress relieving, the travel-time near the weld centerline showed a sharp decrease in travel-time for the hot



rolled plate (1 and 2.25 MHz) and for the cold rolled plate (1 MHz). In general the travel-time increased in regions away from the weld, i.e., in the base metal. This increase is larger in the cold rolled than in the hot rolled plate. Since it is known that residual compressive stresses are introduced during the rolling process, the increase in travel-time shows that the stress in the parent metal has become less compressive, i.e., more tensile as a result of the stress relief treatment. From the acoustoelastic constant in steel [3] for longitudinal waves propagating parallel to the stress axis, the expected travel-time variation is 0.44 nanoseconds per MPa (3 nanoseconds per ksi). This is shown in Figures 2 - 5 on top left corner.

Rolled steel plates are known to have preferred crystallite orientation introduced by the rolling process. To determine the density and distribution of the preferably orientated crystallites, the (001) [110] plate texture was studied by means of a neutron diffraction technique [6]. The technique is through-transmission and yields the through-the-thickness average distribution of a preselected texture of the plates. The fully annealed plate was used to normalize the data obtained from the cold rolled and hot rolled plates, before stress relieving.

The resulting pole figures [5] shown in Figures 6 - 9 indicate that for the hot rolled plate at locations 1 in from the weld (Figure 6) and at the weld (Figure 7), the distribution of the (110) planes (perpendicular to the [110] direction) near the rolling direction is very similar and the density is practically the same (approximately 0.77% lower at the weld). For the cold rolled plate at locations 1 in from the weld (Figure 8) and at the weld (Figure 9), the distribution of the (110) planes is

very similar, but the density is different (approximately 22% higher at the weld). The above results show that the cold rolled plate possesses a larger differential density of the (110) planes near the rolling direction which is parallel to the CRLW propagation direction.

#### Case 2. Shrink Fit Stress in Generator Retaining Rings

Generator retaining rings are subjected to different stress states during operation, installation, and maintenance routines. Principally, hoop stress fluctuates from about 10 ksi at the center of the ring to 45 ksi at the ends of the ring when the ring is shrunk onto the rotor and it is stationary according to a finite element analysis [7] as shown in Figure 10. During operation, the magnitude of the hoop stress depends more on the axial location and operating conditions. When the ring is off the rotor, the hoop stress should be zero in any axial location along the ring. The retaining ring used for this study is a Westinghouse retaining ring with approximate dimensions of 711 mm (28 in) in length and 610 mm (24 in) in radius.

A probe arrangement using one transmitting and one receiving transducer configuration was used. The transducers were made of plexiglass wedges machined to fit the curved surfaces of the ring and highly damped commercial 2.25 MHz transducers were used to excite and receive the CRLW waves. In addition, the obliquity factor technique [8] was used to optimize the energy transmission through the propagating media (alloy steel). The probe was positioned parallel to the circumferential direction (parallel to the hoop stress) to measure travel-time, and was calibrated with a test sample cut off a retaining ring. A more precise and faster digitizing system (100 MHz transient sampling and 300 MHz repetitive bandwidth) as compared

to the system used in the weld plates case was used to capture the CRLW wave, and the travel-time measurements were made when the ring was installed on the rotor and when the ring was off the rotor. The results obtained are shown in Figure 11, where the cross section of the ring is displayed as well as a plot of the hoop direction travel-time variation as a function of axial location on the ring. The acoustoelastic constant for this particular steel is not available at this time, therefore, the stress variation can not be computed. Nonetheless, the travel-time changes follow the same pattern as the predicted hoop stress in [7].

#### SUMMARY

Critically refracted longitudinal waves (CRLW) are demonstrated and found to be a useful way of monitoring residual and/or applied stress changes due to their unique characteristics of being a subsurface longitudinal wave that propagates in a linear manner from the point of excitation. The CRLW can be detected at places in front of the excitation point to precisely measure travel-time between fixed points effectively measuring the wave velocity. Since the velocity of the CRLW waves is sensitive to stress, an unstressed area in a structure should be located and used as a relative zero stress reference as explained in the two cases studied. The CRLW waves are sensitive to stress in the direction they propagate (linear fashion), therefore, if the direction of the stress to be measured is known, the probe should be oriented parallel to that direction. The cases presented demonstrate the versatility and applicability of the technique to different problems either in a laboratory or in the field.

#### ACKNOWLEDGEMENTS

We would like to thank the Texas A&M University NDT lab at the Mechanical Engineering Department, Reinhart & Associates, Inc. lab, W. B. Tuttle Power Plant in San Antonio, Texas, and Hewlett Packard in Austin, Texas, for their support and valuable effort and contribution to make this study possible. Parts of this document are included in the NSF Grant No. ISI-8760214, Phase I Final Report.

#### REFERENCES

1. Cullity, B.D. Elements of X-ray Diffraction, 2nd ed., Addison-Wesley Publishing Co. Inc., Reading, Massachusetts (1978).
2. Gardner, C.G. "Engineering Evaluation of Barkhausen Effect Stress Measurement Instrumentation for Application to Autofrettaged Gun Tubes," AMRC CTR 72-22, Army Materials and Mechanics Research Center, Watertown, Massachusetts (1972).
3. Egle, D.M. and Bray D.E. "Application of the Acousto-Elastic Effect to Rail Stress Measurement," Materials Evaluation, 37, No. 4 (1979), pp. 41-46, 55.
4. Masubuchi, K. "Analysis of Welded Structures," 1st ed., Pergamon Press, Oxford (1980).
5. Leon-Salamanca, T. "Ultrasonic Measurement of Residual Stress in Steels Using Critically Refracted Longitudinal Waves (Lcr)," Ph.D. Thesis (1988).

6. Allen, D.R. and Sayers, C.M. "Neutron Scattering Studies of Texture in Mild Steel," NDT International, 14 No. 5 (1981) pp. 263-269.
7. Structural Integrity Associates, Inc. "Fracture Mechanics Applications to Generator Retaining Rings," Technical Brief S1TB-87-01, November, 1987.
8. Private communication per conversation with Dr. Ronald E. Larsen in July, 1988.

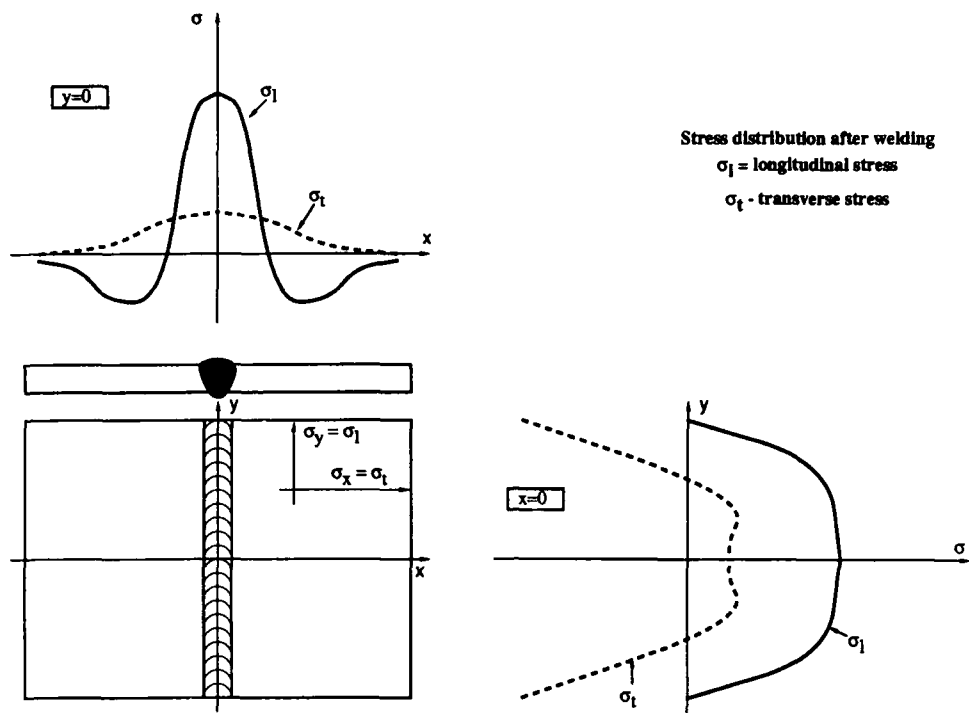


Figure 1. Residual stress distribution after welding a plate.

### CRLW Travel-Time Changes Before and After Stress Relief

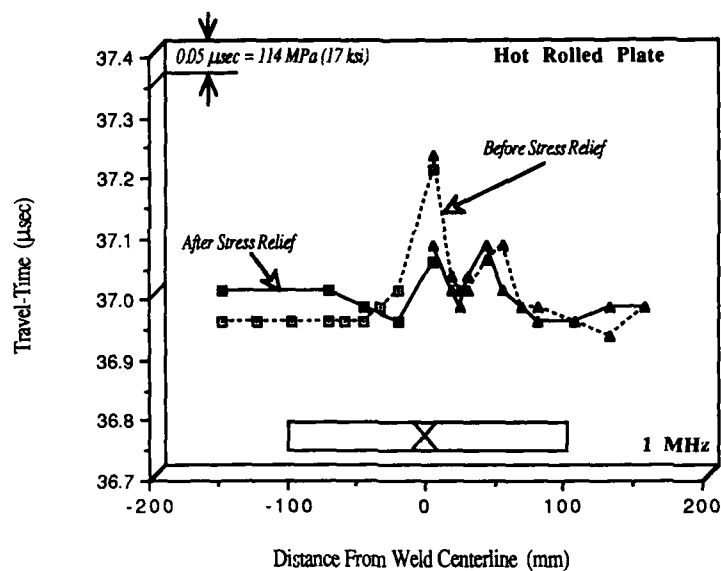


Figure 2. CRLW travel-time changes before and after stress relief (Hot rolled plate, 1 MHz probe).

### CRLW Travel-Time Changes Before and After Stress Relief

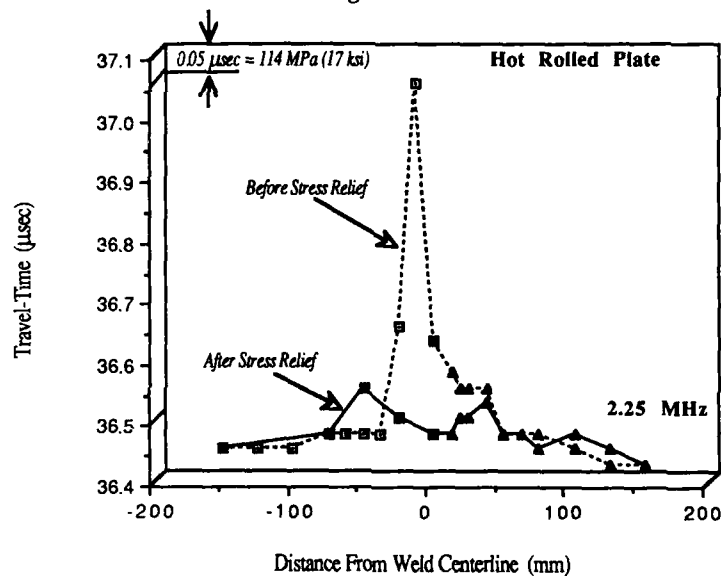


Figure 3. CRLW travel-time changes before and after stress relief (Hot rolled plate, 2.25 MHz probe).

#### CRLW Travel-Time Changes Before and After Stress Relief

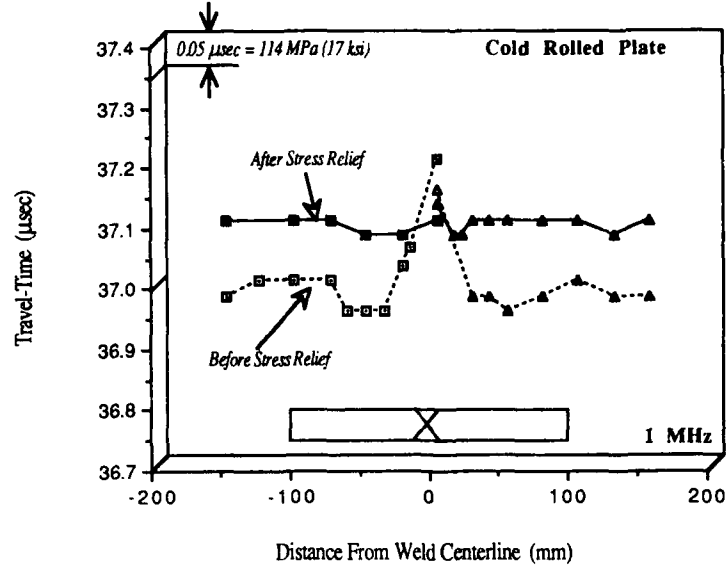


Figure 4. CRLW travel-time changes before and after stress relief (Cold rolled plate, 1 MHz probe).

#### CRLW Travel-Time Changes Before and After Stress Relief

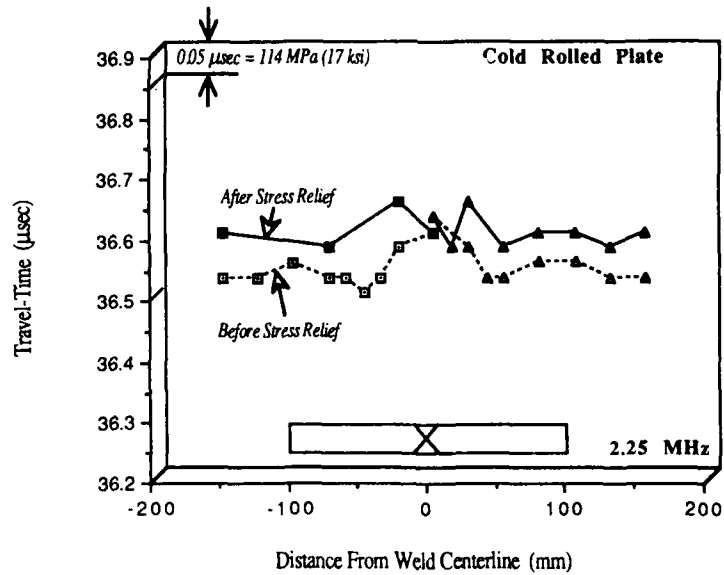


Figure 5. CRLW travel-time changes before and after stress relief (Cold rolled plate, 2.25 MHz probe).

# POLE FIGURE OBTAINED USING A NEUTRON DIFFRACTION TECHNIQUE

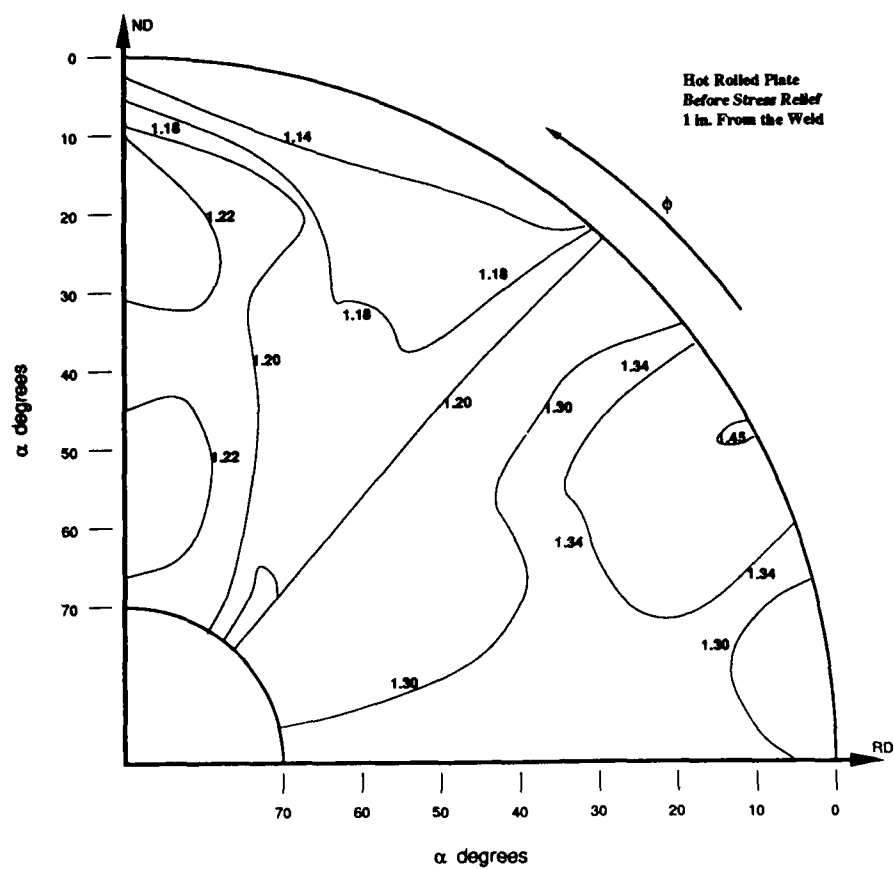


Figure 6. Pole figure from hot rolled plate before stress relief (1 in. from weld).

POLE FIGURE OBTAINED USING A NEUTRON DIFFRACTION TECHNIQUE

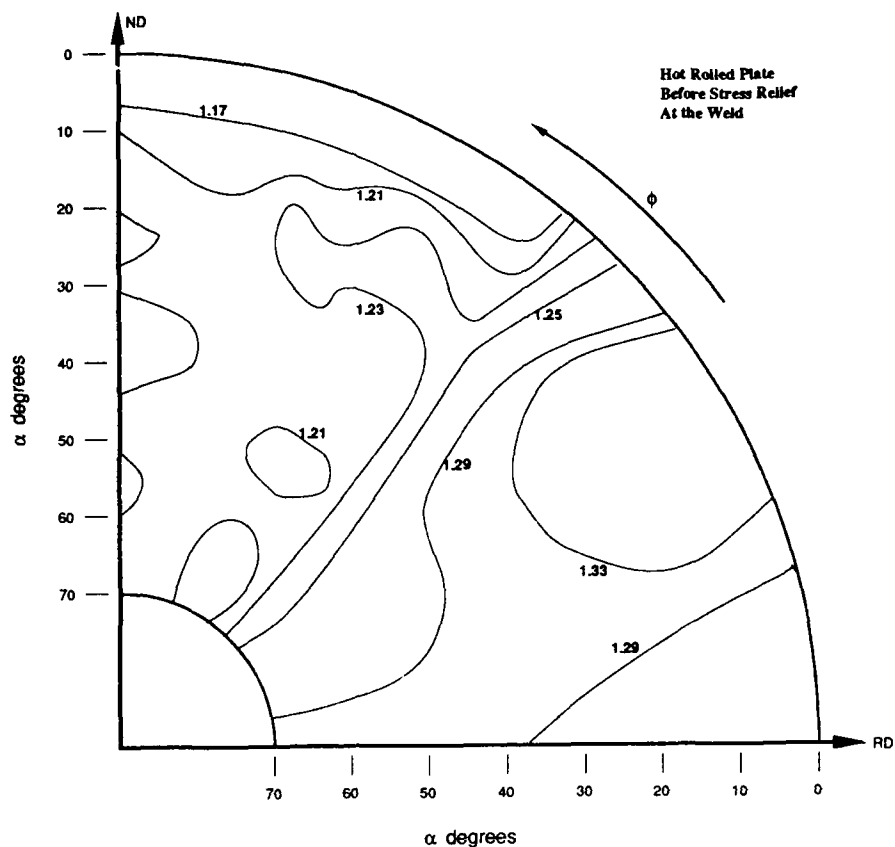


Figure 7. Pole figure from hot rolled plate before stress relief (at the weld).



POLE FIGURE OBTAINED USING A NEUTRON DIFFRACTION TECHNIQUE

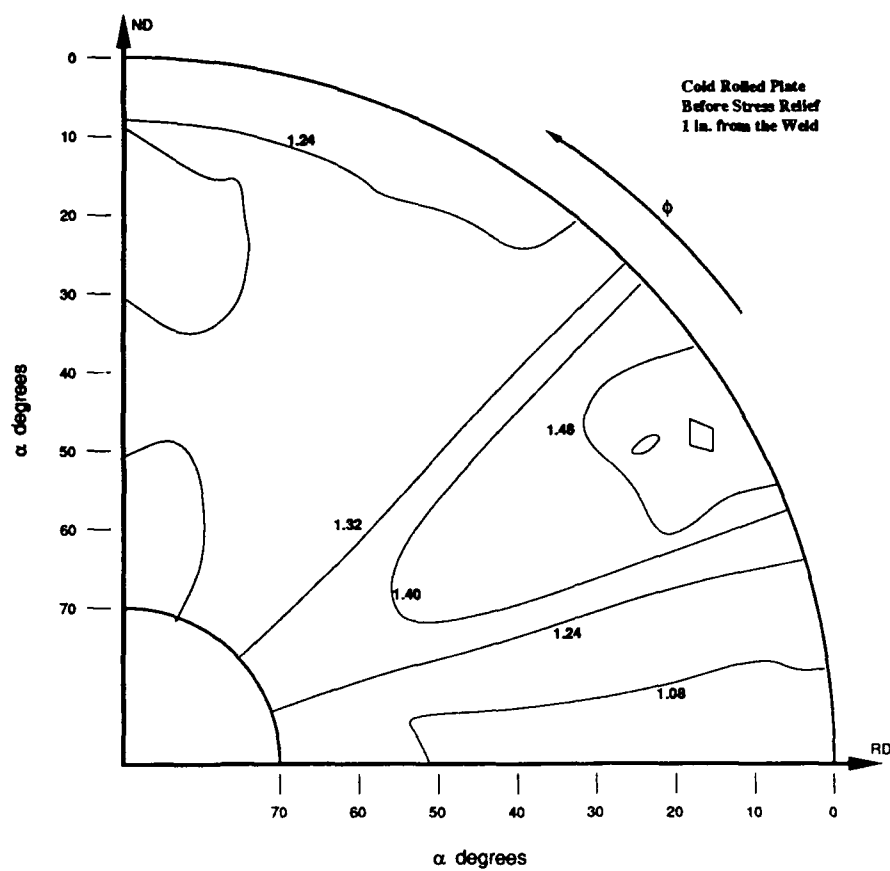


Figure 8. Pole figure from cold rolled plate before stress relief (1 in. from weld).

POLE FIGURE OBTAINED USING A NEUTRON DIFFRACTION TECHNIQUE

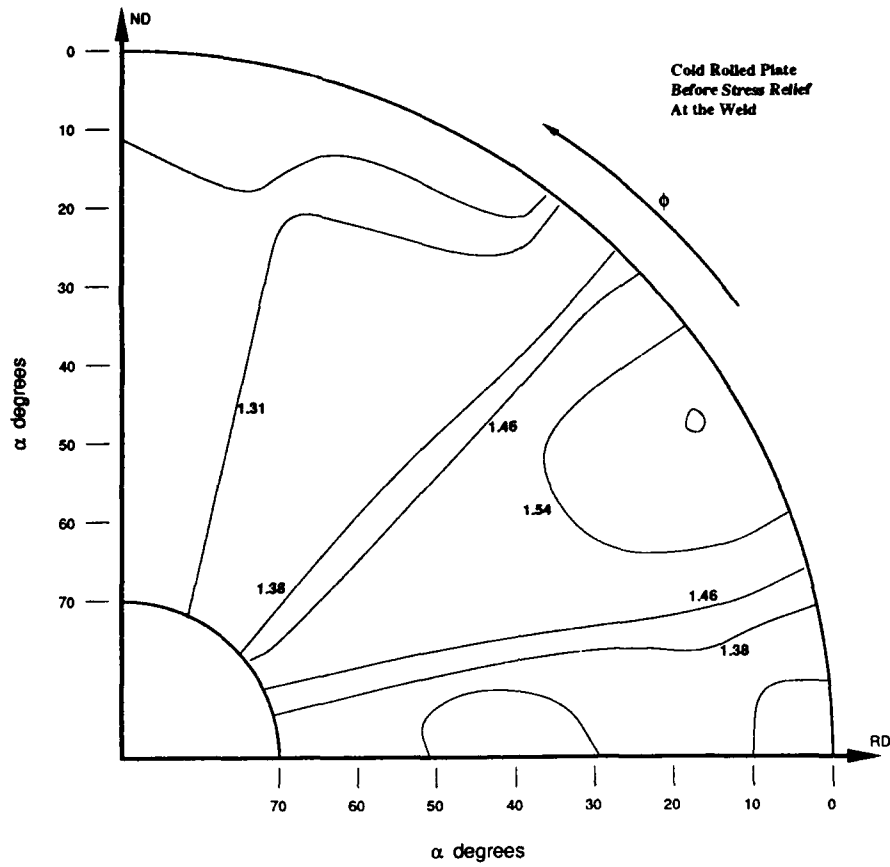


Figure 9. Pole figure from cold rolled plate before stress relief (at the weld).

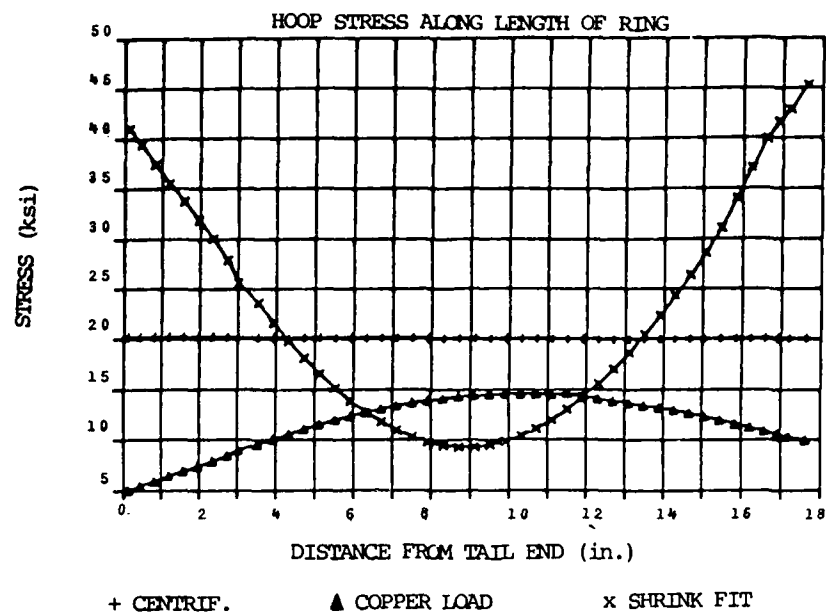


Figure 10. Retaining ring stresses [7] (Reprinted with permission).

### Travel Time vs. Axial Distance

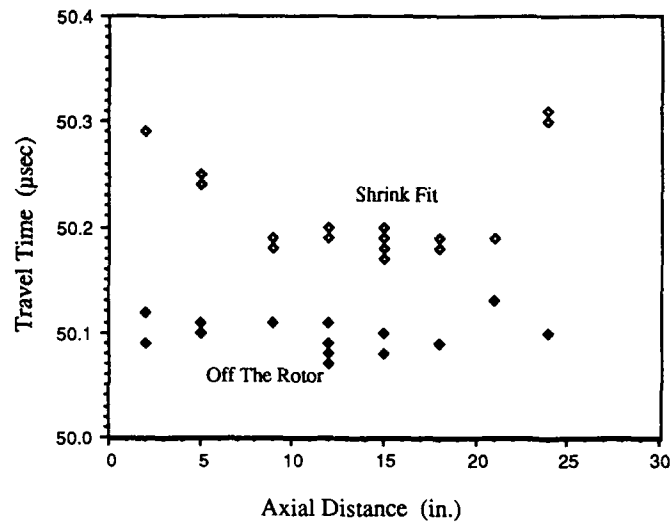


Figure 11. CRLW travel-time changes in the circumferential direction at different axial distances along retaining ring.

## A MODEL FOR MAGABSORPTION AS AN NDE TOOL FOR STRESS MEASUREMENT

M. J. Sablik and W. L. Rollwitz, Southwest Research Institute, San Antonio, TX 78284  
and  
D. C. Jiles, Center for NDE, Iowa State University, Ames, Iowa, 50011

Magabsorption involves measurement of the change in the impedance of an rf coil coupled to a ferromagnetic material in a bias magnetic field. The bias field  $H$  is varied cyclically so that the rf impedance traces out a butterfly-shaped hysteresis loop, which arises because the rf impedance is proportional to the square root of the "reversible" permeability of the material. In this paper, the reversible permeability is taken to be the anhysteretic permeability in the Sablik-Jiles model of stress effects on magnetic hysteresis. It is shown that if the stress axis is parallel to the applied magnetic field, the model predicts for steel that the butterfly-shaped hysteresis loop under tensile stress has more sharply defined peaks which are closer to  $H=0$ . Under compression, the peaks are more diffuse and are further from  $H=0$ . The difference between the peak value and the smallest value of the butterfly loop (i.e. the peak-to-peak amplitude) is a measure of the stress and increases monotonically as stress is varied from negative (compressive) to positive (tensile) values. The predictions of the model agree generally with experimental observations. The peak-to-peak technique for stress measurement has been used for NDE monitoring of stress in compressor blades.

### 1.0 INTRODUCTION

In the "magabsorption" measurement<sup>1,2</sup> a ferromagnetic material is placed inside an rf coil in the presence of a magnetic biasing field. The coil (plus its core) is a part of a resonant circuit. The resonant circuit is fed from a constant current radiofrequency generator. The amplitude varying voltage  $V_M$  across the resonant circuit is the "magabsorption" signal. This signal is a function of the magnetic biasing field. Another name given to this phenomenon in the past is "magnetoabsorption."<sup>1,3</sup>

The resonant circuit in the magabsorption measurement is depicted schematically in Figure 1. A coil with a cylindrical

ferromagnetic core inside it is in a magnetic biasing field. The coil has a self-inductance  $L_o$  which is modified to  $L_o + \Delta L$  because of the presence of the core. Connected to the coil is a resistor. The combination of resistor plus coil plus core has a resistance  $R_o + \Delta R$ , where  $\Delta R$  is the part due to the presence of the core. In parallel with the arm containing the coil and resistor is another circuit arm with a capacitor  $C$ . Into this combined circuit is fed current  $I_c$  from a constant current rf generator at the resonant frequency of the coil capacitor combination.

If the coil is a high  $Q$  coil, the impedance of the coil capacitor combination at resonance is

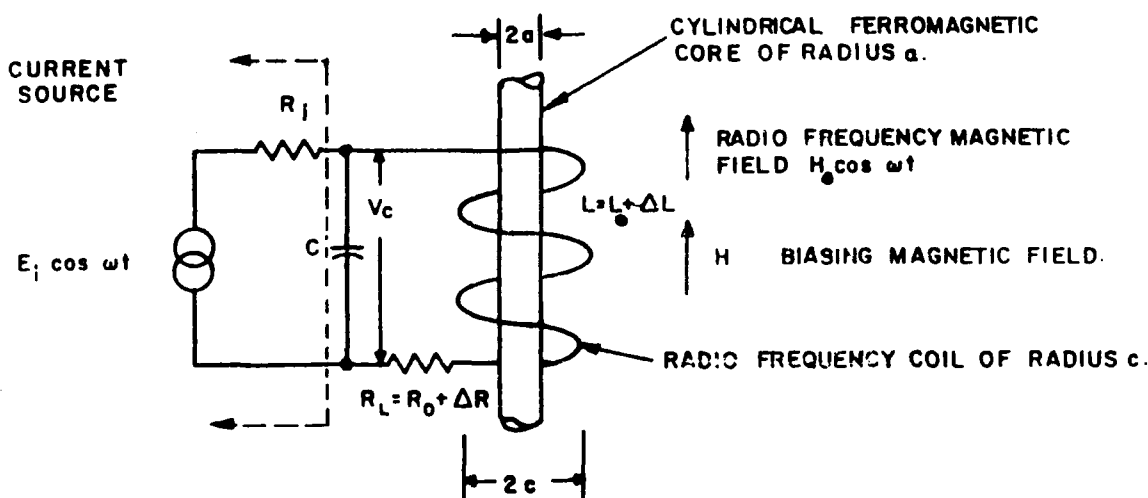


Figure 1 The basic magabsorption circuit composed of an inductance  $L_0$  with the sample core in a biasing field  $H$  and tuned to resonance with capacitance  $C$ . The circuit is fed from a radiotrequency voltage  $e_i = E_i \cos \omega t$ .

$$Z_r \approx X_c Q_r \approx L/RC, \quad (1)$$

where  $X_c$  is the capacitive reactance and where the subscript  $r$  denotes resonance. The magabsorption signal is then

$$V_M = Z_r I_c = (L/RC) I_c, \quad (2)$$

which in turn can be written as

$$V_0 - \Delta V = \frac{(L_0 + \Delta L)}{(R_0 + \Delta R) C} I_c, \quad (3)$$

relative to  $R_0$ ,  $L_0$ , and  $V_0$  of the coil without the core inserted.

The net signal  $\Delta V$  due to the material is given by

$$\Delta V = V_0 - (V_0 - \Delta V),$$

which after appropriate manipulation becomes

$$\Delta V = \left\{ \frac{L_0 \Delta R}{(R_0 + \Delta R) R_0 C} \right\} I_c. \quad (4)$$

Thus, the net magabsorption signal  $\Delta V$  is proportional to  $\Delta R$ , the change in resistance due to the presence of the core.

It can be shown from electromagnetic theory (see Appendix) that  $\Delta R$  is proportional to  $\mu^{1/2}$  and thus  $\Delta V$  is proportional to  $\mu^{1/2}$  if  $R_0 \gg \Delta R$ , which is a condition that can always be satisfied. The magnetic permeability  $\mu$  of the ferromagnetic core is in fact what is called the "reversible" permeability.<sup>4,5</sup>

A radiofrequency bridge for measuring the net signal  $\Delta V$  is shown in Figure 2.

Because the rf excitation signal is small amplitude rf, the domain walls in the ferromagnetic material are not unpinned during their vibratory motion. Hence the  $\mu$  contributing to  $\Delta R$  (and hence  $\Delta V$ ) is the reversible permeability. This "reversible" permeability, which in reality is a differential permeability, nevertheless is hysteretic in behavior as the biasing magnetic field is changed, and a butterfly-shaped hysteresis loop in  $\Delta R$  (and hence  $\Delta V$ ) is found as a function of bias field  $H$ .

In this paper, this butterfly-like hysteresis loop and its stress dependence shall be explained in terms of the model for magnetomechanical effects in the magnetic hysteresis developed by two of the authors of this paper.<sup>6,8</sup>

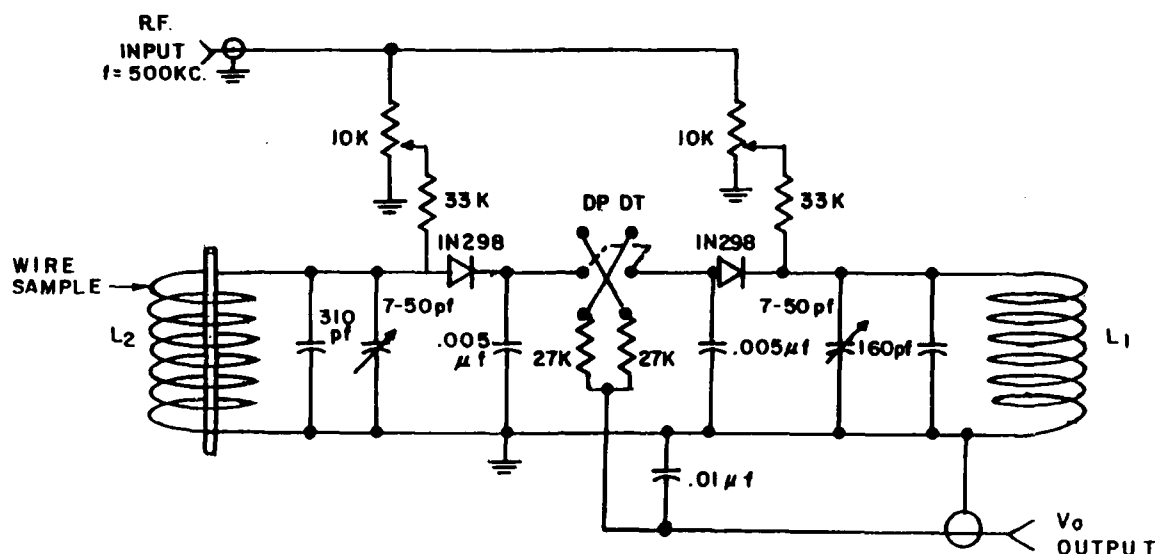


Figure 2 The net magabsorption measurement radiofrequency bridge for the subtraction of peak voltages of two circuits similar to that in Figure 1 but differing in that one of the circuits has the sample core removed.

## 2.0 FORMULATION

In global equilibrium, a ferromagnet has a magnetization given by the anhysteretic magnetization  $M_{an}$ , given as

$$M_{an} = M_s f(H_e/a), \quad (5)$$

where the function  $f$  is the Langevin function

$$f(x) = \coth x - 1/x. \quad (6)$$

Here  $M_s$  is the saturation magnetization of the ferromagnet,  $H_e$  is the effective field inside it, and  $a$  is a parameter of the material.

The effective magnetic field  $H_e$  is

$$H_e = H + \alpha M + H_\sigma(\sigma, M). \quad (7)$$

The second term is the contribution to the effective field from the magnetization and the third term is the contribution to the effective field from mechanical stress  $\sigma$  acting on the material. The parameter  $\alpha$  is known as the effective field parameter.

For the case where the stress axis is parallel to applied field  $H$ ,

the stress contribution  $H_\sigma$  is obtained from thermodynamics.<sup>7</sup> The Gibbs function  $G$ , internal energy  $U$ , and Helmholtz function  $A$  are given respectively as<sup>9</sup>

$$G = U - TS + (3/2) \sigma \lambda, \quad (8a)$$

$$U = (1/2) \kappa M^2, \quad (8b)$$

$$A = G + \mu_0 H M, \quad (8c)$$

where  $\mu_0$  is the permeability of free space and  $\lambda$  is the magnetostriction of the material. It then follows that

$$H_e = \frac{1}{\mu_0} \left( \frac{\partial A}{\partial M} \right)_T, \quad (9a)$$

$$= H + \alpha M + \frac{3}{2} \frac{\sigma}{\mu_c} \left( \frac{\partial \lambda}{\partial M} \right)_T, \quad (9b)$$

so that

$$H_\sigma = \frac{3}{2} \frac{\sigma}{\mu_c} \left( \frac{\partial \lambda}{\partial M} \right)_T, \quad (10)$$

In this,  $\alpha = \kappa/\mu_0$ .

Previous authors<sup>10,11</sup> have used  $H_G = 3\sigma\lambda_s / (2\mu_0 M_s)$ , where  $\lambda_s$  is the saturation magnetostriction. However, this expression is derived on the basis of magnetostriction in a domain. When considering the bulk material, the expression used by previous authors is not appropriate, since bulk magnetostriction changes from zero in a demagnetized state to  $\lambda_s$  at saturation.

The effect of pinning of domain wall motion enters through<sup>12</sup>

$$M = M_{an} - k\delta (dM/dB_e), \quad (11)$$

where  $k$  is the pinning constant,  $B_e$  is the effective flux density, and  $\delta = +1$  or  $-1$ , depending on whether  $H$  is increasing or decreasing. The form of equation (11) ensures that pinning always opposes changes in magnetization. Thus, pinning enters as an irreversible effect in much the same way as mechanical friction.

Considered with previous equations, equation (11) can be rewritten as

$$\frac{dM}{dH} = \frac{M_{an} - M}{\frac{k\delta}{\mu_0} - \left[ \alpha + \frac{3}{2} \frac{\sigma}{\mu_0} \left( \frac{\partial^2 \lambda}{\partial M^2} \right) \right] (M_{an} - M)} \quad (12)$$

This differential equation can be solved numerically for  $M$  and yields the domain wall pinning contribution to  $M$  due to domain wall translation and pinning. The contribution is clearly irreversible and it shall be denoted as  $M_p$ .

A contribution to  $M$  due to bowing of domain walls before and after domain wall translation must be added. Thus, the total magnetization is given as

$$M = M_p + M_b, \quad (13)$$

where bowing contribution  $M_b$  is given by<sup>12</sup>

$$M_b = c(M_{an} - M_p), \quad (14)$$

where  $c$  is the ratio of the initial susceptibilities of the normal ( $M$ ) and the anhysteretic ( $M_{an}$ ) magnetization.

Looking back, one will note that the solution for  $M$  depends on

what is chosen for  $\lambda = \lambda(M)$ . Our choice at present<sup>8</sup> is

$$\lambda = \lambda_0 \hat{I}_{5/2}(H_e/a), \quad (15)$$

where  $\hat{I}_{5/2}(x)$  is a hyperbolic Bessel function. A characteristic of  $\lambda$  obtained from equation (15) is that it depends implicitly on  $M$  through  $H_e$ . Equation (15) is an expression for the magnetostriction which was introduced by Callen and Callen<sup>13,14</sup> and others<sup>15,16</sup> to treat magnetostriction in local moment systems like rare earth metals. In this approximation, the domains are treated as if they are local moments, which may not be a good approximation as saturation is approached.

Finally, the new expression for this paper is the reversible permeability, taken as

$$\mu^{(r)} = \mu_0 (1 + dM_{an}/dH). \quad (16)$$

In other words, the  $M$  contributing to the rf response is really the anhysteretic  $M$ , since domain wall translation and pinning and unpinning does not enter. Alternatively, one sees that it is the  $M$  which depends only on the local effective field  $H_e$  that contributes to the rf impedance response. Because as  $H$  is varied the effective field  $H_e$  displays hysteresis, it follows that the so-called "reversible" permeability also displays hysteresis.

In the following results, normalized curves will be presented in the form

$$\frac{\Delta V}{\Delta V_{max}} = \left( \frac{\mu^{(r)}}{\mu_{max}^{(r)}} \right). \quad (17)$$

### 3.0 COMPARISON OF THEORY AND EXPERIMENT

Figure 3 shows data taken by Rollwitz and Whitney<sup>1</sup> in which the resistance and capacitive reactance of the resonant coil-capacitor combination are measured independently as a function of magnetic biasing field and stress. In particular the changes  $\Delta R$  and  $\Delta X_C$  due to insertion of an iron wire core into the coil are displayed. It is seen that  $\Delta R$  peaks fairly sharply when tensile stress is applied to the iron wire. As stress is increased from 15 ksi to 35 ksi, the difference between the peak value and smallest value of the loop (i.e. the peak-to-peak amplitude) also increases. If  $\Delta R$  were plotted also for negative



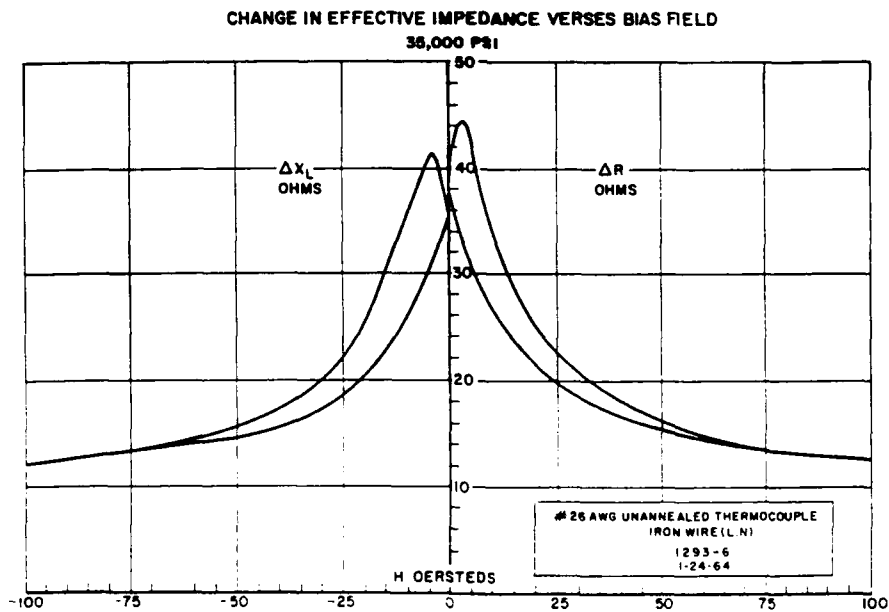
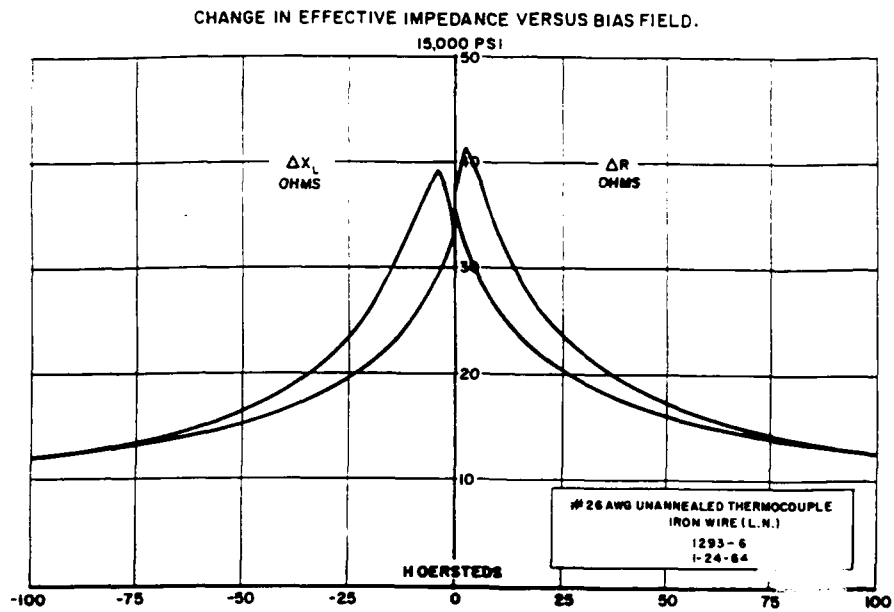


Figure 3 Effect of tensile stress on the hysteretic biasing magnetic field dependence of  $\Delta R$  and  $\Delta X_L$  of an iron thermocouple wire. Stress values for the top and bottom figures are 15 ksi and 35 ksi respectively.  $\Delta R$  and  $\Delta X_L$  denote experimental measurements of the changes in resistance and inductive reactance of the rf coil due to the presence of stressed iron thermocouple wire inside the coil.

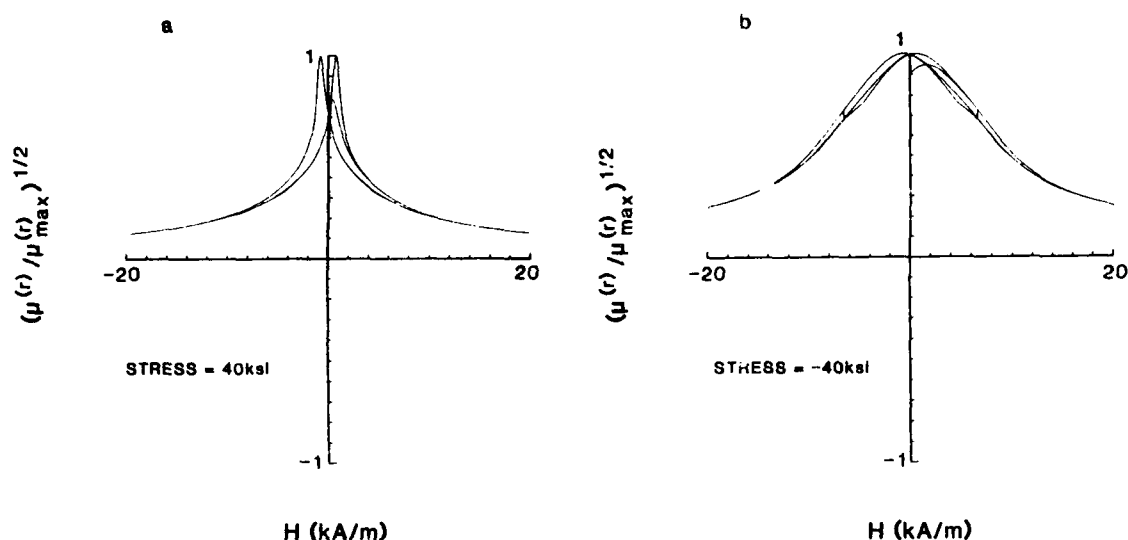


Figure 4 Theoretical variation with magnetic field  $H$  of the square root of the normalized reversible permeability. The value  $\mu_{max}^{(r)}$  denotes the largest value of the reversible permeability attained during the variation of  $H$ . In this case, a family of three hysteresis loops are obtained for different values of maximum  $H$ . Also seen is the initial reversible permeability variation. In (a), the applied stress  $\sigma$  is +40 ksi (tensile); in (b), -40 ksi (compressive). As explained in the text, the net magabsorption signal  $\Delta V$  is related to  $\mu^{(r)}$  as  $\Delta V/\Delta V_{max} = (\mu^{(r)}/\mu_{max}^{(r)})^{1/2}$ . The parameters used for this computation are  $\alpha = 0.002$ ,  $k/\mu_o = 1800$ ,  $c = 0.25$ ,  $a = 3000$  A/m,  $M_s = 1350000$  A/m, and  $\lambda_o = 3.5 \times 10^{-5}$ .

$H$ , one would observe reflective symmetry about  $H=0$  and a butterfly-shaped hysteresis loop. It will be recalled that the magabsorption signal is proportional to  $\Delta R$ .

Figures 4(a) and 4(b) display theoretical results for the normalized quantity  $(\mu^{(r)}/\mu_{max}^{(r)})^{1/2}$  as a function of  $H$  for stress equal to 40 ksi and -40 ksi respectively. A butterfly-shaped hysteresis loop similar to those seen in Figure 3 for  $\Delta R$  is observed in the case of tensile stress ( $\sigma = +40$  ksi). For compressive stress ( $\sigma = -40$  ksi), the peak in  $\Delta V/\Delta V_{max}$  (see equation (17)) is more diffuse. In agreement with experiment, the "peak-to-peak" amplitude increases as stress is increased from compressive to tensile stress. Note that the parameter values chosen for this computation are shown in the figure caption.

Figures 5(a) and 5(b) show corresponding theoretical magnetization hysteresis curves as a function of  $H$ . Notice that the

effect of stress is primarily to change the slope of hysteresis curves with slope increasing as stress is varied from negative (compressive) to positive (tensile) values. This effect was modeled by us previously<sup>6, 17</sup> and noted experimentally by Langman<sup>18</sup> and Kwun and Burkhardt.<sup>19</sup>

Figures 6 and 7 show experimental magabsorption signals for iron and nickel wire respectively. The signals are inverted from what is expected from  $(\mu^{(r)})^{1/2}$  vs.  $H$ . This is because the amplifier configuration produces an output of the form  $V_i - \Delta V$ , which in effect reverses the direction of the peaks. A simulation of this behavior may be seen from a plot of  $1 - (\mu^{(r)}/\mu_{max}^{(r)})^{1/2}$  vs.  $H$ , as obtained theoretically in Figure 8.

Notice the "peaks" in the case of the nickel under tension are more diffuse than in the case of iron under tension. This is because

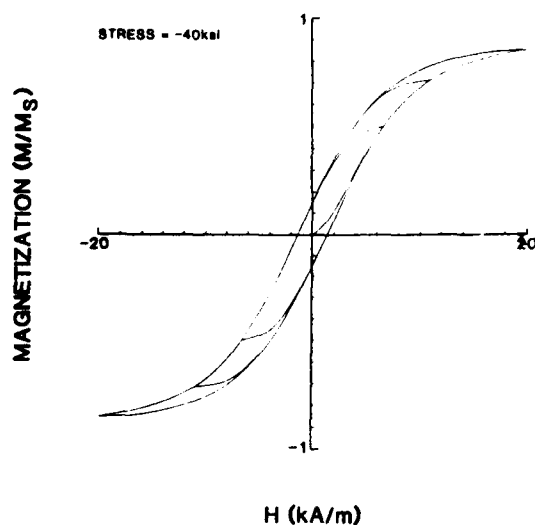
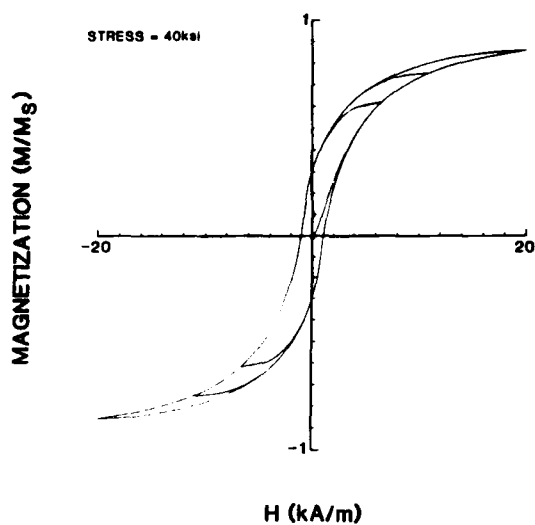


Figure 5 Theoretical variation with  $H$  of the magnetization (normalized by saturation magnetization) for (a)  $\sigma = +40$  ksi and (b)  $\sigma = -40$  ksi. A family of three hysteresis loops are shown for different values of  $H_{max}$ . Parameters used for the computation are the same as in Figure 4.

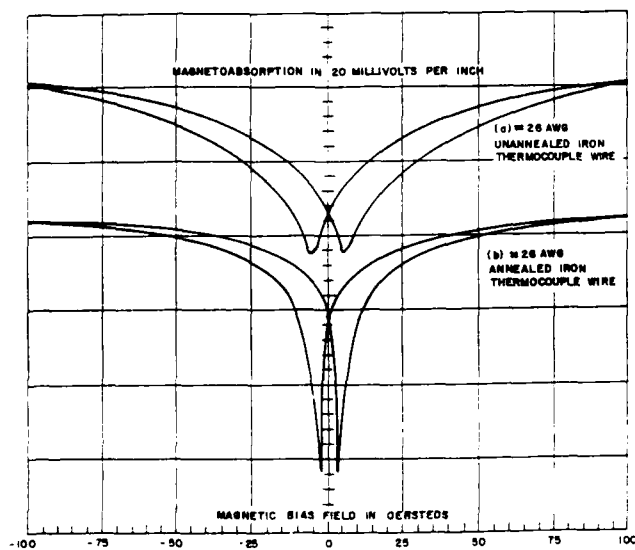


Figure 6 Experimental magabsorption signals for iron thermocouple wire as a function of  $H$ . The signals have been inverted from their expected shape by an amplifier.

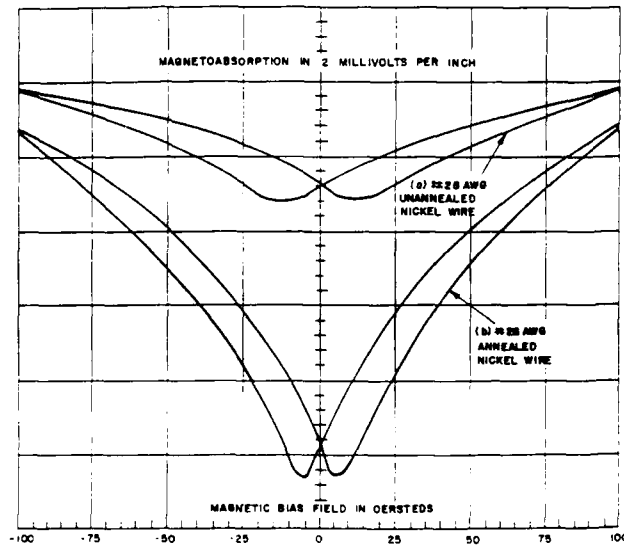


Figure 7 Experimental magabsorption signals for a nickel wire as a function of  $H$ .

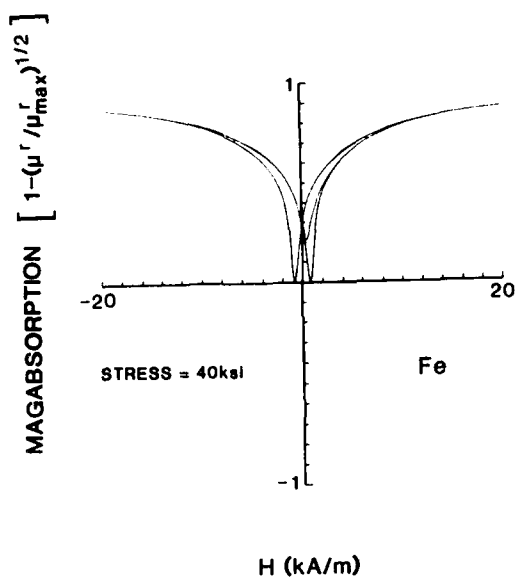


FIGURE a

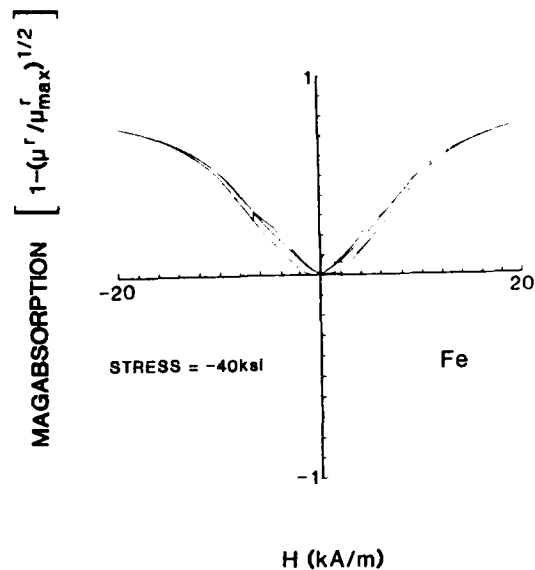


FIGURE b

Figure 8 Theoretical plot of simulated magabsorption signal  $[1-(\mu^{(r)}/\mu_{max}^{(r)})^{1/2}]$  vs. biasing field  $H$ . Parameters used for the computation are again as in Figure 4.

nickel has a magnetostriction constant  $\lambda_o$  from equation (15) that is negative. The contribution of the stress, which comes in with the sign of the combination  $\sigma d\lambda/dM$  (which is proportional in our model to  $\lambda_o \sigma$ ) is qualitatively the same for iron under compression (negative  $\sigma$ ) as for nickel under tension (negative  $\lambda_o$ ).

In Figure 9 is presented the theoretical variation of peak-to-peak amplitude with stress. In this case the "peak-to-peak" change in the unnormalized value  $(\mu^{(r)})^{1/2}$  is plotted. Because the unnormalized value is used, the variation of the "peak-to-peak" magnitude is more clearly displayed. Note that the "peak-to-peak" magnitude monotonically increases with increasing stress, varying more rapidly under tension than under compression.

Figure 10 shows experimental data<sup>20</sup> showing the variation of peak-to-peak amplitude with stress for various steel rods (types 416, 1090 and 4340 steel). The experimental variation of peak-to-peak amplitude with stress is seen to be qualitatively the same as in Figure 9, where the peak-to-peak amplitudes computed for a positive magnetostriction material are obtained.

#### 4.0 SUMMARY

Magabsorption peak-to-peak amplitude is a sensitive function of stress and should be useful as an NDE tool for stress measurement. It is now possible to predict the behavior of the peak-to-peak amplitude with stress using the magnetomechanical hysteretic theory due to Sablik and Jiles. The data in references 1, 2, 3 and 20 indicate that the magabsorption can measure the amount of stress, the type of stress (tension or compression) and the direction of the stress. When calibrated for the type of steel, the stress can be measured to an accuracy of  $\pm 3$  ksi. Also, stress in nonferromagnetic materials can be measured if one first coats the material with a thin nickel coating<sup>21</sup>.

#### 5.0 EPILOGUE

A field-usable unit for measuring stress in ferromagnetic materials has been built. The unit is compact and operates on the principle that the radiofrequency coil only has to be brought near a ferromagnetic material to effect a change in coil resistance and hence produce a magabsorption signal.

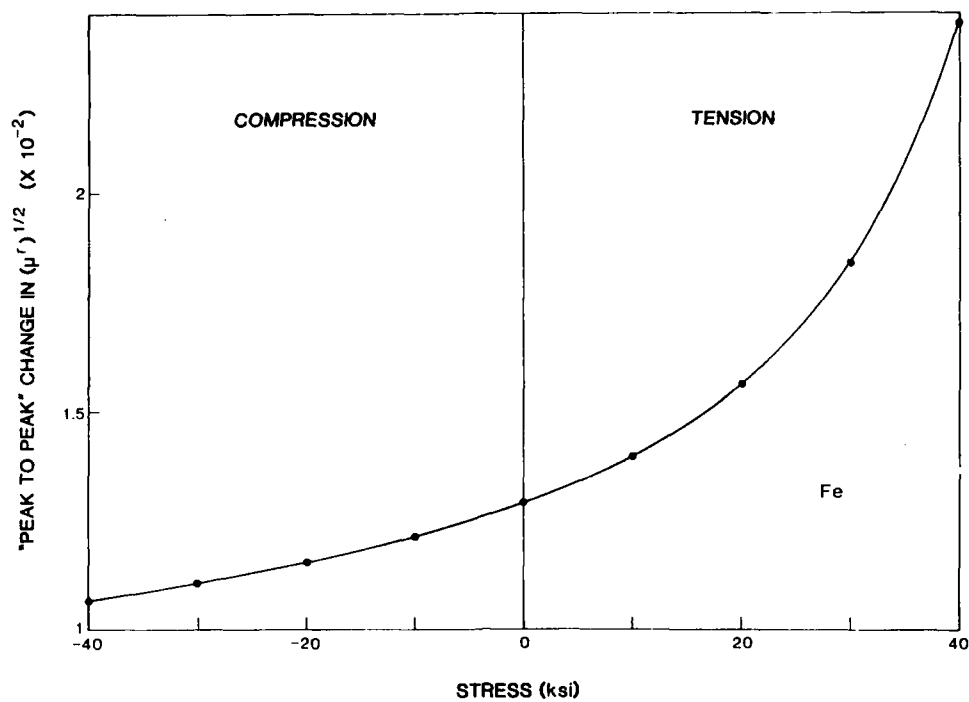


Figure 9 Theoretical variation of "peak-to-peak" change in  $(\mu')^{1/2}$  as a function of stress. Again the parameters used for the computation are as in Figure 4.

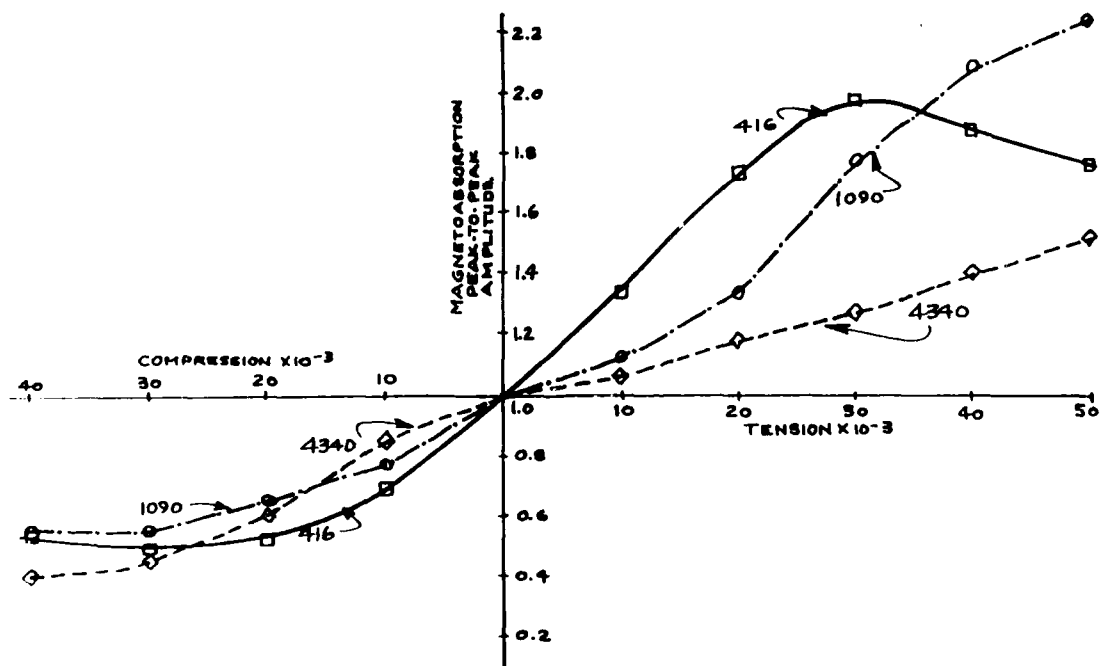


Figure 10 Experimental variation of "peak-to-peak" magabsorption amplitude with applied stress for three different types of steel: 416, 1090 and 4340.

As an example, measurements have been made on compressor blades. The stress at each position was plotted as a function of the number of vibration cycles that the blade experienced. The blade was remounted and cycled more. After many cycles, it was found that at a point near the root of the blade, residual stress would start to rise very rapidly, and the blade would start to crack at that point. It was possible to predict within 1/16 of an inch where the blade would crack, based on the local rise in stress measured by this technique.

Thus the technique discussed in this paper for measuring stress is in fact a very usable technique for NDE.

#### APPENDIX

The relationship that the change in resistance  $\Delta R$  due to the ferromagnetic core is proportional to  $\mu^{1/2}$  is derived<sup>1</sup> via a three-step process. First, the field  $H(r)$  inside the core is obtained. Then the flux threading the coil is computed and the impedance of the coil-core combination is obtained.

To find  $H(r)$  inside the core, start with Maxwell's equation

$$\nabla \times \vec{H} = \vec{J} + \frac{\partial \vec{D}}{\partial t}, \quad (A.1)$$

and take the curl, neglecting displacement current, obtaining

$$\nabla (\nabla \cdot \vec{H}) - \nabla^2 \vec{H} = \nabla \times \vec{J}, \quad (A.2)$$

after using vector identities. From Maxwell's equations and Ohm's law,

$$\nabla \times \vec{J} = \nabla \times \frac{\vec{E}}{\rho} = -\frac{1}{\rho} \frac{\partial \vec{B}}{\partial t}, \quad (A.3)$$

and

$$\nabla \cdot \vec{B} = \nabla \cdot \mu \vec{H} = \mu (\nabla \cdot \vec{H}) = 0. \quad (A.4)$$

In the latter relationship, the spatial dependence of  $\mu$  is neglected, which is reasonable for the core well inside the coil. Thus, equation (A.2) reduces to

$$\nabla^2 \vec{H} = \frac{\mu}{\rho} \frac{\partial \vec{H}}{\partial t}. \quad (A.5)$$

Expressing in cylindrical coordinates and using symmetry of the

geometry so that  $\partial^2 \vec{H} / \partial \phi^2 = 0$ , it is obtained that

$$\frac{1}{r} \frac{\partial}{\partial r} \left( r \frac{\partial \vec{H}}{\partial r} \right) = \frac{\mu}{\rho} \frac{\partial \vec{H}}{\partial t}, \quad (A.6)$$

where  $\partial^2 \vec{H} / \partial z^2 = 0$  if we assume long solenoid behavior. Because the magnetic field is in the z-direction only, its magnitude is a function of radius and time for a given value of the resistivity and reversible permeability.

A radiofrequency magnetic field which is a function of the radius, sinusoidal in time, and in the z-direction is

$$\vec{H} = \hat{k} H(r) e^{i\omega t}. \quad (A.7)$$

When one substitutes equation (A.7) into equation (A.6), one obtains

$$r^2 \frac{\partial^2}{\partial r^2} H(r) + r \frac{\partial}{\partial r} H(r) - i[Kr]^2 H(r) = 0, \quad (A.8)$$

where

$$K = \sqrt{\omega \mu / \rho}, \quad (A.9)$$

Equation (A.8) has a solution which is a Bessel function of zero order,<sup>22</sup>

$$H(r) = C_J J_0(Kr i^{3/2}) + D_K K_0(Kr i^{1/2}). \quad (A.10)$$

Since  $K_0(Kr i^{1/2})$  is undefined or infinite at the origin, it is necessary to set  $D_K = 0$  and obtain

$$H(r) = C_J J_0(Kr i^{3/2}). \quad (A.11)$$

Now apply the other boundary condition that

$$H(a) = H_{gap}, \quad (A.12)$$

where  $a$  is the radius of the cylindrical core and  $H_{gap}$  is the magnitude of the radiofrequency field in the air just outside the core. This boundary condition equates the tangential components of  $H$ . Therefore

$$C_J = H_{gap} / J_0 (Kai^{3/2}), \quad (A.13)$$

and

$$H(r) = H_{gap} \frac{J_0 (Kri^{3/2})}{J_0 (Kri^{3/2})}. \quad (A.14)$$

The magnetic flux  $\Phi$  threading the coil has a component through the core and a component through the gap between the coil and the core. If the coil radius is  $c$ ,

$$\Phi = \int_0^a \mu H(r) 2\pi r dr + \int_a^c \mu_0 H_{gap} 2\pi r dr. \quad (A.15)$$

Well inside the coil,  $H_{gap}$  and  $\mu$  can be treated as constants and

$$\Phi = \frac{\mu H_{gap} 2\pi}{J_0 (Kai^{3/2})} \int_0^a r J_0 (Kri^{3/2}) dr + \mu_0 H_{gap} 2\pi \int_a^c r dr,$$

or, after integration,<sup>22</sup>

$$\Phi = \frac{\mu H_{gap} 2\pi a J_1 (Kai^{3/2})}{Ki^{3/2} J_0 (Kai^{3/2})} + \mu_0 H_{gap} \pi (c^2 - a^2). \quad (A.16)$$

Without the core present, the magnetic flux is

$$\Phi_0 = \mu_0 H_{gap} \pi c^2. \quad (A.17)$$

The next step is to obtain voltage from this flux. From Faraday's Law, for a  $N$ -turn coil,

$$V = -N \frac{d}{dt} \Phi = -i\omega N \Phi. \quad (A.18)$$

The ratio of voltage across the coil with core present to voltage across the empty coil is

$$\frac{V}{V_0} = \frac{i\omega N \Phi}{i\omega N \Phi_0} = \frac{\Phi}{\Phi_0}. \quad (A.19)$$

Also,

$$\frac{V}{V_0} = \frac{(R+i\omega L) I_0}{i\omega L_0 I_0}, \quad (A.20)$$

where  $L_0$  is the self-inductance of the empty coil and  $L$  and  $R$  are the self-inductance and resistance with the core present. A constant amplitude current  $I_0$  is applied to the coil here. Substituting (A.16), (A.17) and (A.19) into (A.20), and simplifying, equating real and imaginary parts, one obtains

$$\frac{\omega L}{\omega L_0} = \text{Re} \left\{ \frac{(\mu/\mu_0) 2a J_1 (Kai^{3/2})}{c^2 Ki^{3/2} J_0 (Kai^{3/2})} + \frac{c^2 - a^2}{c^2} \right\}, \quad (A.21)$$

and

$$\frac{R}{\omega L_0} = \text{Im} \left\{ \frac{(\mu/\mu_0) 2a J_1 (Kai^{3/2})}{c^2 Ki^{3/2} J_0 (Kai^{3/2})} + \frac{c^2 - a^2}{c^2} \right\}, \quad (A.22)$$

Equations (A.21) and (A.22) can be further simplified by using the magnitude and angle representation of the Bessel functions as follows:

$$\frac{\omega L}{\omega L_0} = \frac{\mu 2a}{\mu_0 c^2 K} \left[ \frac{M_1(Ka)}{M_0(Ka)} \right] \times \sin \left[ \theta_1(Ka) - \theta_0(Ka) - \frac{\pi}{2} \right] + (c^2 - a^2)/c^2, \quad (A.23)$$

$$\frac{R}{\omega L_0} = \frac{\mu 2a}{\mu_0 c^2 K} \left[ \frac{M_1(Ka)}{M_0(Ka)} \right] \times \cos \left[ \theta_1(Ka) - \theta_0(Ka) - \frac{\pi}{2} \right]. \quad (A.24)$$

In this formulation the resistance  $R$  is the change in resistance  $\Delta R$  due to the insertion of the core. Inspection of (A.24) reveals that

$$\Delta R \propto \frac{\mu}{K} \propto \mu^{1/2}, \quad (A.25)$$

into which we have substituted (A.9).

# ACKNOWLEDGEMENTS

This work is an extension of research supported by Southwest Research Institute internal research grant 15-9443. One of us (D.C.J.) was supported by funding from the Center for NDE, an NSF-sponsored industry/university cooperative research center. The experimental work (W.L.R.) was supported under Air Force contracts AF33(657)-10326 and AF33(615)-5068.

## REFERENCES

- 1) W. L. Rollwitz and A. W. Whitney, Technical Report No. ML-TDR-64-123, from Southwest Research Institute to Air Force Materials Laboratory, Wright-Patterson AFB (Apr. 1964).
- 2) W. L. Rollwitz, "Magnetic Absorption NDE," ASM Metals Handbook (to be published in 17, Nondestructive Evaluation and Quality Control).
- 3) W. L. Rollwitz and J. P. Claassen, Technical Report No. AFML-TR-65-17 (Jan. 1965).
- 4) R. M. Bozorth, Ferromagnetism. (Von Nostrand, NY, 1951), pp. 538-546.
- 5) M. H. Johnson and G. T. Rado, *Phys. Rev.*, **75**, 841 (1949).
- 6) M. J. Sablik, H. Kwun, G. L. Burkhardt and D. C. Jiles, *J. Appl. Phys.*, **61**, 3799 (1987).
- 7) M. J. Sablik, G. L. Burkhardt, H. Kwun and D. C. Jiles, *J. Appl. Phys.*, **63**, 3930 (1988).
- 8) M. J. Sablik and D. C. Jiles, *J. Appl. Phys.*, **64**, 5402 (1988).
- 9) H. E. Stanley, Introduction to Phase Transitions and Critical Phenomena, (Oxford, NY, 1971), pp. 33-35.
- 10) C. S. Schneider and E. A. Semcken, *J. Appl. Phys.*, **52**, 2425 (1981).
- 11) C. S. Schneider and M. Charlesworth, *J. Appl. Phys.*, **57**, 4198 (1985).
- 12) D. C. Jiles and D. L. Atherton, *J. Magn. Magn. Malls.*, **61**, 48 (1986).
- 13) E. Callen and H. B. Callen, *Phys. Rev.*, **139**, A455 (1965).
- 14) H. B. Callen and E. Callen, *J. Phys. Chem. Solids*, **27**, 127 (1966).
- 15) A. E. Clark, B. F. DeSavage and R. Bozorth, *Phys. Rev.*, **138**, A216 (1965).
- 16) A. E. Clark, J. J. Rhyne, and E. R. Callen, *J. Appl. Phys.*, **39**, 573 (1968).
- 17) P. Garikepati, T. T. Chang and D. C. Jiles, *IEEE Trans. Magn.*, **MAG-24**, 2922 (1988).
- 18) R. Langman, *IEEE Trans. Magn.*, **MAG-21**, 1314 (1985).
- 19) H. Kwun and G. L. Burkhardt, *J. Appl. Phys.*, **61**, 1576 (1987).
- 20) W. L. Rollwitz, Technical Report No. AFML-TR-66-76 (March 1969), Part II.
- 21) W. L. Rollwitz and J. P. Claassen, Technical Report No. AFML-TR-66 (May 1966), Part I.
- 22) N. W. MacLachlan, Bessel Functions for Engineers, (Oxford, London, 1955), p. 137.



## **ELECTROMAGNETIC WELLHEAD TUBULAR INSPECTION**

Clive C. Lam  
Baker Hughes Tubular Services  
Houston, Texas

### **ABSTRACT**

The Wellhead Scanalog (WHS) is a new and effective approach to evaluate used oil field tubing. It is designed to perform tubular inspection while the tubing is being pulled, and it does not interfere with the normal workover operation. WHS provides four separate non-destructive methods to detect and evaluate common used tubing defects, namely, sucker rod wear, corrosion pitting, erosion, holes and splits. A new rotating magnetic field technique is used for sucker rod wear inspection. A modified flux leakage method is used for pitting inspection. The average wall measurement is achieved by measuring the total flux in the tubing. An Eddy current method is used for hole and split detections. These four detections are working simultaneously in a 12 inch long detection area without affecting each other. WHS is designed for wellhead environment. WHS has inspected more than 11 million feet of pipe in 3000 wells. Inspections are not affected by scale, mud, paraffin and water. To ensure reliability of the tool, there are no active moving parts in the sensor package. WHS is a great diagnostic tool for the maintenance of production wells. In addition to traditional pipe inspections and locating tubing pressure leakages, WHS can provide a profile of sucker rod wear and corrosion along the tubing string. This information can be very useful in maintenance programs.

## INTRODUCTION

The Wellhead Scanalog is built to perform on site production tubing inspection and evaluation. The inspection is performed while the tubing is being pulled and it does not interfere with the workover operation. In addition, the inspection will not be affected by poor tubing surface condition such as scale, mud or paraffin.

Kahil<sup>1</sup> has discussed the design criteria thoroughly. An ideal detection system design should be speed independent, non-contact, and with no active mechanical moving parts. These requirements raise problems for commonly used detection systems.

It is a challenge to provide sufficient inspection coverage without mechanical moving parts. Radiation methods are excluded because of the coverage limitation and because of the associated regulatory requirements. Ultrasonic methods are ruled out because of the coverage limitation and the potential poor surface condition of the tubing.

The detection system has to be able to evaluate different kinds of service induced defects. The service induced defects in production tubing are rod-wear, corrosion pitting, erosion, holes and splits. A new electromagnetic system was developed to meet the design criteria. The system includes a rotating magnetic field technique, Eddy current, flux leakage and flux measurement. The newly developed rotating magnetic field technique is used to generate a rotating field without mechanical moving parts. In this paper, we will discuss the detection methods and the oil field application of WHS.

## DETECTION METHODS

The four electromagnetic methods are designed to detect different kinds of production induced tubing defects. The four detection sub-systems overlap but do not interfere with each other. The detection system consists of three drive fields and four sets of detector packages.

A saturating DC magnetic field is applied longitudinally. This DC magnetic field performs three functions: (i) to provide an active field for the flux leakage detection, (ii) to generate a saturated magnetization for the flux measurement, and (iii) to define the magnetic state of the steel for the Eddy current detection. A longitudinal high frequency AC field is used to generate Eddy current. A pair of AC fields at two different phases with the same frequency is applied to generate a radial rotating magnetic field.

### Magnetic Flux Measurement

The application of magnetic flux integration to measure the cross sectional area (CSA) of the ferro-magnetic tubular has been used in the inspection of drill pipe<sup>3</sup>. The basic concept centers around the fact that the cross sectional area is proportional to the total flux in the tubing when (i) the tubing is saturated by a external longitudinal magnetic field, and (ii) the measurement is away from the ends of the tubing.

Figure 1 shows a cross sectional area measurement setup. The total flux ( $\Phi$ ) in the encircling pickup coil is:

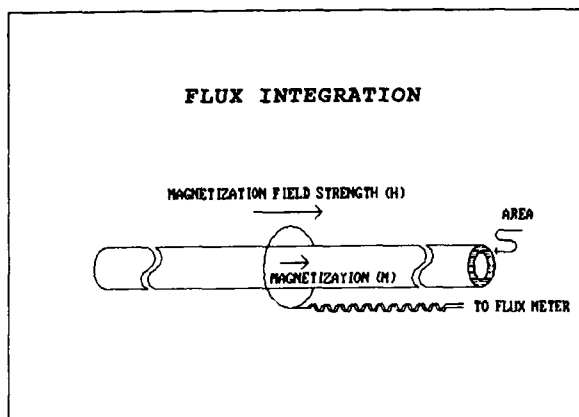


Figure 1

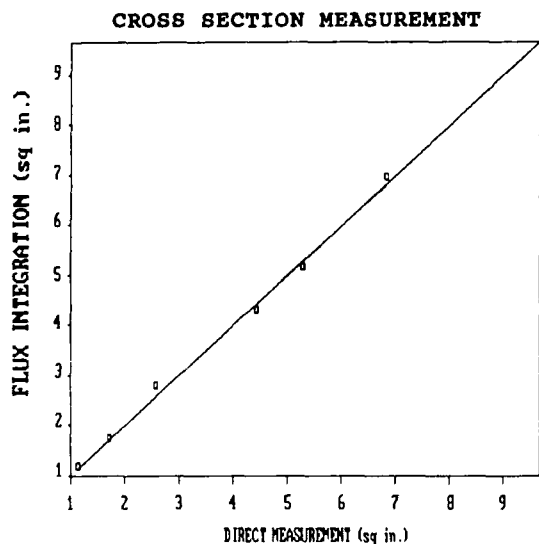


Figure 2

$$\Phi = \int B \, ds$$

If the tubing is saturated by a fixed large magnetic field (H), the magnetization (M) will be a constant. The demagnetizing factor is much smaller than one because the detection coil is away from the ends of the tubing. The flux variation is directly proportional to the cross sectional area of the tubing.

A comparison of the average wall measurement between the magnetic flux integration and a direct measurement is shown in figure 2. The correlation between the two measurements is very good.

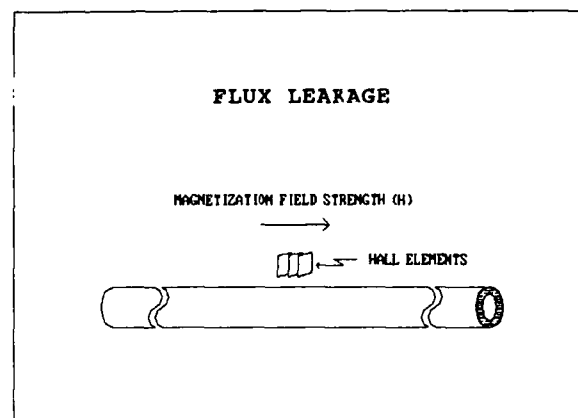


Figure 3

### Magnetic Flux Leakage

A modified magnetic flux leakage method is used for the corrosion pitting inspection. The magnetic flux leakage method is widely used in oil country tubular inspection<sup>2</sup>. A setup of the flux leakage measurement is shown in figure 3. A saturating magnetic field is applied longitudinally along the tube and if a corrosion pit disrupts the magnetic path, magnetic flux leakage will appear outside the tubing surface. A sensor array is used to detect the longitudinal or vertical component of the leakage field. The design is to maximize the correlation between the magnitude of the signal indication and the depth of the corrosion pitting.

The use of Hall elements for sensor arrays provides speed independent flux leakage measurements. The speed of the tubing is totally controlled by the rig operator and it is not predictable during inspection. The tubing speed will go through an acceleration, constant speed and deacceleration cycle for each pull. A speed independent detector will save a velocity correlation step during signal interpretation.

### Eddy Current

An Eddy current method is used for the detection of holes and splits. The ability to identify holes and splits in a tubing string is essential for wellhead tubing inspection. If an oil well is losing production it is important to find the cause during workover. A leak in the tubing string is one of the common causes for production decline. It is sometimes difficult to distinguish between a hole and a deep corrosion pit with the flux leakage method. The Eddy current method is an ideal choice because the discrimination can be obtained from the signature analysis of the phasor diagram.

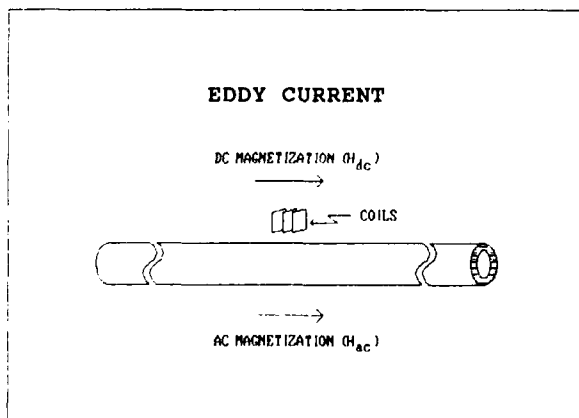


Figure 4

Figure 4 shows an Eddy current detection setup. A longitudinal magnetic field is applied to the tubing to minimize the magnetic permeability of the material. A longitudinal AC magnetic field is used to generate the Eddy current. Sensor arrays are placed around the tubing for circumferential coverage.

The optimal Eddy current frequency is selected experimentally to provide best pit versus hole discrimination. If the frequency is too high, the detection will be too sensitive to external defects and surface anomalies. If the frequency is too low, the detection becomes insensitive. Since the conductivity and the saturated permeability variation of a common grade tubing are small, the frequency is mostly determined by the wall thickness.

Pickup coils are used for the detector array. The coils are arranged in a first derivative configuration. The main purpose is to maximize the defect signal and minimize any off-centering response.

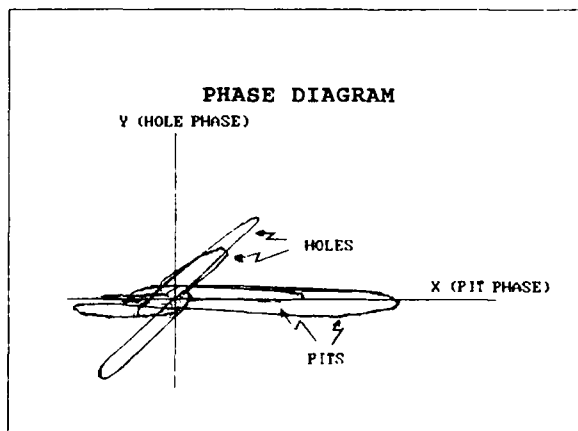


Figure 5

Figure 5 shows the signatures between pits and holes response in the phasor diagram. Since the response of a pit is along the X axis and the response of a hole is about 45 degrees from X axis, the pitting indication will be effectively masked off if we are only interested in the projection of the signal along the Y axis.

#### ROTATING MAGNETIC FIELD

The rotating magnetic field technique (RMFT) is used for rodwear inspection. The advantage of RMFT is that no mechanical rotating part is needed to obtain full circumferential coverage. There are two major differences between RMFT and a conventional Eddy current. (i) In a conventional Eddy current method only one phase is used for the drive current at a given frequency. In the RMFT a two phase drive current is used at the same frequency. With a two phase drive current a rotating magnetic field is generated. (ii) In a conventional Eddy current system, the phasor diagram is used for lift-off or defect geometry interpretation. In the RMFT, the phasor diagrams from two orthogonal detectors are processed to determine the depth and circumferential location of the defect.

A two phase drive field is shown in figure 6. Two uniform AC magnetic fields with equal magnitude and 90 degree phase difference are applied along two orthogonal directions. The magnetic field intensity at an arbitrary angle ( $\theta$ ) around the circumference is the linear combination of the two orthogonal magnetic fields. It can be expressed as

$$H(\theta) = H_0 \cos ( 2\pi ft + \theta )$$

It is interesting to point out that if one measures the phase variation by connecting a pickup coil to a lock-in amplifier (fig 6), the temporal phase is directly proportional to the spatial phase of the pickup coil.

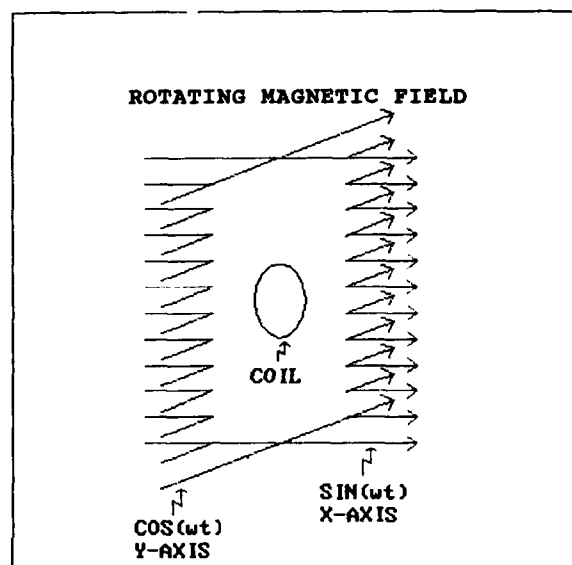


Figure 6

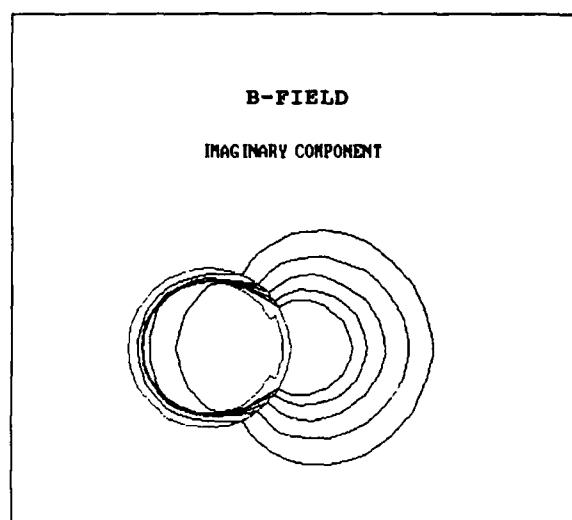


Figure 7

The vector potential  $\mathbf{A}$  of a tube in a rotating magnetic field can be calculated using

$$\nabla^2 \mathbf{A} - \mu \sigma \frac{\partial \mathbf{A}}{\partial t} = 0$$

where  $\sigma$  is the conductivity and  $\mu$  is the permeability. A perturbed magnetic field caused by rodwear is shown in figure 7. The calculation is based on a two dimensional model.

A pair of orthogonal sinusoidal detector coils (OSDC) are used. The signal processing for rotating field detection with a pair of OSDC is very interesting. The first spatial harmonic amplitude and the circumferential angle of the defect is measured. At least two different methods can be used to achieve the same result.

1. The spatial amplitude and phase of the defect can be calculated directly from the in-phase and out-of-phase component of the two coils.
2. A detector channel at any arbitrary angle ( $\theta$ ) around the circumference can be generated electronically by the linear combination of the two detector signals. The induced voltage at an angle  $\theta$  is

$$V(\theta) = V_s \cos(\theta) + V_c \sin(\theta)$$

where  $V_s$  and  $V_c$  are the two induced signals from the OSDC coils. By monitoring the maximum phase shift of various detector channels around the circumference, the defect amplitude is measured.

The wellhead tubing inspection is performed by real time processing. The second method for signal processing was chosen because it requires less CPU processing time. The comparison of a rodwear measurement between RMFT and ultrasonic gauge is shown in figure 8. A compressional UT gauge is used to measure the remaining wall. The results from the two methods appear to be very close.

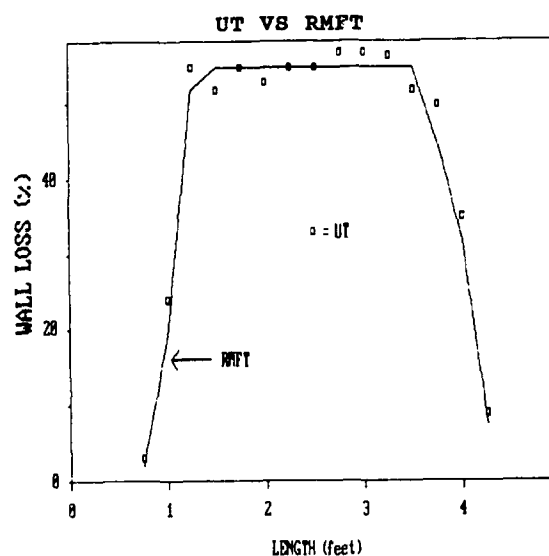


Figure 8

#### WELLHEAD TUBING INSPECTION

The WHS provides more information and cost savings compared to the conventional magnetic tubing inspection at the pipe yard. WHS inspects a tubing string as a whole and provides a complete profile of the string. WHS can reduce some of the operating costs such as pipe transportation, inventory and workover rig time.

## **TUBULAR INSPECTION**

The inspection results are logged using a four channel chart recorder. The chart speed is programmed such that it is proportional to the tubing pulling speed. The four displayed channels are hole, pitting, cross sectional area and rodwear<sup>1</sup>. Control status is displayed on the operator console.

The inspection results are communicated by the inspection operator to the workover rig operator while the tubing is being pulled. The tubing is usually pulled as a single 30 foot joint or a double-joint 60 foot stand. Each joint is graded according to the API bulletin 5C1 or the customer specification. The rejected tubing is laid down. The reusable tubing is segregated according to its grade and hung on the vertical tubing rack. In the case of a double joint stand, the segregation is based on the worse grade of the two joints. The operator will visually check hole and split indications. He will also periodically spot check rodwear with an ultrasonic gauge to confirm the validity of the inspection. The classification and the minimum remaining wall of each tube are logged on an inspection report.

## **WELLHEAD APPLICATIONS**

The wellhead inspection provides useful tubing string information which is related to the wellhead operations. This information is not easily obtainable from a pipe yard inspection service. A corrosion pitting profile and a rodwear profile of a rod pumping oil well are shown in figure 9 and figure 10. This

particular oil well is treated for corrosion. The inhibitor is applied from the top of the well. It is shown on figure 9 that the corrosion problem is progressively worse as the well gets deeper. The well also has a rodwear problem which starts at joint #130. A production well operator can use the well profiles to evaluate the corrosion prevention program and to determine the location and spacing of the rod guides.

## **CONCLUSION**

The WHS is designed and built for the wellhead environment. New technologies, like rotating magnetic field technique, modified flux leakage and flux measurement, are introduced. The WHS provides a tubing log which is very useful for production well diagnosis.

## **REFERENCE**

1. J. Kahil, New Technology For The Inspection Of Used Tubing And Drill Pipe, Proceedings of the 8th International Offshore Mechanics and Arctic Engineering Conference The Hague, The Netherlands, Vol. 1, 327-332, March 1989.
2. D. Bray & R. Stanley, Non-destructive Evaluation McGraw Hill 1989.
3. W.W. Curtis Jr., Standard Buggy Rack Inspection With Continuous Cross Sectional Area Measurement. SPE Drilling Conference Feb 1986.

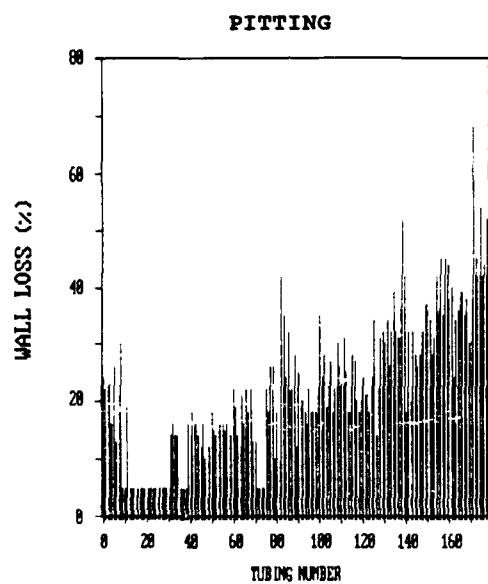


Figure 9

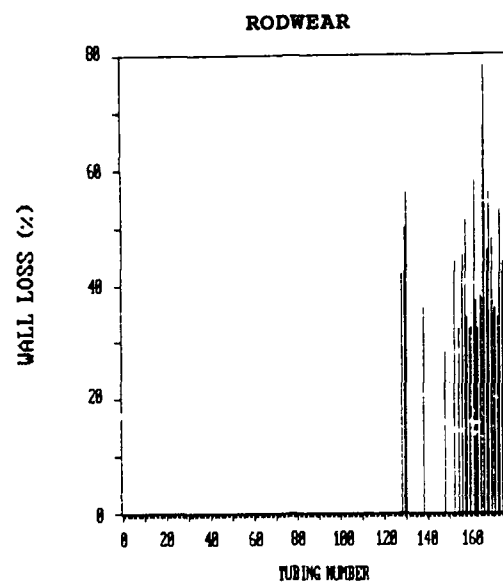


Figure 10



## THEORY OF NON-AXISYMMETRIC EDDY CURRENTS IN CYLINDRICAL CONDUCTORS

R. E. Beissner  
Southwest Research Institute  
San Antonio, Texas

### ABSTRACT

The theory described here is an extension of the Dodd and Deeds axisymmetric eddy current model to the treatment of non-axisymmetric coils. It provides a general theoretical framework for the prediction of the eddy current distribution, and the associated magnetic field distribution, produced by an excitation coil of arbitrary shape and located at an arbitrary position inside a hollow cylinder. By means of the reciprocity theorem for the prediction of eddy current probe response, the same model can also be used to analyze the response of a sensor coil of arbitrary shape and location. Illustrations of such applications are provided by calculations of the effects of excitation coil offset in a nominally axisymmetric system, and by predictions of flaw response signals as a function of sensor coil position and orientation.

### INTRODUCTION

The analytic solutions for eddy current fields presented several years ago by Dodd and Deeds<sup>(1)</sup> have proven useful in a large number of inspection problems, including the inspection of tubular conductors with constant magnetic permeability. The Dodd and Deeds models are, however, limited to axisymmetric and other two-dimensional situations, such as excitation by a current flowing in a circular loop centered on the axis of a cylindrical conductor. Existing analytic models cannot be used to investigate non-axisymmetric cases, such as the generation of spurious signals by a coil that is off-center or tilted with respect to the cylinder axis. Another important application that falls outside the scope of axisymmetric models is the analysis of signals from sensor coils that are not axisymmetric, as is often the case in practical systems used in the inspection of tubular goods.

The problem is illustrated in Figures 1 and 2. Figure 1 is the end view of a pipe with a circular coil centered on the axis. Because the geometry has circular symmetry in this case, the field produced by the coil is independent of azimuthal angle, which is to say it is axisymmetric. The lines shown here in the pipe wall represent the eddy current distribution; lengths are proportional to the magnitude of the current density and the lines are drawn in the direction of current flow. Mathematically this is a simple case because there is only one field component, the field in the azimuthal direction, and it depends on only two variables, the radial distance and the longitudinal distance down the length of the pipe.

If we move the coil off-center (as shown in Figure 2), then the distribution is no longer axisymmetric. In general this means that all three field components must be considered and each is a function of all three spatial variables. This makes the mathematical

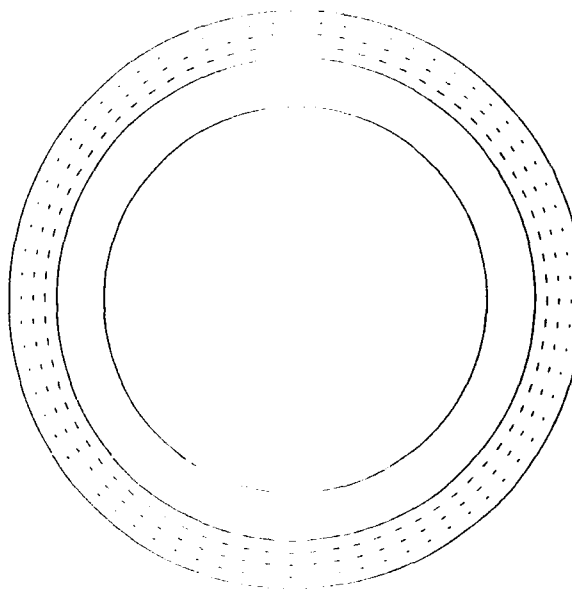


Figure 1. End view of a cylindrical conductor with a circular coil centered on the axis. Lines drawn in the pipe wall represent the axisymmetric eddy current distribution, with the length of each line proportional to the magnitude of the current density.

problem much more complicated, and its analytic solution has not been available for problems of concern in eddy current testing. We know, however, that there are non-axisymmetric situations in many practical test geometries, such as the one shown here where a small transmitter or receiver coil is placed near the wall for greater sensitivity to flaws in a localized region.

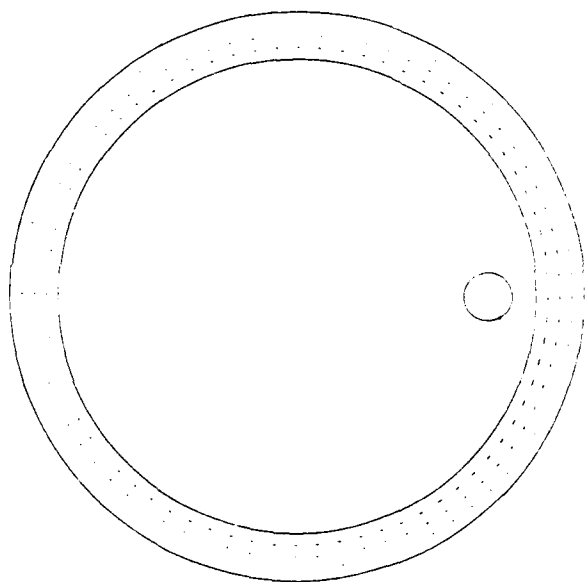


Figure 2. A non-axisymmetric eddy current distribution produced by an off-center coil

Our objectives, therefore, were to develop an analytic model for such non-axisymmetric geometries, and then to apply the model to studies of field distributions and probe response. For the probe response studies, our initial set of calculations was done for the remote field configuration where we examined the effects of off-center coils on the probe impedance in the absence of flaws, and the effects of coil placement and orientation on the response to flaws on the inside pipe wall.

### THEORY

Figure 3 shows the geometry of the problem. Fields are described in terms of the cylindrical coordinates  $r$ ,  $\phi$  and  $z$ , and we will be considering current sources and sensor response for off-center and tilted coils.

For the general three-dimensional case of concern here, the electric and magnetic fields are determined by the vector potential  $\vec{A}$ , which satisfies the vector Helmholtz equation,

$$\nabla \times \nabla \times \vec{A} + i\omega\mu\sigma\vec{A} = 0.$$

In cylindrical coordinates the solution for the vector potential can be written as an inverse Fourier sum and an inverse Fourier transform of a set of vector functions denoted here by the vector  $\vec{a}_n$ . Thus

$$\vec{A}(r, \phi, z) = \frac{1}{2\pi} \sum_{n=-\infty}^{\infty} \int_{-\infty}^{\infty} \vec{a}_n(r, k) e^{ikz} dk e^{in\phi}.$$

The small  $a$ 's, which are the Fourier coefficients of the Fourier transform of the vector potential in the pipe, can be expressed as

$$\vec{a}_n(r, k) = \Lambda_n(r, k) \cdot \vec{a}_n^0(r, k).$$

### GEOMETRY

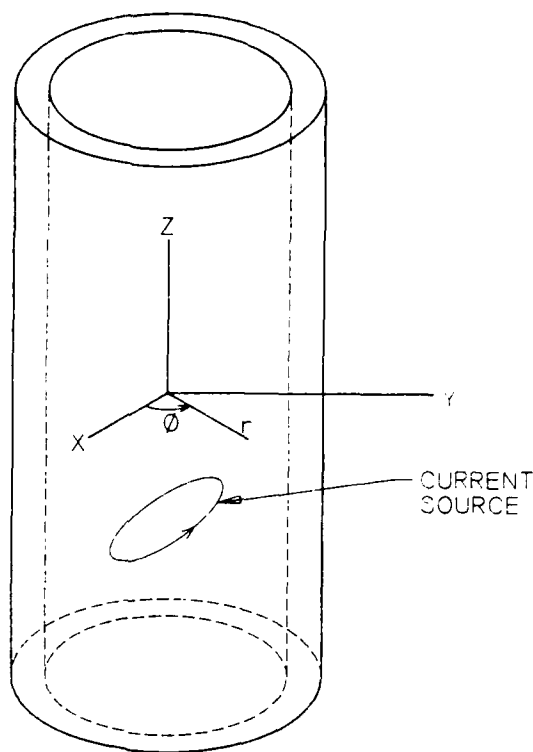


Figure 3. Geometry for the calculation of non-axisymmetric fields

where  $\Lambda$  is a matrix and  $\vec{a}_n^0$  is the transformed vector for the solution in the absence of the pipe. The matrix  $\Lambda$  depends, of course, on the pipe dimensions, permeability, conductivity and frequency, and is derived from the boundary conditions at the inner and outer surfaces of the pipe. The transformed vector  $\vec{a}_n^0$  is related to the vector potential produced by the coil in an infinite medium of air as follows:

$$\vec{a}_n^0(r, k) = \frac{1}{2\pi} \int_{-\infty}^{\infty} \int_0^{2\pi} \vec{A}_0(r, \phi, z) e^{-ikz - in\phi} d\phi dz.$$

A computer program was prepared for calculations of the vector potential and flux density based on the model described above. Given the input data, which are the pipe dimensions, coil diameter and orientation, coil location, material permeability, conductivity and frequency, the first step is the calculation of the source coefficients  $\vec{a}_n^0$ . This is followed by determination of the matrix  $\Lambda$  and calculation of the field coefficients  $\vec{a}_n$ . Then, for a specified set of values of  $r$ ,  $\phi$  and  $z$ , the inverse transform is computed and summed to determine  $\vec{A}$  and the flux density  $\vec{B}$ . The current density is also determined in this last step, because it is simply a constant times  $\vec{A}$ .

We have also written a code to compute the probe impedance in a pipe with no flaws. The calculation is based on the reciprocity theorem<sup>(2)</sup>, which is

$$\Delta Z = \frac{1}{I^2} \int_S [\vec{E}_0 \times \vec{H} - \vec{E} \times \vec{H}_0] \cdot \vec{n} dS.$$

The fields  $\vec{E}$  and  $\vec{H}$  are those produced by the transmitter coil in the pipe, and the fields with subscript 0 are those that would be produced by activating the receiver coil in an infinite medium of air.

Finally, we have also written a code for predicting the change in probe impedance caused by a small flaw in the pipe wall. The theory used here is Burrough's form of the reciprocity theorem<sup>(3)</sup>, in which the flaw is assumed to be small enough that the field is constant inside the flaw, and approximately equal to the field in the absence of the flaw. Burrough's expression for the impedance change due to such a point flaw is

$$\Delta Z = \frac{1}{I^2} \int_V \sigma \vec{E} \cdot \vec{E}_0 dv \sim \frac{V}{I^2} \sigma \vec{E} \cdot \vec{E}_0$$

In this case the  $\vec{E}$  fields are those produced by the transmitter and receiver, and are determined by the procedure described earlier. In applications of this model we will be looking at the receiver response as a function of probe position as the transmitter and receiver are scanned past a flaw on the inside surface of the pipe.

#### APPLICATIONS

In all of the examples presented here the outside pipe diameter is 12cm, the wall thickness is 1cm, the relative permeability is 200, and the conductivity is 0.1.

Figure 4 shows the flux density produced by a centered coil as a function of longitudinal position  $z$  along the pipe wall. The inside surface is to the left and the outside boundary is on the right. This is a section from  $z = 10$  to  $z = 30$ cm, which is 1 to 3 pipe diameters. Of interest is the region at about 1.5 to 2 pipe diameters where the flux density vectors seem to fade out. This is the transition region from the near field to the remote field region. At shorter distances, in the near field region, the flux is greater at the inside wall while in the remote field region it is greater at the outside wall, although this difference is not apparent in the figure. Also, there is a 180 degree phase change as one passes through the transition region from the near to the remote field zone. These are well-known characteristics of the remote field effect, which has been demonstrated several times for axisymmetric systems.

Figure 5 shows the effects of using a small, off-center coil. This is the flux density for the off-center coil over the same region shown in Figure 4 for the symmetric case. A transition zone between the near and remote field regions is again evident as the region where the flux density approaches zero near the outside wall. In this case, however, the transition occurs at a shorter distance from the coil, so that the remote field region begins at about 1.5 pipe diameters rather than 2 pipe diameters as is the case with an axisymmetric system.



Figure 4. Magnetic flux density in the wall of a pipe with axisymmetric excitation as in Figure 1. The inside pipe wall is on the left and the outside is on the right. The region where the flux density approaches zero near the outside wall is the transition region between the near field and remote field zones.

Next we examine the effects of coil orientation on the flux density. In Figure 6 the coil is circular and lies in the plane perpendicular to the plane of the figure. The flux pattern shows how the field is distorted by the presence of the pipe. In the region to the right of the coil the flux distribution in the wall is approximately what one would expect for a coil in the orientation shown here. However, above this region there is a null in the flux density followed by a region where the direction of the flux vector is reversed. This reversal of direction is what we would expect to see above and to the left of center of the coil, if the coil were in air. Evidently the presence of permeable material has pulled flux lines into the wall of the pipe, resulting in a distorted pattern.

Another coil orientation is examined in Figure 7. In this case the flux flows out of the coil and into the pipe on the right, and then returns along paths above and below the coil. A rather interesting effect occurs in the region just to the right of the coil, where crosses appear instead of the usual lines representing the flux density vector. As explained below, this means that the field in this region is elliptically polarized.

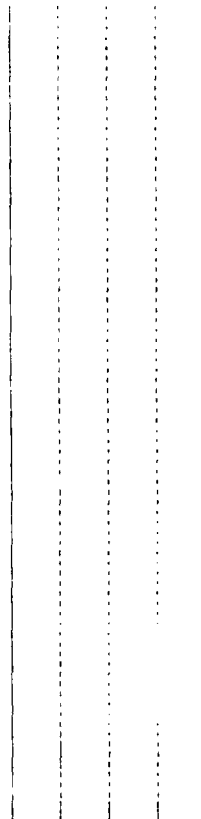


Figure 5. Magnetic flux density with non-axisymmetric excitation as in Figure 2. The transition region is closer to the source than in Figure 4.

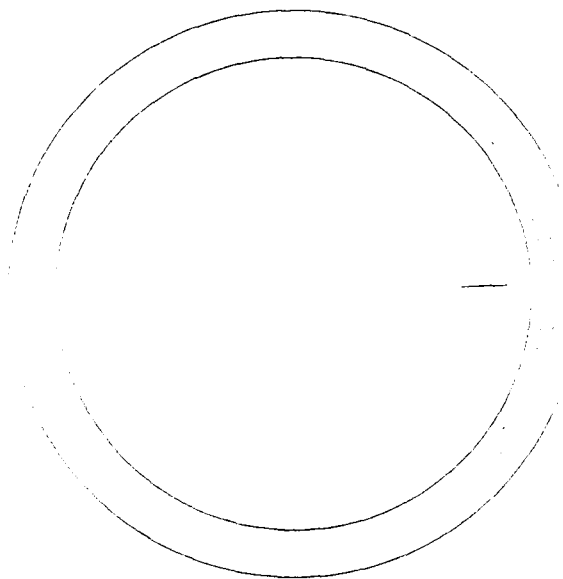


Figure 6. Magnetic flux density produced by an off-center coil with the plane of the coil normal to the plane of the figure

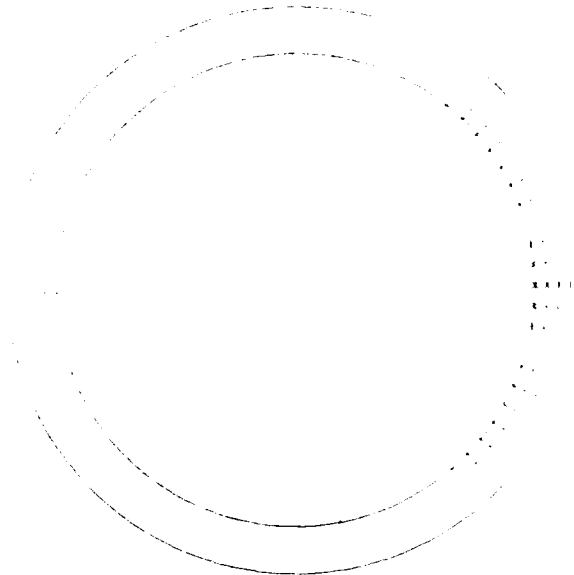


Figure 7. Magnetic flux density map for another coil orientation. The crossed lines in the region to the right of the coil indicate that the field is elliptically polarized.

In most applications of eddy current NDE we can think of field vectors, such as the eddy current or flux density vectors, as quantities that oscillate back and forth, once per cycle, in a specific direction. From electromagnetic theory we know, however, that this need not be the case. In general the end point of field vector at a point traces out an ellipse rather than a straight line, the straight line being a degenerate case of the ellipse. When the pattern is a straight line the field is said to be linearly polarized; otherwise it is elliptically polarized. In the flux plot shown in Figure 7 the flux density is elliptically polarized in the region to the right of the coil, and to indicate the degree of polarization we have plotted the major and minor axis of the polarization ellipse.

The remaining examples are applications to probe impedance predictions in the remote field configuration. We will be looking at coil geometries like that shown in Figure 8. The transmitter is the large coil shown here in the centered position, and the receiver is the small off-center coil located at a distance of 2.5 pipe diameters down the pipe. The curve plotted on the right is the impedance plane trajectory generated by moving the transmitter/receiver system to the right a distance of 4mm. We might think of this as noise due to off-center motion of the transmitter/receiver system. Later we will use the data shown here to obtain a noise figure for comparison with flaw signal predictions. The objective is to calculate relative signal-to-noise figures for different receiver orientations. Similar calculations were performed for the receiver orientations illustrated in Figures 6 and 7.

Next we will look at impedance changes caused by the presence of a point flaw on the inside wall as the transmitter/receiver system is scanned past the flaw.

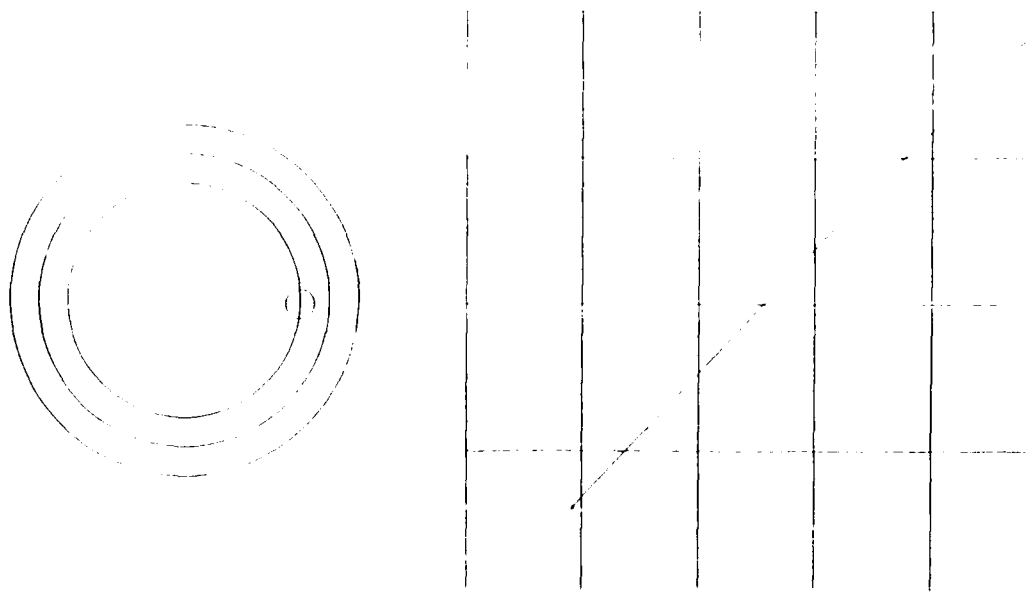


Figure 8. The effect of off-center displacement on the impedance of a sensor coil in the remote field configuration. In the drawing on the left, the transmitter is the large coil and the sensor is the small coil located 2.5 pipe diameters down the axis. Also shown is the impedance plane trajectory generated by moving the transmitter/sensor off-center toward the pipe wall on the right.

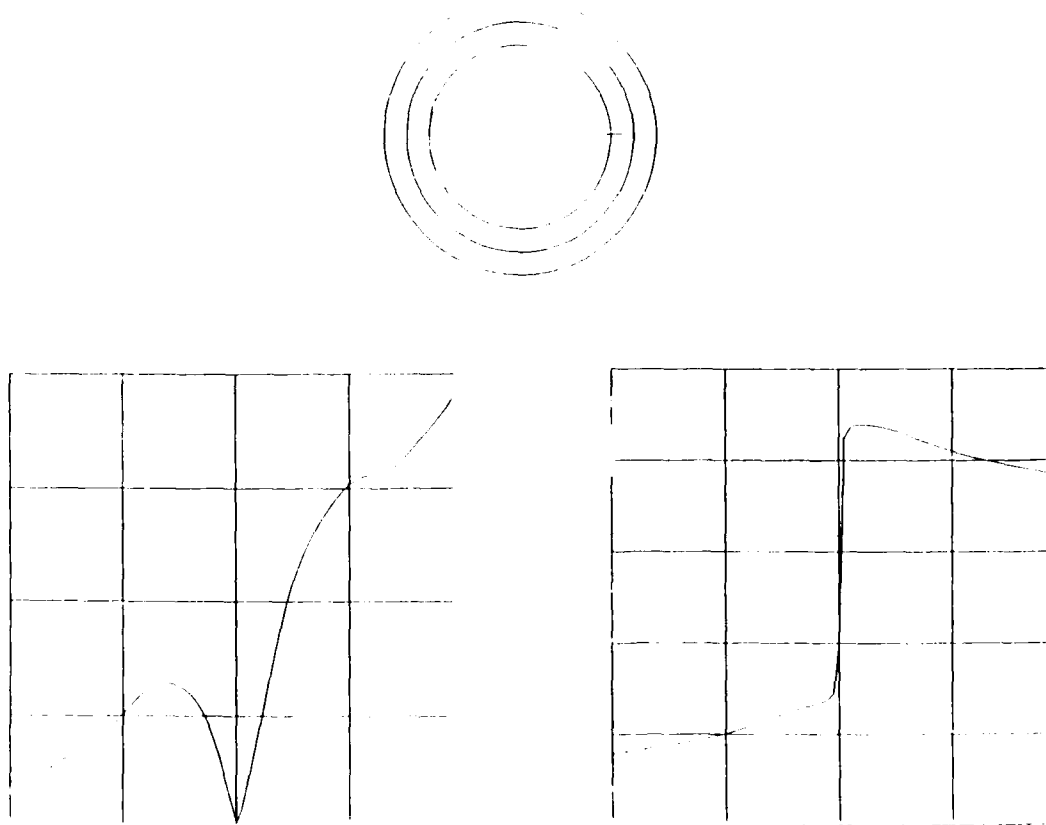


Figure 9. Flaw response as a function of probe position. The coil arrangement is shown at the top of the figure, and the curves on the left and right are the sensor amplitude and phase, respectively, as the system is scanned past a small flaw on the inside surface of the pipe.

Figure 9 shows the amplitude and phase changes caused by the flaw for the transmitter/receiver configuration shown at the top of the figure. The curve on the left is amplitude vs position and that on the right is phase. Calculations like this were also performed for the other two orthogonal receiver orientations.

Now we want to use these data, and the off-center noise data described earlier, to make some estimates of relative signal-to-noise ratios for the three receiver orientations. To do this we will divide the amplitude of the flaw signal, such as that shown in Figure 9, by the amplitude change caused by a 4mm off-center movement of the transmitter/receiver system, which is shown for a different receiver orientation in Figure 8.

The resulting signal-to-noise ratios, normalized to 1 for the configuration shown in the center, are shown in Figure 10. It would appear from these numbers that the configuration at the bottom offers a definite advantage over the other two. However, it should be noted that only one noise source was considered, due to off-center motion, and that the effect of flaw geometry was not considered. These figures must therefore be considered tentative and subject to revision by more refined calculations.

#### SUMMARY

We have reported the development of a general analytic solution for non-axisymmetric fields in tubular conductors, the development of computer programs for calculations of field distributions and receiver response, and some preliminary calculations of signals and noise as a function of receiver orientation in the remote field configuration. In the future we hope to combine the analytic solution described here with boundary element calculations of the fields around a flaw to give a more realistic picture of probe response, including the effects of flaw geometry.

#### REFERENCES

1. C. V. Dodd and W. E. Deeds, *J. Appl. Phys.* 39, 2829 (1968).
2. B. A. Auld, in *Eddy-Current Characterization of Materials and Structures*, ASTM STP 722, edited by G. Birnbaum and G. Free, American Society for Testing and Materials, Philadelphia (1981), p. 332.
3. M. Burrows, dissertation, University of Michigan, University Microfilms, Ann Arbor, Michigan, 1964.

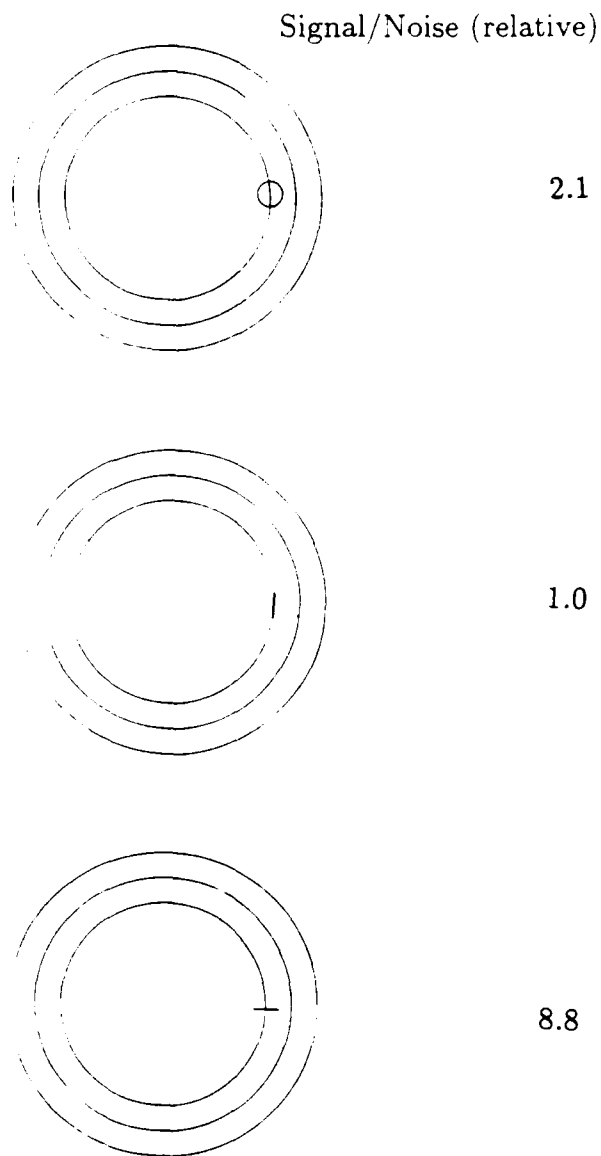


Figure 10. Relative signal-to-noise ratios for three remote field configurations. For these calculations noise was taken to be the magnitude of the impedance change caused by off-center motion, as illustrated in Figure 8, and the signal was the peak amplitude change from a scan over a flaw on the inside pipe surface, as illustrated in Figure 9.

## INFRARED THERMAL WAVE IMAGING OF ADHESION DEFECTS

P.K. Kuo, T. Ahmed, L.D. Favro, H.J. Jin, and R.L. Thomas  
Department of Physics and Institute for Manufacturing Research  
Wayne State University, Detroit, MI 48202

### Abstract

A novel parallel Box-Car Thermal Wave Imaging System, using an IR Video Camera and WSU-designed hardware and software for synchronous, pixel-by-pixel time-gating and averaging is described. Example images are given which illustrate the ability of the system to detect adhesion defects for various specimens of practical interest, including plasma-sprayed coatings on metal substrates, thin boron chips brazed onto copper substrates, and selected polymer-metal interfaces. Because of its synchronous signal averaging capability, the method has considerably better sensitivity than that of conventional thermography. Furthermore, since adjustable time-gating is utilized, it also provides flaw depth information. It is fully automated and operates essentially in real time.

### 1. INTRODUCTION

Conventional infrared video thermography, in which an infrared image is formed either with the natural radiation emitted by a sample or with radiation caused by the artificial heating of the sample, has been used successfully as an NDE technique for imaging gross defects in samples ever since the development of infrared video cameras. However, its direct use has somewhat limited applicability in the study of variations in adhesion because of the subtle nature of most adhesion defects. One approach to improving the sensitivity of the method is to use signal averaging techniques to increase the signal-to-noise ratio. In this work we describe a technique which we have developed to increase the signal-to-noise ratio much further.<sup>(1)</sup> This technique uses active interrogation of the target with a pulsed heat source, followed by *synchronous, real-time* image processing as well as signal averaging. The procedure is to acquire an infrared video image at some fixed, *gated* time after the pulse of heat is applied to the sample (in much the same fashion as a box-car integrator acquires a gated section of a time dependent signal), and to average the resulting images over

multiple pulses of the heat source. The time delay of the gate after each pulse is determined by the characteristic time for a pulse of heat to propagate into the sample, scatter from the defect, and propagate back to the surface where it can be observed with the camera. With typical samples of industrial interest, this time may range from a few tens of milliseconds to a minute or so, although it is not restricted to this range. The width of the time gate may range from several frames for very slow phenomena, to a fraction of a frame for fast phenomena. The apparatus also is capable of using *multiple* (up to four) gates with different delays and gate widths during *each* pulse, thus producing up to four different images corresponding to four different points on the heating and cooling curves for each pixel of the image. The system therefore functions as if it consisted of a large number (roughly a quarter million) of multiple-gate, box-car integrators, one for each pixel of the image, all operating in parallel. The signal-to-noise ratio of these images is enhanced by the averaging of the images corresponding to each of the gate times over several (typically 16) repetitions of the pulse cycle. The resulting images are then post-processed by performing pixel-by-pixel subtractions,

divisions, etc. of the images for different gate times to suppress the background and remove the effects of emissivity variations on the sample surface. The end result is the ability to produce, almost in real time, greatly enhanced thermal-wave images of a variety of different defects which are very difficult to observe with competing technologies.

## 2. DESCRIPTION OF APPARATUS

The box-car imaging apparatus consists of four major components, a heat source consisting of two 5 kJ flash lamps, an Inframetrics IR 600C infrared video camera, a Data-Cube real-time image processing system, and a Sun 3/160 computer workstation. A block diagram of the system is given in Fig. 1. The Sun workstation serves to control the overall operation of the system. This workstation first provides signals to control the timing of the pulses from the flash lamps which heat the sample. These signals may, or may not, be synchronized to the camera's scan rate, depending on the nature of the defects and the time scale

involved in the propagation of thermal waves in the sample. The camera, which is focussed on the sample, scans continuously and sends a standard RS-170 video signal to the DataCube processor, which digitizes the signal at 10 MHz. Then, again under program control from the Sun workstation, gated images are selectively derived from the digitized data stream in the DataCube processor, and stored in four separate frame buffers contained in the processor. Images from subsequent pulses are merged with the images already contained in the buffers to accomplish the desired averaging. Upon completion of the averaging cycle, the images are transferred to the workstation for post-processing, display, and storage.

An example of an averaging and post-processing cycle is indicated schematically in Fig. 2. The graph is a schematic plot of a heating and cooling curve for a typical point on the sample surface. Below it are sketched two possible locations for box-car gates with the suggestion that the second image might be subtracted from the first during post-processing. The purpose of the subtraction in this case

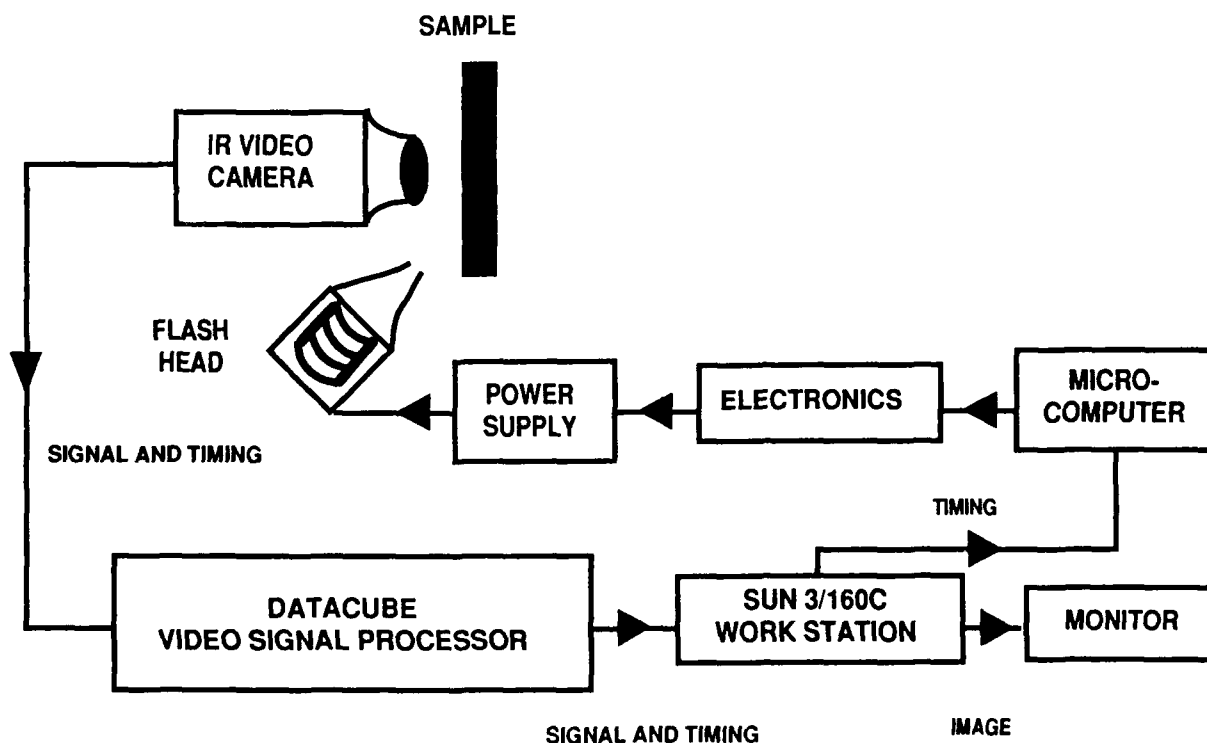


Fig. 1 Block diagram of the box-car video thermal wave imaging apparatus.



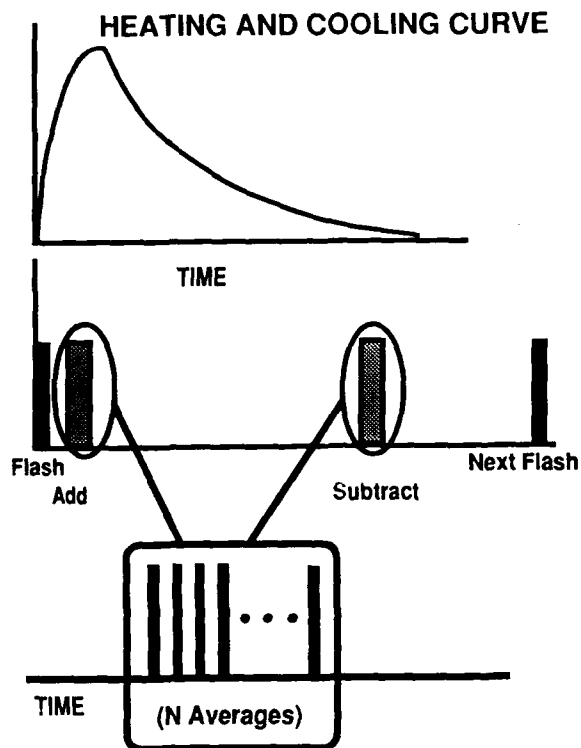


Fig. 2 Schematic diagram of an averaging and post-processing cycle.

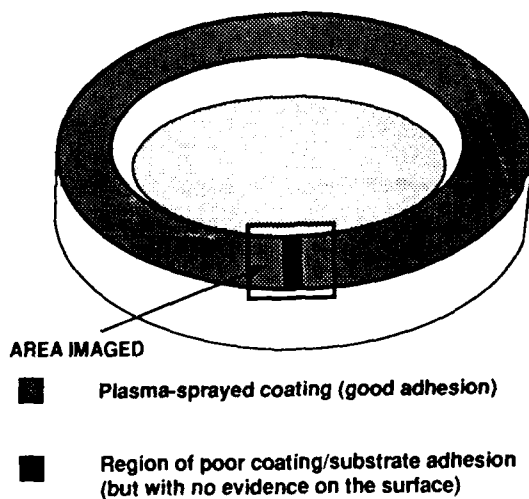


Fig 3 Schematic diagram (left), and box-car video thermal wave image (right), of a plasma-sprayed chromium oxide coating on a steel substrate. The image shows a region of poorer adhesion resulting from inadequate surface preparation prior to coating.

would be the suppression of background effects, which are present at both points on the heating curve, and therefore would tend to cancel. Examples of images obtained with procedures such as this are given in the next section.

### 3. RESULTS

The first example of an adhesion defect we provide consists of a plasma-sprayed coating of chromium oxide on a steel substrate in the form of a ring, about four inches in diameter. The polished surface of the ring was lightly sand-blasted prior to coating, except in a mm-wide strip which is shown schematically in the left half of Fig. 3. Although the resulting difference in adhesion was not observable optically, even after sectioning the sample, the box-car thermal wave image (see right half of Fig. 3) clearly shows the region which was not sand-blasted. A more detailed account of this example may be found in Ref. 1.

As a second example of an adhesion defect in a plasma-sprayed coating, in Fig. 4 we show a thermal wave image of a 0.5 mm-wide defect beneath a coating of magnesium zirconate on a metal substrate.

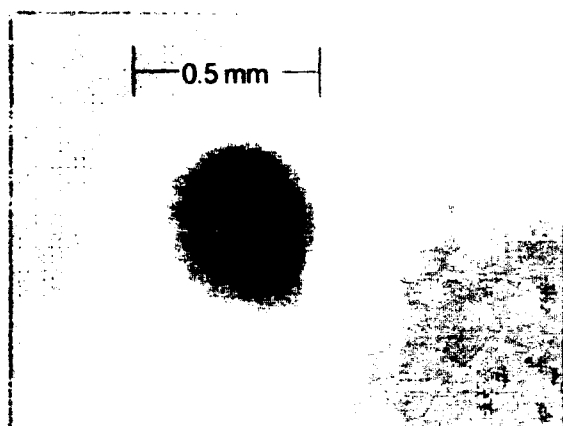


Fig. 4. Thermal wave image of an adhesion defect in a magnesium zirconate plasma-sprayed coating.

Next, we consider the case of an adhesion defect at a brazed joint between a thin (approximately  $10\ \mu\text{m}$ ) boron chip and a copper heat sink. Such chips are used as beam targets in a Van de Graaff accelerator. In Fig. 5, on the left we show the thermal wave image of a target for which the brazing process produced good thermal contact (note the uniform contrast in the image), and on the right we show a corresponding image for which poor thermal contact resulted (note the uneven contrast). Optically, these chips are indistinguishable in quality.

To illustrate the applicability of the thermal wave technique to metal/polymer adhesion defects, we consider the important case of uneven application of an adhesive to the rear surface of a metal panel intended to be joined to some other material. In Fig. 6, we show a pattern of adhesive which was applied to the rear surfaces of two steel panels, one of which is 0.95 mm thick (left image), the other 0.2 mm thick (right image). It may be noted that the left image (of the thicker panel) has poorer resolution of the pattern, and that regions of relatively poorer adhesion may be seen, particularly in the borders of the patterns, in both images.

Another, somewhat more subtle, example of adhesion defects in polymer-metal interfaces is shown in Fig. 7. Here, two painted metal panels were placed side-by-side prior to thermal wave imaging. The panel on the right was nominally of good quality, whereas the panel on the left had been previously subjected to environmental stress in the form of a salt-spray treatment. The left image shows evidence of subsurface corrosion.

## BORON TARGET

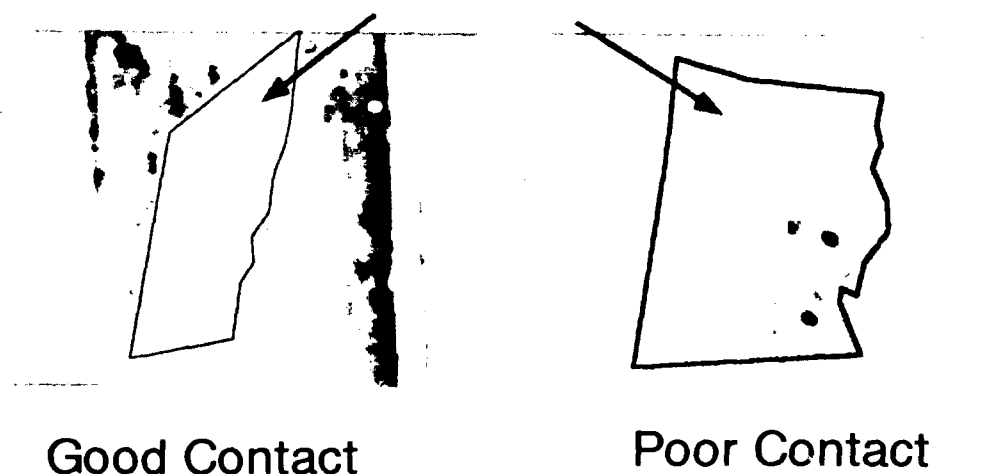
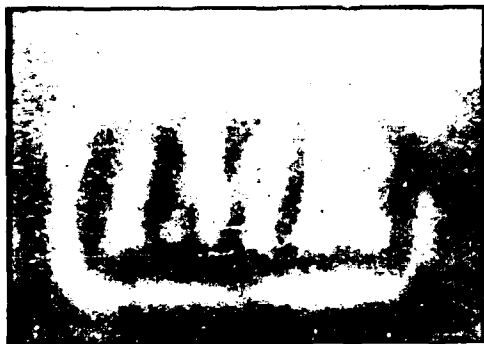


Fig. 5 Thermal wave images of boron chips brazed to a copper heat sink.



0.95 mm Steel



0.2 mm Steel

Fig. 6 Thermal wave images of a pattern of adhesive applied to the rear surfaces of two different thicknesses of steel panels.

Salt-treated

Untreated

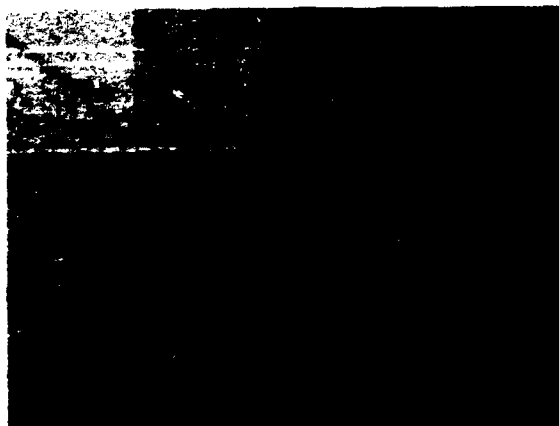


Fig. 7 Thermal wave images of painted metal panels, showing subsurface corrosion.

#### 4. ACKNOWLEDGMENTS

This research was sponsored by the U.S. Army Research Office, under Contract Number DAAL03-88-K-0089, The Institute for Manufacturing Research, and The Ford Motor Company

#### 5. REFERENCE

For a more complete description see "Synchronous Thermal Wave IR Video Imaging for NDE", P.K. Kuo, T. Ahmed, L.D. Favro, H.J. Jin, and R.L. Thomas, *Journal of Nondestructive Evaluation*, in press.

## EFFECT OF SURFACE ROUGHNESS ON THE ULTRASONIC INSPECTION OF SPACE SHUTTLE BOOSTERS

J. K. Hartman and P. W. Karner  
Morton Thiokol, Inc.  
Brigham City, Utah 84302-0524

### Abstract

During the past two years, high ultrasonic signals indicative of steel-to-rubber debonds were found periodically in certain areas on the Space Shuttle Solid Rocket Motors. Since the anomalous signals consistently occurred in the same region, experimental and theoretical tests were done to determine if they were actually due to debonds or some other cause. Peel tests were done on test motors followed by surface roughness measurements on the transducer side of the steel case. The results showed that there were no debonds found in the region of inspection, but surface roughness parameters were found to have a strong correlation with the ultrasonic readings. Theoretical modeling helped confirm the sensitivity of ultrasonic readings to surface conditions which affect the couplant thickness. In order to desensitize the inspection process to surface roughness, three things were done. The ultrasonic frequency of the inspection was lowered, the aperture of the transducer was increased, and a different data processing technique was used. Test motors that showed high signals using the old technique were inspected again after incorporating these improvements, and the resulting images were much more stable and indicative of good steel-to-rubber bonds. Destructive tests also confirmed the integrity of the bond condition.

### 1. INTRODUCTION

For nearly the past two years, ultrasonics has been used to inspect various portions of the steel-to-rubber insulation bondline on Space Shuttle Solid Rocket Motors (SRMs) at Morton Thiokol, Inc. Each SRM is basically made up of four propellant-filled casting segments (as well as a nozzle and "nose cone") which are stacked together. There are two main areas of inspection at the present time. These are the steel/rubber bondlines in (1) the "membrane" region, which consists of the basic cylindrical body of the case, and (2) the joints, which include both the clevis (along with its pinholes) and tang ends where the cases are joined together. The work discussed in this paper has to do with the inspection of the clevis (joint) region.

### 2. BACKGROUND

Figure 1 shows the geometry of the clevis and the areas that are ultrasonically inspected. The figure represents an axial crosssection of the joint. The equipment used presently for the ultrasonic inspection of regions 1 and 2 of the figure is the Amdata I-98 system which incorporates a specially designed tool containing two 5 MHz transducers that fit into the clevis so that the two transducer faces are in direct contact with the steel surface. Water, supplemented with a rust inhibiting agent, is the couplant. The ultrasonic technique that has been used up to now is a pulse-echo, peak amplitude detection method. The whole inspection process involves the use of a calibration block or "reference standard", which consists of a portion of a steel clevis bonded to rubber insulation with a

one-inch wide strip (running axially) cut out of the rubber. This represents a complete one-inch air-backed debond. When a clevis is inspected, the system is first "calibrated" by scanning the calibration block (0.1 in. step size) and adjusting the gain so that the peak amplitude of the 11th multiple reflection (in the steel layer) reaches some predetermined level (> 83 percent full screen height) when positioned directly over the debond. The choice of the 11th multiple was somewhat arbitrary but had to do with choosing a multiple reflection that had a significant debond-to-bond amplitude ratio. After the "cal in", the clevis is scanned and when the scanning session is done the system is ultrasonically calibrated again ("cal out") to insure repeatability. Thus, the system is calibrated to detect an air-backed (or worst case) one inch debond. However, it still seems to be somewhat sensitive to (pseudo) kissing debonds.

A test article was fabricated which consisted of a case segment with rubber insulation attached or "laid up" on the clevis end. Before the rubber was laid up, one-inch wide Teflon tape (whose acoustic impedance is much more similar to rubber than air) was applied to the steel bonding surface. This prohibited the rubber insulation from bonding to the steel in that small area. The bondline stresses experienced in an actual loaded case segment were thus duplicated in this test article. The I-98 system was then calibrated (to the air-backed debond) and the test article was scanned. The one-inch debond was detected quite accurately and was later confirmed to be a debond by destructive tests.

Since its inception, the ultrasonic inspection system has performed reasonably well, but periodically "hot spots" (high amplitudes indicative of debonds) have shown up in the channel one region of the clevis. Since no hot spots ever appeared in the channel two region, but always in the channel one region, and since for a few cases some of the high signals of channel one were detected nearly all around the case, the question arose as to whether or not we were truly seeing debonds or some other artifact. One of the possible causes for the high signals was thought to be surface variations (roughness and waviness). In order to determine what might be causing these high signals, tests were done on a case segment (non-flight hardware, Qualification Motor-6 or QM-6) which showed high near-debond signals in the channel one region of the clevis.

### 3. TEST PROCEDURE AND RESULTS

QM-6 was a test motor that was statically fired at Morton Thiokol (Utah) in the spring of 1988. Before the firing, the case was scanned ultrasonically and near-debond level signals showed up along a 60 degree arc in the clevis region of the center forward case segment. There were four basic tests to be done on QM-6 related to our problem. They were as follows:

- (1) Perform a postfire ultrasonic scan and compare with the prefire scan for consistency.
- (2) Perform peel tests in areas which indicated both a bonded and debonded condition in order to destructively verify the bond condition.
- (3) After the rubber insulation is washed out, perform a bare metal ultrasonic scan and compare the trends.
- (4) Take impression molds every five degrees and compare surface profiles with ultrasonics.

the postfire scans were done in the same manner as the prefire scans, using a 0.25 in. by 0.5 in., 5 MHz transducer with a pulse-echo, peak detection method (on the 11th multiple). Since the inspection of the clevis joint is essentially a one dimensional scan (five passes over the same area), the data is represented graphically in Fig. 2. The value of each data point shown every five degrees is actually the average value of ten measurements (i.e., ten pixels or one circumferential inch of data) centered about each degree location. This was so that the measurements could be correlated with surface roughness measurements every five degrees. The relative error for each amplitude value is probably between 10 to 15 percent. The trends seen in Fig. 2 were the same as those found in the prefire scans, with the highest amplitudes found in the 45 to 50 degree region. This essentially ruled out the possibility of operator error or some other random error as being the cause for the near-debond signals. Again, the amplitude level which is calibrated to represent a (1 inch) debond condition for this peak detection method is anything above 83 percent. The highest value recorded from the postfire scan was 79.7 percent (near 50 degrees). Thus, the amplitude of the signal nearly reached the "debond level" of 83 percent.

The areas chosen for peel tests were located at approximately 2, 37, 50, and 58 degrees around the clevis. The peel strips were about two-inches wide and the peel angle at the bondline was near 135 degrees. The results of the tests showed that there were no debonds present in the areas of ultrasonic inspection. In fact, the bonds were quite strong. When the rubber strips were peeled off, they all failed cohesively (i.e., the failure/tear occurred in the rubber) as opposed to adhesively (failure within the bondline). Therefore, the high ultrasonic signals were not due to bond condition.

Following these tests, the rubber insulation was washed out of

the case. This left a bare metal D6AC steel case (average hardness of 44 Rockwell C) with a very thin (approximately 0.002 in. or 2 mil) film of adhesive on the inside. An ultrasonic scan was again done on the clevis with the same 5 MHz transducers. This time, instead of recording the peak amplitude of the 11th multiple, the absolute sum of the waveform was recorded from the 3rd to the 11th multiple. The image of this scan showed the same trends as the postfire (insulated) images. The values from the bare metal scan are plotted every five degrees along with those from the postfire scan in Fig. 3. The bare metal scan thus confirmed the fact that the trends seen in the previous scans were not due to bond condition but due to the steel itself. Because of the slow spatial changes in the channel one signal and because the channel two signal did not show the same trends, surface roughness (and waviness) became the main suspect.

The primary surface of concern was the steel-to-transducer surface. Since it is located within the clevis, it is a machined surface and is harder to control its surface condition. The steel-to-rubber (or bonding) surface is a grit blasted surface and is much smoother and more uniform and controlled. Both surfaces have surface finish requirements of better (smoother) than 125 Ra. Impression molds were made of the steel-to-transducer surface every five degrees from 0 degrees to 60 degrees. The surface profiles, shown in Fig. 4, revealed a significant amount of variation over the 60 degrees. Most noticeably was a slight bump or ridge that was present most of the way around the case. This ridge was about 0.2 in. wide and 2 to 3 mil high. In order to correlate our ultrasonic measurements with a quantitative parameter of surface roughness, an Ra value was calculated from the "left" (or pinhole) side of each surface profile (cutoff length = 0.3 in.). An Ra value is the mean deviation (over the cutoff length) of a surface about a center horizontal line. The transducer, represented by the dark bar above the 45 degree profile, inspected more in the middle of each profile, so that the areas of measurement (ultrasonics and Ra value) overlapped somewhat. The Ra values are shown in Fig. 5 every five degrees along with the postfire ultrasonic values (normalized to the Ra values). The negative correlation is quite strong, having a correlation coefficient of  $R = -0.94$  (see Fig. 6).

### 4. DISCUSSION

From the strong correlation of Ra value to peak amplitude, one can see that surface variations (either roughness, waviness, or both) are definitely influencing the ultrasonic signal. But exactly how they affect the signal for this particular case is hard to determine. There are probably three physical phenomena which influence the signal the most.

The most obvious is simply scattering of the sound waves. In this situation, the wavelength of the sound waves is larger than the displacements due to surface roughness and usually smaller than the correlation length of the surface. In other words, the surface is still relatively "smooth". When this is the case, the smoother the surface is, the less scattering there is of sound waves off the surface.(1,2) Likewise, the rougher areas will scatter away more sound energy from the specular (normal) axis of the transducer. The data from the postfire and bare metal scans show this trend. In the rougher areas, the wavetrain attenuates or dies off more rapidly than it does in the smoother areas.

Another factor influencing the signal could be attributed to the destructive interference of the sound waves due to varying couplant thicknesses caused by surface roughness.(3) We attempted to model this effect by calculating (approximately) the total acoustical response due to a normally incident, longitudinal spherical wave upon a layered media (transducer, water, steel, and air) with a varying water thickness. This was done by calculating the acoustic response of the layered system for many different water thicknesses and then integrat-

ing or summing these values to obtain an effective acoustical response. The purpose of this was to approximate the effect of varying path lengths in the couplant layer. The model we used was developed by the JSC research and development group at Morton Thiokol<sup>(4)</sup> and is similar to the Thomson-Haskell matrix method.<sup>(5,6)</sup> The results (Fig. 7) show that the amplitude of the 11th multiple reflection can be strongly affected by varying water couplant thicknesses at 5 MHz. The average water thickness on the graph could be thought of as the Ra value of the surface. (Actually, the average water thickness over a small area is probably greater than its Ra value.) When the average water thickness is one mil, the amplitude is down over 50 percent from the amplitude for a completely smooth or flat surface. In contrast, the amplitude of the 11th multiple at 2.25 MHz for 1 mil average water thickness is down only 8% or so from the "smooth surface" amplitude. The destructive interference caused by varying couplant thickness also causes the wavetrain to attenuate more quickly for rougher areas (just as scattering does) according to our modeling.

A third factor which can be influencing the signal is a simple focusing or lens type effect. This is caused by large scale surface variations or surface waviness, such as the slight bump or ridge seen in the surface profiles. The lens effect is strongest when the dimension or width of the ridge approaches that of the transducer diameter (which is nearly the case for the QM-6 profiles). Eric Madaras<sup>(7)</sup> has shown that half inch wide dips and ridges can either greatly enhance or almost destroy the signal from a 5 MHz, one-half-inch diameter circular transducer. The effect of the first two phenomena mentioned (scattering and destructive interference in the couplant layer) is to reduce the amplitude of a reflected sound wave from a rough surface. The effect of surface waviness is to either increase or decrease the amplitude, depending on the shape and location of the surface waviness and the transducer.

#### 5. IMPROVEMENTS

If surface roughness and waviness are the primary problems, then several things can be done that should improve the ultrasonic inspection process. Three basic changes were made for this situation. The most obvious was to lower the frequency. This will reduce the effects of surface roughness such as scattering and destructive interference in the couplant layer. Another improvement that was done was to increase the diameter of the transducer somewhat so that ridges, such as those seen on QM-6, on the order of 0.2 in. wide will not affect the total signal as much. A third change that we implemented was to acquire the sum of the absolute values of a digitized portion of the waveform instead of the peak amplitude (one data point) of one reflection.

A larger (0.625 in. diameter) circular 2.25 MHz transducer was used to inspect the same region that the two 5 MHz transducers used to inspect, and 17 microseconds of data were summed and recorded (the 10th to 13th multiples) instead of just one data point. With these improvements, we rescanned various cases which had previously been scanned using the old methods (5 MHz, peak detect). One such case segment (prob-

ably the "worst" done), whose 5 MHz, peak detect, gray scale C-scan image is in Fig. 8, showed debond indications nearly all around the case. When it was rescanned at 2.25 MHz, the ultrasonic signal showed a low, stable bonded condition (Fig. 9). If the 5 MHz images represented the true bond condition of the joint, then there would have been serious problems when the rocket was fired. This case segment was a part of QM-8, which was static tested with no problems, and, no debonds were detected in the region of inspection during post-fire destructive tests. All the other scans on other case segments using the revised technique indicated a more stable, bonded condition.

#### 6. CONCLUSIONS

Surface roughness and waviness can potentially cause large variations in ultrasonic signals due to scattering, destructive interference, and lens effects. One must take into consideration the frequency and size of the transducer, as well as optimizing data analysis techniques, when trying to minimize the effects of surface variations. It would be desirable to model the surface roughness problem more completely and accurately and obtain an exact digital record (two dimensional profile) of a rough surface in order to compare experimental results with theoretical results.

#### ACKNOWLEDGMENTS

The authors wish to thank Lee Pearson and Eric Madaras for giving helpful insights to the surface roughness problem, and we also thank the many NDT technicians who helped out in the data collection process on QM-6 and other motors.

#### REFERENCES

- (1) P. M. Morse and K. U. Ingard, *Theoretical Acoustics*, Sec. 8.3, McGraw-Hill, New York, 1968.
- (2) J. Krautkramer and H. Krautkramer, *Ultrasonic Testing of Materials*, Sec. 5.5, Springer-Verlag, New York, 1983.
- (3) *Nondestructive Testing Handbook*, ed. by R. C. McMaster, American Society for Nondestructive Testing, Columbus, Ohio, 1959.
- (4) L. H. Pearson, "Theoretical Model for Reflected Ultrasonic Pulse Wave Train Calculation," 2442-FY88-M011, 3 November, 1987.
- (5) W. T. Thomson, "Transmission of Elastic Waves Through a Stratified Medium," *J. Appl. Phys.*, 21, 89-93, 1950.
- (6) N. A. Haskell, "The Dispersion of Surface Waves on Multilayered Media," *Bull. Seismol. Soc. Am.*, 43, 17-34, 1953.
- (7) E. Madaras, "Effects of Small Surface Deformations on Ultrasonic Bond Line Measurements made at 5 MHz", NASA Langley Research Center, 1989.

# Diagram of Clevis Region Showing Areas of Ultrasonic Inspection

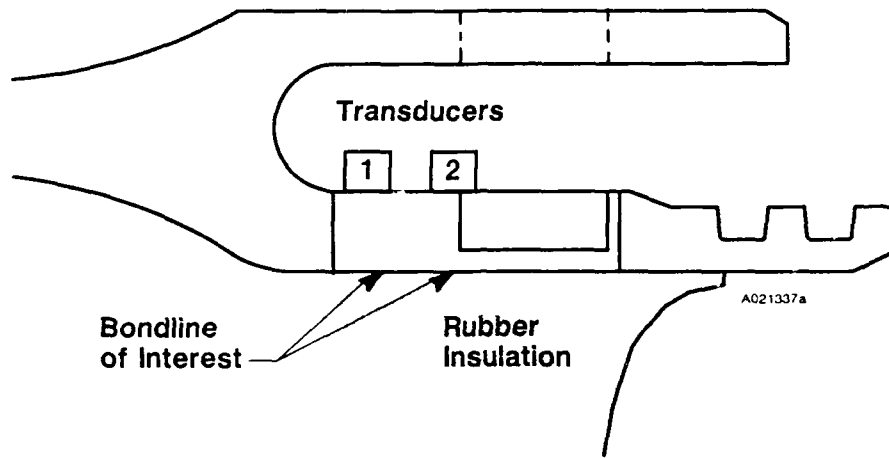


Fig. 1 Clevis Region Showing Areas of Ultrasonic Inspection, Specifically Channel (transducer) 1 and Channel 2.

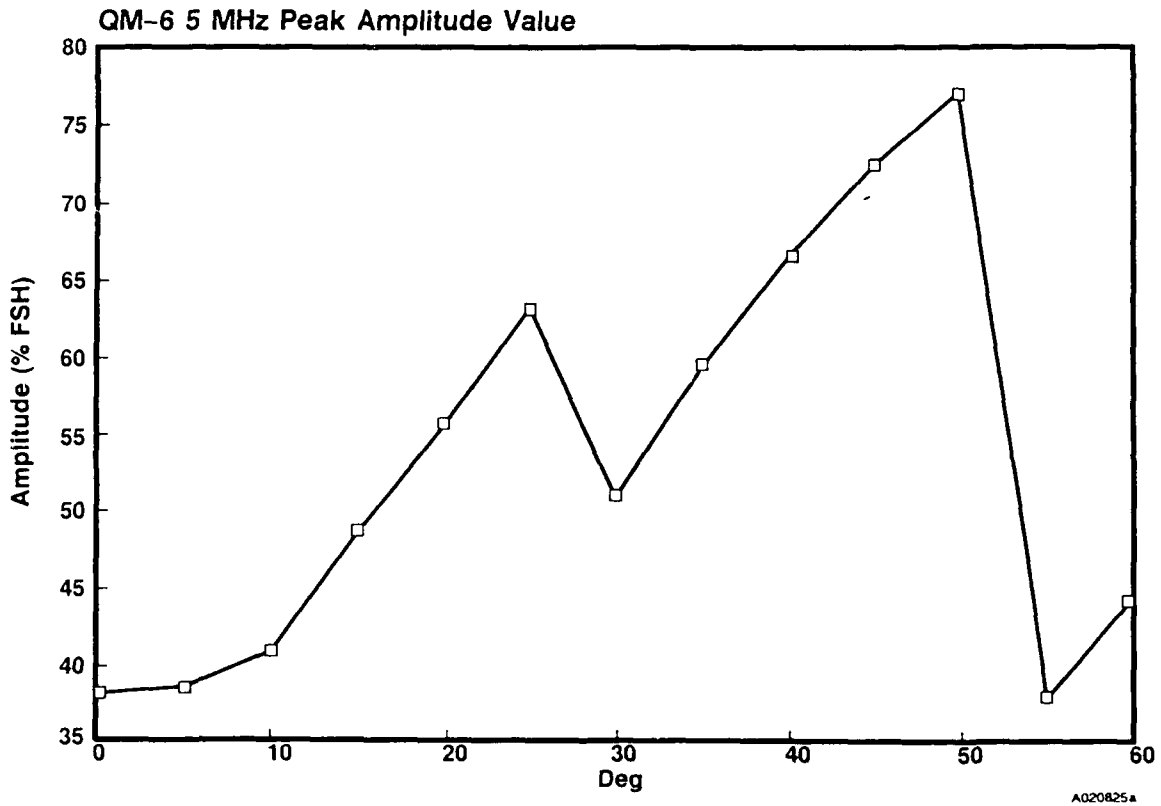


Fig. 2 QM-6 Five MHz Peak Amplitude Values of the 11th Multiple Reflection Off the Steel/Insulation Bondline.

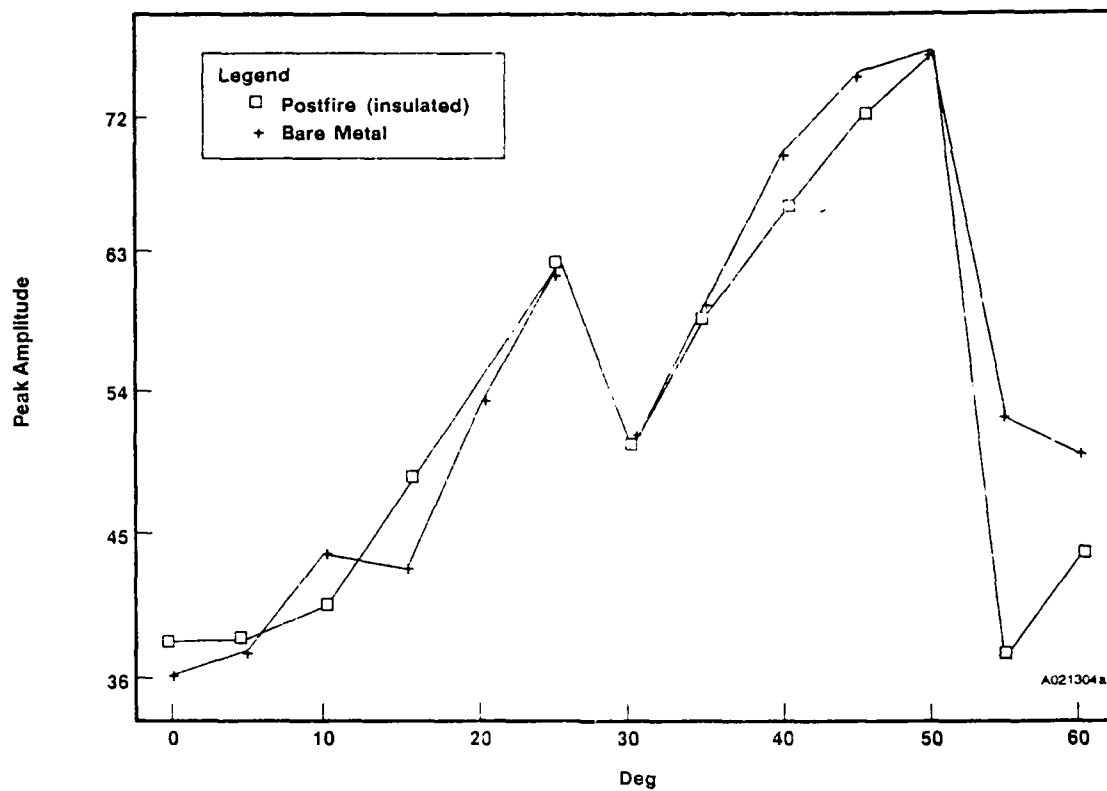


Fig. 3 QM-6 Five MHz Peak Amplitude Values for both Postfire and Bare Metal Scans (normalized at 50 deg).

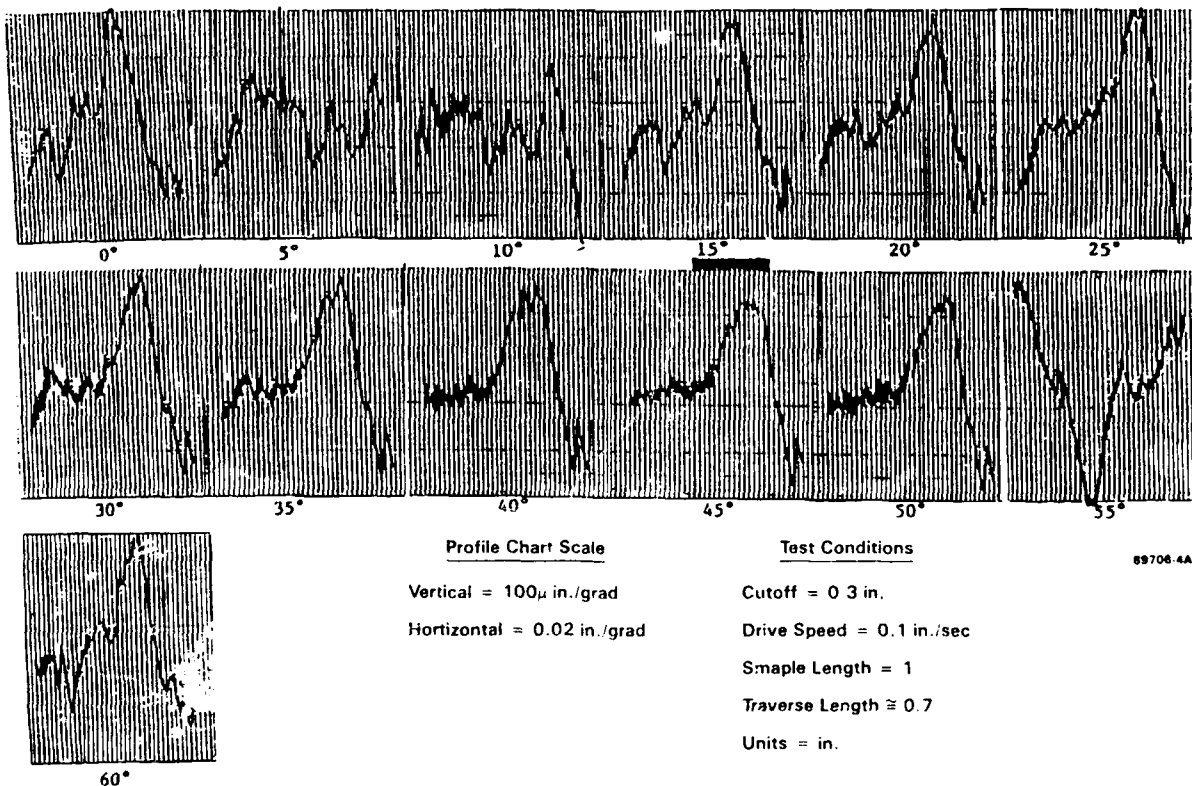


Fig. 4 Surface Roughness Profiles for QM-6 Transducer/Steel Interface (0 to 60 deg).



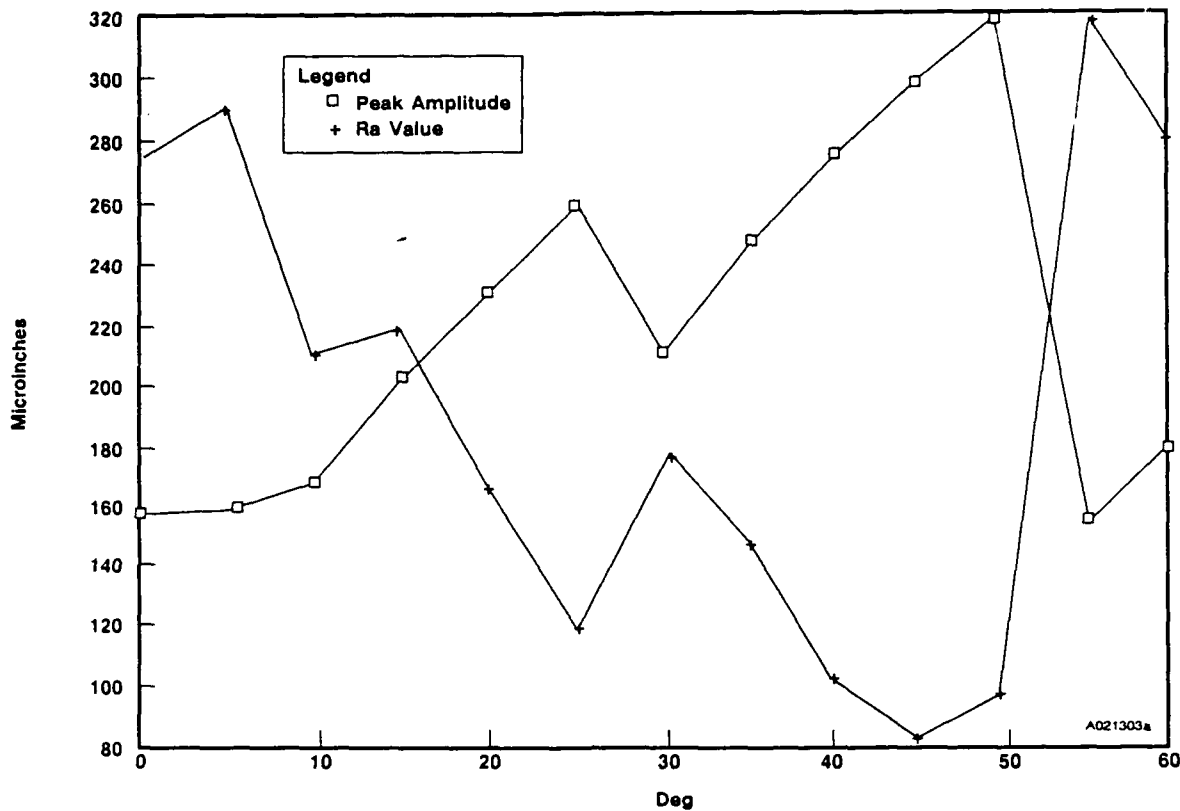


Fig. 5 QM-6 Surface Roughness and Normalized Peak Amplitude Values (postfire).

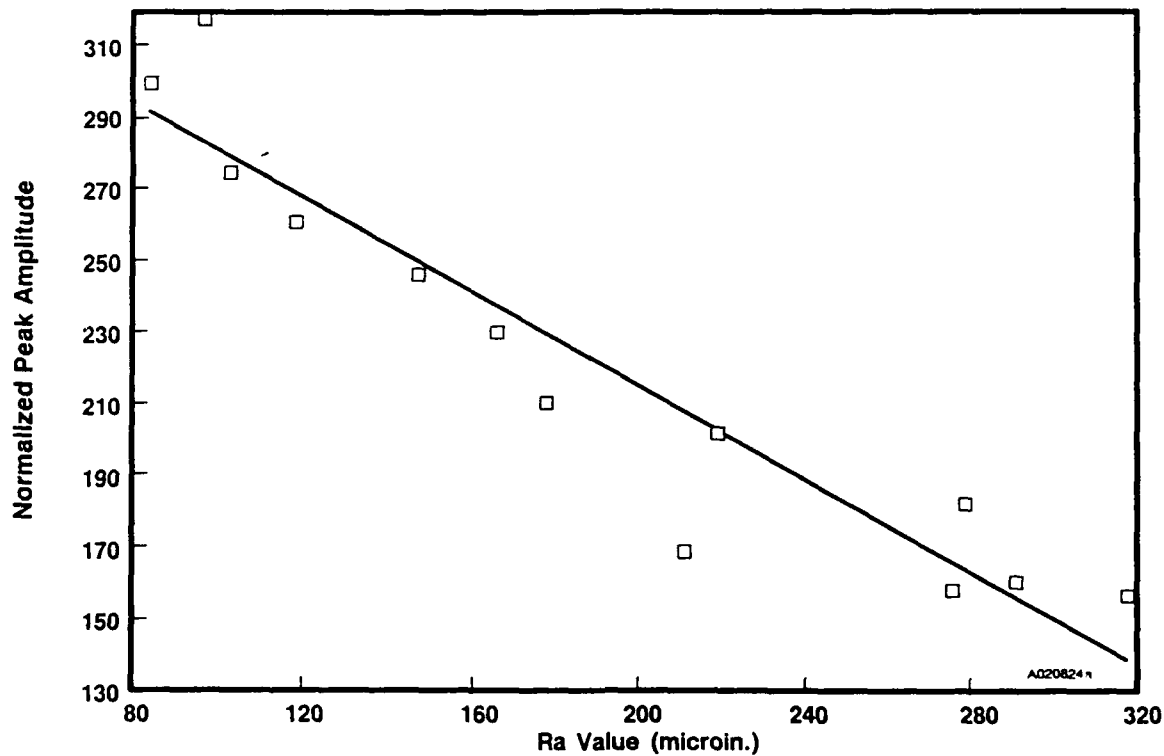


Fig. 6 Scatter Plot of QM-6 Surface Roughness Versus Normalized Peak Amplitude.

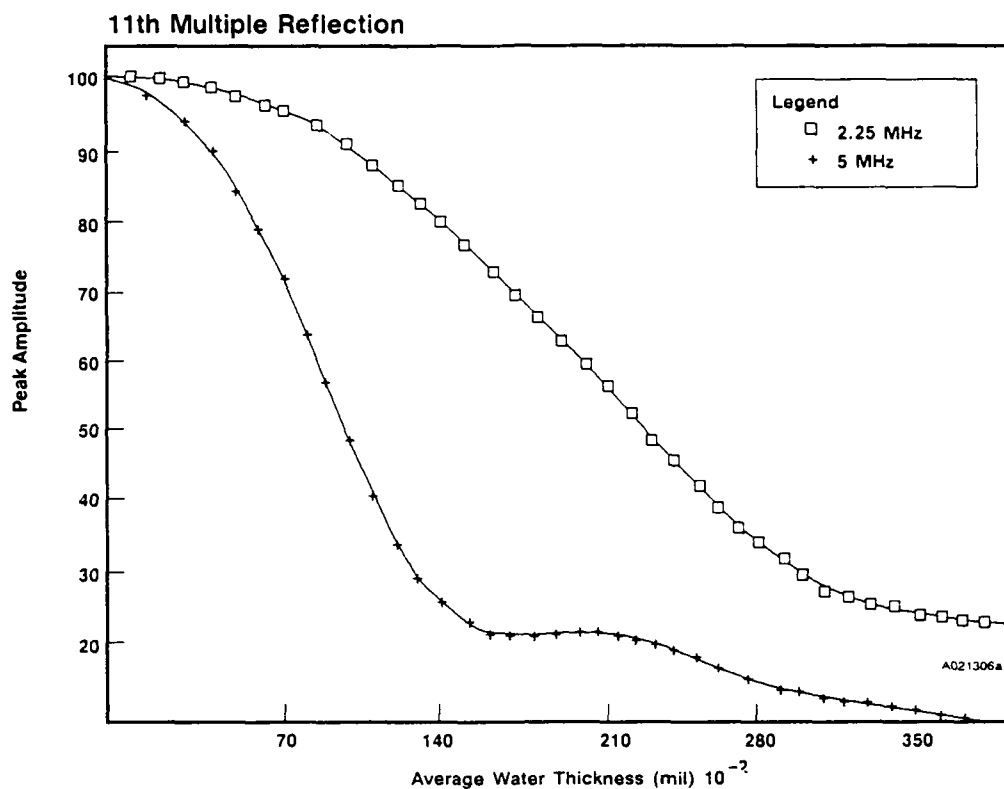


Fig. 7 Theoretical Calculations at 2.25 and 5.00 MHz of the Peak Amplitude of the 11th Reflection Versus Avg Water (couplant) Thickness Corresponding To an Ra (surface roughness) Value.

```

INTRASPECT/98 VIP REV D  RDAS H04  SC5032 D  AMDATA INC., (C) 1987
PN1U75434-06SN00000002  FORM: BA04A21  CH: 1  08/19/88  16:57-17:01
X: 0.00 -> -39.10" / 0.10"  CIRC. SCAN MINUS WELDSIDE GAIN: 22.00 DB
Y: 0.00 -> 0.10" / 0.02"  ANG: 0.00 DAC: OFF GATE  DELAY WIDTH
AMP: % FSH  MP: "  SKW: 0.00 TRG: OFF A (US) 30.00 25.60
TOF: US  DP: "  C (US) 37.95 4.90
SC(X,Y)=( 0.00, 0.00)  AMPLITUDE  T (US) 2.00 1.00
AXIAL DATA : -39.100 -38.700 I/38 AMPLITUDE DATA SUMMARY
CIRC DATA : 0.000 4.980
POINTS ABOVE THRESH: 1250
POINTS BELOW THRESH: 0
AREA ABOVE THRESH : 2.500
MEAN AMPLITUDE : 90.82%
STANDARD DEVIATION : 10.97%
MINIMUM AMPLITUDE : 52.34%
MAXIMUM AMPLITUDE : 100.00%

ZOOM CURSOR H.V=25.0, 0.1 INCHES
MAG WINDOW H.V= 1, 30 TIMES
  
```

0-10%
11-30%
31-49%
50-76%
77-82%
83-87%
88-92%
93-98%
99-100%

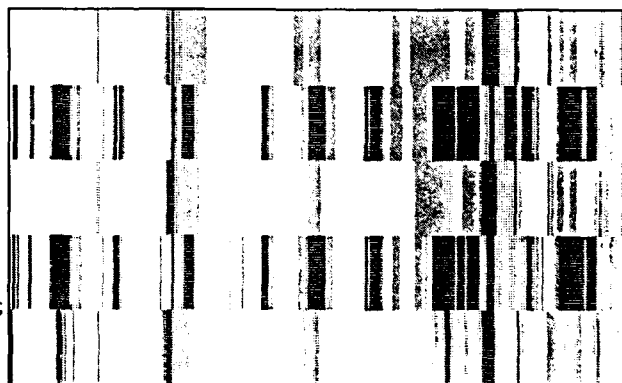


Fig. 8 5 MHz Peak Amplitude Image of QM-8. Image Represents 5 Passes over a 20 Deg Arc on the Case. Debond Level Is Any Signal Above 83 Percent (see legend). Mean Amplitude for the Image Is 90.8 Percent.

INTRASPECT/98 VIP REV D RDAS H04 SC5032 D AMDATA INC., (C) 1987  
 4B AFT S/N00000002 1U75434 FORM: BA04A20 CH: 1 08/28/88 18:09-18:13  
 X: 0.00 -> 39.10" / 0.10" CIRC. SCAN PLUS WELDSIDE GAIN: 12.00 DB  
 Y: 0.00 -> 0.10" / 0.02" ANG: 0.00 DAC: OFF GATE DELAY WIDTH  
 AMP: % FSH MP: " SKW: 0.00 TRG: OFF A (US) 9.00 50.00  
 TOF: US DP: " C (US) 41.00 17.00  
 SC(X,Y)=( 0.00, 0.00) RING-DOWN RATIO T (US) 46.00 4.90  
 AXIAL DATA : 0.000 0.400 I/98 RINGDOWN DATA SUMMARY  
 CIRC DATA : 0.000 4.980  
 POINTS ABOVE THRESH: 1250  
 POINTS BELOW THRESH: 0  
 AREA ABOVE THRESH : 2.500  
 MEAN AMPLITUDE: 1012.895  
 STANDARD DEVIATION : 63.941  
 MINIMUM RATIO : 833.000  
 MAXIMUM RATIO : 1183.000  
 ZOOM CURSOR H.V=25.0, 0.1 INCHES  
 MAG WINDOW H.V= 1, 30 TIMES

	1066.00
	1304.00
	1541.00
	1779.00
	2016.00
	2253.00
	2491.00
	2728.00
	7000.00



Fig. 9 2.25 MHz Image of the Same 20 Deg Arc on QM-8.  
 Debond Level Is Anything Above 2728 (white level). Mean  
 "Amplitude" for the Image Is 1013.

## REVIEW OF NDE METHODOLOGY OF ADHESIVE BOND QUALITY DETERMINATION\*

Glenn M. Light  
Hegeon Kwun  
Southwest Research Institute  
San Antonio, Texas

### ABSTRACT

The aerospace industry has increased its use of adhesively bonded structures to obtain lighter weight, more maneuverable aircraft. Since these structures undergo tremendous environmental weathering and service stresses, it is important to be able to verify the strength of the adhesive bond using nondestructive evaluation (NDE) methods. The NDE community has been studying various methods to inspect these bonds not only for bond vs. debond, but also to determine the strength of the bond. This presentation describes the various bond strength measurement methods that have been tested and how well they have worked. These methods include sonics, ultrasonics, acoustic emission, optical holography, x-ray and neutron radiography, thermography, and nuclear magnetic resonance. Each of these methods has had some limited success in detecting debond conditions. However, at the present time, it appears that only the sonic and ultrasonic methods have the capability to potentially determine the strength of the bond.

### 1. INTRODUCTION

Over the last 20 years, extensive NDE research and development (R&D) has been conducted to determine how to detect and predict the quality of bond in adhesively bonded structures<sup>(1-60)</sup>. The methods investigated include sonics, ultrasonics, acoustic emission, optical holography, radiography, thermography, and nuclear magnetic resonance.

In a 1974 general review of the NDE of adhesive bonds, Norriss<sup>(1)</sup> reported on several techniques including x-ray, holography, sonics, thermography (heat-sensitive coatings and papers), acoustic impedance and emission, and through-transmission and pulse-echo ultrasonics (UT). The most usable methods seemed to be the sonics, through-transmission UT, and acoustic impedance. However, most of these could only detect voids. The preferred method was Fokker Bond Tester for sheet-to-sheet joints; and for the core-to-sheet joints, radiography and through-transmission UT worked best.

In a more recent report (1984), Teagle<sup>(2)</sup> reported that no single NDE technique solved all problems. His studies found that radiography could be used to detect damage to honeycomb, presence of debris and contaminants, and lack of bond due to absence of adhesive. Conventional UT with 1 to 10 MHz can be used in the through-transmission mode to determine attenuation, which gives some information about disbonds, delaminations, and porosity; but these defects cannot be easily distinguished from one another. Approximately the same information can be obtained with pulse-echo UT. Frequency analysis of reflected waves gives information about how the waves have interacted with the materials in the inspection path and can help discriminate between the different bonding problems.

Thermography can successfully monitor the variation in thermal conductivity due to defects in the bonded region. Thermographic techniques, such as infrared scanners and cameras, liquid crystals, treated paper, paints, and phosphors, and thermometric techniques, such as thermocouples and radiometers, were evaluated; but several problems were found. First, it is difficult to get suitable heat/cold sources; second, high anisotropic materials have different thermal properties in different directions, which causes data interpretation problems; and, third, metallic bonded structures can hold temperature gradients for only a short time.

Zurbrick<sup>(3)</sup> reported that the most critical area for NDE R&D was the substrate surface preparation prior to bonding. He developed an equation for predicting bond strength based upon surface energy in which all the controlling variables could potentially be measured using NDE.

The bond strength is primarily determined by the thickness of the bondline, which greatly affects the energy stored in the bond. The ultimate bond strength is related to the solid-surface energy, liquid-surface energy, thickness of the bond, contact angle, and strain. Bond strength can be predicted if bond thickness, contact angle of adhesive-to-substrate, and substrate surface-free energy can be measured nondestructively.

To measure the variables just listed, Zurbrick used NDE techniques including exo-electron emission, ultrasonic gas-phase transmission, electric field reflectometry, and light specular reflectance. Substrate surface-free energy had the most dramatic linear effect. The contact angle was less dramatic. Effective strain was less than anticipated, and the others behaved in a similar manner. Zurbrick's basic premise was that the adhesive bonding is controlled by the surface electron-

\*Supported by U.S. Army Materials Technology Laboratory, Defense Electronics Supply Center, Contract No. DLA900-84-C-0910.

energy state. He took light reflections from the surface using a 45-degree incident white light and a detector at 45 degrees. His data indicated that the reflected light was inversely related to the calculated substrate surface-free energy.

Segal et al.<sup>(4)</sup> divided the problem of nondestructively determining adhesive bond integrity into four parts: (1) detection of the unbond, (2) prediction of the cohesive strength of the bond, (3) detection of adhesive failure, and (4) prediction of a combined cohesive/adhesive strength.

The following sections discuss the work conducted using the various methods and techniques.

## 2. SONIC TECHNIQUES

Several sonic inspection techniques have been used over the years for detecting the quality of bond of an adhesively bonded structure. These include the coin tap test, mechanical impedance, and mechanical resonance<sup>(5)</sup>.

### 2.1 Coin Tap Test

The coin tap test has been used for many years as a quick yet sensitive technique to find large debond areas in laminated and honeycomb structures. This test is usually very subjective, but work by Adams and Cawley<sup>(6)</sup> has shown that the technique can be quantized. The local structural stiffness is affected by the presence of the defect, and the force-time characteristics are dependent upon the local structural impedance. Adams and Cawley found that the impact on a good region had a higher amplitude and a shorter time duration (or contained higher frequencies), while the impact on a defective region had a lower amplitude and a longer duration (or contained lower frequencies). Therefore, by incorporating a force transducer in the impact hammer, the location of adhesive defects can be found. The sensitivity of the technique has not been evaluated.

### 2.2 Mechanical Impedance

The mechanical impedance technique works on the principle that the localized impedance of a sample is dependent upon the defect condition of the sample at that point<sup>(5)</sup>. The point impedance of a structure can be determined by applying a force and measuring the resultant velocity of the structure due to the force.

Most commercially available instruments work between 1 and 10 kHz. In general, as the impedance of the structure decreases, the quality of the bond decreases. The impedance, however, is very dependent upon the flexibility of the base structure. Because the sensitivity of this technique is directly related to the contact stiffness of the material being tested, it has not been very reliable. In addition, this technique does not work well with a composite structure.

### 2.3 Mechanical Resonance

If a planar disbond is modeled as a plate restrained around the edges by the surrounding structure<sup>(6)</sup>, then as the frequency of excitation increases, the disbond approaches resonance. At resonance, the impedance

over the defective region decreases, and the response for a given force input increases. If the excitation frequency is close to the fundamental frequency, the response amplitude for the defective region will be much higher than for the surrounding region. When the layers above a defect were modeled as a disk, and the resonant frequency of the disk was directly related to the depth of the defect and the radius of the defective region, as well as the square roots of Young's modulus, the density, and a function of Poisson's ratio. The typical operating frequencies for instruments using this technology are 20 to 30 kHz.

Another mechanical resonance method used to evaluate adhesive bonds utilizes a lower frequency. Low-frequency (~10 Hz) dynamic measurements of the shear modulus of epoxy phenolic and other adhesive systems have been shown to vary greatly during curing and, in fact, to provide a measure of the degree to which curing has progressed<sup>(7)</sup>. Damping of the vibrations of adhesive rod specimens also correlates with cure and strength.

Meyer and Chapman<sup>(8)</sup> reported that the Ford Motor Company has used the low-frequency Automation Industries' Sondicator S-2B to monitor the bond strength of adhesively joined fiberglass-reinforced plastic (FRP). They found that three factors affected the strength of FRP; namely, the substrate, primer, and adhesive. To address the potential problem with quality assurance of bonds, Ford developed three concepts: quality bonding environment, bond-strength profile, and bond merit factor (BMF). The BMF was used to estimate the severity of a partial bond that exists but is not detected. Meyer and Chapman developed an empirical equation that incorporated the length of the joint to be inspected, the length of the total disbond, and the length of the partial disbond.

In a review paper, Thompson et al.<sup>(7)</sup> pointed out that a number of survey experiments have suggested that the adhesive bond strength of honeycomb sandwich panels also can be nondestructively determined by measurements of vibrational response. The data show that both the damping characteristics of panel vibrations as a whole and the velocity of the propagation of elastic waves that travel along the surface and the sample bondline can be correlated with destructively determined bond strengths. These results are a consequence of the viscoelastic properties of the adhesive whereby changes in the elastic moduli and damping capacity of the adhesive can be related to the molecular structure and hence the strength of the adhesive.

## 3. ULTRASONIC TECHNIQUES

A tremendous amount of work has been conducted to evaluate the capability of ultrasonic techniques to determine the quality of adhesive bonds. The work has consisted of studying longitudinal, shear, surface, and interface waves. Some techniques utilize the time-amplitude domain, while others use frequency amplitude. These techniques include those that measure the response of the signal reflected from or transmitted through the bonded interface region and those that interact directly with the adhesive layer. These techniques are described in more detail in the following paragraphs.

### 3.1 Amplitude-Domain Reflection/Transmission at the Bond Interface

The amplitude-domain reflection/transmission techniques attempt to determine the quality of the bond by evaluating the interaction of the ultrasonic beam with the adhesive boundary interfaces. For the pulse-echo mode, as the ultrasonic beam interacts with the boundary of the adhesive, certain reflections should occur. [See Figure 1<sup>(9)</sup>.] If a good bond exists, little reflection should be observed (except due to pure impedance matching). If a defective bond exists, then reflection would increase because the impedance mismatch is due not only to the impedances of the adherents and adhesive, but also to the presence of air or other inclusions. The through-transmission technique would interact with the same boundaries, but good bonds would have high transmission, while poor bonds would have decreased transmission.

Work by Adler and Whaley<sup>(10)</sup> showed experimental dependence of spectral variations within a reflected broadband ultrasonic pulse on the size and orientation of the reflector. An analytical model was developed assuming that the interference of the waves received from the edges of the reflecting surface was responsible for the variations of the received frequency spectra. Their work was aimed at developing a method for determining the size of arbitrarily oriented flaws of crack-like geometry. When an object was placed in the path of a sound beam, the object produced waves which constructively interfered (added in phase) for frequencies (f) given by

$$f_n = nv/(2d \sin a) \quad (1)$$

where  $n$  is an integer,  $d$  is the diameter of the circular object in the path of the ultrasound,  $v$  is the velocity of the sound in the medium, and  $a$  is the angle of the transducer relative to the object.

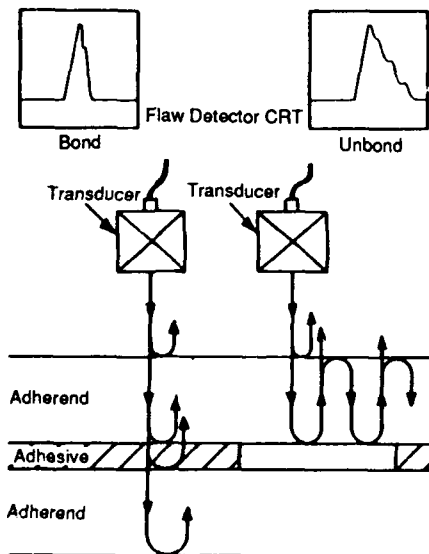


Figure 1. Illustration of pulse-echo techniques and how the ultrasonic wave interacts with the bond region for the cases of bond and unbond

Tattersall<sup>(11)</sup> found that flaws are commonly detected by their ability to reflect a burst of ultrasound back to the piezoelectric transducer. Relying on the existence of a reflected signal, however, is not adequate to detect the difference between a weak and a good bond because both good and bad bonds can reflect ultrasound. He developed a theory that provides expressions for the coefficients of the reflected and transmitted amplitude and phase. The formula for the reflected amplitude ( $A$ ) from an adhesively bonded area is

$$A = \frac{Z_1 - Z_2 + i\omega(Z_1 Z_2 / K)}{Z_1 + Z_2 + i\omega(Z_1 Z_2 / K)} \quad (2)$$

where  $Z_1$  and  $Z_2$  are the ultrasonic impedances of the adherent and adhesive, respectively,  $K$  is a constant, and  $\omega$  is  $2\pi f$ . By determining the amplitude, the quality of the bond can be derived from the Argand diagram shown in Figure 2.

Rose and Meyer<sup>(12)</sup> and Biggiero et al.<sup>(13)</sup> utilized ultrasonic immersion and spectroscopic procedures for predicting and evaluating bond strength in aluminum-to-aluminum step-lap joints made with Scotch-Weld 2216 structural adhesive joint. The UT tests were conducted using a medium-focused, 1/4-inch diameter, 10-MHz transducer in the immersion mode. The frontwall echo (FWE) and the backwall echo (BE) were compared. The results showed that as the ratio of FWE/BE increased, the adhesive bond strength increased.

Meyer and Rose<sup>(14)</sup> demonstrated the application and use of analytical models in the experimental ultrasonic evaluation of interface conditions in an aluminum-to-aluminum adhesively bonded system. Their results showed that a variation in bond strength due to surface preparation can be detected ultrasonically through careful inspection and signal-processing analysis.

UT data were collected using 1/4-inch, 10- and 20-MHz transducers in an immersion mode. Several samples were destructively tested to determine the bond strength. Their results indicated that a variation

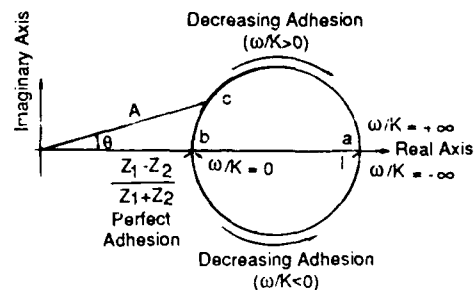


Figure 2. Argand diagram illustrating how reflected amplitude should vary as a function of quality of adhesive bond. If  $A = 1$ , then there is complete debond. The case of complete adhesion is shown as point "b" on the Argand diagram. Intermediate bond quality gives values between "b" and 1.

in the interfacial condition of the bond was most noticeable ultrasonically by an amplitude change in the interface echo. As the quality of the interfacial bond decreased, the amplitude of the reflection from the adhesive-substrate interface increased.

The 10-MHz data did not correlate well; the 20-MHz data, however, showed clearly which sample had good surface preparation and which did not. Because some of the data were unclear, more experimentation is needed using the model developed by Rose and Meyer.

In 1979 Chernobelskaya et al.<sup>(15)</sup> developed a quantitative method of testing adhesive bonded joints using a high-resolution ultrasonic probe. The probe resolved echoes from the two interfaces of the bondline. The method was tested on aluminum-to-aluminum joints bonded with Metlbond 328 of Narmco Corp. Their method first tested the unbonded piece and obtained a set of echoes from the free surface, and then data were taken from the bonded joint. The effective reflection coefficient of the interface was derived from the measured amplitude ratio, which takes into account the loss in the aluminum. The true reflection coefficient can be derived from the measured transit times, thicknesses, and known densities of the aluminum and the adhesive. The ratio of the effective reflection coefficient to the true reflection coefficient was the measure of the adhesive bond strength.

This model was simple; but it was only tested on two samples, and the data stated that the two samples were good. No destructive tests were conducted on the samples to correlate the findings.

Alers et al.<sup>(16)</sup> felt that the basic premise on which ultrasonic methods can be used to predict the cohesive and adhesive strength of a metal-to-adhesive bond was the argument that measurable changes in the elastic properties of the adhesive or the interface should be associated with changes in the cohesive or adhesive strength. Their work showed that the cohesive strength of a bond can be predicted from quantitative measurements of the velocity of sound and the attenuation in the adhesive layer.

What needed to be addressed was the lack of cohesive strength with the bulk of the adhesive and the lack of adhesive strength at the polymer-to-metal interface. When adhesive cures, it becomes hard and less attenuative to ultrasound. By measuring these two parameters, a cure-monitoring system can be made. Alers pointed out that the bond is really not between the adhesive and the metal, but between the oxide of the metal surface and the primer. The oxide/primer interface is usually between 0.02 and 0.2 micron thick, and ultimately the NDE test has to target this thickness.

Expressions for the various reflection coefficients were given based upon impedances. For very thin adhesive layers, the resonance and antiresonance dips become coupled and it is difficult to determine the thickness and adhesive properties without a computer.

The cohesive strength of a polymeric adhesive should be closely correlated with its bulk physical properties. An improper mixture of chemical constituents of an incorrect curing procedure is apparent in cohesive

strength and also modifies the ultrasonic velocity and attenuation. The Fourier transform of the adhesive interface reflection is taken and divided by the Fourier transform of the front surface reflection. The minima in the spectrum is related to the layer thickness, and the depth is related to the attenuation as a function of frequency. The ultrasonic attenuation showed knee-type relation with bond strength (as shown in Figures 3 and 4). Velocity was linearly related to bond strength. The resonance frequency was correlated with bond strength, but showed that the shift in resonance frequency was small for changes in adhesive strength.

Segal et al.<sup>(4)</sup> found that the best ultrasonic technique for predicting adhesive quality was high-frequency ultrasonics using signal processing, as described by Raisch and Rose<sup>(17)</sup>. Williams and Zwicke<sup>(18)</sup> utilized various ultrasonic resonance methods to inspect adhesively bonded joints, but were disappointed in the correlation between the ultrasonic data and joint strength.

A good bond is determined by several variables, and the ultrasonic interaction also depends upon variables that are difficult to separate. Williams and Zwicke categorized the bond variables into two areas: intrinsic and extrinsic. The intrinsic properties affecting cohesive bond strength included degree of cure, adhesive

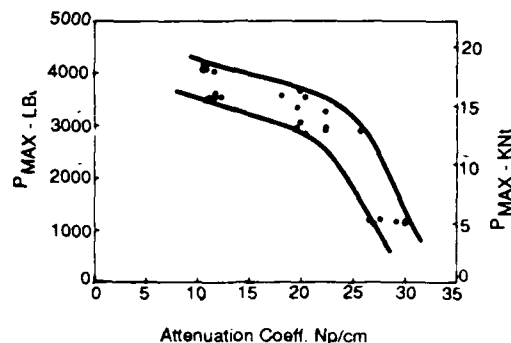


Figure 3. Correlation between the measured attenuation of the adhesive and the strength of the adhesive bond

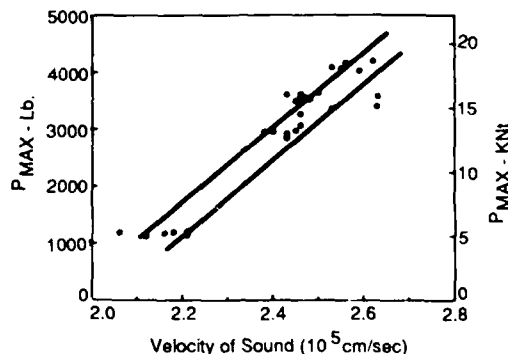


Figure 4. Correlation between the measured velocity of sound in the adhesive and the strength of the adhesive bond

chemistry, bondline thickness, and voids. The extrinsic properties affecting adhesive bond strength included surface cleanliness, surface contamination, etchant type and time, primer type and application, and wetting properties of the adhesive. They found that even if all the intrinsic properties were within proper tolerances, the bond might still fail due to extrinsic factors. They included joint geometry and loading, and the presence of defects.

A multidisciplinary approach was required that combined NDE and fracture mechanics to form a basis for a comprehensive quality assurance solution. NDE could detect defects and measure intrinsic cohesive and adhesive properties and, in the case where no defects were present, could assess bond strength. Fracture mechanics was employed to determine acceptable defect sizes (to be detected by NDE) for a given set of intrinsic bond properties. The interaction of ultrasonic waves with certain properties of the bond varied as shown in Table 1. For example, longitudinal (L)-waves were strongly influenced by the cure state and bondline thickness, but did not do well for chemistry, porosity, etch, defects, or surface condition.

The experimental work was conducted on 6061 aluminum using Eastman EA 9649 adhesive. The L-waves were generated with a polyvinylidene fluoride (PVDF) transducer which had high internal damping and broadband frequency response (1 to 35 MHz). Shear (S)-wave work was conducted with an S-wave transducer using a UTRC (United Technologies Research Corporation) proprietary couplant. The signals from the front and back surfaces were digitized and processed. UTRC developed a pattern-recognition analysis algorithm called REcursive Structure IDentification (RESID) based upon a theory developed by Ivakhnenko<sup>(19)</sup>. The algorithm involved five features (S-wave velocity, L-wave attenuation, S-wave attenuation, L-wave attenuation versus frequency, and S-wave attenuation versus frequency).

The RESID algorithm was applied to ultrasonic amplitude data. These amplitudes, shown in Figures 5 and 6, were the positive and negative RF amplitudes of the reflections from the adherent/adhesive interface and the positive and negative RF amplitudes of the adhesive/adherent interface. The features used in the algorithms are listed in Table 2.

Using the developed algorithms, experimentally predicted bond properties such as bond strength, shear strength, and percent cure were correlated with destructively measured properties, shown in Figures 7 and 8.

Rose et al.<sup>(20)</sup> developed a combined NDE technique that used signal processing, pattern recognition, and a high-density ultrasonic scan in a hybrid scheme for assessing the integrity of an adhesively bonded structure.

Experimentally, they used a 10-MHz transducer in the immersion mode and performed a raster scan over the test plate. The test plate consisted of a sandwich configuration and contained curing defects, adhesive contamination, and voids in the adhesive. They looked at ten different samples. The RF waveform was digitized and analyzed using several feature-extraction

algorithms. The ratio of the adhesive layer reflection to the front-surface reflection was one of 14 features evaluated.

### 3.2 Spectral Domain Reflection/Transmission at the Bond Interface

The spectral domain reflection/transmission techniques attempt to determine the quality of the bond by evaluating the interaction of the frequency content of the ultrasonic beam with the adhesive boundary interfaces. Frequency parameters such as center frequency, bandwidth, power spectrum, and others can be calculated from the Fourier transform of the reflected or transmitted ultrasonic beam. These features can be extracted from waveforms obtained from test samples that simulate various bond conditions and an algorithm using weighted values of the features that are best correlated to the bond quality.

Ciang et al.<sup>(21)</sup> analyzed the frequency spectrum of ultrasonic plane waves transmitted through a multilayered laminate structure at normal incidence to determine the amplitude distribution of the frequency components. In supporting the theoretical calculations, the wave equation was solved to evaluate the displacement field with the appropriate boundary conditions in a six-region laminate. Cavity resonance of the plane waves in the layers produced peaks in the transmission-frequency spectrum. Experiments were conducted using a pair of broadband acoustical transducers transmitting a pulsed ultrasound wave with a center frequency of 5 MHz through multilayer adhesively bonded aluminum plates with different thicknesses. Resonant peaks in the experimental frequency spectra were compared with those theoretically calculated from regions of good bond and disbond.

The theory gave expressions for the transmitted energy and transmitted flux coefficient, and the effects of air gap and good adhesive layers were shown. Also, the effect of the adhesive-layer density, adhesive-layer sonic velocity, and adhesive sonic impedance on the theory were described. The experimental results looked promising, but more work was needed.

Chang et al.<sup>(22)</sup> in 1975 reported that NDE parameters evaluated from the ultrasonic spectroscopic method could be correlated with adhesive bond strength in multilayered structures. Selected portions of the reflected or transmitted RF signals were digitized and Fourier transformed, and resonance peaks or anti-resonance dips in the frequency spectrum characterized the thickness of the substrate plates and the adhesive gap. The shape and the Q-value of the peaks and dips determined the bond strength.

The Q of the resonance was related to the ratio (r) of acoustic impedances in the two media by

$$Q = 180/(\sin^{-1}(2r/r^2-1)) \quad (3)$$

The Q values were measured at the half-width of the curves in the frequency spectrum.

The UT pulse-echo amplitude ratio did not give good correlation, but did show a generalized trend of A1/A2 decreasing as bond strength increased (where A1/A2 is the ratio of signal amplitude for the top and bottom



Table 1  
EFFECTS OF BOND VARIABLES ON ULTRASONIC MEASUREMENTS <sup>(18)</sup>

Ultrasonic Measurements	Bond Variables						
	Cure State	Chemistry	Porosity	Bondline Thickness	Etch	Surface Condition	Defects
Longitudinal Wave Velocity, $V_L$	S	W		S	W		
$V_L$ vs. Wavelength			W				
Longitudinal Wave Hysteresis Atten., $\alpha H_L$	S	S			W	W	S
Longitudinal Wave Scattering Atten., $\alpha S_L$			S			S	S
$\alpha S_L$ vs. Wavelength			S				
Shear Wave Velocity, $V_T$	S	W		S	S		
$V_T$ vs. Wavelength			W				
Shear Wave Hysteresis Atten., $\alpha H_T$	S	S			S	W	S
Shear Wave Scattering Atten., $\alpha S_T$			S			S	S
$\alpha S_T$ vs. Wavelength			S				

S = Strong Dependence; W = Weak Dependence

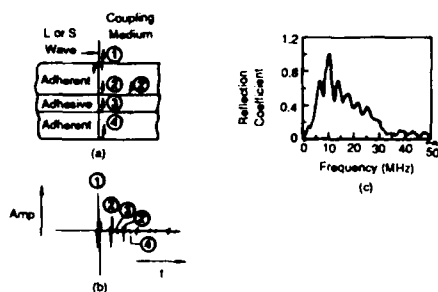


Figure 5. Schematic diagram of a typical specimen, with (a) time domain, (b) frequency domain, and (c) ultrasonic signals. A longitudinal (L) or shear (S) wave is excited in the specimen, and the reflections from surfaces 1, 2, 3, and 4 observed. (Wave 2' is the second round trip in the top adherent.)

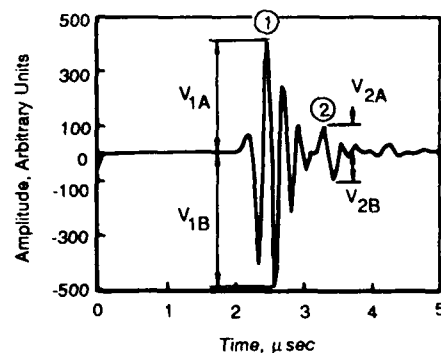


Figure 6. Typical time domain waveform showing reflections from the adherent/adhesive (1) and adhesive/adherent (2) interfaces.

Table 2

ULTRASONIC FEATURES EXTRACTED FROM WAVEFORMS<sup>(18)</sup>

## (a) Longitudinal Wave Features

Feature	Determined by*	Related to
$L_P$	$(V_{2A} + V_{2B})/(V_{1A} + V_{1B})$	Total Attenuation, $\alpha_L$
$L_M$	$V_{2B}/V_{1B}$	Total Attenuation, $\alpha_L$
$L_0$	$F_0$	Longitudinal Velocity, $V_L$
$L_1$	$F_1$	$V_L$ (Dispersion)
$L_2$	$F_2$	$V_L$ (Dispersion)
$L_5$	$1/A_1$	Total Attenuation, $\alpha_L$
$L_6$	$[\log(1/A_2) - \log(1/A_1)]/[\log F_1 - \log F_0]$	$\alpha_L = \alpha_L(F)$
$L_7$	$[\log(1/A_3) - \log(1/A_2)]/[\log F_2 - \log F_0]$	$\alpha_L = \alpha_L(F)$

## (b) Shear Wave Features

Feature	Determined by*	Related to
$S_P$	$(V_{2A} + V_{2B})/(V_{1A} + V_{1B})$	Total Attenuation, $\alpha_T$
$S_M$	$V_{2B}/V_{1B}$	Total Attenuation, $\alpha_T$
$S_0$	$F_0$	Longitudinal Velocity, $V_T$
$S_1$	$F_1$	$V_T$ (Dispersion)
$S_2$	$F_2$	$V_T$ (Dispersion)
$S_5$	$1/A_1$	Total Attenuation, $\alpha_T$
$S_6$	$[\log(1/A_2) - \log(1/A_1)]/[\log F_1 - \log F_0]$	$\alpha_S = \alpha_S(F)$
$S_7$	$[\log(1/A_3) - \log(1/A_2)]/[\log F_2 - \log F_0]$	$\alpha_S = \alpha_S(F)$

\* $V_{MN}$ ,  $A_N$ , and  $F_M$  are defined in Figures 5 and 6.

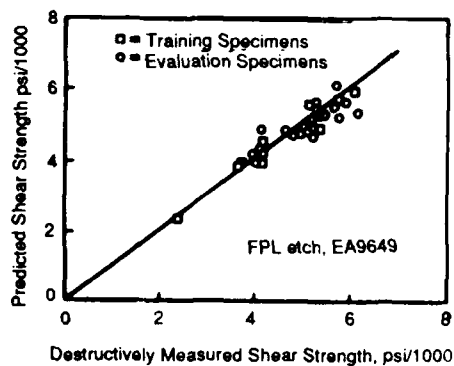


Figure 7. Experimentally predicted shear strength versus actual shear strength in a defect-free specimen (measured destructively) as obtained using the RESID network.

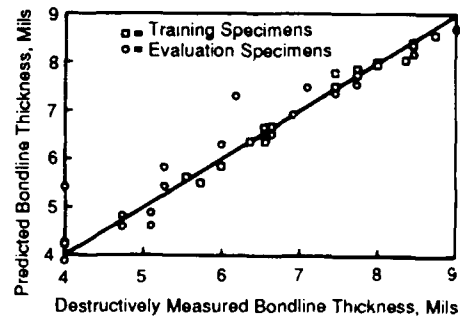


Figure 8. Experimentally predicted bondline thickness versus actual bondline thickness (measured by sectioning) as obtained using the RESID network.

adhesive interfaces). The shear strength was found to vary directly with Q-value.

Chang et al.<sup>(23)</sup> used an ultrasonic-frequency, spectral-analysis method for detecting flaws in composite materials. This technique depended on the phenomenon of resonance interference of acoustical waves in materials. When the material thickness was an integral multiple of the half-wavelength of the sound waves, destructive interference of a return echo by multiple reflections in the materials produced antiresonance dips in the frequency spectrum for the reflected signal.

Their experimental results showed that a well-bonded region of the composite had a very different frequency spectrum from a delaminated region. They could detect defects as small as 1.5 mm but were not able to differentiate between different sizes of defects.

Chang et al.<sup>(24)</sup> utilized ultrasonic spectroscopy to evaluate the quality of the bond. They theorized that in adhesively bonded structures, destructive interference of the pulsed sound waves at the boundaries of the bond layer produced spectral information characteristic of the bond. The bondline thickness could be determined accurately from the frequency minima in the spectra. The width of the antiresonance dipped at half-power points, and the amplitude of the dips was related to the acoustic properties at the interfaces of the adhesive layer.

They provided an analytical calculation for the sound-wave interference in the bondline using a notation developed by Brekhovskikh<sup>(25)</sup>. This calculation included the ultrasonic attenuation of the adhesive layer which, in effect, decreased the amplitude differences between the resonance peaks and dips in the frequency spectrum. Also, the acoustic impedance was directly related to the elastic modulus of the adhesive by  $A = (E \rho)^{1/2}$  where  $E$  was the modulus and  $\rho$  was the density.

The experimental setup used 15-MHz, L-wave pulse echo; a wideband pulser/receiver; and plates of 2024 Al and RB-398 adhesives. Fabrication processes included low curing temperature, unetched substrate surfaces, adhesive sheet cutout, and insufficient bonding pressure.

Their test results showed that the amplitude ratio correlated well with bond strength. Also, excellent correlation between the reciprocal of the half-power bandwidth ( $1/B$ ) and shear strength was found (see Figure 9). The amplitude ratio and the  $1/B$  had a linear relationship, which provided a basis for a mathematical model to predict bond strength.

Raisch and Rose<sup>(17)</sup> examined the potential of selected ultrasonic signal features and the ability of these features to predict performance on an adhesively bonded structure. Adhesive, rather than cohesive, problems were considered. They claimed that the cohesive strength prediction had been solved by Flynn<sup>(26)</sup> using measurements of wave speed and attenuation in the bulk adhesive, provided that adhesive-type failure did not occur. The cohesive-strength prediction problem was also studied by Yee et al.<sup>(27)</sup> using ultrasonic spectroscopy measurements to characterize

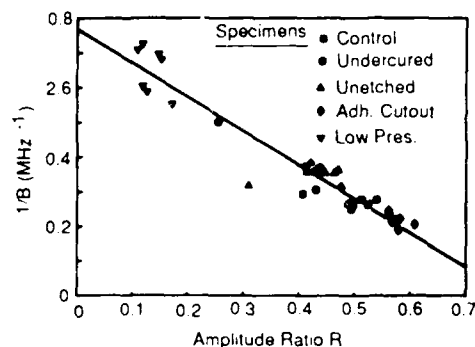


Figure 9. Correlation of ultimate shear strength with  $1/B$

the physical state of the adhesive in a bonded laminate.

The experimental work of Raisch and Rose<sup>(17)</sup> was conducted using 0.25-inch (0.63-cm) diameter, 10-MHz transducers at normal incidence in the immersion mode. The data were acquired, digitized, and then operated in the amplitude-time and amplitude-frequency domain. Thirteen features were extracted for evaluation. Those in the amplitude-time domain included (1) peak-to-peak pressure variation, (2) the activity region (obtained by using a spline curve containing all the relative maximums of the rectified bond echo), (3) the area enclosed by the rectified amplitude-time bond echo within the activity region, and (4) the ratio of positive-to-negative area enclosed by the amplitude-time bond echo within the activity region. The remaining nine features were in the amplitude-frequency domain. They included (1) the maximum amplitude of the Fourier Spectrum, (2) the 6-dB down point on each side of the maximum amplitude frequency peak, and (3) the number of relative maximums and minimums occurring within the bandwidth region of the spectrum. The frequency locations of the maximums and minimums that occurred at lower and higher frequencies relative to the spectrum maximum also were picked, and then ratios of these amplitudes and their associated frequencies were used. Using this technique on 45 specimens yielded an overall 84-percent accuracy of calls.

Rose and Thomas<sup>(28)</sup> showed that ultrasonic C-scan techniques can be used to detect delaminated bonds. A completely automated ultrasonic inspection system was developed for predicting bond strength in metal-to-metal bonded step-lap joints. Results to date provide a 91-percent reliability for solving the problem of predicting the adhesive bond performance. The system used pattern-recognition techniques, especially the nearest neighbor rule and the Fisher linear discriminator algorithm, which separated the bond data into strong and weak bonds.

A 10-MHz transducer was used in the tests. The results using three different transducers showed correct prediction of 95, 95, and 89 percent (the training set was done with the first transducer). However, the algorithm was still felt to be very much transducer-dependent (especially on the pulse shape). A transducer test was developed to evaluate the use of

different transducers. This deconvolution basically made all the transducers equal in their capability to predict good versus bad bond.

Ultrasonic pulse waveforms reflected from the interface of bonded joints were digitally recorded by Alers and Elsley<sup>(29)</sup>. Certain frequency-dependent features of the reflected waves such as the lowest frequency of resonance and the highest split resonance frequency were correlated to the mechanical strength of the bond. The pulse-echo method was used in the immersion mode. The signals from the top of the metal surface and from the interface bonded region could be separated. A drawback of looking just at the amplitude ratios was that the bond strength was really determined by a very thin layer at the metal-to-adhesive interface, and the reflection from this critical layer was dominated by the metal-polymer impedance discontinuity rather than the structure of the interface. Their method was to Fourier transform the entire signal through the composite structure and to look at the frequency features.

The results showed that resonant frequency was very dependent upon bondline thickness. Other frequency-dependent variables needed to be evaluated and then correlated to the bond strength.

Thomas and Rose<sup>(30)</sup> studied the problem of predicting adhesive bond performance for both surface preparation and undercure defects using an ultrasonic experimental test bed system. The experimental test bed incorporated ultrasonic and computer equipment necessary to acquire and process data from various types of adhesively bonded test specimens. A set of 154 bond specimens was used to develop an algorithm that was 91 percent reliable in separating good and poor bond samples. A Fisher Linear Discriminant function was selected as the best pattern-recognition routine for this classification problem.

The features selected were:

- (1) Peak-to-peak ratio of the echo and the reference signal-frequency shift
- (2) Peak frequency
- (3) Deepest depression frequency (dip frequency)
- (4) Difference between the dip frequency and the peak frequency
- (5) Ratio of dip amplitude to peak amplitude
- (6) Difference between the first and second dip frequencies
- (7) Standard deviation of the transfer function
- (8) 6 dB beam width of the first dip

Lloyd<sup>(31)</sup> worked with A-scan and frequency spectrum data from one substrate of the adhesively bonded composite. Using the same transducer and equipment, he took data through the adhesively bonded substrate and compared the two sets of data. The unbond condition was expected to be similar to the data taken from the substrate. A discussion of the theory was

given, which basically stated that when the transducer was over the bonded region, a mixed frequency spectrum was obtained which was a measure of the compliance of the adhesive layer.

Recent work conducted by Joshi<sup>(32)</sup> also utilized the ultrasonic spectrum obtained from the interface region of the bond. The method he used was called the Chirp-Z Transform (CZT). The CZT is obtained by taking the Fourier transform of the A-scan (time-amplitude data display) and determining the location of dips in the frequency spectrum. These dips are caused by interference between the bond interface layers. The frequencies of the dips were used as center frequencies in the CZT to expand the frequency resolution.

Joshi tested his technique on symmetric double-lap specimens fabricated from 6061T6 aluminum and the Dexter Hyson adhesive EA 9628. The samples had different surface preparations and were fabricated in different humidity level environments. His conclusion was that the frequency dip intervals or the successive cutoff frequencies could be correlated to the condition of the surface preparation and the level of humidity under which the bond was made.

### 3.3 Low-Frequency Techniques

Thompson et al.<sup>(7)</sup> reported results of several experiments that suggested the adhesive bond strength of honeycomb sandwich panels can be nondestructively determined by measurements of vibrational response. The data showed that both the damping characteristics of panel vibrations and the velocity of the propagation of elastic waves traveling along the surface and sample bondline can be correlated with destructively determined bond strengths. These results were a consequence of the viscoelastic properties of the adhesive, whereby changes in the elastic moduli and damping capacity of the adhesive can be related to the molecular structure and hence the strength of the adhesive.

Data collected on honeycomb at 7 kHz showed a relationship between the modulus and cohesive strength of the bond with the damping of the UT signal. The frequency and temperature at which the damping reached its maximum were interrelated through the expression  $\omega t = 1$  where  $\omega$  is  $2\pi f$  and  $t$  is the relaxation time according to the Arrhenius equation

$$t = t_0 e^{W/kT} \quad (4)$$

where  $t_0$  is a temperature-independent factor,  $W$  is the activation energy,  $k$  is Boltzmann's constant, and  $T$  is the absolute temperature. Damping of the vibrations of the adhesive rod specimens also correlated with cure and strength.

Averbukh and Gradinar<sup>(33)</sup> conducted work with the Fokker Bond Tester. They placed the piezoelectric transducers on a sheet of material and determined the acoustic characteristics. Then the composite material (composed of the first sheet cemented to another sheet) was monitored to determine its acoustic characteristics. The composite produced a shift in frequency and acoustic impedance. The shift in frequency was indirectly proportional to the bond strength. The Bond Tester, however, had some shortcomings: (1) it

required that the adhesive strength exceed or be equal to the cohesive strength and (2) it imposed sometimes unattainable technological requirements on the cementing.

Budenkov et al.<sup>(34)</sup> showed that the Bond Tester and the Stabmeter work only where the adhesive strength is higher than the cohesive strength. Bond strength can be determined by correlating the strength and the characteristic impedance of the glue using ultrasonics.

### 3.4 Rayleigh and Surface Waves

Staecker and Wang<sup>(35)</sup> studied the application of acoustic Rayleigh wave propagation in a layered medium. A theoretical derivation was made for the propagation in a fluid between two solids. Experimentally, they used 30-MHz Rayleigh waves of 2-microsecond duration on the exposed region of the second layer (see Figure 10). The wave traveled into the bonded region and excited characteristic waves of the layer. Their work demonstrated that acoustic waves could be propagated in a solid-fluid-solid guiding structure.

Thompson et al.<sup>(7)</sup> also did some surface work and found that the surface-wave velocity increases with the adhesive bond strength.

### 3.5 Lamb and Interface Waves

Rokhlin<sup>(36)</sup> analyzed diffraction of Lamb waves by a finite crack situated on the plane of symmetry of an elastic layer. The surface of the crack and the layer were assumed to be stress-free. The field of the reflected and transmitted waves as well as the field in the vicinity of the crack were given as expansions of natural waves of the elastic layer. The amplitudes of these waves were found from exponentially converging infinite systems of equations.

The interaction of waves at bonded interfaces was studied by Jones and Whittier<sup>(37)</sup>. They looked at plane-strain elastic-wave propagation for two dissimilar half-spaces joined together at a plane interface by an elastic bond. The bond thickness was assumed to be small compared to the wavelength; the existence of interface waves was shown to be governed by a parameter involving bond stiffness and wavelength. The infinitely stiff bond case (fully cured) would reduce to the Stoneley wave data; and the infinitely soft bond

would produce two Rayleigh surface waves, one in each medium.

They also found that as the bond became stiff, the Rayleigh waves could change into two interface waves, each involving motion of both media. One of these waves, the one with the higher speed, disappeared for a sufficiently stiff bond. With further increase in bond stiffness, the remaining interface wave either went into a Stoneley wave or disappeared, depending on whether or not Stoneley waves were possible. Furthermore, when the Rayleigh wave speed in the faster medium was greater than the S-wave speed in the slower medium, the Rayleigh wave in the faster medium existed only for zero bond stiffness. As soon as the stiffness became finite, the wave disappeared, and only a wave similar to the Rayleigh wave in the slower medium might occur.

A new technique for analyzing interfacial conditions in completed adhesive bonds was suggested by Claus and Kline<sup>(38)</sup>. The method was based on the sensitivity of Stoneley waves, which propagate along the boundary between dissimilar solid media, to changes in the material properties of the interface region. Stoneley wave attenuation measured after polishing was found to increase as a function of increasing surface roughness in specimens of borosilicate crown glass bonded with an anaerobic cement to a substrate of 7740 Pyrex mirror glass.

The experimental setup utilized surface acoustic waves from an x-cut piezoelectric crystal mounted on a conventional Rayleigh-angle water-coupled wedge. As the waves passed into the adhesively bonded region, they became Stoneley waves, which are affected by the boundary condition. The outgoing waves were detected with an optical interferometer. In these experiments, the Stoneley wave attenuation increased as the surface roughness of the two adherents increased.

The use of ultrasonic wave-velocity measurements of surface, plate, or interface waves for the evaluation of adhesive bond strength was studied by Pilarski<sup>(39)</sup>. His work dealt with two classes of problems: (1) cases where a step-like change occurred in the acoustic impedance such as bimetals or glued metal bonds and (2) cases where the bond was a thin intermediate layer whose thickness was much less than the wavelength of the ultrasonic wave.

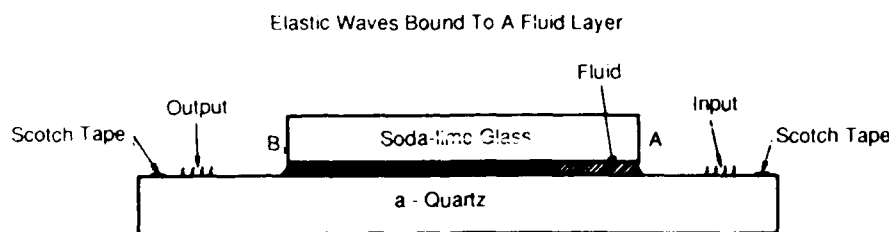


Figure 10. Experimental layered geometry configuration used to generate Rayleigh wave data

One way to evaluate the adhesive strength of a layered joint is based upon the measurements of the pressure coefficient of the reflected wave for the bond interface. Another way is to use ultrasonic waves propagating parallel to the bond surface. These waves are called subsurface waves in the case of a layer on a base, plate waves in the case of one or more solid layers, and interface waves in the case of two elastic half-spaces (i.e., a solid medium of thickness several times the wavelength of a surface mode). Previous work had used the decay of the surface, plate, or interface waves in evaluating the bond strength.

The purpose of Pilarski's paper<sup>(39)</sup> was to use velocity measurement of waves propagating along the bonded surfaces to determine the bond strength. The theory considered two types of boundary conditions, i.e., welded and adhesively bonded boundaries. For the welded case, a continuity of displacement and stress occurred. For the adhesively bonded case, a vanishing tangent stress can occur. Decrease in adhesive strength yields a decrease in the phase velocity of the surface waves, as shown in Figure 11.

Experimentally, the phase velocity of the ultrasonic waves can be measured using critical-angle reflectivity. The change in the critical angle is related to the change in velocity which, in turn, is related to the quality of the bond. In general, the higher the phase velocity, the greater the bond.

Most of the previous UT methods used for determination of strength of adhesive bonds used 0-degree L-waves, which are not extremely sensitive to the adhesion properties between the adhesive and the adherents. Rokhlin<sup>(40)</sup> used guided waves to produce shear stress on the interface. Interface waves were applied for monitoring curing of the adhesive, and Lamb waves were used to study adhesive joints of the thin sheets.

An interface wave can be obtained in the adhesive joint by generating a surface wave into the lower substrate. The thickness of the layer must be smaller than

the UT wavelength. Bond failure can occur inside the adhesive (called cohesive failure) and between the adhesive and adherent (called adhesive failure).

When contact between the adhesive and the substrate is not ideal, the interface wave velocity decreases. By monitoring two interface waves, one through an unbonded region (calibration) and one through an adhesively curing region, it can be observed that as the adhesive cures, the phase velocity between the two waves increases. (See Figures 12 and 13.)

When the thicknesses of the bonded substrates are comparable to the wavelength, Lamb waves are used. The dispersion characteristic of Lamb waves can be useful to monitor the slip (liquid) and rigid (bonded) boundary conditions. During the curing process (liquid to solid), the Lamb wave propagation mode is transformed with a change in phase from the mode in the slip condition to the mode in the rigid condition.

Data were collected using 0.5-, 1-, 1.5-, and 2-MHz transducers on adhesive films that were 80 to 90 microns thick (approximately 3 to 4 mils). The 1- to 2-MHz data were good; the 0.5-MHz data, however, did not show good results due to edge problems.

Rokhlin<sup>(41)</sup> studied a thin adhesive film between two bonded adherents and showed that it was capable of localizing the energy of elastic waves in the form of an interface wave. The phase velocity and transmission losses of the interface wave were measured during the course of polymerization of the adhesive. The phase velocity of the interface wave and the effective shear

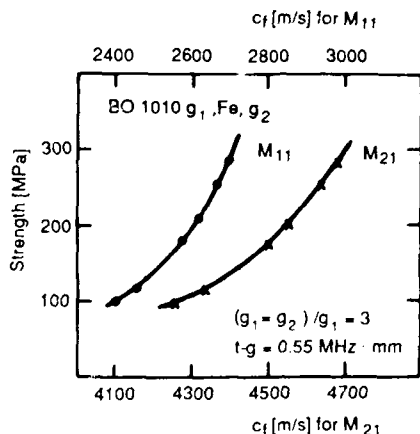


Figure 11. Relationship between phase velocity of the first two modes of plate waves and shear strength of the adhesive joint in bimetal

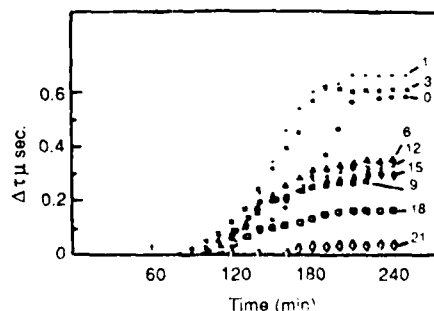


Figure 12. Change in interface-wave velocity as a function of curing time for aged specimens

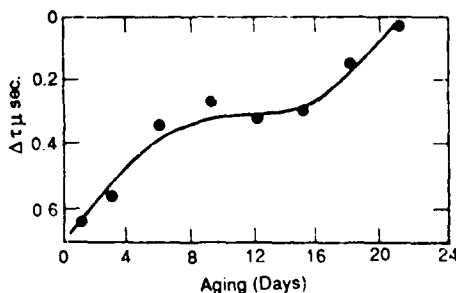


Figure 13. Change in time delay as a function of aging time

modulus of the interface film were related to the strength of the adhesive bond, as shown in Figure 14.

The thin film located between plates exhibited waveguide properties if the shear modulus of the film was smaller than that of the substrates. When the film thickness was much smaller than the wavelength, the interface wave produced shear stress only in the film.

Their study was conducted in the following way. First, a Rayleigh wave was propagated on the surface of the top part. If two plates were put together with a thin layer between them with the layer thickness much smaller than the Rayleigh wavelength and much larger than the hydrodynamic boundary layer, then the phase velocity of the interface wave ( $V_i$ ) was smaller than the Rayleigh wave velocity ( $V_r$ ). The relationship is

$$V_i/V_r = 1 - K_t h B_r \rho_0 / 4 \rho a_r \quad (5)$$

where  $B_r = (a_r^2 - 1)^{1/2}$ , and  $a_r = K_r/K_t$  are the wave numbers for the Rayleigh and shear waves in the substrates,  $\rho$  is the substrate density, and  $h$  is half of the layer thickness.

Now if the layer thickness was smaller than the boundary layer, then the shear displacement was not damped out across the film thickness and was transmitted from the lower to the upper substrate without a break in continuity. Thus, as the film solidified, the phase velocity tended toward the shear velocity. The measured velocity and damping factor of the interface waves could be used to calculate the complex shear modulus of the interface film. When there was an absence of shear bonding between the adhesive and at least one substrate, then velocity of the interface wave was close to the Rayleigh wave velocity.

Two 1.2-MHz narrow-band transducers were used for the tests. The greater the change in velocity, the greater was the strength. Also, the greater the transmission loss, the greater was the strength.

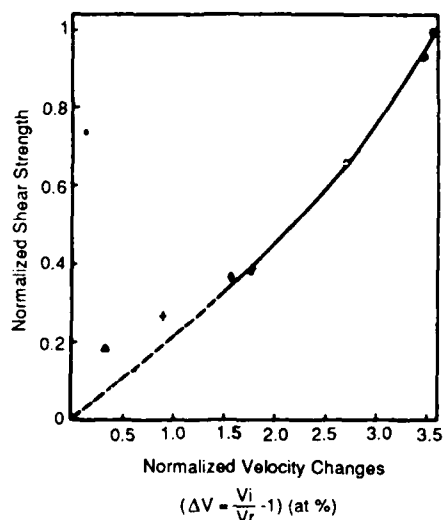


Figure 14. Experimental relationship between interface wave velocity and normalized shear strength

Rokhlin et al.<sup>(42)</sup> also studied the waveguide properties of a thin film separating two elastic half-spaces possessing a shear modulus higher than the shear modulus of the film. It was shown analytically and experimentally that such a film was capable of localizing the energy of elastic waves near the interface. The velocity of the interface wave was determined by the shear modulus, density, thickness of the film, and elastic properties of the substrates. The velocity of the interface wave was between the Rayleigh and the shear wave in the solid substrates. It was shown that the interface wave could be used to estimate the elastic and dissipation properties of thin interface layers.

### 3.6 Stress-Wave Factor

Vary et al.<sup>(43-45)</sup> showed that the ultrasonic parameter called the stress-wave factor correlated with the tensile strength and interlaminar shear strength of graphite fiber composites. Williams and Lampert<sup>(46)</sup> looked at impact damage to composites and compared the through-thickness attenuation and the stress-wave factor measurements to the degradation.

Experimentally, they used two 0.1 to 3-MHz broadband through-transmission transducers to determine the attenuation through the damage composite, and a 0.1 to 3-MHz broadband-transmitting transducer with a 375-kHz receiving transducer to measure the stress-wave factor. They defined the stress-wave factor as

$$e = g r n \quad (6)$$

where  $g$  is the accumulation time after which the counter was automatically reset,  $r$  is the transmitter repetition rate, and  $n$  is the number of cycle oscillations exceeding a fixed threshold in the output waveform generated by the input pulses. The stress-wave parameter characterized the specimen length, while the through transmission characterized the specimen's thickness. They concluded that both inspection techniques provided adequate means to determine strength of the composite.

Dos Reis et al.<sup>(47)</sup> conducted tests to evaluate the adhesive bond strength between rubber and steel plates using the stress-wave factor measurement technique. This technique measured the relative efficiency of energy transmission into the specimen. A UT pulse was injected with a transducer mounted on the surface of the specimen. The number of oscillations higher than a chosen threshold were monitored. The more internal damage, the greater was the attenuation and the less efficient the energy transmission (lower ringing). The ringing was detected by another transducer on the surface.

Experimentally, the stress-wave factor measurements were obtained using the portable Acoustic Emission Technology (AET) acousto-ultrasonic instrument. The pulsing transducer had a flat response from 0.1 to 3 MHz. The receiving transducer was resonant at 375 kHz. The injected pulse was 150V at a rate of 250 pulses/second.

### 3.7 Horizontally Polarized Shear Waves

Yew<sup>(48)</sup> performed a preliminary study using horizontally polarized shear (SH) waves on a bonded plate to

estimate the bonding strength of the adhesive bond. The concept was that the characteristics of the SH waves in the bonded structure were dependent upon the bonding stiffness of the adhesive; thus, an estimation of the adhering strength can be made by observing the behavior change of the SH wave motion. Two measurable modes of SH waves are in the structure during the early stages of adhesive curing, and the amplitude of the second-mode SH wave decreases as the adhesive cures and finally disappears after the adhesive-curing process is completed.

In addition, Yew studied the propagation of Stoneley waves in the interface of the two bonded solids. It was shown that the attenuation and the propagation speed of sonic waves in the medium were related to the bonding strength and the stiffness of the adhesive. When the cohesive strength was low, the wave behavior of the bond was similar to that of a free plate. The wavelength of the applied SH wave was so long in comparison with the plate thickness that a standing wave was established along the thickness of the plate.

The experimental tests were conducted on aluminum test plates bonded with DER 332 epoxy resin with a T403 amine curing agent and 399 accelerator. The SH waves were generated with a 0.5-MHz transducer. A 600-kHz wave-train frequency, 30 microseconds long, was delivered to the strip at a rep rate of 500 Hz using an Arenburg pulsed oscillator. After the wave train had traveled 4 inches (10 cm), it was detected by a 5-MHz, SH transducer. This set up two modes in the plate. The second mode signal clearly decreased as the adhesive cured, while the first mode stayed relatively constant. One problem with this technique was ensuring proper coupling of the SH waves. Another issue was that the width of the receiver transducer should be shorter than the SH wavelength.

### 3.8 Obliquely Incident Ultrasonic Waves

Rokhlin and Marom<sup>(49)</sup> demonstrated that changes of the amplitude of the reflected UT wave during adhesive curing occurred simultaneously with changes of the UT velocity in the adhesive. The sensitivity of the method to evaluate the interface properties was higher for thinner adhesive-interface films. It was shown by Kuhn and Lutsch<sup>(50)</sup> in 1961 that the reflection coefficient for obliquely incident L-waves from a slip interface may be higher in some cases than from a free surface; thus, the value of the reflection coefficient can be used for evaluating the interface properties.

They measured (1) the amplitude of the reflected signal at the joint and (2) the L-wave velocity and attenuation in the bulk of the sample. The change in phase velocity was determined by measuring the phase shift of the RF signal. Transducers used were 1.3 MHz. The reflected signal amplitudes as a function of cure time for three different adhesive thicknesses (8, 35, and 75 microns) were plotted, as shown in Figure 15. The thinnest showed the most dramatic effect, changing approximately 11 dB over the cure cycle, while the thickest samples only changed 3 dB over the cure cycle. That is, the technique worked best when the ratio of the adhesive layer thickness to the UT wave velocity was approximately 0.01.

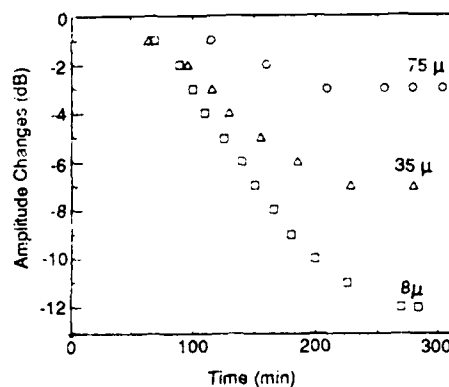


Figure 15. Dependence of reflected signal amplitude on time of adhesive curing for different adhesive thicknesses (metal-metal bond)

Similar results were obtained by Pilarski and Rose<sup>(51)</sup> using obliquely incident shear waves. They looked at adhesively bonded aluminum samples and found that the reflection coefficient as a function of angle through a bonded structure varied as a function of the bond rigidity.

## 4. ACOUSTIC EMISSION TECHNIQUES

Acoustic emission<sup>(34)</sup> can also be used to monitor bond defects. The defective bond produces a large increase in AE during loading. These methods, however, are not being used in practical applications because they have not been sufficiently developed or have been applied for only a few cases. Averbukh and Gradinar<sup>(33)</sup> collected data on bonded composites and found that the amount of acoustic emission as a function of load varied depending upon the strength of the bond.

## 5. OPTICAL HOLOGRAPHIC TECHNIQUES

Mueller et al.<sup>(52)</sup> developed a holographic weak-signal-enhancement technique (WSET) which enhanced the image of the source of a weak signal of interest in the presence of an unwanted strong signal with very little *a priori* knowledge. The feasibility of the WSET was shown by simulating a two-solid-layer acoustic problem on a digital computer. The enhancement method was based upon the use of the signal field for reconstruction and high-pass filtering of some of the information.

## 6. RADIOGRAPHIC TECHNIQUES

Radiography can be used to detect damage to honeycomb, presence of debris and contaminants, and lack of bond due to absence of adhesive<sup>(2)</sup>. Neutrons are attenuated by nuclear processes, while x-rays interact with atomic electrons. Most organic adhesives contain between 8 and 12 percent hydrogen, so neutron radiography becomes a viable tool to inspect for adhesive problems. Dance and Petersen<sup>(53)</sup>, using a californium-252 source, did experiments in which they added gadolinium oxide to the epoxy.



## 7. THERMOGRAPHIC TECHNIQUES

Thermography can be separated into two techniques, passive and active<sup>(5)</sup>. The passive method utilizes an external heat source, while the active method utilizes internal temperature changes when an external force is applied that produces internal frictional heating. The thermographic method makes use of the difference in thermal conductivity of a good bond and a poor bond. In the poor bond, there could be a discontinuity at the adhesive/adherend interface which would produce a poorer thermal conductor.

In practice, passive thermography utilizes an external heat source and an infrared camera (or other imaging system sensitive to thermal radiation). Monitoring of thermal transients is the most effective method. Monitoring of absolute temperatures is difficult because of variations in thermal emissivities, nonuniform heating, and many other problems. The defects appear as cooler regions (if a through-transmission technique is used) because of the lower thermal conductivity through them. If the camera and the heat source are on the same side, then the defects will appear hotter because they do not transmit the heat as well. In addition, the sensitivity of the method decreases as the thermal conductivity and depth of the defect increase.

Work by McLaughlin et al.<sup>(54)</sup> and Reynolds and Wells<sup>(55)</sup> has shown that thermography can be used to detect delaminations and voids. Very little work has been done to determine its capability to actually determine the quality of the bond.

Active thermography makes use of an externally applied force and an infrared camera. For example, by vibrating the surface of a bonded structure, the defective regions will experience a local rise in temperature due to frictional heating. These defects can then be observed using the infrared camera. Work by Russell and Henneke<sup>(56)</sup> has shown that defects in composite structures can be detected if the vibrational frequency is that of the defect membrane resonance. Again, however, very little work has been conducted to determine the capability of active thermography to determine the quality of the bond.

## 8. NUCLEAR MAGNETIC RESONANCE TECHNIQUES

Nuclear magnetic resonance (NMR) is primarily used to detect the presence of hydrogen, especially in the form of moisture. This method has not been used to determine bond quality; however, it is believed that work should be conducted using NMR since one of the major causes of bond failure is the ingestion of moisture. This method requires the use of a large magnetic field and an RF exciter coil. This method cannot be used for metals, but should be of practical use for composite structures.

## 9. SUMMARY

This paper has presented a synopsis of information on the subject of NDE of adhesively bonded joints. Most of the NDE methods employed to date involve ultrasonic techniques such as:

- (1) Through-transmission or pulse-echo reflection of longitudinal waves from the adherend/adhesive/adherend layer (in both time and frequency domain)
- (2) Stoneley waves interacting with the adhesive layer
- (3) Rayleigh waves
- (4) Obliquely incident waves
- (5) Horizontally polarized shear waves

Work using all these techniques has indicated results that correlate with bond quality in a limited number of tests.

Additional work has been conducted using sonic waves, and the body of evidence shows that sonic waves can be used to detect defective bonds. The coin tap technique has been used throughout the industry as a quick and easy method to detect large, near-surface delaminations.

Other methods also were evaluated including acoustic emission, optical holography, radiography, and thermography. Application of these methods to certain bonding problems has shown good success in differentiating between a good and bad bond, but very little capability in quantifying the quality of the bond. Radiography is used to detect defects such as inclusions and voids in the adherend/adhesive layer that can cause poor bond quality. Nuclear magnetic resonance has some potential for determining bond quality in nonmetallic structures by detecting the presence of moisture in the bond. Little work, however, has been done with this technique.

## 10. CONCLUSIONS

Almost every NDE method has been utilized at one time or another in an attempt to develop a technique to adequately describe bond quality in a bonded structure. Most of the work to date has centered around application of ultrasonic techniques. The interaction of the through-transmitted (or reflected) longitudinal (L) wave with the adherend/adhesive/adherend interfaces can be used to easily detect the difference between the good bond and the total disbond. The L-wave, however, does not perturb the adhesive layer in a way that would provide a means to interrogate the strength of the adhesive layer or the adherend/adhesive interface. Other ultrasonic waves such as the Stoneley and interface waves directly interact with the adhesive layer so that the strength of the adhesive or adherend/adhesive interface can be measured. Unfortunately, the application requirements make it almost impossible to use these techniques for field inspections. Horizontally polarized shear waves launched from the top surface into the material will interact with the adherend/adhesive interface, but more work must be done to further evaluate this technique.

Based upon the amount of work conducted to date, the most promising approach for the largest variety of bonding inspections is application of one of the

ultrasonic techniques. The information in this report is based upon multiple case studies, some of which were correlated with destructive testing; the one point, however, that seems apparent is that no one technique was tested on a large variety of different bond types with known bond strength.

A program should be conducted using a large number of ultrasonic techniques on a carefully produced set of samples that would cover most bonding situations.

The test plan should be coordinated with experts in both NDE and adhesive bonding. After a thorough evaluation, the samples should be destructively tested to determine the actual bond strength.

# 11. REFERENCES

1. Norriss, T. H. "Nondestructive Testing of Bonded Joints: The Control of Adhesive Bonding in the Production of Primary Aircraft Structures." *Nondestructive Testing*. December 1974, pp. 335-339.
2. Teagle, R. R. "Recent Advances in Mechanical Impedance Analysis Instrumentation for the Evaluation of Adhesive Bonded and Composite Structures." *3rd European Conference on Nondestructive Testing*. Florence, Italy, October 15-18, 1984, pp. 139-162.
3. Zurbrick, John R. "Techniques for Nondestructively Characterizing Metallic Substrate Surfaces Prior to Adhesive Bonding." *International Advances in Nondestructive Testing*. 5 (1977), pp. 41-70.
4. Segal, E., G. Thomas, and J. L. Rose. "Hope for Solving the Adhesive Bond Nightmare." *Proceedings of the 12th Symposium on NDE*. San Antonio, Texas: Nondestructive Testing Information Analysis Center (NTIAC), April 1979, pp. 269-281.
5. Guyott, C. C. H., P. Cawley, and R. D. Adams. "The Non-Destructive Testing of Adhesively Bonded Structure: A Review." *Journal of Adhesion*. 20 (1986), pp. 129-159.
6. Adams, R. D., and P. Cawley, *Research Techniques in Non-Destructive Testing*. 8th ed., Chap. 7. R. S. Sharpe, ed. London: Academic Press, 1985, pp. 303-360.
7. Thompson, D. O., R. B. Thompson, and G. A. Alers. "Nondestructive Measurement of Adhesive Bond Strength in Honeycomb Panels." *Materials Evaluation*. April 1974, pp. 81-85.
8. Meyer, F. J., and G. B. Chapman. "Nondestructive Testing of Bonded FRP Assemblies in the Auto Industry." *Adhesives Age*. April 1980, pp. 21-25.
9. Segal, E., and J. L. Rose. "Nondestructive Testing Techniques for Adhesive Bond Joints." *Research Techniques in NDT*. 1V (1980), pp. 275-316.
10. Adler, L., and H. L. Whaley. "Interference Effect in a Multifrequency Ultrasonic Pulse Echo and Its Application to Flaw Characterization." *Journal of the Acoustical Society of America*. 51 (3 Part 2) (1972), pp. 881-887.
11. Tattersall, H. G. "The Ultrasonic Pulse-Echo Technique as Applied to Adhesive Testing." *Journal of Physics D: Applied Physics*. 6 (1973), pp. 819-832.
12. Rose, Joseph L., and Paul A. Meyer. "Ultrasonic Procedure for Predicting Adhesive Bond Strength." *Materials Evaluation*. June 1973, pp. 109-114.
13. Biggiero, G., G. Canella, and S. Cicchinelli. "Ultrasonic Testing for Bond Efficiency of Carbon to Stainless Steel Adhesive Joints." *3rd European Conference on Nondestructive Testing*. Florence, Italy, October 5-18, 1984, pp. 206-223.
14. Meyer, Paul A., and Joseph L. Rose. "Ultrasonic Determination of Bond Strength Due to Surface Preparation Variations in Aluminum to Aluminum Adhesive Bond System." *Journal of Adhesion*. 8 (1976), pp. 145-153.
15. Chernobelskaya, T., S. Kovnovich, and E. Harnik. "The Testing of Adhesive-Bonded Joints by a Very High Resolution Ultrasonic Probe." *Journal of Physics D: Applied Physics*. 12 (1979).
16. Alers, G., P. L. Flynn, and J. J. Buckley. "Ultrasonic Techniques for Measuring the Strength of Adhesive Bonds." *Materials Evaluation*. 35, No. 4, April 1977, pp. 77-84.
17. Raisch, J. W., and J. L. Rose. "Computer Controlled Ultrasonic Adhesive Bond Evaluation." *Materials Evaluation*. May 1979, pp. 55-64.
18. Williams, R. S., and P. E. Zwicke. "Assessment of Adhesive Properties Using Pattern Recognition Analysis of Ultrasonic NDE Data." *Materials Evaluation*. 40, March 1982, pp. 312-317.
19. Ivakhnenko, A. G. "Polynomial Theory of Complex Systems." *IEEE Transactions on Systems, Man and Cybernetics*. SMC-1, No. 4, October 1971.
20. Rose, J. L., M. J. Avioli, and R. Bilgram. "A Feasibility Study on the NDE of an Adhesively Bonded Metal to Metal Bond: An Ultrasonic Pulse Echo Approach." *British Journal of Nondestructive Testing*. March 1983, pp. 67-71.
21. Chang, F. H., J. C. Couchman, and B. G. W. Yee. "Transmission Frequency Spectra of Ultrasonic Waves Through Multi-Layer Media." *Proceedings of the 1973 Ultrasonic Symposium*. New York: The Institute of Electrical and Electronics Engineers, Inc. (IEEE), November 5-7, 1973, pp. 209-215.

22. Chang, F. H., J. C. Couchman, J. R. Bell, and D. E. Gordon. "Correlation of NDE Parameters with Adhesive Bond Strength in Multi-Layered Structures." *Proceedings of the 10th Symposium on NDE*. San Antonio, Texas: NTIAC, April 1975.
23. Chang, F. J., B. G. W. Yee, and J. C. Couchman. "Spectral Analysis Technique of Ultrasonic NDT of Advanced Composite Materials." *Nondestructive Testing*. August 1974, pp. 194-198.
24. Chang, Francis H., Paul L. Flynn, David E. Gordon, and Jerry R. Bell. "Principles and Application of Ultrasonic Spectroscopy in NDE of Adhesive Bonds." *IEEE Transactions on Sonics and Ultrasonics*. SU-23, No. 5, September 1976, pp. 334-338.
25. Brekhovskikh, L. M. *Waves in Layered Media*. New York: Academic Press, 1960, p. 53.
26. Flynn, P. L. "Cohesive Bond Strength Prediction." *Interdisciplinary Program for Quantitative Flaw Definitions, Semiannual Report*. Thousand Oaks, California: Rockwell International Science Center (Rockwell), September 4, 1976, to February 1, 1977.
27. Yee, B. G. W., F. H. Chang, and P. L. Flynn. "Signal Processing Methods for Measuring Cohesive Bond Strength." *Interdisciplinary Program for Quantitative Flaw Definitions, Semiannual Report*. Thousand Oaks, California: Rockwell, July 18, 1975, to January 1, 1976.
28. Rose, J. L., and G. H. Thomas. "The Fisher Linear Discriminant Function for Adhesive Bond Strength Prediction." *British Journal of Nondestructive Testing*. 21, No. 3, May 1979, pp. 135-139.
29. Alers, G. A., and R. K. Elsley. "Measurement of Metal to Adhesive Bond Quality Using Digital Signal Analysis." *1977 Ultrasonics Symposium Proceedings*, IEEE Catalogue No. 77CH1264-1SU. New York: IEEE, 1977.
30. Thomas, Graham H., and Joseph L. Rose. "An Ultrasonic Evaluation and Quality Control Tool for Adhesive Bonds." *Journal of Adhesion*. 10 (1980), pp. 293-316.
31. Lloyd, E. A. "Nondestructive Testing of Bonded Joints, A Case for Testing Laminated Structures by Wide-Band Ultrasound." *Nondestructive Testing*. December 1974, pp. 331-334.
32. Joshi, N. R. *Technical Report to the U.S. Army Materials Technology Laboratory*. Contract No. DAAL03-86-D-0001. Watertown, Massachusetts: U.S. Army Materials Technology Laboratory, September 1988.
33. Averbukh, I. I., and V. V. Gradinar. "Inspecting the Strength Characteristics of Composite Materials." *Soviet Journal of Nondestructive Testing*. 9, No. 3, May-June 1973, pp. 261-264. (English Translation, March 1974.)
34. Budenkov, G. A., Yu. V. Volegov, V. A. Pepelyaev, and V. I. Red'ko. "Inspecting the Strength of Glued Joints with Ultrasonic Interference Waves." *Soviet Journal of Nondestructive Testing*. 13, March-April 1977, pp. 138-145. (English Translation, January 1978.)
35. Staecker, P. W., and W. C. Wang. "Propagation of Elastic Waves Bound to a Fluid Layer Between Two Solids." *Journal of the Acoustical Society of America*. 53, No. 1 (1973), pp. 65-74.
36. Rokhlin, S. "Diffraction of Lamb Waves by a Finite Crack in an Elastic Layer." *Journal of the Acoustical Society of America*. 67, No. 4, April 1980, pp. 1157-1165.
37. Jones, J. P., and J. S. Whittier. "Waves at a Flexibly Bonded Interface." *Journal of Applied Mechanics*. December 1967, pp. 905-909.
38. Claus, Richard O., and R. A. Kline. "Adhesive Bondline Interrogation Using Stoneley Wave Methods." *Journal of Applied Physics*. 50, No. 12, December 1979, pp. 8066-8069.
39. Pilarski, A. "Ultrasonic Evaluation of the Adhesion Degree in Layered Joints." *Materials Evaluation*. 43, May 1985, pp. 765-770.
40. Rokhlin, S. I. "Adhesive Joint Evaluation by Ultrasonic Interface and Lamb Waves." *Proceedings of Analytical Ultrasonics in Material Research and Testing*. Cleveland, Ohio: NASA-Lewis, November 13-14, 1984, pp. 299-310.
41. Rokhlin, S. I., M. Hefets, and M. Rosen. "An Ultrasonic Interface-Wave Method for Predicting the Strength of Adhesive Bonds." *Journal of Applied Physics*. 52, No. 4, April 1981.
42. Rokhlin, S. I., M. Hefets, and M. Rosen. "An Elastic Interface Wave Guided by a Thin Film Between Two Solids." *Journal of Applied Physics*. 51, No. 7, July 1980.
43. Vary, A., and K. J. Bowles. "Ultrasonic Evaluation of the Strength of Unidirectional Graphite-Polyimide Composites." NASA Technical Memorandum TM-73646. Cleveland, Ohio: NASA-Lewis, April 1977.
44. Vary, A., and K. J. Bowles. "Use of an Ultrasonic-Acoustic Technique for Nondestructive Evaluation of Fiber Composite Strength." NASA Technical Memorandum TM-73813. Cleveland, Ohio: NASA-Lewis, February 1978, pp. 185-91. Also published in *ASTM Journal of Testing and Evaluation*. 7, No. 4 (1979).
45. Vary, A., and R. F. Lark. "Correlation of Fiber Composite Tensile Strength with the Ultrasonic Stress Wave Factor." NASA Technical Memorandum TM-78846. Cleveland, Ohio: NASA-Lewis, April 1978.

46. Williams, J. H., and N. R. Lampert. "Ultrasonic Evaluation of Impact Damaged Graphite Fiber Composite." *Materials Evaluation*. December 1980, pp. 68-72.
47. Dos Reis, H. L. M., L. A. Bergman, and J. H. Bucksbee. "Adhesive Bond Strength Quality Assurance Using the Acousto-Ultrasonic Technique." *British Journal of Nondestructive Testing*. November 1986, pp. 357-358.
48. Yew, Ching H. "Using Ultrasonic SH Waves to Estimate the Quality of Adhesive Bonds: A Preliminary Study." *Journal of the Acoustical Society of America*. 76, No. 2, August 1984, pp. 525-531.
49. Rokhlin, S. I., and D. Marom. "Study of Adhesive Bonds Using Low Frequency Obliquely Incident Ultrasonic Waves." *Journal of the Acoustical Society of America*. 80, No. 2, August 1986, pp. 585-590.
50. Kuhn, G. J., and A. Lutsch. "Elastic Wave Mode Conversion at a Solid-Solid Boundary with Transverse Slip." *Journal of the Acoustical Society of America*. 33 (1961), pp. 949-954.
51. Pilarski, A., and J. L. Rose. "A Transverse-Wave Ultrasonic Oblique-Incidence Technique for Interfacial Weakness Detection in Adhesive Bonds." *Journal of Applied Physics*. 63, No. 2, January 15, 1988.
52. Mueller, R. K., R. R. Gupta, and P. N. Keating. "Holographic Weak-Signal Enhancement Technique." *Journal of Applied Physics*. 43, No. 2, February 1972, pp. 457-462.
53. Dance, W. E., and D. H. Petersen. "Verification of the Structural Integrity of Laminated Skin-to-Spar Adhesive Bondlines by Neutron Radiography." *Journal of Applied Polymer Science: Applied Polymer Symposium*. 32 (1977), pp. 399-410.
54. McLaughlin, P. V., E. V. McAssey, and R. C. Deitrich. "Nondestructive Examination of Fibre Composite Structures by Thermal Field Techniques." *NDT International*. 13 (1980), pp. 56-62d.
55. Reynolds, W. N., and G. M. Wells. "Video-Compatible Thermography." *British Journal of Non-destructive Testing*. 26 (1984), pp. 40-43.
56. Russell, S. S., and E. G. Henneke. "Dynamic Effects During Vibrothermographic NDE of Composites." *NDT International*. 17 (1984), pp. 19-25.
57. Cotter, J. L., and M. G. D. Hockney. "Metal Joining with Adhesives." *International Metallurgical Reviews*. Review 183 (1974), pp. 103-115.
58. Joiner, Neil. "Adhesive Bond Testing." *Nondestructive Testing-Australia*. April 1983, pp. 17-23.
59. Francke, W., and A. W. J. de Gee. "A Nondestructive Method for the Measurement of the Adhesive Bond Strength of Thermally Sprayed Nonfused Coating." *Advances in Surface Coating Technology, Vol. I-Papers*. Abington, Cambridge CB16AL: The Welding Institute, Abington Hall, 1978, pp. 99-109.
60. McBrearty, M., M. Negin, A. Zielensk, and M. Weilerstein. "Realtime Nondestructive Evaluation in Ultrasonic Wire Bonding." *1983 Ultrasonic Symposium*. New York: IEEE, 1983, pp. 861-865.

## CHIRP Z-TRANSFORM IN ULTRASONIC INTERFERENCE SPECTROSCOPY FOR ADHESIVE BONDS

Narayan R. Joshi, Ph.D.  
Associate Professor  
Department of Mechanical Engineering  
Lamar University  
Beaumont, Texas

### ABSTRACT

Nondestructive testing (NDT) of adhesive bonds and bond strength determination using NDT parameters has become the subject of intensified research activity in recent years. A total of 48 bonds on 12 symmetrical double lap-shear specimens with different target features in bondlines were examined by ultrasonic interference spectroscopy strengthened by the modern technique of zoom spectroscopy utilizing chirp z-transform. Different target features such as unprepared surfaces, trapped humidity, and defects of known sizes and shapes produced different ultrasonic interference frequency dips. The quantities of average maximum load per failed bond and average maximum elongation per failed bond were consistent with target features incorporated in bondlines. The ultrasonic interference frequency dip intervals could, therefore, be related to the average maximum load per failed bond.

### 1. INTRODUCTION

Ultrasonic spectroscopy is being used in a growing number of applications in the field of nondestructive characterization of materials properties since its introduction by Gericke. Chang et al.<sup>(1)</sup> used the principle of ultrasonic interference spectroscopy to develop a spectral analysis of ultrasonic nondestructive testing (NDT) of advanced composite materials. The principle and technique were extended by Chang et al.<sup>(2)</sup> to the problem of correlating NDT parameters with adhesive bond strength. When the RF waveforms reflected from the top and bottom adhesive interfaces were included in the digitizing window, the interference effect in the frequency spectrum produced dips of the bondline thickness. They related the Q of the resonances in the frequency spectra to the ultimate shear strength (USS) of bonds, higher Q implying higher USS.

Chang et al.<sup>(3)</sup> reported analytical calculations of the soundwave interferences in the bondline which included the attenuation in the adhesive. They found that increasing the attenuation in the adhesive layer had the effect of broadening the resonance, and decreasing resonance quality was a strongly decreasing function of the acoustic impedance of the adhesive. The shear strength of the adhesive bond was directly dependent on the acoustic impedance of the adhesive. This dependence originated from the relationship between the acoustic impedance and the elastic modulus of the adhesive.

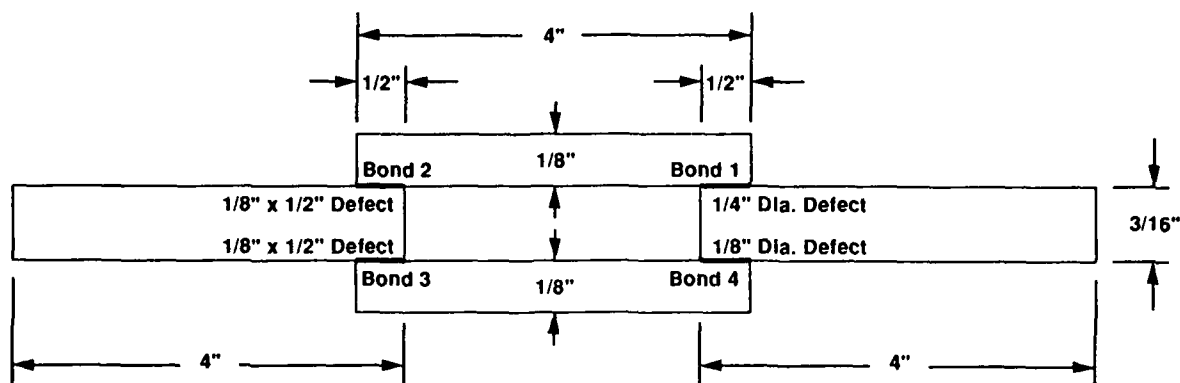
Alers et al.<sup>(4)</sup> used the ultrasonic spectroscopy technique on lap joints of aluminum plates glued together with Chemlok 304. The value for the velocity of sound in the adhesive was calculated from a knowledge of the bondline thickness D and the separation

between minima  $\Delta f$  in the frequency spectrum using the expression, adhesive sound velocity  $V = 2D \cdot \Delta f$ . They found that a linear relationship existed between shear strength of bond and ultrasonic velocity in adhesive.

Nondestructive testing on adhesive bond is followed by destructive testing if the aim is to relate a non-destructive parameter to the adhesive bond strength. In many instances of destructive testing, a simple lap-shear tensile specimen is used. In a simple lap-shear tensile specimen, the stress is not true shear due to deformation immediately upon loading. The new configuration places the joint under a combination of shear and peeling forces, as well as a flexural moment enhancing tearing of the adherent. One way to measure a more accurate bond shear strength is to increase the shear component at the adhesive-adherend interface by loading along the neutral axis, thereby reducing distortion-induced tearing. The second way is to use a symmetrical double lap-shear specimen (Figure 1). All specimens used in this work were, therefore, fabricated in the form of symmetrical double lap-shear.

### 2. THEORY

Spectral analysis measurements<sup>(5)</sup> are based on the measurements of  $\Delta f = 1/T$ , the interval between two antiresonances on the frequency spectrum. However, as the first cutoff of the spectrum occurs at zero frequency, the smallest measurable thickness is related to the greatest  $\Delta f$ --the difference between zero frequency and the highest frequency at which a cancelling out of the spectrum can be observed. In other words, the smallest measurable thickness corresponds to the shortest significant half-wavelength in the emitted signal. An appreciable gain in comparison with classical measurement is therefore obtained.



Width of Each Coupon = 1 Inch

Figure 1. A symmetrical double lap-shear specimen

With classical measurement, the shortest measurable propagation time corresponds to a few periods associated with the center frequency of the transducer. According to Paradis et al.<sup>(5)</sup>, it is thus possible to measure the thickness of steel foil or adhesive layer thinner than 4 mils provided the transducer has a component at about 30 MHz, even at -15 dB from the maximum. The adhesive bondline behaves as a selective periodic filter with cutoff frequencies

$$f_n = \frac{n}{t}$$

where  $n$  takes only integral values 1, 2, 3, etc., and time

$$t = \frac{2d}{v}$$

where  $d$  = adhesive bondline thickness and  $v$  = ultrasonic longitudinal wave velocity in the cured in situ adhesive bondline.

Different bondline target features such as unprepared surfaces, trapped humidity and defects are expected to produce different values of  $d$  which in turn will produce different cutoff frequencies or different  $\Delta f$ . Different bondline features will affect bond strength differently. It is theoretically possible to relate an ultrasonic nondestructive testing parameter such as  $\Delta f$  to the parameter related to bond strength.

### 3. SPECIMEN PREPARATION

Four groups of symmetrical double lap-shear specimens were prepared from strips of grade 6061 T6 aluminum. Each specimen consisted of four strips of aluminum 1 inch wide and 4 inches long. The outer two adherent strips were 1/8 inch thick and the central two adhered strips were 3/16 inch thick. The four strips were bonded together with four 0.5 inch overlaps (Figure 1). The adhesive used in the bond assembly was EA 9628 manufactured by Dextor Hyson of Pittsburgh, California.

Group 1 consisted of 20 control group specimens. The coupons of this group were grit blasted, ideally cleaned and dried. They were primed with close attention to complete wetting. Adhesive was applied with similar care to assure 100 percent wetting of all interfaces, exclusion of voids, and a bondline approximately 3 mils thick. The specimens were cured at the prescribed temperature of 250°F for 1 hour. Pressure was applied with G clamps to the coupons before heating and was maintained until cooldown of the assembly. Heatup rate to the cure temperature was approximately 5°F per minute. The specimens were cured in a controlled, low-humidity environment.

Group 2 consisted of specimens that were assembled using towel-wiped, uncleaned, unsanded, or unabraded aluminum coupons. The primer and adhesive were applied as carefully as in the control specimen fabrication process. The specimens were cured at the prescribed temperature and pressure in a low-humidity environment.

Group 3 consisted of specimens assembled in a 90-percent relative humidity environment using cleaned and abraded aluminum coupons. The primer and adhesive were applied as carefully as in the control specimen fabrication process. The specimens were cured at the prescribed temperature and pressure in a low humidity environment.

Group 4 consisted of specimens containing unbonded areas fabricated using cleaned, abraded, and dried coupons. In the four bonds of each specimen, four different types of unbonded areas, one in each bond, were created. Bond 1 contained a circular void 1/4 inch in diameter. Bond 4 contained a circular void 1/8 inch in diameter. Bonds 2 and 3 each contained a rectangular void 1/8 x 1/2 inch. The 1/2-inch dimension of the rectangular void was set parallel to the 1-inch dimension of the coupon (Figure 1). Each defect was located exactly at the center of each overlap area. Bond G111 identified Bond 1 of Specimen 1 belonging to Group G1; Bond

223 identified Bond 3 of Specimen 2 of Group G2, and so on.

#### 4. EXPERIMENTAL APPARATUS AND PROCEDURES

The experimental apparatus is shown schematically in Figure 2. The broadband short pulse-echo immersion technique was used with a 30 MHz, 1/4-inch diameter focused Panametrics transducer. The transducer carried a delay line of 4.25  $\mu$ s and had a focal length of 1.86 inches in water. The specimen assembly was held under temperature equalized water in the MIS-100 immersion tank manufactured by Test Tech, Inc. The tank was provided with the transducer carriage having translations along the X, Y, and Z axes and rotations about the Y and Z axes. The transducer can be positioned on a specimen in the tank with accuracy of 1 mil.

Since the film thickness and stress distribution may vary at the edges of the overlap area, the ultrasonic beam was always focused exactly at the center of an overlap area. By using all movements, the beam was focused first on the top plate maximizing the pulse-echo signal on the oscilloscope. The Z axis vertical adjustment then was lowered in order to focus

the beam on the bondline. With this setting, it was decided to examine two signals, the front wall echo coming from the top surface of the top aluminum plate (1/8 inch thick) and the bond echo returning from the top surface of the second aluminum plate (3/16 inch thick). Four bonds on a single specimen were examined in the order of 1, 2, 3, and 4. The ultrasonic data was collected in both time domain and frequency domain. The highly damped transducer was excited by a Panametrics ultrasonic pulser/receiver Model 5601. The pulse repetition rate chosen was 5 MHz and the damping setting was chosen so as to produce a highly damped negative-going pulse with the fastest recovery time available.

The time domain pulse echoes were gated for the purpose of obtaining their ultrasonic spectra. The gate width chosen was equal to 500 ns covering fully the pulse widths of approximately 200 to 300 ns. A Panametrics stepless gate Model 5605A was used for gating the signals. In order to display, gate, and photograph the time domain signals, a Tektronix 7704A cathode ray oscilloscope with various plug-in modules was used. The vertical sensitivity chosen was 200 mv/div and the horizontal time scale was 100 ns/div for all ultrasonic time domain data.

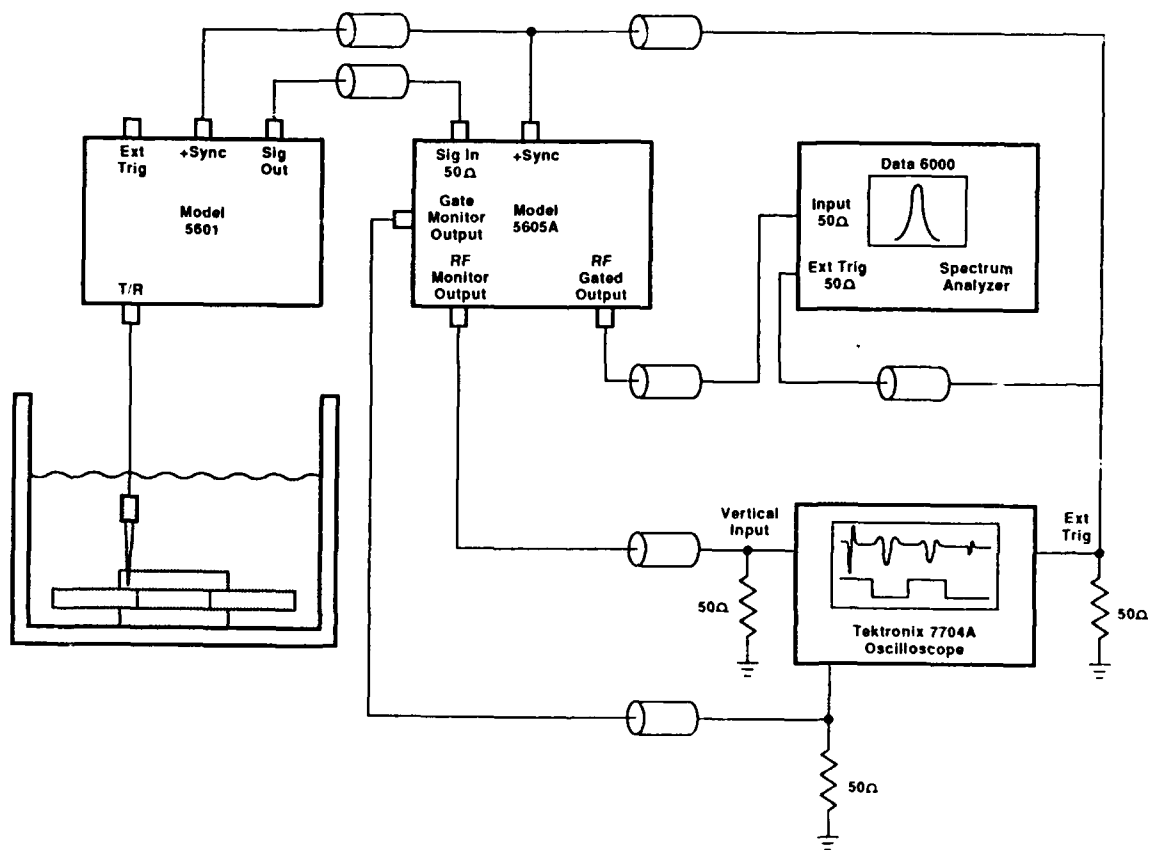


Figure 2. Schematic of experimental apparatus

Ultrasonic magnitude spectra were obtained with the digital signal processing equipment/digital oscilloscope Data 6000A equipped with Model 620A plug-in module. The unit was provided with two floppy disk drives in order to transfer data from the memory of the Data 6000 to the external memory of the floppy disk.

The sampling frequency used in all digital operations was 100 MHz with a horizontal resolution of 512 points and a vertical resolution of 8 bits or 256 points giving the FFT resolution of 195.3125 KHz. For each bond, the various ultrasonic observations were identified by the following scheme. The pulse-echo waveform from the top surface of the aluminum plate (1/8 inch thick) was named T1. Its ultrasonic spectrum, called the reference spectrum, was named S1. The pulse-echo waveform from the bond was named T2. Since the adhesive bondline was thin, separate pulse-echo waveforms from the top of the bond (from the bottom of the 1/8-inch thick plate) and from the bottom of the bond (from the top of the 3/16-inch thick plate) were not separated in the time domain. The ultrasonic spectrum of the bond echo was named S2.

When frequency dips due to ultrasonic interference effects appeared in the ultrasonic spectrum, the frequencies of these dips were measured by X-Y axis crosswire lines aligning them at the deepest point of the dip. These dip frequencies were next used as the center frequencies in the process of expanding the frequency resolution (zoom effect) by the process of chirp Z-transform (CZT). Each zoom spectrum of the regular FFT spectrum S was named Z1, Z2, etc.

In order to obtain CZT on the dip frequency, the dip frequency measured by the X-Y crossline method from the spectrum S2 was chosen as the center frequency. The choice of zero width automatically set the width at 1.56252 MHz full screen by default when the sampling frequency was set at 100 MHz. Thus, the zoom CZT resolution for 512 points along the horizontal frequency axis was equal to 1.56252 MHz/512 points = 3.05180 KHz per point. In order to reduce noise and improve the signal-to-noise ratio, the time domain signals T1 and T2 were averaged 128 times for observations on all bonds.

After ultrasonic testing, the 12 specimens were pulled using an Instron testing machine in order to determine their tensile lap-shear strengths. The tests were performed in an environmental chamber with relative humidity controlled at 50 percent and temperature at 72°F. For all tests, the crosshead speed was set at a constant value of 0.01 inch per minute.

## 5. EXPERIMENTAL RESULTS

Figures 3A, 3B, and 3C show time domain and frequency domain data on Bond G123. The specimen belonged to Group 1, control specimens. The average of 12 ultrasonic dip frequencies on 12 bonds of this group was 19.9125 MHz. The first cutoff frequency was at 0 MHz. G123Z1 is the CZT spectrum of G123S2 obtained in order to determine the exact frequency of the dip. Since other CZT spectra of frequency dips of bonds from specimens of other groups have similar appearances, they were not

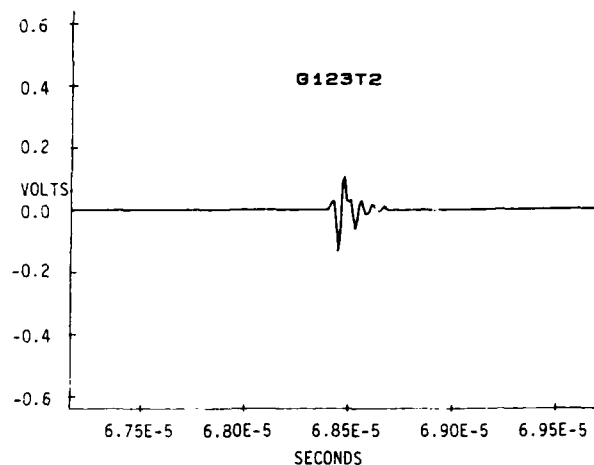


Figure 3A. Control specimen bond echo

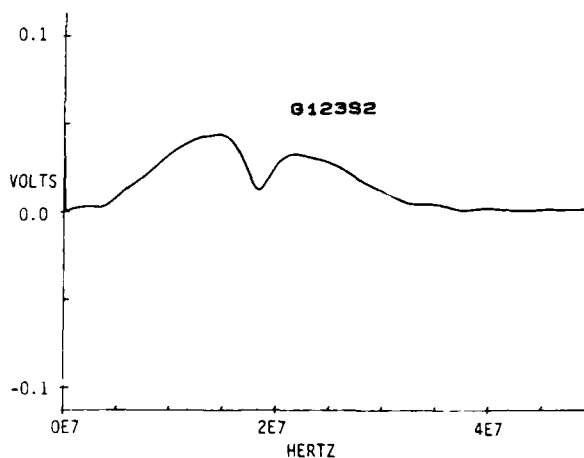


Figure 3B. Control specimen bond spectrum

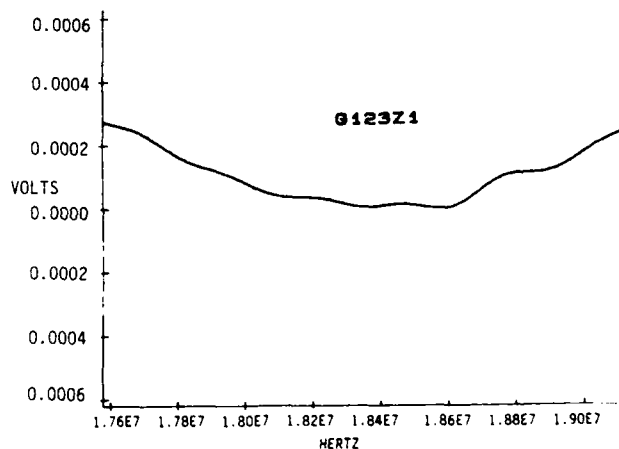


Figure 3C. Control specimen zoom spectrum



included in the figures for other groups in the following discussion.

Figures 4A and 4B show time domain and frequency domain data on Bond G213. This specimen belonged to Group 2, specimens assembled without preparing the adherend surfaces. It showed two ultrasonic dip frequencies instead of the one shown typically by specimens of Group 1. The average of 12 ultrasonic dip frequencies of the first dip was 11.5028 MHz. The average of 12 ultrasonic dip frequencies of the second dip was 23.9358 MHz.

Figures 5A, 5B, and 5C show time domain and frequency domain data on Bond G324. This specimen belonged to Group 3, specimens assembled in a humid environment. It showed two ultrasonic dip frequencies similar to a specimen belonging to Group 2. However, other specimens showed three dip frequencies (Figure 5C) instead of two. The average of 12 ultrasonic dip frequencies of the first dip was 11.9500 MHz. The average of 11 ultrasonic dip frequencies of the second dip was 24.4876 MHz. The average of three ultrasonic dip frequencies of the third dip was 17.0801 MHz.

Figures 6A and 6B show time domain and frequency domain data on Bond G414. The specimen belonged to Group 4, specimens carrying one defect in each bond. The ultrasonic beam was focused on the edge of the defect. As many as seven cutoff frequencies appeared in the spectrum. The frequency dips were located at approximately 3 MHz, 7 MHz, 11 MHz, 15 MHz, 19 MHz, 23 MHz, 27 MHz, etc. The average frequency interval between two successive dips was 4.1279 MHz.

In order to compare the results of the NDT tests to the results of the destructive tests, Tables 1 and 2 were constructed. Table 1 gives the nature, adhesive or cohesive, of bond failures. Since more than one bond failed simultaneously in the tensile lap-shear tests, new concepts of average maximum elongation per failed bond and average maximum load per failed bond were developed. The average load per failed bond is the highest for the control specimens, Group G1, and is the lowest for the no surface preparation specimens, Group G2, as expected.

The average load per failed bond for the specimens of Group G3 assembled in a humid environment was lower than that for the specimens of Group G1 but was higher than that for the specimens containing known defects of Group G4, as expected.

A similar picture evolves for values of average elongation per failed bond. If the tensile lap-shear strength of a bond is assumed to be proportional to the average elongation per failed bond, then the control Group G1 showed the highest bond strength; the trapped humidity Group G3 showed the next lower value of bond strength; the defect Group G4 showed the next lower value of bond strength; and, finally, the no surface preparation Group G2 showed the lowest bond strength.

The ultrasonic interference dips in bond spectra clearly identified bonds with different target features characteristic of each group. Each group showed

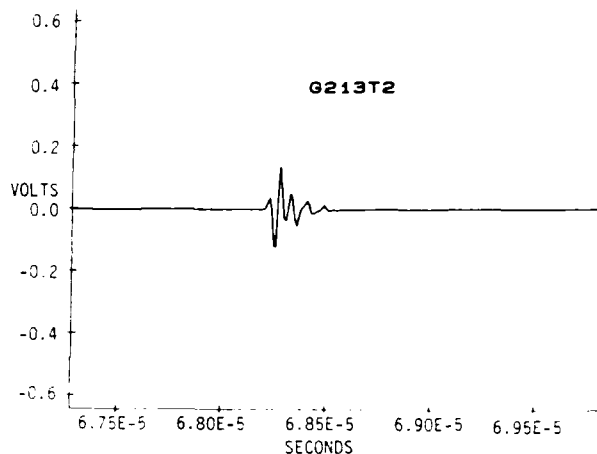


Figure 4A. Unprepared surfaces bond echo

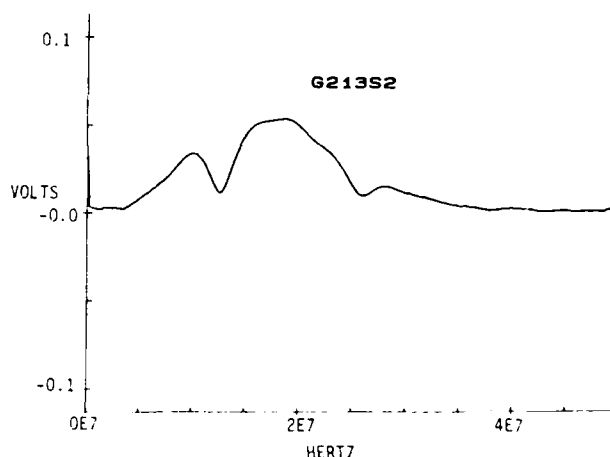


Figure 4B. Unprepared surfaces bond spectrum

distinct average maximum load per failed bond and average maximum elongation per failed bond. It can be said, therefore, that the NDT technique using ultrasonic interference spectroscopy worked successfully in identifying specimens with different target bondline features and, hence, with different mechanical properties.

## 6. CONCLUSIONS

Ultrasonic interference frequency dip data and tensile lap-shear ultimate strength data on 48 bonds of 12 specimens with different target features were examined. Based on these data values, it was concluded that NDT parameters--frequency dip intervals or successive cutoff frequencies--can be used to identify the various target features of bondlines. These target features included bondlines attached to surfaces of coupons prepared according to ASTM standards, without surface preparations and carrying different amounts of humidity. In some specimens, the target features were created by embedding defects of known sizes and shapes.

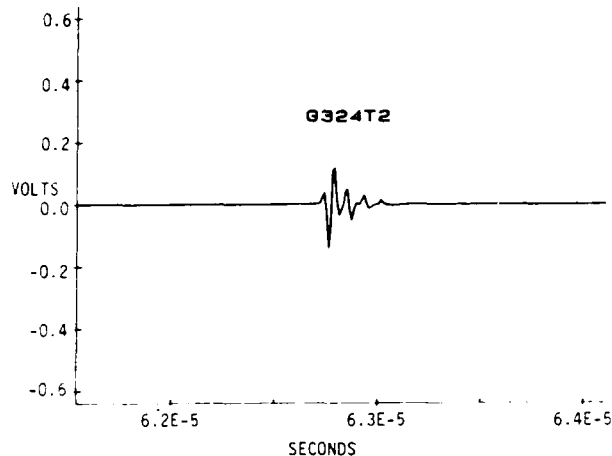


Figure 5A. Trapped humidity bond echo

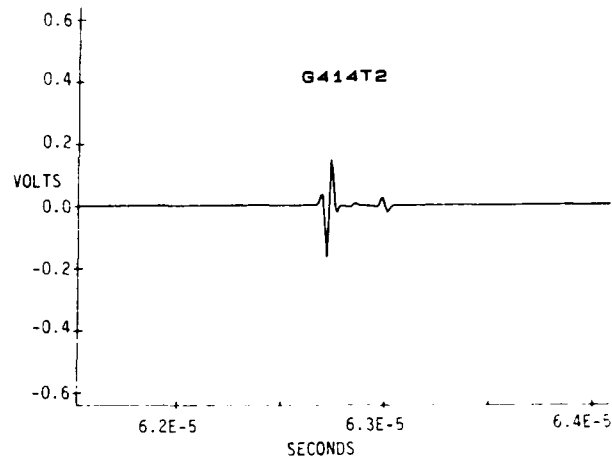


Figure 6A. Defect bond echo

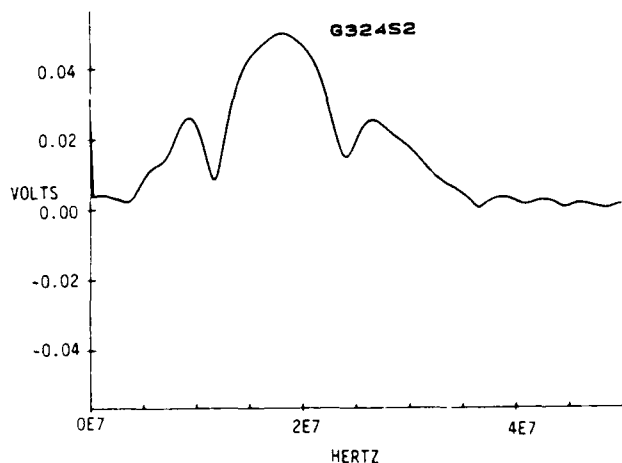


Figure 5B. Trapped humidity bond spectrum

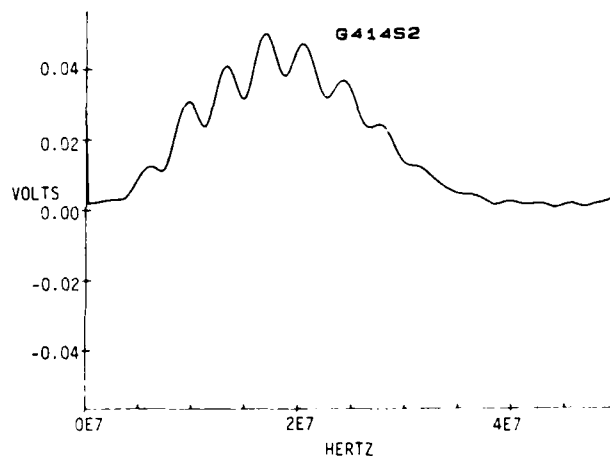


Figure 6B. Defect bond spectrum

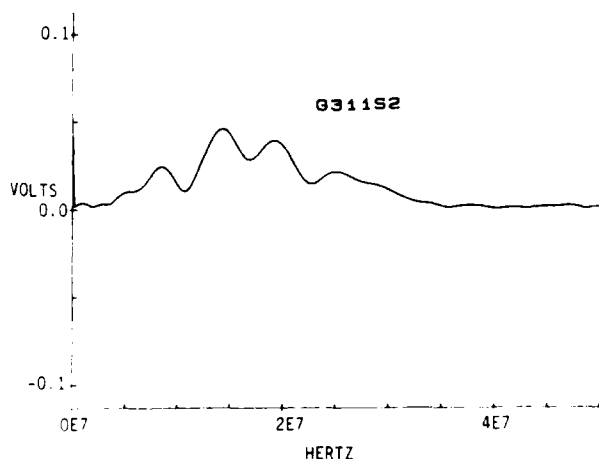


Figure 5C. Trapped humidity bond spectrum

All target features were successfully identified by the method used except in the case of bonds with trapped humidity. These bonds showed a scatter in data greater than that shown by the specimens of the remaining three groups.

Each symmetrical double lap-shear specimen consisted of four bonds. The observed simultaneous failure of more than one bond in the tensile lap-shear test led to development of the concepts of average maximum elongation per failed bond and average maximum load per failed bond. Both quantities were found to be directly related to the target features.

The bonds without surface preparation showed the lowest values for these two quantities. The bonds of control specimens showed the highest values, as expected.

Table 1  
TYPE OF BOND FAILURES

SPECIMEN NO.	BOND THAT FAILED - NO.	TYPE OF FAILURE	TOTAL NO OF BONDS FAILED AMONG 3 SPEC
G1-1	3	COHESIVE	4
G1-2	4	MIXED	CONTROL SPECIMENS
G1-3	1	COHESIVE	
	4	COHESIVE	
G2-1	1	ADHESIVE	5
	3	ADHESIVE	NO. SURFACE PREPARATIONS
G2-2	4	ADHESIVE	
G2-3	2	ADHESIVE	
	3	ADHESIVE	
G3-1	1	COHESIVE	6
	4	COHESIVE	SPECIMENS WITH TRAPPED HUMIDITY
G3-2	1	COHESIVE	
	4	ADHESIVE	
G3-3	2	COHESIVE	
	3	COHESIVE	
G4-1	2	ADHESIVE	5
G4-2	2	ADHESIVE	SPECIMENS WITH DEFECTS
	4	ADHESIVE	
G4-3	2	ADHESIVE	
	3	ADHESIVE	

Table 2  
AVERAGES OF TENSILE LAP-SHEAR STRENGTH TESTS DATA

I	II	III	IV	V	VI	VII
GROUP NO.	AVERAGE NO. OF BONDS FAILED	AVERAGE LOAD LBS	AVERAGE ELONGATION MICROIN.	AVERAGE LOAD PER FAILED BONDS LBS	AVERAGE ELONGATION PER FAILED BONDS MICROIN.	TARGET FEATURES OR CONDITIONS OF BONDS
G1	1.33	4017	60000	3020	45113	CONTROL SPECIMENS OF PERFECT BONDS
G2	1.66	2108	27667	1270	16667	BONDS WITHOUT SURFACE PREPARATION
G3	2	5083	85333	2542	42667	BONDS ASSEMBLED UNDER 80-90 RH ENVIRONMENT
G4	1.66	3567	60333	2149	36345	BONDS WITH DEFECTS

## 7. ACKNOWLEDGEMENTS

The author would like to thank Dr. Alfred Broz, Mr. Otto Gericke, Mr. Walter Roy, Mr. Paul Kenny, Mr. Jeffrey Gruber, Mr. John Nunes, Mr. Jonathan Fazli, and Dr. Stanley Wentworth, all of the U.S. Army Materials Technology Laboratory, Watertown, Massachusetts, and Mr. David Goonan, student assistant, in completing this work. The author would also like to thank Mr. Garry Hill of Battelle RTP for providing the project with needed financial support through the U.S. Army Summer Faculty Research and Engineering Program.

## 8. REFERENCES

1. Chang, F. H., W. G. W. Yee, and J. C. Couchman. "Spectral Analysis Technique of Ultrasonic NDT of Advanced Composite Materials." *Nondestructive Testing*, August 1974, pp. 194-198.
2. Chang, F. H., J. C. Couchman, J. R. Bell, and D. E. Gordon. "Correlation of NDE Parameters With Adhesive Bond Strength in Multi-layered Structures." *Proc. 10th Symposium on NDE*, San Antonio, April 23-25, 1975.
3. Chang, F. H., P. L. Flynn, D. E. Gordon, and J. R. Bell. "Principles and Application of Ultrasonic Spectroscopy in NDE of Adhesive Bonds." *IEEE Transactions on Sonics and Ultrasonics*, Vol. SU-23, No. 5, September 1976, pp. 334-338.
4. Alers, G. A., P. L. Flynn, and M. J. Buckley. "Ultrasonic Techniques for Measuring the Strength of Adhesive Bonds." *Materials Evaluation*, April 1977, pp. 77-84.
5. Paradis, L., Y. Serruys, and R. Saglio. "Ultrasonic Signal Processing for Thickness Measurements and Detection of Near-surface Defects." *Materials Evaluation* 44, October 1986, pp. 1344-1349.

FEATURE MAPPING METHODOLOGY  
FOR ULTRASONIC INSPECTION OF ADHESIVE BONDS

J.L. Rose, T.D.K. Ngoc, D. Jiao and K. Balasubramaniam  
Department of Mechanical Engineering and Mechanics  
Drexel University  
Philadelphia, PA 19104

Abstract

The feature mapping methodology is an integrated approach to ultrasonic NDE that optimally combines the physical insights offered by wave mechanics and the advanced signal processing techniques in order to make the best possible decision for defect characterization. This methodology has been applied to inspection of adhesive bonds for two reasons: the material structure is a highly absorptive and multi-layered system and the typical defects are very weak reflectors. The conventional ultrasonic technique of using peak amplitude and travel time at L-wave normal incidence is no longer sufficient for inspecting such defects. Other features and techniques that are more sensitive to subtle changes in boundary conditions and material microstructure must be included to improve the inspection capabilities. The considered features are contained not only in the RF waveform, but also in the frequency spectrum. In addition, ultrasonic modes other than the conventional bulk wave modes and advanced signal processing techniques can be employed to enhance the desired feature. In this paper, the feature mapping technique is applied to the inspection of adhesively bonded Aluminum-Aluminum samples with built-in disbonds and weak bonds which are introduced by chemical contaminants.

1. FEATURE MAPPING METHODOLOGY

The traditional ultrasonic inspection techniques typically produces scanning images by using the peak amplitude of the time-gated pulse. This approach has proven to be adequate for inspecting simple defects in iso-

tropic, homogeneous materials. With the increasing demand of material performance, the needs for inspecting subtler defects in advanced materials, whose microstructure turns out to be quite complex, call for new, innovative approaches to practical NDE.

In dealing with tougher defects and more complicated materials, one should explore the use of all available features of the received signal. The ultrasonic technique and the optimal feature should therefore be chosen such that they in combination would provide the most sensitive mechanism to characterize the targeted type of defects. This approach opens up a broad, diversified range of NDE procedures that are defined by judiciously selecting an optimal combination of feature and technique for a given type of defect. Let us review the fundamental ultrasonic techniques and features.

It is probably best to group the numerous ultrasonic techniques by their wave mode and basic transducer configuration. In terms of the wave mode type, the ultrasonic techniques can be identified with either bulk or guided waves. In isotropic media, bulk waves are one of three modes: P, SV and SH. In anisotropic media, it is only meaningful to describe the three bulk wave modes as either quasilongitudinal or quasitransverse. There exist many guided wave modes associated with each geometrical structure of the media. Of the more established modes, one must mention the surface, plate, cylindrical and spherical guided waves. Together with the wave mode, an ultrasonic NDE technique is also defined by the specific transducer configuration. Most basic is the number of transducers deployed, single, dual, or array. Of course, the single transducer arrangement is preferred because of the ease of implementation. The transducer configuration is also further specified by the manner in which the ultrasonic waves are generated and received. Thus one often talks about such arrangements as pulse echo, through transmission, reflection, corner reflection, etc.

Once the technique is chosen, the information on the material characteristics, including the possible defects, is extracted from the received signals. The signals themselves represent a complicated signature of the material under investigation, which contains many usable features. The time-honored, most frequently used features are the arrival time and peak amplitude. From these two pieces of information, one can construct an image of the test piece, which indicates the possible existence of a defect, describing where and how strong it is as an ultrasonic scatter or reflector.

The above practice is adequate for many NDE applications. However, for more difficult problems, one has to resort to other features also contained in the received signals, which may turn out to be more sensitive to the presence of defects, and thus are more useful for defect characterization. For example, we have reported [1-2] on the use of the amplitude of a selected frequency band for inspecting adhesive bonds. Recently, our research results also suggested [3-4] an innovative use of the resonant frequencies associated with a plate structure to determine the porosity content of the resin-based composites.

In general, the features available from the received signals after processing can be grouped into three categories: temporal, spectral and spatial. In the time domain, one can select such features as arrival time, sound velocities, rise time, fall time and other pulse shape characteristics. In the frequency domain, useful features include peak frequency amplitude, center frequency amplitude, selected band amplitude, resonant frequencies and other spectral features. With regard to the spatial fea-

tures, among the more established features are the critical angles and nonspecular beam reflection effects. Finally, we also wish to point out that some features vary with the chosen techniques while others are independent of techniques. Therefore, it is advisable to use the most appropriate technique to highlight the desirable feature.

Indeed, in the past we recognized the practical potential of the feature mapping methodology and emphasized its flexibility in adapting to different NDE applications [5-8]. In the preceding discussion, we have provided a more coherent formulation of this methodology. In the following, we demonstrate its use in the problem of inspecting weak adhesive bonds.

## 2. WEAK ADHESIVE BONDS

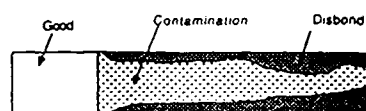
### 2.1 SAMPLES

In general, there are two types of defects that might exist in the bonding layer sandwiched between two solid substrates, cohesive and adhesive defects. The cohesive defects include porosity, inclusions, cracks, poor cure and voids. Adhesive defects refer to lack of adhesion at one of the solid-adhesive interfaces. The results presented here deal with weak adhesive defects introduced into Al-adhesive-Al samples.

We attempted to simulate adhesive defects with various degrees of bond strength in two sets of samples. In one set, we used Teflon spray to create three distinct bonding conditions: good, debond and weak. Good bond means the adhesion between adhesive and Al is perfect, debond means there is a discernable air gap at the interface; while a weak bond is the area where the adhesive strength is reduced because of the mixing

with Teflon. In the other set, two circular areas of weak bonding were created by applying a release agent to one Al surface. The release agent was baked at 250 degrees under strong static loading. The resulting condition is that there is no adhesion, but the adhesive layer and the Al substrate is in tight contact. We will refer to the first set of samples as Sample I and the second set as Sample II. Figure 1 illustrates the areas of different bonding conditions in these samples.

Sample 1



Sample 2

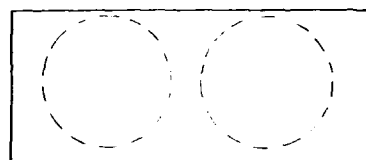


Fig.1: Samples with Weak Bonding Areas

### 2.2 PHYSICAL MODEL

The data interpretation in this study was carried out on the basis of a physical model of solid-adhesive layer-solid, in which the boundary conditions at the adhesive-solid interfaces are generalized to represent intermediate conditions between smooth and welded interfaces. In the frequency range under consideration (5-15 MHz) and an adhesive thickness of about 0.010", the bonding is seen as a layer of finite thickness by the probing ultrasonic wave. A numerical model was developed to calculate the reflectivity as a function of wave type, incident angle and frequency or  $fd$ , the product of frequency times thickness.

From the computational results of the above model, we made the following key observations:

- (1) The shear incident wave is more sensitive to changes in the adhesive layer, and thus is expected to be a better means to interrogate the bonding conditions.
- (2) The oblique incidence in general leads to more pronounced changes in reflectivity at some critical angles.
- (3) Since reflectivity is also strongly dependent on the frequency, for a broad band pulse a judicious choice of the desirable frequency band would significantly enhance defect characterization.

As a result, we chose to investigate the bonding layer with a 30 degree SV broadband beam in the 5-15 MHz range. Figure 2 shows how the reflectivity varies as function of frequency at this incidence for two cases: good bonding and weak bonding. It is shown there that in the 5-15 MHz range, the reflectivity from the weak bond can be either higher or lower than that from the good bond, depending on the specific frequency band selected.

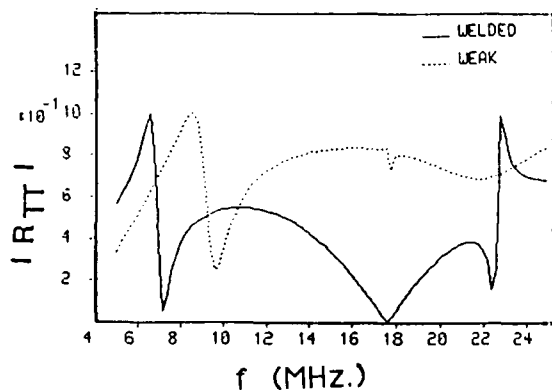


Fig.2: Shear-Shear Reflectivity

## 2.3 INSPECTION TECHNIQUE

The theoretical predictions suggest that we should use the shear oblique incidence to investigate the bonding conditions. Figure 3 presents the experimental arrangement with the typical values being indicated in the drawing. As the transmitter-receiver pair is scanned over the samples, the RF waveforms at each position are digitized and stored in a data file. Each waveform is then Fourier transformed and the split-spectrum processing algorithm is performed to enhance the signal-to-noise ratio. In the present study, the scanning images of the samples can be formed by either using the peak amplitude or the amplitude of a selected frequency band that is most sensitive to changes in the elastic properties of the adhesive layer. This selection is guided by such theoretical analysis as that presented in Fig.2.

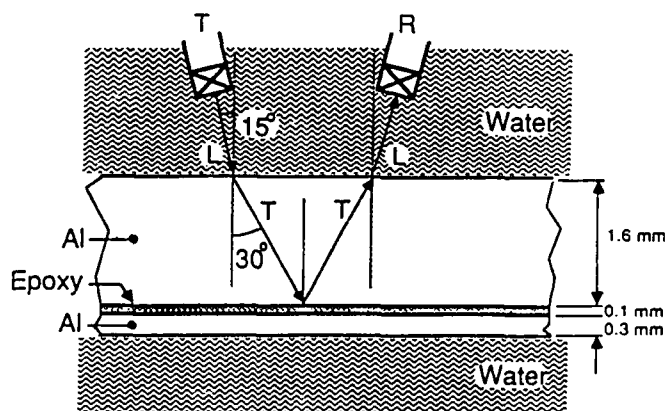


Fig.3: Experimental Arrangement

## 2.4 EXPERIMENTAL RESULTS

In Fig.4, an image of Sample I is constructed from the peak amplitude of the broad band pulse and can clearly distinguish the



good, bad and weak bond areas. In this case, we did not have to go into the frequency domain to search for the desirable frequency band. On the other hand, the defects present in Sample II are more subtle, the simple use of the peak amplitude does not produce the best image of the defects. The defects are better defined with good contrast when the images are formed with the amplitude of either 5 MHz or 10 MHz frequency bands. It is interesting to note that the relative intensity at the defect area with respect to the surrounding good area is reversed as one goes from 5 MHz to 10 MHz. This is clearly predicted from the computational results described in Fig.2.

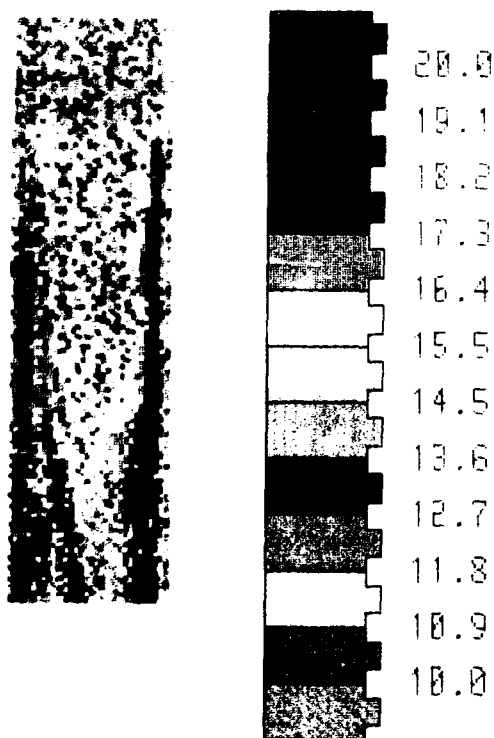
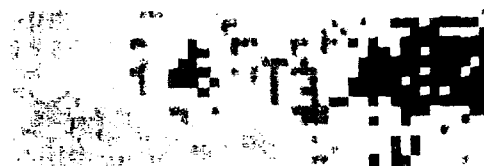


Fig.4: Feature-Based Imaging, Sample I

## Transverse 32° Incidence



Broad Band



5 MHz Spectral Amplitude



10 MHz Spectral Amplitude

Fig.5: Feature-Based Imaging, Sample II

## 3. CONCLUSION

In this paper, we have reviewed the fundamentals of the feature mapping methodology developed for ultrasonic NDE. This approach offers viable alternatives for inspecting subtler defects where conventional ultrasonics reaches its limits. As an example, this methodology was applied to the problem of inspecting weak adhesive bonds. We demonstrated that by using a selected spectral amplitude we can identify weak bond areas that cannot be resolved by normal incidence L-wave C-scan.

# References:

1. A. Pilarski and J.L. Rose, "A transverse wave ultrasonic oblique-incidence technique for interfacial weakness detection in adhesive bonds," J. Appl. Phys. 63, 300 (1988).
2. A. Pilarski and J.L. Rose, "Ultrasonic oblique incidence for improved sensitivity in interface weakness determination," NDT Int. 21, 241 (1988).
3. K. Balasubramaniam, "Guided plate waves and reflection factor for NDE of composite materials," Ph.D. Thesis, Drexel University (1989).
4. J.B. Nestleroth, J.L. Rose, M. Bashyam and K. Subramaniam, "Physically based ultrasonic feature mapping for anomaly classification in composite materials," Mat. Eval. 43, 541 (1985).
5. J.L. Rose, J.B. Nestleroth and K. Balasubramaniam, "Utility of feature mapping in ultrasonic nondestructive evaluation," Ultrasonics 26, 124 (1988).
6. J.L. Rose, "Elements of a feature-based ultrasonic inspection system," Mat. Eval. 42, 210 (1984).
7. J.L. Rose, J.B. Nestleroth, L. Niklas, O. Ganglbauer, J. Ausserwoeger and F. Wallner, "Flaw classification in welded plates employing a multidimensional feature-based decision process," Mat. Eval. 42, 433 (1984).
8. J.L. Rose, "A feature based ultrasonic system for reflector classification," in New procedures in nondestructive testing (Ed. P. Holler), Springer-Verlag, Berlin-Heidelberg (1983).

## DEVELOPMENT OF A RESONANT PROBE FOR EVALUATING THE INTEGRITY OF RUBBER-TO-METAL BONDED JOINTS

R. Lowell Smith, Alan V. Bray, and Cecil M. Teller  
Texas Research Institute Austin, Inc.  
9063 Bee Caves Road  
Austin, TX 78733-6201

### Abstract

A prototype contact resonator probe for the nondestructive evaluation of rubber-to-metal bonds in Navy sonar transducers was designed, fabricated and tested. The design employs two piezoelectric elements driven in a balanced manner such that the mass between them is essentially a node, and a third piezoelectric element that senses the vibration of the "node" when the probe is coupled to a sample. This design makes the probe extremely sensitive to changes in the stiffness, mass and especially damping of the bond/debond condition under the probe face. Debonds were consistently detected in samples comprising a 1/8-inch neoprene rubber layer over a metal substrate of 1/4-inch stainless steel or 1/2-inch aluminum. The use of a special coupling agent to couple the probe to the sample resulted in a detection accuracy of 100% for flaws as small as one-half the probe tip diameter using amplitude measurements alone. Direct probe output differences between bonded and debonded areas averaged over 5 dB in samples with rather subtle prepared flaws. Derived numerical measures of the bond/debond condition produced excellent discrimination as well. Results compared favorably with hand scans obtained using the NDT Bondascope 2100, a commercial unit designed to address the same general problem area. Phase information between the probe drive voltage and the "nodal" mount ceramic output allowed additional debond sites as small as one-quarter the probe diameter to be detected. However, the phase information lacked the stability of the amplitude detection technique and appears to require further development.

### 1. INTRODUCTION

This paper deals with work directed toward the development of a robust, relatively simple method for the nondestructive evaluation (NDE) of bond-line integrity in structures involving rubber adherends vulcanized to metal substrates. It summarizes portions of Phase I, the feasibility study, of a project conducted under the Small Business Innovation Research (SBIR) Program, with inspection of rubber covered sonar transducers as the long-term objective. There are already more than 50 commercial hardware offerings that may be generally characterized as ultrasonic NDE equipment adapted to a broad spectrum of test applications. Most of these use some form of pulse/echo technology. Measured delay times, changes in pulse shape, or tone-burst attenuation effects are used to draw inferences about the structures

being examined. These methods generally fail to detect rubber-to-metal debonds where the two materials remain in intimate contact because a rubber-to-metal interface exhibits essentially the same acoustic impedance characteristics whether bonded or not.

A few commercial test equipments operate on the principle of measuring the electrical impedance of a transducer mechanically coupled to a sample of interest. This approach is often referred to as impedance spectroscopy and employs simple mechanical coupling (mass, spring, dashpot) as opposed to acoustic interaction with the sample. Impedance spectroscopy is an approach that better lends itself to the detection of debonds. Debonds can be detected as a mechanical impedance interrogated under clamped (good bond) or free (debond) interfacial boundary conditions. To date,

impedance spectroscopy hardware, ranging from the venerable Fokker Bond Tester developed in the 1960's to modern versions of the Bondascope 2100 manufactured by NDT Instruments, couple a single transduction element to the sample. The Bondascope is considered by many to represent the present state of the art in terms of debond detection performance.

Our Phase I approach to rubber-to-metal debond detection makes use of a contact resonator (CR) approach involving mechanically coupling a probe to the sample of interest. The method is discussed in greater detail in Section 2. There are two basic distinctions between it and conventional acoustic NDE methods. We employ a symmetrical driver and separate motion detector, and a unique coupling agent with significant dynamic tensile strength is employed. Additional perspective is provided in the next few paragraphs.

A number of contact resonator NDE approaches have been investigated for a variety of applications. Some of the earliest work in this area was by Bell Laboratories in the mid-fifties for determining bond adherence in the emerging technology of circuit board fabrication, and wire bond testing continues to be an active research area in CR probe development.<sup>(1)</sup> CR bond testing techniques relating to rubber-to-metal bonds have recently been reviewed in two NDE publications.<sup>(2,3)</sup> Both of these review articles characterize the commercially available CR equipments as single frequency, single transducer, impedance measuring devices (see Section 5.2 for more detail on commercial hardware).

A recent series of papers by Guyott, Cawley, et al.<sup>(4,5,6)</sup> examined the physics of CR detection of debonds and included extensive experimental work with the Fokker Bond Tester series of products. A major theoretical contribution in this series included a mass and stiffness dominated receptance model of a joint undergoing CR testing. They concluded that the model can be simplified to a three body vibration problem consisting of the cylindrical regions of adherend (rubber in this case), adhesive, and substrate (metal in this case) directly below the probe. They were able to predict the frequency shifts of a Fokker CR probe quite accurately for a limited frequency region in the vicinity of a number of probe resonances for a joint of known material characteristics. They also highlighted the major disadvantage of mass-stiffness CR detection probes as being the interference problems that result when the frequency shifts observed become large enough to cause mode coupling with lower resonances. This inherent design problem with mass-stiffness CR detection devices is particularly degrading in the rubber-to-metal joint application. Single transducer CR probes performed best for similar material joints (e.g., metal-to-metal) in laboratory tests.

Material thickness effects in CR probe/sample interactions have also been investigated. The standing vibrational wave in the material under test is an odd multiple of the wavelength of the propagating wave equal to the effective thickness of the material.<sup>(7,8)</sup> This thickness is inversely related to resonant frequency, and therefore, an unbonded material gives rise to a higher resonant frequency. The thicker the sample the larger the effect as long as attenuation does not become a major factor. It is this phenomenon which has led to a number of attempts to characterize bond strength by looking for changes in adhesive layer depth.<sup>(9,10)</sup> In limited cases these attempts have been successful, but never outside of the laboratory environment. This historical perspective convinced the authors to avoid attempting a bond strength characterization in the proposed Phase II effort.<sup>(11)</sup> By thresholding at the bond/debond point without attempting to specify the occurrence of intermediate bond strength, very little is lost in the transducer inspection application.

We are unaware of any previously published work devoted specifically to CR bond testing using damping effects as a primary bond/debond indicator. However, the computational power now available in small computers makes the damping emphasis in CR design feasible. A number of researchers have acknowledged the potential use of damping effects as a bond/debond detection mechanism,<sup>(4,5,8,12)</sup> but to our knowledge this is the first detailed investigation of this technology.

## 2. PHASE I TECHNICAL APPROACH

As explained in greater detail in Section 1, this project has to do with establishing the feasibility of an appropriate acoustic method for detecting unbonded regions in rubber-to-metal bonded structures. The original intent was to evaluate an approach generally referred to as impedance spectroscopy, discussed in Section 2.1. It was anticipated that the data obtained would be interpreted with respect to bond condition using standard equivalent circuit modeling techniques. But during the execution phase of the project, simpler, more efficient figures of merit relating to bond state were developed. This work is described in Section 5. In order to preserve the greatest flexibility of approach in the experimental work (Section 4), a special piezoelectric driver/receiver was designed. This structure can be operated as a reentrant Tonpilz in either in-phase or quadrature modes. In addition, the driver/receiver configuration allowed operation as a nominally balanced transducer with a nodal accelerometer readout. This latter arrangement ultimately proved most useful in addressing the debond detection problem, and is the primary emphasis of this paper (particularly Sections 2.3, 4 and 5).

## 2.1 THE IMPEDANCE SPECTROSCOPY METHOD

In Section 1, it was noted that there are a number of acoustic approaches to, and a great deal of commercial hardware for, nondestructive testing. Detecting a degraded or nonexistent interfacial bond between materials in contact, however, remains a significant concern. A small subset of available ultrasonic testing hardware operates on the principle of measuring the electrical impedance of a transducer mechanically coupled to a specimen of interest. This approach typically involves a sequence of steady-state, sinusoidal excitation measurements over a range of discrete frequencies and is referred to as impedance spectroscopy. Impedance spectroscopy is distinct from other acoustic testing methods (such as pulse/echo or time of flight) in that it can be understood in terms of simple mechanical (mass, spring, dashpot) coupling as opposed to acoustic (sound propagation) interaction with the sample. For this reason, it appears to be an approach that better lends itself to the detection of debonds. In simple terms, one might think of debonds or unbonded areas as regions lacking tensile strength across an interface. This can be detected as a mechanical impedance interrogated under clamped (good bond) or free (debond) interfacial boundary conditions with data displayed to emphasize the differences. To date, commercial impedance spectroscopy hardware ranging from early models of the Fokker Bond Tester developed in the 1960's to modern versions of the Bondascope 2100 manufactured by NDT Instruments, typically couples a single transduction element (piezoelectric ceramic or crystal) to the sample. The Bondascope is considered by many to represent the present state of the art in terms of debond detection performance.

In Phase I, two closely related variations of the classic impedance spectroscopy method were investigated. The first is the reentrant Tonpilz oscillator. This is a special sort of inside-out transducer configured so that both the "headmass" and a surrounding annular "tailmass" (both driven by piezoelectric elements) can be arranged to interact symmetrically with the sample under study. This approach represents standard impedance spectroscopy in the sense that inferences are drawn from ordinary two-terminal impedance or admittance measurements. The balanced design transducer discussed in Section 2.3 is less conventional in that two piezoelectric sections are driven while a third ceramic is employed to monitor the motion of the center of symmetry or "nodal" mount of the driver. The output is a function of mechanical loading, i.e., the bond/debond state of the sample in contact with the probe tip.

## 2.2 PHYSICAL BASIS FOR BOND/DEBOND DETECTION

NDE techniques for discriminating between bonded and debonded areas in rubber-to-metal joints generally exploit the nature of the interaction between the probe or sensor and the inspected area to highlight detectable differences. In a contact resonator approach to this, the frequency response or impedance at a given reference frequency, of a piezoelectric element in air or in contact with a good bond is compared to its response when placed in contact with a debond site. Focusing the discussion on the former case, the CR probe frequency response in air depends upon the inherent stiffness, or spring constant, of the probe; the damping, or internal dissipation, associated with this structure; and its inertial mass distribution. When the probe contacts a rubber-to-metal bond, the probe/bond system has a modified frequency response.

This is simply illustrated in the mechanical analogy shown in Figure 1. Imagine that a force  $F(t)$  is applied to the system inertial mass, and that the foundation, analogous to the substrate of the bonded joint, responds with a displacement  $x(t)$ . The equation of motion for the system is dependent upon the stiffness,  $k$ , the damping coefficient,  $b$ , and the inertial mass,  $m$ . The CR probe analogy is that in the three states of interest, i.e., operation in air, in contact with a bond, or in contact with a debond, the foundation response  $x(t)$  is determined by three different sets of constants since each of these interactions affects the system parameters,  $k$ ,  $b$ , and  $m$  differently. The result is a different equation of motion for each of the three situations of interest. Since the system frequency response is the Fourier transform of the displacement  $y(t)$  for a unit impulse displacement of the foundation; three different frequency response functions are implied.

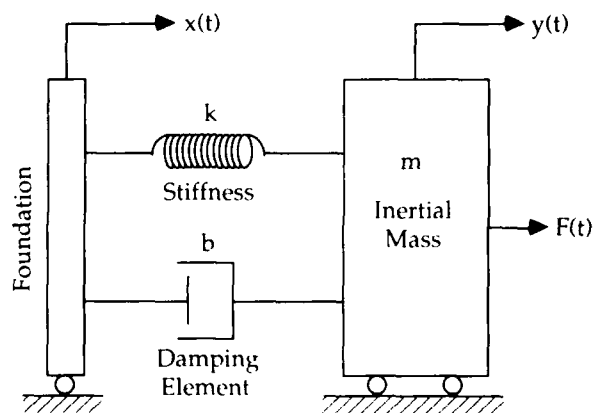


Figure 1. Mechanical System with Foundation Motion and Forcing Function

A well-bonded rubber-to-metal joint exhibits an adhesive strength not present in the unbonded state. When a resonator contacts a good bond, relatively little mass moves with the resonator, and the stiffness and damping involved are determined by the clamped nature of the sample. In an unbonded situation more of the rubber mass is free to move with the resonator and the unclamped condition reduces damping and stiffness. As a result of these effects, in comparing a debond to a good bond, the resonance frequency shifts downward due to added mass, and upward due to reduced incremental stiffness; and the response is less attenuated by a reduction in damping. Previous contact resonator designs have been optimized to observe frequency shifts as an indicator of the debonded condition.<sup>(4,5)</sup> The inertial mass of the probe is made as low as possible, such that the added mass of the debond has a large downward frequency shifting effect. Since the stiffness of the probe in these systems is much larger than the sample stiffness, the mass changes dominate, and frequency shifts are the primary detection mechanism. The disadvantages of this approach relate to the overlap of these large shifts with other resonances.<sup>(13)</sup>

The CR probe design investigated in this work exploits primarily the damping coefficient change to distinguish the bonded and debonded situations. This approach includes using a large inertial mass in the probe; thus

frequency shifts due to added sample mass and stiffness are small. By incorporating lightly damped resonators, the design is optimized to observe significant changes resulting from the difference in bond and debond damping effects. In addition, the design employs a special nodal mount technology which accentuates overall probe/sample coupling detection sensitivity.

### 2.3 MEASUREMENT SYSTEM AND PROBE DESIGN

Phase I of the project emphasized taking a very flexible posture toward probe design options and ways of interacting with the sample. This approach was facilitated by centering the data acquisition system around the versatile HP-4192A Low Frequency Impedance Analyzer. The experimental setup is quite simple as sketched in Figure 2. The 4192 is controlled using an IBM PC computer and IEEE-488 interface. Menu-driven software developed for the project allows measurement mode, frequency scanning, and data display and storage choices to be made easily. A screen graphics section of the code permits real-time display of the current run data. A screen dump to the printer is available as a low-resolution graphic output. Data files are also written to floppy disk storage. Here the data remain available for numerical post-processing or direct display using a high-resolution pen plotter.

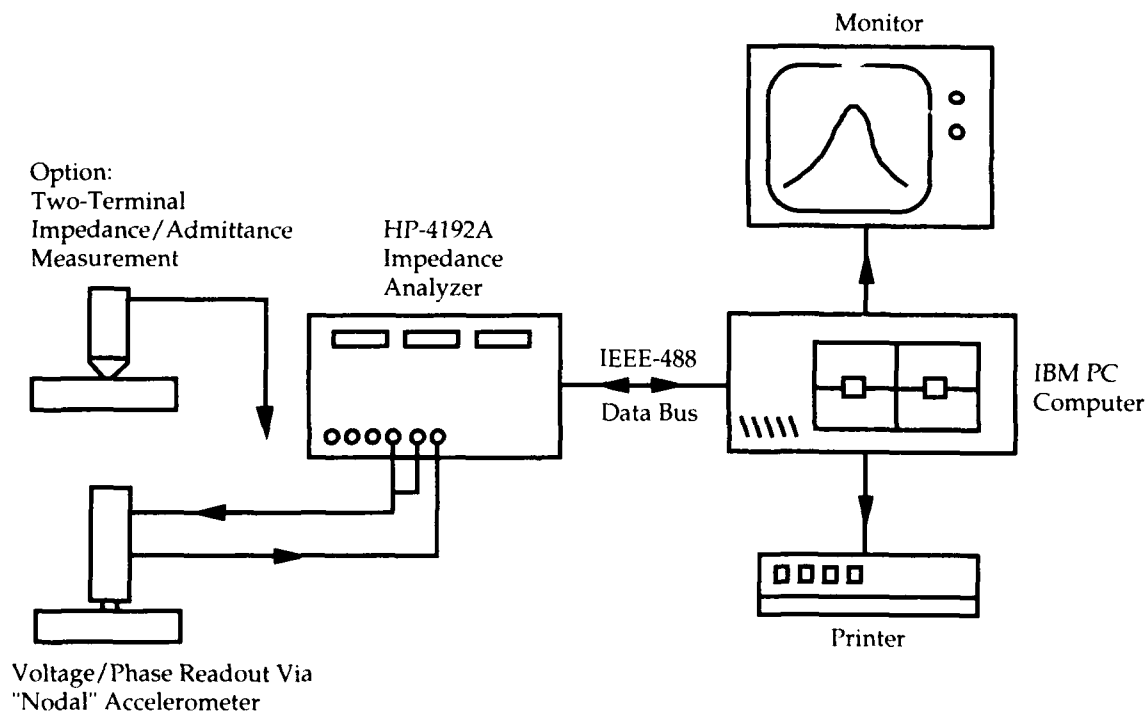


Figure 2. Schematic Layout of Phase I Debond Detection System

The HP-4192A is basically a tracking lock-in or phase-sensitive detector set up to process two coherent signal channels. We used the instrument in two different ways. A two-terminal measurement of the in-phase and quadrature components of impedance (or more commonly admittance) was one operating mode. Even more useful for debond detection purposes was what might be referred to as a four-terminal measurement. The 4192 local oscillator output was used to drive the balanced probe driver and provide a phase reference signal (to input A). Input B of the impedance analyzer received the nodal accelerometer output signal; and the instrument was used to output stepped frequency, amplitude and phase information.

The preferred probe design is discussed in more detail in the next paragraph. However, to keep several experimental options open, a modular approach was taken to probe-configuration alternatives. The basic radially poled piezoelectric tubes had threaded brass terminations bonded to each end. The threaded fittings allowed considerable flexibility in coupling, terminating, mounting, and supporting the active piezoelectric elements.

Figure 3 is a photograph of one experimental conformation showing a closeup view of the probe, the test specimen and support frame isolated from other data acquisition components.

The balanced (symmetrical) driver fitted with a nodal mount accelerometer readout is illustrated schematically in Figure 4. The ceramic segments can be driven in or out of phase, although there appears to be no practical advantage associated with the latter. In-phase operation means that the matched ceramic drivers lengthen and shorten together when AC voltage is applied. Coupling to the specimen under investigation is via a single brass nose piece. Actually four nose pieces were fabricated as matched pairs (by mass). They had four different footprints or sample-contact areas so that spatial resolution effects could be studied. Bond/debond discrimination was by far most successful using the "nodal" motion detection scheme. Therefore the several classes of experimental data discussed in Section 4 represent this approach exclusively. Variations of a balanced oscillator with accelerometer readout were proposed for further development in Phase II of the project.<sup>(11)</sup>

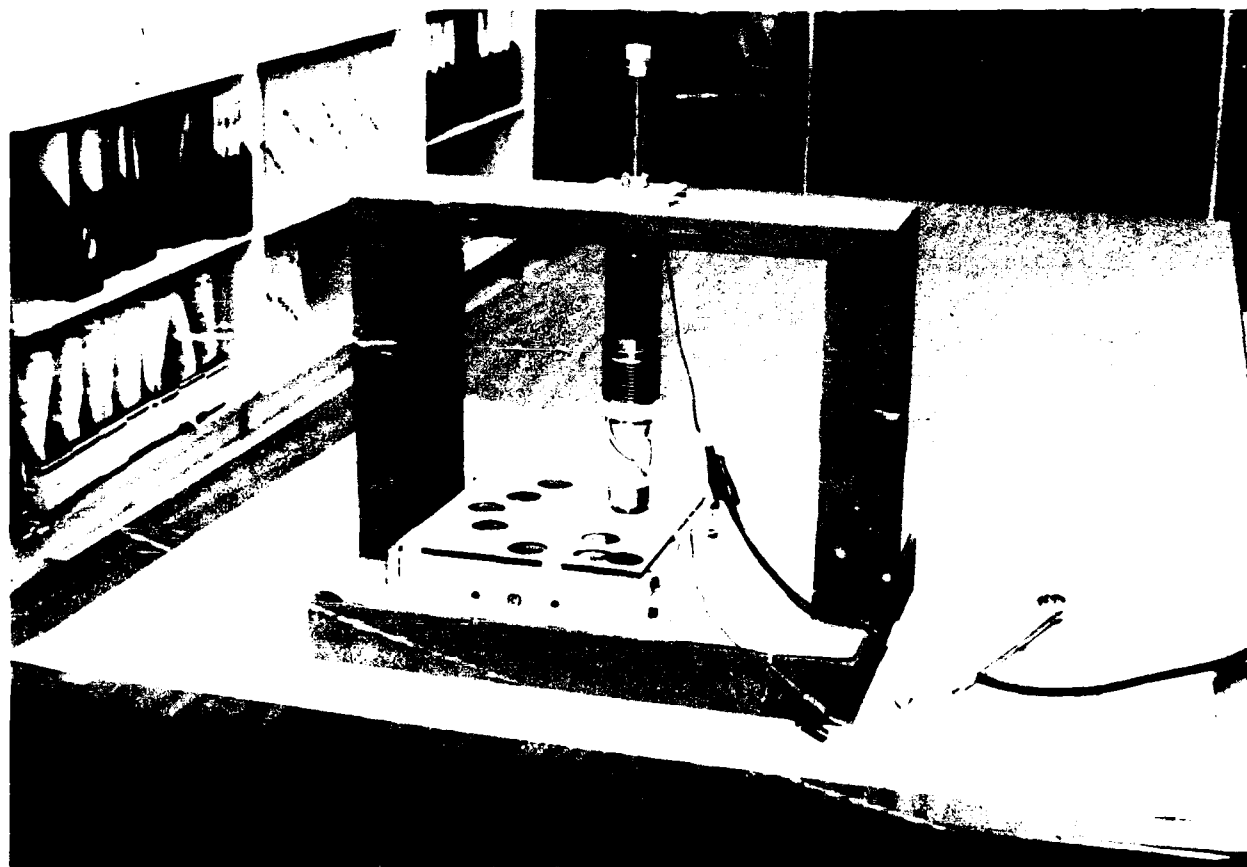


Figure 3. Photograph of the Probe, Test Specimen, and Support Frame

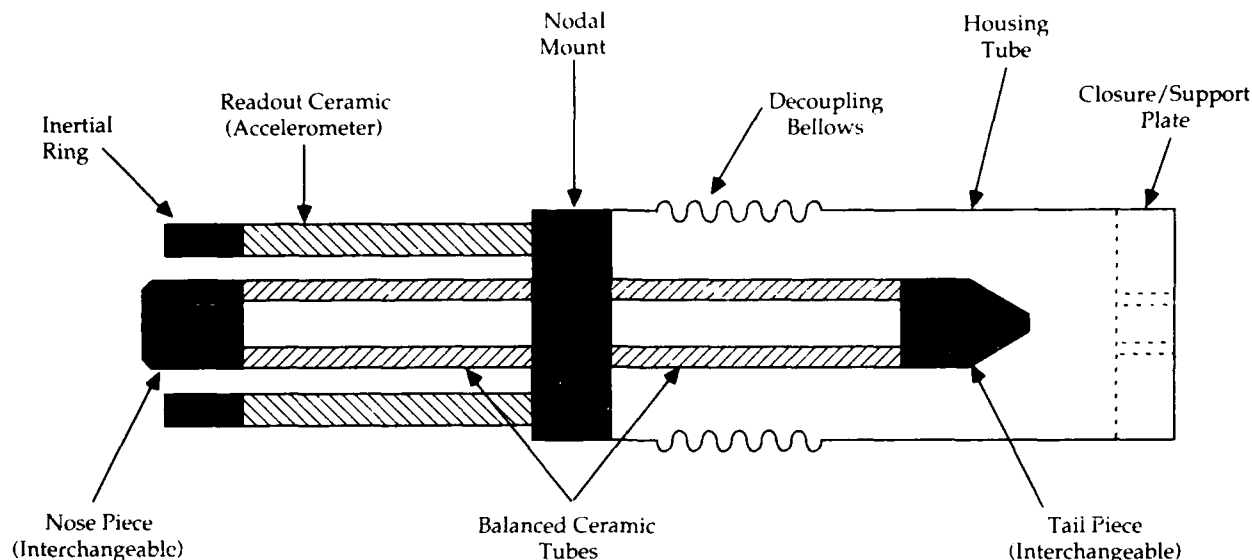


Figure 4. Schematic Diagram of the Balanced Transducer with Nodal Accelerometer

### 3. SAMPLE PREPARATION

Phase I experimental work depended upon exercising the various probe configurations in the context of test specimens having reasonably well understood bond/debond properties. Two specially designed structures were fabricated to meet these requirements. Their physical conformations are discussed in the next two subsections. But first let us consider some more general background material concerning how specimens with controlled flaws are fabricated in our laboratory. Conventional rubber molding facilities and procedures are used to produce test articles from a variety of materials in different formats. Substrates have included steel (stainless and others), aluminum, monel, and brass. The elastomeric layer worked with most commonly is neoprene 5109S because of its wide application in Navy transducers and its use in a related adhesives evaluation program, but various urethanes have been molded as well. The simplest specimen configuration is a flat plate with rubber bonded to one of the open face areas. We have worked with a variety of plate thicknesses ranging up to one inch. Elastomeric layer thicknesses are ordinarily 0.125 to 0.25 inch unless an actual operational item is being emulated.

Specimens are prepared according to fairly generally accepted procedures. The metal surface is vapor degreased, then grit blasted with the abrasive size recommended for use with the substrate material selected. The surface is then cleaned with a solvent and degreased again. Thereafter, the plate (or other substrate structure) is handled using clean rubber gloves. Bonding neoprene requires application of a primer and adhe-

sive to the prepared surface before vulcanizing the rubber to it. Vulcanizing is done at the temperature recommended for the material used, typically 315°F, at a pressure of 1.5-1.7 ksi. Urethanes generally do not require a primer/adhesive and are simply appropriately oven cured.

There are several ways of producing programmed debonds in a test specimen. The substrate surface can be masked or painted with a mold release prior to application of the primer/adhesive. The same procedures are effective for urethane materials. One alternative is to leave the masking material in place to form an inclusion flaw. The mask can also be removed leaving an unprimed, bare metal region. This results in a weakly adhering, but not well-bonded, rubber-to-metal interface. Surfaces painted with mold release yield layers in intimate contact, but not bonded.

#### 3.1 STRIP-DEBOND SAMPLE WITH MODIFICATIONS

The strip-debond sample is a 6 inch by 6 inch by 1/4 inch square stainless steel plate to which a 1/8 inch layer of neoprene 5109S is bonded. Prior to the application of the Chemloc 205/220 primer/adhesive, a 1/2 inch wide by 6 inch long strip of the metal substrate was masked with teflon tape. After primer/adhesive application, the tape was removed leaving a region of bare metal. When the rubber adherend was cured, the weak attachment in the unprimed region was mechanically disrupted with a 0.01 inch thick spatula to a penetration depth of about 1.25 inches at each end, creating a true unbonded condition. The resulting structure is referred to at this point



as a strip-debond sample. Not infrequently in delamination studies, a debond (adherend and substrate in contact but not attached) will mature such that there is void space between the two material layers. To simulate this situation the strip-debond sample was modified by machining several holes through the stainless steel substrate but not into the neoprene rubber layer. In particular a 3/4 inch diameter hole was cut behind the unbonded strip itself and three smaller holes were cut behind well-bonded regions of the sample. The large hole was machined in stages using flat-faced milling tools of increasing diameter. The last, thin disk of metal removed from each hole was preserved for inspection. What was observed was cohesive failure of the rubber in bonded regions. In contrast, in the unbonded region adhesive failure was experienced; i.e., the metal and rubber separated cleanly without damage to the rubber.

Figure 5 provides a schematic graphic representation of the modified strip-debond sample and how it relates to measurements and data display discussed further in Sections 4.2 and 5.1. When measurements are made, the test specimen is fitted with a cardboard overlay (such as seen on the model headmass assembly in Figure 3). Circular cutouts in the overlay facilitate reproducible placement of the CR probe tip for data acquisition purposes. Figure 5 is reproduced at approximately one-half actual size.

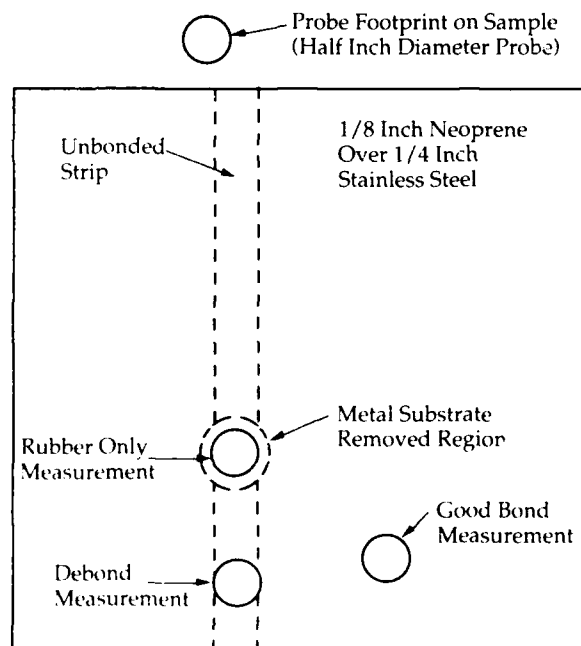


Figure 5. Profile Diagram of the Modified Strip-Debond Test Specimen

### 3.2 MODEL HEADMASS ASSEMBLY

A much more sophisticated debond evaluation test specimen was also designed and fabricated for Phase I. This is a structure, the dimensions and configuration of which were chosen to simulate the major features of the headmass/shroud assembly of the TR-317 transducer. That is, a central "headmass" with a square face area was surrounded on four sides by a metal annulus. Neoprene 5109S was molded over one face and down the sides of the central mass filling the gap between the headmass and the surrounding metal annulus. This test fixture is referred to as the model headmass assembly, and it was used quite extensively in the data acquisition phases of the project.

Twenty intentional debonds (including all three types discussed in Section 3) were introduced in the model headmass assembly. A debond configuration map showing flaw size, placement, and type is presented as Figure 6. The flaws are sized and placed to represent a wide range of detection difficulties. Most Phase I experimental work emphasized flaw detection through the face rubber. But sample interrogation from the metal side of the annulus was also investigated. The model headmass assembly was used to compare our Phase I results with the corresponding debond detection capabilities of commercial equipment as discussed in Section 5.2.

### 4. EXPERIMENTAL WORK

In this section we discuss significant experimental aspects of the project. A few points should be clarified. First of all, this was a feasibility study. Although substantial quantities of data were generated, there is little justification for reviewing other than representative examples of same here. Much of this is done in the data analysis section (Section 5). Greatest attention is given to describing those techniques considered to represent a basis for further development in Phase II. Bond/debond comparison data developed from the rubber side of the test samples represented the overwhelming emphasis of the Phase I effort as discussed briefly in Section 4.2. The corresponding data analysis is dealt with in Section 5. Edge sensitivity and resolution measurements, and debond detection through the metal annulus of the model headmass assembly were successfully conducted during Phase I of the project, but are not considered further here in order to limit the scope of the discussion.

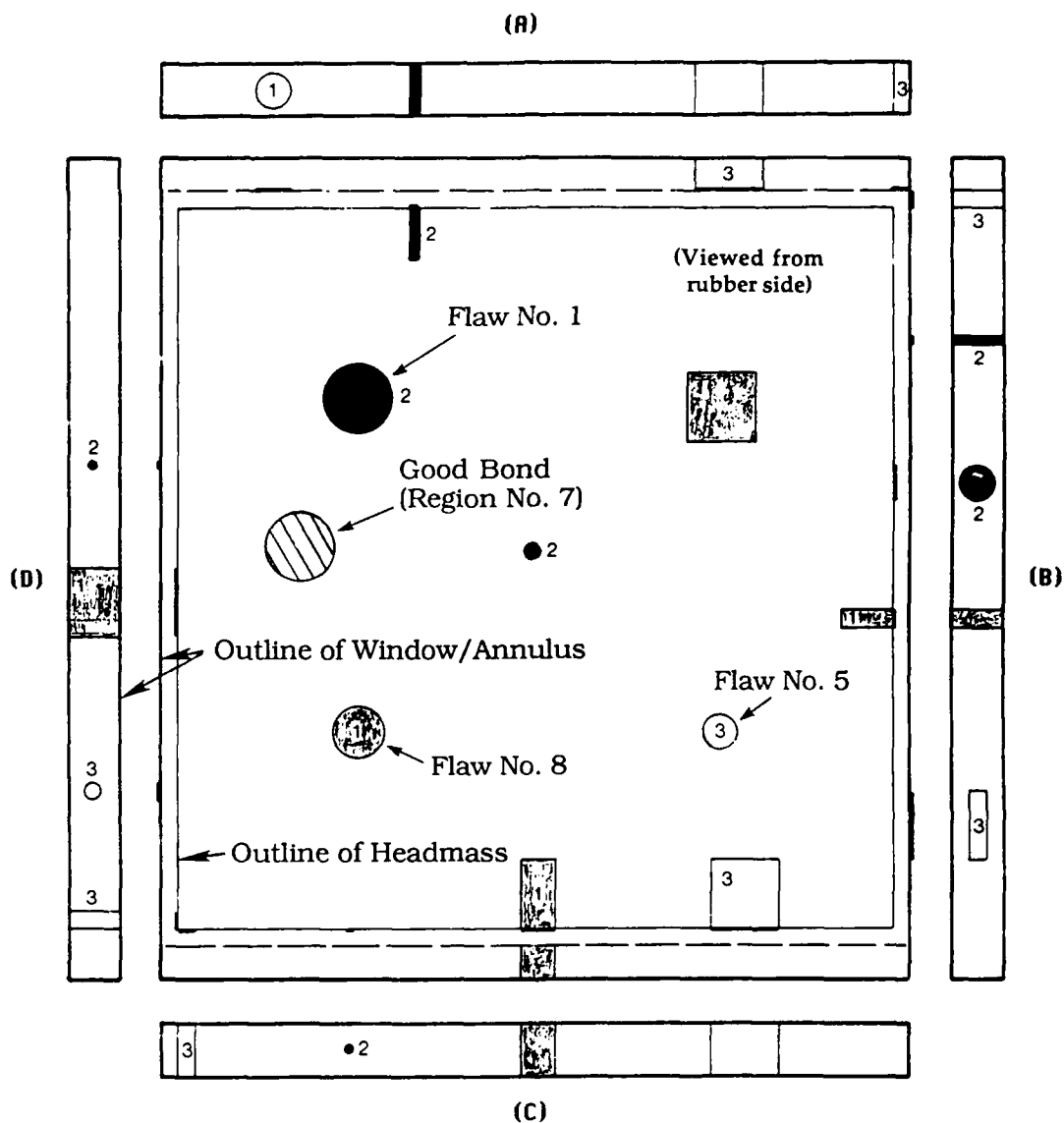


Figure Legend: Explanation of the Three Distinct Types of Debonds Induced

Flaw Designation/ Description	Aluminum Substrate Surface Preparation	Nature of Induced Defect	Anticipated Detection Difficulty
Type 1 (Shaded Gray)	Grit Blasted and Cleaned Bare Metal	Substrate Masked, Primer and Adhesive Applied and Dried, Mask Removed Exposing Bare Metal	Most Difficult
Type 2 (Shaded Black)	Same	Substrate Masked and Mask Left in Place for Adhesive Application and Molding Procedures	Intermediate Difficulty
Type 3 (not Shaded)	Same	Metal Surface Painted with Mold Release Material Before Application of Adhesive	Least Difficult

Figure 6. Debond Configuration Map of the Phase I Model Headmass Assembly Test Fixture

#### 4.1 USE OF SPRAY-ON ADHESIVE COUPLANT

All ultrasonic nondestructive testing equipment depends on the transmission of acoustic energy into or from the specimen of interest. Quite frequently, efficiency is significantly enhanced by using special coupling agents—silicone grease, mineral oil, or water, for example. During Phase I of the project we obtained superior results with a rosin-based spray-on adhesive commercially available from sporting goods stores.

#### 4.2 RUBBER-SIDE BOND/DEBOND COMPARISONS

All of the experimental work during Phase I made use of the specially prepared flawed samples discussed in Sections 3.1 (strip debond) and 3.2 (model headmass assembly). The latter specimen emulates the headmass assembly of the TR-317 transducer, with rubber vulcanized over the the headmass face and forming a rubber annulus between the sides of the headmass and a surrounding ring of metal. Some transducers have a rubber-covered shroud, a booted endseal enclosure, or are fully encapsulated with rubber. It is clear that detecting debonds from the rubber side of the rubber-to-metal interface is an extremely important application. This was the major emphasis during Phase I. A great deal of data was collected and several methods of analysis developed. The data analysis for bond/debond comparisons is presented in detail in Section 5.

### 5. DATA ANALYSIS

There were two primary forms of data analysis used in Phase I; direct display of the voltage and phase spectra, and numerical discriminants. The first of these provided a means of examining the raw data for location of rubber sensitive resonances, a quick-look capability for comparing air, bonded, and unbonded samples, and system operability checks. The second technique included off-line processing of the spectral data to produce a set of discriminants which are sensitive to the bond/debond condition under the probe. Numerical discriminants are not discussed further here because they are largely a precursor to the shaping of Phase II development recommendations. Direct data display methods and a comparison between our data analysis and presentation approach and outputs of two commercial NDE contact resonator systems are presented.

#### 5.1 DIRECT DISPLAY OF PROBE OUTPUT VERSUS FREQUENCY

The output of the probe is processed by the HP-4192A impedance analyzer, resulting in a voltage spectrum which is proportional to the output of the nodal-mount accelerometer. The output of the HP-4192A is routed to

the IBM/PC computer via an IEEE-488 interface. Display and plotting of the data is handled by the computer code called XINT. This software handles the data transfer and assigns the spectra to a file storage and retrieval protocol which is used in post-processing. The data are displayed in real time and hard copy plots are also available in near real time if desired. The XINT program was originally developed under contract to the Navy for the acquisition of data supporting the accelerated life testing of sonar transducers. The XINT program was modified for this project to accommodate rapid processing of the probe output spectra.

Normal experimental procedure was to precede a new series of contact measurements by obtaining an in-air spectrum (probe output voltage versus frequency) over the same frequency region. By subtracting the two types of spectra it is possible to isolate those frequency regions which are sensitive to contact with the elastomer adherend. The difference spectrum shown in Figure 7 clearly illustrates that there are two frequency regions which can be exploited for their sensitivity to elastomer contact, 10-14 kHz and 65-70 kHz. In this study, the former region was the primary one used to investigate the bond/debond detection capability of the probe.

Figure 8 represents a series of measurements, which included an air spectrum, a bonded spectrum, and spectra from two unbonded sample sites (one of which had no substrate) on the strip-debond sample of Figure 5. The highest amplitude curve in the figure is the in-air spectrum, while the lowest amplitude result corresponds to the bonded site. Since the largest damping is associated with the bonded site, the relationship between the air and bonded spectra is as expected. The data from the site without the metal substrate is the next largest in amplitude to the air spectrum, and is higher than the debonded site spectrum. This is also an expected result since the site without the substrate should be damped less than the debonded site from physical considerations (see Section 2.2).

The ability to distinguish between the two debonded sites in this sample is an example of the sensitivity of the probe to small changes which are important in the production transducer inspection application. Repeated tests over a period of four days resulted in a 95% (20 of 21) success ratio in distinguishing the difference between the two types of debond conditions. The final success ratio for distinguishing between bonded and debonded regions in the final system configuration was over 97% for all tests conducted with the strip-debond sample. Although the testing process was not actually designed to establish a success ratio which can be compared to other systems, the results stated above are still a clear indication that the CR probe debond detection concept is viable.

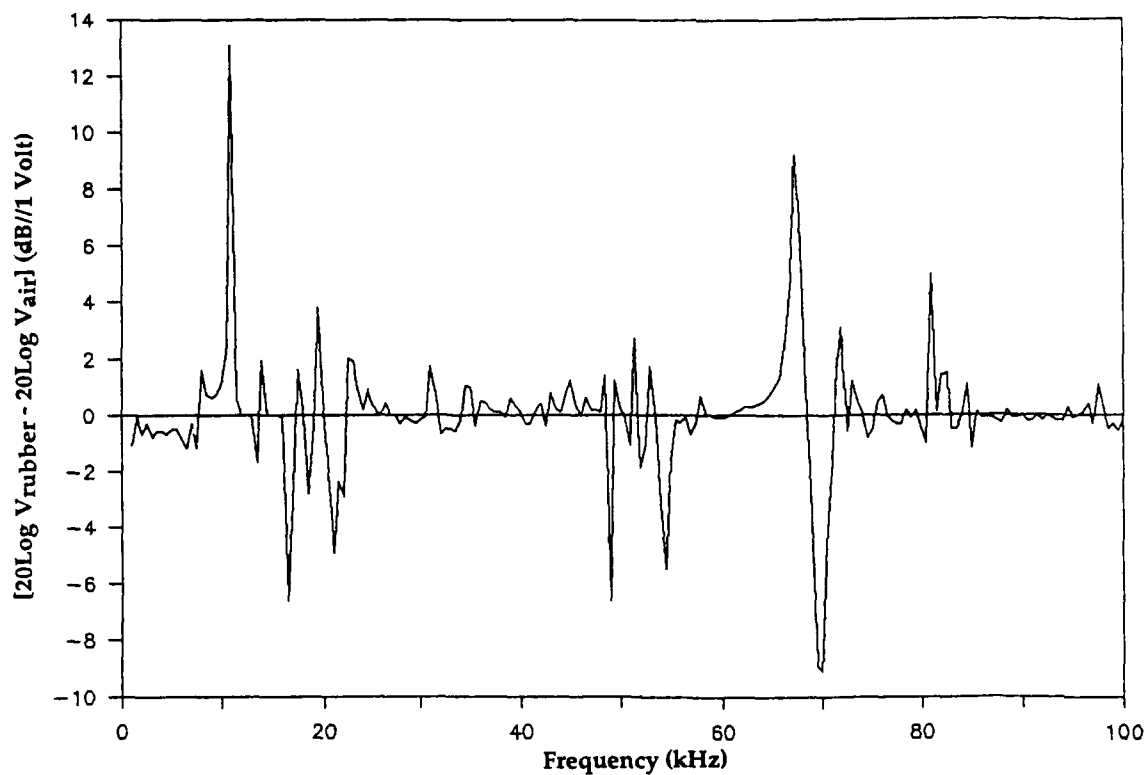


Figure 7. Difference Spectrum Emphasizing the Frequency Regions Dramatically Affected by Sample Coupling

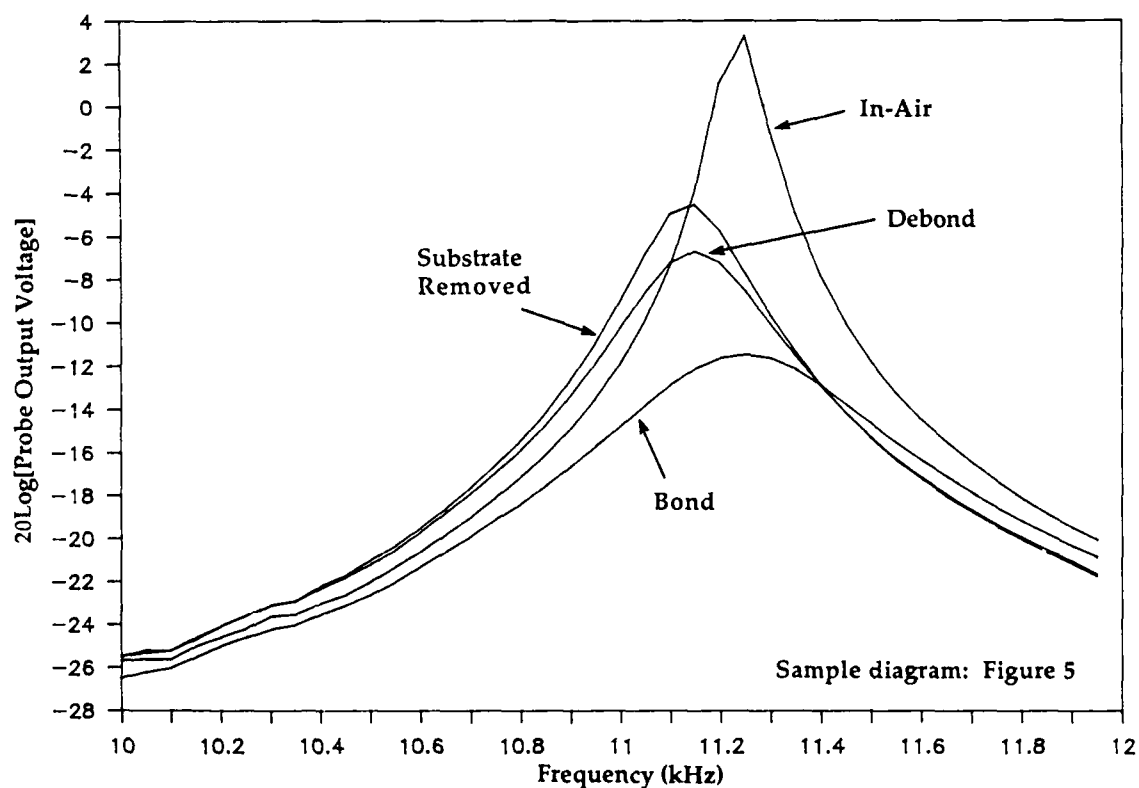


Figure 8. Bond/Debond Comparison for Test Sample Containing Strip Debond and Substrate Relief

### 5.1.1 Phase Measurements

The phase between the drive voltage and the nodal mount accelerometer output was measured to determine its sensitivity to differences in bond integrity. Two factors concerning phase measurement are important to bond/debond discrimination—essentially the position and width of the sample-sensitive resonance. The frequency corresponding to a phase angle of  $90^\circ$  ( $\phi=90^\circ$ ) is the resonant frequency (position aspect) of the probe loaded by the test specimen. Bond, debond, and air measurements all go through the  $\phi=90^\circ$  point at different frequencies, which are characteristic of the site; i.e., debond spectra typically exhibit a  $90^\circ$  phase shift at lower frequencies than bond spectra due to the mass dominance of the combined mass and stiffness differences in the former case. The slopes (width aspect) of phase spectra in the vicinity of  $\phi=90^\circ$  are directly related to the damping of the probe motion. Lower (less vertical) slopes indicate higher damping. In plots of probe output amplitude versus frequency this corresponds to reduced signal levels and, again, broader resonances.

Figure 9 is an example of a phase spectrum in the 10 to 12 kHz region. Notice that the in-air, debond, and bond data all cross  $90^\circ$  degrees at different frequencies. The

nature of this shift is difficult to determine a priori since both stiffness and mass changes affect the degree and direction of the frequency shift. Relative to the resonance in air, the debond shows a much larger frequency shift than does the well-bonded region of the sample. In the latter case the downward frequency shift due to added mass and upward shift associated with increased stiffness nearly add to zero. However, the interaction of the probe with the debond site is clearly mass controlled for the data presented in the figure.

In contrast to the situation for the resonance frequency itself, the relative slopes of the phase spectra in the region near resonance can be predicted based on the nature of the sample site, as indicated above. The bonded site had the lowest (least vertical) slope, followed in sequence by the debond and in-air measurements. This is the order which one would expect based solely on the degree of damping for each case. During the Phase I effort, the slopes of the phase spectra in the resonance region were not quantitatively evaluated, but in every instance in which phase data were obtained with the preferred probe configuration, the slope differences were discernable by inspection and conformed to the ordering displayed in Figure 9.

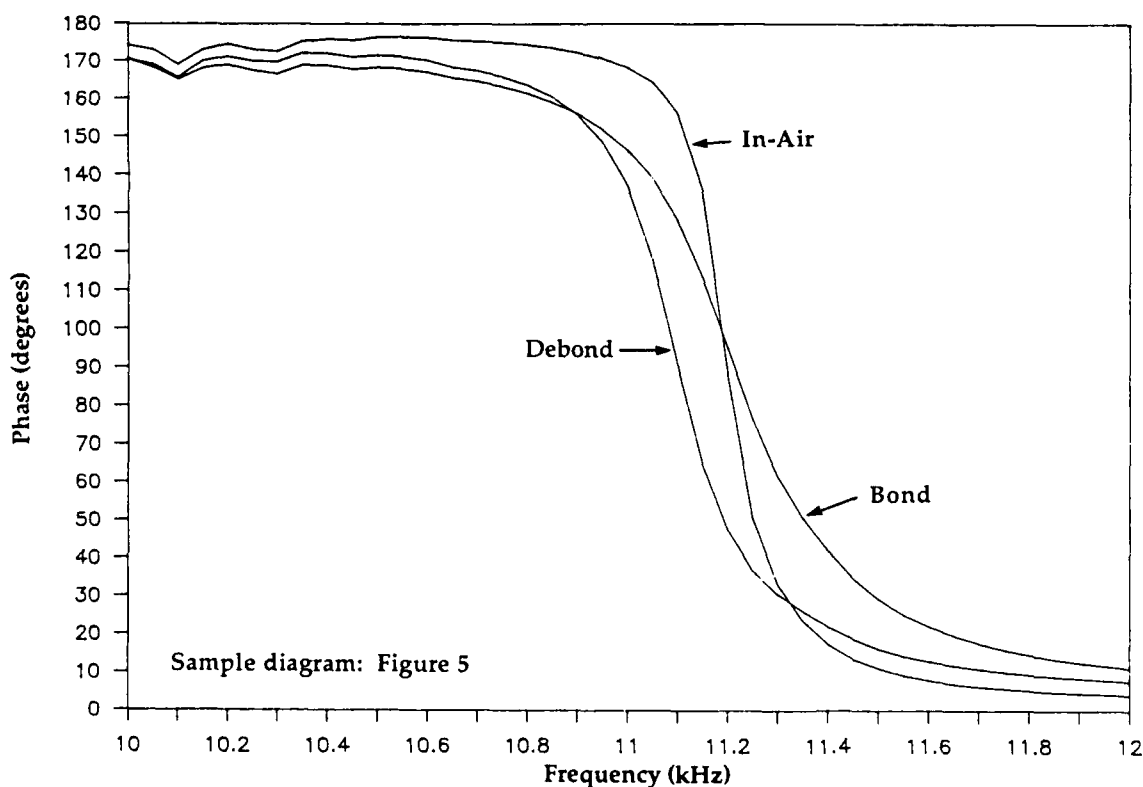


Figure 9. Phase Differences Between Probe Drive and Output Voltages as a Function of Frequency

### 5.1.2 Stability Measurements

The repeatability of the bond/debond decision is predicated on a comparison of the current measurement and an historical measure of a bonded or an in-air spectrum. The system must remain stable during the intervening period between the reference and the current measurement for the comparison to be of value. Stability measurements were made by averaging spectra (incoherently) over time. The standard deviation of a series of measurements at each frequency is an indicator of the stability of the process. Both short term, (three hour), and long term, (three day), standard deviations as a function of frequency were computed. This is a complete compilation of deviations from the mean for spectra associated with reference and measurement data record types; i.e., all in-air spectra were averaged and their deviations from the mean included in the calculation. The spectra for the bonded sites were treated in the same manner. These two types of deviations were combined to form the short and long term stability figures of merit.

A short term variability at resonance of about 0.5 dB (reference 1 Volt) was observed, but was not limiting in terms of the ability to discriminate between the debonded and bonded states during Phase I. Using the half-inch diameter probe tip, the amplitude difference between an in-air sample and a bonded sample averaged approximately 12 dB, while the difference between debonded and bonded sites was approximately 6 dB. The decision that a given spectrum acquired is associated with a debond is not compromised by the 0.5 dB variability. The long term stability was as much as five times greater at certain frequencies, however, suggesting the need to update the reference spectrum on a regular basis. This approach was taken during Phase I and no discrimination failures were attributed to instability effects. Procedures to upgrade the probe/inspection system stability during Phase II by controlling the probe contact force have already been defined.<sup>(11)</sup>

### 5.2 COMPARISON WITH COMMERCIAL HARDWARE RESULTS

Through a subcontract with Douglas Aircraft Company, we arranged a direct comparison of the Phase I CR probe performance with the Fokker Bond Tester and the NDT Bondascope 2100. The model headmass assembly was selected as the test specimen. None of the flaws were detectable using the Fokker unit. The Bondascope produced an oscilloscope complex-impedance-plane output as shown in Figure 10a. Debond signal levels indicated correspond to the spatial debond map presented as Figure 10b. Figure 10b was produced by hand-scanning the face of the model headmass assembly using a 1/2 inch diameter probe operating at a single

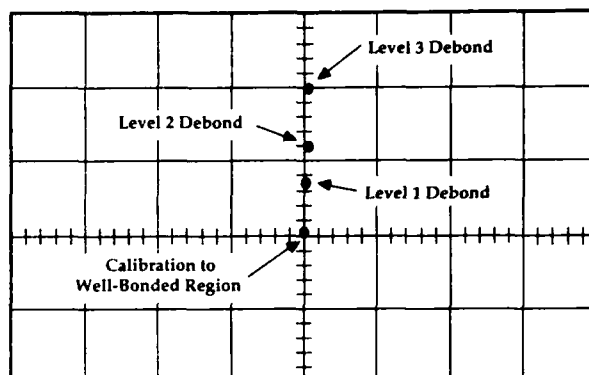


Figure 10a. Bondascope 2100 Impedance Readout for Flaws Detected in the Model Headmass Assembly

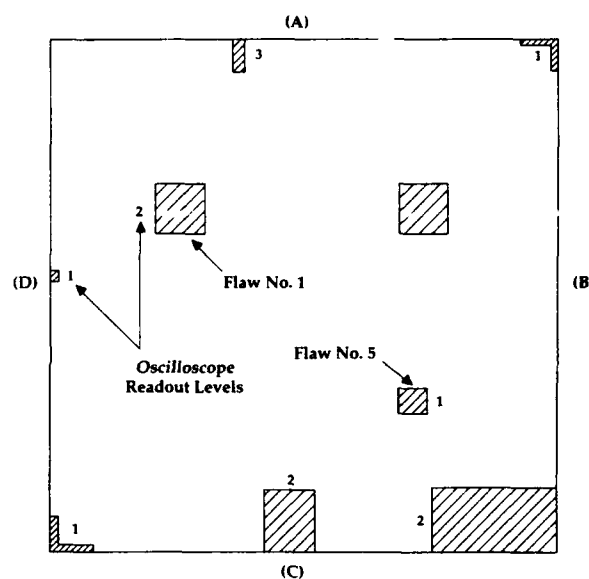


Figure 10b. Hand-Scan Debond Map of the Model Headmass Assembly Using the Bondascope 2100

frequency, and calibrated so that a "good bond" produced a null output.

Figure 11 shows corresponding results using the Phase I CR probe. Static local measurements detected flaws (commensurate in size with the probe tip) that produced level 1 and level 2 signals on the Bondascope 2100. There were two anomalous results of interest. Flaw site No. 8 (see Figure 6) was undetectable by any method and was probably actually bonded by adhesive migration. Pitting of the rubber or surface holidays confounded both the Bondascope and CR probe measurements in the lower right hand corner region of the test specimen.

It is of particular interest that all the Bondascope readings shown in Figure 10a are closely aligned with the

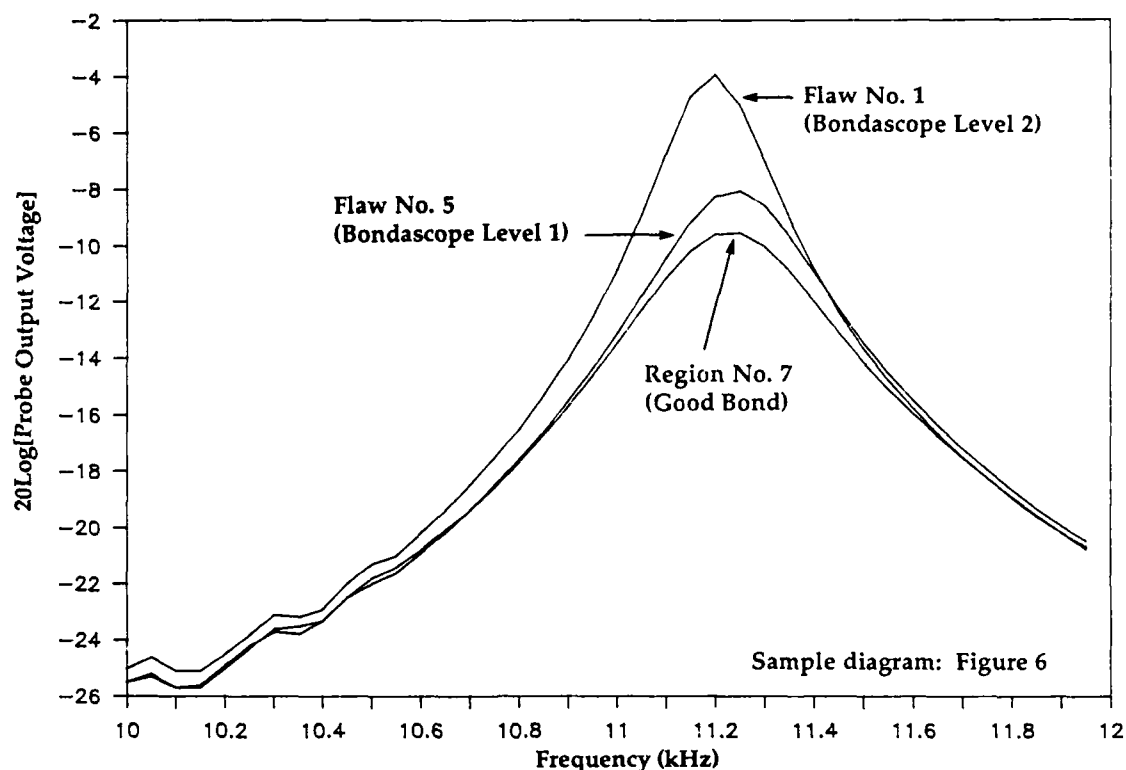


Figure 11. Model Headmass Assembly Bond/Debond Comparison Using the Phase I CR Probe

imaginary axis of the display. This corresponds to a situation where damping effects and not incremental mass or stiffness constitute the primary basis for debond detection. The same conclusion is obvious from Figure 11 where shape, level, width, or Q information (different perspectives of the same situation) is more important than the minor frequency shifts. The latter are often ambiguous because of the competition of added mass and increased stiffness to shift frequency in opposite directions. One would have to conclude that single-site swept frequency data (Figure 11) are more informative than the corresponding single frequency measurements (Figure 10a) because a much more robust quantification of damping effects is possible.

## 6. CONCLUSIONS

This Phase I feasibility study demonstrated quite convincingly that debonds at a rubber-to-metal interface are highly observable using a balanced oscillator fitted with an accelerometer to detect motion of the "nodal" support. A tacky coupling agent (as discussed in Section 4.1) appears to be very important to the success of the method. A Phase II proposal<sup>(11)</sup> was written and favorably received by the Navy's technical review committee. Reference 11 indicates how both the physical probe structure and numerical data processing can be significantly improved and automated, targeting

utility for debond detection in the commercial production environment. In Phase II we anticipate integrating a CR probe with spatial scanning hardware and software to provide essentially complete inspection coverage of manufactured end items. Perhaps the only additional observation that might be mentioned to establish perspective is the following:

One of the piezoelectric ceramic cylinders used to fabricate the Phase I CR probe was accidentally chipped during handling. The unit had to be reworked resulting in a slightly unbalanced "balanced oscillator". This is obvious from a number of data records associated with probe operation in air (Figure 8 for example). The output from the nodal mount accelerometer is maximum when ideally it should be very small. We believe that bonds and debonds will be more highly distinguishable if the test specimen is coupled to a truly balanced probe, i.e., one that produces a null output in the absence of sample material. It is recommended that future work pursue this avenue of investigation.

## 7. ACKNOWLEDGMENTS

We would like to express our appreciation to the Naval Sea Systems Command for supporting this work under the Small Business Innovation Research (SBIR) Program. The project was conducted under Contract No.

N00024-88-C-5123 and administered by Mr. Charles Clark as the Contracting Officer's Technical Representative (COTR). Dr. Yoseph Bar-Cohen and Mr. David Del Rio of Douglas Aircraft, Co. were instrumental in helping us compare the Phase I CR probe with commercial instrumentation.

#### REFERENCES

1. Bilgutay, N.M., Xing, L. and McBearty, M., "Development of Non Destructive Bond Monitoring Techniques for Ultrasonic Bonders," *Ultrasonics*, **24**, 307 (1986).
2. Bar-Cohen, Y., Mal, A.K., and Yin, C.C., "Ultrasonic Evaluation of Adhesive Bonding," to be published in the *Journal of Adhesion*, 1989.
3. Kwun, H. "Through Transmission/Pulse-Echo Ultrasonic Equipment Evaluation," Southwest Research Institute, San Antonio, TX, Final Report SwRI Project 17-7958-834, September 1987.
4. Guyott, C.C.H., Cawley, P., and Adams, P., "Use of the Fokker Bond Tester on Joints With Varying Adhesive Thickness," *Proc. Instn. Mech. Engrs.*, **201**, (B1), 41 (1987).
5. Guyott, C.C.H., Cawley, P., "The Ultrasonic Vibration Characteristics of Adhesive Joints," *J. Acoust. Soc. Am.* **83**(2), 632 (1988).
6. Guyott, C.C.H., Cawley, P., and Adams, R.D. "The Non-Destructive Testing of Adhesively Bonded Structure: A Review," *J. Adhes.* **20**, 129 (1986).
7. Botsco, R.J. and Anderson, R.T., "Ultrasonic Impedance Plane Analysis of Aerospace Laminates," *Adhesives Age*, June 1984, pp. 22-25.
8. NDT Instruments, Inc., "Ultrasonic Physics of the Bondascope," Huntington Beach, CA, Report No. 2100, March 1982.
9. Cagel, C.V., "Ultrasonic Testing of Adhesive Bonds Using the Fokker Bondtester," *Materials Evaluation*, **24**, 362 (1966).
10. Hagemaiier, D.J., "NDT of Adhesive Bonded Structure," presented to the Air Transport Association of America, 1977 NDT Forum, Hartford, CN, September 13-15, 1977, Paper No. 6652 published by Douglas Aircraft Company.
11. Teller, C. M., Bray, A.V., and Smith, R.L., "Improved Transducer Production Testing for Rubber-to-Metal Bonded Joints, Phase II," Texas Research Institute, Inc. proposal 8048:CMT submitted under the NAVSEA SBIR Program, June 8, 1988.
12. Widener, M.W. "The Development of High-Efficiency Narrow-Band Transducers and Arrays," *J. Acoust. Soc. Am.* **67**(3), 1051 (1980).
13. Guyott, C.C.H., Cawley, P., and Adams, R., "Vibration Characteristics of the MK II Fokker Bond Tester Probe," *Ultrasonics*, **24**, 318 (1986).



# NON-DESTRUCTIVE TESTS OF MOISTURE-INDUCED CURRENT LEAKAGE ON IC PACKAGES

D. Kenyon, E. Thumm, C. O'Brien, R. Maglic  
Honeywell Solid State Electronics Division  
Colorado Springs, Colorado 80906

An IC device having high input impedance may drift when in humid environment. Package surface conductance between input leads is found to be of the order of  $10M\Omega$  and dependent on relative humidity. For low humidities, surface resistance ( $R_s$ ) becomes large ( $100 G\Omega$ ) and negligible in comparison to input impedance.

Complex time dependence of  $R_s$  can be satisfactorily fit assuming a water dominated resistor and a parallel resistor operating with different mechanisms: although lead-to-lead current on surface is small, significant power is pumped into the water-based resistor. Evaporation of the water accounts for sharp rise in time of observed resistance  $R_s(t)$ .

For later times ion motion becomes dominant, causing a minimum of  $R_s(t)$ .

By applying evaporation/ion-motion model, a completely coherent model for leakage current is obtained. Basically, it agrees with results of some published work on humid surface resistance. Our model can explain experimental results without invoking "negative capacitance" at low frequencies.

## INTRODUCTION

Surface resistance of most IC packages becomes low in presence of humid environment. Current leakage resulting may have unpredictable and fatal consequences for the packaged unit. In this paper we describe a standard, high gain operational amplifier, Figure 1 shows its partial block diagram. The particular problem encountered with the

packaged unit was significant voltage output drift in time, drift that was totally unacceptable. Figure 2 shows an especially bad case of the drift occurring during only 70 sec; note that our experimental set up allowed measurement of the input current  $I_{IN}$ . Drift of  $I_{IN}$  caused a proportional drift of  $V_{out}$  since the gain of the opamp was

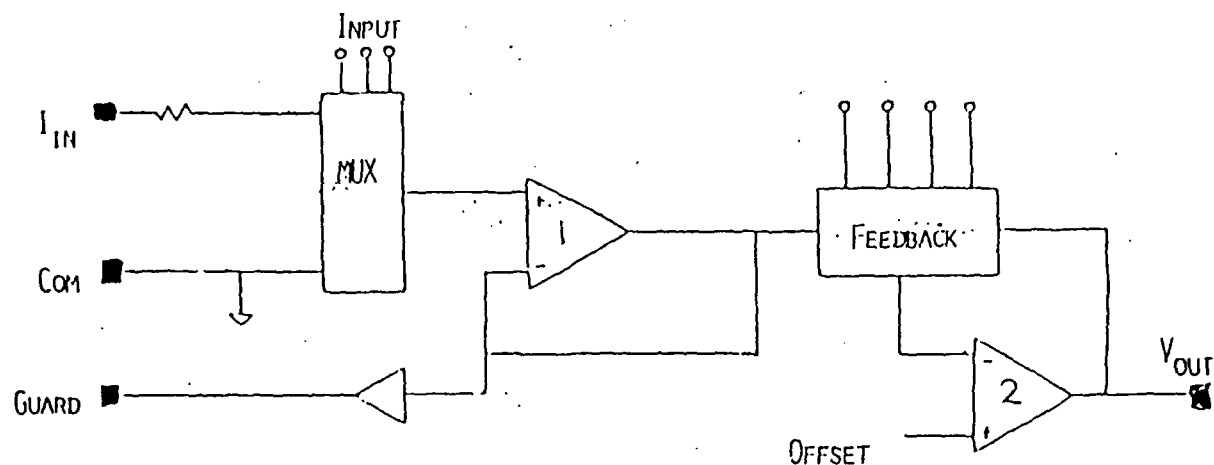


FIGURE 1. SIMPLIFIED BLOCK DIAGRAM OF PREAMPLIFIER CIRCUIT

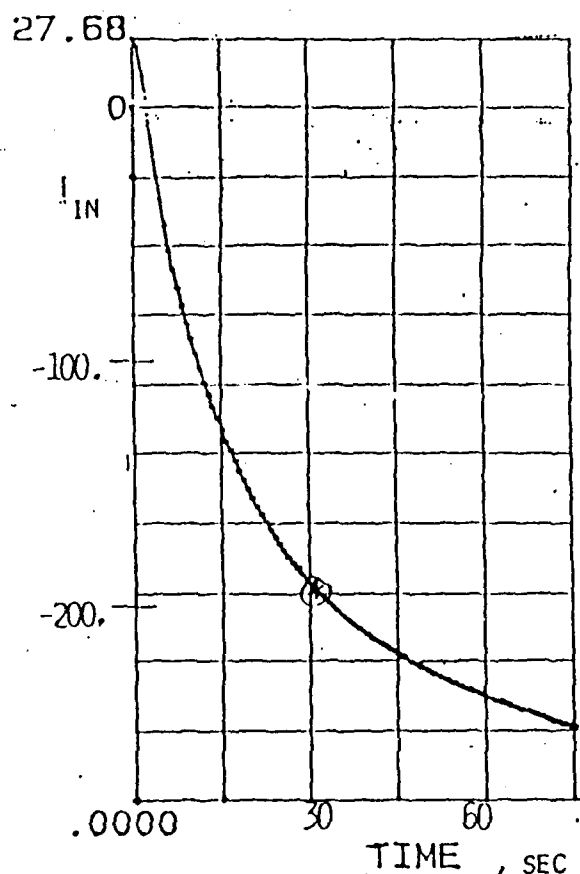


FIGURE 2. INPUT CURRENT DRIFT EXAMPLE; MAXIMUM ALLOWABLE DRIFT IS 2nA.

essentially constant in time and temperature independent. High gain value defined acceptable/unacceptable current drift value: 2nA in 150 sec.

#### MOS INVERSION

In looking for sources of drift, almost the first candidate was formation of a parasitic MOS transistor. Such a leakage path for current could be created throughout an OSFET (a MOSFET without a metal, Figure 3b). If an inversion of mildly doped N-Epi could be achieved by the presence of negative ionic charges accumulated on the silicon dioxide top surface, a parasitic P-channel would be formed. It would conduct current for P-type drain of a JFET, Figure 3a,

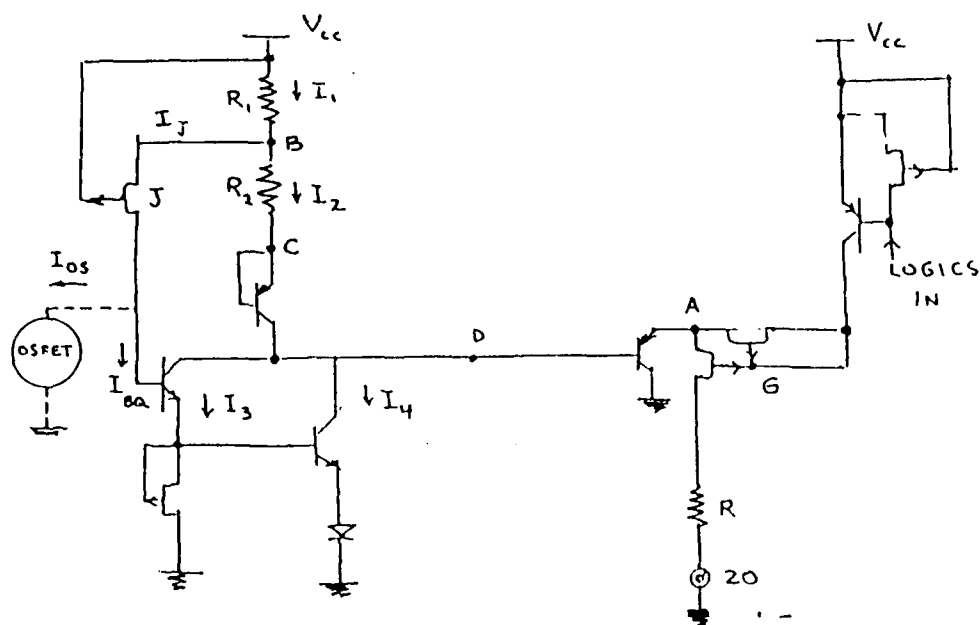


FIGURE 3A. SIMPLIFIED PORTION OF OPAMP INPUT

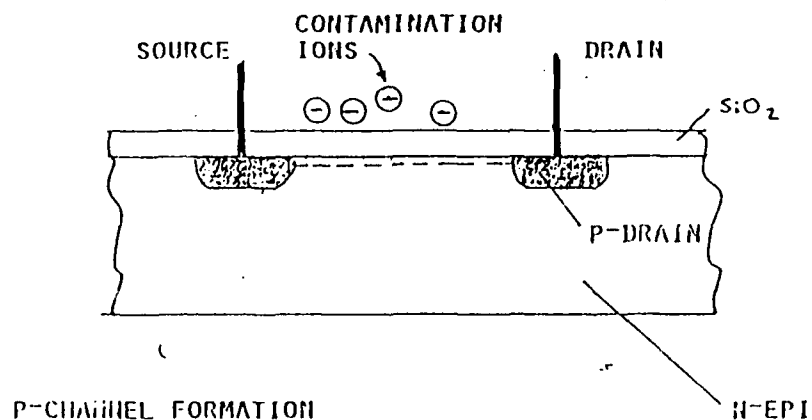


FIGURE 3B. PHYSICAL ORIGIN OF OSFET

eventually causing a drift. Figure 3a gives a portion of the input circuit for our opamp. It can be shown that an increase in  $I_{os}$  of the OSFET would result in  $dI_1 < 0$  of Figure 3a. This raises potential of points B, D, and eventually A, "opening" JFET near it and finally increasing  $I_{IN}$  in the negative direction. This would account for the observed drift. Our detailed circuit

analysis showed however, that quantitatively, insufficient drift was caused this way to explain the drift result.

A possible method for parasitic P-channel formation is, of course, to increase the value of  $V_T$ , threshold voltage for N-Epi inversion. This reduces the leakage current which would be equivalent, in our case, to JFE

current, given by (saturated unit)

$$I_{SD} = K(V_{SG} - V_T)^2$$

with S, G and D standing for words source, gate and drain. Increased  $V_T$  (higher Epi implant) helped indeed make units more resistant to noise.

#### MOISTURE INDUCED DRIFT

A curious, simple test led us to examine moisture on the package

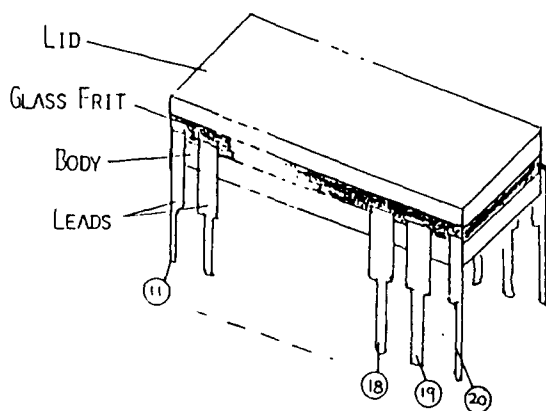


FIGURE 4. CERAMIC PACKAGE FOR THE OPAMP

as a cause of drift: while testing the drift of the input current  $I_{IN}$  we noticed large effect of moisture as coming from human breath. A series of subsequent experiments reinforced this finding however. A particularly sensitive package area was pins 19 and 20 as shown on Figure 4. These leads enter through a Glass Frit into the package; the opamp is situated inside the package body. The cavity is normally closed at 360° C with the lid (also shown).

Extensive studies were performed on cavity gas content, particularly its moisture content. Residual Gas Analyzers (RGA) were used for this purpose. The leading idea was that, perhaps, a gas leak through the frit may cause the drift. For this particular reason the frit material was changed from KC400 to KC1M both manufactured by Kyocera INC. As shown, eventually, an improvement resulting from this switch was due to the surface state of the frit, in addition to it's other advantages.

During our drift test a DC voltage of 8 volts is applied between pins 19 and 20. If 2nA drift current is the allowed limit, minimal resistance is 4GΩ. Superficial resistance measurement between pins 19 and 20 gave low, MΩ readings, depending on relative humidity RH, in the environment.

#### MOIST SURFACE RESISTANCE

In order to measure  $R_S$  between pins 19 and 20 without any bias from the circuit, an empty package was selected.  $R_S$  was measured, with a Keithley 617 electrometer, under controlled environmental conditions: relative humidity, air pressure and temperature. These were regulated with a device ("coffee pot") shown in Figure 5. The RH meter was a commercially available instrument HI 8564 thermo-hygrometer capable of temperature measurements as well. Air pressure/humidity was adjusted at constant temperature by allowing water evaporation into the chamber; a vacuum system was used to obtain right pressure.

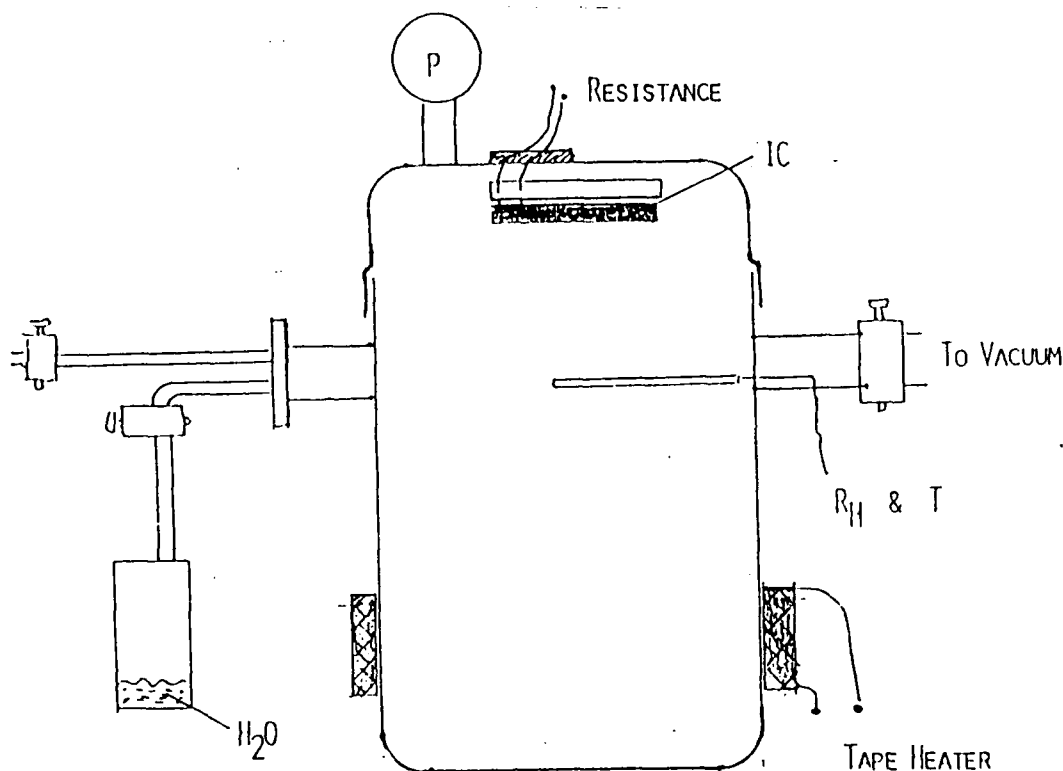


FIGURE 5. CHAMBER FOR CONTROLLED MEASUREMENT OF RESISTANCE; RELATIVE HUMIDITY, AIR PRESSURE AND TEMPERATURE MAINTAINED CONSTANT

First resistance measurement  $R_s(t)$  showed shape, Figure 6, we could fit only after developing our "evaporation theory" given below.

Between leads 19 and 20 there is a "blanket" of water of length  $a \approx 1\text{mm}$  width  $b \approx 1\text{mm}$  and about 15A/layer thickness. the number of water layers are related to relative humidity as reviewed in literature [1]. For  $R_H \approx 98\%$  the number of layers is roughly 100: thus  $h = 1500A = .15\mu\text{m}$ , and

$$V = abh \sim 1.5 \cdot 10^{-7} \text{ cm}^3$$

To evaporate this volume of water in time  $t_0$

$$P \cdot t_0 = \rho^* L V \quad (1)$$

where  $\rho^* = 1 \text{ gm/cm}^3$  is water density and  $L = 539.55 \text{ cal/gm}$  is heat of evaporation for water;  $P = U^2/R = .32\mu\text{W}$  (input power when surface resistance is  $200 \text{ M}\Omega$ ). Equation (1) gives for  $t_0 \sim 17.6 \text{ min.}$ , in rough agreement with

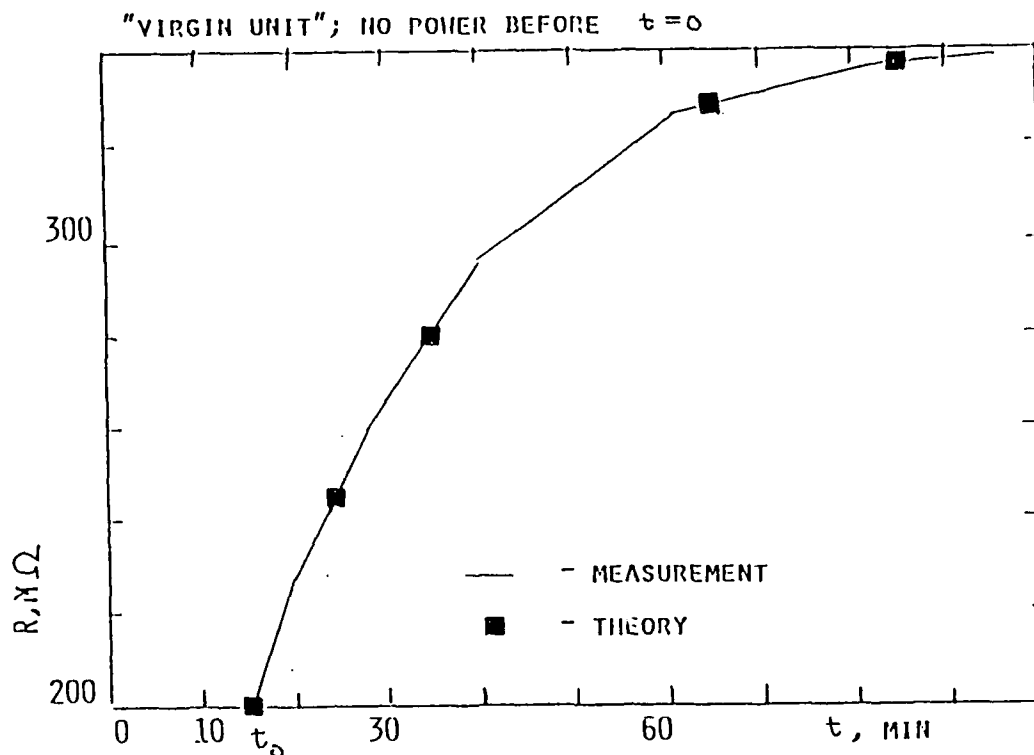


FIGURE 6. SURFACE RESISTANCE MEASUREMENT

experiment, Figure 6.

Water evaporates in time with "blanket" thickness  $h$  reducing and resistance  $R_s$  increasing

$$dR = -\rho \frac{a}{b} \frac{dh}{h^2} = -\frac{R}{h} dh \quad (2)$$

and

$$\frac{dr}{dt} = -\frac{R}{h} \frac{1}{ab} \frac{dV}{dt}$$

But change in volume due to evaporation (power  $P$ ) is

$$dV = -\frac{Pdt}{\rho^*L} = -\frac{U^2}{\rho^*LR}dt \quad (3)$$

Finally, upon substitution

$$\frac{dR}{R} = \frac{dt}{\tau}$$

where we introduced

$$\tau = \frac{a^2 \rho^* L \rho}{U^2} \quad (4)$$

thus

$$R_t = R_o e^{\frac{t}{\tau}} \quad (5)$$

Numerically  $\tau$  can be very small, of order of 5 sec and up to a minute, depending on specific resistance  $\rho$  of contaminated water.

We obtained an excellent fit to measured resistance curve  $R_s(t)$ , Figure 6, by assuming  $R_t$  parallel to a constant resistance  $R_p$ . The origin of  $R_p$ , although logical, can not be claimed with certainty. It

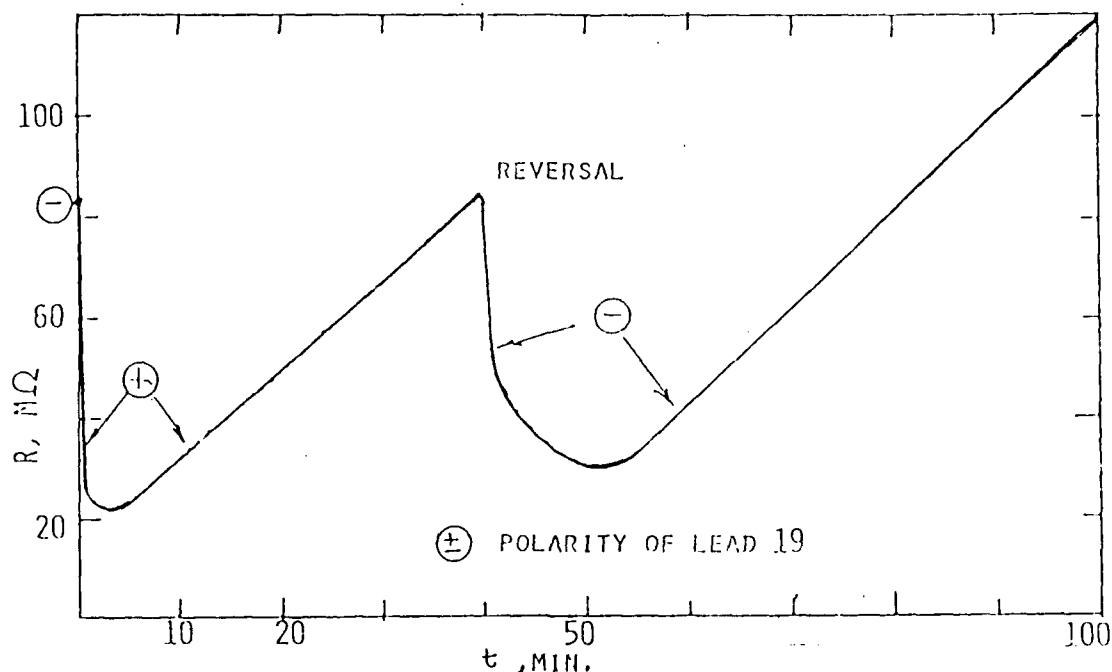


FIGURE 7. RESISTANCE MEASUREMENT WITH REVERSIBLE DC VOLTAGE POLARITIES

may be due to last couple of water layers + dissolved glass frit. Or, it may be due to the surface layer of frit itself after absorbing the moisture. In any case, the value of  $R_p$  is  $\sim 340\text{M}\Omega$ , as seen from the data, Figure 6.

Thus

$$R_s = \frac{R_t R_p}{R_p + R_t} = \frac{R_p}{1 + \frac{R_p}{R_t} e^{-\frac{t}{\tau}}} \quad (6)$$

Fit of experimental  $R(t)$  was obtained with

$$\tau = 17\text{min.} \quad R_0 = 486\text{M}\Omega \quad (7)$$

Value of  $\tau = 17\text{min.}$  implies from equation (4)  $\rho = 3000\Omega\text{cm}$  (a rather high value, characteristic for clean water).

Ion motion was suspected for the shape of  $R_s(t)$  shown of Figure 7. Note that the resistance between pins 19 and 20 was measured with, first negative power at pin 19; then power polarity was reversed and after some 40 min. reversed again. After removing the power the internal voltage source was measured,  $U_s^+$  and  $U_s^-$ . One half of the difference

$$\Delta U = \frac{1}{2} (U_s^+ - U_s^-) \quad (8)$$

was identified as true internal emf; the result was .82 volts. Now since the capacitance between 19 and 20 was measured to be 30pF, the moving ion charge is

$$q = C \cdot \Delta U = 2.5 \cdot 10^{-11} \text{ C} \quad (9)$$

and number of ions is,

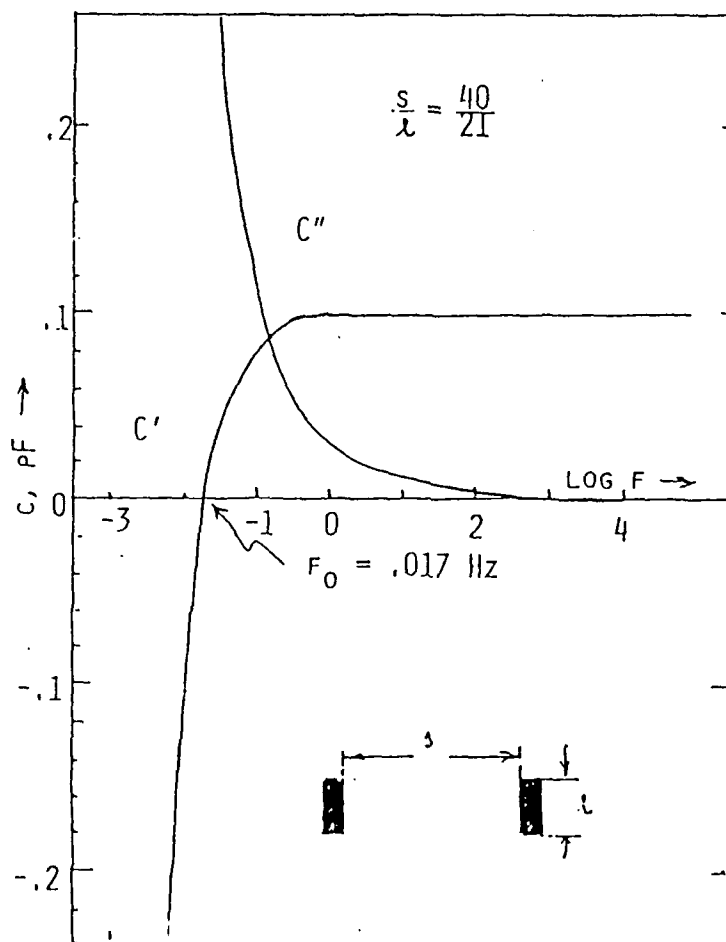


FIGURE 8. JONSCHER'S IMPEDANCE MEASUREMENT FOR  $s/l = 40/21$

$N_T = q/e = 1.5 \cdot 10^8$ . Since these ions are on the surface  $a \cdot b = .01 \text{ cm}^2$ , we have

$$N_S = 1.5 \cdot 10^{10} \text{ cm}^{-2} \quad (10)$$

for the surface density of contamination. This number seems to be in the right range.

Finally, one can speculate of the origin of  $R_0$ , maximum resistance of water, at  $t = 0$ . If  $N_T$  ions are inside volume  $abh$ ,

$$R_0 = \frac{1}{eNv} \frac{a}{bh} = 486 \cdot 10^6 \Omega \quad (11)$$

giving  $Nv = 8.6 \cdot 10^{12} \text{ cm}^{-2} \cdot \text{sec}^{-1}$ . By using  $N$  from equation (10), one finds ion velocity

$$v = .0086 \text{ cm/sec}$$

and travel time  $\Delta t = 11.6 \text{ sec}$ . The latter number is born out by experimental data. It is interesting to note that if an AC signal was applied to pins 19 and 20, a resonance would occur according to above at

$$f = \frac{1}{\Delta t} = .086 \text{ Hz} \quad (12)$$

#### NEGATIVE CAPACITANCE

Recently Owede and Jonscher [2] measured surface impedance  $Z^*$  of dielectric surfaces such as glass, silicone nitride etc. They interpreted the impedance  $Z^*$  as due to a capacitance exclusively

$$Z^* = \frac{1}{i\omega C^*} \quad (13)$$

with

$$C^* = C' - iC''$$

Measurements were done with flat electrodes (width  $l$ ) spaced at distance  $s$  from each other. For  $s/l = 40/21$ , see Figure 8, their  $C'$  goes through zero at  $f = 0.017 \text{ Hz}$ . If the impedance  $Z$  was represented as normally done by EE engineers

$$Z = R + iX$$

their  $C'$  and  $C''$  could be related to  $R$  and  $X$  by

$$R = \frac{1}{\omega} \frac{C''}{C'^2 + C''^2} > 0 \quad (14)$$

$$X = -\frac{1}{\omega} \frac{C'}{C'^2 + C''^2} \geq 0$$



When  $C' < 0$  it follows that the reactance

$$X = L\omega - \frac{1}{C\omega}$$

is positive, the circuit behaves as an inductance

$$L_{ef} = - \frac{1}{\omega^2} \frac{C'}{C'^2 + C''^2} \quad (15)$$

At  $\omega = 2\pi \cdot 0.017 \text{ rad/sec}$

$L_{ef} \sim 2.5 \cdot 10^{13} \text{H}$ , a very large inductance, hardly due to some magnetic field coupling. Since  $L$  in the resonant circuit is an inertial element, we propose it's origin in ion masses. Indeed, if one writes Newton's equation for a charged particle of mass  $m$  moving in a media (dielectric constant  $\epsilon$ ) in direction  $x$ , under influence of an electric field  $E$ ,

$$\frac{dx}{dt} = - \frac{eE}{m} t + v_0 \quad (16)$$

— where we assumed  $E$ -field in negative  $x$ -direction and particle velocity  $v_0$  half-way between pins 19 and 20. The electric field will slow down the particle and eventually reverse its velocity; half-way back it will be  $-v_0$ . If the frequency of the AC-field is right, the field direction will then change and the process repeats. Quarter of period is thus from (16)

$$\frac{T}{4} = \frac{v_0}{eE} m = \sqrt{\frac{ma}{eE}} \quad (17)$$

since  $v_0 = 2x_0 \frac{eE}{m}$  and amplitude of oscillation  $x_0 = a/2$ . Thus

$$\omega = \frac{2\pi}{T} = \frac{\pi}{2} \sqrt{\frac{eE}{am}} \quad (18)$$

Now, if we equate above frequency to an equivalent  $L/C$  circuit,

$$\omega^2 = (LC)^{-1} \text{ and}$$

$$L = \frac{4}{\pi^2} \frac{a^2 m \epsilon}{e CU} \quad (19)$$

with  $E = U/\epsilon$ .

Numerically, for  $a = 1 \text{mm}$ ,  $m = 1.64 \cdot 10^{-27} \text{ n Kgm}$ ,  $e = 1.6 \cdot 10^{-19} \text{ C}$ ,  $U = 8 \text{ volts}$  and  $C/\epsilon \sim 2.2 \cdot 10^{-20} \text{ F}$  we get

$$L = 2300 \text{ n Henry}$$

$n$  in above result is the ratio of ion mass to that of a proton. It is noteworthy to mention that Eq. (19) gives for,  $L$  mega, Henries for parameters of reference cited, [2]; further improvements of Eq. (19) would bring it closer to the  $L$ -value extracted from the data in [2]. This origin of observed inductance seems to us more acceptable than the one offered by Jonscher [3].

Acknowledgement: We wish to thank Floyd Buhler, of Honeywell SSEd for his continuing support and Dr. Sekela and M. Todd for early discussions on the topic.

#### REFERENCES

- [1] W.A. Yager and S.O. Morgan, J. Phys. Chem. 3, 2026 (1931)
- [2] E.F. Owede and A.K. Jonscher, J. Electrochem. vol 135, 7, 1757 (1988)
- [3] A.K. Jonscher, J. Chem. Soc. Faraday Trans. 2, 1986, 82, 75-81

# COMPUTER-BASED INSTRUCTION TO TRAIN NDE TECHNICIANS

G.P. Singh  
W.R. Tweddell  
Karta Technology, Inc.  
San Antonio, TX

## ABSTRACT

Over the past 20 years computers have been increasingly used for training in business, industry, and the military. However this technology has not been used until recently for training NDE technicians. This paper describes two general types of computer based training methods, computer aided instruction (CAI) and intelligent tutoring systems (ITS, a.k.a. intelligent computer aided instruction). It also examines a CAI program, the Expert Training System Version 3.0, used for training and testing NDE technicians. Other topics include a view of some potential uses of computer simulators to train NDE personnel, and benefits realized by other industries using computers to supplement conventional training procedures.

## 1. INTRODUCTION

Computer-based training has its roots in early teaching machines developed by Pressey in 1927 and Skinner in 1958<sup>(1)</sup>. These were the first attempts at building interactive teaching devices. The foundation of Skinner's work was based on the theory of operant psychology. This theory of instruction was the foundation for the linear-programmed instruction methodology used in the 60's and early 70's, and which is still used for much of the classroom training of NDE technicians.

Computer based training can be divided into two general types: computer aided instruction (CAI) and intelligent tutoring systems (ITS). Computer aided instruction comes from an application of Skinnerian behaviorism in which a linear small-step immediate feedback scheme of learning is advocated. Intelligent tutoring systems incorporate artificial intelligence (AI) modules and are based on the Socratic and other methods which advocate learning by discovery.

The development of intelligent tutoring systems entailed combining experience from computer science, psychology, and education to simulate a one-to-one student/teacher relationship using a computer acting as the teacher. CAI is an extension of the linear-program methods in which there is no modification in the instruction given to meet a student's specific needs and/or weaknesses.

In a recent review of published and unpublished studies dating from 1980 to 1987 that dealt with the effectiveness of computer based training<sup>(2)</sup>, two discoveries reflect the potential benefits of aggressively pursuing its use for training NDE technicians. First, it was found that adult and college population benefit most from computer-based training. Second, science or technical simulations seem to be the most effective application than other content areas.

Some of the benefits realized by other industries using computer based training are cost effectiveness, availability,

consistency, retention of knowledge, and documentation<sup>(3)</sup>. These are self contained systems that require no additional staffing. Often training can be accomplished without removing personnel from their job sites. Computer-based training is less expensive than consultants and training schools.

Computer-based training is always available and can be in operation 24 hours a day. Personnel can use intelligent systems as job-aids when experts are not available. It can also promote training by eliminating overtime and shift coverage expenses while shortening training time. Personnel can leave a training session and they are automatically able to return to where they left off.

Computer-based training is consistent and not dependent on the available time and training skills of supervisors. Computers also have an infinite amount of patience and free supervisor's time for other tasks.

Intelligent tutoring systems have the capability to retain an expert's knowledge and preserve it for job aids and instructional purposes. Turnover rates would no longer cause a threat to efficiency due to a drain of man-years of experience.

And finally it is extremely important today to maintain complete and accurate documentation of operator training. The computer can be used to track each trainee through their training and formal testing. It also assures trainee honesty.

## 2. COMPUTER-AIDED INSTRUCTION (CAI)

Frame-based CAI uses three methodologies for training, tutorials, drill and practice, and simulation. Tutorials present segments of information generally related to or extended from the previous lesson. They consist of presenting stimulus information, providing learning guidance, and in some instances provide feedback. Tutorials are particularly useful when the material is new.

A drill and practice session consists of some sort of performance elicitation combined with feedback. They are particu-

larly useful for practicing rule using, discrimination, and concepts.

Simulation consists of presenting the objective, presenting the stimulus, eliciting performance and providing feedback. This type of instruction places the student in a somewhat real world environment. Simulations are especially useful for teaching rule using and problem solving.

Computer aided instruction is usually frame based in the nature of its presentation. Many people think of CAI to be unrealistic, rigid, and uninteresting. One of the keys to the emerging success of CAI lies in its increasing use of interactive graphics and visuals. The success of interactive video instruction stems from the fact that people learn more through sight than through all the other senses. Studies have shown that these systems can reduce learning time by as much as 50% while increasing retention by as much as 80%<sup>(4)</sup>.

For example the University of Illinois chemistry department at Champaign-Urbana has developed a CAI system to supplement laboratory requirements for general chemistry<sup>(5)</sup>. It uses CD ROM disks to store visual information and is linked to an IBM PS/2 Model 30 using IBM InfoWindow displays. The InfoWindows display includes a touch screen, audio capabilities, and a voice synthesizer. In lessons students can combine different quantities of reactants, set temperatures, and observe the results. Many experiments can be performed that are too complicated, dangerous, or time consuming to be performed under actual lab conditions. The program has helped to reduce the strain on laboratory space, time, and supervisors.

At this time there are only a few CAI systems available for training NDE personnel. One of these is the Expert Training System (ETS) Version 3.0 developed by Karta Technology. The program contains question files that administer either exams or training sessions. The question files are composed of questions and answers taken from the ASNT test booklets. Question modules are available for ultrasonic testing (UT), radiographic testing (RT), magnetic particle testing (MT), penetrant testing (PT), and eddy current testing (ET). Levels

I, II, and III. These are contained in separate files as shown in Figure 1.

ETS can be used to generate sets of questions to be printed out for written exams, or to administer exams or training sessions on the computer. An example of the exam screen is shown in Figure 2. Questions are shown in the upper portion of the screen and the student selects one of the choices listed below it by typing in A, B, C, or D. Scores are not displayed during exams, but are automatically recorded in a separate database file that corresponds to the trainee's Social Security Number. This database can only be accessed by using a special administrator password.

Figure 3 illustrates the screen that a trainee would see when using the program in the training mode. Note that an accumulative score is shown in the bottom right hand of the screen. When an incorrect answer is chosen a hint appears in the middle of the screen (Figure 4) to aid the trainee in selecting the correct answer on their next attempt. Even correct

answers are followed in many cases by an explanation on why the answer was correct.

ETS is capable of presenting visual images for tests and training purposes through a random access 35mm slide viewer. Karta Technology is currently investigating using slide modules that will offer visual interaction with the program. These programs will focus on the fundamentals of different NDE methods especially RT, PT, and MT, and can be customized to meet the end user's requirements. ETS is also an authoring system. It contains a built-in word processor so users can create your own question files, with or without visual aids.

This system is classified as CAI because it does not incorporate an AI module to continually adapt the learning environment. Questions are presented in a random fashion and even though a primitive coaching method is used in the form of hints and explanations the program does not diagnose misconceptions or take any corrective actions to further explore the level of knowledge the student already has.

Test	Certification	Files	Exit
Train			
Exam			
Print			
	ETLEV_1	25k	
	ETLEV_2	24k	
	ETLEV_3	20k	
	MTLEV_1	44k	
	MTLEV_2	42k	
	MTLEV_3	27k	
	PTLEV_1	68k	
	PTLEV_2	44k	
	PTLEV_3	41k	
	RTLEV_1	77k	
	RTLEV_2	93k	
	RTLEV_3	115k	
Question File Database			
File Name : ETLEV_1			
Category : Eddy Current Testing Level I			
Sub Category : Copyright (1980) ASNT			
Remarks : This file not accessible when using FILES options.			

Figure 1. ETS test selection screen showing the listing of separate question files for ET, MT, PT, and RT, Levels I, II, and III.

Examination Question

Upon completing an x-ray exposure and turning the equipment off:

Choices

- A. personnel should wait for a few minutes before entering the exposure area.
- B. personnel should wear a lead-lined apron before entering the exposure area.
- C. personnel should enter the exposure area without fear of radiation exposure.
- D. personnel should take a reading with a survey meter before entering the exposure area.

Press choice letter:                      Question: 3 of 10

Figure 2. An example of an ETS test screen when in the exam mode.

Training Question

Upon completing an x-ray exposure and turning the equipment off:

Choices

- A. personnel should wait for a few minutes before entering the exposure area.
- B. personnel should wear a lead-lined apron before entering the exposure area.
- C. personnel should enter the exposure area without fear of radiation exposure.
- D. personnel should take a reading with a survey meter before entering the exposure area.

Press choice letter:                      Question: 7      Score: 1 out of 10

Figure 3. An example of an ETS test screen when in the training mode. Note the score keeper at the bottom right of the screen.

<p align="center"><b>Training Question</b></p> <p>Upon completing an x-ray exposure and turning the equipment off:</p>
<p align="center"><b>HINT</b></p> <p>A. Why? Once the power is off no more X-rays are being produced and they don't linger about.</p>
<p>B. personnel should wear a lead-lined apron before entering the exposure area.</p> <p>C. personnel should enter the exposure area without fear of radiation exposure.</p> <p>D. personnel should take a reading with a survey meter before entering the exposure area.</p>

A is INCORRECT, press any key ...      Question: 7      Score: 1 out of 10

Figure 4. An example of an ETS test screen showing a hint which appears only when the program is in the training mode.

This is only the beginning of what today's powerful desktop computer systems can offer to increase the efficiency and effectiveness of NDE training. The next section focuses on intelligent tutoring systems which are the first steps in fully utilizing a modern PC's capabilities. They have not been applied, as of yet, to training NDE technicians.

### 3. INTELLIGENT TUTORING SYSTEMS

Intelligent tutoring systems or intelligent computer assisted instruction use an AI module to create a learning environment that closely resembles what actually occurs in a one-on-one student/teacher relationship. Intelligent tutors focus on the learning strategies ignored or only partially addressed by traditional CAI or other non-technology instruction. Designers of ITS are interested in distinguishing the difference between experts and novices. They then use these distinctions between the groups to allow the presentation of instruction to be changed in order to convert novice behavior into expert behavior.

There are five approaches used in ITS to convey this knowledge: the Socratic method, coaching, diagnostic tutors, the

microworld concept, and articulate expert systems. In the Socratic method the program engages the student in a two-way conversation to find concepts in which the student is having difficulty understanding. Socratic teaching then uses what the student already knows to modify their misconceptions. The Socratic method is best suited for teaching conceptual or procedural learning tasks. Coaches observe student learning and provide advice to improve the student's performance and mainly used to teach problem solving. Diagnostic tutors "debug" a student's work and are guided by a "bug catalog". They find the misconceptions students have in solving a problem and attempt to correct them. Diagnostic tutors are used to teach subjects that deal with less conceptual more rule intensive subjects such as computer programming and algebra. The microworld concept involves the use of realistic graphics that allow a student to explore a problem domain such as geometry, physics, or music. Articulate expert systems allow a student to practice decision-making and problem-solving skills. They can be also used as job aids. Of these five approaches the Socratic method and coaching have gained the most widespread use.

Intelligent tutoring systems are composed of three modules in order to carry out these functions: the expertise module, the

student model, and the tutorial module. Interaction between the three modules is illustrated in Figure 5. The expertise, or problem solving module contains the domain knowledge the system intends to teach. The information is obtained through consultation between a knowledge engineer and a subject matter expert. This is usually combined with knowledge from manuals and texts. The idea is to have a knowledge base module that can both generate solutions to previously encountered teaching situations and make inferences from incomplete measures of student input data.

The student model assesses the users current state of knowledge and makes hypotheses about their conceptions and reasoning strategies used to achieve their current knowledge state. One method used to accomplish this is the overlay method in which the student's knowledge is considered as a subset of the expert's knowledge. This comparison is used to set the pace, subject area, and level of difficulty.

The tutorial module contains rules on what information is to be presented and when it is to be presented. This is done by an inference engine which makes decisions such as selecting problems to be solved, critiquing performance, providing assistance upon request, and selecting remedial materials.

One way to expand on the Expert Training System idea would be to incorporate an inference mechanism that would allow a further degree of coaching. A student's misconceptions in an area, say transducers, could be diagnosed and appropriate written, graphical, or visual information could be given to clarify the error. This would be followed by more questions concerning transducers. A certain skill level would have to be reached before progressing onto a higher level of difficulty. Automatic reviews of previous sessions would also be included.

Using a Socratic approach for ETS, questioning would cover general principles in the beginning working towards more specific concepts. For example the properties of radiation would begin with the question "How do X-rays differ from gamma rays?" From here the program could follow a number of paths branching into the various aspects of radiation such as scatter radiation, its effects on film, dosage limitations, etc.

The ability to make the ETS more interactive though the addition of graphics and visuals provided by a slide projector or even a video disk would be much simpler than creating a full blown ITS, but the advantages an ITS offers is worth the extra effort and development cost. Once complete the knowledge contained in an ITS can be continuously updated and easily transferred for distribution.

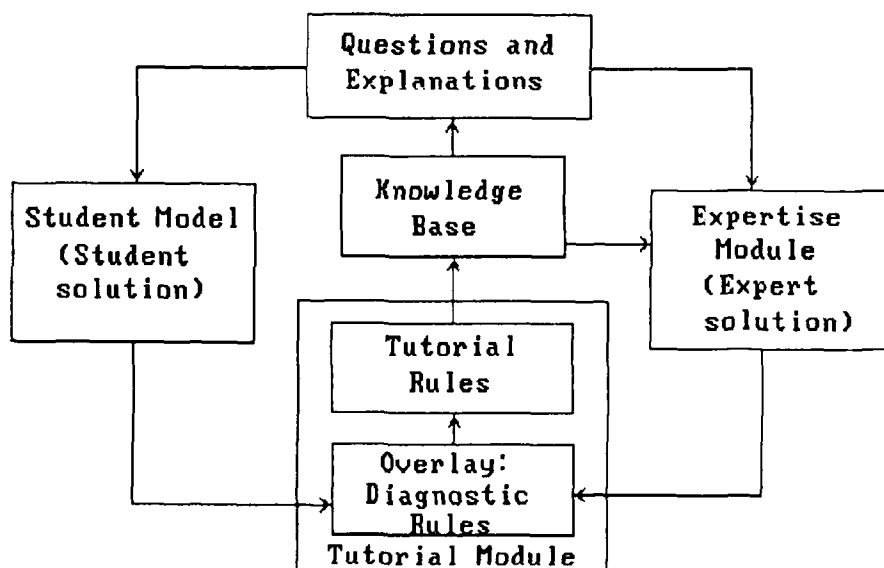


Figure 5. Block diagram illustrating the interaction of the different modules in an intelligent tutoring system.

#### 4. POTENTIAL USES OF COMPUTER BASED TRAINING FOR NDE

One example of what lies ahead in using computer based training for NDE is an ultrasonic simulator developed in England. In this system a computer is connected to the analog display of actual A-scanning equipment and generates various defect signals. The student scans a special test block with an actual transducer and the computer generated results are shown on the equipment's CRT. Defect signals from actual scans are stored in the computer's memory. The type of defect to be shown and its position on the flat test block are set by the instructor. The program also records the scanning pattern used by the student which can be analyzed later. Modifications are under way to simulate curved surfaces and angled-probe skewing. There are also plans to extend the simulator to an eddy-current model<sup>(6)</sup>.

Another type of CAI simulator for training RT technicians could also be developed. Within the program a true to life X-ray machine would be shown on the screen and controlled from there. They would be given a part to radiograph or they could select one of their own choice. The proper operating parameters would be stored in the computer's memory and the trainee's responses would be compared to this ideal radiograph.

The trainee would be responsible for entering the kV, mA, source-to-subject distance, exposure time, film type, etc., selected from an on-screen display. The computer would be connected to an external slide projector or video disk player and a copy of the resulting radiograph using parameters set by the trainee would then appear for their interpretation. Trainees could see the visual effects a change in kV or film speed would make on the resulting radiographic image. All this could be done without the danger of operating a real X-ray machine and without the expense of film and processing.

This type of system would be similar to the chemistry tutor developed at the University of Illinois in that it would allow the user to experiment and make possibly serious errors without serious consequences. It would also allow trainees and certified

personnel to gain experience beyond their normal working conditions.

Other RT modules would contain lessons on radiograph interpretation, manual film processing, automated film processing, gamma radiography, etc. The point is that the technology available today is far ahead of the methods in use today to train NDE technicians.

#### 5. CONCLUSION

CAI and ITS have much to offer in reducing the training time while increasing the performance of NDE technicians. CAI is only beginning to be used in NDE training and there are only a few fundamental systems currently being offered. CAI is usually frame-based, but can interact with the student by using visual and graphic displays. Intelligent tutoring systems model student knowledge to create a flexible learning environment. CAI is beginning to see use as a training tool for NDE training, but as of yet has not approached the level of sophistication found in its use in other industries. Interactive videos combined with CAI systems could act as the first step to developing intelligent tutoring systems for various NDE methods. From the success of computer-based training in other industries its use has much to contribute to the rigorous training and on the job experience needed to make a fully qualified NDE technician. It is cost effective, the technology is available, and it works when properly developed and applied.

#### REFERENCES

1. Kearsley, G. (1987) *Artificial Intelligence and Instruction*, Reading Massachusetts: Addison-Westley.
2. Furgang, S.R., Train Better by Computer: *Hydrocarbon Processing*, Jan. 1989, pp. 86-89.
3. Roblyer, M.D., The Effectiveness of Microcomputers in Education: A Review of Research from 1980-1987: *Technical Horizons in Education*, Vol. 16 No. 2, 1988.



4. Therrien, L. *Videos are Starring in More and More Training Programs. Business Week* 7 Sep 1987, pp 108-110.
5. Jones, L. & Smith, S. Lights, Camera, Reaction! The Interactive Videodisc: A Tool for Teaching Chemistry, *Technical Horizons In Education*, Vol. 16, No.7 1989.
6. Personal Communication, Phil Stoor, Riscley Lab, National NDE Centre Harwell, U.K.

FATIGUE INDUCED CHANGES IN THE  
MAGNETIC PROPERTIES OF FERRITIC  
STEELS

D. C. Jiles and D. Utrata<sup>+</sup>  
\*Center for NDE  
Iowa State University  
Ames, Iowa 50011

<sup>+</sup>Association of American Railroads  
South Federal Street  
Chicago, Illinois 60616

Abstract

Fatigue failures are the most commonly occurring modes of mechanical failure encountered in constructional components. Such failures, which occur without prior indication and therefore appear to be spontaneous, can have catastrophic effects. The objective of this study was to determine the suitability of magnetic inspection methods for detection of incipient fatigue failure. This paper discusses the existing state of knowledge of the mechanism of fatigue and reports on some promising preliminary results of magnetic inspection of fatigued specimens.

1. INTRODUCTION

Since fatigue failures are the most commonly occurring mode of mechanical failure in constructional components it is natural to look for some nondestructive method of predicting the remaining service life of a component. Dieter [1] has stated that more than 90% of service failures due to mechanical causes are a result of fatigue, and consequently it would be of great commercial benefit to retire the components for cause at an appropriate time. This should be neither too soon, because of the additional cost of unnecessary replacement, nor too late because of the cost of a catastrophic failure.

2. MECHANISM OF FATIGUE

An extensive introductory review of the mechanisms of metal fatigue has been given by Grosskreutz [2,3]. In

this it is shown that the continual stress cycling causes a build up of dislocations in the metal. If the stress amplitude is well below the normal yield strength  $\sigma_y$  of the material the number of stress cycles needed before fatigue occurs can be very large (eg.  $10^6 - 10^8$  cycles). Below a certain stress amplitude,  $\sigma_e$ , the endurance limit, it appears that the material can be cyclically stressed indefinitely without failure occurring. Fatigue failure therefore is only of interest for stresses in the range between  $\sigma_e$  and  $\sigma_y$ .

The fatigue properties of a specimen are normally plotted on an S-N curve which is a plot of stress amplitude against number of cycles to failure. However we should note immediately an important fact: the form of these curves is not solely a materials property. It depends strongly upon the surface finish of the material. Therefore two specimens cut from the same bar and otherwise identical would yield different S-N curves if their surface finishes were different. This crucial factor will be discussed later in our treatment of the fatigue crack initiation and growth. Attempts have been made to make the S-N curve characteristic of the material by using highly polished specimens.

2.1 DISLOCATION DENSITY AND THE  
FATIGUE PROCESS

The initial dislocation density in a very pure metal, before fatiguing

takes place can be as low as  $10^7$  per  $\text{cm}^2$ . Stressing the material, whether cycling in tension, compression or symmetrically about zero stress, causes the dislocations to move. In the early stages of fatigue the dislocations coalesce into bundles of dislocations which are separated by large volumes of material which are relatively free of dislocations. This is known as the "rapid hardening" stage since the mechanical hardness changes quickly in the early stages of fatigue. The dislocation density in the bundles can be as high as  $10^{13}$  per  $\text{cm}^2$ .

As the fatiguing progresses the number density of the bundles increases leaving smaller and smaller volumes between the bundles. In the saturation or equilibrium stage of fatiguing the mechanical hardness does not change much and the whole process seems to have settled into a kind of equilibrium. However as the process of fatiguing continues the bundles form together to give "cell walls" which eventually can divide grains into subgrains. The principal difference between the dislocation structures produced in fatiguing and unidirectional plastic deformation is that the arrangement of dislocations in a fatigue specimen is highly inhomogeneous whereas in unidirectional plastic deformation the dislocations are more evenly distributed. Furthermore the size of the dislocation "cells" formed during fatigue decreases with the stress amplitude.

## 2.2 FINAL STAGES OF FATIGUE: CRACK GROWTH AND FAILURE

The penultimate stage of fatigue, crack growth, almost always occurs in the last few percent of the fatigue process, and this leads to failure. It is difficult to give any more reliable general statement since the details are likely to be very specific to each given case. It is also difficult to give a meaningful statement about crack initiation since as Grosskreutz has noted there is no definition of how large a flaw has to be before it qualifies as a "crack".

In almost all cases the fatigue crack begins on the outer surface of the material or on an internal interface, such as a grain boundary. The cracks begin at regions with a high

stress concentration, and therefore any surface irregularity can seriously reduce the fatigue life. In materials such as steel which consist of two phases, fatigue cracks can also begin at the interface between the two phases.

## 2.3 CHANGES IN SURFACE CONDITION DURING FATIGUE

It has been suggested by Kramer [4] that the mechanism of fatigue is dependent only upon the mechanical properties of the surface layer. In his paper it was found that the strength of the surface layer increased with fatigue cycling and when the strength reached a critical value, independent of the cyclic stress amplitude, a fatigue crack began.

This lead to further investigations by Pangborn, Weissman and Kramer [5,6] of the surfaces of fatigued specimens using x-ray diffraction. In studies of aluminum 2024 alloy it was found that the surface layers did work harden more rapidly than the bulk material. It was also found that the dislocation density in the surface layer increased quickly during the first 20% of fatigue life, then remained fairly constant between 20 and 90% of fatigue life and increased rapidly again in the last 10%. These studies seemed to confirm the original work by Kramer which suggested that it was the accumulation of dislocations and associated stresses in the surface layer which control the fatigue failure.

## 2.4 DEPENDENCE OF FATIGUE ON MICROSTRUCTURE

The fatigue properties of materials are dependent on the microstructure, as might be expected given that the fatigue cracks can initiate on internal interfaces such as grain or phase boundaries. Aita and Weertman [7] have investigated fatigue in iron carbon alloys. In this it was found that the fatigue cracks propagated preferentially through the ferrite phase. A decrease in fatigue crack growth rate with increasing volume of brittle phases was observed in these alloys.

### 3. NDE OF FATIGUE

In view of the importance of fatigue failures there have been a number of studies designed to identify viable NDE methods for prediction of incipient failure. Among these there have been studies of the magnetic properties by Sanford-Francis [8,9,10] by Bose [11,12] and Mughrabi, Kutterer, Lubitz and Kronmuller [13].

Sanford-Francis [8,9] used an A.C. magnetic technique to detect changes in magnetic properties with fatigue. These results did show some changes in the response of this "magnaprobe" which were related to hardness of the material. These were related to changes in permeability. More recently an improved version of the "magnaprobe" has been used [10] to obtain advanced warning of impending fatigue failure.

Bose [11,12] has investigated the use of ferromagnetic hysteresis measurements for the evaluation of fatigue damage. The approach in the work of Bose has much in common with the present investigation. In his work he was able to show that the magnetic properties of steels were very sensitive to fatigue damage, in particular coercivity and remanence were found to correlate with the number of stress cycles at a given amplitude. The sharp increase in coercivity in the early stages of fatigue can be correlated with the rapid increase in dislocation density noticed by earlier workers.

#### 3.1 SCOPE OF THE PRESENT STUDY

Our investigations have been concerned with understanding the effects of applied stress, plastic deformation and fatigue damage on the magnetic properties of steels with the longer term objective of devising magnetic NDE techniques for determining the mechanical condition of steels.

Earlier studies of plastic deformation [14] indicated that the coercivity of steels increases after plastic deformation because of the resulting increase in dislocation density. The dislocations impede domain wall motion. Applied stress within the

elastic region however has a quite different effect [15] because the stress essentially changes the anisotropy of the material via the magnetostriction coefficient. In fact it appears that results can best be described by considering long and short range stresses, each of which alters the magnetic properties in a different way. Short range stresses, which exist over a range of 10-100 mm are comparable in range to the widths of magnetic domain walls. These stresses, which are mostly associated with dislocations are very effective in pinning magnetic domain walls. These lead to increased coercivity.

Longer range stresses with a range  $1 \mu\text{m} - 0.1 \text{ mm}$  are not effective in pinning domain walls, but do affect the anisotropy field seen by the domains. These primarily cause changes in the differential susceptibility.

#### 3.2 EXPERIMENTAL PROCEDURE

We have made a study of the effects of fatigue on the magnetic properties of AISI 4140 steel and some unspecified constructional steel removed from a railroad bridge by the Association of American railroads. Only results on the former will be presented here.

The magnetic properties of the specimens, which were in the form of rods of length 100 mm and diameter 7 mm, were measured using a multiparameter magnetic inspection system which has been described previously [16].

### 4. RESULTS

The specimens were divided into two groups according to the strain amplitude of the fatigue cycling which was either  $\frac{dI}{I} = 0.002$  or  $0.007$ .

Measurements were made of several magnetic properties including initial permeability, anhysteretic permeability at the origin, maximum differential permeability, coercivity, remanence and hysteresis loss. It was found from these results that hysteresis loss and coercivity were the most promising measurements for monitoring the progress of fatigue, as shown in Figs. 1 and 2.

Studies of the effect of unidirectional plastic deformation on the magnetic properties of specimens of the same material also showed a significant increase in coercivity, Fig. 3, but other properties such as maximum differential permeability were unaffected over most of the range of deformation.

Finally studies of the effect of applied stress on the magnetic properties of specimens of the same material showed that the maximum differential susceptibility and the anhysteretic susceptibility at the origin Fig. 4 were both strongly affected and that these parameters are useful for monitoring applied stress.

#### 4.1 INTERPRETATION

Previously it had been quite difficult to interpret the effects of various mechanical treatments on the magnetic properties of steels. This was due in part to the lack of understanding of the information given by the magnetic hysteresis curve. Recently this situation has changed with the publication of a viable hysteresis model [17], in which both pinning effects and anisotropy can be accounted for. The former is explicitly included as a parameter in the model, the latter is implicitly included in the orientation of the hysteresis curve.

The effect of mechanical treatment on the internal stress is, we believe, best treated by the model of Cullity [18] which is shown in diagrammatic form in Fig. 5. This model was originally devised for describing the effects of unidirectional tensile plastic deformation on the internal stress in steels, however it applies equally to compressive plastic deformation, if the signs of the stresses are inverted, and to fatigue damage. In fatigue the main difference is a qualitative one: the stress concentrations become even more inhomogeneous.

It is well known from x-ray diffraction studies that a material which has been plastically deformed in tension and then released, appears to have a net residual compressive stress. Magnetic and mechanical-stress-relief investigations do not

show the material to be in compressive stress and therefore some authors have called this residual stress a "fictitious" stress. These contradictory results can be explained on the basis of Fig. 5. Clearly the material is in equilibrium after deformation and unloading, so the total stress when integrated over the volume of the material is zero. The x-ray results although limited to the surface do sample the major volume component, which in this case is in residual compressive stress, as shown in Fig. 5. Hence the well known result that x-ray diffraction indicates residual compressive stress. In order that the material be in overall equilibrium therefore, the tensile stress regions must exist only over a very small fraction of the total volume, and they must have much greater stress magnitude than the compressive stress regions.

From this model then we can interpret the observed results. Overall the material is in stress equilibrium. Locally however the situation is very different. The small volume, high stress regions, which are associated with dislocations, act as pinning sites for magnetic domain walls and therefore as their number and stress amplitude increases with plastic deformation so does the coercivity.

The compressive regions that exist over most of the volume do not impede domain wall motion. Instead they have the effect of altering the anisotropy seen by the domains, and this leads to a change in differential susceptibility. This variation of differential susceptibility with stress has been successfully explained in an earlier paper [15].

#### 5. CONCLUSIONS

Stress and plastic deformation alter the magnetic properties of steels in distinct ways. Fatigue cycling leads to changes which are qualitatively similar to the effects of plastic deformation. The principal difference is the greater inhomogeneity of dislocation density after fatigue cycling. Coercivity and hysteresis loss measurements show promise for monitoring the progress of fatigue.

## 6. REFERENCES

1. G. E. Dieter, "Mechanical Metallurgy" 3rd Edition, Chapter 12, (McGraw-Hill, New York, 1986).
2. J. C. Grosskreutz, Phys. Stat. Sol. B 47, 11, 1971.
3. J. C. Grosskreutz, Phys. Stat. Sol. B 47, 359, 1971.
4. I. R. Kramer, Met. Trans. 5, 1735, 1974.
5. R. N. Pangborn, S. Weissman and I. R. Kramer, Met. Trans. A. 12, 109, 1981.
6. S. Weissman, R. N. Pangborn and I. R. Kramer, Scripta Met. 17, 807, 1983.
7. C. R. Aita and J. Weertman, Met. Trans. A 10, 535, 1979.
8. C. H. A. Sanford-Francis, Brit. J. NDT 20, 119, 1978.
9. C. H. A. Sanford-Francis, Brit. J. NDT 23, 241, 1981.
10. C. H. A. Sanford-Francis, Brit. J. NDT 29, 83, 1987.
11. M. B. Shah and M. S. C. Bose, Phys. Stat. Sol. A 86, 275, 1984.
12. M. S. C. Bose, NDT International 19, 83, 1986.
13. H. Mughrabi, R. Kutterer, K. Lubitz and H. Kronmüller, Phys. Stat. Sol. A 38, 261, 1976.
14. D. C. Jiles and D. Utrata, J. NDE 6, 129, 1988.
15. P. Garikepati, T. T. Chang and D. C. Jiles, IEEE Trans. Mag. 24, 2922, 1988.
16. D. C. Jiles, J. Appl. Phys. 63, 3946, 1988.
17. D. C. Jiles and D. L. Atherton, J. Mag. Mag. Mater. 61, 48, 1986.
18. B. D. Cullity, Met. Trans. 277, 356, 1963.

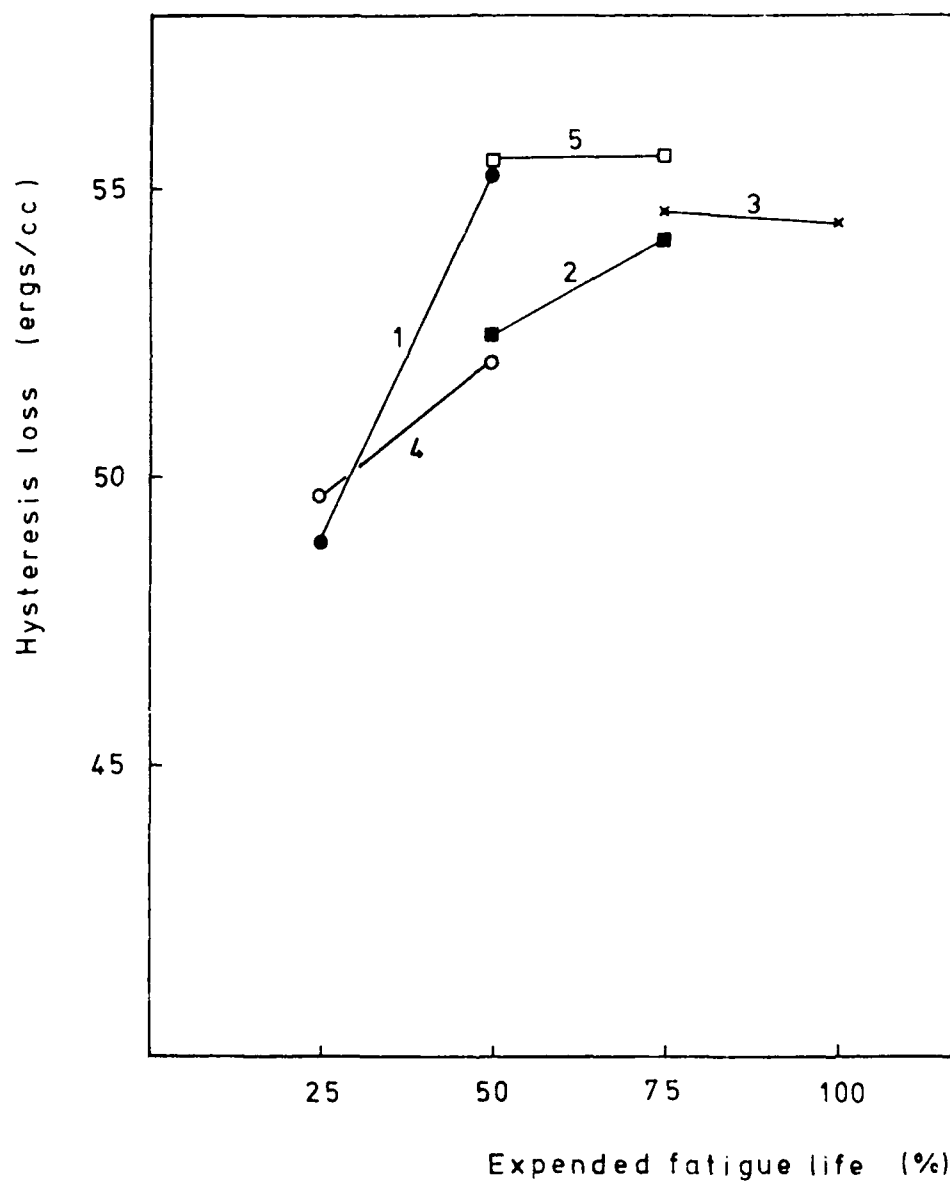


Fig. 1. Variation of hysteresis loss with expended fatigue life for five specimens of AISI 4140 steel. Specimens 1, 2, and 3 strained at an amplitude of  $d1/l = 0.002$ , specimens 4 and 5 strained at an amplitude of  $d1/l = 0.007$ .

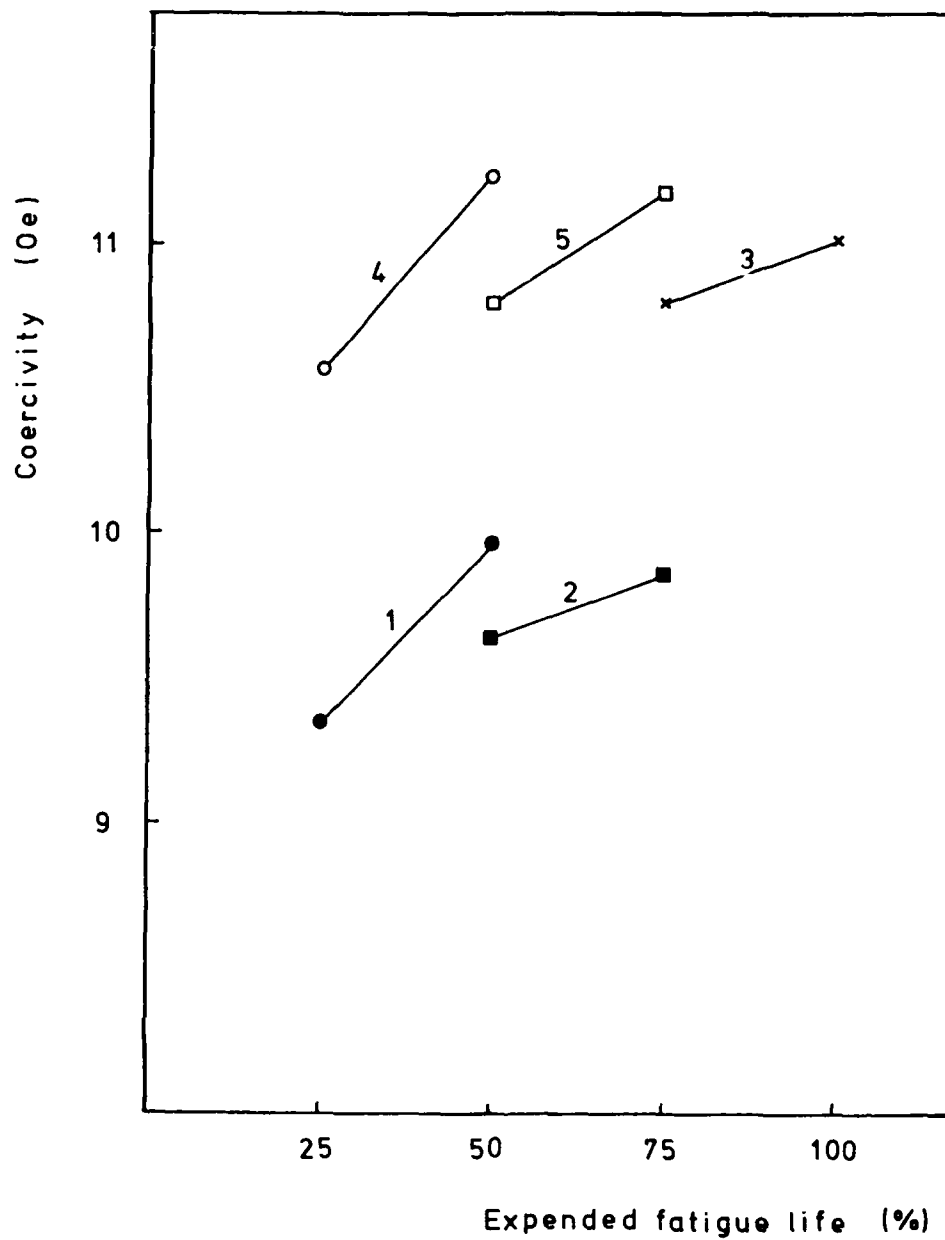


Fig. 2. Variation of coercivity with expended fatigue life for the same five specimens of AISI 4140 steel as in Fig. 1.



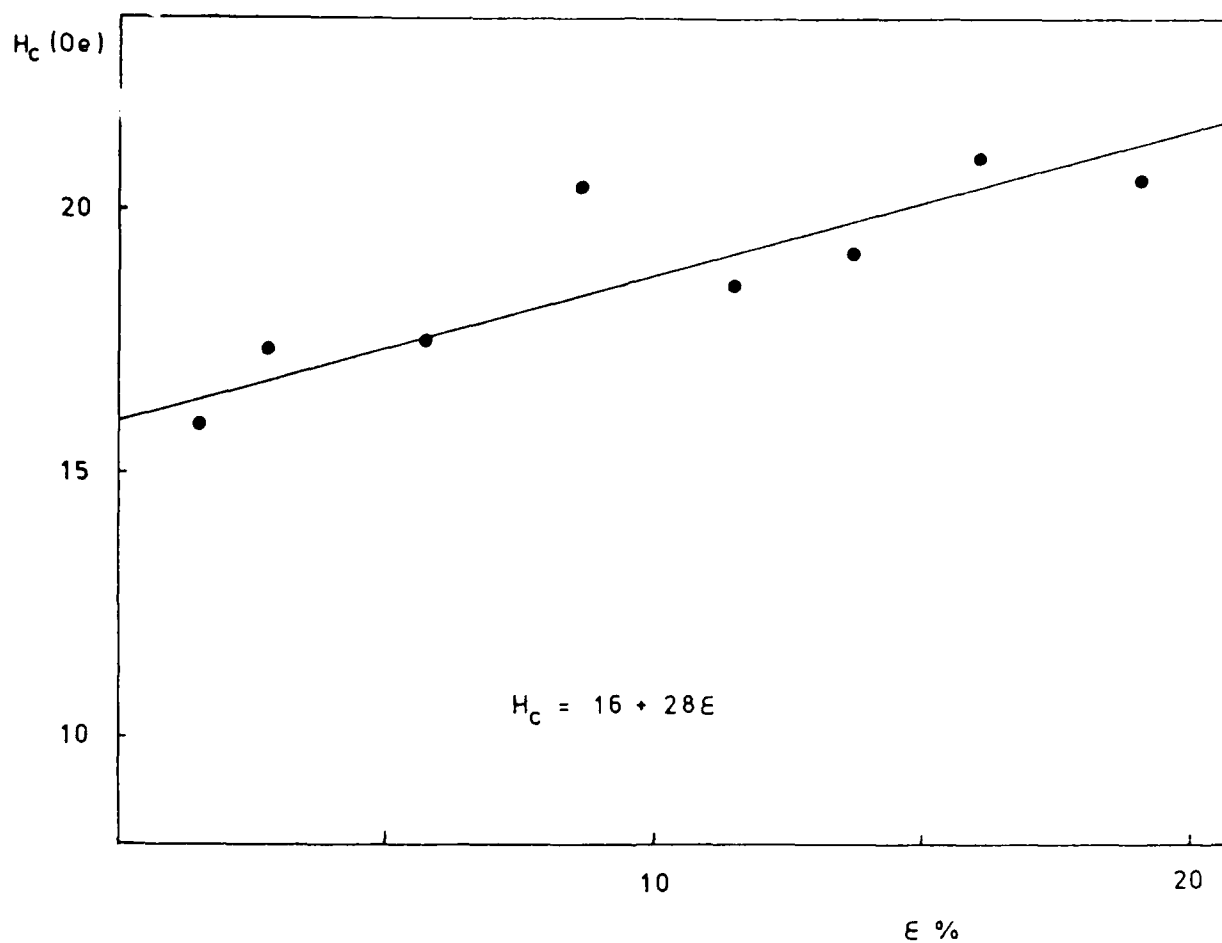


Fig. 3. Dependence of coercivity on unidirectional compressive plastic deformation.

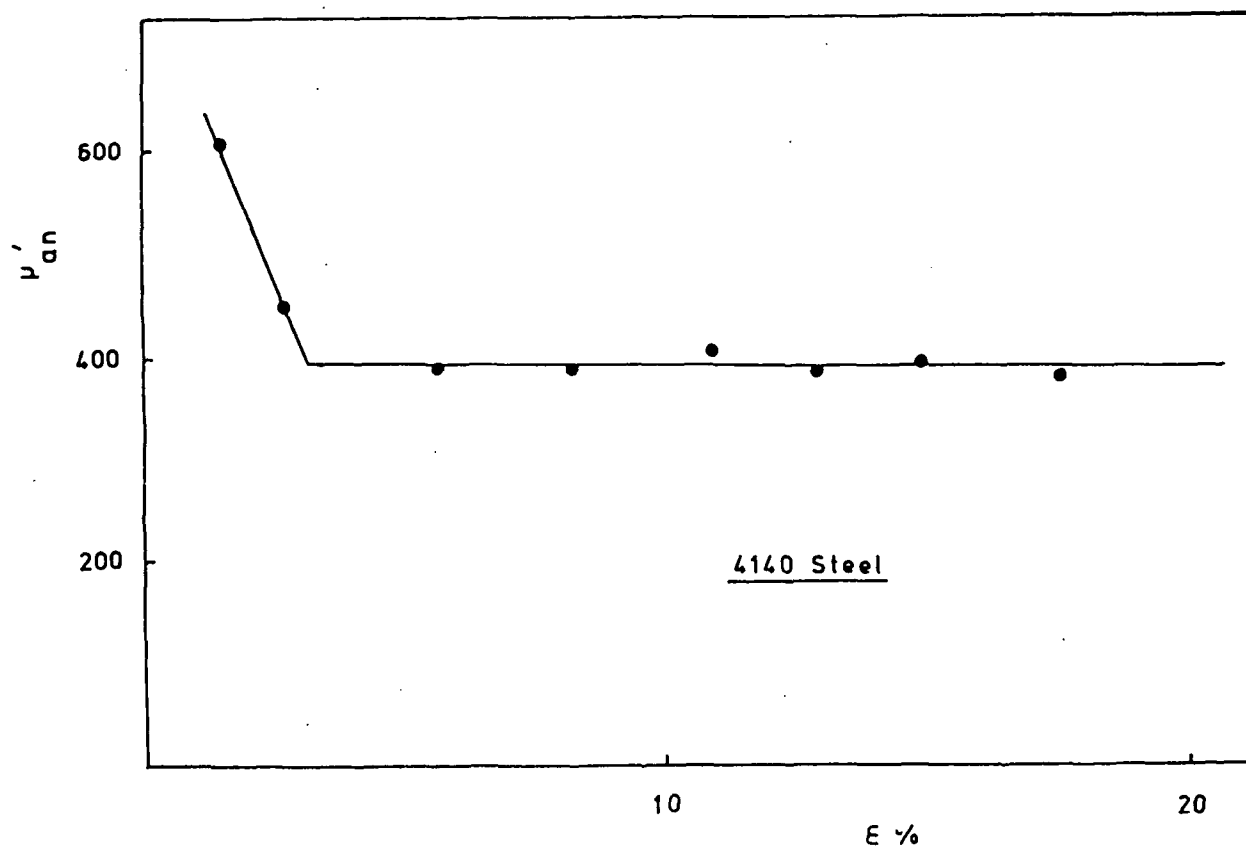


Fig. 4. Dependence of the anhyseretic susceptibility at the origin on unidirectional compressive plastic deformation.

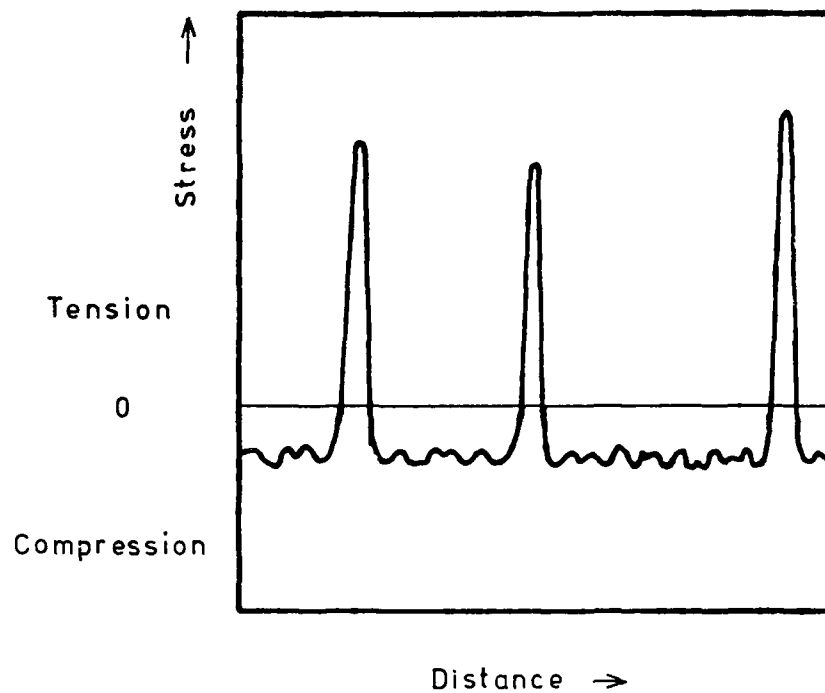


Fig. 5. Model of the effects of tensile plastic deformation on the residual stress (after Cullity reference 18).

PROGRAMMABLE ULTRASONIC REFLECTANCE  
OF ARTIFICIAL FLAWS IN MATERIALS

Ronald E. Larsen, Ph.D.  
Reinhart & Associates, Inc.  
Austin, Texas

Matthew J. Golis, Ph.D.  
Advanced Quality Concepts, Inc.  
Columbus, Ohio

ABSTRACT

An experimental study was conducted to evaluate the feasibility of producing a programmable ultrasonic reflectance standard for use in calibrating ultrasonic pulse-echo equipment. The physical basis of the standard is that interfaces between two flat surfaces might be made transparent, or nearly transparent, to ultrasound by an application of sufficient pressure across the interface. Investigated in this research was the physical basis for the standard and the use of a voltage-activated piezoelectric stack to produce the required pressures. In ultrasonic tests conducted at 2.25 MHz, it was found that the interface echo amplitude could be reduced by 16 dB (84 percent) by applying only 75 lb-in. torque to a lead screw driving element in the fixture. Application of 2,000 volts to the piezoelectric stack reduced the interface echo amplitude by 5.8 dB (49 percent). Careful evaluation of the fixturing and specimens suggests that a factor of two in echo amplitude (in dB) should be achievable at 2,000 volts by improvements in surface finishing of specimens and elimination of spurious compliances by improvements in the fixturing. It is concluded that the technique is feasible and that a multi-element standard merits development. A standard fitted with a multi-element contact array should have wide application in nondestructive evaluation since it would be capable of simulating reflectors having a wide range of shapes, sizes, and reflectivities.

INTRODUCTION

Calibration standards, often called reference on test blocks by inspectors, are a vital adjunct to any ultrasonic pulse-echo materials evaluation system. Typically fabricated by drilling flat-bottomed holes of several diameters and at several depths in material acoustically equivalent to the material under test, they have the disadvantage of being incapable of simulating the shapes of actual flaws, which are seldom circular. With this limitation in mind, a Phase I Small Business Innovative Research program was performed to evaluate the feasibility of developing a programmable ultrasonic reflectance standard.

The physical basis of the standard is that the interface between two flat, smooth surfaces may be made transparent, or nearly transparent, to ultrasound by applying sufficient normal force to the surfaces. Removing the force, therefore, produces a perfect reflector. A programmable standard might consist of a multi-element array of steel rods with smooth, flat ends that has been clamped tightly to the smooth, flat face of a polished steel block. Selective retraction of elements will then create a reflector having nominally any size or shape. The required expansion and retraction forces might be applied with a screw mechanism or piezo-electric stack.

This paper reports on evaluation of a single-element array that was actuated by a screw mechanism and that was actuated by a stack.

#### APPARATUS AND SPECIMENS

Figure 1 shows the test fixture set-up with a piezo-electric stack. A hardened steel ball presses against the bottom of the stack. The screw beneath the ball is used to apply pre-loading force. For tests in which mechanical screw loading was to be used, the stack was replaced with a solid cylinder.

The contacting specimens were 1/2-inch diameter steel cylinders with either ground or polished end surfaces. The polished end surfaces were ground and polished to a flatness of 1/4 wave length (green light). The polished surfaces had an estimated roughness of 15 microinches. The contacting portion of the fixture top piece was ground and polished to the same tolerances.

The top step in the frame was angled to produce 45-degree refracted shear waves in the test pieces. The search unit was used in conjunction with a conventional pulser-receiver.

#### RESULTS

Figure 2 shows the results of tests using screw loading of a polished cylinder on the interface and cylinder back wall amplitudes. A sizeable change is obtained with relatively low applied torque.

Figure 3 shows the results obtained when the spacer rod in the fixture was replaced with the stack. The stack was rated for use up to 2,000 volts. The largest amplitude decrease obtained was 5.8 dB. Nominally, a 5 dB decrease in echo amplitude was obtained for this voltage.

The results for the screw and stack tests are summarized in Figure 4. Torque values were converted to pressures using classical screw theory. The maximum stack pressure, determined by plotting the maximum amplitude change attained with the stack on the curve obtained by mechanical loading, is about 280 psi. This value is considerably lower than had been anticipated. However, calculation of the deflection of the loading ball by Hertz contact pressures revealed that resulting number would account for this pressure deficit. Other improvements, chiefly in fixturing and in specimen surface finishing procedures, may also be required but echo-amplitude decreases of 12 dB or more are thought to be achievable.

#### CONCLUSIONS

It is concluded that the calibration standard concept is feasible and that a standard should be developed. The standard is anticipated to have wide potential application in the nondestructive evaluation industry.

#### ACKNOWLEDGEMENTS

This research was partially supported by Phase I Small Business Innovative Research funding furnished under Contract No. DTRS-57-87-C-00100 by the U. S. Department of Commerce. The contract was issued by the DOT/Transportation Systems, Kendall Square, Cambridge, Massachusetts. Technical monitor for this project was Mr. Allen Bowers, U. S. DOT, Federal Railroad Administration, Washington, D.C.

The authors wish to express their gratitude for assistance furnished by Professor Don Bray and Mr. Howard Strahan, both at the Department Mechanical Engineering, Texas A&M University.

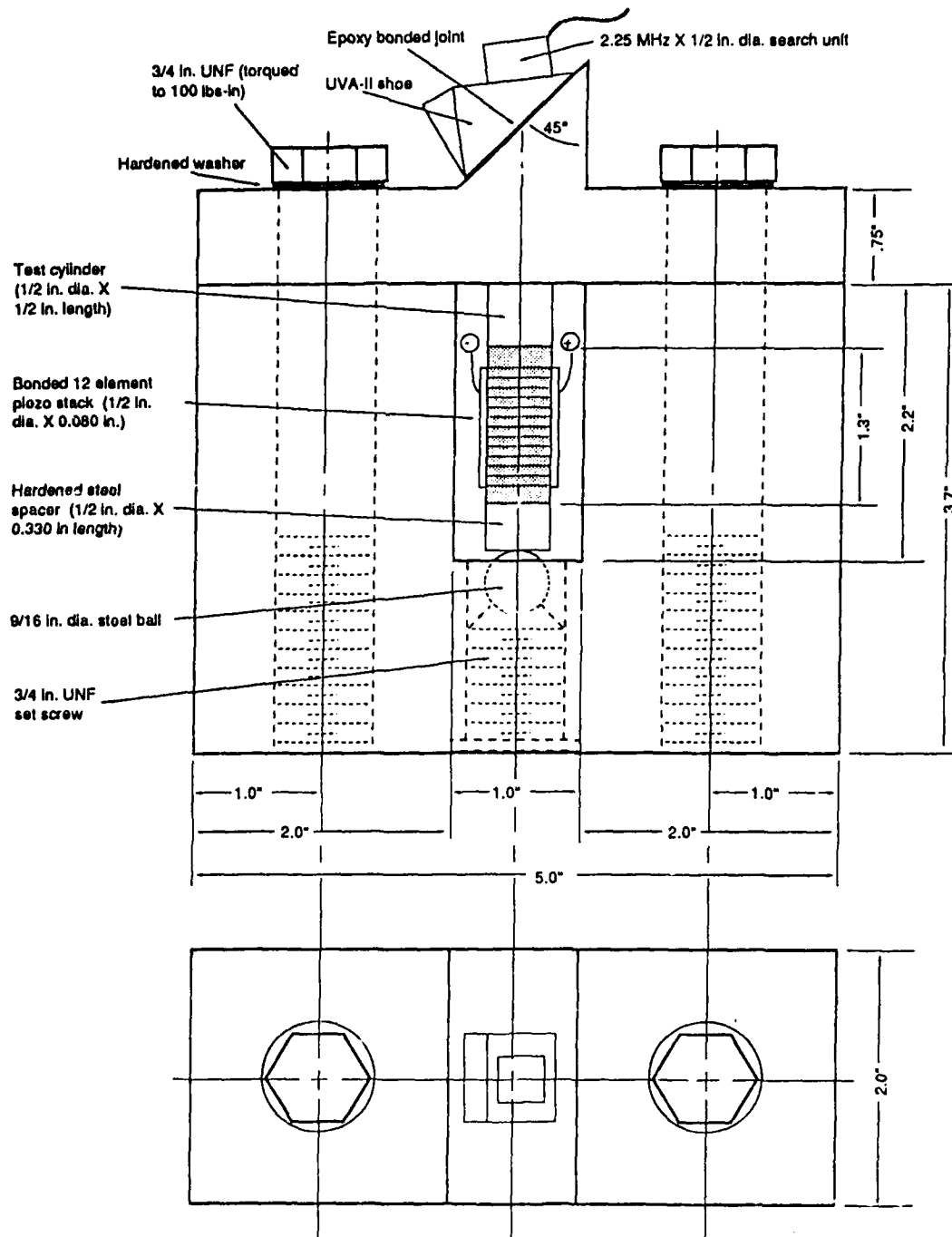


Figure 1. Engineering drawing of assembled compact test fixture.

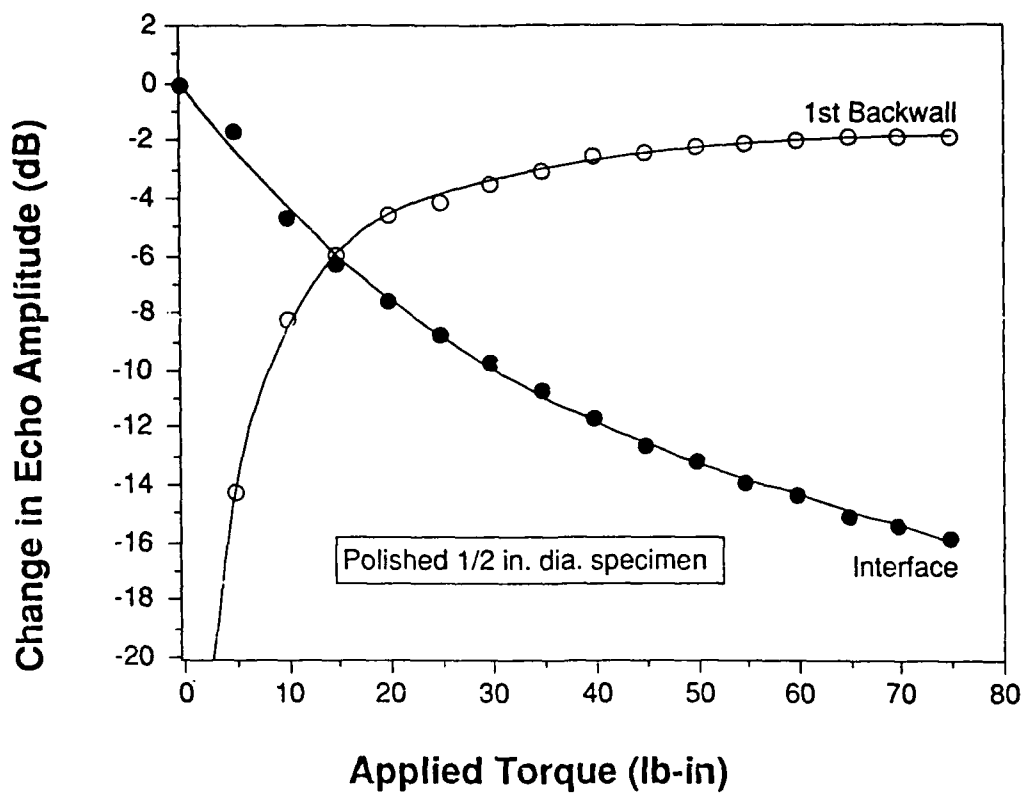


Figure 2. Variation of interface and first backwall echo amplitudes with torque applied to loading screw during tests with the "dummy" (steel) rod in-place. A polished specimen was used.

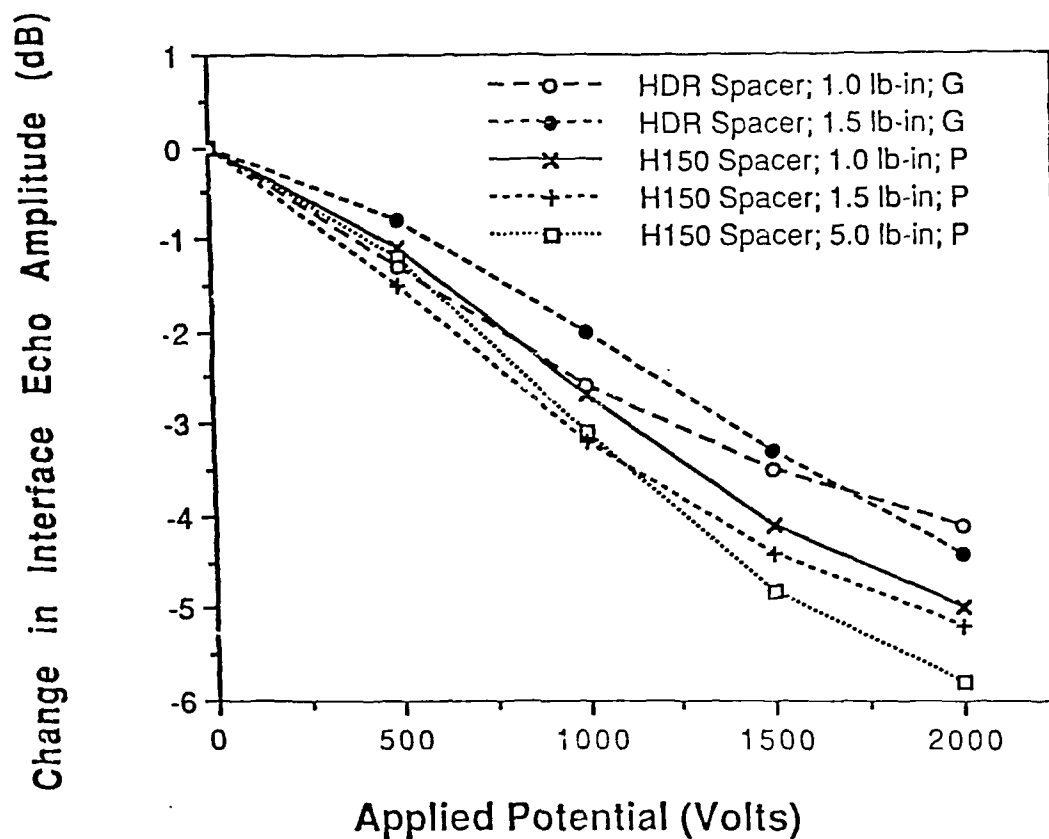


Figure 3. Variation of interface echo amplitude with applied potential on piezoelectric stack for ground (G) and polished (P) specimens and various preloads. Notice that polishing and preloading both enhance the decrease in reflectivity.



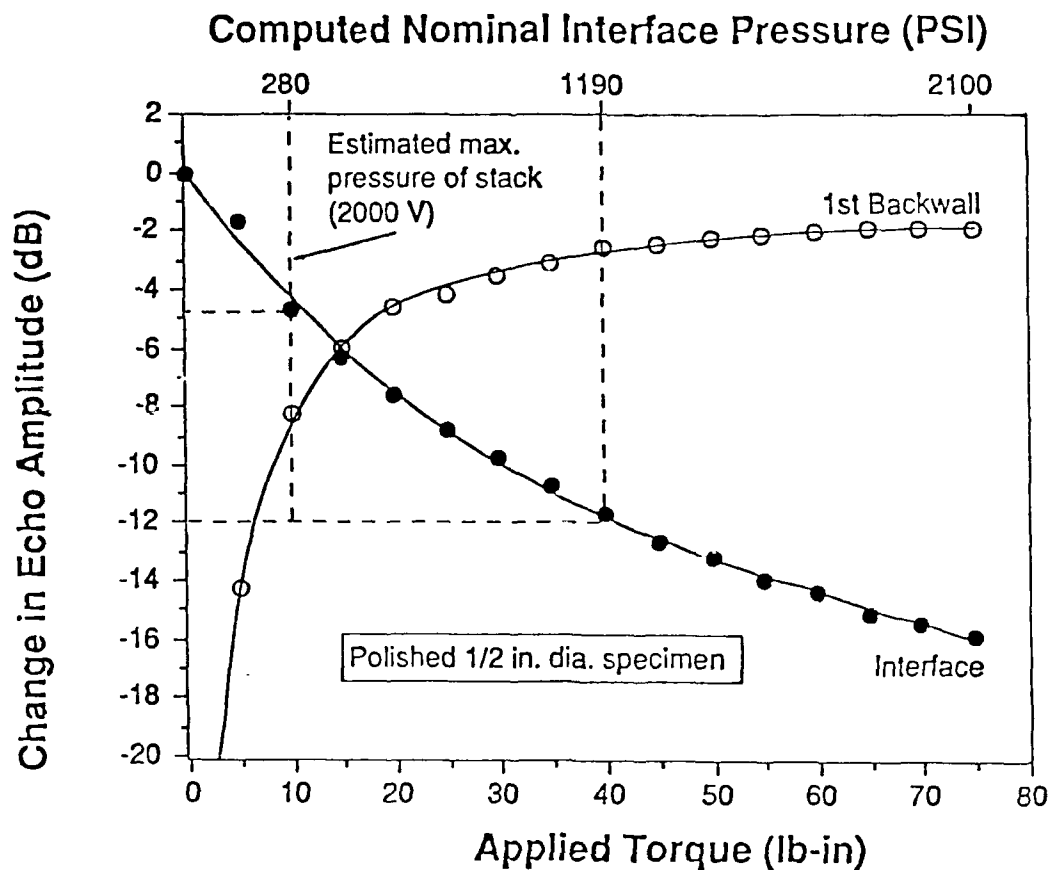


Figure 4. Analysis of variation of echo amplitudes with applied mechanical loading. Nominal pressures were computed from torque using simple screw thread theory.

## NONDESTRUCTIVE EXAMINATION OF STEAM TURBINE ROTORS BY AUTOMATED SYSTEMS

Gerald A. Lamping  
Southwest Research Institute  
San Antonio, Texas

L. D. Nottingham  
Electric Power Research Institute  
EPRI NDE Center  
Charlotte, North Carolina

### ABSTRACT

The Electric Power Research Institute is currently sponsoring a project to improve existing turbine rotor life assessment capabilities. The project involves a variety of disciplines with activities in nondestructive evaluation, metallurgy, fracture mechanics, material characterization, and life prediction methodologies. The nondestructive evaluation activities include examination of retired rotors using several different bore inspection methods and techniques. To date, six rotors have been examined using three boresonic examination systems—one focused, immersion test system and two contact systems. In addition to bore examination for internal and surface-connected flaws, the rotors have undergone nondestructive tests for creep damage assessment.

Currently, the rotors are being sectioned to remove flaw coupons, which will undergo metallographic evaluation to characterize the flaws and correlate them with the examination findings. Extensive material property tests will also be conducted to add data to existing material property databases and to correlate the creep assessment findings with creep damage. This paper describes the project and its objectives and presents preliminary results of completed examination activities.

### INTRODUCTION

Because of the high levels of stored energy in massive rotating components, such as turbine rotors, the consequences of a failure can be severe. Accordingly, emphasis in the utility industry has been placed on reducing the potential for failure. For new forgings, utilities have relied on the steel manufacturers to provide rotors with improved mechanical properties and less severe flaws. For older rotors, life assessment methodologies have been developed to predict the onset of failure before it occurs. Traditionally, evaluation procedures have been conservative to account for the uncertainties associated with many of the evaluation parameters. However, as emphasis in the electric utility industry has shifted toward plant life extension, increased importance has been placed on reducing conservatism and eliminating premature retirements.

Rotor remaining life assessment involves several disciplines, including: nondestructive examination for flaws, determination of material properties, stress analysis, duty cycle evaluation, and fracture mechanics analysis. The Electric Power Research Institute (EPRI) has supported the development and evolution of evaluation procedures through research and development projects in each of these disciplines, directed specifically toward turbine life assessment. Early projects involved nondestructive examination and destructive correlation, development of the Stress and Fracture Evaluation of Rotors (SAFER) rotor life prediction computer code, and material properties measurements<sup>(1-3)</sup>. EPRI has also

sponsored performance evaluations of several rotor examination systems<sup>(4-6)</sup> and has recently completed a major upgrade of SAFER<sup>(7)</sup>.

Reliable flaw detection and sizing in the near-bore material of turbine and generator rotors are prerequisites for accurate remaining life evaluation. Relative to other locations, near-bore material in older rotors is prone to concentrations of inherent flaws and less desirable material properties as a result of rotor manufacturing processes. In addition, the near-bore material is subjected to significant tensile stresses arising from rotation and thermal gradients. The combination of high stresses, concentrations of discontinuities, and less desirable properties makes the near-bore a critical area in terms of predicted remaining life.

Ultrasonic inspection of turbine and generator rotors, conducted from the rotor's central bore (boresonic inspection), has become an accepted method for examination of the near-bore material over the past several years. A variety of boresonic test systems are commercially available for this inspection. However, no approach is available to determine that test results are compatible with the analysis methods and to factor the test system measurement uncertainties into a life prediction model. Late in 1986, EPRI initiated a program to improve existing rotor life prediction capabilities. In one portion of this program, basic examination approaches will be compared to determine if one approach is more applicable than others under certain circumstances or in general. In addition, measurements will be made to

enable integration of system performance uncertainties into a life prediction model.

#### EPRI TURBINE ROTOR LIFE ASSESSMENT PROGRAM

The EPRI program that was initiated in 1986 involves five independent tasks related to rotor remaining life prediction. Together, these represent a major commitment to improve all phases of rotor evaluation.

##### RP 2481-4 -- Handbook of Rotor Materials

Material Properties Council, Inc. (MPC) is the contractor for this task, which calls for literature review, analysis, and documentation of available material mechanical properties relevant to rotor life prediction. The materials of interest include CrMoV, NiCrMoV, NiMoV, NiCrMo, and NiMo, made to forging specifications. High and low temperature properties over the entire range of possible thermal exposure are included.

##### RP 2481-5 -- NDE and Mechanical Property Evaluation of Retired Rotors

Southwest Research Institute (SwRI) is the prime contractor on this task, which has three primary objectives:

- To correlate conventional and focused beam boresonic indications in retired rotors with the metallurgical conditions of the rotors;
- To perform a critical assessment of the capabilities of boresonic inspections to detect cracks located within inclusion clusters; and,
- To develop mechanical property data for incorporation into lifetime assessment codes.

Six retired rotors have been examined under this task. The rotors are now being sectioned to remove coupons containing flaws which will undergo metallographic evaluation to determine the size and nature of the flaws. Additional coupons will be used for material properties tests.

##### RP 2481-6 -- Cyclic Life Evaluation

The objectives of this task are to develop a personal computer (PC)-based preprocessor for rotor remaining life analysis and to develop a PC-based expert system for life extension studies. The preprocessor would handle near-bore flaws, bore creep-fatigue, creep-fatigue of blade attachments and heat and seal grooves, and stress corrosion cracking in shrunk-on disks. The expert system for life extension would provide a probabilistic analysis of failure and a cost-benefit analysis, and would be compatible with the EPRI three-level approach to life extension. Failure Analysis Associates (FaAA) is the prime contractor.

##### RP 2481-7 -- Coordination of Steam Rotor Life Assessment Tasks

MPC is also the contractor on this task, which involves coordinating the selection and shipment of the program rotors, coordinating interactions between the other tasks and contractors, and coordinating the activities of a utility advisory group.

##### RP 2481-8 -- NDE Techniques for Creep and Fatigue Damage Assessment

This project has four main tasks:

- To perform thermal and stress analyses on the selected rotors;
- To develop and perform detailed NDE of the rotors using hardness, replication, and X-ray diffraction techniques;
- To make a creep life prediction for each of the program rotors; and,
- To make a fatigue life prediction for each of the rotors.

Mitsubishi Heavy Industries (MHI) had previously developed the Material Characteristic Nondestructive Evaluation System (MACH NDE). MACH I equipment measures hardness and extracts replicas from the bore; MACH P equipment performs X-ray diffraction surveys on selected areas on the periphery. MHI is the contractor for this project and is using the MACH equipment for their NDE activities.

#### PROGRAM ROTORS

Each task undertaken in this program presented a unique set of requirements for the rotor selection process. The rotor boresonic inspection and correlation activities require rotors with near-bore and bore-connected flaws, preferably covering a range of types and sizes. For activities related to creep properties and creep life expenditure determination, rotors with high temperature steam conditions, preferably in excess of 1050° F, are required. Fatigue life expenditure studies require rotors that have undergone many start/stop cycles. And, of course, the selected rotors are to represent both major domestic manufacturers, Westinghouse (W) and General Electric (GE). To minimize costs, it was desirable to locate rotors that possess all of these characteristics.

As expected, locating retired rotors with all of the required characteristics was not an easy task. The high temperature steam condition requirement immediately limited candidates to high pressure (HP) rotors, high pressure/intermediate pressure (HP/IP) rotors, and sections of certain intermediate pressure/low pressure (IP/LP) elements. NDE records were often incomplete; that is, once critical defects sufficient to cause retirement had been found in one area of the rotor, other examinations were cancelled or discontinued.

Originally, the project was to include four rotors. However, only one rotor that seemed to meet all of the imposed requirements, a GE HP/IP rotor from the Moss Landing #4 unit at Pacific Gas and Electric, could be found. Two GE IP/LP rotors from Centenor Energy's Eastlake station were selected on the basis of prior bore examinations and possible creep damage, although with some reservations on both criteria.

Because the three rotors selected were all built by GE, a concerted effort was made to locate W-built candidate rotors. Two W HP/IP rotors from the Niles Station of Ohio Edison were procured for the program on the basis of retirement from creep in the blade attachment areas. No boresonic examination records were available, so both rotors were brought into the program in the hope that one would be useful.

After performing boresonic evaluations of the five rotors, a decision was made to bring another rotor into the project for the boresonic activities and to separate this work from the material property activities as best possible. The Moss Landing #4 HP/IP and the two Niles HP/IP rotors will be used for material characterization. The two Niles rotors are particularly interesting for this study because they are from identical units that saw similar service yet they have different chemical compositions. The Niles #1 rotor is a NiCrMo forging and the Niles #2 rotor is a CrMoV forging. The Moss Landing rotor is also of interest in terms of boresonic indications, and sections will be used in the correlation efforts as well. The Eastlake #1 IP/LP and the sixth rotor brought into the program, a GE IP/LP from the Riverbend #7 unit of Duke Power Company, will also be used for the boresonic correlation efforts. The Eastlake #2 IP/LP will not be used for any further studies.

#### ROTOR BORE DEFECT BLOCK

In the earlier program<sup>(7)</sup> that upgraded the SAFER computer code, a computer subroutine was developed to assess the significance of boresonic examination findings. In this subroutine, the rotor is divided into pixels and the boresonic data are assigned to the appropriate pixels according to their spatial relationships. The significance of a particular pixel is determined statistically on the basis of the number and strength of the ultrasonic reflections contained in that pixel and the significance of all neighboring pixels. For this subroutine to work properly, the statistical treatment of the data must be calibrated on known reflectors for the particular test system supplying the data.

All reflectors in the flaw blocks that were used in earlier boresonic system studies<sup>(4,6)</sup> are located very near the bore, within about 1/2 inch radially. This has always been perceived as a shortcoming of the existing blocks; consequently, as part of the NDE activities of this program, a task to build a new bore block containing deeper seated reflectors was undertaken.

The new block contains glass beads and radial-axial disks over a radial depth range of 1/2-inch through 4 inches. The reflectors were inserted using a hot isostatic pressing (HIP) process that bonds the fusion lines between adjoining segments of the block so that the bond lines are transparent to an ultrasonic examination. Reflectors are placed in the block as single, isolated reflectors and in clusters to assess test system resolution capabilities. Rotor material removed from a retired rotor at the EPRI NDE Center was used to construct the block. The new block, which has now been completed, will be used for this project and then will be added to the NDE Center's rotor boresonic sample library for use in system performance evaluations.

#### NDE TASK ACTIVITIES AND STATUS

Duke Power examined the two Niles, two Eastlake, and Moss Landing rotors, using a PHased Optics Computerized Ultrasonic System (PHOCUS) for the rotor boresonic examinations. PHOCUS is an immersion-type test system that operates in a water-flooded bore<sup>(8)</sup>. The system utilizes two phased array transducers to perform focused examination of the first approximately 4 inches of rotor material, measured from the bore surface. Two transducers provide shear wave examination, at a refracted angle of approximately 45° from radial, in clockwise and counterclockwise directions. The system is completely automated in terms of scan control and data acquisition.

These examinations revealed very few significant indications in the Eastlake #2 rotor and both Niles rotors. As a result, an additional rotor was sought for the boresonic activities. Duke Power's Riverbend #7 IP/LP rotor had been examined previously using PHOCUS and had been retired on the basis of the findings. Relative to the other five rotors examined, the Riverbend rotor appeared to contain more and larger indications; consequently, Duke Power donated this rotor to the project.

The addition of another rotor for the boresonic activities also permitted the mechanical property testing to be separate from the NDE activities, allowing the former to proceed without having first completed the NDE activities. It appears that the Moss Landing rotor and the two Niles rotors are the strongest candidates for the mechanical property tests. The results of the MHI inspections will provide additional information regarding this selection.

Public Service Electric and Gas (PSE&G) completed their examinations of the three rotors selected for further NDE studies, i.e., the Moss Landing, Eastlake #1, and Riverbend rotors. PSE&G uses a contact test system built in their own development laboratories for their boresonic inspections<sup>(9)</sup>. The system uses contact transducers that provide S-wave examination at a refracted angle of approximately 60° from radial. The PSE&G system also provides clockwise and counterclockwise examination and is fully automated in terms of scan control and data acquisition.

MHI has used their MACH inspection equipment on the Moss Landing, Eastlake #1, and both Niles rotors<sup>(10)</sup>. Surface replication tests were conducted in the blade attachment regions of the high temperature zones to inspect for creep damage. The MACH P equipment was used to inspect for fatigue damage on the first blade groove of the Niles #1 and #2 rotors. The MACH I equipment was used to inspect for bore surface damage on the Moss Landing and Eastlake #1 rotors. Results from the MHI inspections have not been released at this time.

#### CONCLUSION

The electric power industry is responding to the challenge for more accurate turbine rotor life assessments. New NDE systems have been developed by utilities and manufacturers which have greater capabilities to detect and characterize rotor defects. Data from these new automated NDE systems must be rationalized for use as inputs in the enhanced fracture mechanics analysis method which is applied to predict the remaining service life. NDE data has now been collected from the new NDE systems, and activities are underway to correlate this data with material properties tests and metallographic examinations.

Additional examinations performed before the rotors were sectioned include examinations using the Ultrasonic Data Recording and Processing System (UDRPS), by Dynacon Systems, Inc.<sup>(11)</sup> and by the Ansaldo Componenti Company. The Turbine Rotor Examination and Evaluation System (TREES) also was used to examine the Buck #6 test piece<sup>(12)</sup>. Results from these examinations are not yet available.

#### ACKNOWLEDGEMENTS

The authors wish to acknowledge the support of the Electric Power Research Institute through its research project

RP-2481. The Project Manager is Dr. R. Viswanathan and Task Managers are Dr. Stephen Gehl and Dr. R. Dooley.

#### REFERENCES

1. *Steam Turbine Rotor Reliability - Task Details*. Palo Alto, CA: Electric Power Research Institute, November 1978. NP-923.
2. *Nondestructive Testing of Large Steam Turbine Rotors*. Palo Alto, CA: Electric Power Research Institute, December 1982. NP-2736.
3. *Verification of SAFER Code for Rotor Lifetime Prediction*. Palo Alto, CA: Electric Power Research Institute, September 1984. NP-3693.
4. *Repeatability of TREES Bore Inspection System*. Palo Alto, CA: Electric Power Research Institute, November 1982. NP-2640.
5. *Evaluation of the Prototype Westinghouse PHOCUS BoreSonic System*. Palo Alto, CA: Electric Power Research Institute, July 1985. NP-4167.
6. *Evaluation of the Commercial Machine Works BorSonic System*. Palo Alto, CA: Electric Power Research Institute, August 1988. NP-5948.
7. *Life Assessment Methodology for Turbogenerator Rotors*. Palo Alto, CA: Electric Power Research Institute, March, 1988. CS/EL-5593-CCM.
8. L. O. Nottingham and W. S. Beal, "The Phocus Rotor BoreSonic Inspection Tool," *Proceedings of EPRI Seminar on Life Assessment and Improvement of Turbo-Generator Rotors for Fossil Plants CS-4160*, New York: Pergamon Press, 1985.
9. T. J. McGarvey, J. Murray, and D. Roller, "An Automated Ultrasonic Data Acquisition and Evaluation System," in *Corrosion Monitoring in Industrial Plants Using Nondestructive Testing and Electrochemical Methods*, ASTM STP908, Philadelphia: American Society for Testing and Materials, 1986, pp. 102-111.
10. T. Gota, et al., "Life Assessment and Extension of Steam Turbine Rotor - Overview of MHI's Activities," in *Conference Proceedings on Life Extension and Assessment of Fossil Power Plants, CS5208*, Palo Alto: EPRI, 1987, pp. 649-658.
11. S. R. Buxbaum, "Turbine/Generator Examinations Using the Ultrasonic Data Recording and Proceeding System," in *Proceedings of Fossil Plant Inspections Conference, CS5320*, Palo Alto: EPRI, August 1987, Section 4, pp. 17-22.
12. B. M. Jacobs, "Computer-Automated Inspection and Lifetime Analysis for Large Steam Turbine Rotors," *Materials Evaluation*, Vol. 42, No. 13, Columbus, Ohio: American Society for Nondestructive Testing (ASNT), December 1984, pp. 1631-1637.

# AN IMPROVED AVERAGING METHOD TO PREDICT THE TECHNICAL CONSTANTS FROM THE ELASTIC CONSTANTS

Mahmoud Harmouche\*  
Alan Wolfenden  
Texas A&M University  
Mechanical Engineering Department  
College Station, Texas 77843

## ABSTRACT

An improved averaging method pertinent to predicting the technical constants from the elastic constants is presented. The averaging scheme employs the principles of the Debye theory of lattice vibrations, where the averaged reciprocal squared velocities of polycrystalline and single-crystal materials are equated with the underlying assumption of the existence of one quasi-longitudinal and two quasi-transverse waves traveling with their own velocities. The present averaging method requires solving the secular equation for the three velocities and performing numerical integration in the reciprocal lattice space. An analytical solution to the secular equation, simplified computational procedures, some selective numerical results, and suggestions for practical applications are presented.

## INTRODUCTION

Hill<sup>(1)</sup> showed that the classical averaging methods of Voigt<sup>(2)</sup> and Reuss<sup>(3)</sup> represent upper and lower bounds, respectively, for the technical constants. Numerical observations suggest, as Hill stated, that either their arithmetic or geometric means should be taken. A host of other averaging methods aimed at improving the method of either Voigt or Reuss or both also appear in the literature. The work of Zeller et al.,<sup>(4)</sup> Kromer,<sup>(5)</sup> Hershey,<sup>(6)</sup> Hashin,<sup>(7)</sup> Alenkovson et al.,<sup>(8)</sup> Peresada,<sup>(9)</sup> and Povoto et al.<sup>(10)</sup> may be cited. Predicting accurate values for the technical constants from the elastic constants remains intractable in practice, as set forth by Voigt and/or Reuss, due to the complexity of the state of stress and/or strain within and across the grains.

Alternative averaging methods based on dynamic deformations of crystalline solids were proposed by Ledbetter et al.<sup>(11)</sup> based on equal elastic Debye<sup>(12)</sup> temperature for single crystals and polycrystals of the same materials. Most recently, Middya et al.<sup>(13)</sup> proposed the use of computer-simulated sound velocity measurements to calculate the technical constants. Both methods were presented in variant forms but were applied to cubic symmetries only.

This paper describes an improved averaging method to calculate the technical constants from the elastic constants using sound velocity measurements. The proposed averaging method averages the squared velocities, on which the technical constants actually depend, in the reciprocal lattice space. It is shown that averaging methods based on dynamic deforma-

\*Presently employed at Southwest Research Institute, San Antonio, Texas

tions follow the trend of those based on static deformations, where the present averaging method produces intermediate values for the technical constants, which always fall between Ledbetter et al. and Middya et al. values, just as Hill expected values which fall between Voigt and Reuss values. It is also shown that the present averaging method yields values in excellent agreement with observations and, surprisingly, with Hill's method.

## THEORETICAL DESCRIPTIONS

In order to formulate the relationships between the technical constants and the elastic constants, the following assumptions are made:

- (1) The grain boundaries contribute nothing to the elastic properties of polycrystals.
- (2) The crystallites' size is small so that their number is large enough, but not too small that their crystallinity is lost.
- (3) No texture exists in the crystalline aggregates.
- (4) The elastic stiffnesses are homogenous within and across the grains.
- (5) There exist a quasi-longitudinal and two quasi-transverse modes, independent of the vibrational frequencies, with marked differences in their velocities for every set of crystallographic directions.

Furthermore, we regard a crystalline solid as a lattice of atoms in which the three phase velocities are orthogonal throughout the solid.

In his review of the Debye<sup>(12)</sup> theory of lattice vibration, Alers<sup>(14)</sup> showed that the cutoff frequency  $\nu_n$  is related to the average phase velocity  $V$  of a plane wave by the relationship

$$N = \frac{4\pi M \nu_n^3}{9\rho V^3} \quad (1)$$

where  $N$  is the Avogadro's number,  $M$  is the atomic mass, and  $\rho$  is the density

Equation (1) is derived without reference to the modes of vibration available for a solid. For the purpose of the Debye theory of lattice vibration,  $1/V^3$  is taken to represent the average of the three velocities with which a wave may propagate. Since we are concerned with deriving expressions for the technical constants in terms of the elastic constants, we rearrange Equation (1) and specialize it to each mode of vibration; that is

$$\nu_l^2 = k(V_l^2) \quad (2)$$

$$\nu_{t1}^2 = k(V_{t1}^2) \quad (3)$$

$$\nu_{t2}^2 = k(V_{t2}^2) \quad (4)$$

Here,  $k$  is a constant representing the quantity  $((9\rho N)/(4\pi M))^2/3$ . The subscript  $l$  represents longitudinal vibrations, and  $t1$  and  $t2$  represent transverse vibrations.

The present averaging method assumes equal cutoff frequencies for single crystals and polycrystals of the same materials for every mode of vibration, that is,

$$(V_l^2)_{\text{poly}} = (V_l^2)_{\text{c.c.}} = l, t1, t2 \quad (5)$$

The three phase velocities are the roots of the secular equation expressed in the form given by Christoffel<sup>(15)</sup> as

$$\det [\Gamma_{ij} - \rho V^2 \delta_{ij}] = 0 \quad (6)$$

The secular equation does not factor out in a straightforward manner. However, we can and do expand it to yield a cubic polynomial in  $\rho V^2$  for which an analytical solution exists in standard textbooks (see, for example, Mishina et al.<sup>(16)</sup>). In the present notations, the three roots are given by

$$\rho V_l^2 = -b/3 + 2\sqrt{-p/3} \cos((\psi + 6\pi)/3) \quad (7a)$$

$$\rho V_{t1}^2 = -b/3 + 2\sqrt{-p/3} \cos((\psi + 4\pi)/3) \quad (7b)$$

$$\rho V_{12}^2 = -b/3 + 2\sqrt{-p/3} \cos((\psi + 2\pi)/3) \quad (7c)$$

where  $\psi$  is the smallest positive angle satisfying the condition

$$\cos \psi = Q/2 \sqrt{(-3/p)^3}$$

Here,  $p = C - b^2/3$  and  $Q = \frac{2b^3}{27} + d - c b/3$ .

The coefficients of the cubic equation  $b$ ,  $c$ , and  $d$  are defined by

$$b = (\Gamma_{11} + \Gamma_{22} + \Gamma_{33}),$$

$$c = \Gamma_{11} \Gamma_{22} + \Gamma_{22} \Gamma_{33} + \Gamma_{33} \Gamma_{11} - \Gamma_{12}^2 - \Gamma_{13}^2 - \Gamma_{23}^2,$$

$$d = \Gamma_{11} \Gamma_{23}^2 + \Gamma_{22} \Gamma_{13}^2 + \Gamma_{33} \Gamma_{12}^2 - 2\Gamma_{12} \Gamma_{13} \Gamma_{23} - \Gamma_{11} \Gamma_{22} \Gamma_{33}.$$

The  $\Gamma_{ij}$ s are defined in terms of the elastic constants and the direction cosines. They take on long expressions and are not given here.

In general, these velocities depend on the crystallographic orientations. Thus, their averages are determined by

$$(V_i^2)_{\text{avg}} = \int V_i^2(r) \frac{d\Omega}{4\pi} \quad (8)$$

where  $d\Omega$  is the element of the solid angle and  $4\pi$  is the surface area of the sphere.

For polycrystals, the phase velocities are given by

$$\rho V_\ell^2 = B + 4G/3 = G \left( \frac{4G + E}{3G - E} \right), \quad (9a)$$

$$\rho V_{11}^2 = \rho V_{12}^2 = G. \quad (9b)$$

where  $B$ ,  $G$ , and  $E$  are the bulk, shear, and Young's modulus, respectively.

Therefore,

$$G = \frac{1}{2} \left[ \int \frac{1}{\rho} \left( V_{11}^2(r) + V_{12}^2(r) \right) \frac{d\Omega}{4\pi} \right]^{-1} \quad (10a)$$

$$B = \left[ \int \frac{1}{2} \left( V_\ell^2(r) \right) \frac{d\Omega}{4\pi} \right]^{-1} - 4G/3 \quad (10b)$$

Similar expressions may be derived for  $E$  as indicated in Equation (9a).

Analytical solutions to Equations (10a) and (10b) are not practical because the expressions for the phase velocities are too rigorous for the purpose of performing the integration called for in Equations (10a) and (10b). Consequently, we used Simpson's 1/3 rule to perform the integration. We found it sufficient for convergence to use about 121 nodal points in 1/4 section of the sphere where orthorhombic materials are the lowest symmetry considered.

## RESULTS AND DISCUSSIONS

### TECHNICAL CONSTANTS FOR SOME CUBIC MATERIALS

To see how the present averaging scheme fares against others and how well it compares with observations, we have employed the same input elastic constants used by Middya et al. and Ledbetter et al. in Equations (10a) and (10b), as shown in Table 1.

Table 2 lists the observed shear modulus and the theoretical values computed by Middya et al., Ledbetter et al., the Hill geometric mean value, the present method, and the percentage difference between the present method and that of Hill. The same type of information is listed for the bulk modulus  $B$  and the Young's modulus  $E$  in Tables 3 and 4, respectively. Several major observations may be deduced from these tables.

First, the agreement in results for  $G$  (Table 2) and  $E$  (Table 4) of the present averaging scheme and the geometric mean values of Hill is rather remarkable despite the fact that the starting premises of the two averaging schemes are entirely different. Comparison of the results of the two methods with observations



indicates a slight advantage of the present averaging scheme over that of Hill. However, this advantage remains too small to be measurable.

Second, averaging methods derived from sound velocity measurements follow the scheme of those derived from static deformation measurements. That is, averaging the reciprocal velocity (Middya et al. method) tends to yield results representing an upper bound for the technical constants similar to that of Voigt's classical work. Averaging the reciprocal cubed velocity (Ledbetter et al. method) tends to yield results representing a lower bound for the technical constants similar to Reuss's classical work. Averaging the squared reciprocal velocity on which the technical constants actually depend predicts results which always fall between Ledbetter et al. and Middya et al. values. This finding is depicted in Figure 1, where the ratio of  $G$  (theoretical) over  $G$  (observed) is plotted versus the Zener anisotropy factor. As can be seen from this figure, the present method yields ratios falling between those of Middya et al. and Ledbetter et al. and closer to observation than either of theirs. The concordance between the present method and Hill's is also illustrated in Figure 1.

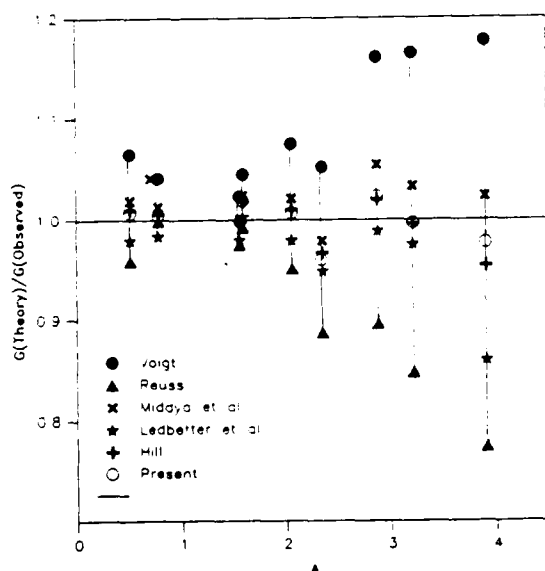


Figure 1. Reduced shear modulus  $G$  (theory)/ $G$  (observed) versus Zener elastic anisotropy factor  $A = 2C_{44}/(C_{11} - C_{12})$  for some cubic material

Third, both the present method and that of Middya et al. predict values for  $B$  which are artificially higher than the observed values. We believe this is due to the nature of the equation involving  $B$ , since  $E$  and  $B$  are both predicted from the same Equation (9a).

#### TECHNICAL CONSTANTS FOR SOME NONCUBIC MATERIALS

The technical constants for some hexagonal, tetragonal, trigonal, and orthorhombic materials have been computed using the present averaging scheme and that of Hill (geometric mean value only). All other averaging schemes have been applied to cubic symmetries only, so they will be discussed in this section. There appear to be large discrepancies among the published results for the stiffnesses as well as the technical constants. For this reason, two data sets for the elastic constants were used to compute the technical constants wherever this has been possible. The elastic constants are taken from the data compiled by Simmons et al.<sup>(17)</sup> The technical constants are taken from the data compiled by Koster et al.<sup>(18)</sup> and Gschneid-er.<sup>(19)</sup> Additionally, some useful data for Young's modulus were listed by Barrett et al.<sup>(20)</sup>

The input elastic constants are listed in Table 5. Table 6 provides a list of the observed values (column 2), the computed values using the Hill method (column 3), the computed values using the present averaging scheme (column 4), and the percentage deviation between the present averaging scheme and that of Hill (column 5) for the shear modulus. The same type of information is provided for the bulk modulus and Young's modulus in Tables 7 and 8, respectively.

As can be seen from these tables, the concordance of the results of the shear modulus and Young's modulus between the present averaging scheme and that of Hill's is rather good. The average deviation is 1.3 percent. True comparison between the observed values and the theoretical ones of either averaging scheme seems to be unobtainable because of the discrepancies among the observed values. Broadly speaking, the agreement between the theoretical values and the

observed ones is satisfactory. The fact that the theoretical values are in agreement with observations for most of the materials under consideration suggests that the apparent discrepancies between theory and observation may be due to metallurgical effects (mainly texture) in polycrystalline materials and/or experimental error in measuring the elastic constants. As was the case for cubic symmetry, the present averaging scheme yields theoretical values for the bulk modulus that are higher than the observed values as well as higher than the theoretical value of Hill, and his method yields theoretical results in better agreement with observations than the present method.

Again, it is argued that the discrepancy between the present theoretical and observed values of the bulk modulus may be an artifact and is largely due to error propagation because of the nature of the equation used to compute its value. This is especially true in the case of antimony. As can be seen from Table 6, this is an odd case. The stiffnesses producing the larger percentage deviations appear to be questionable since the margin of difference between Hill's theoretical value and the observed value is objectionably large in comparison to the results of the other data set for antimony and other materials under consideration. Nonetheless, this trend exists throughout Table 6. One should be discouraged, therefore, from using the present averaging scheme to compute the bulk modulus; it is best computed by the Voigt averaging method.

## CONCLUSIONS

1. Averaging schemes based on dynamic deformation follow the trends of the averaging schemes based on static deformation. That is, averaging the reciprocal cubed velocities and the actual reciprocal velocities produces lower and upper bounds similar to those of the Reuss and Voigt methods, respectively. These bounds, however, are much closer to observations than either the Voigt or Reuss bounds.

2. The proposed averaging scheme which averages the reciprocal squared velocities produces intermediate values for the technical constants in excellent

agreement with Hill's method and observations. A drawback of the proposed averaging scheme occurs in calculating the bulk modulus which is artificially high due to the nature of the equation employed to calculate its final value.

3. Solving the secular equation analytically and the use of the Simpson 1/3 rule in performing direct numerical integration in 1/4 of the sphere made it possible to obtain convergence of the integration using only 121 iterations for all crystal symmetries (excluding the triclinic system). This is about a tenfold reduction in the computational time required by previous methods. Consequently, the technical constants can be calculated from sound velocity measurements using the simplest computer available today.

## REFERENCES

1. Hill, R. W. (1952), *Procedures of the Physical Society* (London), A65, 349.
2. Voigt, W. (1928), "Lehrbuch der Kristallphysik," B. G. Teubner, Leipzig, 962.
3. Reuss, A. (1929), *Z. angew. Math. Mech.*, 9, 49.
4. Zeller, R., and Dederichs, P. H. (1973), *Physical Status of Solids*, B55, 831.
5. Kromer, E. (1967), *Journal of Mechanical Physics of Solids*, 15, 319.
6. Hershey, A. V. (1954), *Journal of Applied Mechanics*, 21, 36.
7. Hashin, Z., and Shtrikman, S. (1962), *Journal of Mechanical Physics of Solids*, 10, 343.
8. Alenksondrov, K. S., and Ryzhova, T. V. (1961), *Soviet Physics*, 10, 893.
9. Peresada, G. I. (1971), *Physical Status of Solids* (a), K23, 4.
10. Povoto, F., and Bolmaro, R. E. (1987), *Physical Status of Solids* (a), 99, 423.
11. Ledbetter, H. S., and Naimon, E. R. (1973), *Journal of Applied Physics* [1] 45, 66.
12. Debye, P. (1912), *Ann. Phys. (Leipzig)*, 39, 789.
13. Middya, T. R., Basu, A. N., and Serdupta, S. (March 1985), *Journal of Applied Physics*, [6] 57, 1984.
14. Alers, G. S. (1965), *In Physical Acoustics*, edited by W. P. Mason, Academic, New York, IIIB, 1.

15. Christoffel, E. B. (1877) *Ann. di Mat.*, 89, 193.
16. Mishina, A. P., and Proskuryako, I. V. (1965), "Higher Algebra," Pergamon Press Ltd., Oxford, 20, 172.
17. Simmons, G., and Wang, H. (1971), "Single Crystal Elastic Constants and Calculated Aggregate Properties," M.I.T. Press, Cambridge, Massachusetts.
18. Koster, W., and Franz, H. (1961), *Metals Reviews*, London: Institute of Metals, 6, 1.
19. Gschneider, K. A., Jr. (1964), "Solid State Physics," Edited by F. Seitz and D. Turnbull (Academic, New York), 16, 275.
20. Barrett, G. R., Nix, W. D., and Teleman, A. S. (1973), "The Principles of Engineering Materials," Prentice-Hall, Inc., Englewood Cliffs, New Jersey, 540.

TABLE 1

Input stiffnesses  $C_{ij}$  data at room temperature for Tables 2 to 4 in units of  $10^{11}$  N/m<sup>2</sup>.

Material	$C_{11}$	$C_{12}$	$C_{44}$	References
Cu <sup>**</sup>	1.661	1.199	0.756	1
Cu <sup>*</sup>	1.6809	1.2145	0.7511	1
Ag <sup>**</sup>	1.222	0.907	0.454	1
Ag <sup>*</sup>	1.21	0.899	0.426	1
Au <sup>*1**</sup>	1.929	1.638	0.415	1
Ni <sup>*</sup>	2.52	1.51	1.04	1
Pb <sup>*</sup>	0.4765	0.4028	0.1441	1
V <sup>*</sup>	2.287	1.19	0.4315	1
Fe <sup>*</sup>	2.42	1.465	1.12	1
Nb <sup>*</sup>	2.465	1.345	0.9873	1
Ta <sup>*</sup>	2.667	1.608	0.8249	1
Mo <sup>*</sup>	4.696	1.676	1.068	1
W <sup>*</sup>	5.0085	1.98	1.5267	1
Pt <sup>*</sup>	3.467	2.507	0.765	1
Mgo <sup>**</sup>	2.7908	0.9536	1.5613	1
Mgo <sup>*</sup>	2.893	0.877	1.5477	1
CaF <sub>2</sub> <sup>**</sup>	1.642	0.4398	0.337	1
CaF <sub>2</sub> <sup>*</sup>	1.62	0.53	0.337	1
$\beta$ -ZnS <sup>**</sup>	1.0462	0.6534	0.4613	1
$\beta$ -ZnS <sup>*</sup>	0.942	0.568	0.436	1
ZnSe <sup>*1**</sup>	0.81	0.488	0.441	1
CdTe <sup>*1**</sup>	0.5351	0.3681	0.19 <sup>a</sup> 4	1

\*Data used by Ledbetter et al. (1973)

\*\*Data used by Middya et al. (1984)

<sup>a</sup>References

1. Simmons and Wang (1971)

TABLE 2

Comparison of the results of  $G$  in units of  $10^{11}$  N/m<sup>2</sup>: present, Middya et al., Ledbetter et al., and Hill methods with experiment.

$G$							
Material et al.	Observed et al.	Middya	Ledbetter	Hill (%) <sup>b</sup>	Present	Difference	Reference <sup>a</sup>
Cu <sup>**</sup>	0.483	0.483	0.4557	0.465	0.4657	+0.16	1
Cu <sup>*</sup>	0.477	0.4826	0.4559	0.461	0.4659	-0.17	1
	0.451						2
	0.455						3
Ag <sup>**</sup>	0.294	0.3045	0.2858	0.2947	0.2858	+0.37	1
Ag <sup>*</sup>	0.291	0.2911	0.2735	0.7825	0.2836	+0.35	1
	0.288						2
	0.286						3
Au <sup>***</sup>	0.2817	0.282	0.2643	0.2706	0.2743	+1.36	1
	0.278						1
	0.276						2
	0.277						3
Ni <sup>*</sup>	0.785	0.7844	0.7637	0.7768	0.7737	-0.4	1
	0.75						2
	0.77						3
Pb <sup>*</sup>	0.086	0.088	0.074	0.082	0.084	+2.33	1
V <sup>*</sup>	0.474	0.4754	0.4647	0.475	0.4747	-0.06	1
	0.819						1
	0.815						2
	0.831						3
Nb <sup>*</sup>	0.376	0.3791	0.3647	0.3761	0.3747	-0.36	1
	0.375						2
	0.366						3
Ta <sup>*</sup>	0.700	0.6931	0.6795	0.6904	0.6895	-0.12	1
	0.687						2
Mo <sup>*</sup>	1.18	1.228	1.2141	1.2271	1.2241	-0.24	1
	1.158						2
	1.197						3
W <sup>*</sup>	1.526	1.5217	1.5117	1.5127	1.5217	-0	1
	1.514						1
	1.53						2
	1.485						3

TABLE 2 (continued)

Material et al.	Observed et al.	Middya	Ledbetter	Hill (%) <sup>b</sup>	Present	Difference	Reference <sup>a</sup>
Pt <sup>*</sup>	0.637	0.6383	0.6247	0.6344	0.6347	+0.04	1
	0.622						1
	0.61						3
HgO <sup>**</sup>	1.306	1.3092	1.2924	1.3101	1.3024	-0.58	1
HgO <sup>*</sup>	1.292	1.3017	1.2852	1.3029	1.2952	-0.59	4
CaF <sub>2</sub> <sup>**</sup>	0.409	0.4256	0.4119	0.4252	0.4219	-0.83	1
CaF <sub>2</sub> <sup>*</sup>	0.411	0.4123	0.3996	0.4118	0.4096	-0.54	4
$\beta$ -ZnS <sup>**</sup>	0.317	0.3311	0.3148	0.3263	0.3248	-0.45	1
$\beta$ -ZnS <sup>*</sup>	0.318	0.3158	0.2979	0.3094	0.3076	-0.57	4
ZnSe <sup>**, *</sup>	0.289	0.2977	0.2799	0.2925	0.2899	-0.91	1
	0.285						4
CdTe <sup>**, *</sup>	0.138	0.1428	0.138	0.1404	0.1401	-0.06	1
	0.139						4

<sup>a</sup>For the sources of the observed G, see the following references:

1. Middya et al. (1984)
2. Gschneider (1964)
3. Koster et al. (1961)
4. Ledbetter et al. (1973)

<sup>\*</sup>, <sup>\*\*</sup>Footnotes in Table 1

<sup>b</sup>percentage difference reflects comparison between the present averaging scheme and that of Hill

TABLE 3

Comparison of the results of E in units of  $10^{11}$  N/m<sup>2</sup> obtained by the present, Middy et al., and Hill methods with experiment.

Material	E				Difference (%)
	Observed	Middy et al.	Hill	Present	
Cu**	1.2668	1.3084	1.2501	1.2639	+1.1
Cu*		1.3047	1.2521	1.2665	+1.07
Ag**	0.7959	0.8336	0.8054	0.8125	+0.89
Ag*		0.7989	0.7744	0.7805	+0.8
Au**,*	0.7924	0.8034	0.7714	0.7827	+1.4570
Ni*	2.0699	2.0704	2.0433	2.0468	+0.17
Pb*	0.2422	0.2466	0.2312	0.2372	+0.17
V*	1.2956	1.2948	1.2934	1.2931	-0.25
Fe*	2.1269	2.1099	2.0704	2.0769	+0.32
Nb*	1.0507	1.0605	1.0514	1.0491	-0.2
Ta*	1.8844	1.8623	1.8536	1.8540	+0.03
Mo*	3.1011	3.2006	3.1942	3.1924	-0.06
W*	3.9062	3.9028	3.9029	3.9029	-0
Pt*	1.7585	1.7817	1.7707	1.7724	+0.1
MgO**	3.0904	3.1184	3.098	3.1080	-0.16
Mg*		3.0734	3.0527	3.0639	+0.36
CaF <sub>2</sub> **	1.0779	1.0977	1.0919	1.0901	-0.12
CaF <sub>2</sub> *		1.0761	1.0719	1.0704	-0.14
ZnSe**,*	0.7434	0.7735	0.7526	0.7570	+0.6
CdTe**,*	0.3747	0.3865	0.3784	0.3799	+0.41

<sup>b</sup>See Footnotes for Table 1

\*\*, \*See Footnotes for Table 1

<sup>c</sup>E is calculated from the relation

$$E = \frac{9BG}{(3B + G)}$$

where B and G are the averaged observed values listed in Tables 2 and 3

TABLE 4

Comparison of the results of B in units of  $10^{11}$  N/m<sup>2</sup> obtained by the present, Middya et al., and Hill methods with experiment.

Material	B					Reference <sup>a</sup>
	Observed	Middya et al.	Hill	Present	Difference (%) <sup>b</sup>	
Cu <sup>*</sup>	1.376 1.3974	1.4667	1.370	1.4583	+8.4	1
Ag <sup>*</sup>	1.027	1.0438	1.0027	1.0523	+4.9	1
Au <sup>**, *</sup>	1.766	1.7715	1.735	1.7808	+2.6	1
Ni <sup>*</sup>	1.90	1.914	1.8467	1.9254	+4.3	1
Pb <sup>*</sup>	0.438	0.447	0.4274	0.4516	+5.7	1
V <sup>*</sup>	1.537	1.5601	1.5557	1.5909	+0.34	1
Fe <sup>*</sup>	1.795	1.8807	1.7833	1.8969	+6.4	1
Nb <sup>*</sup>	1.736	1.7444	1.7183	1.7494	+1.86	1
Ta <sup>*</sup>	2.04	1.9824	1.9610	1.9863	+1.3	
Mo <sup>*</sup>	2.779	2.7105	2.6827	2.7144	+1.2	
W <sup>*</sup>	3.055 2.963 3.296	2.9895	2.8995	2.9895	-0	1 1 1
Pt <sup>*</sup>	2.838	2.8459	2.8270	2.8501	+0.8182	1
MgO <sup>*</sup>	1.641 1.663	1.5037	1.549	1.6097	+3.92	1 1
CaF <sub>2</sub> <sup>*</sup>	0.999 0.438	0.9198 0.447	0.90 0.4274	0.9224 0.4516	+2.5 +5.7	1 1
$\beta$ -ZnS <sup>*</sup>	0.775 0.766	0.7302	0.6927	0.7364	+6.3	1 1
ZnSe <sup>*</sup>	0.598	0.6475	0.5953	0.6557	+1.02	1
CdTe <sup>*</sup>	0.424	0.4985	0.4238	0.4429	+4.5	1

<sup>\*\*</sup>, <sup>\*</sup>See Footnotes in Table 1

<sup>b</sup>See Footnotes in Table 1

<sup>a</sup>See Footnotes in Table 1

1 Middya et al. (1984)



TABLE 5  
Input stiffness  $C_{ij}$ s at room temperature for Tables 6 to 8.

Material	$C_{11}$	$C_{12}$	$C_{13}$	$C_{14}$	$C_{22}$	$C_{23}$	$C_{33}$	$C_{44}$	$C_{55}$	$C_{66}$	References <sup>a</sup>
Cd	1.145	0.395	0.399	0	-	-	0.5085	0.1985	-	-	1
	1.2100	0.4810	0.4420	0	-	-	0.445	0.185	-	-	2
Co	3.071	1.650	1.027	0	-	-	3.5810	0.755	-	-	2
	2.63	1.52	1.33	0	-	-	2.83	0.52	-	-	1
Mg	0.595	0.2612	0.2180	0	-	-	0.6155	0.1635	-	-	2
	0.5858	0.2502	0.2079	0	-	-	0.611	0.1658	-	-	1
Zn	1.6110	0.3420	0.503	0	-	-	0.6110	0.3830	-	-	2
	1.785	0.2418	0.6088	0	-	-	0.764	0.3984	-	-	1
Zr	1.4340	0.7280	0.6530	0	-	-	1.648	0.3200	-	-	1
Hf	1.811	0.772	0.6610	0	-	-	1.969	0.5570	-	-	1
Ti	1.624	0.92	0.69	0	-	-	1.8070	0.467	-	-	1
Sb	0.7916	0.2474	0.2613	0.162	-	-	0.4273	0.2852	-	-	1
	0.994	0.3090	0.9640	0.2160	-	-	0.445	0.3950	-	-	1
	1.013	0.345	0.2920	0.209	-	-	0.450	0.3930	-	-	1
Bi	0.628	0.3503	0.2114	-0.424	-	-	0.4397	0.1084	-	-	2
	0.6370	0.249	0.247	0.0717	-	-	0.382	0.1123	-	-	1
Se	1.9	0.30	1.9	-0.6	-	-	8.4	1.8	-	-	3
	1.88	0.7	2.71	-0.50	-	-	7.44	1.25	-	-	3
Te	5.79	2.18	1.78	0.8	-	-	3.31	5.26	-	-	4
	3.28	0.91	2.45	-1.24	-	-	7.07	3.18	-	-	4
In	0.4450	0.3950	0.4050	0	-	-	0.444	0.0655	-	1.22	2
Sn	0.8391	0.4870	0.2810	0	-	-	0.870	0.220	-	0.2265	1
	0.723	0.594	0.3578	0	-	-	0.884	0.2203	-	0.240	1
$\alpha$ -U	2.125	0.483	0.226	0	1.934	1.064	2.51	1.176	0.659	0.696	1
Ga	0.98	0.33	0.28	0	0.876	0.42	1.33	0.342	0.42	0.392	5

<sup>a</sup>References

1. Simmons et al. (1971)
2. Edgar (1967)
3. Meibner et al. (1970)
4. Hearmon (1984)
5. Hearmon (1967)

TABLE 6

Comparison of the results of  $G$  in units of  $10^{11}$  N/m<sup>2</sup> obtained by Hill and the present method with experimental for some hexagonal, trigonal, tetragonal, and orthorhombic materials.

$G$					
Material	Observed	Hill	Present	Difference (%)	References <sup>a</sup>
Cd	0.241	0.2392	0.2308	-3.54	1
		0.2157	0.2061	-4.5	
Co	0.764	0.8233	0.8172	-0.74	1
	0.750	0.570	0.5735	+0.15	2
Mg	0.1736	0.2435	0.2396	-1.591	1
	0.174	0.1737	0.1736	+0.062	2
Zn	0.372	0.3893	0.3805	-2.26	2
Zr	0.3610	0.3602	0.3594	-0.22	
Hf	0.53	0.5581	0.5577	-0.06	1
Ti	0.3934	0.4335	0.4328	0.17	1
	0.3980				2
Sb	0.2	0.2264	0.2194	-3.08	1
		0.2698	0.2524	-6.45	
Bi	0.1285	0.1173	0.1158	-1.35	1
	0.1290	0.1249	0.1209	-3.2	2
Se	0.217				2
Te	0.154				2
In	0.0373	0.469	0.048	+2.12	1
Sn	0.204	0.2287	0.2281	-0.3	1
	0.1844	0.1775	0.1831	+3.1	2
$\alpha$ -U	0.7044	0.7921	0.7814	-1.4	1
	0.7360				
Ga	0.43	0.3684	0.3666	-0.5	1
	0.346				

<sup>a</sup>References for Table 6

1. Koster et al. (1961)
2. Gschneider (1964)

<sup>b</sup>Difference (%) is given between the present method and that of Hill.

TABLE 7

Comparison of the results of  $B$  in units of  $10^{11}$  N/m<sup>2</sup> obtained by Hill and the present method with experimental for some hexagonal, trigonal, tetragonal, and orthorhombic materials.

$B$					
Material	Observed	Hill	Present	Difference <sup>b</sup> (%)	Reference <sup>a</sup>
Cd	0.467	0.5278	0.5948	+12.7	1
	0.476	0.5261	0.6447	+22.5	2
Co	1.920	1.9033	1.9435	+2.1	1
	1.835	1.8278	1.8365	+0.48	2
Mg	0.289	0.3460	0.3800	+9.8	1
	0.333	0.3461	0.3471	0.30	2
Zn	0.599	0.7561	0.8831	+16.8	1
	0.605	0.6547	0.7840	+19.8	2
Zr	0.833	0.953	0.96	+0.73	1
	0.898				2
Hf	1.09	1.0865	1.0892	+0.25	1
	1.098				2
Ti	1.052	1.0727	1.0831	+0.91	1
	1.236				
Sb	0.3924	0.3781	0.4405	+16.5	1
	0.3828	0.4204	0.5868	+39.6	2
Bi	0.315	0.3483	0.3655	+4.94	1
	0.353	0.3361	0.3759	+11.9	2
Se	1.058				2
Te	0.418				2
In	0.412	0.4159	0.4314	+3.72	1
	0.436				
Sn	0.51	0.5145	0.5237	+1.8	1
	0.542	0.5494	0.5790	+5.4	2
$\alpha$ -U	1.02	1.1166	1.1993	+7.4	1
	0.988				2
Ga	0.5	0.5744	0.5897	+2.6	1
	0.52				2

<sup>a</sup>References

1. Koster (1961)
2. Gschneider (1964)

<sup>b</sup>See Footnotes in Table 6

TABLE 8

Comparison of the results of  $E$  in units of  $10^{11} \text{N/m}^2$  obtained by Hill and the present method with experimental for some hexagonal, trigonal, tetragonal, and orthorhombic materials.

Material	$E$				References <sup>a</sup>
	Observed	Hill	Present	Difference <sup>b</sup> (%)	
Cd	0.623	0.623	0.6234	+0.61	1
	0.5528	0.5693	0.5588	-1.85	3
Co	2.001	2.1586	2.1503	-0.4	2
	2.073	1.5597	1.5583	-0.08	3
Mg	0.444	0.5914	0.5939	+0.43	2
	0.435	0.4465	0.4465	0	3
Zn	0.9259	1.0758	1.0927	+1.58	3
	0.922	0.9746	0.9825	+0.81	1
Zr	0.9467	0.9598	0.9587	-0.12	3
	0.9560				2
Hf	1.370	1.4294	1.4292	-0.02	1
	1.382				3
Ti	1.161	1.1461	1.1457	-0.04	3
	1.06				1
Sb	0.5494	0.5660	0.5645	-0.26	1
	0.780	0.6661	0.6624	-0.56	3
Bi	0.318	0.3165	0.3141	-0.75	3
	0.340	0.333	0.3276	-1.69	2
Se	0.580				2
Te	0.412				2
In	0.1105	0.1356	0.1388	+2.33	3
	0.105				2
Sn	0.55	0.5976	0.5974	-0.02	1
	0.4146	0.4804	0.4968	+3.414	3
$\alpha$ -U	1.766	1.9217	1.9259	+0.22	
	1.864				
Ga	1.20	0.9108	0.911	+0.21	
	0.965				

<sup>a</sup>References

1. Koster et al. (1961)
2. Gschneider (1964)
3. Barrett et al. (1973)

<sup>b</sup> See Footnotes in Table 6